6)

Microstructure of Polyphase Rocks:
Effects on Friction, Deformation Behavior
and Melt Distribution.

By

Margaretha M. Eckhardt

B.S. Geology
University of Minnesota, 1991

B. Arch., B.F.A. Architecture
Rhode Island School of Design, 1975, 1974

Submitted to the Department of Earth, Atmospheric and Planetary Sciences
in Partial Fulfillment of the Requirements for the Degree of
Doctor of Philosophy in Geophysics

at the

Massachusetts Institute of Technology
March, 1997

Signature of Author...
Department of Earth, Atmospheric and Planetary Sciences
26 March, 1997

Certified by..
J. Brian Evans
Professor of Geophysics
Thesis Supervisor

Accepted by...
Thomas H. Jordan
Department Head

Microstructure of Polyphase Rocks:
Effects on Friction, Deformation Behavior
and Melt Distribution.

By

Margaretha M. Eckhardt

Thesis Abstract

The development of constitutive laws for the prediction of the mechanical behavior of geological structures requires a detailed understanding of the interactions between phases in Earth materials. I have conducted three studies designed to evaluate interactions between minerals during physical and chemical processes of geological significance: frictional sliding, ductile deformation of two-phase aggregates, and partial melting.

Geological evidence strongly suggests that plowing of asperities into opposing surfaces occurs during frictional sliding of rocks, but little is known about the contribution of this phenomenon to the total friction on a fault. I examined the evolution of plowing friction for a single asperity, through room temperature scratch and indentation tests using a rigid conical diamond indenter with a rounded tip on polished calcite cleavage surfaces, r_1. Tests were performed at constant load or constant penetration velocity in a microindentation instrument. Normal loads ranged from 3 to 36 mN; scratch velocities, v_s, were 0, 0.13, 1.0 or 100 μm/s, roughly parallel to $[r_1{:}r_2]^-$. Data on scratch depth, i, normal load, N, and tangential load, T, were used to calculate the apparent friction coefficient, $\mu_{app} = T/N$, normal hardness, $H_{nor} = N/A_{\perp N}$, and tangential hardness, $H_{tan} = T/A_{\perp T}$, as they evolved with time and scratch distance. μ_{app} increased with changing conditions, according to three scratch damage regimes which were identified within the range of conditions tested. Regime I represented calcite response at low normal loads, where elastic and possible minor plastic deformation were accompanied by the removal of submicron-sized gouge. As normal load increased from 3 to 6 mN in Regime I, μ_{app} increased dramatically from ~0.2 to ~0.4. Regime II began at slightly higher loads, above 5-7 mN, where, in addition to the mechanisms observed at the lowest loads, localized low-temperature plastic deformation occurred either by slip on f_1 systems or twinning on e_1 systems. In Regime II, as the normal load increased to 12 mN, μ_{app} increased to ~0.55. Regime III, where the normal load exceeded 25 mN, was characterized by brittle fracture on r_3 cleavage planes, twinning the e_1 system, finely notched scratch edges, cracks and shallow triangular pits from which chips of calcite were removed. In Regime III, μ_{app} was relatively insensitive to normal load, but increased from ~0.55 to ~0.65 with an increase in scratch velocity, v_s, from 0.13 μm/s to 100 μm/s.

The plowing coefficient of friction in calcite can be described by a simple expression:

$$\mu_{app} = (A_{\perp T}/A_{\perp N}) \cdot (H_{tan}/H_{nor})$$

where the area ratio, $A_{\perp T}/A_{\perp N}$, is a geometric factor which accounts for the shape of the asperity. For a conical asperity of included angle 2α, with a rounded tip, $A_{\perp T}/A_{\perp N}$ evolves with scratch depth toward a constant value of $(2/\pi) \cdot \cot\alpha$. The hardness ratio, H_{tan}/H_{nor}, reflects the anisotropic stress distribution due to loading conditions, active damage mechanisms, crystal structure and contact friction. For our test conditions on calcite, H_{tan}/H_{nor} evolved with increasing normal load toward a value close to 1.0. At high normal loads H_{tan}/H_{nor}, and therefore μ_{app}, showed a positive correlation with v_s.

Strain localization in geological structures suggests that the ductile behavior of polyphase rocks at elevated temperatures and pressures in the Earth is sensitive to the relative proportions of minerals with different physical properties. I studied the strengthening effect of a varying fraction of non-deforming particles in a plastically deforming matrix through conventional triaxial deformation experiments on synthetic aggregates. Deformation experiments were performed on samples of a calcite matrix with 0%, 5% or 20% quartz particles. I evaluated the mechanical data collected during experiments in terms of existing mechanical mixing theories. Additional interpretation of data included assessment of microstructural observations of sample material before and after tests. The results of experiments conducted at 600°C and 200 MPa at a strain rate of $3\times10^{-5}s^{-1}$ suggest that, under these conditions, the presence of relatively strong quartz particles strengthens the synthetic marble by enhancing strain hardening, through the development of local strain gradients around the strong particles. The magnitude of strengthening is greater than that predicted by existing models.

Experiments on partially molten geological materials demonstrate that processes involved in melt segregation within a planetary interior are controlled in part by the relative interfacial energies of contacts between coexisting phases. In order to provide constraints on the formation history of the parent body of the Brenham pallasite, I assessed the interfacial energy between a metallic melt and a silicate mantle, through detailed textural observations and the analysis of interfacial angles between phases. Interfacial angle data were used to estimate the values of interfacial energy along interfaces between given phases, and to predict the conditions for formation of a connected network of metallic melt. The value calculated for olivine/metal interfaces was 660 mJ/m^2, followed by 636 mJ/m^2 for olivine/schreibersite and 615 mJ/m^2 for olivine/troilite. Further calculations provided rough estimates of interfacial energy for metal/schreibersite interfaces of less than 50 mJ/m^2, for schreibersite/troilite interfaces of approximately 50 mJ/m^2, and for metal/troilite interfaces of close to 100 mJ/m^2. The large wetting angles, all close to 90°, between olivine and non-silicate phases suggested that original chondritic material must have experienced both melting and fracturing before the observed connected network of metallic melt could have formed. During subsequent cooling of this melt, blebs of sulfide exsolved from the iron-nickel melt, followed by exsolution of phosphide blebs. The resulting minerals, troilite and schreibersite, crystallized adjacent to olivine grains. A later low-temperature deformation event opened fractures between and within olivine grains, thereby drawing non-silicate phases into cracks.

Thesis supervisor: J. Brian Evans

Title: Professor of Geophysics

Table of Contents

Chapter 4: Conditions for Melt Migration in Planetary Interiors: Evidence from the Brenham Pallasite

Acknowledgments

"Through how many dimensions and how many media will life have to pass? Down how many roads among the stars must man propel himself in search of the final secret? The journey is difficult, immense, at times impossible, yet that will not deter some of us from attempting it. We can not know all that has happened in the past, or the reason for all of these events, any more than we can with surety discern what lies ahead. We have joined the caravan, you might say, at a certain point; we will travel as far as we can, but we cannot in one lifetime see all that we could like to see or learn all that we hunger to know."

Loren Eiseley 1957, in The Immense Journey.

It would take many pages to thank all those for whose companionship in this journey I am grateful. But it is quite clear that during my time at M.I.T. certain people have had key roles. I begin by thanking my advisor, Brian Evans, for his support, insightful discussions and for his understanding of my goals in my work. His grasp of the diverse phenomena of mineral physics and rock mechanics will continue to serve as inspiration for me in years to come. I am also grateful to Tim Grove for encouraging me in my study of topics in petrology, ranging from meteorites to mid-ocean ridges. It was my privilege to work as teaching assistant for Brian and Tim during the semester when they created their new course in Earth Materials, and I thank them for a tremendous learning experience along the way. I must also thank the students of that class for their interest, hard work and occasional indulgence of my crazy enthusiasm for aspects of mineralogy.

Two of the three projects on which I worked for this thesis were collaborations with other researchers. I am grateful to Sriram Viswanathan for performing the microscratch experiments at the University of Minnesota on samples I prepared and report upon in Chapter 2. Sriram and David Kohlstedt also provided helpful conversations on the interpretation of the data, and Ming Liu gave me expert help with transmission electron microscopy. I thank Georg Dresen and David Olgaard for their work in preparing synthetic marble for the experiments described in Chapter 3 and I also appreciated Georg's guidance and participation during some of those experiments. Carl Francis and Bill Metropolis at Harvard University Museum were of great help in the loan and preparation of the meteorite sample I analyzed in Chapter 4. My committee members have also given me helpful feedback and valuable discussions. Many thanks go to Chris Marone and Greg Hirth.

My fellow graduate students have been an incredible resource, helping me to learn laboratory procedures, sharing the struggles over problem sets, discussing ideas, and finding moments for sharing a walk or a coffee. Big thanks to Gunter Siddiqi, John Olson, Chantal Chauvelier, Steve Karner, Mousumi Roy, Helen Webb, Tom Wagner, Glenn Gaetani, Steve Parman, Paula Waschbusch and many others. In the day to day life of M.I.T., Marie Senat and Jock Hirst have provided unfailing, friendly help. Mike Frongillo in the electron microscopy facility has also been of assistance in my work.

Three people, whose teaching inspired me to pursue studies and research in this field, have given me moments of much appreciated encouragement during the past five years: Neil Jorgensen, who introduced me to the excitement of science in 7th grade, John Lukens who inspired my fascination with geology during a course in Terrain Analysis at R.I.S.D., and Paul Weiblen at the University of Minnesota, from whom I learned of the world which can be explored through observations of rocks under optical and electron microscopes.

Outside the academic community are my family and friends, and members of several communities, with whom I have conversed, shared meals, hiked, sung, danced and prayed. I acknowledge the wonderful help of many, many people in my pursuit of balance and some degree of sanity in my life as a graduate student. I have space only to mention three who have been outstandingly supportive through thick and thin: my father Homer Eckhardt, for continuing to remind me of the joys of learning and thinking, which he taught me since the day I was born, and my friends Dania Jekel and Marilyn Richards for listening and being there to help in many ways.

I would like to dedicate this thesis to the memory of my mother, whose life as an artist strongly influenced my belief in the importance and meaning of the shapes of things, and to three people who died during my third year at M.I.T., each of whom, among his or her many accomplishments, served as a model of courage and inspiration to me:

Mary Grinnell Post, *my mother* 1923-1983
Elisabeth Peckham Morrissey, *my great aunt* 1892-1993
Abigail Dewing Avery, *environmental activist and friend* 1912-1993
Roger Burns, *Professor of Mineralogy*, 1937-1994.

Chapter 1: Introduction

Since, then, we agreed that the cause of the imposed six-cornered shape lay with an agent, we of course wondered what that agent was, and how it acted: could it be as immanent form or as efficient cause from outside? Did it stamp the six-cornered shape on the stuff as the stuff demanded, or out of its own nature - a nature, for instance in which there is inborn either the idea of the beauty inherent in the hexagon or knowledge of the purpose which that form subserves?

Johannes Kepler, 1611

The relationship between physical processes and the morphology and internal structure of Earth materials has been a topic of interest to scientists in Western culture for at least four centuries. Johannes Kepler was an early pioneer with his short book, A New Year's Gift: The Six-cornered Snowflake. He convincingly linked the three-dimensional geometry generated by the packing of spheres with processes which would produce regular crystal forms, including hexagonal snow crystals. While his concept of invisibly small spheres composed of the "moist element" has proven incorrect in the light of modern atomic theory, his idea of a repeating structural unit demonstrated remarkable insight. Following Kepler, further investigations into the "facultas formatrix", or form-generating cause, laid the foundations of much of our current understanding of the atomic structure of solids. Thus when x-ray diffraction patterns were first produced from crystalline materials, exactly 300 years after the publication of Kepler's book, all the chemical and mathematical theory was in place to use this new information to fully determine the crystal structures of minerals. Idealized structures are expressed in terms of the composition, symmetry and dimensions of a structural unit cell. Subsequent developments have permitted scientists to examine defect structures within crystals as they relate to processes of crystallization and deformation.

At present, Earth scientists would like to determine the structure and physical properties of bodies measuring up to thirteen orders of magnitude larger than the unit cell

10

of a crystal. These geological materials comprise aggregates of rock-forming minerals, most of which are well understood individually. A new scale of relationship between morphology, structure and physical processes is required. The internal structure of rocks can not be thought of as essentially identical units stacked in a regular manner. Coexisting phases of varying compositions, properties, sizes and shapes, possibly including fluids, are generally assembled in an irregular manner. The possibility of developing constitutive laws to predict aggregate properties depends in part on understanding of how these individual units interact along their shared interfaces.

I have pursued three research topics which address interactions between minerals under varied conditions. Two properties have proven useful in this work: mineral hardness and interfacial energy. Hardness measures the deformation response of one material to indentation by another. No simple method exists to predict hardness from other mechanical data. The concentrated stresses are distributed within the indenter and indented material in a manner which depends upon their elastic moduli, yield strengths, indenter geometry, contact friction and other physical properties. I have found hardness to be a useful quantity for examining the micromechanics of friction in Chapter 2. Hardness contrast also plays a role in the heterogeneous deformation which occurs at the microscopic scale in aggregates of minerals with different hardnesses, which I describe in Chapter 3.

Interfacial energy arises at the boundary of a homogeneous material, where the equilibrium bonding conditions within the volume of the material are abruptly interrupted. The material tries to minimize the excess energy associated with the boundary by reducing the ratio of boundary area to volume. This situation is complicated by the presence of an adjacent volume of material beyond the opposite face of the boundary. Interfacial energy is influenced by the compositions and the character and orientation of structure in the materials on both sides of the interface. While in most cases we can not predict the resulting energy from first principles, it can be measured as a distinct property through a variety of methods. One method, which I have used in Chapter 4, is to measure angles at which interfaces intersect. These angles correspond to a force balance between the

tension developed in each interface as it tries to minimize its area. Interfaces with higher energy will generate correspondingly higher tensile forces. The angle between the interfaces thus can be used to determine relative magnitudes of the three interfaces which meet at a triple junction.

While it is not currently possible to predict hardness or interfacial energy from atomic principles, these quantities summarize the effects of important phenomena. By assembling data on their measurement and considering their meanings in terms of processes at both smaller and larger scales, I hope to contribute to our understanding of the behavior of heterogeneous Earth materials.

Chapter 2: Micromechanics of Friction in Calcite

Abstract

Geological evidence strongly suggests that plowing of asperities into opposing surfaces occurs during frictional sliding of rocks, but little is known about the contribution of this phenomenon to the total friction on a fault. I examined the evolution of plowing friction for a single asperity, through room temperature scratch and indentation tests using a rigid conical diamond indenter with a rounded tip on polished calcite cleavage surfaces, r_1. Tests were performed at constant load or constant penetration velocity in a microindentation instrument. Normal loads ranged from 3 to 36 mN; scratch velocities, v_s, were 0, 0.13, 1.0 or 100 μm/s, roughly parallel to $[r_1: r_2]^-$.

Data on scratch depth, i, normal load, N, and tangential load, T, were used to calculate the apparent friction coefficient, $\mu_{app}=T/N$, normal hardness, $H_{nor}=N/A_{\perp N}$, and tangential hardness, $H_{tan}=T/A_{\perp T}$, as they evolved with time and scratch distance. μ_{app} increased with changing conditions, according to three scratch damage regimes which were identified within the range of conditions tested. Regime I represented calcite response at low normal loads, where elastic and possible minor plastic deformation were accompanied by the removal of submicron-sized gouge. As normal load increased from 3 to 6 mN in Regime I, μ_{app} increased dramatically from ~0.2 to ~0.4. Regime II began at slightly higher loads, above 5-7 mN, where, in addition to the mechanisms observed at the lowest loads, localized low-temperature plastic deformation occurred either by slip on f_1 systems or twinning on e_1 systems. In Regime II, as the normal load increased to 12 mN, μ_{app} increased to ~0.55. Regime III, where the normal load exceeded 25 mN, was characterized by brittle fracture on r_3 cleavage planes, twinning the e_1 system, finely notched scratch edges, cracks and shallow triangular pits from which chips of calcite were removed. In Regime III, μ_{app} was relatively insensitive to normal load, but increased from ~0.55 to ~0.65 with an increase in scratch velocity, v_s, from 0.13 μm/s to 100 μm/s.

The plowing coefficient of friction in calcite can be described by a simple expression:

$$\mu_{app} = (A_{\perp T}/A_{\perp N}) \cdot (H_{tan}/H_{nor})$$

where the area ratio, $A_{\perp T}/A_{\perp N}$, is a geometric factor which accounts for the shape of the asperity. For a conical asperity of included angle 2α, with a rounded tip, $A_{\perp T}/A_{\perp N}$ evolves with scratch depth toward a constant value of $(2/\pi) \cdot \cot\alpha$. The hardness ratio, H_{tan}/H_{nor}, reflects the anisotropic stress distribution due to loading conditions, active damage mechanisms, crystal structure and contact friction. For our test conditons on calcite, H_{tan}/H_{nor} evolved with increasing normal load toward a value close to 1.0. At high normal loads H_{tan}/H_{nor}, and therefore μ_{app}, showed a positive correlation with v_s.

Introduction

Friction on faults is a complex process which Earth scientists would like to be able to quantify in order to improve our ability to assess and model earthquakes. An accurate understanding of frictional forces under varying conditions is also critical to estimating the physical properties of the lithosphere (Kohlstedt et al., 1995). Geological evidence shows that sliding on rock surfaces frequently involves a variety of interactions between asperities, flat surfaces and gouge material. Asperities are known to interact with other asperities through adhesion between surface areas in direct contact with each other. Dieterich and Kilgore (1994) performed experiments in which they showed that friction on some surfaces is primarily controlled by adhesive contacts between asperities, and they found a simple method to quantify the evolution of this process. However, it is clear from the quantity of scratches and carrot-shaped grooves on fault surfaces that the plowing of asperities into rock surfaces is a common phenomenon which may contribute significantly to frictional forces during sliding on faults (Engelder, 1976; Jaeger and Cook, 1976; Scholz, 1990). Because the nature and magnitude of this contribution is not well understood, the present study was undertaken in order to explore the micromechanics of plowing friction.

In experiments on frictional sliding of rocks, Engelder (1976) produced carrot-shaped grooves on sample surfaces, which he concluded were the results of asperity plowing. Mini-stick-slip events were explained as being due to a population of asperities plowing into the opposite surface, then shearing off. Each asperity plowed more deeply into the surface, in response to a local increase in the normal load. Engelder (1976) ascribed the associated increase in frictional force to enlargement of the contact area between asperity and surface, and the resulting increase in adhesive contact force. When shear stress due to this frictional force exceeded the shear strength of a population of asperities, he predicted that the asperities would fail, resulting in a sudden drop in frictional force.

In a related series of experiments, Engelder and Scholz (1976) used single asperities and flat surfaces prepared from minerals of various hardnesses to perform scratch tests,

during which the normal force was constant, and the tangential force on the asperity was monitored. They examined the nature of the frictional wear and correlated it with the evolution of the apparent coefficient of friction for a single asperity. Their results demonstrated that friction of an asperity on a flat surface was strongly influenced by the degree of hardness contrast between asperity and surface materials. The highest friction coefficients were measured where an asperity with much higher hardness than the flat plowed into the surface of the flat. These tests produced scratches accompanied by series of tension fractures.

In the study described in this chapter, I examined friction due to a single nondeforming asperity plowing into a soft opposing surface. By evaluating the evolution of the apparent coefficient of friction with time and changes in normal load and scratch velocity, I have provided new data along with a method for quantifying plowing friction, for eventual incorporation in constitutive laws for friction on fault surfaces.

Background

In discussing the micromechanics of friction, it is important to clarify the distinction between bulk stresses acting on the macroscopic plane, and concentrated stresses supported only on asperities, or portions of the surfaces which are in actual contact. Typically, σ and τ are used to designate bulk normal and shear stresses respectively. For the assessment of forces acting upon an individual asperity, I have used N and T to refer to normal and tangential forces, respectively. Other symbols defined below represent estimates of contact stresses on an individual asperity.

Adhesive friction: Rabinowicz (1965) and Bowden and Tabor (1964) considered the case where friction on an entire surface is controlled by adhesive contacts between asperities. In referring to stresses concentrated on actual contact areas, they defined S as the contact shear stress during slip, while P represents the inverse of contact normal stress. Assuming that all asperities have the same yield strength, conversion from σ and τ to S and P can be done by dividing measurements of bulk stresses by the ratio of contact area, A_{con}, to total area, A_{total}, where contacts are assumed to be parallel to the surface as a whole:

contact area ratio: $\alpha = A_{con}/A_{total}$

inverse contact normal stress: $P = 1/(\sigma/\alpha)$

contact shear: $S = \tau/\alpha$

A steady-state adhesive friction coefficient for sliding surfaces controlled by adhesive contacts would be:

$$\mu_{adh} = \tau/\sigma = S \cdot P$$

Hardness measurements: Where Dieterich and Kilgore (1994) and other workers have expressed either contact area or contact depth as a function of normal load, an indentation hardness has been used as a material property which links these parameters. For example, in the above expression, Dieterich and Kilgore (1994) assumed that $P \sim 1/H_{ind}$, where H_{ind}

is the static indentation hardness of the asperity, as defined below. In fact, hardness can be defined in a number of ways and the values obtained depend on indenter shape, contact time and interfacial friction at the contact between indenter material and sample. Tabor (1951) and Williams (1996) have provided discussions of commonly used hardness tests. Detailed analysis of stress distributions was given by Johnson (1977).

Static indentation hardness tests are performed by lowering an indenter slowly onto the sample surface, where it remains in contact for 10-15 seconds under constant load, at zero scratch velocity. For Vickers indentation tests the indenter is a square pyramid of diamond. Knoop indentation tests are performed with an indenter which produces a diamond-shaped contact area, whose long diagonal is approximately seven times the length of the short diagonal. The elongated indentation provides a rough means of assessing the anisotropy of static indentation hardness on the sample surface. Spherical and conical indenters are also commonly used.

Historically, static indentation hardness values have been calculated in terms of the mass used to load the indenter, divided by actual contact area, A_{con}. By multiplying the mass times acceleration due to gravity, units of force can be obtained, and units of stress can be calculated in terms of force per contact area. An alternative calculation is based on contact area projected on a plane perpendicular to the force, $A_{\perp force}$, rather than on actual contact area, A_{con}. I have referred to the resulting value as the static indentation hardness, $H_{ind} = F/A_{\perp force}$. Williams (1996) claimed that this method of calculating hardness could be interpreted as equivalent to mean static indentation pressure, $p_m = H_{ind}$.

An advantage of calculating hardness using area projected perpendicular to the force is that, because it estimates a mean contact pressure, it also expresses the energy consumed per unit of volume displaced as the indenter moves a distance, dx, parallel to the force:

$$H_{ind} = p_m = force/A_{\perp force} = (force \cdot dx)/(A_{\perp force} \cdot dx) = energy/volume$$

A calculation of normal force per projected contact area can be used to define a hardness, $H_{nor} = N/A_{\perp N}$, maintained during scratch tests. Williams (1996) showed that H_{nor}

during scratch tests was not necessarily equal to H_{ind} measured using static tests on the same material. For example, the ratio H_{nor}/H_{ind} in work-hardened copper and steel increases with increasing included angle, 2α, of a conical indenter, and $H_{nor} \sim H_{ind}$ where $2\alpha \sim 160°$.

During scratch tests a plowing hardness, $H_{tan} = T/A_{\perp T}$, can also be defined as the relationship between tangential force and the projected contact area perpendicular to it. Williams found an increase in this quantity with included angle for many metals. In general, H_{tan} is not equal to H_{nor}, and the relationship between $A_{\perp T}$ and $A_{\perp N}$ depends upon A_{con} and the geometry of the asperity.

The precise measurement of static indentation hardness, H_{ind}, scratch hardness, H_{nor}, and plowing hardness, H_{tan}, have proven useful in the examination of the micromechanics of friction. Authors typically assume that these quantities have constant values. However, the observation that indentation depth and contact area increase with time during static indentation tests (Engelder and Scholz, 1976a) indicates that hardness is a time-dependent value and therefore is likely to vary in response to imposed scratch and indentation velocities. I have analyzed our data below, in terms of hardness evolution with respect to scratch distance, normal load, indentation velocity, scratch velocity and coefficient of friction. From this analysis, I have concluded that in fact velocities can have a significant effect upon H_{nor} and H_{tan} calculated from our data.

Plowing friction: Hardness values can be related to plowing friction, as described by Bowden and Tabor (1986), who examined the case where asperities plow into the opposing surface under constant normal load, N. They considered the total frictional or tangential force, T, to be the sum of a force needed to overcome adhesive contact, T_{adh}, and a force required to move material aside as a permanent scratch was plowed into the surface, T_{plow}. The authors assumed that the magnitude of the contact area, A_{con}, between the asperity and the plowed surface was controlled by the normal load and a hardness, H_{nor}, measured normal to the surface, and predicted:

$$A_{\perp N} = N/H_{nor}$$

A distinct plowing hardness, H_{tan}, and the particular geometric relationship between A_{con}, $A_{\perp T}$ and $A_{\perp N}$ determined the plowing force, T_{plow}, such that:

$$T_{plow} = H_{tan} \cdot A_{\perp T}$$

$$T = T_{adh} + T_{plow} = S \cdot A_{\perp N} + H_{tan} \cdot A_{\perp T}$$

$$\mu_{total} = T/N = S/H_{nor} + (H_{tan} \cdot A_{\perp T})/(H_{nor} \cdot A_{\perp N}) = \mu_{adh} + (H_{tan}/H_{nor}) \cdot (A_{\perp T}/A_{\perp N})$$

Authors such as Scholz (1990) who assumed that $H_{ind} \sim H_{plow}$ have simplified the expression:

$$\mu_{total} = \mu_{adh} + (A_{\perp T}/A_{\perp N})$$

Interactions between asperities may include deformation of asperities as well as adhesive and plowing effects. Sin, Saka and Suh (1981) expressed the three effects as additive, and proceeded to derive expressions for each independently. However, interactions between adhesion, plowing and deformation at an individual asperity may be significant. Therefore it is important to examine the assumption that frictional effects are simply additive.

Rate and state law: Because friction typically evolves over time and changes in conditions, calculations must ultimately consider dependence on elapsed time, slip velocity and other possible factors. Dieterich (1979) introduced a form of the rate and state law which has been used successfully to model friction on rock surfaces in conjunction with experimental data:

$$\mu = \tau/\sigma = \mu_0 + A \cdot \ln(1+v/v^*) + B \cdot \ln(1+\theta/\theta^*)$$

where v is slip velocity, θ is a state parameter measured in units of time, and μ_0, A, B, v^* and θ^* are empirically derived constants for given pairs of surfaces.

Dieterich and Kilgore (1994) examined the micromechanics of a rate and state law for surfaces where friction was controlled by adhesive contacts between asperities, so that

plowing and deformation effects could be neglected. They performed frictional sliding experiments with translucent materials on the stage of a long working distance microscope. During each experiment the ratio $\alpha = A_{con}/A_{total}$ was monitored continuously, along with applied σ and τ. Data from their sliding experiments indicated that $\sigma/\alpha = 1/P$ was close to the indentation hardness of their sample materials. As bulk normal stress σ was increased, the local load on asperities increased. The material at asperities responded by indentation creep, resulting in an increase in contact area ratio α. The normal load was thus redistributed until local stress decreased to the value of indentation strength, or $1/P$. Dieterich and Kilgore (1994) found that the bulk shear stress τ in turn depended on α. Their data supported the linear relationships:

$$\alpha = \sigma \cdot P$$

$$\tau = S \cdot \alpha$$

where S and P were constant for a given velocity and state. Because the extent to which creep processes enlarge contact area at a given normal load depends upon elapsed time, they proposed that P is a function of time, or state. The authors claim that S may be a function of slip velocity, due to the fact that for creep processes shear strength is a strain-rate sensitive property.

The contact area at an individual asperity may at any moment grow, shrink or coalesce with another contact area. The apparent existence of a critical distance D_c, over which the friction coefficient reaches a steady state value after a change in velocity, is a quantity against which the state of friction can be evaluated. Dieterich and Kilgore (1994) interpreted the steady state value of $\theta = D_c/v$ as the average contact age of an asperity during sliding, from initiation to loss of contact. After an elapsed time greater than θ, the asperity population has responded to the combined effects of time-dependent and velocity dependent processes, and no longer preserves the memory of previous velocity.

Because various authors have used different symbols for quantities which may or may not be equivalent to those I will consider, I have defined my symbols as listed in Table 1.

Experimental Method

Mechanical tests were performed on polished calcite cleavage surfaces at the University of Minnesota, using a microindentation apparatus built according to specifications developed by IBM's research laboratory (see Wu, 1991). This equipment was calibrated and servo-controlled to execute indentation and scratch tests, with a choice of maintaining a constant normal load or a constant indentation rate; constant horizontal velocity was provided for all scratch tests. Motion of the indenter was monitored and controlled through the use of piezoelectric translators, and normal and tangential forces were measured by Be-Cu load cells. During a given test, depth of indentation, horizontal displacement, normal force and horizontal shear force were monitored with respect to time, so that the evolution of the apparent friction coefficient for a single asperity could be calculated and analyzed. Scratches and indentations were made by a conical diamond indenter whose spherical tip had a radius of 1 μm. Indenter geometry and relationship to scratch dimensions are shown in Figure 1. Scratch axis orientations were parallel within 5° to $[r_1:r_2]$, an edge of the cleavage rhomb. The direction of most scratch tests was in a negative sense, away from the c-axis, although a few were done in the reverse direction. Each scratch was approximately 120 μm long.

All tests were performed on 3 mm by 3 mm calcite rhombs which were prepared for the ultimate purpose of examination by transmission electron microscopy. Thin slabs of Iceland Spar calcite were cut on a rock saw, ground and polished to approximately 100 μm thickness, cleaved into rhombs of the desired size, mounted to steel stubs using superglue, and given a final polish with 1 μm alumina grit.

Constant load tests were performed at normal loads of 3, 6, 11 or 36 mN. The scratch speed for these tests was either 0.13 or 100 μm/s. For *constant penetration rate tests*, a constant indentation velocity was imposed, and the ratio between scratch and indentation velocities was maintained at approximately 50. The scratch speed for these tests was

either 1.0 or 100 μm/s. *Constant indentation rate tests* were performed at 20 nm/s indentation rate and zero scratch speed.

We observed fluctuations in our data which may have been due to several causes. The fluctuations were most pronounced at low normal loads and fast velocities, and thus could have been noise due to oscillations in the indenter beam. Any surface flaws and imperfections in the original polish would have served to produce variations in effective hardness over short, possibly periodic scratch distances. Tilt of the polished calcite surface with respect to the indenter axis and scratch direction also caused some uncertainty in the scratch depth data. Before the first scratch test on each sample, a tilt profile was measured at ~zero load, for use in correcting these data. Because the surface remote from the tilt profile may have been tilted slightly differently than at the profile, the correction was most accurate for the first few tests and less reliable for the remaining tests. Tilt profiles were not performed on samples tested under constant load, so the first scratch on each of these samples was used as a source of tilt information. The scratches produced were of constant width, after an initial period of evolution, and so constant depth was assumed for the major portion of each scratch, and corrections to the data made accordingly. As a result, depth data for these tests have uncertainty with respect to whether or not slight increases observed were due to actual increases in depth, or to the tilt of the surface. The zero point for depth measurements in constant load tests was also less precise than in the constant penetration rate tests. In the latter the zero point was clearly the depth datum at which normal and tangential load began to increase above zero, whereas in the former each test began with a hold at zero scratch velocity during which depth change was monitored with respect to an assumed zero point.

Additional *Knoop indentation tests* at constant load were performed at M.I.T. on a Tukon hardness tester. A diamond Knoop indenter tip was used to explore anisotropic features of calcite hardness and the nature of the damage caused by concentrated deformation at higher normal loads.

Optical microscopic examination of the samples was performed at M.I.T. using Leitz Ortholux and MetalluxII microscopes in reflected and transmitted light. A 45x objective and a 16x eyepiece micrometer provided 720x magnification for measurement of the finest details, with a maximum resolution of approximately 0.5 μm. A layer of gold, approximately 100 nm thick, was vacuum-deposited on the scratched surfaces of four of the samples. The highly reflective surface made it possible to obtain interferometric images of scratches on those samples in reflected light by the Tolansky method, through the installation of a Leitz incident-light interference device on a 10x or 32x objective. The gold coating also provided a reflective layer for additional reflected light microscopy.

After each sample had been thoroughly documented using optical methods, it was prepared for transmission electron microscopy. The back surface (without scratches) was dimpled on a VCR Dimpler to provide a minimum thickness of 10 μm near the center of the rhomb. This procedure sometimes caused the sample to fracture along a cleavage plane. Dimpled samples, or fragments of samples, were mounted on copper TEM grids, for further thinning in an ion mill. Four to over ten hours of milling was required to obtain a satisfactory hole in each sample.

Observations of intracrystalline deformation features were made on a Jeol [200] CX transmission electron microscope with a LaB_6 electron source in the Center for Materials Science and Engineering at M.I T.

A summary of test conditions is provided in Table 2.

Results: Mechanical Data

For each scratch test, data on normal load, N, tangential load, T, and scratch depth, i, were plotted against scratch distance. Plots for typical tests shown in Figure 2 display the evolution of these quantities over distance and thus through time. The apparent friction coefficient, μ_{app} = T/N was calculated and also plotted against scratch distance. Oscillations in μ_{app} were consistently due to drops in T, and were influenced to a smaller extent by changes in N. The magnitude of ΔT relative to ΔN may have been due in part to the fact that machine stiffness with respect to tangential load was less than that of the entire indentation apparatus ($\sim 10^9$ N/m). Within the range of normal loads and scratch velocities tested, the apparent friction coefficient μ_{app} displayed a pronounced sensitivity to changes in N, but variable sensitivity to changes in scratch velocity, v_s (Figures 3a, 3b). Where N and v_s remained constant, μ_{app} either remained constant or increased very slowly once the indenter has adjusted its depth to a steady state value.

Constant Load Tests. At low loads, 3 or 6 mN, values of μ_{app} oscillated around a mean value near 0.3 to 0.4. When these tests were done at the fast scratch velocity, v_s = 100 μm/s, both N and i evolved initially by decreasing after the initial hold at v_s = 0, over a scratch distance of approximately 20 μm, to reach apparent steady-state values. Corresponding evolution of μ_{app} consisted of increasing apparent slip stability through a gradual reduction in the magnitude of oscillations over a scratch distance of $\sim$ 40 μm, at which point it reached a more stable condition where the magnitude of the oscillations was approximately $\Delta \mu_{app} \sim$ 0.2. At slow velocity, v_s = 0.13 μm/s, slip was more steady, with typical oscillations $\Delta \mu_{app}$ < 0.04, and no distinct period of evolution of μ_{app}. Our data indicate possible very slight, steady increases in both i and μ_{app} over the entire scratch length during these slower tests.

At an intermediate constant load of 11 mN, scratch tests done at the fast scratch velocity displayed mean values of μ_{app} close to 0.5, with oscillations $\Delta \mu_{app}$ < 0.2. Again after an initial hold, N and i evolved to steady values over a scratch distance of

approximately 20 μm. Slip became stable as oscillations in μ_{app} decreased in magnitude for at least 60 μm.

Scratch tests with a constant load of 36 mN exhibited higher μ_{app}, and smaller oscillations, continuing the apparent trend of more stable slip with increasing N. At this load μ_{app} may have been sensitive to v_s as well. At fast scratch velocity, v_s=100 μm/s, μ_{app} was close to 0.65, with oscillations of $\Delta\mu_{app} < 0.04$. Following the initial hold, N and i decreased to steady-state values over scratch distance of 20 μm. Over the same distance, μ_{app} increased to its steady-state value. At slow scratch velocity, $v_s = 0.13$ μm/s, oscillations in μ_{app} were greater than at the fast velocity, due to frequent drops in T, and the mean value for μ_{app} was 0.55. Constant values of i and N were reached immediately after the initial hold, with no measurable period of evolution.

Results from all of our constant load tests are summarized in a plot of μ_{app} versus N in Figure 3a. The function $\mu_{app}(N)$ suggested by these data is most sensitive to changes in N at low N, and begins to level off at the highest value of N tested. At this high value, $\Delta\mu_{app}$ also appears to be influenced by v_s.

Constant Penetration Rate Tests. Data from scratch tests performed at a constant penetration rate show relationships between N, i and μ_{app} within each test which follow trends similar to those observed in the constant load tests as a whole. Apparent oscillations in slip at initial conditions were damped during evolution toward more stable slip with increasing sample distance. The controlled constant increase in scratch depth, i, was accompanied by a nearly linear increase in N and more irregular, gradual increases in T and μ_{app}. At fast scratch velocity $v_s = 100$ μm/s, initial oscillations in μ_{app} were extremely large, at values of $\Delta\mu_{app} > 1.0$ as the indenter first penetrated the calcite, but oscillations decreased steadily as i and N increased. Scratches performed at slow velocity $v_s = 1.0$ μm/s showed increases in i, N and μ_{app} of similar magnitude to those at faster velocity, but oscillations were much smaller. Data for a typical constant penetration rate test at each velocity are superimposed upon the constant load data in Figure 3b. Each

constant penetration rate test exhibited a trend in sensitivity to N essentially the same as the trend which summarizes the constant load test data.

Indentation Tests. Indentation test data recorded the response of calcite to a normal load on a cleavage surface with no lateral motion. Constant load indentation tests, performed using a Knoop indenter, demonstrated the effect of the orientation of the long diagonal with respect to the anisotropic calcite surface structure. The greatest depth was obtained for a given load when the diagonal was parallel to a cleavage trace. When a constant indentation velocity was imposed, N increased with i, slowly at shallow i and with increasing sensitivity as the indenter penetrated to greater depth (Figure 4a). Results from indentation tests are most appropriately interpreted through the calculation of indentation hardness for each indenter geometry under the given test conditions. Hardness calculations are discussed further below.

Results: Optical Microscopy

Detailed investigation was made of typical scratch damage features using optical microscopy and interferometry. Scratch morphology as it corresponds to variations in load and scratch velocity can be well-characterized by the presence of damage features with dimensions on the order of microns to tens of microns. Figure 5 shows examples of typical scratches.

Damage features. The basic damage feature present in all scratches is the trough plowed by the indenter. Other features include the traces of active slip or twin planes, cleavage fractures, pits and notches, as sketched in Figure 6. In general, the width of the trough is even for constant load tests, whereas for constant penetration rate tests it is tapered. The edges and bottom of scratches produced at loads of less than 20 mN appear to be smooth. Optical interferograms of these scratches display notches in the interference fringes where each scratch interrupts the flat cleavage surface. The sharp corners where these notches meet the background fringes show that the original surface of the calcite continues flat up to each smooth scratch edge, within the 15 nm depth resolution of this technique. The absence of ridges along scratch edges suggests that the plastic pileup of material either had not occurred or was very gradual. Removal of submicron-sized gouge was thus inferred, although no gouge fragments were identified.

At the normal load of 36 mN a notched scratch edge was produced. Notches are fairly evenly spaced, at 3 to 5 μm. One edge of each notch is parallel to the trace of the r_3 cleavage plane. Deformation of the calcite surface appears to end abruptly at the outer edges of the notches. I inferred removal of small chips of calcite from notches.

Along scratches produced under moderate normal load, fine linear features intersect one edge of the trough at 39°. Optical observations suggest that they represent traces of planes of deformation extending to some depth, at a high angle to the surface. Birefringence of the wedge of calcite enclosed between each of these planes and the surface does not exceed first order grey-white, indicating that they extend no more than 2

μm below the surface. Their projected width is approximately 1 μm. These dimensions permit an estimation of the angle between these planes and the sample surface of roughly 60°. The linear traces of these planes on the polished surface display sufficient relief to be visible in reflected light after coating with up to 100 nm of gold. Interferometry confirms a displacement of approximately 0.05 μm normal to the surface across each trace. Interpretation of these measurements in conjunction with stereographic plots of known low-temperature intracrystalline slip and twinning systems in calcite (deBresser, 1991; Turner et al, 1954) suggests that these damage features represent either negative slip on the f_l plane or twinning on e_l plane. Both deformation planes dip 72° relative to the r_l sample surface but in opposite directions. Because of the apparent lack of pairs of planes, I have assumed that they are not twins, and have referred to these features as slip planes below.

In some cases, the trace of a slip plane terminates in a short cleavage fracture at its outer edge (remote from the scratch axis), but this cleavage fracture does not intersect the scratch itself. The position of these fratcures at the terminations of the slip planes suggests that they may be secondary features which accomodated displacement along the edges of primary slip planes.

Among the tests in our study, the greatest amount of damage was produced in the form of triangular pits, during tests where relatively high normal loads were reached. Each pit is defined by a short r_3 cleavage fracture whose trace is 102° from the $[r_l:r_2]$ scratch axis. The deepest portion of the pit occurs at the apex where the r_3 cleavage fracture meets the scratch. A set of parallel striations intersect both the scratch axis and the trace of the cleavage fracture at an angle of 39°. The striations appear to be the edges of shallow steps in the sample surface which descend gradually toward the apex. The surface of the flat portion of each step is parallel to r_l, the cleavage plane represented by the polished surface of the sample; the risers connecting adjacent steps have an orientation consistent with traces of cleavage or slip on c (basal), e_l (twin) or f_l planes. Extension of riser planes below the steps was observed to tilt in a direction consistent with e_l planes.

Table 3 documents damage features identified and measurements made along scratches.

Scratch types. Microstructural observations for the scratch tests can be summarized in terms of scratch types. Three distinct types of scratch were produced by constant load tests at different loads and a fourth type from the constant penetration rate tests. These scratch damage types are illustrated in Figure 6b.

Low constant load tests at 3 and 6 mN produced smooth scratches of even width. The ends of these scratches were marked with smooth round indentations where the indenter had been held stationary under load for a period of time. At the initial end where scratch depth evolved, the scratch is slightly tapered in width for 20 -40 μm.

Smooth, even width scratches were also produced by moderate constant load tests at 11 mN. This scratch type is distinguished by the additional presence of traces of slip planes along one side of the scratch.

For tests conducted under the relatively high constant load of 36 mN, scratches were notched and accompanied by a series of overlapping pits.

Constant penetration rate tests produced a distinct type of scratch with a tapered outline and cross-section, from a shallow, sharp beginning, where the indenter first made a permanent impression, to a broad, deep end. These scratches are smooth along their entire length. At the point where i > 1 μm and n > 5 to 7 mN, many but not all of these scratches begin to be accompanied by a series of traces of slip planes. These planes increase in size as i and N increase. Interferometry reveals that the calcite surface is depressed slightly in the region around the slip planes. The orientation of the planes with respect to the depression further supports their interpretation as slip on an *f*-system.

Results: Transmission Electron Microscopy

Transmission electron microscopy of samples 9 and 10 revealed a well-defined dislocation damage zone of high dislocation density around the perimeter of each scratch. Extending across the zone were planar features whose character and orientation were consistent with the slip-planes observed optically (Figures 7a, 7b). The smooth, clean appearance of these features, and the fact that some of them appeared to consist of closely spaced pairs, supports the interpretation of these features as twin planes. However, diffraction patterns did not exhibit the characteristic double spots of twinning, so the possibility of their being f-slip planes was not discounted. Along the c^- edge of the scratch, the planes ended at the edge of the zone, but on the c^+ side they extended some distance outside it. Beyond the margin of the zone on either side of the scratch, a much broader region exhibited a dislocation density elevated somewhat above background level.

Scratch 9-4, produced at a constant load of 11 mN and v_s = 100 μm/s, displayed a dislocation damage zone of a fairly even width. The radius of the zone, defined as the distance from the scratch axis to the margin, was ~1.5 μm on either side. Within the zone, planar features could be faintly discerned, but the thickness of the sample did not permit their detailed examination.

The best transmission electron microscopy results were obtained from the broad ends of scratches 10-5 and 10-6, which had been produced at a constant penetration rate, with v_s = 1 μm/s. Along the c^- edge of the scratch, the dislocation damage zone radius was 3.5 μm, and planar features were spaced approximately 1.0 μm apart. The zone radius along the c^+ edge was at least 5.0 μm, and the planar features, spaced at 1.5 μm, extended some distance beyond the margin. At the prow of the scratch, the zone radius was 2.5 μm, slightly narrower than along the edges (Figure 7c). A planar feature within this zone appeared to have formed ahead of the moving indenter (Figure 7d). Along the narrower portions of these tapered scratches, the dislocation damage zone radius decreased and was more variable than at the broad end.

Results: Correlation of Damage Features with Mechanical Data

Scratch damage regimes. Interpretation of scratch damage in terms of deformation mechanisms requires the comparison of feature type and magnitude with the data on normal and tangential loads and scratch velocity. In broad terms, three distinct damage regimes can be defined tentatively, through correlation of each of the constant load scratch types with a region of the normal load versus μ_{app} plot (Figure 8). Regime I comprises smooth scratches produced at normal loads of 3 or 6 mN. Here μ_{app} was very sensitive to changes in the normal load. Regime II is defined by the introduction of localized slip on f-planes, when normal load is 11 mN, and where the slope of the μ_{app} versus N curve decreases. The highest load tests which produced pits and notches along scratches define Regime III. In this regime, the curve has begun to level off, so that μ_{app} is not very sensitive to N. However, in this regime μ_{app} may have been influenced by changes in scratch velocity. The fourth scratch type, resulting from constant penetration rate tests, overlaps Regimes I and II, as each scratch responded to increasing N by evolving from a smooth scratch to a smooth scratch with slip planes after N > 5-7 mN. The fact that no slip planes occurred in constant load tests at the depths when they begin in constant penetration rate tests suggests that the imposition of indentation velocity $v_i > 0$ may alter the stress state around the moving indenter, in such a way as to enhance the activation of this damage mechanism. No slip planes were observed along scratches produced at 100 μm/s on sample 14. In this case, tilt of the sample surface may have altered scratch conditions.

Elastic recovery. Interpretation of damage features in terms of the extent to which elastic deformation is significant contributes to calculations of energy due to plowing friction. I evaluated the elastic recovery of calcite after scratch tests through correlation of the scratch depth data collected during the tests with dimensions measured on the tested samples using optical microscopy and interferometry. Typical interferograms are shown in Figure 9, and results are tabulated in Table 4.

Data collected during the constant load tests with N = 3mN indicated a scratch depth of 0.6 to 0.8 μm, whereas the depth after recovery was 0.3 μm (Figure 9a). Scratch widths during the tests, estimated using depth data and an assumed ideal indenter geometry, were 1.9 to 2.4 μm, compared to the 1.4 μm permanent width of most scratches. Together, the depth and width recovery mean that at least 50% of the volume displaced by the indenter at small normal loads was accommodated elastically.

Recovered depth data for other constant load tests are not available for comparison with mechanical data. However, a comparison of final width with the width calculated from depth data suggests that at constant loads of 11 mN elastic recovery is not significant. Data for sample 9 do not show any measurable elastic recovery, although uncertainties in depth data may account for this. Nevertheless, a greater proportion of permanent damage is consistent with the fact that these tests exhibited localized slip or twinning.

Constant penetration rate tests also exhibited varying degrees of elastic recovery. The permanent length of these scratches was commonly ~10 μm shorter than the recorded scratch distance, suggesting that calcite response to loads up to 1 or 2 mN was 100% elastic. The tapered shape of the trough produced by these tests makes it difficult to use interferometry to determine the exact scratch depth at a given point, but the slope can be estimated (Figure 9b). Again, at low loads of less than 5 mN, elastic recovery was substantial, and permanent scratch depth appears to be less than half the depth measured during the tests. As the load and depth increase, interference fringes begin to merge, so that further estimation of final depth at the broad end of the scratch is not possible. Elastic recovery of scratch width at this end, estimated as for the constant load tests, resulted in a reduction from 4.0 - 5.5 μm during the test to 2.9 - 4.6 μm permanent width. At this point, the value of N was typically 14 mN, and so this result is not consistent with the result described above for tests at a lower constant load of 11 mN. Uncertainties in depth data for the latter tests suggest that the constant penetration rate test results are more reliable.

Correlation of individual events with specific features. Along each scratch, occurrences of specific features can be examined for correspondence with events in the mechanical data recorded at the given scratch distance (Table 5). Because there are oscillations in the data which may represent noise or instabilities in the testing equipment, only those characteristics of plots which involve several data points can be unambiguously identified as slip events. For this reason it was not possible to match sudden drops in either N or T with the occurrence of individual slip planes, closely spaced at 2 to 5 μm. Where a cluster of f-slip planes spaced at less than 5 μm was produced during the constant load tests, N or T sometimes showed a slight decrease, and i a slight increase.

For the scratches produced at a high normal load, N = 35 mN, some of the pits observed optically correlate with drops in the normal and tangential loads, as well as with transient increases in scratch depth. At fast velocity, v_s = 100 μm/s, r_3 fractures bounding pits were up to 20 μm long and generally spaced between 6 and 10 microns apart, but occasionally were as close together as 2 microns. The damage resulting from each pit overlapped and obscured some of the features of earlier pits. Associated with each pit was a smooth drop in N of less than 1 mN, and a more abrupt drop in T of as much as 2 mN. Changes in depth were less than 0.05 μm. Transient decreases in μ_{app} of approximately 0.02 appear to correlate with drops in depth as well as load. At some larger pits with more data points, it was possible to observe a gradual decrease in μ_{app} to a minimum, followed by an abrupt increase to its previous value.

Closely spaced mechanical data points from the 35 mN constant load tests at the slow velocity, v_s = 0.13 μm/s, exhibit pit formation in greater detail than at the fast velocity. Fracture dimensions are variable, with lengths from 10 to 50 μm and 6 to 10 μm spacing between fractures. At each fracture, the drop in N was less than 2mN, and at the same time, the drop in T could be as large as 8 mN. Load drops were accompanied by increases in scratch depth of up to 1.0 μm. Many events began as an abrupt increase in depth with concurrent decrease in T and μ_{app}, followed by more gradual recovery to the previous depth but a more abrupt increase in T.

Several scratch tests produced anomalous results. On three samples, scratch direction of the first test was "positive", or in the opposite sense from that of the majority of tests. Data for the positive direction tests at constant penetration rate were very irregular. Damage features observed along the resulting scratch included fractures and pits which formed at N as low as 5 mN, and i as shallow as 0.25 μm. Individual pits correlate fairly well with simultaneous drops in N and T of 20 to 100% of the magnitude of the load just prior to pit formation. Fractures without pits correlate with smaller load drops, ~5% of the prior load. In most cases, the drops in N and T associated with a given pit were similar in magnitude, so that their effect upon $T/N = \mu_{app}$ is very small. While there are not enough data to prove it, these three tests suggest that resolved shear stresses on fracture planes are much higher at given N and i when the scratch direction is positive. However, formation of individual pits and fractures do not generally have a large impact on μ_{app}, because they tend to result from roughly equivalent drops in N and T.

Scratches 12-9 and 12-10 produced pits in constant penetration rate tests, done in the negative direction as in the majority of tests. It appears that either the tilt of the sample surface or a quirk in the loading mechanism resulted in initial contact of the indenter at significantly higher loads than in other constant penetration rate tests. Pits occurred near the beginning of scratches when v_i was probably very high, and again later when N > 25 mN. Pits were associated with load drops of ~20% for N and T, but had only a small effect on μ_{app}. An exception occurred at the end of 12-9 where pit formation lowered T more than N, resulting in a 10% drop in μ_{app}. The depth of these scratches is not known, due to ambiguity of the zero point. Data from these two tests suggest that N > 25mN is sufficient for pit formation during constant penetration rate tests at 1 μm/s.

Discussion: Hardness and Stress Calculations

Hardness values provide simple and useful means for quantifying the stress response of a sample to a concentrated load. Indentation or scratch hardness, $H_{ind} = N/A_{\perp N}$ or $H_{nor} = N/A_{\perp N}$, gives a means for establishing a relationship, under the given test conditions, between the normal force and the indentation or scratch depth, through calculation of projected contact area based upon the geometry of the indenter. Similarly, plowing hardness $H_{tan} = T/A_{\perp T}$ provides a relationship between scratch depth i and the tangential force T. Figures 1 and 10a show the idealized geometry I assumed in making calculations of these quantities. During constant penetration rate tests, the scratch velocity was approximately 50 times greater than the indentation velocity, so that the penetration vector of the indenter was only 1° from parallel to the tangential force. I therefore used the same calculation of $A_{\perp T}$ perpendicular to the sample surface for both constant penetration rate and constant load scratch tests.

Hardness values calculated from data: For each scratch or constant indentation rate test, I calculated hardnesses from the simultaneously collected data on forces and scratch depth, as they evolved during the test. Figure 11 exhibits typical plots for several types of scratch test. The value at a particular point during a test could be compared with the static indentation hardness of calcite, to assess the effect of imposed scratch or indentation velocity.

Vickers static indentation tests are the basis of many studies linking hardness and other mechanical properties of the sample. Brace (1960) performed Vickers indentation tests on the polycrystalline calcite in fine-grained Solnhofen limestone. His results gave a Vickers hardness of $H_v = 147$ kg/mm^2 = 1.44 GPa, which is equivalent to mean contact pressure $p_m = H_{ind} = 1.55$ Gpa, where $H_{ind} = N/A_{\perp N}$ for static indentation tests.

Because the mechanical properties of calcite are generally very anisotropic, I performed Knoop indentation tests at various orientations on calcite cleavage surface to determine the magnitude of hardness anisotropy. Normal loads were those which generate

reproducible results on the Tukon Tester, and at 491 or 245 mN were significantly larger than normal loads for the scratch tests. Where the long diagonal of the indenter was nearly parallel to $[r_1:r_2]$, and thus to the orientation of our scratch tests, a hardness of H_k = 130 kg/mm^2 = 1.28 GPa, was measured. The Knoop hardness number is calculated using a projected area, so that $H_k = H_{ind} = p_m$. For all other orientations, the hardness was greater than this value, increasing with the angle between long diagonal of the indenter and the trace of a cleavage plane. Maximum Knoop hardness measured was $H_k = H_{ind} = p_m$ = 175 kg/mm^2 = 1.71 Gpa.

Whereas a single value of H_{ind} was determined by each static indentation test, the value of H_{nor} was not in general constant during any given test where a constant indentation or scratch velocity was imposed. The effect of a constant indentation velocity, v_i, alone upon hardness H_{nor} is shown in a plot based upon data for indentation tests with $v_s = 0$ and v_i = 20 nm/s (Figure 4b). Hardness calculations display an interesting result: H_{nor} increased initially as the indenter was pushed into the sample, reached a maximum value of 2.6 GPa at i~1.0 μm, and then decreased toward its initial value.

For scratch tests, calculations of hardness H_{nor} express the response of the calcite to the normal load which was also influenced by the fact that the indenter was moving at a particular scratch velocity. Hardness calculations for constant load tests give results which are variable, corresponding at least in part to the uncertainty in scratch depth. Nevertheless there are some consistent characteristics. After an initial unstable interval, H_{nor} and H_{tan} both oscillated about a constant value and no hardening was observed. At constant load N = 3 mN and v_s = 100 μm/s, values for H_{nor} ranged from 1.0 to 1.5 GPa, and H_{tan} from 0.8 to 1.0 GPa. Larger and more variable values were calculated for tests conducted at the same velocity with constant load, N = 11 mN, where both H_{nor} and H_{tan} ranged from 1.5 to over 5.0 GPa. For each test, however, H_{nor} and H_{tan} were approximately equal. Hardness values for tests with the highest constant load, N = 35 mN, were fairly steady after an initial period of evolution, but showed a strong sensitivity to scratch velocity. At v_s = 100 μm/s this high load generated H_{nor} ~ 3.5 Gpa and H_{tan} ~

3.7 Gpa. The slower tests, with v_s = 0.13 μm/s showed H_{nor} ~ 1.1 Gpa and H_{tan} ~ 1.0 Gpa, hardness values that were significantly lower than the static indentation hardness.

Hardnesses H_{nor} and H_{tan} during constant penetration rate tests also generally appear to evolve toward constant values. For tests done at v_s = 1.0 μm/s, H_{nor} was very high initially, but within a 40 μm scratch distance it decreased to a constant or slightly decreasing value of between 1.5 and 2.0 GPa. At the same time, H_{tan} was either slightly increasing or constant, around 1.0 to 1.5 GPa. At the scratch distance where a cluster of f-slip planes occurred along a particular scratch, the slopes of both H_{nor} and H_{tan} decrease slightly, generally causing the hardness curves to level off. Toward the end of the scratch, curves for H_{nor} and H_{tan} approached each other but did not meet.

Constant penetration rate tests performed at v_s = 100 μm/s evolved in a manner similar to those performed at the slower velocity. The major difference is that mean values for the faster tests were higher, with H_{nor} ranging from 2.5 to 3.0 GPa and H_{tan} from 1.5 to 2.5 GPa. However, the evolution of H_{nor} and H_{tan} approached equal values, as before. Higher hardness values for both H_{nor} and H_{tan} during faster tests suggest that calcite responded to the moving indenter through strain-rate sensitive mechanisms. The fact that H_{nor} during most scratch tests was also significantly greater than the static Knoop indentation hardness, H_k = 1.28 Gpa, further supports this conclusion.

Williams (1996) has found microstructural evidence in most scratch experiments for plastic deformation ahead of and below the indenter. The presence of a zone of dislocations ahead of the moving indenter, as exhibited in TEM observations of sample 10, demonstrates that this may be true of calcite under the conditions of our tests. The evolution of H_{tan} may reflect any hardening of the calcite ahead of the indenter which resulted from the activity of plastic mechanisms. The initial periods of evolution in most tests, where H_{tan} increased to reach a fairly steady value, may represent accumulation of dislocations which soon reaches a constant level.

Contact friction. The relationship between hardness measurements and local stress depends in part upon the magnitude of the coefficient of contact friction, μ_{con}, between indenter and sample at the atomic scale. I examined our data to assess the degree to which contact friction may have been a factor in hardness results. For isotropic materials whose perfectly plastic deformation response to static indentation can be estimated by predicting displacement along sliplines, Hankin (1923) found that yield pressure depends upon included angle α and μ_{con}. Tabor (1951) presented an expression based upon his results for the effect of μ_{con} during static indentation tests using a conical indenter

$$p_m = p_0 \cdot (1/(1+ \mu_{con} \cdot \cot\alpha))$$

where p_m is the mean indentation pressure or hardness, H_{ind}, which is actually measured, and p_0 is the value which would be obtained for $\mu_{con} = 0$. The simplicity of this relationship is due to the assumption of perfectly plastic deformation and the circular symmetry of the contact area, for which the horizontal components of μ_{con} cancel each other out, and only the vertical component must be considered. A more complicated situation pertains to scratch tests, where response to two forces, T and N were asymmetric. The anisotropy of the calcite yield surface and the presence of evidence for elastic and brittle mechanisms suggest factors which cause further deviation of our results from the situation described by Tabor's expression. One feature of the expression is nevertheless significant for our results: in even the simplest case where $v_s = 0$, contact friction has an effect on hardness. For this reason, μ_{con} and μ_{plow}, for scratch tests where $v_s > 0$, are not likely to be simply additive, as implied by Bowden and Tabor (1986). In all cases μ_{con} must be incorporated into hardness calculations with consideration for the indenter geometry and other factors influencing local stress distribution.

Two-dimensional force balance: One means which I used to estimate μ_{con} in our experiments was to make the assumption that the shear force on the contact at a given instant simply corresponded to a two-dimensional force balance between the normal and tangential loads. This would be the case only for non-deforming planar contact surfaces with unrestricted motion in either direction along the plane. Our non-planar contact

surface was in fact deforming, and the downward motion of the indenter was restricted by the volume of calcite, so this force balance at best provides an upper bound for μ_{con}.

A net force, F, can be calculated to estimate the maximum force acting upon the contact surface:

$$F = N/\cos\theta$$

where $\theta = \tan^{-1}(\mu_{app})$ and $\mu_{app} = T/N$. The force F meets the contact surface at a maximum angle of $(\theta + \alpha)$, in the plane defined by N and T (Figure 10b), where α is the angle between the contact surface and N. (Note that 2α is the included angle of the conical portion of the indenter.) For $(\theta + \alpha)<90°$, the net effect of μ_{con} is to inhibit increase in scratch depth at this portion of the contact, whereas for $(\theta + \alpha)>90°$, it inhibits forward motion. Where $(\theta + \alpha)=90°$, the effect of contact friction will be zero. Our data give a maximum value of $\mu_{app} \sim 0.65$, for which $\theta \sim 33°$, and because our indenter geometry has $\alpha = 45°$, $(\theta + \alpha) = 78° < 90°$. In our experiments where $\mu_{app} \leq 0.65$, we have $\theta \leq 33°$, so that $(\theta + \alpha) < 90°$ in all cases. Expressions for estimating the mean stresses on the contact area in the N-T plane are as follows:

$$\sigma_{con} = (F/A_{\perp F})\cdot\sin^2(\theta + \alpha)$$

$$\tau_{con} = (F/A_{\perp F})\cdot\cos(\theta + \alpha)\cdot\sin(\theta + \alpha)$$

$$\mu_{con} = \tau_{con}/\sigma_{con} = \cot(\theta + \alpha)$$

Table 6 shows a range of values for μ_{con} calculated in this manner from our data. My convention is that positive values of τ_{con} represent contact shear downward into the sample, whereas negative values predict the opposite shear sense, up and out of the sample in the scratch direction. This method associates increases in the apparent friction of the moving indenter with decreases in contact friction, if α is considered constant. The values range from $\mu_{con} = 0.2$, calculated for $\mu_{app} = 0.65$, to $\mu_{con} = 0.65$ calculated for $\mu_{app} = 0.3$. However, the correct value of μ_{con} is not likely to vary widely among scratch tests. It

happens that the smaller μ_{app} associated with the higher estimates for μ_{con} were generated during tests with shallow scratch depths, where different damage mechanisms were active and the spherical tip of the indenter would have dominated the geometry of the contact between indenter and calcite.

In order to examine this effect, I estimated and plotted the force balance-based relationship between μ_{con} and μ_{app} for a variety of angles α (Figure 12). Assuming that $\mu_{con} = 0.2$, estimated for $\mu_{app} = 0.65$, is a correct value for all tests, this plot suggests that tests with lower μ_{app} had a lower effective included angle, α_{eff}. The lowest values occurred where $\mu_{app} = 0.30$, $\mu_{con} = 0.20$ and $\alpha_{eff} \sim 60°$. Such tests had scratch depths of 0.6 - 1.0 μm, which is only two to three times 0.293 μm, the depth of the spherical portion of the indenter. By considering indenter geometry in this way, the estimate of $\mu_{con} = 0.2$ appears to be reasonable, but I looked at three other means of assessing contact stresses which take into account the stress or strain state of the contact surface.

Stress resolution. A two-dimensional Mohr's circle approximation of the stress resolution on the contact surface can be used to calculate contact friction, where $\mu_{con} = \tau_{con}/\sigma_{con}$. The assumption behind these calculations is that stress is static, whereas our tests involved dynamic stresses. Nevertheless this method has the advantage over the previous approach, in that it permits incorporation of hardness data reflecting the actual stress response of the calcite. The assignment of the orthogonal hardness values as principal stresses, such that $\sigma_1 = H_{nor}$ and $\sigma_2 = H_{tan}$, leads to the following expressions

$$p_m = \sigma_{con} = H_{nor} \cdot \cos^2(\alpha) + H_{tan} \cdot \sin^2(\alpha) = (H_{nor} - H_{tan})/2 + (H_{nor} + H_{tan}) \cdot \cos(2\alpha)/2$$

$$\tau_{con} = (H_{nor} - H_{tan}) \cdot \sin(2\alpha)/2$$

$$\mu_{con} = \tau_{con}/\sigma_{con} = ((H_{nor} - H_{tan}) \cdot \sin(2\alpha))/((H_{nor} - H_{tan}) + (H_{nor} + H_{tan}) \cdot \cos(2\alpha))$$

With our indenter included angle of $2\alpha = 90°$, these expressions become

$$p_m = \sigma_{con} = (H_{nor} + H_{tan})/2$$

$$\tau_{con} = (H_{nor} - H_{tan})/2$$

$$\mu_{con} = (H_{nor} - H_{tan})/(H_{nor} + H_{tan})$$

If, as suggested by the discussion on the force balance approach, it is appropriate to use $\alpha_{eff} \sim 60°$ for results from tests done at low normal load, then $2\alpha = 120°$, and

$$p_m = \sigma_{con} = H_{nor}/4 + 3 \cdot H_{tan}/4$$

$$\tau_{con} = \sqrt{3} \cdot (H_{nor} - H_{tan})/4$$

$$\mu_{con} = \sqrt{3} \cdot (H_{nor} - H_{tan})/(H_{nor} +3\ H_{tan})$$

Calculations of contact stresses and friction for some typical values of H_{nor} and H_{tan} are given in Table 7, based on either $\alpha_{eff} \sim 45°$ or $\alpha_{eff} \sim 60°$. These values for μ_{con} vary significantly, from 0.25 to 0, as the ratio H_{tan}/H_{nor} ranges from 0.6 to 1.0, but μ_{con} does not show much sensitivity to α_{eff}, nor is it directly related to μ_{app}. Tests with low ratios of H_{tan}/H_{nor}, which tend to be associated with low μ_{app}, are predicted to have higher contact friction than tests with high H_{tan}/H_{nor} and μ_{app}.

Adhesive contact friction: The expression for adhesive friction, $\mu_{adh} = S \cdot P$, (Bowden and Tabor, 1986) provides a means of estimating contact friction, which is based upon the creep response an asperity along a planar surface. The geometry assumed is quite different from that in our tests, where it was the surface rather than the asperity which was deforming. However, if contact friction were primarily a function of atomic adhesive forces, the geometry may have minimal effect on its magnitude. The shear strength, S, of the contact can be estimated, given von Mises bulk shear strength for the initiation of plastic deformation,

$$S \sim k = \sigma_y/\sqrt{3}$$

The extent to which deformation during indentation is either plastic or elastic was examined by Johnson (1970). He concluded that the factor $(E/\sigma_y) \cdot \cot\alpha$ is a useful

measure of material response to a concentrated load. In our tests $\alpha=45°$. For compression perpendicular to r_1 in single crystals of calcite at room temperature with a confining pressure of 50 MPa and a strain rate of 2.5×10^{-4}/s, data from Turner et al (1954) provide $E \sim 90$ GPa and $\sigma_y \sim 450$ MPa. Thus we have $(E/\sigma_y)\cdot\cot\alpha = 200$.

Because the normal load in a static indentation test is supported by a volume of material substantially larger than the contact surface itself, hardness values calculated as force per actual or projected contact area are typically greater than the differential yield stress σ_y of the material, frequently by a factor close to 3. Johnson (1970) described a hemispherical core immediately surrounding the contact area, within which a hydrostatic pressure p_h was assumed. The radius of the core is equal to a, the projected radius of the contact area. He derived a theoretical expression which relates p_h to σ_y, for a conical indenter

$$C = p_h/\sigma_y = 2/3\cdot(1 + \ln((1/3)\cdot(E/\sigma_y)\cdot\cot\alpha))$$

and found values calculated for p_h to agree fairly well with experimentally determined hardness, or p_m, of metals. Johnson (1970) provided a plot of the elastic-plastic model, expressed by this equation, which predicts $C = p_m/\sigma_y$ is close to 3.0 for materials with $(E/\sigma_y)\cdot\cot\alpha = 200$. This relationship provides an estimate for P,

$$P \sim 1/H_v \sim 1/(3\cdot\sigma_y)$$

Substitution produces

$$\mu_{adh} = S\cdot P \sim (\sigma_y/\sqrt{3})\cdot(1/(3\cdot\sigma_y)) = 1/(3\sqrt{3}) = 0.193.$$

This quantity has the advantage of providing a constant value, independent of parameters such as μ_{app} which vary from test to test. This same fact however means that it does not reflect the actual stress state during the tests, nor does it represent the actual contact friction between calcite and diamond which may not be accurately described as adhesive. Tabor (1951) reported contact friction between a diamond indenter and a metal

sample to range from 0.1 to 0.15, lower than for contacts between metal and most other indenter materials. Contact friction between calcite and diamond need not have the same value, but this information supports the likelihood of μ_{con} for calcite and diamond being less than 0.2. Contact friction is also likely to be greater than zero for real materials which will experience some degree, if small, of adhesion.

Perfectly plastic deformation: Williams (1996) used the model from Johnson (1970) to plot 2α versus (E/σ_y), in order to outline the conditions of elastic and plastic response. Our value of $\mu_{app} = 0.65$ plots in the fully plastic regime, given our values of α and (E/σ_y). However, at shallow scratch depths where $\mu_{app} = 0.3$, the spherical tip of our indenter would dominate the geometry so that the effective $\alpha > 45°$. For a larger included angle the response of calcite would plot within the elastic-plastic regime, consistent with the elastic recovery we observed at shallow scratch depths. It is therefore reasonable to examine methods of estimating contact stresses which include some consideration of plasticity.

Challen and Oxley (1979) and Black et al (1988) have studied deformation regimes in metals under varied scratch test conditions. Their two-dimensional models are based upon the assumption of perfectly plastic deformation in a material with an isotropic yield surface, which can be analyzed in terms of displacement along slip lines. The authors plotted the relationship of the shear strength of the contact between asperity and sample to apparent friction coefficient and included angle of the indenter. Our indenter angle $\alpha = 45°$, and values of friction coefficient μ_{app} ranging from 0.3 to 0.65, plot in a region where they predict the formation and removal of chips of sample material. Chip removal is consistent with my optical observations and inferrence of gouge and chip removal described above. In this regime, the cutting model of Challen and Oxley (1979) predicts

$$\mu_{app} = \tan((90°-\alpha)-45°+(\cos^{-1}f)/2)$$

where they defined the ratio f, rather than a coefficient of contact friction, such that

44

$$f = \tau_{con}/k = \text{(shear strength of contact)/(bulk shear strength of material)}$$

This result is interesting in that it considers the shear condition at the contact not to result from some constant coefficient of contact friction, μ_{con}, but to have a particular strength which is related only to α and μ_{app}. According to the discussion in Black et al (1988), the nature of chip formation is such that lower values of μ_{app} are associated with higher contact strengths, due to the increased ability of the plowing indenter to remove material which is well adhered to it.

Values of shear stress obtained by $\tau_{con} = f \cdot k$, and the corresponding values of μ_{app} for α = 45° or 60°, are shown in Table 8, and can be compared with those obtained by stress resolution in Table 9. Our data agree most closely with calculations based upon the expression from Challen and Oxley (1979) for f = 0.4 to 0.5, which result in τ_{con} = 111 to 139 MPa. Given a typical contact pressure, p_m = 1.4 GPa, the contact friction would be $\mu_{con} \sim 0.1$. Higher values of p_m would generate smaller coefficients of contact friction, μ_{con} < 0.1, if contact shear strength were constant as predicted by this model.

The varied methods of estimating contact friction and stresses are based upon simplifying assumptions, none of which completely describes our scratch tests in calcite. However, some conclusions can be reached, which provide the basis for further interpretation of damage features. The coefficient of contact friction, μ_{con}, appears to be between 0.1 and 0.2. The value of μ_{con} may not be constant, as it is likely to be intimately dependent upon indenter geometry, active deformation mechanisms and the stress state in the calcite. Mohr's circle analysis of stress resolution on the contact surface provides a means of obtaining realistic estimates for mean contact stress, p_m.

Discussion: Shear Stress on Calcite Deformation Systems

Among all the room temperature experiments reported in Turner et al (1954), the minimum resolved shear stress at yield for each of the active systems was:

twinning on e_1: $\tau_c \geq 4$ MPa

slip on r_1: $\tau_c \geq 115$ MPa

slip on f_1: $\tau_c \geq 200$ MPa

For comparison, I have tabulated the minimum normal load, scratch depth, H_{nor} and H_{tan} at which particular damage features were generated along each scratch in our tests (Table 9). I have then used these data in the following calculations in order to estimate stresses available to activate different damage mechanisms.

Maximum radial stress σ_{pp} due to a moving indenter, can be calculated using values for p_m and μ_{con} in an expression from Lawn and Wilshaw (1975). This maximum stress would be a tensile force at the trailing edge of the contact between indenter and sample. The expression is based upon the Hertzian analysis in Hamilton and Goodman (1966) for a moving circular contact area. For these calculations, I have assumed $v = 0.32$ and considered p_m to be the value estimated using Mohr's circle method.

$$\sigma_{pp}/p_m = ((1-2v)/2) \cdot (1+A \cdot \mu_{con}) = 0.18 \cdot (1+A \cdot \mu_{con})$$

where

$$A = (3\pi/8) \cdot (4+v)/(1-2 \cdot v) = 14.14.$$

Examination of this expression reveals that σ_{pp}/p_m increases rapidly with increasing μ_{con}. I performed further calculations for hardness values typical of our tests, assuming $\mu_{con} = 0.1$ or $\mu_{con} = 0.2$. These results (Table 10) show that for fixed μ_{con} and a given H_{nor}, σ_{pp} increases slightly with increasing ratio H_{tan}/H_{nor}, due to the corresponding increase in p_m.

If μ_{con} increases, results of all calculations for maximum contact stress, σ_{pp}, increase dramatically. In these calculations, changes in α_{eff} do not have a significant effect. Thus, even if μ_{app} does not have a direct relationship with μ_{con}, the ratio H_{tan}/H_{nor}, which correlates positively with μ_{app} as shown below, is associated with the effect of μ_{con} on local stress distribution, which in turn can influence the activity of damage mechanisms.

Values calculated for σ_{pp} are generally high when compared with the minimum resolved shear stresses on active slip and twinning systems from Turner et al (1954). However, the location and orientation of σ_{pp} may not have been ideal with respect to resolution on these systems. I used the values for hardness from Table 9 and the expression from Lawn and Wilshaw (1975) to calculate maximum stresses associated with the minimum conditions for the occurrence of particular damage features in our tests.

Localized plastic deformation by slip on f_l planes or twinning on e_l planes first occurred in the constant penetration rate tests at $v_s = 100$ $\mu m/s$ on sample 10 when N $\sim$ 5mN and i $\sim$1.0 μm. At this point, $H_{nor} \sim 1.9$ Gpa, $H_{tan} \sim 1.5$ Gpa, $p_m = 1.7$ Gpa and, assuming $\mu_{con} = 0.1$, the estimated maximum contact stress was

$$\sigma_{pp} = 0.43 \cdot p_m = 731 \text{ Mpa}.$$

Fracture on r_3 planes occurred along the scratches on sample 4 which were produced during fast constant load tests at $v_s = 100$ $\mu m/s$, with N ~ 35 mN and i ~ 2.0 μm. Mean hardnesses for these tests were $H_{nor} \sim 3.5$ Gpa, $H_{tan} \sim 3.7$ Gpa, $p_m = 3.6$ Gpa and, assuming $\mu_{con} = 0.1$, the estimated maximum contact stress was

$$\sigma_{pp} = 0.43 \cdot p_m = 1548 \text{ Mpa}.$$

Fractures produced during tests with constant load N ~ 35 mN at the slower scratch velocity of $v_s = 0.13$ $\mu m/s$ were associated with much lower hardnesses, $H_{nor} \sim 1.1$ Gpa, and $H_{tan} \sim 1.0$ Gpa, $p_m = 1.05$ Gpa and, assuming $\mu_{con} = 0.1$, the estimated maximum contact stress was

$$\sigma_{pp} = 0.43 \cdot p_m = 452 \text{ MPa}.$$

This maximum stress was much lower than for fracture producing tests at the same load but a faster scratch velocity. It is interesting to note that in the slow constant load test the maximum stress calculated is almost identical to the yield stress of calcite; and the much higher value calculated for faster tests provides another indication of strain-rate sensitivity of the damage mechanisms.

These estimates of maximum contact stress, σ_{pp}, are thus of a magnitude sufficient to generate the damage features observed, but their resolution on the deformation systems also depended upon their relative orientation. Mean contact pressures, p_m, were also in the range of critical resolved shear stresses, so that if the deformation system was not ideally oriented with respect to the location of σ_{pp}, there may still have been orientations of normal stress on the contact surface which met the criteria for activation of slip or twinning.

In our tests, the normal force N was oriented perpendicular to r_1, but the conical shape of the indenter would have resulted in a large range of normal stress orientations on the actual contact area. For indentations, Evans and Goetze (1979) argued that because the plastic core and surrounding deformation zone have hemispherical symmetry, all slip systems may be active. During a scratch test, asymmetrical deformation is expected, but a wide range of slip systems must nevertheless be considered.

The conical shape of the contact area can be viewed as an infinite set of planes described by poles which are 45° from the indenter axis and which form a semicircle pointing toward the half-cone not in contact with the sample, as shown in a stereographic plot (figure 13). A compressive stress orientation which would produce a maximum resolution of stress on a particular deformation system would have its pole in the plane defined by the normal to the deformation plane and the slip or twinning vector, and this pole would be 45° from both the normal and the vector. Figure 13 shows that there is a pole within this semicircle which comes close to the ideal orientation with respect to $[f_2 \cdot r_3]$

slip on the f_1 plane. Thus the resolved shear stress on that system would be close to $\sigma_{con} \cdot \cos(45°) \cdot \cos(45°) = 0.5 \cdot \sigma_{con}$. Contact normal stress calculated above for minimum N and i associated with slip planes in our tests are $\sigma_{con} = p_m = 1.7$ Gpa and $\tau_{con} = 200$ MPa. Thus at the nearly ideal orientation the resolved shear stress exceeded the critical value of 200 MPa for that system from Turner et al (1954). There is no pole in the semicircle with an ideal orientation for twinning, but the low critical resolved shear stress for twinning on e means that it could easily have been activated at non-ideal orientations.

Discussion: Interpretation of Damage Features

The data in Table 9 summarize the relationships between hardness and damage features under varied test conditions. As discussed in the results section, three damage regimes can be defined according to characteristic damage features, where each regime represents a particular range of normal loads and apparent friction coefficients. Some of the damage features were further correlated with specific events in the mechanical data.

Engelder and Scholz (1976) have studied some of the effects of scratch velocity and normal load upon the apparent friction coefficient and damage features. Their experiments were done using spherical indenters, at normal loads measuring 10 to over 100 times the magnitude of the maximum loads in our scratch tests, but their scratch velocities, 1.0 and 50 $\mu m/s$, were similar to ours. They varied the minerals used for both sample and indenter, in order to test the influence of hardness contrast on damage features and the evolution of the friction coefficient. For an asperity with much higher hardness than the flat, as in our diamond indenter on calcite, they predicted a high μ_{app} due to the fact that the asperity would plow into the surface of the flat. Their scratch tests on Solnhofen limestone demonstrated that spherical asperities of hardness as low as apatite and as high as topaz all generated similar coefficients of friction, $\mu_{app} \sim 0.45$.

The damage on the limestone was not discussed in detail by Engelder and Scholz (1976), but for other materials tested at high normal loads they identified ring cracks along the scratches which could be correlated with features of the mechanical data. Their tests at high loads exhibited time-dependent stick-slip behavior, which they predicted would occur only under normal loads great enough to generate fracture under static indentation. The scratches produced by these tests contained series of partial ring cracks formed during slip events, which they interpreted to result from the high tensile stresses at the trailing edge of the contact between asperity and sample. Periodic full ring cracks were correlated with individual events when the tangential stress was rising, interpreted as time intervals of static contact.

Misra and Finnie (1979) described the production of cracks during indentation and scratch tests. They interpreted vertical median cracks as a reponse to loading, whereas lateral, or cone, cracks propagated from the median crack as the load was removed, sometimes reaching the surface, thereby releasing chips of material. Among results of scratch tests they observed a series of partial cone cracks forming behind a moving spherical indenter, or a series of chevron cracks when the moving indenter had a sharp point.

Engelder and Scholz (1976) considered full ring cracks along the scratch tracks to provide evidence that the normal load exceeded the value that would cause fracture during an indentation tests. This condition for formation of full ring cracks at high loads would be modified by increasing the time of contact, which would enhance the possibility of forming fractures. Increased contact time also increased the depth to which the indenter penetrated the sample, and thereby increased the contact area and, in their view, the apparent friction coefficient. Therefore they predicted that slower scratch tests would have higher coefficients of friction.

Our scratch tests also generated fractures when normal loads exceeded a certain value, approximately 25 mN, and the fractures produced during slow tests were larger than those from fast tests. However, increases in fracture size and scratch depth in our tests were associated with lower apparent friction coefficients. Another difference from the results of Engelder and Scholz is that among our damage features there is no apparent distinction between full and partial ring cracks. The cleavage fractures on r-planes resulting from our scratch tests on calcite are all similar to fractures produced by static indentation tests, and may be characterized as chevron cracks (Misra and Finnie, 1979). Along the scratches which exhibit fractures, some but not all fractures were correlated with events in the mechanical data. This suggests that even though they appear to be the same kind of feature, some fractures may have formed during a period of static contact while others were caused by high maximum contact stress during slip.

During our tests on sample 3, at v_s = 0.13 μm/s and a constant load of 35 mN, a more detailed correlation of changes in N, T and i suggests that scratch motion proceeded at a shallower depth with higher friction until twins developed and a fracture formed. Opening of the newly formed fracture in response to tensile stresses along the trailing edge of the indenter contact permitted an increase in scratch depth and a transient lowering of tangential load, T, which ended when scratch motion pulled the indenter up and out of the pit. The slow velocity meant that these features formed rapidly relative to the motion of the indenter, so that the opening of the fracture and resulting decrease in T occurred while the indenter was still close to its maximum depth within the pit. T then returned to its previous value as soon as the indenter moved beyond the fracture, while the indenter climbed up out of the pit more gradually. The actual removal of the large chip from the stepped portion of the pit may have occurred in response to the elastic recovery and closing of the fracture after the indenter had moved out of the pit.

At a faster scratch velocity, v_s = 100 μm/s and a constant load of 35 mN, smaller fractures due to shallower scratch depth did not have time to open and lower T. Instead the effect of the fracture was to increase scratch depth, and in this case T increased because the indenter suddenly had more material ahead of it which must be deformed in order for it to move ahead. Friction in this case only decreased when the indenter had climbed out to its original depth. For these reasons, the effect of scratch velocity upon friction during tests in Regime III was such that μ_{app} increased with an increase in velocity, even though this increase resulted in a shallower scratch depth.

The TEM observation of a planar feature forming ahead of the moving indenter suggests that in some cases the apparent slip-planes may actually form in compression rather than as a response to maximum tensile forces. As mentioned in the section where damage features were correlated with mechanical data, I was not able to associate slip-planes with individual events. The 2-5 μm spacing between these features may however be related to the effective contact time of the indenter on the sample during a scratch test. When the indenter plowed through calcite at constant load of 11 mN, generating slip-

planes where the mean scratch depth was 1.1 μm, the radius of the contact area projected perpendicular to N was approximately 1.5μm. The depth at which slip-planes began to form during constant penetration rate tests was 0.7 to 1.1 μm, with projected area radius of 1.1 to 1.5 μm. Within the resolution of our optical measurements and scratch depth data, scratch velocity did not have a measurable effect on this dimension. However, this depth and radius occurred at a higher load in the faster tests, because the increased velocity resulted in shallower scratch at a given normal load. The projected radius of contact represents the distance over which the indenter moved before the contact area was completely replaced. The similarity of this dimension to spacing between planar features observed optically and under TEM suggests that it may be a critical distance with respect to mini-stick-slip events. In a test conducted at v_s = 100 μm/s, the time taken for the indenter to travel this distance was a mere (1.5 μm)/(100 μm/s) = 0.15 seconds.. A longer contact time of 11.5 seconds would have occurred during tests at v_s = 0.13 μm/s. This length of time is comparable to the 15 second contact time used in static indentaion tests, which explains in part the reason that the slower tests had values of H_{nor} much closer to the static hardness than did the faster tests.

Discussion: Damage Zone Energy

Rough estimates of the scratch damage energy budgets for typical scratches in the three regimes are tabulated in Table 11. For each scratch, an energy input was calculated based upon the work represented by the product of the tangential force and the distance over which it moved the indenter. This work energy could then be compared with the energy stored in various damage features in order to determine assess the partitioning of energy into elastic, brittle or plastic mechanisms.

Elastic deformation in Regime I was estimated above as 50% of the total deformation, so I assume that 50% of the work energy was absorbed by that process. Additional energy would have been used to fracture the calcite in the production of gouge. For this calculation I assumed a gouge particle size of 10 nm and surface energy or 0.200 J/m^2. The sum of energies calculated for elastic and gouge producing mechanisms does not balance the work energy input, and the balance may have been used in minor plastic deformation or heat production. The energy budgets in Regime II include the added energy sink represented by slip planes. Table 11 shows calculations based upon alternative interpretation of these features as slip on the f-system and for twinning on the e-system. The energy calculated for twinning is smaller than the work input by four orders of magnitude and that for f-slip by three orders of magnitude. Elastic response is probably no more than 25% of the deformation, and gouge production measures about one order of magnitude smaller. Again, the sum of damage energies does not balance the work input. I calculated a separate energy budget for each velocity in Regime III. Because of the low value of surface energy in calcite, even in these scratches with extensive fracture, damage energy does not balance the work input. It appears that in Regime III, gouge production was the most significant use of damage energy. In all three regimes, dislocation densities within the damage zones may store significant damage energy. The results of Viswanathan and Kohlstedt (1996) also show a discrepancy between work energy input and damage energy calculated from observed features. Heat production would have been a possible energy sink, both in their experiments and in the ones I have examined.

Discussion: Plowing Friction

Analysis of our data for calcite displays a strong dependence of plowing friction on normal load, and at high normal load, a sensitivity to scratch velocity. In order to incorporate these results into models of friction on rock surfaces, it is necessary to understand the microphysics behind this response and to identify the effects of rate and state variables.

Normal load is likely to influence friction through its control of the depth at which the indenter plows through the calcite. Engelder and Scholz (1976) found this to be the case in their scratch tests on minerals, at a normal load of 3.5 N. For our constant load tests, performed at much smaller normal loads, Figure 14a shows a plot of scratch depth, i, versus normal load, N. The calcite clearly responded to higher normal forces on the indenter with greater scratch depths. For reference, a constant hardness curve for the indentation depth response to an indenter of our geometry was calculated and plotted assuming that $H_{nor} = H_k = 1.28$ GPa, the static Knoop indentation hardness. It can be seen that at N less than 6 mN, the calcite responded to normal load on a moving indenter with a hardness H_{nor} close to the static value and velocity did not appear to have a measurable effect upon scratch depth. At higher loads, an increase in scratch velocity increased the effective hardness H_{nor}, as shown by the decrease in scratch depth for a given load. This increase was most dramatic for the highest normal load, N = 36 mN.

Figure 14b shows a similar plot for two typical constant penetration rate tests. The increase in scratch depth with increasing N for each test generally is very close to the trend shown for the constant load tests as a whole. Below 5 mN, scratch hardness H_{nor} was essentially the same as for static indentations. At N > 5 mN, the calcite responded to the slower velocity with a lower effective indentation hardness H_{nor}, resulting in a deeper scratch. As the normal load continued to increase, data from scratches performed at the two velocities diverged, suggesting a lower H_{nor} at slower v_s.

The extensive literature on the interpretation of static indentation hardness demonstrates that the shape of the indenter has an influence on stress distribution due to

normal load at the contact of the indenter with the material being tested. Asperity shape must therefore be considered a possibly significant factor in the relationship between normal force and scratch depth during scratch tests. One way of expressing the three-dimensional shape of the indenter is to calculate the ratio between $A_{\perp T}$ and $A_{\perp N}$, the projections of the contact area perpendicular to the tangential and normal forces, respectively. For a simple cone of included angle 2α, the ratio would be constant:

$$A_{\perp T}/A_{\perp N} = (2/\pi)\cdot\cot\alpha$$

For a hemispherical asperity of radius r_t, the ratio would evolve to a maximum depth of $i = r_t$, according to:

$$A_{\perp T}/A_{\perp N} = r_t^2\cdot(2\cdot\cos^{-1}((r_t\text{-}i)/\ r_t)\text{-}\sin(2\cdot\cos^{-1}((r_t\text{-}i)/r_t)))/\pi\cdot(2\cdot r_t\cdot i\text{-}i^2)$$

As scratch depth increased, the contact shape of our rounded conical indenter, with $\alpha = 45°$ and spherical tip radius $r_t = 1.0$ μm, initially evolved according to the equation for a hemispherical indenters, and after reaching a scratch depth, $i = 0.293$ μm:

$$A_{\perp T}/A_{\perp N} = (2/\pi)\cdot(\cot\alpha\text{-}(K2/((i+K1)^2\cdot\tan^2\alpha)))$$

where K1 and K2 are constants for indenter geometry of a given α and r_t:

$$K1 = r_t\cdot((\cos^2\alpha/\sin\alpha)\text{-}1+\sin\alpha)$$

$$K2 = r_t^2\cdot((\cos^3\alpha/\sin\alpha)\text{-}((\pi/2\text{-}\alpha)\text{-}\cos\alpha)/2)$$

A plot of $A_{\perp T}/A_{\perp N}$ versus i for our indenter geometry is given in Figure 15. The plot demonstrates that with increasing depth the effect of the spherical tip diminished and the ratio approaches a constant value, based on the conical portion of the indenter.

The relationship between $A_{\perp T}/A_{\perp N}$ and i expresses the three-dimensional response at contact of a solid surface to a given indenter geometry. For a larger tip radius, the spherical geometry dominates to a greater depth, thus increasing the range of i(N) over which $A_{\perp T}/A_{\perp N}$ evolves significantly. Where the conical portion of the indenter makes contact with the solid, the effect of the spherical tip gradually diminishes as $A_{\perp T}/A_{\perp N}$

approaches an asymptotic value with increasing i. Indenters with cones of larger included angles generate lower asymptotic values of $A_{\perp T}/A_{\perp N}$.

Figure 16a displays a plot of the apparent friction coefficient μ_{app} versus $A_{\perp T}/A_{\perp N}$ calculated from our constant load test data. Figure 16b is a similar plot for the results from two typical constant penetration rate tests. The large scatter in the data on this plot is likely to be due in part to uncertainties in i data, which are magnified in calculating areas. Nevertheless, the shape of indenter contact area, as expressed by $A_{\perp T}/A_{\perp N}$, clearly influences μ_{app}.

If μ_{app} can be expressed as a linear function of $A_{\perp T}/A_{\perp N}(N)$ at a given scratch velocity, then it would have the form:

$$\mu_{app} = m \cdot (A_{\perp T}/A_{\perp N}) + b$$

For all data for which $v_s = 100$ μm/s, the slope suggested by a rough evaluation of the plot is m ~ 3.6 and the intercept b ~ -0.29. A micromechanical interpretation of these values may determine whether the linear function represents the data appropriately.

According to Bowden and Tabor (1986) friction of an indenter or asperity plowing into a perfectly plastic surface would obey a linear expression:

$$\mu = T/N = \mu_{adh} + (H_{tan}/H_{nor}) \cdot (A_{\perp T}/A_{\perp N})$$

For functions implied by plots in Figures 17a and 17b, this would require that the slope equals the hardness ratio, $H_{tan}/H_{nor} = m = 3.6$. and the intercept represents adhesion friction, $\mu_{adh} = b = -0.29$. Because the slope m is greater than 1.0, this implies that $H_{tan} \gg H_{nor}$, which does not seem likely, since the proximity of the surface means that the effective confining pressure for the tangential loading condition is less than for the normal load. However, it could be the case if the calcite were hardening ahead of the moving indenter through accumulation of dislocations. Viswanathan (personal communication) reported hardening ahead of an indenter in scratch tests on olivine, garnet and calcite in a related study. As described in more detail above, my TEM observations also indicated

hardening ahead of the indenter in calcite, but its magnitude may in some cases have been less than the hardening occurring beside and below the indenter.

The negative value for intercept b is more difficult to explain, because it appears to imply that the shear strength of the calcite is less than zero. One possible explanation is based upon the argument presented above in the analysis of contact friction. Because our geometry and data result in $(\alpha+\theta) \geq 90°$, the shear stress on the contact surface may have been downward, resulting in a component of motion which opposed the scratch velocity. Substituting contact friction for adhesive friction, the net effect could have meant that μ_{adh} = $\mu_{con} \leq 0$. In either case, μ_{con} is not likely to have had a direct additive effect on μ_{app}.

A different and simpler interpretation of Figures 16a and 16b is provided by recognizing that the plot can be divided into the three scratch damage regimes identified above in Figure 8. For each regime, different mechanisms are operative and therefore different constants may obtain. Superposition of these regimes upon data from Figures 16a and 16b is shown in Figure 16c. Because the effect of μ_{con} is intimately connected with measurement of hardness, it appears appropriate to assume that its effects are included in H_{nor} and H_{tan} rather than as a separate additive term. In this case, b = 0 and for each regime:

$$\mu_{app} = (H_{tan}/H_{nor}) \cdot (A_{\perp T}/A_{\perp N})$$

In Regime I, when the calcite responded to a low normal load on the indenter through elastic and minor plastic deformation, accompanied by submicron gouge removal, average values suggest that:

$$\mu_{app} \sim 0.5 \cdot (A_{\perp T}/A_{\perp N}) \text{ and thus } H_{tan} \sim 0.5 \cdot H_{nor}$$

After the threshold at 5 to 7 mN was reached, in Regime II, localized slip was added to the deformation mechanisms. The particular orientation of the slip plane and vector changed the ratio of hardnesses so that:

$$\mu_{app} \leq (A_{\perp T}/A_{\perp N}) \text{ and thus } H_{tan} \leq H_{nor}$$

When brittle fracture and twinning were active damage mechanisms, in Regime III, the expression remained:

$$\mu_{app} \geq (A_{\perp T}/A_{\perp N}) \text{ and thus } H_{tan} \geq H_{nor}$$

The normal load can be seen to have influenced μ_{app} in two ways. It controlled the scratch depth and thus $A_{\perp T}/A_{\perp N}$. In addition, it determined which damage mechanisms were operative, which in turn controlled the magnitude of H_{tan}/H_{nor}. In an anisotropic mineral like calcite, the orientations of deformation planes and vectors relative to applied forces are likely to have an effect on H_{tan}/H_{nor}.

The plots in Figure 16 also exhibit a degree of sensitivity of μ_{app} to v_s. In Regime II, tests done at 6 mN produced deeper scratches, which therefore show higher values of $A_{\perp T}/A_{\perp N}$, at slow v_s, but this does not appear to have had an effect on μ_{app}. In contrast, Regime III tests at both velocities produced scratch depths very different from each other, as shown in Figure 14a, but in both cases great enough to have nearly reached the same self-similar $A_{\perp T}/A_{\perp N} = (2/\pi)\cdot\cot\alpha = 0.637$. Even so, for nearly all the slow tests at the high constant load, μ_{app} was lower than that for the fast tests. As observed above in the μ_{app} versus N plot, velocity sensitivity only occurred where damage mechanisms included brittle fracture and twinning.

Given this interpretation of our data it would be useful to determine how the variables $A_{\perp T}/A_{\perp N}$ and H_{tan}/H_{nor} could be expressed in terms of a rate and state law. For friction controlled by adhesive contacts, Dieterich and Kilgore (1994) suggested that values of S and P can be used to calculate parameters in the rate and state equation. Where S is a function of velocity and P a function of elapsed time or state, they showed that for a single adhesive contact or a surface with many adhesive asperities of equal strength:

$$S = S_1 + S_2 \cdot \ln(1+v/v^*)$$

$$P = P_1 + P_2 \cdot \ln(1+\theta/\theta^*)$$

$$\mu = S \cdot P \sim S_1 \cdot P_1 + S_2 \cdot P_1 \cdot \ln(1+v/v^*) + S_1 \cdot P_2 \cdot \ln(1+\theta/\theta^*)$$

For the plowing friction expression, the arguments above suggest that I could propose similar expressions for (H_{tan}/H_{nor}) and $(A_{\perp T}/A_{\perp N})$. At shallow penetration, $A_{\perp T}/A_{\perp N}$ measures the three-dimensional response of the sample to a given indenter geometry under increasing normal load. However, at deeper penetration, where conical geometry of the indenter dominates the shape function, further increases in N and I have a diminishing effect on $A_{\perp T}/A_{\perp N}$. Our indenter geometry therefore can be defined by an asymptotic or steady-state value of $A_{\perp T}/A_{\perp N} = (2/\pi) \cdot \cot\alpha$. The relationship between N and the apparent friction coefficient, μ_{app}, appears to vary over the conditions represented by our tests, and can be divided into three regimes.

Regime I is defined at low loads which produce smooth shallow scratches, and where both i and $A_{\perp T}/A_{\perp N}$ depend on normal load, N, but appear to be independent of scratch velocity, v_s. Here, μ_{app} is also dependent upon N but not v_s. For our indenter geometry on calcite, a critical normal load of 5-7 mN, associated with a scratch depth of ~1.0 μm, signals the initiation of Regime II, with localized slip on f-planes. Here both $A_{\perp T}/A_{\perp N}$ and i are sensitive to N, and slightly sensitive to v_s, but μ_{app} appears to depend only upon N. At high loads in Regime III, $A_{\perp T}/A_{\perp N}$ is close to the steady-state value, where it is relatively independent of both N and v_s,. It thus does not represent the dependence of scratch depth, i, upon N and v_s. From these observations, I conclude that $A_{\perp T}/A_{\perp N}$ represents the state of sliding for an individual asperity, as controlled by elapsed time through asperity shape and N. This ratio is a weak function of scratch velocity only in Regime II. In Regime I, $A_{\perp T}/A_{\perp N}$ is a function of N, and in Regime III it is a constant

The other variable in the plowing friction law, H_{tan}/H_{nor}, also evolves toward an apparently constant value, in this case close to 1.0. However, this steady-state value is quite sensitive to scratch velocity. Interpretation of H_{tan}/H_{nor} in Regime I is difficult, due to the large fluctuations in data at low loads. Here, the mean value of $H_{tan}/H_{nor} \sim 0.5$ may reflect the stress distribution for a shallow rounded contact surface, which may be distinct from that for the conical geometry. Scratches produced in Regime II show H_{tan}/H_{nor} approaching 1.0 which value may itself be controlled by shape function $A_{\perp T}/A_{\perp N}$, as well

as by μ_{con} and anisotropy in the calcite yield surface. This increased H_{tan}/H_{nor} is associated with initiation of the damage features described as f-slip planes. A possible reason for this association is that resolved stresses had reached an orientation which maximized the resolved shear stress on the f-system, while the mean pressure, p_m had increased to produce high enough stress to activate that system. Throughout Regime II, H_{tan}/H_{nor} may have had a relatively constant value, slightly less than 1.0, for a given scratch velocity. It may or may not have been sensitive to v_s. Although each hardness value represents a potentially strain-rate dependent response of calcite to stress imposed by the indenter, the ratio between hardnesses may be less strain-rate dependent. This conclusion is supported by the fairly uniform distribution of dislocations ahead of and alongside the scratch, according to my TEM observations.

In Regime III, the ratio H_{tan}/H_{nor} displays sensitivity to scratch velocity, v_s. Initiation, propagation and Mode I opening of r_f fractures, accompanied by twinning, were associated with drops in both normal and tangential stress. The relative magnitude and sequential timing of these drops resulted in changes in μ_{app}. It appears that at slow v_s pit formation temporarily lowered μ_{app}, whereas at fast v_s it caused a brief, abrupt increase in μ_{app}. It is therefore reasonable to suggest that H_{tan}/H_{nor} is a function of v_s in Regime III.

With increasing N, $A_{\perp T}/A_{\perp N}$ reaches a constant value, resulting in a diminishing sensitivity to state, whereas the velocity dependence of μ_{app} increases through the evolution of H_{tan}/H_{nor}. A distinct law for each regime would comprise different constants and functions. In Regime I:

$$A_{\perp T}/A_{\perp N} = (A_{\perp T}/A_{\perp N})_1^{\ I} + (A_{\perp T}/A_{\perp N})_2^{\ I} \cdot f^I(N, H_{nor})$$

$$H_{tan}/H_{nor} = (H_{tan}/H_{nor})_1^{\ I} + (H_{tan}/H_{nor})_2^{\ I} \cdot g^I(A_{\perp T}/A_{\perp N})$$

In Regime II:

$$A_{\perp T}/A_{\perp N} = (A_{\perp T}/A_{\perp N})_1^{\ II} + (A_{\perp T}/A_{\perp N})_2^{\ II} \cdot f^{II}(N, H_{nor})$$

$$H_{tan}/H_{nor} = (H_{tan}/H_{nor})_1^{\ II} + (H_{tan}/H_{nor})_2^{\ II} \cdot g^{II}(v_s, A_{\perp T}/A_{\perp N})$$

In Regime III:

$$A_{\perp T}/A_{\perp N} = (A_{\perp T}/A_{\perp N})_1{}^{III} = (2/\pi)\cdot\cot\alpha$$

$$H_{tan}/H_{nor} = (H_{tan}/H_{nor})_1{}^{III} + (H_{tan}/H_{nor})_2{}^{III}\cdot g^{III}(v_s)$$

Without slip rate stepping experiments, our data are not sufficient to determine the empirical constants, nor whether the functions are logarithmic. Changes in mechanisms may in fact result in a discontinuous function, such that different constants obtain for each regime. Nevertheless, it is possible to suggest that, for an individual conical asperity with a spherical tip, scratch tests within a particular regime on calcite generate an apparent friction coefficient according to an expression of the form:

$$\mu_{app} = (H_{tan}/H_{nor})\cdot(A_{\perp T}/A_{\perp N})$$

$$\sim(H_{tan}/H_{nor})_1\cdot(A_{\perp T}/A_{\perp N})_1+(H_{tan}/H_{nor})_1\cdot(A_{\perp T}/A_{\perp N})_2\cdot f(N,H_{nor})+(H_{tan}/H_{nor})_2\cdot(A_{\perp T}/A_{\perp N})_1\cdot g(v_s)$$

where $(H_{tan}/H_{nor})_i$ and $(A_{\perp T}/A_{\perp N})_i$ and the precise functions would be determined empirically. It appears that this relation would pertain to any asperity shape whose curvature relative to N is zero except at its rounded tip. Constants would vary to account for variations in included angle and symmetry with respect to N. For example, at pyramidal asperities with rounded tips $(A_{\perp T}/A_{\perp N})_{steady\ state} = \cot\alpha$.

The form of this expression contains an important property for a conical asperity with a spherical tip, as well as for asperities with related geometries: plowing friction does not depend upon contact area directly, but upon two ratios which may approach steady-state values. The evolution of these ratios may not be continuous with increasing normal load or scratch velocity, and therefore the identification of the damage regime controlling deformation may be critical to the application of the correct expression and constants. Because many asperities result from fracture, the flat-sided geometry with a worn, rounded apex may be a good approximation for a single asperity in a geological context

Asperities on a fault surface vary in shape, dimensions and degree of contact with the opposing surface. Each one may be subject to internal deformation and removal by fracture, while at the same time passing through a series of adhesion or plowing regimes. The presence of gouge, or wear particles, provides additional possible damage

mechanisms. Therefore the plowing friction expression I have proposed will not alone be applicable to friction on the entire surface. However, it may help to explain certain transitions in sliding behavior. Sin, Saka and Suh (1979) have examined the evolution of friction on surfaces which generates wear particles. In their experiments on sliding between metal surfaces, they identified six regimes, each of which represented a combination of deformation mechanisms. Regimes where plowing was significant exhibited a gradually increasing coefficient of friction, as would be predicted by my expression for surfaces making initial contact. A more constant value of the coefficient of friction occurred where further evolution involved the removal of asperities, the formation of wear particles and an increase in adhesion where surfaces became flatter.

Friction generated by geological materials also displays evidence for the existence of distinct slip regimes. In their experiment on the frictional sliding of dolomitic marble, Weeks and Tullis (1985) found velocity strengthening behavior, in agreement with our results on calcite. The normal stress, σ_n, = 75 MPa, maintained in their experiment is comparable to stresses of geological significance (Hickman, 1991). If asperities similar to our indenter were spaced 20 μm apart (one asperity per 400 μm^2) 75 MPa would produce a normal load, N = 30 mN, on each asperity, comparable to the normal load at which we observed velocity strengthening. In order to model their results using a rate and state law, Weeks and Tullis (1985) found that different parameters were required to describe slip behavior at different velocities, which suggested a velocity influence on deformation regimes. They also identified a transition velocity of 0.1 μm/s, below which unstable sliding occurred, with $\Delta\mu \sim 0.005$. Our high normal load experiments conducted at v_s = 0.13 μm/s displayed oscillations of a magnitude $\Delta\mu_{app} \leq 0.2$, and at v_s = 100 μm/s, oscillations were $\Delta\mu_{app} \leq 0.05$. The difference in stability was likely due to the difference between considering the behavior of an individual asperity and a population of asperities.

Regime controlled sliding on Westerly granite was also observed by Kilgore et al (1993), who performed sliding experiments for a wide range of velocities, from 10^{-4} to 1000 μm/s. Normal stresses on the surfaces were 5 < σ_n < 150 MPa. The results from their lower velocity experiments showed velocity weakening for $v_s \leq 1$ μm/s at all normal

stresses tested. At faster velocities their results diverged. σ_n > 30 MPa continued to generate velocity weakening for v_s > 10 μm/s. However, velocity neutral behavior was observed at σ_n = 15 Mpa and velocity strengthening at σ_n = 5 Mpa for the higher velocities. The authors suggested that the transition at v_s = 1 μm/s, above which frictional behavior was sensitive to σ_n, may have represented a change in relative contributions of different deformation mechanisms. In our tests on a different material, calcite, single asperities exhibited velocity neutral behavior at smaller loads, and velocity strengthening at higher loads, a trend which also appears to have been due to changes in mechanisms, but which is opposite in sense to that reported for granite by Kilgore et al. (1993).

An accurate expression for friction due to asperity plowing may also contribute to our understanding of the relationship between fault strength and dilation across a fault during sliding. Marone (1991) observed that dilation in gouge layers could occur under load in the absence of shear. Beeler and Tullis (1996) examined the increase in indentation depth and contact area with time for a stationary indenter, as a model for shear independent dilation. They developed an expression for the energy of friction on a dilating fault which recognizes the separate contributions of elapsed time and shear to the strength of the fault. They commented that their model does not account for the velocity strengthening observed in experiments with sliding on gouge-filled faults. If the strength of faults depends linearly on the contact area of plowing asperities, as they and other workers (i.e., Engelder and Scholz, 1976) have assumed, then velocity weakening would be predicted, due to decreased effective time of contact at faster velocities. In contrast to this prediction, our data at the highest loads displayed velocity strengthening, and my expression shows how a coefficient of friction may become independent of scratch depth, or dilation, when the ratio $A_{\perp T}/A_{\perp N}$ reaches a steady-state value.

Application of our results to the behavior of fault surfaces will require a statistical evaluation of the competing effects of coexisting damage mechanisms for a population of asperities of varied penetration depths. I believe that the simple plowing friction expression I have presented will be a useful tool for incorporating rate and state effects due to asperity plowing into constitutive laws for frictional sliding on faults.

Conclusions

Results from asperity plowing tests performed on calcite, at normal loads, 3 mN < N < 35 mN and scratch velocities, v_s, = 0.13, 1 or 100 μm/s, suggest that three scratch damage regimes can be identified within this range of conditions. Each regime corresponds to different partitioning between elastic, brittle and plastic damage mechanisms. Regime I occurred at N < 5 mN, where gouge removal and elastic recovery were observed or inferred. In Regime II, normal loads of 5 mN < N < 14 mN generated localized slip or twinning in addition to the damage features produced in Regime I. The appearance of pits comprising fractures and twinning at 25 < N ≤ 35 mN characterized Regime III.

Our results also suggested that the plowing friction coefficient can be described as the product of a hardness ratio and an area ratio:

$$\mu_{app} = T/N = (H_{tan}/H_{nor}) \cdot (A_{\perp T}/A_{\perp N})$$

where $A_{\perp N}$ is the indenter contact area projected normal to N, $A_{\perp T}$ is the contact area projected normal to T, plowing hardness is H_{tan}, = $T/A_{\perp T}$, and scratch hardness, H_{nor} = $N/A_{\perp N}$. I found that the evolution of the ratio, $A_{\perp T}/A_{\perp N}$ was a function of asperity geometry, whereas H_{tan}/H_{nor} was controlled by the nature of damage produced under the given conditions, as well as by $A_{\perp T}/A_{\perp N}$. In our tests the asperity was a cone with a rounded tip, for which $A_{\perp T}/A_{\perp N}$ increased rapidly at shallow depths, later evolving toward a nearly constant value. In Regime I scratch depth and the resulting value of $A_{\perp T}/A_{\perp N}$ were primarily a function of N. These dimensional factors were influenced by N and possibly v_s in Regime II. Regime III occurred at scratch depths great enough that $A_{\perp T}/A_{\perp N}$ could be considered constant.

The ratio H_{tan}/H_{nor} was a more complicated function of v_s and v_t, N and contact friction between asperity and sample. It also likely responded to the anisotropy of the yield surface in calcite. Our tests displayed hardness ratios which reached constant values when N, v_s and geometry were kept constant. In all regimes, H_{tan}/H_{nor} increased with increases in N. In Regime III, H_{tan}/H_{nor}, and therefore μ_{app}, had a positive correlation with v_s.

References.

Beeler, N. M.; Tullis, T. E., 1996. The roles of time and displacement in velocity dependent dilation of faults. (submitted for publication)

Black, A.J.; Kopalinsky, E.M.; Oxley, P.L.B., 1988. An investigation of the different regimes of deformation which can occur when a hard wedge slides over a soft surface: the influence of wedge angle, lubrication and prior plastic working of the surface. Wear. 123:97-114.

Bowden, F.P.; Tabor, D., 1986. The Friction and Lubrication of Solids. Oxford University Press.

Challen, J.M.; Oxley, P.L.B., 1979. An Explanation of the Different Regimes of Friction and Wear Using Asperity Deformation. Wear 53:229-243

DeBresser, J.H.P., 1991. Intracrystalline Deformation of Calcite. PhD. Thesis, Rijksuniversiteit te Utrecht.

Dieterich, J.H.; 1979. Modeling of rock friction: 1. Experimental results and constitutive equations. J. Geophys. Res. 84:2161-2168.

Dieterich, J.H.; Kilgore, B.D., 1994. Direct observation of frictional contacts: New insights for state-dependent properties. Pure Appl. Geophys.

Engelder, J.T., 1976. Effect of Scratch Hardness on Frictional Wear and Stick-Slip of Westerly Granite and Cheshire Quartzite. In Proceedings of NATO Advanced Study Institute on Petrophysics. John Wiley, New York.

Engelder, J.T.; Scholz, C.H., 1976. The Role of Asperity Indentation and Ploughing in Rock Friction - I: Asperity Creep and Stick-Slip. Int. J. Rock Mechanics, Mineral Science and Geomechanics Abstracts. 13:149-154.

Engelder, J.T.; Scholz, C.H., 1976. The Role of Asperity Indentation and Ploughing in Rock Friction - II: Influence of Relative Hardness and Normal Load. Int. J. Rock Mechanics, Mineral Science and Geomechanics Abstracts. 13:155-263.

Evans, B., 1984. The effect of temperature and impurity content on indentation hardness of quartz. J. Geophys. Res. 89:4213-4222.

Evans, B.; Goetze, C., 1979. The temperature variation of hardness of olivine and its implication for polycrystalline yield stress. J. Geophys. Res. 84:5505-5524.

Hickman, S.H., 1991. Stress in the lithosphere and the strength of active faults. U. S. Natl. Rep. Int. Union. Geod. Geophys. 1987-1990, Rev. Geophys. 29:759-775.

Jaeger, J.C.; Cook, N.G.W., 1976. Fundamental of Rock Mechanics. London: Chapman and Hall.

Johnson, K.L.; 1970. The correlation of indentation experiments. J. Mech. Physics Solids 18:115-126.

Johnson, K.L., 1985. Contact Mechanics. Cambridge University Press.

Kilgore, B.D.; Blanpied, M.L.; Dieterich, J.H.; 1993. Velocity dependent friction of granite overa wide range of conditions. Geophys. Res. Lett. 20:903-906.

Kohlstedt, D.L.; Evans, B.; Mackwell, S.J.; 1995. Strength of the lithosphere: Constraints imposed by laboratory experiments. J. Geophys. Res. 100:17,587-17,602.

Lawn, B.; Wilshaw, R., 1975. Review: indentation fracture: principles and applications. J. Mater. Sci. 10: 1049-1081.

Linker, M.F.; Dieterich, J.H., 1992. Effects of variable normal stress on rock friction: observations and constitutive equations. J. Geophys. Res. 97:4923-4940.

Marone, C.J., 1991. A note on the stress-dilatancy relation for simulated fault gouge. Pure appl. Geophys. 137:409-419.

Misra, A.; Finnie, I., 1979. On the scribing and subsequent fracturing of silicon semiconductor wafers. J. Mater. Sci. 14:2567-2574.

Rabinowicz, E., 1965. Friction and Wear of Materials. John Wiley and Sons, Inc.

Scholz, C. H., 1990. The Mechanics of Earthquakes and Faulting. Cambridge University Press.

Sin, H; Saka, N.; Suh, N.P., 1979. Abrasive wear mechanisms and the grit size effect Wear 55:163-190.

Tabor, 1951. The Hardness of Metals. Oxford University Press.

Tolansky, S., 1955. An Introduction to Interferometry. John Wiley and Sons, Inc.

Tullis, T.E., 1986. Friction and faulting--Editor's note, Pure Appl. Geophys. 124:375-381

Turner, F.J.; Griggs, D.T; Heard, H., 1954. Experimental Deformation of Calcite Crystals. Bulletin, Geol. Soc. America 65:883-934.

Viswanathan, S.; Kohlstedt, D.L,, 1966. Evolution of friction coefficient during sliding of a single asperity on semi-brittle mineral surfaces. EOS 77:F696.

Weeks, J.D.; Tullis, T.E., 1985. Frictional Sliding of Dolomite: A Variation in Constitutive Behavior. J. Geophys. Res. 90:7821-7826.

Williams, J.A., 1996. Analytical models of scratch hardness. Tribology Int. 29: 675-694.

Wu, T.W., 1991. Microscratch and load relaxation tests for ultra-thin films. J. Mater. Res. 6: 407-426.

List of Tables

Legend for Tables 3 and 5:

Scratch types: A = smooth, even width; B = finely notched, even width; C = smooth, tapered width increases toward c^-; D = smooth, tapered width increases toward c^+; E = coarsely notched, even width; F = notched, tapered width increases toward c^-; G = notched, tapered width increases toward c^+.

End types: A = rounded with slight taper in scratch near end; B = rounded with small fracture; C = pit with r fracture and twinning; D = slightly tapered with no other feature; E = sharp; F = blunt.

Wedge types: A = pit with r fracture and twinning, chip removed; B = partial r fracture and twinning or slip-planes; C = slip plane.

TABLE 1: SYMBOLS

Variables controlled or measured during experiments:

v_i = indentation rate, measured in nanometers/second (nm/s)

v_s = scratch velocity, measured in microns/second (μm/s)

i = indentation or scratch depth, measured in microns (μm)

SD = scratch distance, measured in microns (μm)

t = elapsed time, measured in seconds (s)

N = normal force, measured in Newtons, converted to milliNewtons (mN)

T = tangential force, measured in Newtons, converted to milliNewtons (mN)

Friction coefficients:

μ_{app} = T/N = apparent friction coefficient for a single asperity

$\theta = \tan^{-1}(\mu_{app})$

μ_{con} = contact friction coefficient between indenter and sample at area of contact

Areas:

A_{con} = actual contact area between indenter and sample (μm^2)

$A_{\perp N}$ = contact area projected onto a plane perpendicular to N (μm^2)

$A_{\perp T}$ = contact area projected onto a plane perpendicular to T (μm^2)

Hardnesses and stresses:

$H_v = N/A_{con, Vickers} = H_{ind} \cdot \sin(68°)$ = Vickers hardness (GPa)

$H_k = N/A_{\perp N, Knoop} = H_{ind}$ = Knoop hardness (GPa)

$H_{ind} = N/A_{\perp N}$ = static indentation hardness (GPa)

$H_{nor} = N/A_{\perp N}$ = normal hardness during scratch test (GPa)

$H_{tan} = T/A_{\perp T}$ = tangential hardness during scratch test (GPa)

p_m = mean indentation pressure (GPa or MPa)

σ_n = normal stress on surface (MPa)

τ = shear stress on surface (MPa)

S = k = shear strength of asperity (MPa)

$P \sim 1/H_{ind}$ = inverse normal indentation strength of asperity (1/MPa)

σ_{con} = contact normal stress at asperity (MPa)

τ_{con} = contact shear stress at asperity (MPa)

σ_{pp} = maximum contact stress at asperity (MPa)

Other quantities:

2α = indenter included angle (°)

γ = surface energy (J/m^2)

v = Poisson's ratio

Calcite deformation systems (hexagonal structural cell):

c = <0001> =axis of 3-fold rotational symmetry

e^+_i = {(-1)018}<40(-4)1> = low-temperature twinning system

f_i = {(-1)012}<(-2)20(-1)> = low temperature slip system

r_i = {10(-1)4} = rhombohedral cleavage plane

TABLE 2: Experimental conditions

sample	scratch numbers	type of test	scratch velocity (μm/s)	normal load (mN)	measurements: optical	interfer	TEM	tilt (μm/μm)
CAT1	1 to 7	CL	0.13	6				0.0107
CAT2	1 to 9	CL	100	6				0.0041
CAT3	1 to 10	CL	0.13	35	(X)			-0.0144
CAT4	1 to 10	CL	100	35	X			-0.0013
CAT7	1 to 9	CL	100	3	X			-0.0063
CAT8	1 to 9	CL	100	3	X	X		-0.0036
CAT9	1 to 11	CL	100	11	X		X	-0.0120
CAT10	1 only	profile	1		X	X		-0.0113
	2 to 14	CPR	1	0 to 1	X	X	X	-0.0113
CAT11	1 to 14	CPR	1	0 to 2	X			-0.0126
CAT12	1 only	profile	1		X	X		0.0015
	2 to 8, 1	CPR	1	0 to 1	X	X		0.0015
	9, 10	anom.	1	0 to 3	X	X		0.0015
CAT13	1 only	profile	100		X	X		-0.0050
	2 to 10	CPR	100	0 to 1	X	X		-0.0050
CAT14	1 only	profile	100		X			-0.0036
	2 to 14	CPR	100	0 to 1	X			-0.0036

LEGEND:
CL = constant load test
CPR = constant penetration rate test
profile = test at ˜zero load to determine sample tilt
anom = anomalous test

TABLE 3: DAMAGE FEATURES

width magnification = (40x objective)*(16x ocular)=640x; 1grat=7.14 microns
length magnification = (16x objective)*(16x ocular)=256x; 1grat=17.5 microns

sample <CAT 7> constant load = 3 mN, scratch velocity = 100 microns/second

scratch:						ends:				features:				
number	type	width(grat)	width(μm)	length(grat)	length(μm)	type		width(grat)	width(μm)	quantity	type	width(grat)	width(μm)	spac(grat)	spac(μm)
7	1 A |	0.10	0.6	7.15	125 A	c+	0.55	3.2	0					
	v					B	c-	0.30	1.7						
7	2 A |	0.10	0.6	6.90	121 C		1.50	8.7	0						
	v			1.10	19 D		0.25	1.5							
7	3 A |	0.15	0.9	7.15	125 A		0.60	3.5	0						
	v				0 D		0.30	1.7							
7	4 A |	0.10	0.6	7.20	126 A		0.55	3.2	0						
	v				D										
7	5 A |	0.15	0.9	7.00	123 C		2.20	12.8	0						
	v			0.60	11 A										
7	6 A |	0.20	1.4	7.15	125 A		0.85	6.1	0						
	v				A		0.55	3.9							
7	7 A |	0.20	1.4	7.15	125 A		0.60	4.3	0						
	v				A		0.30	2.1							
7	8 A |	0.20	1.4	7.15	125 A		0.80	5.7	0						
	v				A		0.35	2.5							
7	9 A |	0.20	1.4	7.20	126 A		0.90	6.4	0						
	v				A		0.35	2.5							

sample <CAT 8>   constant load = 3 mN, scratch velocity = 100 microns/second

scratch:							ends:				features:				
number	type	width(grat)	width(μm)	length(grat)	length(μm)	type		width(grat)	width(μm)	quantity	type	width(grat)	width(μm)	spac(grat)	spac(μm)
8	1 A |	0.20	1.4	7.20	126	A	c+	0.70	5.0	0					
	v					A	c-	0.40	2.9						
8	2 A |	0.20	1.4	7.20	126	A	c+	0.60	4.3	0					
	v					A	c-	0.40	2.9						
8	3 A |	0.20	1.4	7.15	125	A	c+	0.70	5.0	0					
	v					A	c-	0.40	2.9						
8	4 A |	0.20	1.4	7.20	126	A	c+	0.85	6.1	0					
	v					A	c-	0.45	3.2						
8	5 A |	0.20	1.4	7.20	126	A	c+	0.75	5.4	0					
	v					A	c-	0.45	3.2						

sample <CAT 9>   constant load = 11 mN, scratch velocity = 100 microns/second

scratch:						ends:			features:					
number	type	width(grat)	width(μm)	length(grat)	length(μm)	type	width(grat)	width(μm)	quantity	type	width(grat)	width(μm)	spac(grat)	spac(μm)
9	1 D |	0.55	3.9	6.40	112	E c-	0.00	0.0	3	A	2.80	20.0	0.65	4.6
	v					D c+	1.10	7.9	3	A	1.60	11.4	0.60	4.3
									9	B	1.10	7.9	0.45	3.2
9	2 E ∧	0.70	5.0	7.00	123	C	4.00	28.6	3	B	1.80	12.9	0.60	4.3
	|			3.00	53	C	8.60	61.4	11	C	1.80	12.9	0.60	4.3
9	3 B ∧	0.35	2.5	7.05	123	C	2.75	19.6	1	A	1.10	7.9		0.0
	|			0.80	14	C	2.30	16.4						
9	4 B ∧	0.40	2.9	6.80	119	F	0.40	2.9	3	C	0.80	5.7	0.50	3.6
	|			1.40	25	C	2.95							
9	5 B ∧	0.50	3.6	6.95	122	A	0.90	6.4	1	A	1.00	7.1		
	|			1.10	19	C	2.30		2	C	0.75	5.4		
9	6 B ∧	0.45	3.2	6.70	117	C	3.70	26.4	4	C	0.80	5.7	0.40	2.9
	|			1.55	27	C	6.30	45.0	5	C	0.80	5.7	0.40	2.9
9	7 B ∧	0.50	3.6	6.70	117	C	3.40	24.3	0					
	|			1.65	29	C	3.60	25.7						
9	8 B ∧	0.45	3.2	7.65	134	F	0.45	3.2	5	C	0.85	6.1		
	|			0.85	15	C	4.00	28.6						
9	9 B ∧	0.40	2.9	6.40	112	F	0.40	2.9	0					
	|			1.95	34	C	3.80	27.1						
9	10 B ∧	0.40	2.9	6.50	114	C	4.00	28.6	3	C	0.50	3.6	0.30	2.1
	|			2.25	39	C	5.30	37.8						
9	11 B ∧	0.45	3.2	7.55	132	F	0.45	3.2	5	C	0.55	3.9	0.30	2.1
	|					A	2.40	17.1						

sample <CAT 10> constant penetration rate with scratch velocity = 1 microns/second

		scratch:				ends:				features:				
number	type	width(grat)	width(μm)	length(grat)	length(μm)	type	width(grat)	width(μm)	quantity	type	width(grat)	width(μm)	spac(grat)	spac(μm)
10	1 G │	0.30	2.1	5.65	99 E c-	0.00	0.0	2 A	2.30	16.4	0.65	4.6		
	V					F c+	0.60	4.3	2 B	1.10	7.9	0.60	4.3	
									1 B	1.50	10.7	0.45	3.2	
10	2 C ∧	0.25	1.8	6.45	113 F	0.50	3.6	7 C	0.60	4.3	0.30	2.1		
	│				0 E	0.00	0.0							
10	3 C ∧	0.23	1.6	6.60	116 F	0.45	3.2	9 C	0.70	5.0	0.60	4.3		
	│				0 E	0.00	0.0							
10	4 C ∧	0.20	1.4	6.15	108 F	0.40	2.9	10 C	0.60	4.3	0.50	3.6		
	│				0 E	0.00	0.0							
10	5 C ∧	0.20	1.4	6.00	105 F	0.40	2.9	2 B	0.70	5.0			
	│				0 E	0.00	0.0	6 C	0.55	3.9				
10	6 C ∧	0.25	1.8	7.75	136 F	0.50	3.6	10 C	0.65	4.6	0.40	2.9		
	│				0 E	0.00	0.0							
10	7 C ∧	0.20	1.4	6.30	110 F	0.40	2.9	7 C	0.60	4.3			
	│				0 E	0.00	0.0							
10	8 C ∧	0.25	1.8	6.40	112 F	0.50	3.6	7 C	0.50	3.6			
	│				E	0.00	0.0							
10	9 C ∧	0.25	1.8	6.45	113 F	0.50	3.6	5 C	0.50	3.6			
	│				E	0.00	0.0							
10	10 C ∧	0.23	1.6	6.35	111 F	0.45	3.2	10 C	0.55	3.9			
	│				E	0.00	0.0							
10	11 C ∧	0.28	2.0	6.15	108 F	0.55	3.9	6 C	0.65	4.6			
	│				E	0.00	0.0							

sample <CAT 10> continued

scratch:						ends:			features:					
number	type	width(grat)	width(μm)	length(grat)	length(μm)	type	width(grat)	width(μm)	quantity	type	width(grat)	width(μm)	spac(grat)	spac(μm)
10	12 C	0.23	1.6	6.25	109	F	0.45	3.2	7	C	0.45	3.2		
						E	0.00	0.0						
10	13 C	0.23	1.6	6.05	106	F	0.45	3.2	6	C	0.40	2.9		
						E	0.00	0.0	5	C	0.65	4.6		
10	14 C	0.25	1.8	6.50	114	F	0.50	3.6	11	C	0.50	3.6		
						E	0.00	0.0						

sample <CAT 11>   constant penetration rate with scratch velocity = 1 microns/second

scratch: number	type		width(grat)	width(μm)	length(grat)	length(μm)	ends: type		width(grat)	width(μm)	features: quantity	type	width(grat)	width(μm)	spac(grat)	spac(μm)
11	1 C	$\wedge$	0.20	1.4	6.15	108	F	c-	0.40	2.9	2	C	0.40	2.9		
		|					E	c+	0.00	0.0	9	C	0.65	4.6		
11	2 C	$\wedge$	0.28	2.0	6.15	108	F		0.55	3.9	6	C	0.55	3.9	0.50	3.6
		|					E		0.00	0.0	15	C	0.85	6.1	0.50	3.6
11	3 C	$\wedge$	0.30	2.1	6.30	110	F		0.60	4.3	1	A	2.05	14.6		
		|					E		0.00	0.0	1	A	1.50	10.7		
											9	C	0.75	5.4		
11	4 C	$\wedge$	0.28	2.0	6.55	115	F		0.55	3.9	4	~B	1.10	7.9		
		|					E		0.00	0.0	17	C	0.85	6.1		
11	5 C	$\wedge$	0.33	2.3	6.45	113	F		0.65	4.6	7	C	0.50	3.6		
		|					E		0.00	0.0	6	C	0.90	6.4		
11	6 C	$\wedge$	0.28	2.0	6.30	110	F		0.55	3.9	5	C	0.60	4.3		
		|					E		0.00	0.0	9	C	0.90	6.4		
11	7 C	$\wedge$	0.25	1.8	6.45	113	F		0.50	3.6	2	~B	0.90	6.4		
		|					E		0.00	0.0	3	C	0.55	3.9		
											7	C	0.85	6.1		
11	8 C	$\wedge$	0.33	2.3	6.35	111	C		3.50	25.0	2	B	0.95	6.8		
		|					E		0.00	0.0	7	C	0.70	5.0		
											4	C	0.40	2.9		
11	9 C	$\wedge$	0.33	2.3	6.50	114	F		0.65	4.6	5	C	0.70	5.0		
		|					E		0.00	0.0	10	C	1.05	7.5		
11	10 C	$\wedge$	0.28	2.0	6.45	113	F		0.55	3.9	1	~B	1.10	7.9		
		|					E		0.00	0.0	12	C	0.80	5.7		

sample <CAT 11> continued

scratch: number	type		width(grat)	width(μm)	length(grat)	length(μm)	ends: type	width(grat)	width(μm)	features: quantity	type	width(grat)	width(μm)	spac(grat)	spac(μm)
11 11	C	∧	0.23	1.6	6.45	113	F	0.45	3.2	2	A	1.25	8.9		
		|					E	0.00	0.0	1	C	0.85	6.1		
11 12	C	∧	0.25	1.8	6.35	111	F	0.50	3.6	13	C	0.95	6.8		
		|					E	0.00	0.0						
11 13	C	∧	0.25	1.8	6.40	112	F	0.50	3.6	1	A	2.30	16.4		
		|					E	0.00	0.0	1	A	1.2	8.6		
										3	~B	0.90	6.4		
										9	C	0.60	4.3		
11 14	C	∧	0.23	1.6	6.40	112	F	0.45	3.2	14	C	0.90	6.4		
		|					E	0.00	0.0						

sample <CAT 12>   constant penetration rate with scratch velocity = 1 microns/second

scratch: number	type		width(grat)	width(μm)	length(grat)	length(μm)	ends: type		width(grat)	width(μm)	features: quantity	type	width(grat)	width(μm)	spac(grat)	spac(μm)
12	1 C	|	0.20	1.4	6.45	113	E	c+	0.00	0.0	0					
		V					F	c-	0.40	2.9						
12	2 C	|	0.25	1.8	6.25	109	E		0.00	0.0	10	C	0.60	4.3		
		V					F		0.50	3.6						
12	3 C	|	0.28	2.0	6.25	109	E		0.00	0.0	11	C	0.75	5.4		
		V					F		0.55	3.9						
12	4 C	|	0.23	1.6	6.10	107	E		0.00	0.0	9	C	0.55	3.9		
		V					F		0.45							
12	5 C	|	0.28	2.0	7.10	124	E		0.00	0.0	12	C	0.65	4.6		
		V					F		0.55		1	B	0.85	6.1		
12	6 C	|	0.28	2.0	6.20	109	E		0.00	0.0	10	C	0.55	3.9		
		V					F		0.55	3.9						
12	7 C	|	0.28	2.0	6.25	109	E		0.00	0.0	8	C	0.70	5.0		
		V					F		0.55	3.9						
12	8 C	|	0.28	2.0	6.60	116	E		0.00	0.0	7	C	0.85	6.1		
		V					F		0.55	3.9						
12	9 F	|	0.68	4.8	6.55	115	C		0.45	3.2	1	A	1.65	11.8		
		V			0.55	10	C		3.15	22.5	1	A	1.00	7.1		
											10	B	0.70	5.0		
12	10 F	|	0.60	4.3	7.00	123	C		2.40	17.1	1	B	2.35	16.8		
		V					F		0.80	5.7	1	B	1.1	7.9		
											13	C	0.85	6.1		
12	11 C	|	0.25	1.8	6.40	112	E		0.00	0.0	10	C	0.75	5.4		
		V					F		0.50	3.6						

77

sample <CAT 13> constant penetration rate with scratch velocity = 100 microns/second

scratch:							ends:				features:					
number	type		width(grat)	width(μm)	length(grat)	length(μm)	type		width(grat)	width(μm)	quantity	type	width(grat)	width(μm)	spac(grat)	spac(μm)
13	1 D	∧	0.23	1.6	7.10	124	E	c-	0.00	0.0	1	A	1.55	11.1		
		Ι					F	c+	0.45	3.2	1	A	1.25	8.9		
											1	A	0.85	6.1		
											4	B	0.50	3.6		
13	2 F	Ι	0.50	3.6	6.70	117	F		1.00	7.1	2	A	3.60	25.7		
		V					E		0.00	0.0	2	~B	1.40	10.0		
											7	C	1.00	7.1		
13	3 C	Ι	0.25	1.8	6.30	110	F		0.50	3.6	3	C	0.85	6.1		
		V					E		0.00	0.0						
13	4 C	Ι	0.23	1.6	5.65	99	F		0.45	3.2	1	C	0.85	6.1		
		V					E		0.00							
13	5 C	Ι	0.23	1.6	5.35	94	F		0.45	3.2	0					
		V					E		0.00							
13	6 C	Ι	0.18	1.2	5.40	95	F		0.35	2.5	0					
		V					E		0.00	0.0						
13	7 C	Ι	0.18	1.2	4.80	84	F		0.35	2.5	0					
		V					E		0.00	0.0						
13	8 C	Ι	0.15	1.1	4.60	81	F		0.30	2.1	0					
		V					E		0.00	0.0						
13	9 C	Ι	0.20	1.4	5.45	95	F		0.40	2.9	2	C	0.40	2.9		
		V					E		0.00	0.0						
13	10 C	Ι	0.18	1.2	4.75	83	F		0.35	2.5	3	C	0.65	4.6		
		V					E		0.00	0.0						

sample <CAT 14>   constant penetration rate with scratch velocity = 100 microns/second

scratch:						ends:				features:				
number	type	width(grat)	width(μm)	length(grat)	length(μm)	type	width(grat)	width(μm)	quantity	type	width(grat)	width(μm)	spac(grat)	spac(μm)
14 1 C	|	0.25	1.8	7.05	123 E	c+	0.00	0.0	8	C	0.70	5.0		
	V				F	c-	0.50	3.6						
14 2 C	|	0.15	1.1	5.40	95 E		0.00	0.0	0					
	V				0 F		0.30	2.1						
14 3 C	|	0.15	1.1	5.15	90 E		0.00	0.0	0					
	V				0 F		0.30	2.1						
14 4 C	|	0.18	1.2	5.30	93 E		0.00	0.0	0					
	V				0 F		0.35	2.5						
14 5 C	|	0.13	0.9	4.20	74 E		0.00	0.0	0					
	V				0 F		0.25	1.8						
14 6 C	|	0.15	1.1	4.25	74 E		0.00	0.0	0					
	V				0 F		0.30	2.1						
14 7 C	|	0.18	1.2	4.70	82 E		0.00	0.0	0					
	V				0 F		0.35	2.5						
14 8 C	|	0.15	1.1	3.95	69 E		0.00	0.0	0					
	V				F		0.30	2.1						
14 9 C	|	0.15	1.1	4.90	86 E		0.00	0.0	0					
	V				F		0.30	2.1						
14 10 C	|	0.18	1.2	4.75	83 E		0.00	0.0	0					
	V				F		0.35	2.5						

sample <CAT 14> continued

				scratch:				ends:			features					
	number	type		width(grat)	width(μm)	length(grat)	length(μm)	type	width(grat)	width(μm)	quantity	type	width(grat)	width(μm)	spac(grat)	spac(μm)
14	11	C	|	0.13	0.9	4.00	70	E	0.00	0.0	0					
			V					F	0.25	1.8						
14	12	C	|	0.08	0.5	3.20	56	E	0.00	0.0	0					
			V					F	0.15	1.1						
14	13	C	|	0.13	0.9	4.85	85	E	0.00	0.0	0					
			V					F	0.25	1.8						
14	14	C	|	0.13	0.9	4.20	74	E	0.00	0.0	0					
			V					F	0.25	1.8						

TABLE 4: ELASTIC RECOVERY

CONSTANT LOAD TESTS: load = 3mN; v_s=100μm/s

sample	scratch number	MME inter i = indent depth(μm)	MME data w = scratch width(μm)	SV plot i = indent depth(μm)	MME calc d = indent dia (μm)	elastic rebound: i_e = elastic depth(μm)	w_e= elastic width(μm)	w_e/2
7	1	(na)	0.6	1.2	3.1	(na)	2.5	1.3
	2	(na)	0.6	0.4	1.5	(na)	0.9	0.5
	3	(na)	0.9	0.5	1.8	(na)	1.0	0.5
	4	(na)	0.6	0.6	2.1	(na)	1.5	0.8
	5	(na)	0.9	1.2	3.1	(na)	2.3	1.1
	6	(na)	1.4	0.9	2.6	(na)	1.2	0.6
	7	(na)	1.4	0.7	2.2	(na)	0.8	0.4
	8	(na)	1.4	0.8	2.3	(na)	0.9	0.5
	9	(na)	1.4	0.9	2.5	(na)	1.1	0.6
8	1	0.3	1.4	0.8	2.4	0.5	1.0	0.5
	2	0.3	1.4	0.7	2.2	0.4	0.8	0.4
	3	0.3	1.4	0.6	2.0	0.3	0.6	0.3
	4	0.3	1.4	0.8	2.3	0.5	0.9	0.5
	5	0.3	1.4	0.6	1.9	0.3	0.5	0.3

CONSTANT LOAD TESTS: load = 11mN; v_s=100μm/s

sample	scratch number	MME inter i = indent depth(μm)	MME data w = scratch width(μm)	SV plot i = indent depth(μm)	MME calc d = indent dia (μm)	elastic rebound: i_e = elastic depth(μm)	w_e= elastic width(μm)	w_e/2
9	1	(na)	3.9 (varies)			(na)		
	2	(na)	5.0 (?)			(na)		
	3	(na)	2.5	1.8	4.4	(na)	1.9	1.0
	4	(na)	2.9	1.0	2.8	(na)	-0.1	0.0
	5	(na)	3.6	1.0	2.8	(na)	-0.8	-0.4
	6	(na)	3.2	1.8	4.4	(na)	1.2	0.6
	7	(na)	3.6	1.0	2.8	(na)	-0.8	-0.4
	8	(na)	3.2	1.0	2.8	(na)	-0.4	-0.2
	9	(na)	2.9	1.0	2.8	(na)	-0.1	0.0
	10	(na)	2.9	1.0	2.8	(na)	-0.1	0.0
	11	(na)	3.2	0.8	2.4	(na)	-0.8	-0.4

82

CONSTANT INDENTATION RATE TESTS: v_s=1.0µm/s; v_i=20nm/s

sample	scratch number	MME inter i = indent depth(µm)	MME data W_{max}=max width(µm)	SV plot i_{max} = max depth(µm)	MME calc d = indent dia (µm)	i_e = elastic depth(µm)	W_e= elastic width(µm)	$W_e/2$
10	1		4.3	0.4	1.6		**-2.7**	-1.3
	2		3.6	2.1	4.9		**1.3**	0.7
	3		3.2	2.1	4.9		**1.7**	0.9
	4		2.9	1.9	4.6		**1.7**	0.9
	5		2.9	2.0	4.8		**1.9**	1.0
	6		3.6	1.9	4.6		**1.0**	0.5
	7		2.9	2.0	4.8		**1.9**	1.0
	8		3.6	2.0	4.8		**1.2**	0.6
	9		3.6	2.0	4.8		**1.2**	0.6
	10		3.2	1.9	4.6		**1.4**	0.7
	11		3.9	2.0	4.7		**0.8**	0.4
	12		3.2	2.0	4.7		**1.5**	0.8
	13		3.2	2.0	4.7		**1.5**	0.8
	14		3.6	2.0	4.7		**1.1**	0.6
11	1 (na)		2.9	1.9	4.5 (na)		**1.6**	0.8
	2 (na)		3.9	2.3	5.4 (na)		**1.5**	0.8
	3 (na)		4.3	2.4	5.5 (na)		**1.2**	0.6
	4 (na)		3.9	2.3	5.4 (na)		**1.5**	0.8
	5 (na)		4.6	2.4	5.5 (na)		**0.9**	0.5
	6 (na)		3.9	2.3	5.4 (na)		**1.5**	0.8
	7 (na)		3.6	2.3	5.4 (na)		**1.8**	0.9
	8 (na)		4.6	2.4	5.5 (na)		**0.9**	0.5
	9 (na)		4.6	2.3	5.4 (na)		**0.8**	0.4
	10 (na)		3.9	2.4	5.6 (na)		**1.7**	0.9
	11 (na)		3.2	2.3	5.4 (na)		**2.2**	1.1
	12 (na)		3.6	2.3	5.4 (na)		**1.8**	0.9
	13 (na)		3.6	2.4	5.5 (na)		**1.9**	1.0
	14 (na)		3.2	2.3	5.4 (na)		**2.2**	1.1
12	1		2.9	1.1	2.9		**0.0**	0.0
	2		3.6	1.5	3.7		**0.1**	0.1
	3		3.9	1.5	3.8		**-0.1**	0.0
	4		3.2	1.5	3.8		**0.6**	0.3
	5		4.0	1.6	3.9		**-0.1**	0.0
	6		3.9	1.6	4.0		**0.1**	0.1
	7		3.9	1.6	4.0		**0.1**	0.1
	8		3.9	1.6	4.0		**0.1**	0.1
	9		9.6	1.7	4.2		**-5.4**	-2.7
	10		8.6	1.5	3.8		**-4.8**	-2.4
	11		3.6	1.6	3.9		**0.3**	0.2

CONSTANT INDENTATION RATE TESTS: v_s=100μm/s; v_i=2000nm/s

sample	scratch number	MME inter i = indent depth(μm)	MME data SV plot w_{max}=max width(μm)	i_{max} = max depth(μm)	MME calc elastic rebound: d = indent dia (μm)	i_e = elastic depth(μm)	w_e= elastic width(μm)	w_e/2
13	1		3.2	1.5	3.7		0.5	0.3
	2		7.1	2.8	6.4		-0.7	-0.3
	3		3.6	1.6	4.0		0.4	0.2
	4		3.2	1.7	4.1		0.9	0.5
	5		3.2	1.4	3.6		0.4	0.2
	6		2.5	1.5	3.8		1.3	0.7
	7		2.5	1.5	3.8		1.3	0.7
	8		2.1	1.3	3.4		1.3	0.7
	9		2.9	1.4	3.6		0.7	0.4
	10		2.5	1.3	3.3		0.8	0.4
14	1 (na)		3.6	1.2	3.2		-0.4	-0.2
	2 (na)		2.1	1.3	3.4		1.3	0.7
	3 (na)		2.1	1.4	3.5		1.4	0.7
	4 (na)		2.5	1.2	3.2		0.7	0.4
	5 (na)		1.8	1.1	3.0		1.2	0.6
	6 (na)		2.1	1.1	2.9		0.8	0.4
	7 (na)		2.5	1.2	3.1		0.6	0.3
	8 (na)		2.1	1.1	2.9		0.8	0.4
	9 (na)		2.1	1.2	3.1		1.0	0.5
	10 (na)		2.5	1.3	3.4		0.9	0.5
	11 (na)		1.8	1.1	2.9		1.1	0.6
	12 (na)		1.1	1.0	2.7		1.6	0.8
	13 (na)		1.8	1.3	3.4		1.6	0.8
	14 (na)		1.8	1.0	2.7		0.9	0.5

TABLE 5: DAMAGE PROFILES

sample <CAT 3>   constant load = 35 mN; scratch velocity = 0.13 microns/second
distances estimated from photograph

scratch 3-1
SD (grat)   1.0
SD (μm)   6   (DATA STORED ELSEWHERE AT THE MOMENT)
wedge   A
time (s)   48

sample <CAT 4>   constant load = 35 mN; scratch velocity = 100 microns/second
magnification = (45x objective)*(16x ocular)=720x; 1grat=7.14 microns

scratch 4-3

SD (grat)	3.3	4.4	4.9	6.4	7.8	8.8	10.3	10.9	13.3	14.8	16.0	17.3	19.1	19.4
SD (μm)	20	27	30	39	48	54	64	67	82	91	99	107	118	120
wedge	A	A	A	A	A	A	A	A	A	A	A	A	A	end
time (s)	0.20	0.27	0.30	0.39	0.48	0.54	0.64	0.67	0.82	0.91	0.99	1.07	1.18	1.20

scratch 4-4

SD (grat)	1.9	3.3	4.5	6.9	8.2	9.1	10.6	12.3	13.1	15.9	17.2	18.8	19.9
SD (μm)	12	20	28	43	50	56	66	76	81	98	106	116	123
wedge	A	A	A	A	A	A	A	A	A	A	A	A	end
time (s)	0.12	0.20	0.28	0.43	0.50	0.56	0.66	0.76	0.81	0.98	1.06	1.16	1.23

scratch 4-5

SD (grat)	1.1	2.3	3.1	3.9	4.9	5.9	7.3	7.8	9.3	13	14	15	17	18
SD (μm)	7	14	19	24	30	36	45	48	57	81	87	92	102	111
wedge	A	A	A	A	A	A	A	A	A	A	A	A	A
time (s)	0.07	0.14	0.19	0.24	0.30	0.36	0.45	0.48	0.57	0.81	0.87	0.92	1.02	1.11

scratch 4-6

SD (grat)	1.7	2.6	4.2	6.6	7.6	8.4	9.1	9.7	11	12	13	15	16	19
SD (μm)	11	16	26	41	47	52	56	60	69	75	81	91	97	116
wedge	A	A	A	A	A	A	A	A	A	A	A	A	A
time (s)	0.11	0.16	0.26	0.41	0.47	0.52	0.56	0.60	0.69	0.75	0.81	0.91	0.97	1.16

scratch 4-7

SD (grat)	0.3	1.5	3.5	4	4.6	6.1	6.9	8.9	10	11	13	13	14	15
SD (μm)	2	9	22	25	28	37	43	55	63	70	78	83	87	93
wedge	A	A	A	A	A	A	A	A	A	A	A	A	A
time (s)	0.02	0.09	0.22	0.25	0.28	0.37	0.43	0.55	0.63	0.70	0.78	0.83	0.87	0.93

scratch 4-7 continued

SD (grat)	18	20
SD (μm)	109	124
wedge	A	A
time (s)	1.09	1.24

scratch 4-8

SD (grat)	1.3	2.4	2.9	3.7	4.7	6	7	7.6	8.3	10	11	13	14	15
SD (μm)	8	15	18	23	29	37	43	47	51	63	66	83	87	95
wedge	A	A	A	A	A	A	A	A	A	A	A	A	A
time (s)	0.08	0.15	0.18	0.23	0.29	0.37	0.43	0.47	0.51	0.63	0.66	0.83	0.87	0.95

scratch 4-8 continued

SD (grat)	17	19	20
SD (μm)	107	115	124
wedge	A	A	A
time (s)	1.07	1.15	1.24

scratch 4-9

SD (grat)	1.6	3	4.3	5.1	5.8	7.4	10	13	16	18	19	19
SD (μm)	**10**	**19**	**27**	**32**	**36**	**45**	**63**	**83**	**101**	**109**	**115**	**120**
wedge	A	A	A	A	A	A	A	A	A	A	A	A
time (s)	0.10	0.19	0.27	0.32	0.36	0.45	0.63	0.83	1.01	1.09	1.15	1.20

scratch 4-10

SD (grat)	0.2	1.8	2.6	4.2	4.9	5.6	6.5	7.6	8	9	9.5	10	12	12
SD (μm)	**1**	**11**	**16**	**26**	**30**	**34**	**40**	**47**	**49**	**55**	**59**	**62**	**71**	**74**
wedge	A	A	A	A	A	A	A	A	A	A	A	A	A	A
time (s)	0.01	0.11	0.16	0.26	0.30	0.34	0.40	0.47	0.49	0.55	0.59	0.62	0.71	0.74

scratch 4-10 continued

SD (grat)	14	15	15	17	19	20
SD (μm)	**85**	**91**	**95**	**106**	**120**	**123**
wedge	A	A	A	A	A	A
time (s)	0.85	0.91	0.95	1.06	1.20	1.23

sample <CAT 9>   constant load = 11 mNscratch velocity = 100 mi· *updated 24 July, 1996*
magnification = (40x objective)*(16x ocular)=640x; 1grat=7.14 microns

scratch 9-1 (reverse direction)

SD (grat)	4.2	5	5.9	6.4	7.7	8	8.6	9.1	10	11	12	13	14
SD (μm)	**30**	**36**	**42**	**45**	**55**	**57**	**61**	**65**	**75**	**78**	**87**	**96**	**101**
wedge	B	A	B	B	C	B	B	B	B	A	A	A	A
time (s)	0.30	0.36	0.42	0.45	0.55	0.57	0.61	0.65	0.75	0.78	0.87	0.96	1.01

scratch 9-2

SD (grat)	0.4	5.5	6	6.3	6.6	7.2	8.2	8.5	9.3	9.7	10	10	11	12	12	13
SD (μm)	**118**	**82**	**78**	**76**	**74**	**70**	**63**	**60**	**55**	**52**	**49**	**48**	**42**	**36**	**33**	**28**
wedge	end	C	C	C	C	C	~B	C	C	~B	C	C	C	C	C
time (s)	1.18	0.82	0.78	0.76	0.74	0.70	0.63	0.60	0.55	0.52	0.49	0.48	0.42	0.36	0.33	0.28

scratch 9-2 continued

SD (grat)	15	16	17
SD (μm)	**16**	**10**	**0**
wedge	C	C	end
time (s)	0.16	0.10	0.00

scratch 9-3

SD (grat)	8.5	10	11	11	11	12	13	16	16	17
SD (μm)	**59**	**49**	**43**	**40**	**38**	**35**	**31**	**8**	**4**	**0**
wedge	(C)	(C)	(C)	(C)	(C)	(C)	(C)	B	A	end
time (s)	0.59	0.49	0.43	0.40	0.38	0.35	0.31	0.08	0.04	0.00

scratch 9-4

SD (grat)	0.5	0.9	1.5	1.9	2.2	4.7	6.4	6.7	12	12	17
SD (μm)	**117**	**115**	**110**	**108**	**105**	**88**	**76**	**73**	**39**	**35**	**0**
wedge	C	C	C	C	C	C	C	C	C	C	end
time (s)	1.17	1.15	1.10	1.08	1.05	0.88	0.76	0.73	0.39	0.35	0.00

scratch 9-5 (broken)

SD (grat)	3.5	4.9	5.6	6.3	9.6	10	11	12	12
SD (μm)	**97**	**87**	**82**	**77**	**54**	**49**	**45**	**40**	**35**
wedge	C	C	C	C	C	C	C	C	C
time (s)	0.97	0.87	0.82	0.77	0.54	0.49	0.45	0.40	0.35

scratch 9-6 (broken)

SD (grat)	0.3	3.5	3.7	4	4.3	4.7	4.9	5.3	5.6	6	6.6	7.1	7.6	7.9	8.2	8.7
SD (μm)	**115**	**92**	**91**	**88**	**86**	**84**	**82**	**79**	**77**	**74**	**70**	**66**	**63**	**61**	**58**	**55**
wedge	C	C	C	C	C	C	C	C	C	C	C	C	C	C	C	C
time (s)	1.15	0.92	0.91	0.88	0.86	0.84	0.82	0.79	0.77	0.74	0.70	0.66	0.63	0.61	0.58	0.55

scratch 9-6 (broken) continued

SD (grat)	10	11	11	11
SD (μm)	**44**	**41**	**38**	**36**
wedge	(C)	(C)	(C)	(C)
time (s)	0.44	0.41	0.38	0.36

scratch 9-7 (broken)
SD (grat) 0.4
SD (μm) 117
wedge   end
time (s)   1.17

scratch 9-8 (broken)
SD (grat) 0.8 1.2 2.1 6.8
SD (μm)   **115 111 105   71**
wedge   C   C   C   C
time (s)   1.15 1.11 1.05 0.71

scratch 9-9   no brittle damage apparent
scratch 9-10   no measurements
scratch 9-11   no measurements

sample <CAT 10> constant penetration rate with scratch velocity = *updated 24 July, 1996*
magnification = (40x objective)*(16x ocular)=640x; 1grat=7.14 microns

scratch 10-1 =>

SD (grat)	3.8	5.3	5.7	6.8	8.2
SD (μm)	**27**	**37**	**41**	**49**	**58**
wedge	B	B	B	A	A
time (s)	27	83	79	71	62

scratch 10-2 <=

SD (grat)	0.2	1.1	1.5	2.1	2.5	2.8	3.3	4.8	5.6	6.1	6.6	7.6
SD (μm)	**112**	**106**	**103**	**98**	**95**	**93**	**89**	**79**	**73**	**70**	**66**	**59**
wedge	C	C	C	C	C	C	C	(C)	(C)	(C)	(C)	(C)
time (s)	112	106	103	98	95	93	89	79	73	70	66	59

scratch 10-3

SD (grat)	0.4	0.9	1.4	2.0	2.5	3.7	4.0	5.0	5.8
SD (μm)	**113**	**110**	**106**	**102**	**98**	**90**	**87**	**81**	**75**
wedge	C	C	C	C	C	C	C	C	C
time (s)	113	110	106	102	98	90	87	81	75

scratch 10-4

SD (grat)	1.7	2.1	2.6	3.1	3.5	3.9	4.3	4.9	5.2	5.6	5.9	6.7	6.8	7.2
SD (μm)	**96**	**93**	**89**	**86**	**83**	**80**	**77**	**73**	**71**	**68**	**66**	**61**	**59**	**57**
wedge	C	C	(C)	C	C	C	C	C	C	C	C	(C)	(C)	C
time (s)	96	93	89	86	83	80	77	73	71	68	66	61	59	57

scratch 10-5

SD (grat)	1.0	1.5	1.9	2.2	2.6	2.9	3.3	4.0	4.6	5.0	5.9	6.9
SD (μm)	**98**	**94**	**91**	**89**	**86**	**84**	**81**	**77**	**72**	**70**	**63**	**56**
wedge	C	C	C	C	C	(C)	~B	~B	(C)	C	C	C
time (s)	98	94	91	89	86	84	81	77	72	70	63	56

scratch 10-6

SD (grat)	1.1	1.6	2.9	3.2	3.8	4.2	4.9	5.4	5.9	6.3	6.7	7.1	8.0
SD (μm)	**128**	**125**	**116**	**113**	**109**	**106**	**101**	**97**	**94**	**91**	**88**	**86**	**79**
wedge	C	C	C	C	C	C	C	C	C	C	C	(C)	C
time (s)	128	125	116	113	109	106	101	97	94	91	88	86	79

scratch 10-7

SD (grat)	0.3	0.7	1.0	1.9	2.5	2.8	3.4	4.0	4.4	4.9	5.7	5.9	6.2
SD (μm)	**108**	**105**	**103**	**96**	**92**	**90**	**86**	**82**	**79**	**75**	**70**	**68**	**66**
wedge	(C)	C	C	C	(C)	C	C	C	C	C	(C)	(C)	(C)
time (s)	108	105	103	96	92	90	86	82	79	75	70	68	66

scratch 10-8

SD (grat)	0.2	0.7	1.3	1.9	2.2	2.9	3.6	4.1	4.6	5.3
SD (μm)	**111**	**107**	**103**	**99**	**96**	**92**	**87**	**83**	**79**	**75**
wedge	(C)	~B	~B	C	C	C	C	C	C	C
time (s)	111	107	103	99	96	92	87	83	79	75

scratch 10-9

SD (grat)	1.0	1.3	2.0	3.4	3.7	4.5	6.0	6.3
SD (μm)	**106**	**104**	**99**	**89**	**87**	**81**	**70**	**68**
wedge	(C)	~B	C	(C)	C	C	(C)	C
time (s)	106	104	99	89	87	81	70	68

scratch 10-10

SD (grat)	0.8	1.3	1.8	2.1	2.6	3.2	3.9	4.4	5.1	5.5	5.9	6.6	7.0
SD (μm)	**106**	**102**	**99**	**96**	**93**	**88**	**84**	**80**	**75**	**72**	**69**	**64**	**61**
wedge	C	C	C	C	C	C	C	C	C	C	C	C	C
time (s)	106	102	99	96	93	88	84	80	75	72	69	64	61

scratch 10-11

SD (grat)	1.3	1.9	2.7	3.1	3.6	4.3	4.8	6.0
SD (μm)	**99**	**94**	**89**	**86**	**82**	**77**	**74**	**65**
wedge	C	C	C	C	C	C	C	(C)
time (s)	99	94	89	86	82	77	74	65

scratch 10-12

SD (grat)	0.3	0.7	1.3	2.2	2.8	3.4	3.8	5.0	6.9	7.4
SD (μm)	**107**	**104**	**100**	**93**	**89**	**85**	**82**	**74**	**60**	**57**
wedge	C	C	C	C	C	C	C	C	C	(C)
time (s)	107	104	100	93	89	85	82	74	60	57

scratch 10-13

SD (grat)	0.4	0.9	1.4	1.9	2.6	3.4	4.3	4.5	4.9	5.6	6.1	6.4	7.0	7.4
SD (μm)	**103**	**100**	**96**	**93**	**87**	**82**	**76**	**74**	**71**	**66**	**63**	**61**	**56**	**54**
wedge	C	C	C	C	C	C	C	C	C	C	C	C	C	(C)
time (s)	103	100	96	93	87	82	76	74	71	66	63	61	56	54

scratch 10-14

SD (grat)	0.7	1.4	1.9	2.5	3.1	4.0	4.5	5.4	5.9	6.3	6.9
SD (μm)	**109**	**104**	**100**	**96**	**92**	**85**	**82**	**75**	**72**	**69**	**65**
wedge	C	C	C	C	C	C	C	C	(C)	C	(C)
time (s)	109	104	100	96	92	85	82	75	72	69	65

sample <CAT 12> constant penetration rate with scratch velocity = 1 micron/second
magnification = (40x objective)*(16x ocular)=640x; 1grat=7.14 microns

scratch 12-1 no brittle damage apparent

scratch 12-2

SD (grat)	0.4	1	1.4	2.1	2.5	3.2	3.4	3.8	4.2	4.7	5.3	5.8	6.2	6.6	7	7.3
SD (μm)	**106**	**102**	**99**	**94**	**91**	**87**	**85**	**82**	**79**	**75**	**71**	**68**	**65**	**62**	**59**	**57**
wedge	(C)	(C)	(C)	~B	~B	C	C	C	C	C	C	C	C	C		(C)
time (s)	106	18	21	26	29	33	35	38	41	45	49	52	55	58	61	63

scratch 12-2 continued

SD (grat)	7.7	8	8.3	8.7
SD (μm)	**54**	**52**	**50**	**47**
wedge	(C)	(C)	(C)	(C)
time (s)	66	68	70	73

scratch 12-3

SD (grat)	0.5	1	2	2.3	3	3.6	4	4.4	4.8	5.5	6.2	7.1	10
SD (μm)	**106**	**102**	**95**	**93**	**88**	**83**	**81**	**78**	**75**	**70**	**65**	**59**	**38**
wedge	(C)	C	C	C	C	C	C	(C)	C	C	C	C	(C)
time (s)	14	18	25	27	32	37	39	42	45	50	55	61	82

scratch 12-4

SD (grat)	0.7	0.9	1.9	2.5	3	3.5	3.9	4.3	5.2	5.6	6.3
SD (μm)	**102**	**101**	**94**	**89**	**86**	**82**	**79**	**76**	**70**	**67**	**62**
wedge	(C)	(C)	C	C	C	C	C	C	C	C	C
time (s)	18	19	26	31	34	38	41	44	50	53	58

scratch 12-5

SD (grat)	1.3	2	2.5	3.6	4	4.5	5.1	5.7	6	6.6	7	7.4	7.7	8.3
SD (μm)	**115**	**110**	**107**	**98**	**96**	**92**	**88**	**84**	**81**	**77**	**74**	**71**	**69**	**65**
wedge	C	~B	C	C	C	C	C	C	C	C	C	C	C	C
time (s)	5	10	13	22	24	28	32	36	39	43	46	49	51	55

scratch 12-6

SD (grat)	0.3	1.2	1.5	2.1	2.5	3.3	3.9	4.8	5.4	6.2	7	8.1	8.7
SD (μm)	**107**	**101**	**98**	**94**	**91**	**86**	**81**	**75**	**70**	**65**	**59**	**51**	**47**
wedge	C	C	C	C	C	C	C	C	C	C	C	C	C
time (s)	13	19	22	26	29	34	39	45	50	55	61	69	73

scratch 12-7

SD (grat)	0.3	0.7	1.2	1.6	2	2.3	2.6	3.1	3.5	4	4.3	5	5.4	5.8	9.2	9.8
SD (μm)	**107**	**104**	**101**	**98**	**95**	**93**	**90**	**87**	**84**	**80**	**79**	**73**	**71**	**68**	**43**	**39**
wedge	C	C	C	C	C	C	C	C	C	C	C	C	C	C	(C)	(C)
time (s)	13	16	19	22	25	27	30	33	36	40	41	47	49	52	77	81

scratch 12-8

SD (grat)	0.4	1	1.5	1.9	2.3	2.7	3.1	5.9	6.4	7.3	7.8	8.1	8.6	9.3
SD (μm)	113	109	106	102	100	97	94	74	70	64	60	58	55	50
wedge	C	C	C	C	C	C	C	C	C	C	C	C	C	C
time (s)	7	11	14	18	20	23	26	46	50	56	60	62	65	70

scratch 12-9

SD (grat)	0.6	2.3	3.7	5.3	6	6.6	6.8	8.3	9.6	10	11	12	13	14	16	16
SD (μm)	117	105	95	83	78	74	72	62	52	48	45	37	25	20	7	4
wedge	end	A	A	C	C	C	B	B	C	C	C	B	B	B	B	B
time (s)	3	15	25	37	42	46	48	58	68	72	75	83	95	100	113	116

scratch 12-9 continued

SD (grat)	17
SD (μm)	0
wedge	end
time (s)	120

scratch 12-10

SD (grat)	0.9	2.5	4	4.1	4.6	5	6.2	6.8	7.6	8	8.3	8.7	9.8	10	11	11
SD (μm)	118	107	95	95	91	88	80	75	70	67	65	62	54	50	46	44
wedge	end	B	C	B	B	B	C	C	C	C	C	C	C	C	C	C
time (s)	2	13	25	25	29	32	40	45	50	53	55	58	66	70	74	76

scratch 12-10 continued

SD (grat)	11.9	13	14	14	15	16	16	17	17
SD (μm)	39	28	25	24	16	13	10	6	0
wedge	C	(C)	C	B	C	C	C	~B	end
time (s)	81	92	95	96	104	107	110	114	120

scratch 12-11 no brittle damage apparent

sample <CAT 13>

constant penetration rate with scratch velocity = 100 microns/second
magnification = (40x objective)*(16x ocular)=640x; 1grat=7.14 microns

scratch 13-1 (reverse direction)

SD (grat)	2.3	2.7	3.1	4.3	5.4	5.7	6.1	8	9.1
SD (μm)	16	19	22	30	39	40	44	57	65
wedge	B	B	A	A	B	B	A	gap	gap
time (s)	0.16	0.19	0.22	0.30	0.39	0.40	0.44	0.57	0.65

scratch 13-2

SD (grat)	0.8	1.3	1.9	2.7	6.7	7	7.4	7.7	8.3	9.1	9.7	9.9	10	11	11
SD (μm)	111	108	104	98	70	67	64	62	58	52	48	46	45	42	38
wedge	B	A	A	A	C	B	C	C	C	C	C	(C)	C	C	C
time (s)	1.11	1.08	1.04	0.98	0.70	0.67	0.64	0.62	0.58	0.52	0.48	0.46	0.45	0.42	0.38

scratch 13-3

SD (grat)	0.4	0.9	1.3	1.6
SD (μm)	107	104	101	99
wedge	C	C	C	(C)
time (s)	1.07	1.04	1.01	0.99

scratch 13-4

SD (grat)	1.4	2
SD (μm)	89	85
wedge	C	C
time (s)	0.89	0.85

scratch 13-7

SD (grat)	0.4
SD (μm)	81
wedge	(C)
time (s)	0.81

scratch 13-10

SD (grat)	0.7	1.1	1.5	1.8
SD (μm)	78	75	72	70
wedge	C	C	C	(C)
time (s)	0.78	0.75	0.72	0.70

scratch 13-5

no brittle damage apparent

scratch 13-8

no brittle damage apparent

scratch 13-6

SD (grat)	1.3
SD (μm)	86
wedge	(C)
time (s)	0.86

scratch 13-9

SD (grat)	2.6	3.1
SD (μm)	77	73
wedge	C	C
time (s)	0.77	0.73

94

TABLE 6: CONTACT FRICTION FROM FORCE BALANCE

a) conical indenter with α = 45 degrees

μ_{app}	θ (rad)	θ (deg)	$\theta+\alpha$ (rad)	$\theta+\alpha$ (deg)	μ_{con}
0.30	0.29	17	1.08	62	0.54
0.40	0.38	22	1.17	67	0.43
0.50	0.46	27	1.25	72	0.33
0.60	0.54	31	1.33	76	0.25
0.70	0.61	35	1.40	80	0.18
0.80	0.67	39	1.46	84	0.11
0.90	0.73	42	1.52	87	0.05
1.00	0.79	45	1.57	90	0.00
1.10	0.83	48	1.62	93	-0.05
1.20	0.88	50	1.66	95	-0.09

b) conical indenter with α_{eff} = 60 degrees

μ_{app}	θ (rad)	θ (deg)	$\theta+\alpha$ (rad)	$\theta+\alpha$ (deg)	μ_{con}
0.30	0.29	17	1.34	77	0.24
0.40	0.38	22	1.43	82	0.14
0.50	0.46	27	1.51	87	0.06
0.60	0.54	31	1.59	91	-0.02
0.70	0.61	35	1.66	95	-0.09
0.80	0.67	39	1.72	99	-0.15
0.90	0.73	42	1.78	102	-0.21
1.00	0.79	45	1.83	105	-0.27
1.10	0.83	48	1.88	108	-0.32
1.20	0.88	50	1.92	110	-0.37

TABLE 7: MOHR'S CIRCLE CONTACT STRESS

a) conical indenter with α = 45 degrees, ν = 0.32

H_{nor} (GPa)	H_{tan} (GPa)	H_{tan}/H_{nor}	p_m (MPa)	τ_{con} (MPa)	μ_{con}	σ_{pp} (MPa)
0.5	0.3	0.6	400	100	0.25	327
1.5	0.9	0.6	1200	300	0.25	980
2.5	1.5	0.6	2000	500	0.25	1633
3.5	2.1	0.6	2800	700	0.25	2286
0.5	0.4	0.7	425	75	0.18	267
1.5	1.1	0.7	1275	225	0.18	802
2.5	1.8	0.7	2125	375	0.18	1337
3.5	2.5	0.7	2975	525	0.18	1872
0.5	0.4	0.8	450	50	0.11	208
1.5	1.2	0.8	1350	150	0.11	625
2.5	2.0	0.8	2250	250	0.11	1041
3.5	2.8	0.8	3150	350	0.11	1458
0.5	0.5	1.0	500	0	0.00	90
1.5	1.5	1.0	1500	0	0.00	270
2.5	2.5	1.0	2500	0	0.00	450
3.5	3.5	1.0	3500	0	0.00	630
0.5	0.6	1.2	550	-50	-0.09	-28
1.5	1.8	1.2	1650	-150	-0.09	-85
2.5	3.0	1.2	2750	-250	-0.09	-141
3.5	4.2	1.2	3850	-350	-0.09	-198

b) conical indenter with α_{eff} = 60 degrees, ν = 0.32

H_{nor} (GPa)	H_{tan} (GPa)	H_{tan}/H_{nor}	p_m (MPa)	τ_{con} (MPa)	μ_{con}	σ_{pp} (MPa)
0.5	0.3	0.6	350	87	0.25	283
1.5	0.9	0.6	1050	260	0.25	850
2.5	1.5	0.6	1750	433	0.25	1417
3.5	2.1	0.6	2450	606	0.25	1984
0.5	0.4	0.7	388	65	0.17	235
1.5	1.1	0.7	1163	195	0.17	705
2.5	1.8	0.7	1938	325	0.17	1175
3.5	2.5	0.7	2713	455	0.17	1645
0.5	0.4	0.8	425	43	0.10	187
1.5	1.2	0.8	1275	130	0.10	560
2.5	2.0	0.8	2125	217	0.10	934
3.5	2.8	0.8	2975	303	0.10	1307

TABLE 8: CONTACT STRENGTH FROM CHALLEN & OXLEY METHOD

a) conical indenter with α = 45 degrees, k = 277 MPa

f	τ_{con} (MPa)	μ_{app}
0	0	1.00
0.1	27.7	0.90
0.2	55.4	0.82
0.3	83.1	0.73
0.4	110.8	0.65
0.5	138.5	0.58
0.6	166.2	0.50
0.7	193.9	0.42
0.8	221.6	0.33
0.9	249.3	0.23
1	277	0.00

b) conical indenter with α_{eff} = 60 degrees

f	τ_{con} (MPa)	μ_{app}
0	0	0.58
0.1	27.7	0.51
0.2	55.4	0.45
0.3	83.1	0.39
0.4	110.8	0.33
0.5	138.5	0.27
0.6	166.2	0.20
0.7	193.9	0.14
0.8	221.6	0.06
0.9	249.3	-0.04
1	277	-0.27

TABLE 9: CORRELATION OF DAMAGE FEATURES WITH MECHANICAL DATA
tabulation of minimum values for the appearance of slip planes (f) and cleavage fractures (r)

a) constant load tests at 0.13 μm/s

V_s(μm/s)	sample	scratch feature	N_{min} (mN)	ΔN (mN)	i_{min} (μm)	Δi (μm)	H_{nor}(GPa)	ΔH_{nor}(GPa)	H_{tan}(GPa)	ΔH_{tan}(GPa)	H_{tan}/H_{nor}
0.13 c-	1 (CL)	(no damage features observed)									
0.13 c-	3 (CL)	1 r	35	3	4	1.2	1.1	0.2	0.9		0.82
0.13 c-	3 (CL)	2 r	35	4	4.2	0.8	1	0.3	0.8		0.80
0.13 c-	3 (CL)	3 r	35	5	4	0.8	1.1	0.2	0.9		0.82
0.13 c-	3 (CL)	4 r	35	6	5.4	1	0.6	0.1	0.5		0.83
0.13 c-	3 (CL)	5 r	35	8	3	0.6	1.4	0.3	1.3		0.93
0.13 c-	3 (CL)	6 r	35	4	3.6	0.6	1.2	0.2	1		0.83
0.13 c-	3 (CL)	7 r	35	4	3.4	0.4	1.5	0.2	1.4		0.93
0.13 c-	3 (CL)	8 r	35	3	2	0.8					
0.13 c-	3 (CL)	9 r	35	2	3	0.8					
0.13 c-	3 (CL)	10 r	35	2	3.2	0.4					
		mean	**35**		**3.6**		**1.13**		**0.97**		**0.85**

b) constant penetration rate tests at scratch velocity = 1 μm/s

v_s(μm/s)	sample	scratch	type	N_{min} (mN)	ΔN (mN)	i_{min} (μm)	Δi (μm)	H_{nor}(GPa)	ΔH_{nor}(GPa)	H_{tan}(GPa)	ΔH_{tan}(GPa)	H_{tan}/H_{nor}
1 c+	10(CPR)	1	r (A,B)	7.5	5	0.25	0.3					
1 c-	10(CPR)	2	f	4.5 ~0		1 ~0		1.9 ~0		1.4 ~0		0.74
1 c-	10(CPR)	3	f	5.5 ~0		1.3 ~0		1.6 ~0		1.3 ~0		0.81
1 c-	10(CPR)	4	f	4.5 ~0		0.9 ~0		1.9 ~0		1.5 ~0		0.79
1 c-	10(CPR)	5	f	5 ~0		0.9 ~0		1.9 ~0		1.4 ~0		0.74
1 c-	10(CPR)	6	f	8.5 ~0		1.2 ~0		2.1 ~0		1.7 ~0		0.81
1 c-	10(CPR)	7	f	5 ~0		1.1 ~0		1.9 ~0		1.5 ~0		0.79
1 c-	10(CPR)	8	f	6.5 ~0		1.2 ~0		1.9 ~0		1.6 ~0		0.84
1 c-	10(CPR)	9	f	6 ~0		1.15 ~0		1.8 ~0		1.55 ~0		0.86
1 c-	10(CPR)	10	f	5.5 ~0		0.9 ~0		2.1 ~0		1.65 ~0		0.79
1 c-	10(CPR)	11	f	5.5 ~0		1.1 ~0		2.1 ~0		1.6 ~0		0.76
1 c-	10(CPR)	12	f	4.5 ~0		0.9 ~0		1.9 ~0		1.5 ~0		0.79
1 c-	10(CPR)	13	f	4.5 ~0		0.9 ~0		2 ~0		1.6 ~0		0.80
1 c-	10(CPR)	14	f	5.5 ~0		1.05 ~0		1.8 ~0		1.35 ~0		0.75
		mean		5.5		1.0		1.9		1.5		0.79

| 1 c- | 11(CPR) | (no damage profile taken) | | | | | | | | | | |

1 c+	12(CPR)	1 (no damage features observed)										
1 c-	12(CPR)	2	f	6 ~0		0.65 ~0		3.9 ~0		3.3 ~0		0.85
1 c-	12(CPR)	3	f	5 ~0		0.55 ~0		3.5 ~0		3 ~0		0.86
1 c-	12(CPR)	4	f	7 ~0		0.8 ~0		3 ~0		2.2 ~0		0.73
1 c-	12(CPR)	5	f	9 ~0		0.9 ~0		3.3 ~0		2.7 ~0		0.82
1 c-	12(CPR)	6	f	5 ~0		0.6 ~0		3.1 ~0		2.2 ~0		0.71
1 c-	12(CPR)	7	f	5 ~0		0.6 ~0		3.1 ~0		2.3 ~0		0.74
1 c-	12(CPR)	8	f	7 ~0		0.7 ~0		3.5 ~0		2.8 ~0		0.80
1 c-	12(CPR)	9	r	12?	~0	unknown ~0		unknown ~0		unknown ~0		
1 c-	12(CPR)	9	f	18 ~0		unknown ~0		unknown ~0		unknown ~0		
1 c-	12(CPR)	10	r	24 ~0		unknown ~0		unknown ~0		unknown ~0		
1 c-	12(CPR)	10	f	11 ~0		unknown ~0		unknown ~0		unknown ~0		
1 c-	12(CPR)	11 (no damage features observed)										
		mean		6.3		0.7		3.3		2.6		0.79

c) constant load tests at scratch velocity = 100 μm/s

v_s(μm/s)	sample	scratch	type	N_{min} (mN)	ΔN (mN)	i_{min} (μm)	Δi (μm)	H_{nor}(GPa)	ΔH_{nor}(GPa)	H_{tan}(GPa)	ΔH_{tan}(GPa)	H_{tan}/H_{nor}
100 c-	2 (CL)	(no damage features observed)										
100 c-	4 (CL)	1 r		35	1	2.3	~0	2.8	<0.1	3.1	0.1	1.11
100 c-	4 (CL)	2 r		35	~0	2.2	~0	2.9	<0.1	3.1	0.1	1.07
100 c-	4 (CL)	3 r		35	1	2.4	<0.1	2.7	<0.1	2.9	0.2	1.07
100 c-	4 (CL)	4 r		35	<1	2.1	<0.1	3.6	0.1	3.7	0.1	1.03
100 c-	4 (CL)	5 r		35	1	2.1	0.1	3.3	0.1	3.5	0.2	1.06
100 c-	4 (CL)	6 r		35	<1	2	<0.1	3.8	0.1	4	0.2	1.05
100 c-	4 (CL)	7 r		35	1	1.9	0.1	4	0.1	4.2	0.2	1.05
100 c-	4 (CL)	8 r		35	<1	2.1	<0.1	3.8	0.1	4.1	0.2	1.08
100 c-	4 (CL)	9 r		35	1	1.8	0.1	4.3	0.2	4.6	0.2	1.07
100 c-	4 (CL)	10 r		35	2	1.8	0.2	4	0.1	4.1	0.2	1.03
		mean		**35.0**		**2.1**		**3.5**		**3.7**		**1.1**
100 c-	7 (CL)	(no damage features observed)										
100 c-	8 (CL)	(no damage features observed)										
100 c+	9 (CL)	1 r (A,B)		6	4 to 13	1	0.2 to 0.7	0.6 to	0.4 to 1.1	0.6	0.3 to 0.8	
100 c-	9 (CL)	3 f		11	~0	1.8	~0	1.6	~0	1.5	~0	0.94
100 c-	9 (CL)	4 f		11	~0	1	~0	3.5	~0	4	~0	1.14
100 c-	9 (CL)	5 f		11	~0	1	~0	3.7	~0	4	~0	1.08
100 c-	9 (CL)	6 f		11	~0	1.6	~0	1.7	~0	1.7	~0	1.00
100 c-	9 (CL)	7 f		11	~0	1	~0	3.7	~0	3.7	~0	1.00
100 c-	9 (CL)	8 f		11	~0	1	~0	3.5	~0	3.5	~0	1.00
100 c-	9 (CL)	9 f		11	~0	1	~0	4.3	~0	4.3	~0	1.00
100 c-	9 (CL)	10 f		11	~0	1	~0	3.3	~0	3.2	~0	0.97
100 c-	9 (CL)	11 f		11	~0	0.8	~0	5.4	~0	5.8	~0	1.07
		mean		**11.0**		**1.1**		**3.4**		**3.5**		**1.02**

d) constant penetration rate tests at scratch velocity = 100 μms/s

$v_s(\mu m/s)$	sample	scratch	type	N_{min} (mN)	ΔN (mN)	i_{min} (μm)	Δi (μm)	H_{nor}(GPa)	ΔH_{nor}(GPa)	H_{tan}(GPa)	ΔH_{tan}(GPa)	H_{tan}/H_{nor}
100 c+	13(CPR)	1	r	5	5	0.5	0.3	3.3		3		0.91
100 c-	13(CPR)	2	f	10		1		3.5		3.7		1.06
100 c-	13(CPR)	3	f	11		1.3		2.2		1.8		0.82
100 c-	13(CPR)	4	f	8		1.15		2		1.6		0.80
100 c-	13(CPR)	5	f	(no damage features observed)								
100 c-	13(CPR)	6	f	8		1.2		2		2.7		1.35
100 c-	13(CPR)	7	f	?								
100 c-	13(CPR)	8	f	(no damage features observed)								
100 c-	13(CPR)	9	f	7		0.9		2.5		1.5		0.60
100 c-	13(CPR)	10	f	7		0.9		2.7		1.8		0.67
		mean		8.5		1.1		2.5		2.2		0.88

100 c-   14 (no damage features observed)

TABLE 10: MAXIMUM CONTACT STRESS: CONSTANT μ_{con}

a) conical indenter with α = 45 degrees, ν = 0.32

H_{nor} (GPa)	H_{tan} (GPa)	H_{tan}/H_{nor}	P_m (MPa)	σ_{pp} (MPa) μ_{con} = 0.1	σ_{pp} (MPa) μ_{con} = 0.2
0.5	0.3	0.6	400	172	276
1.5	0.9	0.6	1200	516	827
2.5	1.5	0.6	2000	860	1378
3.5	2.1	0.6	2800	1204	1929
0.5	0.4	0.7	425	183	293
1.5	1.1	0.7	1275	548	878
2.5	1.8	0.7	2125	914	1464
3.5	2.5	0.7	2975	1279	2050
0.5	0.4	0.8	450	194	310
1.5	1.2	0.8	1350	581	930
2.5	2.0	0.8	2250	968	1550
3.5	2.8	0.8	3150	1355	2170
0.5	0.5	1.0	500	215	345
1.5	1.5	1.0	1500	645	1034
2.5	2.5	1.0	2500	1075	1723
3.5	3.5	1.0	3500	1505	2412
0.5	0.6	1.2	550	237	379
1.5	1.8	1.2	1650	710	1137
2.5	3.0	1.2	2750	1183	1895
3.5	4.2	1.2	3850	1656	2653

b) conical indenter with α_{eff} = 60 degrees, ν = 0.32

H_{nor} (GPa)	H_{tan} (GPa)	H_{tan}/H_{nor}	P_m (MPa)	σ_{pp} (MPa) μ_{con} = 0.1	σ_{pp} (MPa) μ_{con} = 0.2
0.5	0.3	0.6	350	151	241
1.5	0.9	0.6	1050	452	723
2.5	1.5	0.6	1750	753	1206
3.5	2.1	0.6	2450	1054	1688
0.5	0.4	0.7	388	167	267
1.5	1.1	0.7	1163	500	801
2.5	1.8	0.7	1938	833	1335
3.5	2.5	0.7	2713	1166	1869
0.5	0.4	0.8	425	183	293
1.5	1.2	0.8	1275	548	878
2.5	2.0	0.8	2125	914	1464
3.5	2.8	0.8	2975	1279	2050

TABLE 11: DAMAGE ENERGY

quantities calculated in kg-m-s, per micron scratch distance
assumptions: 10 nm gouge particles; surface energy = 0.200 joules/m²

	T (N)	i (m)	vol(m³)	length of feature(m)	surface area (m²)	C.R.S.S. (Pa)	force (N)	dx (m)	energy/ feature (j)	features/ micron	energy/ length (J/μm)
Regime I											
work applied	1.0E-03										1.0E-09
elastic response											5.0E-10
gouge produced		6.0E-07	3.6E-19		2.2E-10						4.3E-11
plastic deformation											na
Regime II											
work applied	2.5E-03										2.5E-09
elastic response											6.3E-10
gouge produced		1.0E-06	1.0E-18		6.0E-10						1.2E-10
plastic deformation											na
slip on f-system				5.0E-06	1.3E-11	2.0E+08	2.5E-03	5.0E-08	1.3E-10	0.50	6.3E-11
twinning on e-planes				5.0E-06	1.3E-11	1.0E+06	1.3E-05	5.0E-08	6.3E-13	0.50	3.1E-13
Regime IIIa (fast)											
work applied	2.3E-02										2.3E-08
elastic response											na
plastic deformation											na
gouge produced		2.0E-06	4.0E-18		2.4E-09						4.8E-10
twinning on e-planes				2.0E-05	2.0E-10	1.0E+06	2.0E-04	5.0E-08	1.0E-11	0.67	6.7E-12
fracture on r-planes				2.0E-05	2.0E-10				8.0E-11	0.17	1.3E-11
Regime IIIb (slow)											
work applied	1.9E-02										1.9E-08
elastic response											na
plastic deformation											na
gouge produced		4.0E-06	1.6E-17		9.6E-09						1.9E-09
twinning on e-planes				4.0E-05	8.0E-10	1.0E+06	8.0E-04	5.0E-08	4.0E-11	0.67	2.7E-11
fracture on r-planes				4.0E-05	8.0E-10				3.2E-10	0.17	5.3E-11

List of Figures

104

Figure 1. Indenter Geometry
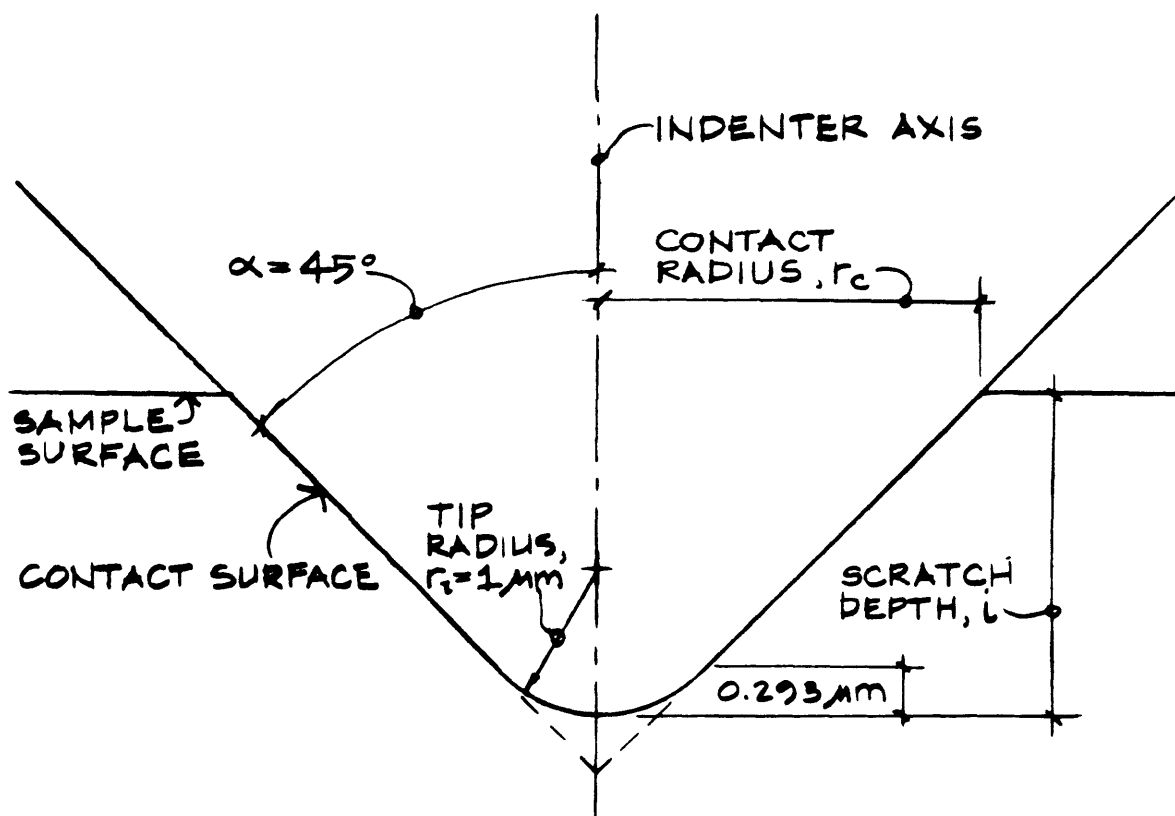
Figure 2a. Plots of mechanical data for scratch 3-1: constant load = 35mN, scratch velocity = 0.13 μm/s

scratch 3-1 normal load
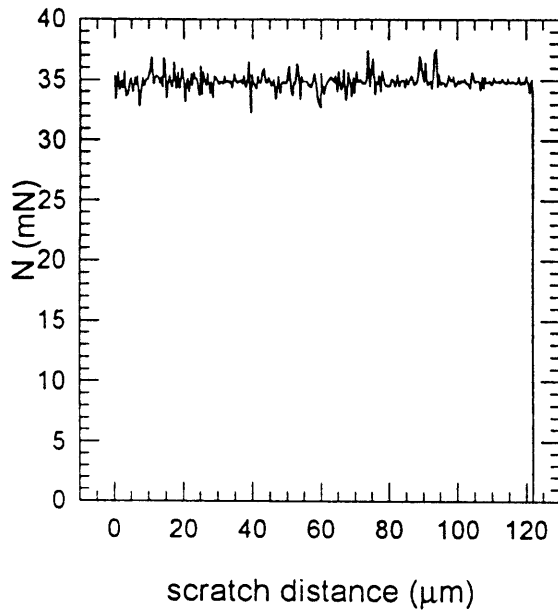
scratch 3-1 tangential load
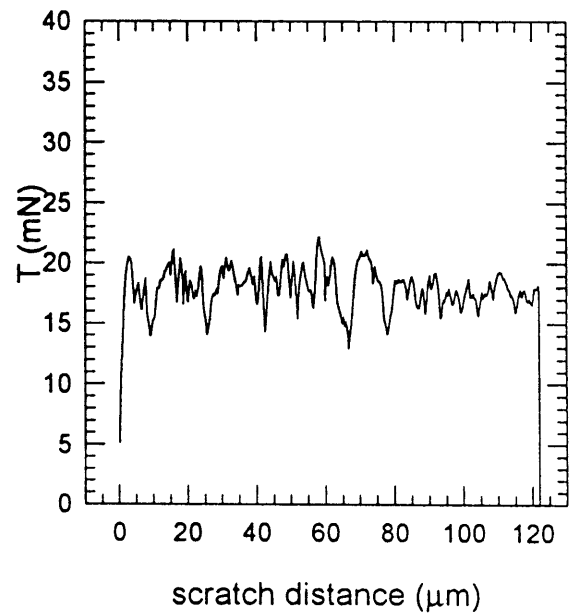
scratch 3-1 scratch depth
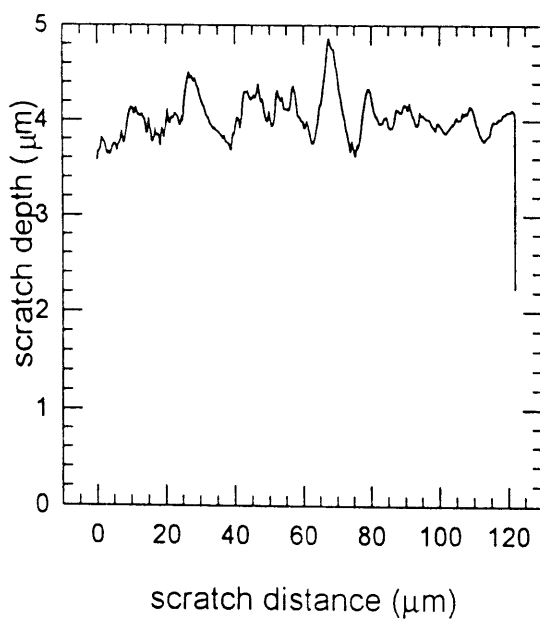
scratch 3-1 friction
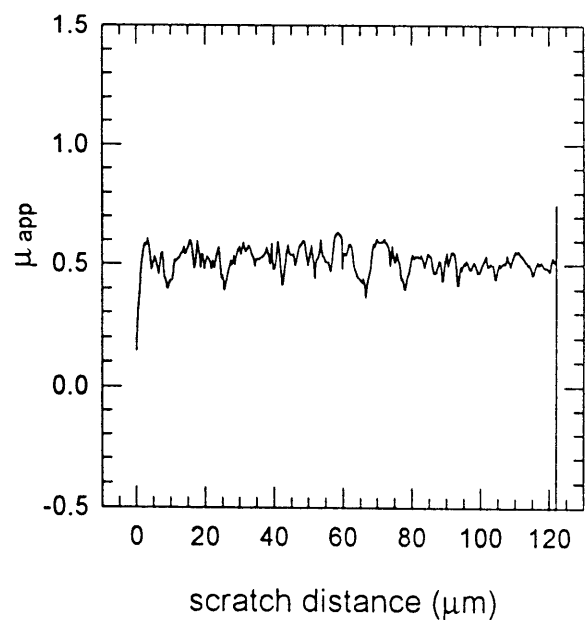
Figure 2b. Plots of mechanical data for scratch 4-4: constant load = 35mN, scratch velocity = 100 μm/s

scratch 4-4 normal load

scratch 4-4 tangential load

scratch 4-4 scratch depth

scratch 4-4 friction
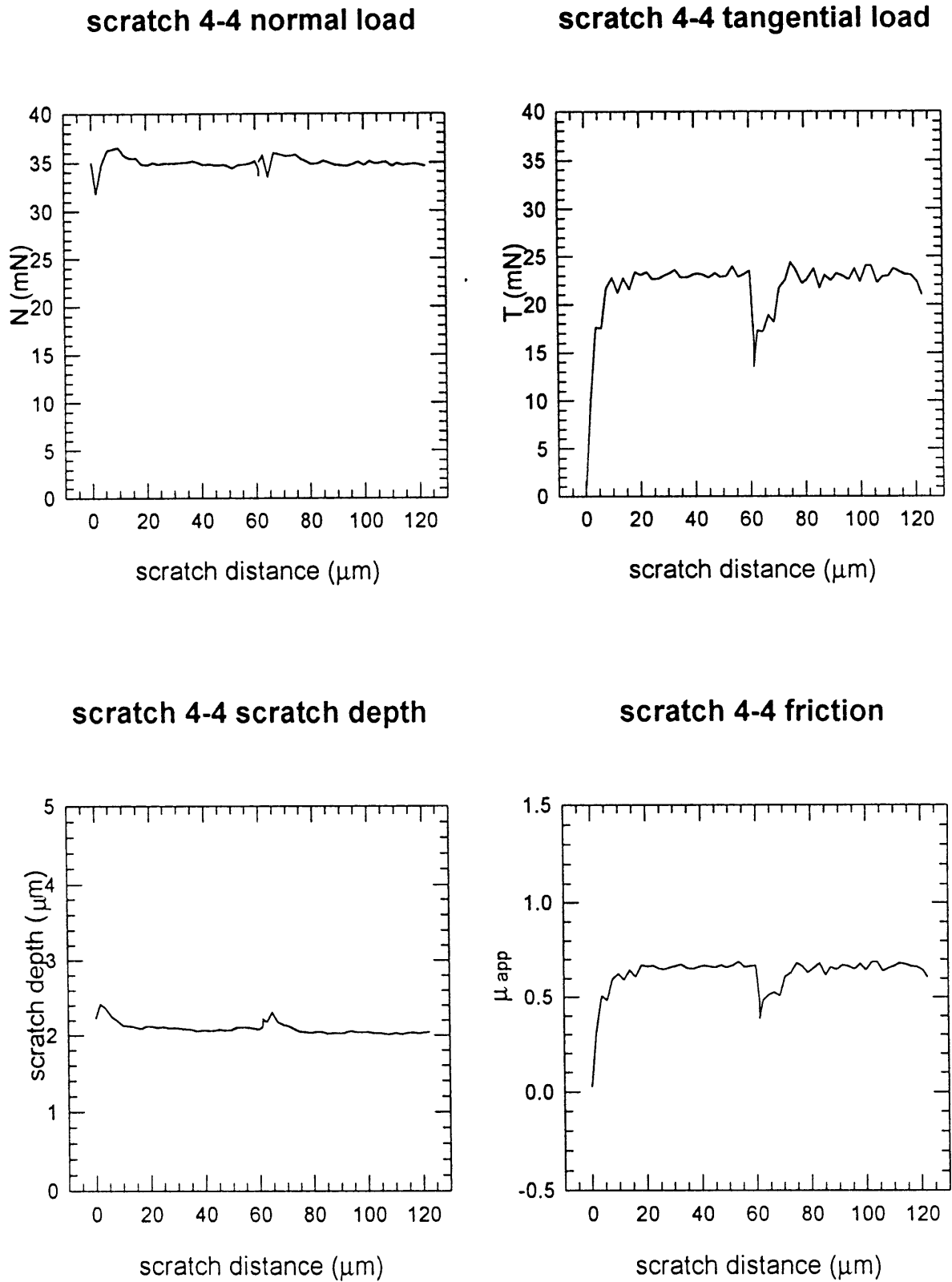
Figure 2c. Plots of mechanical data for scratch 8-2: constant load = 3mN, scratch velocity
= 100 μm/s

scratch 8-2 normal load
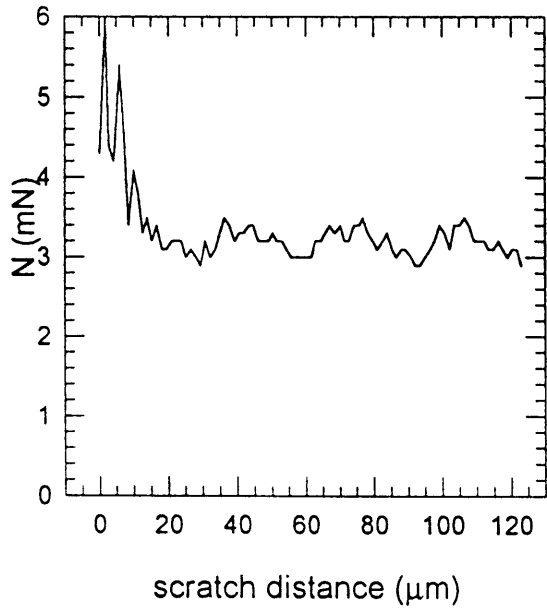
scratch 8-2 tangential load
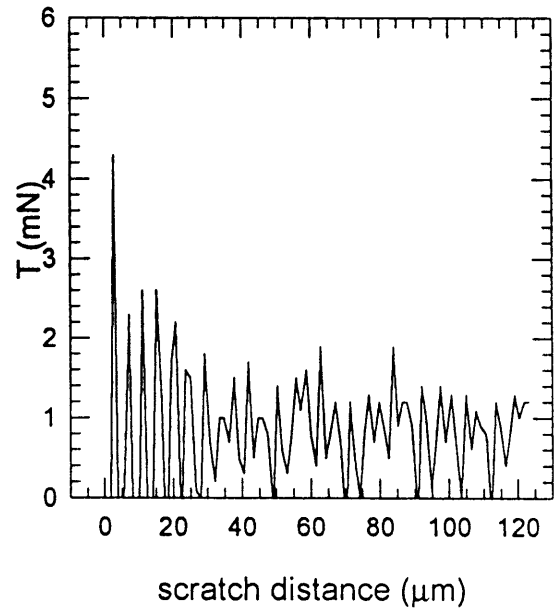
scratch 8-2 scratch depth
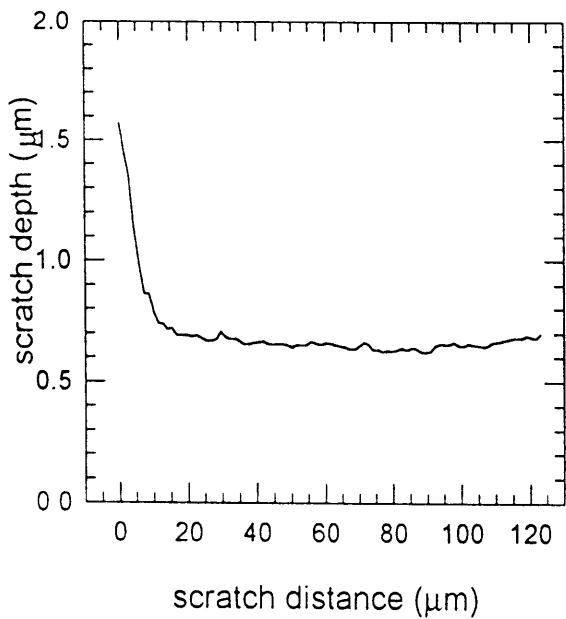
scratch 8-2 friction
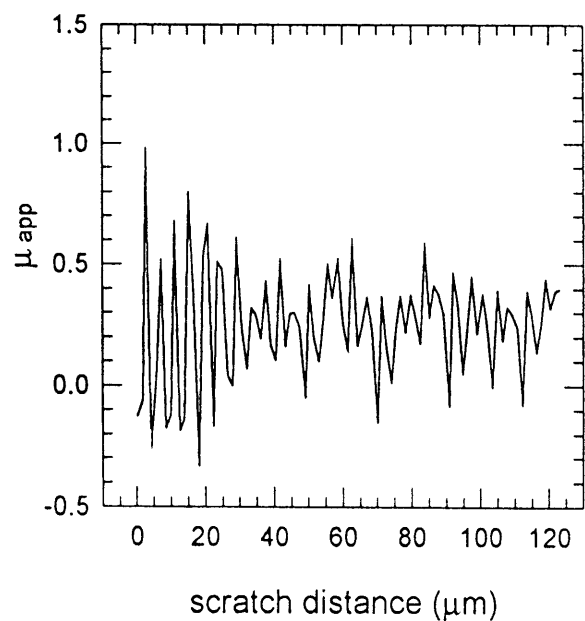
Figure 2d. Plots of mechanical data for scratch 10-5: constant penetration rate, scratch velocity = 1 μm/s

scratch 10-5 normal load

scratch 10-5 tangential load

scratch 10-5 scratch depth

scratch 10-5 friction
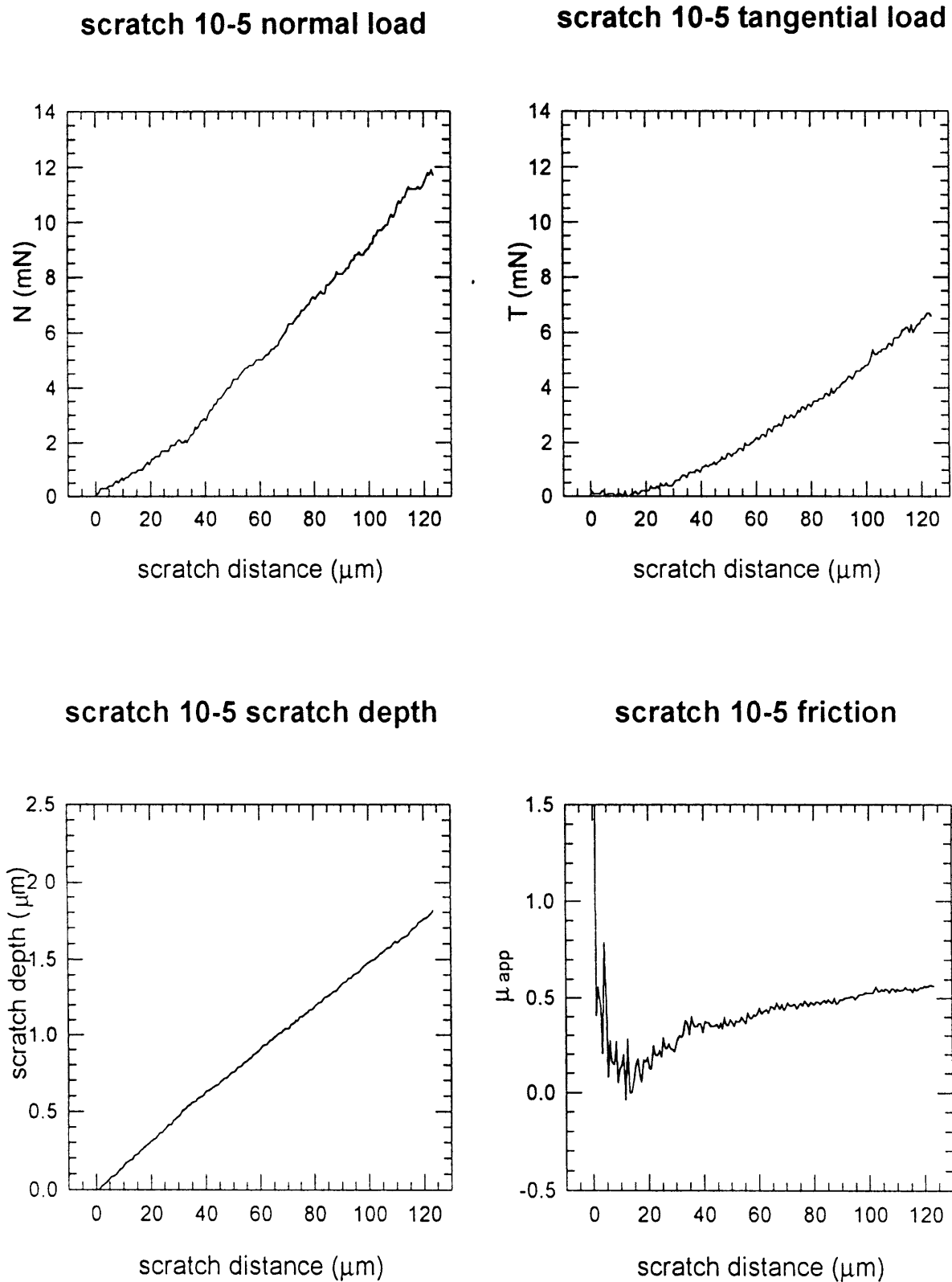
Figure 2e. Plots of mechanical data for scratch 13-4: constant penetration rate, scratch velocity = 100 μm/s

scratch 13-4 normal load
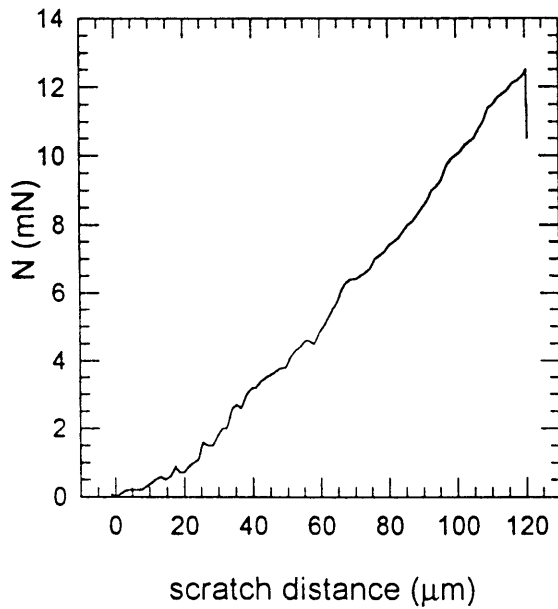
scratch 13-4 tangential load
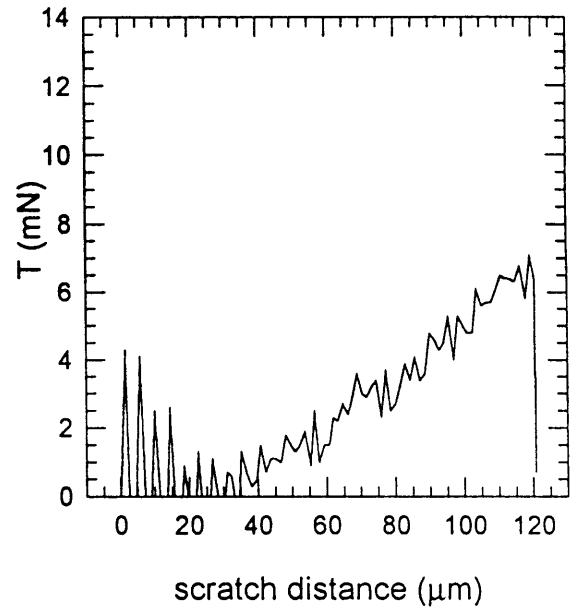
scratch 13-4 scratch depth
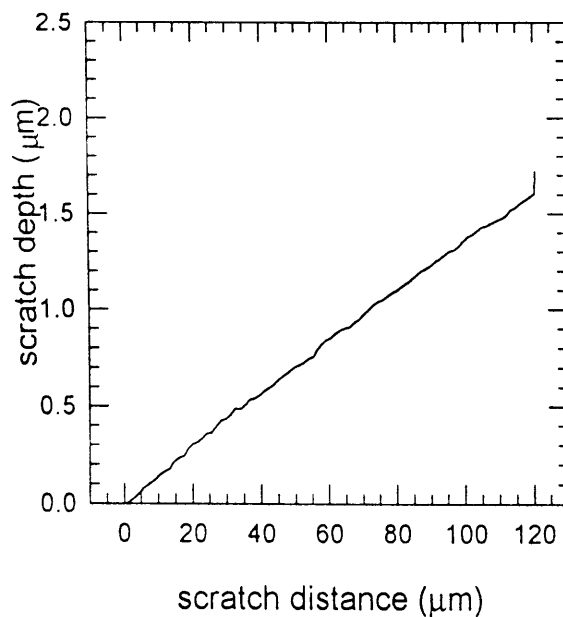
scratch 13-4 friction

Figure 3a: Plot of μ_{app} versus N: Constant Load Tests

constant load tests

Legend:
- ○ $v_s = 0.13\ \mu m/s$
- ● $v_s = 100\ \mu m/s$

X-axis: N (mN)

Y-axis: apparent friction coefficient
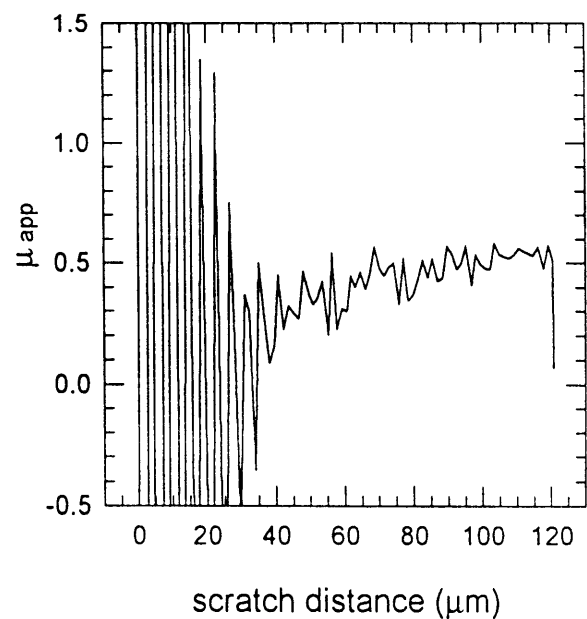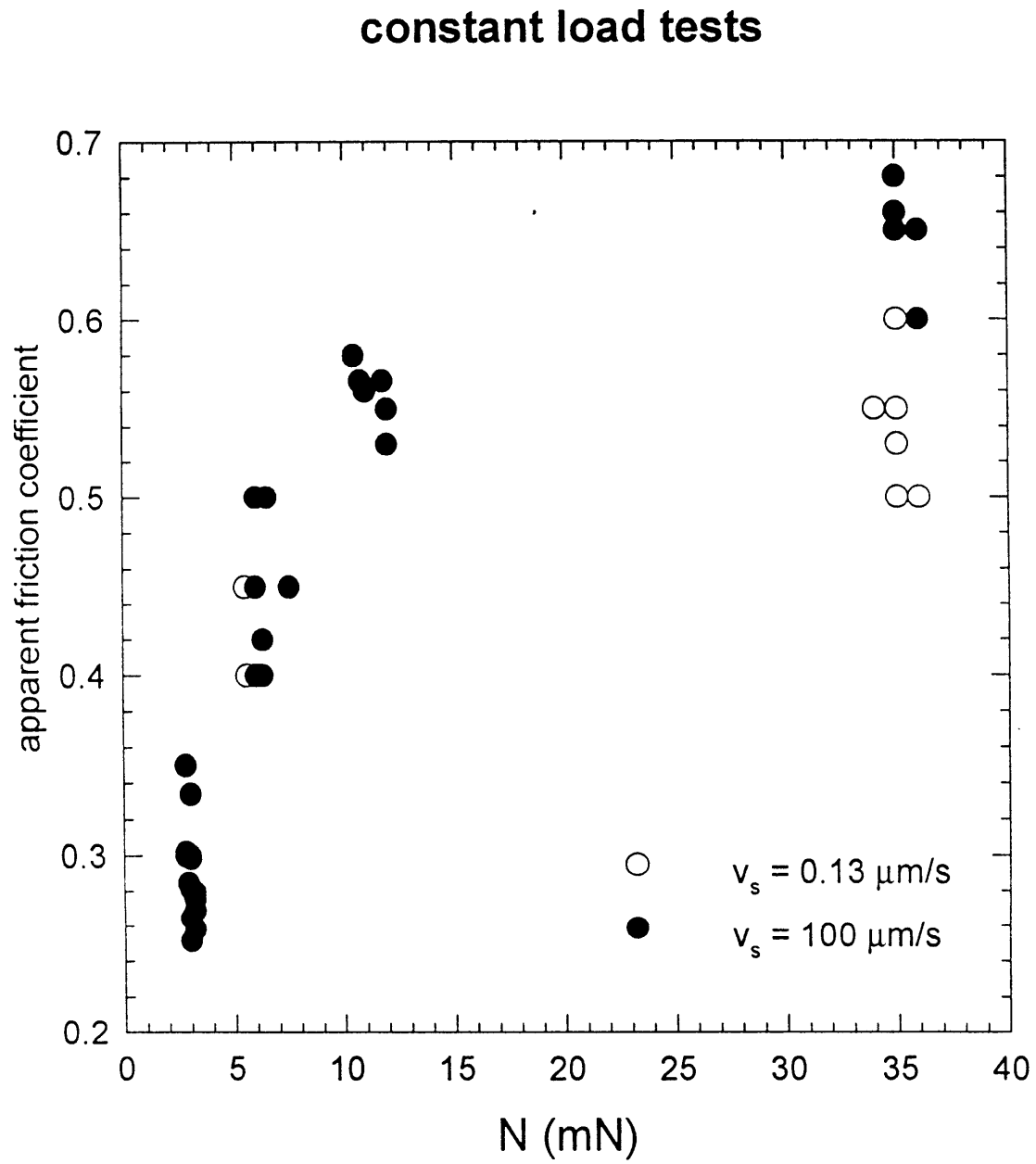
Figure 3b: Plot of μ_{app} versus N: Constant Penetration Rate Tests (examples)

constant load and typical constant penetration rate tests
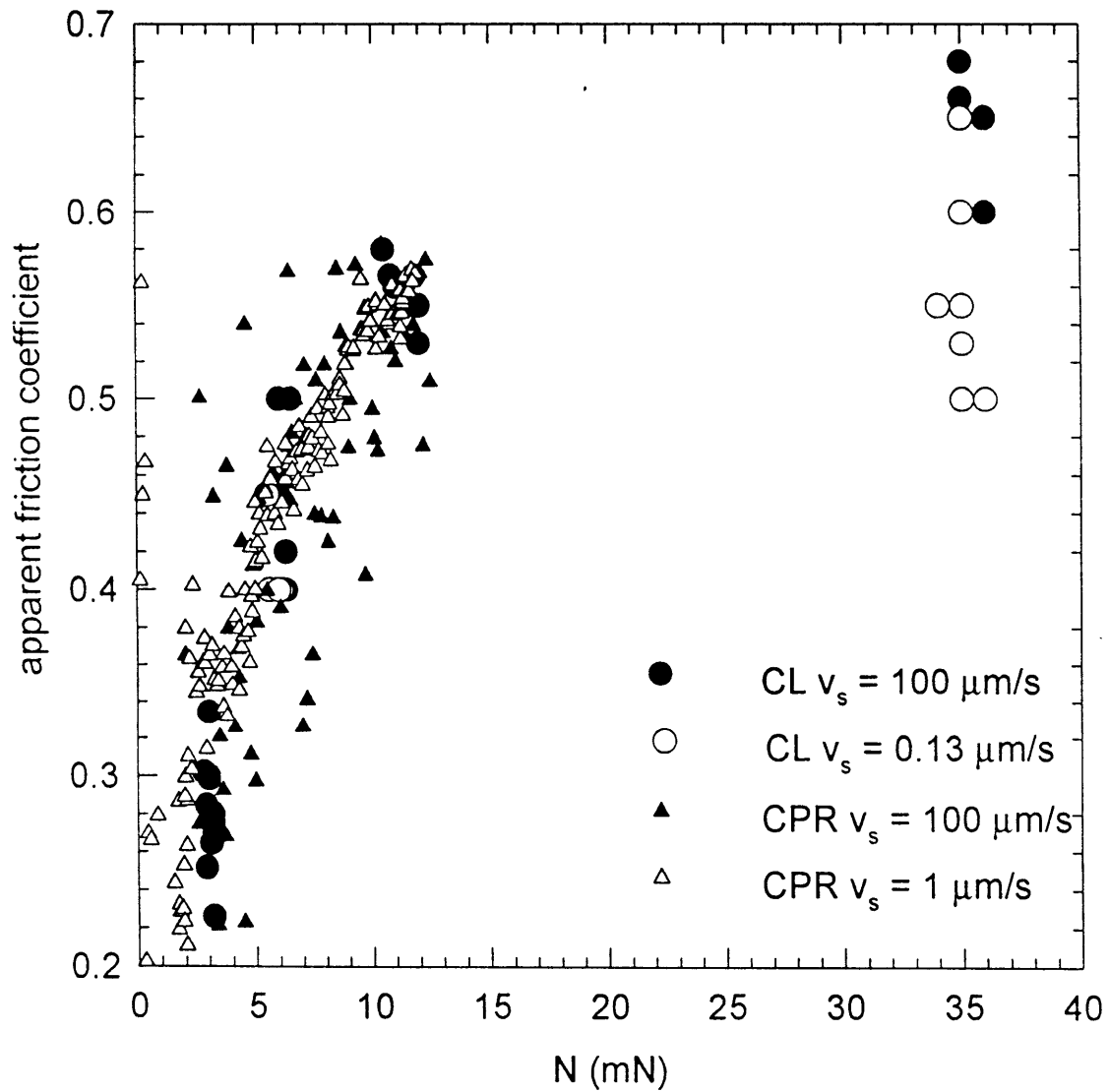
Figure 4a: Plot of Data from Indentation Test: Scratch Depth versus Normal Load
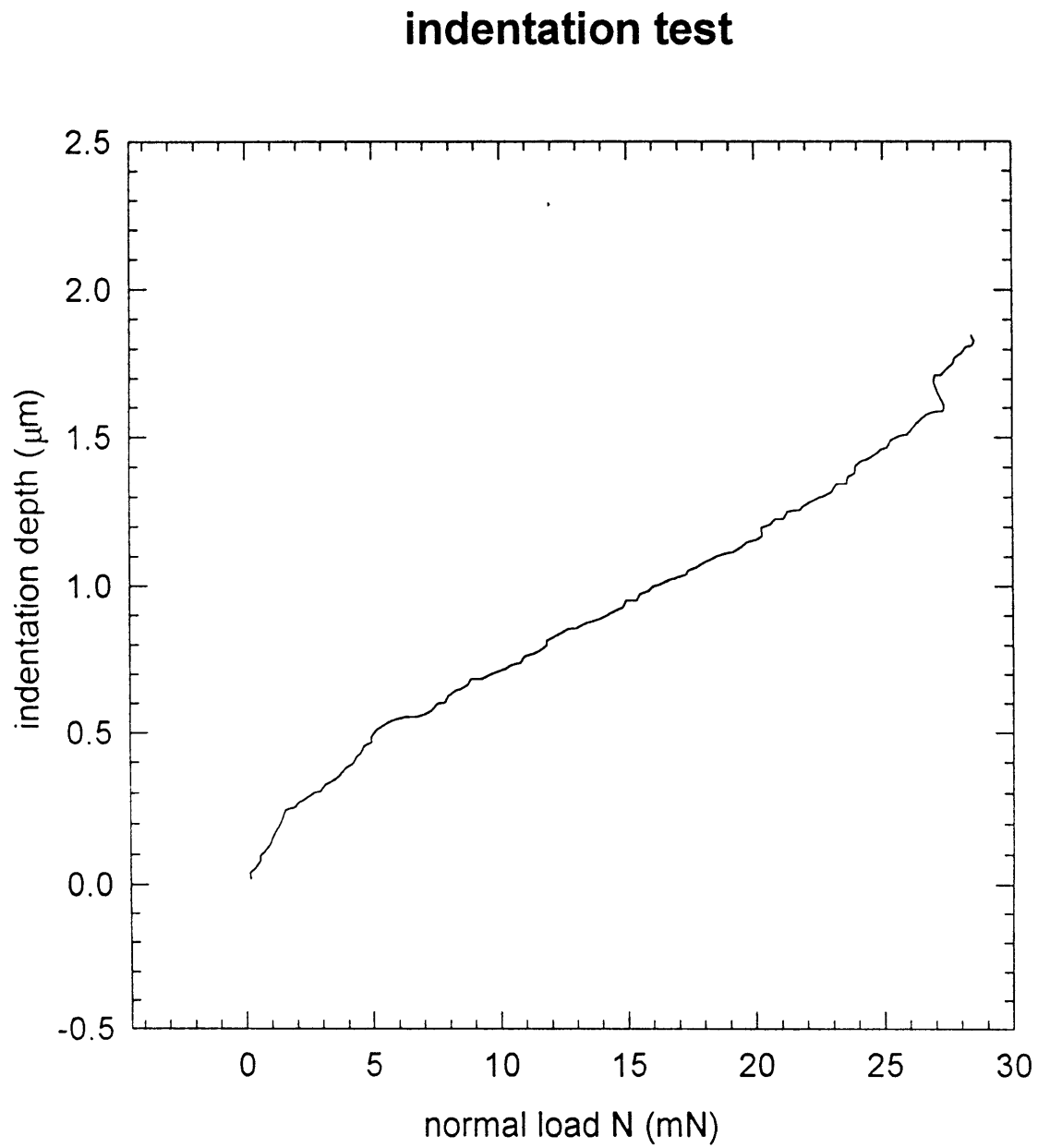
indentation test

Figure 4b: Plot of Data from Indentation Test: H_{nor} versus Scratch Depth

indentation hardness
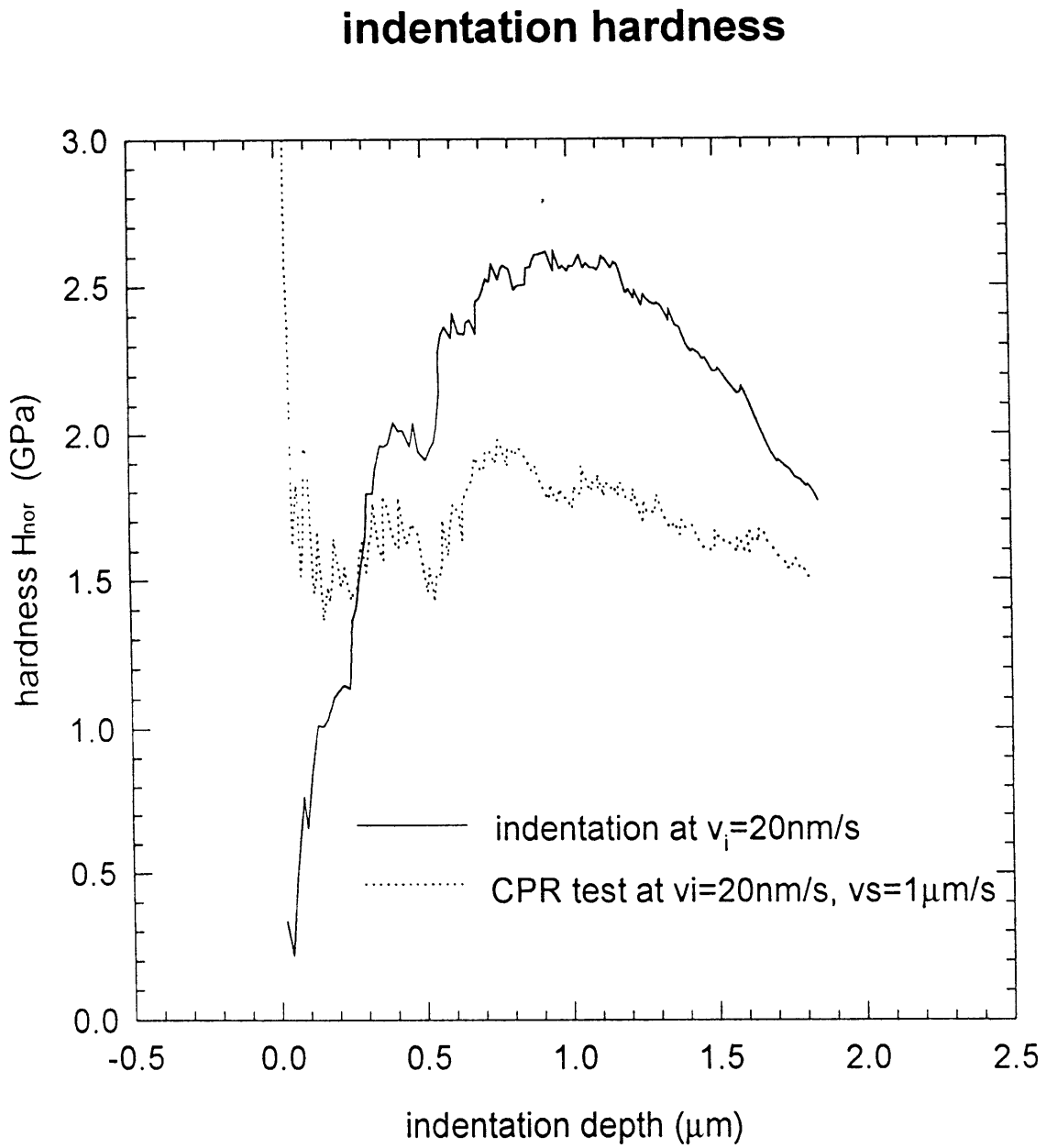
Figure 5a: Optical Photograph of Sample 1: constant load = 6 mN, scratch velocity = 0.13 μm/s.
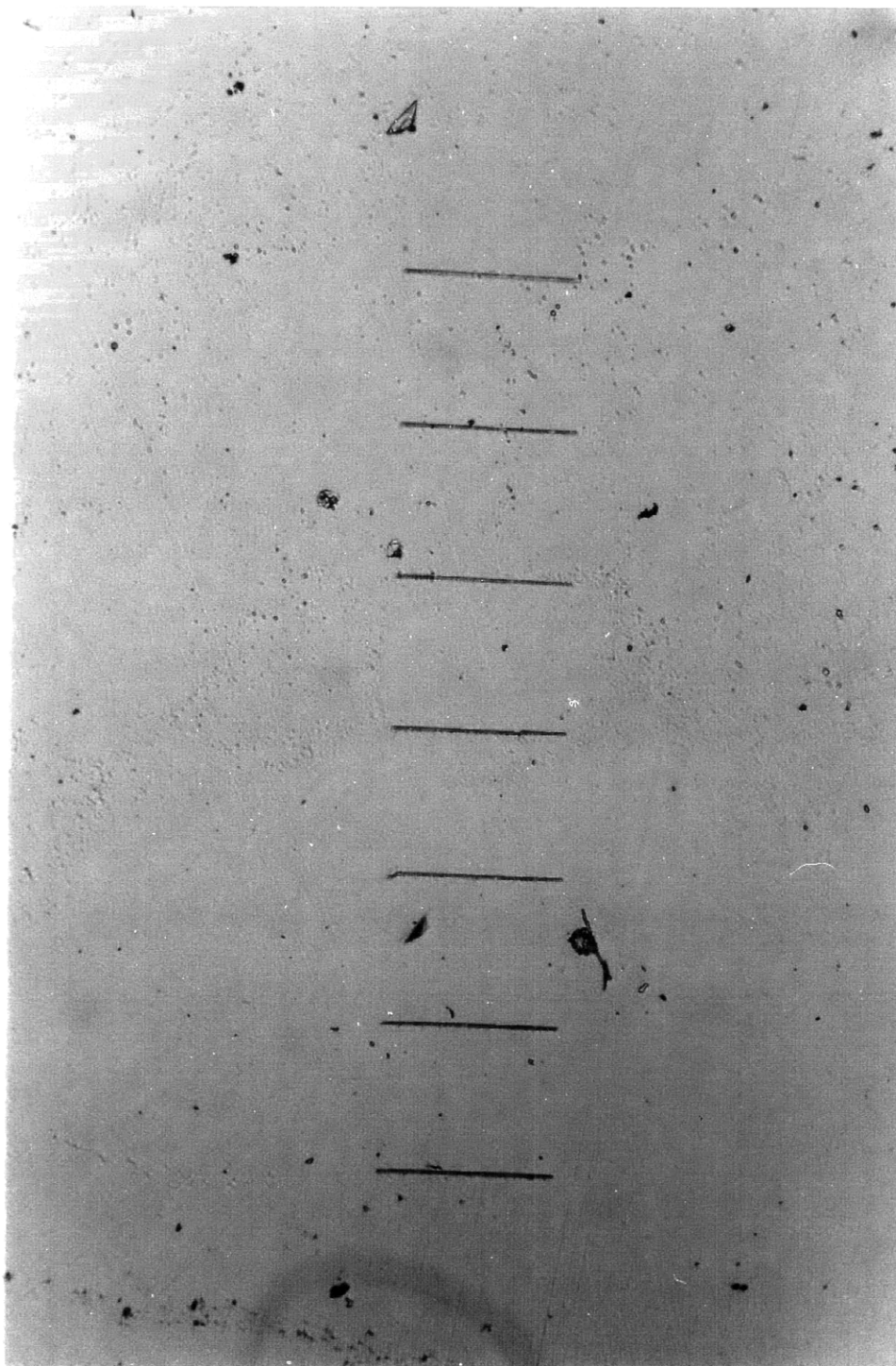
Figure 5b: Optical Photograph of Sample 2: constant load = 6 mN, scratch velocity = 100 μm/s.

Figure 5c: Optical Photograph of Sample 3: constant load = 35 mN, scratch velocity = 0.13 μm/s.
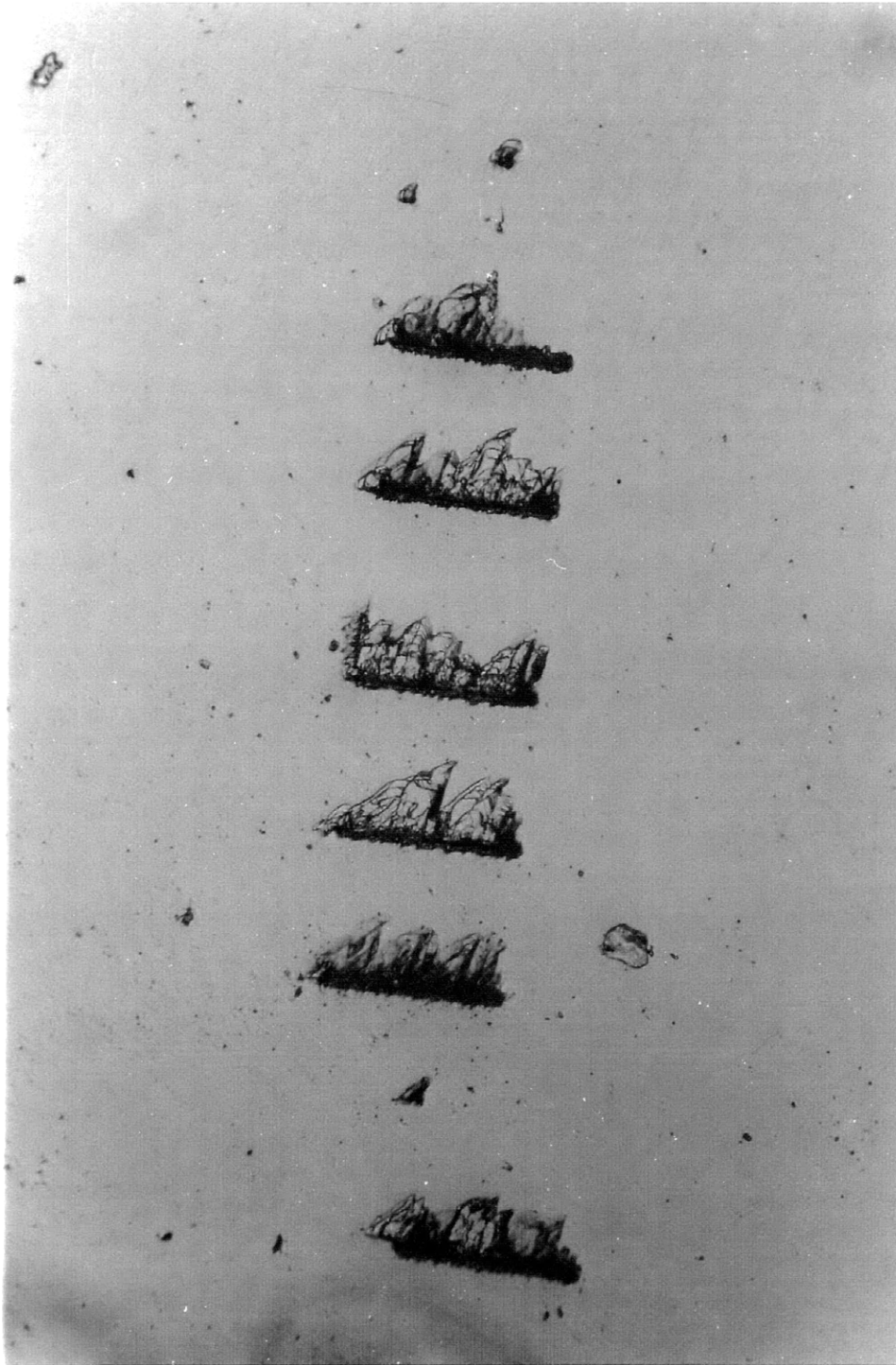
Figure 5d: Optical Photograph of Sample 4: constant load = 35 mN, scratch velocity = 100 μm/s.
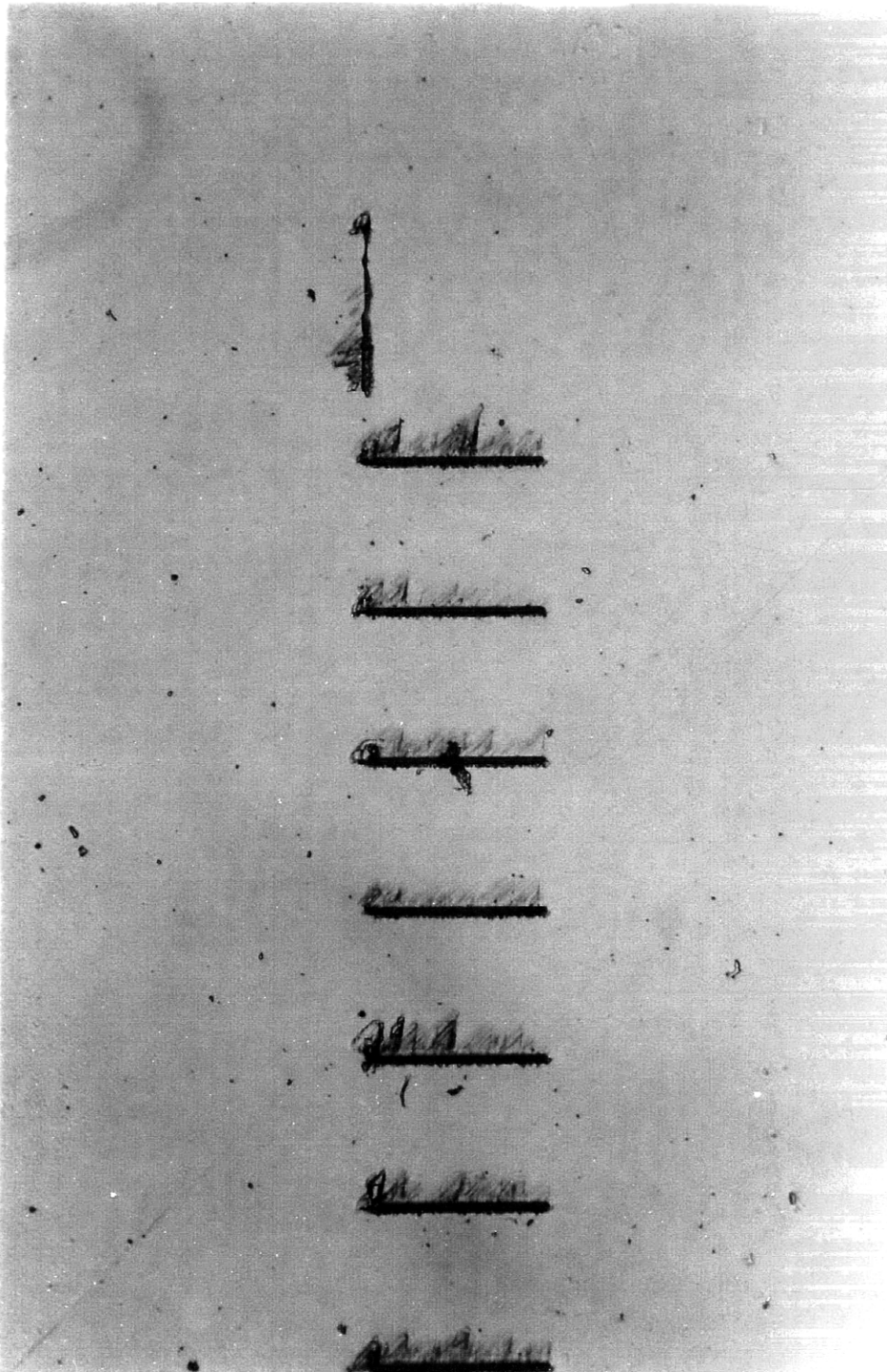
Figure 5e: Optical Photograph of Sample 7: constant load = 3 mN, scratch velocity = 100 µm/s.
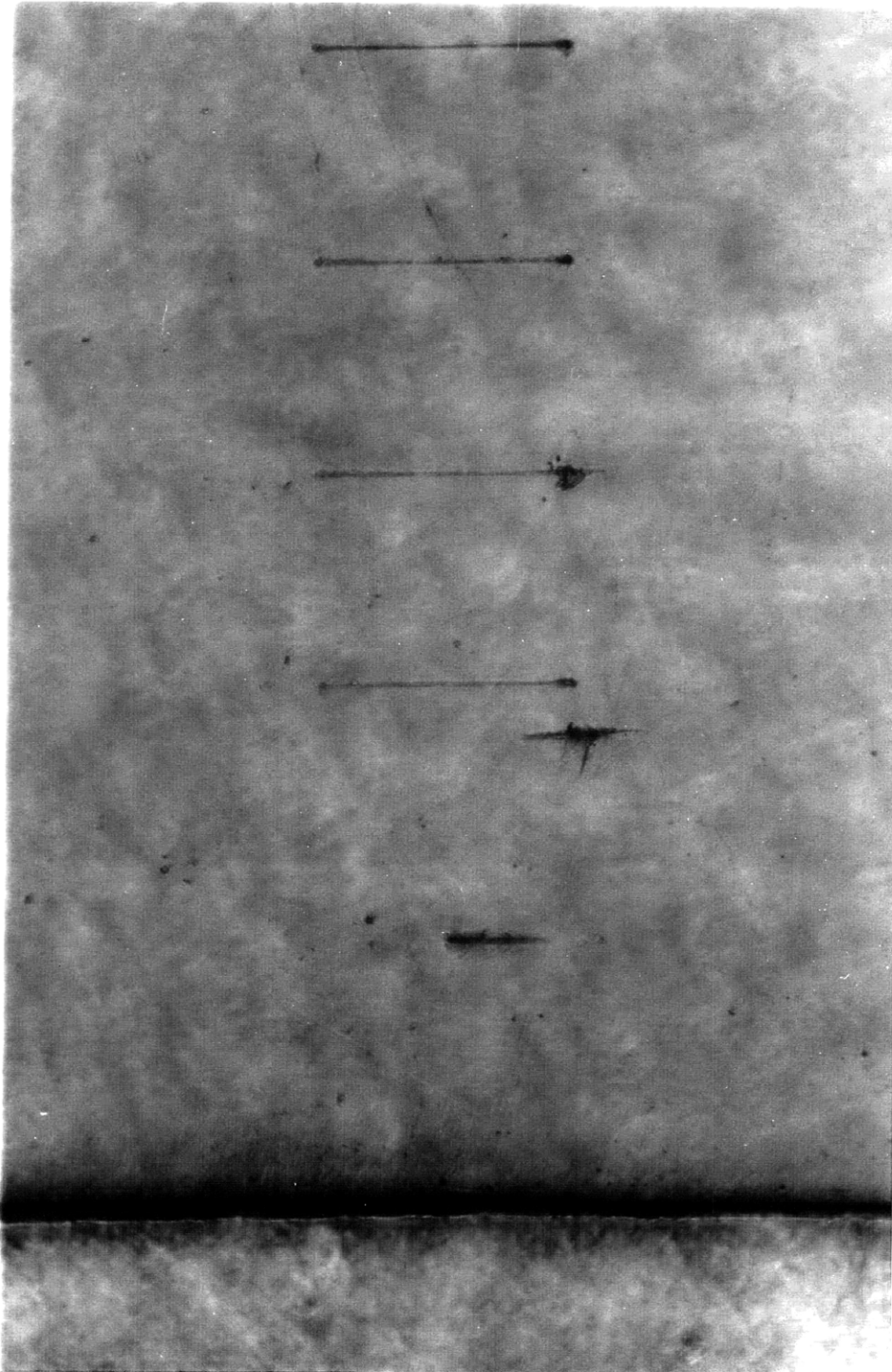
Figure 5f: Optical Photograph of Sample 8: constant load = 3 mN, scratch velocity = 100 μm/s.
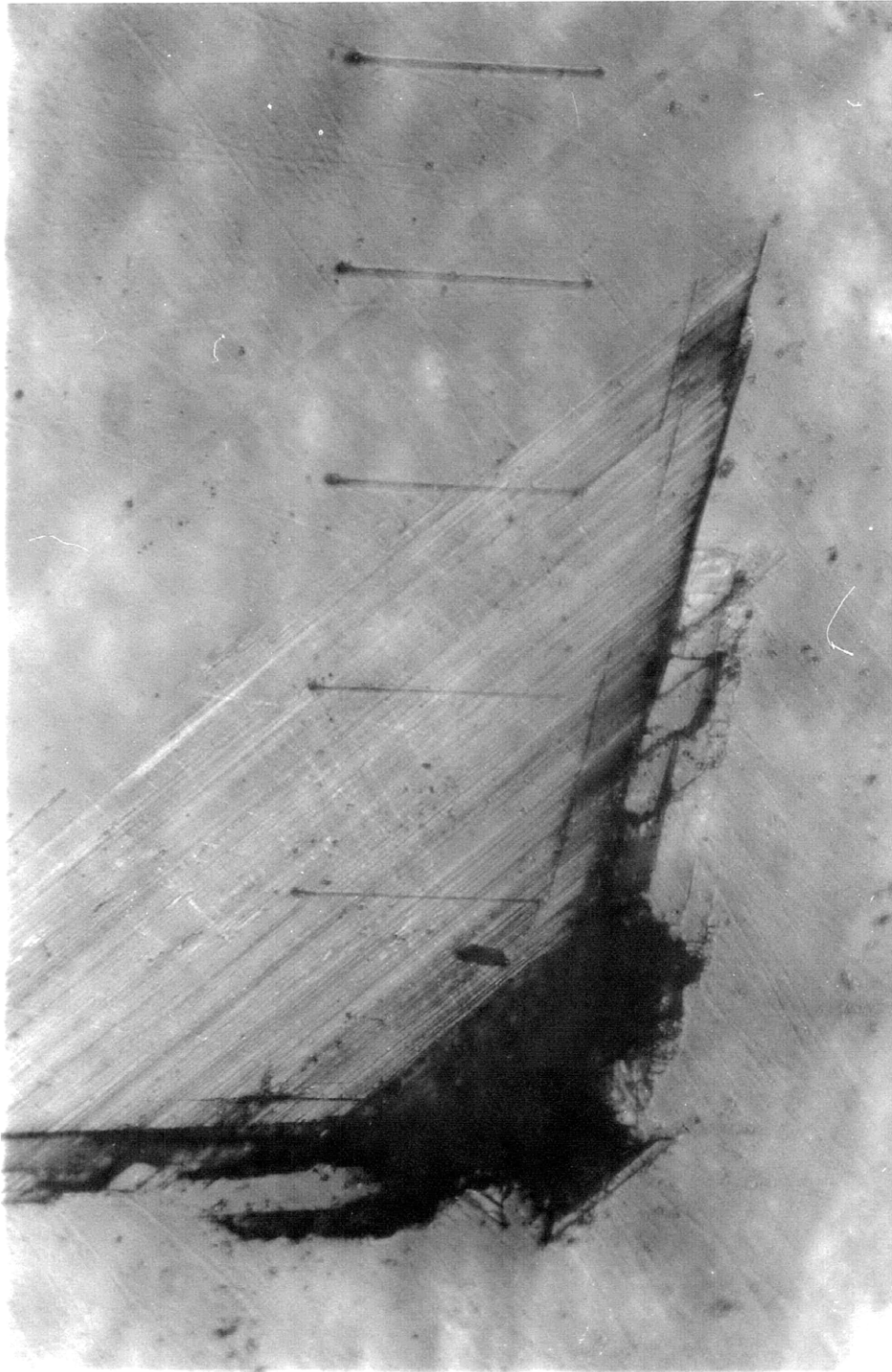
Figure 5g: Optical Photograph of Sample 9: constant load = 11 mN, scratch velocity = 100 µm/s.
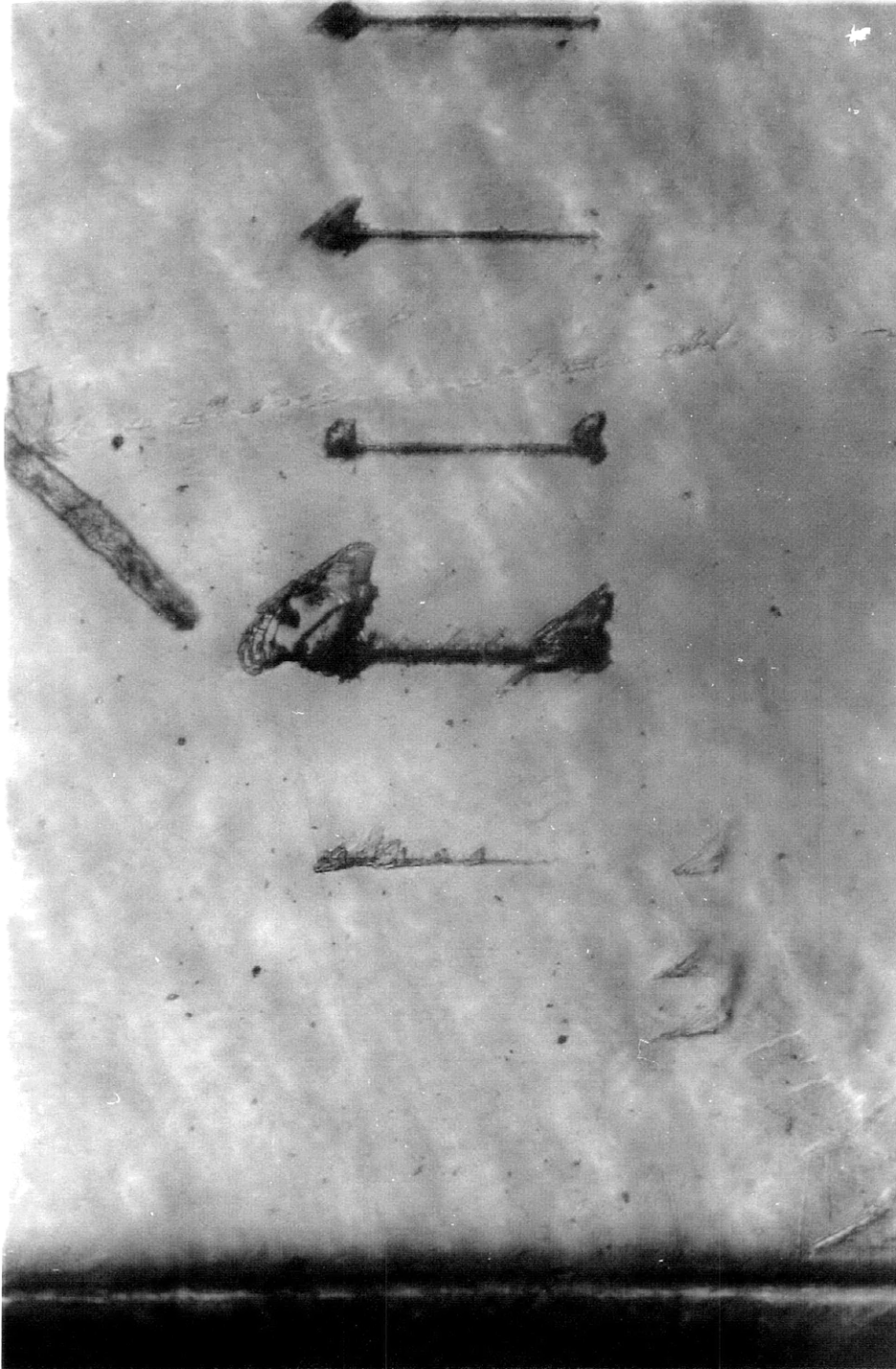
Figure 5h: Optical Photograph of Sample 10: constant penetration rate, scratch velocity = 1 μm/s.
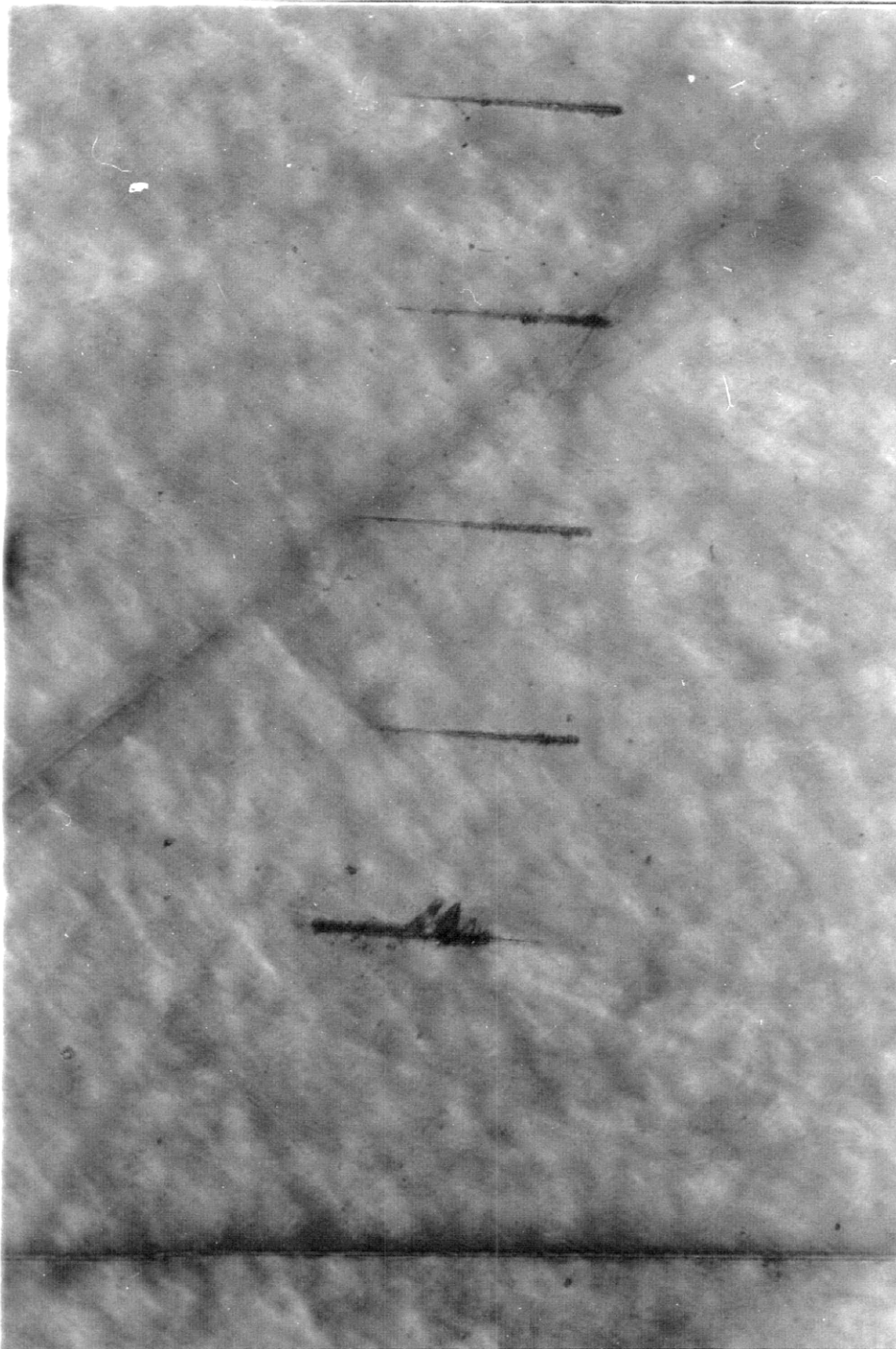
Figure 5i: Optical Photograph of Sample 11: constant penetration rate, scratch velocity = 1 µm/s.
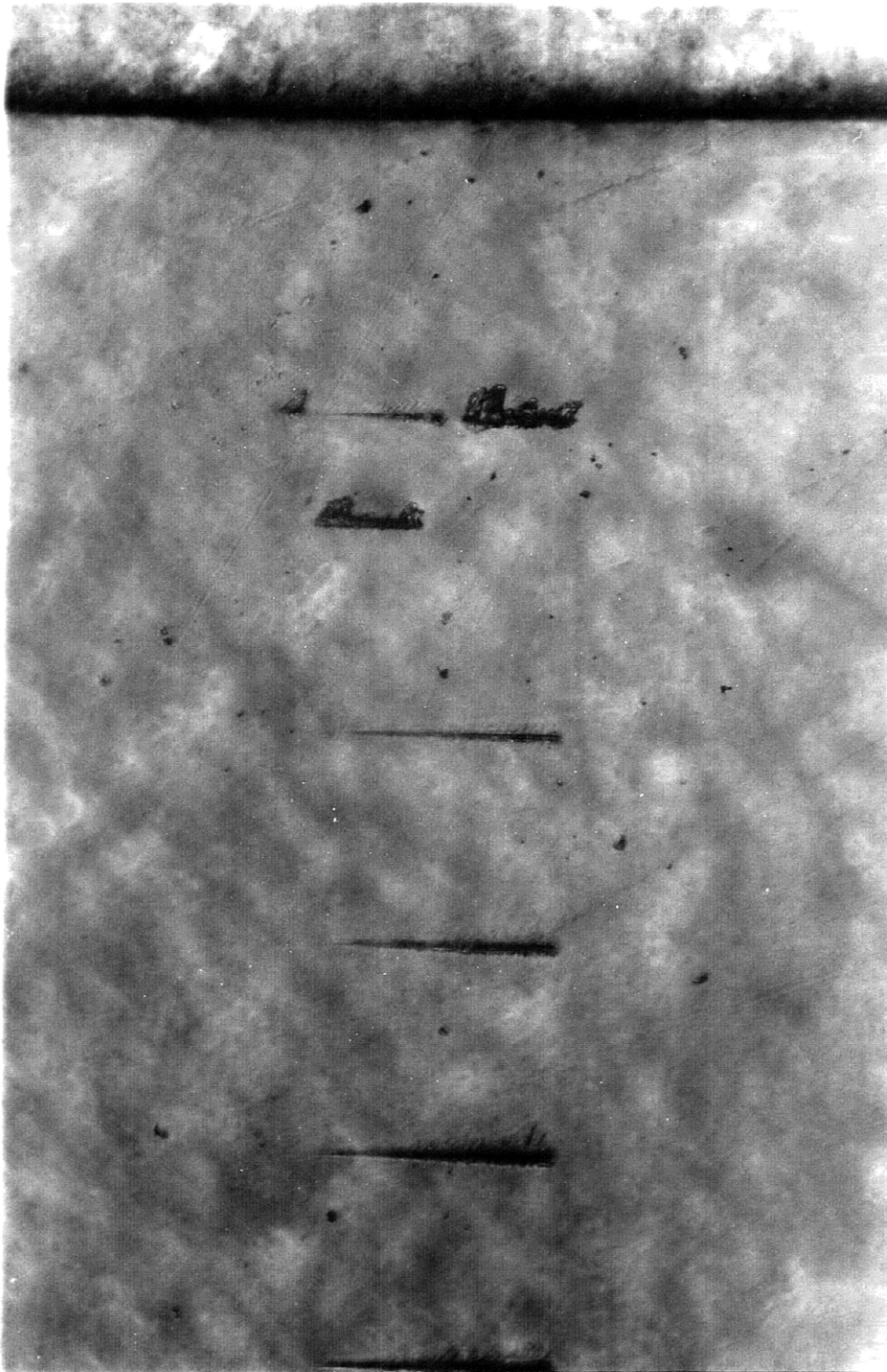
Figure 5j: Optical Photograph of Sample 12: constant penetration rate, scratch velocity = 1 μm/s.
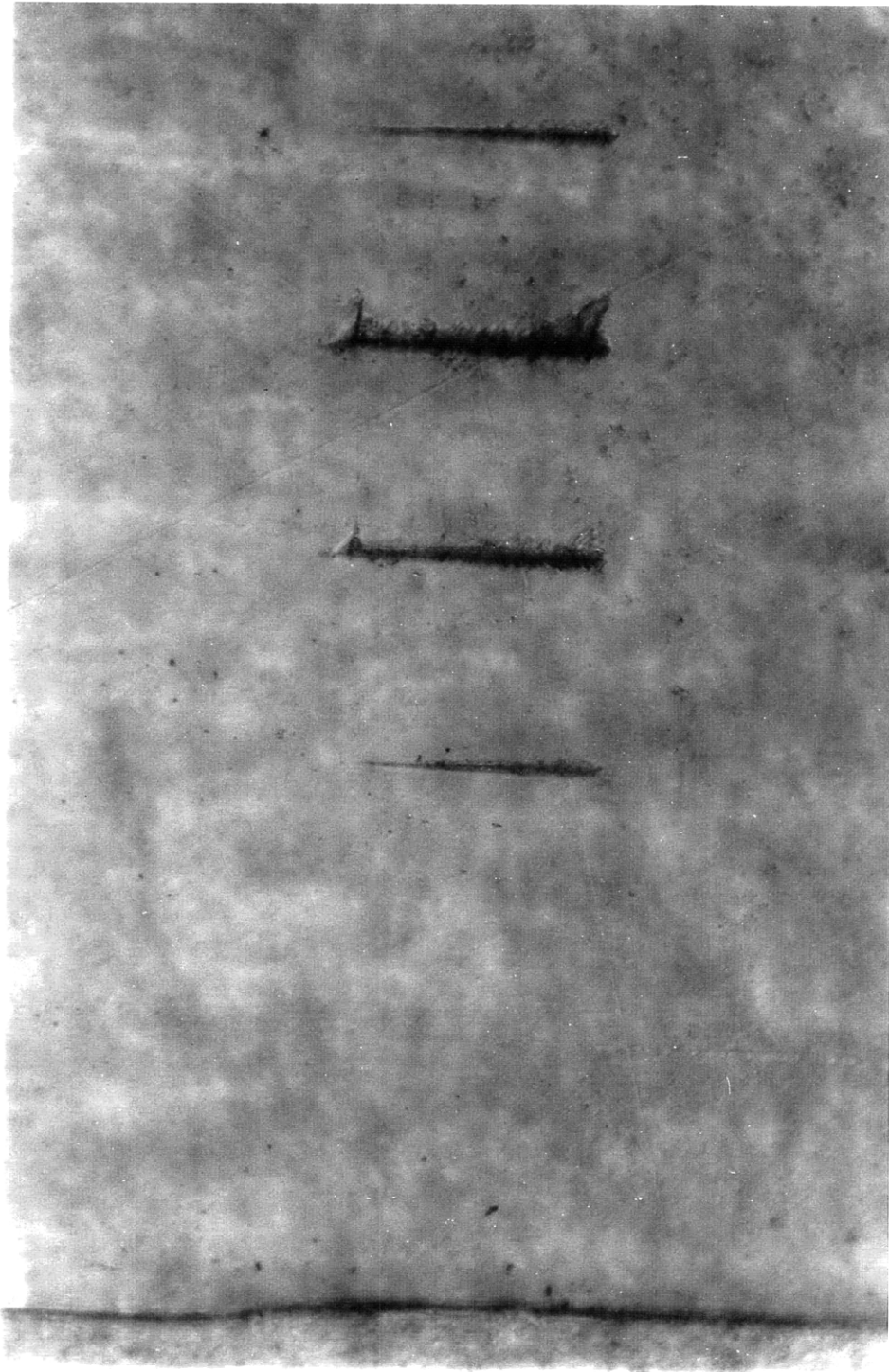
Figure 5k: Optical Photograph of Sample 13: constant penetration rate, scratch velocity = 100 μm/s.
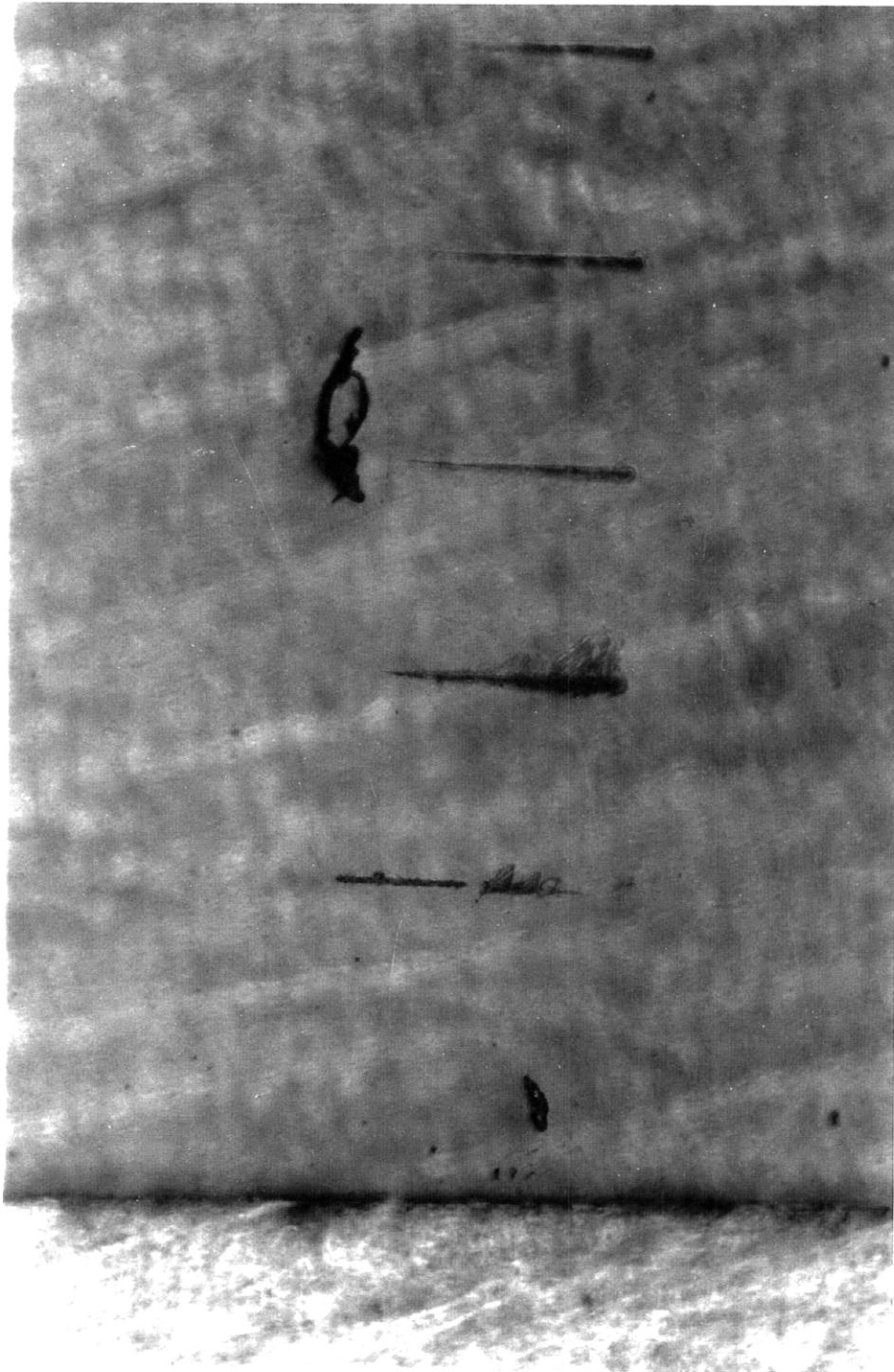
Figure 5l: Optical Photograph of Sample 14: constant penetration rate, scratch velocity = 100 µm/s.
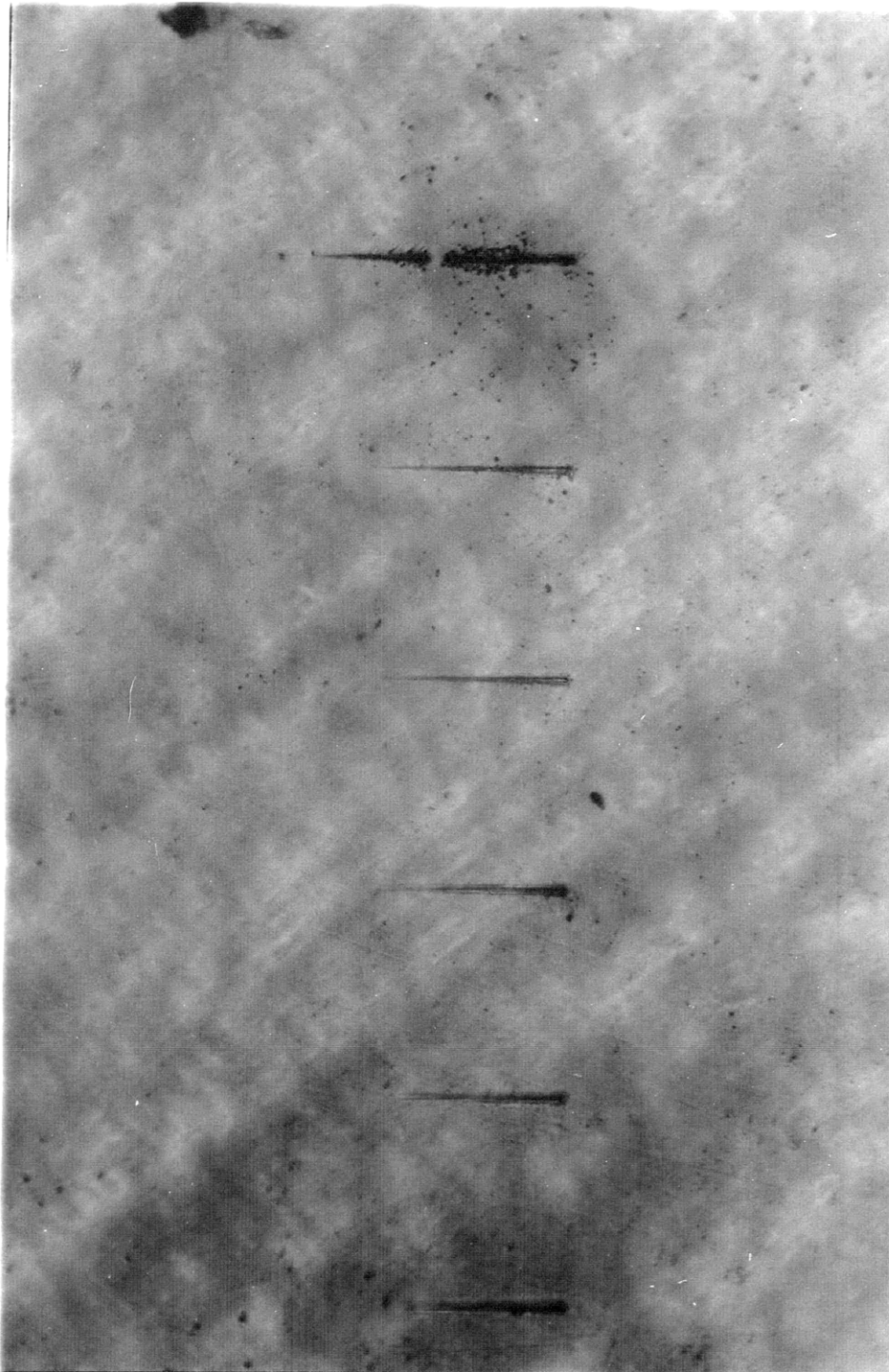
Figure 5m: Optical Photograph of Knoop Indentation.
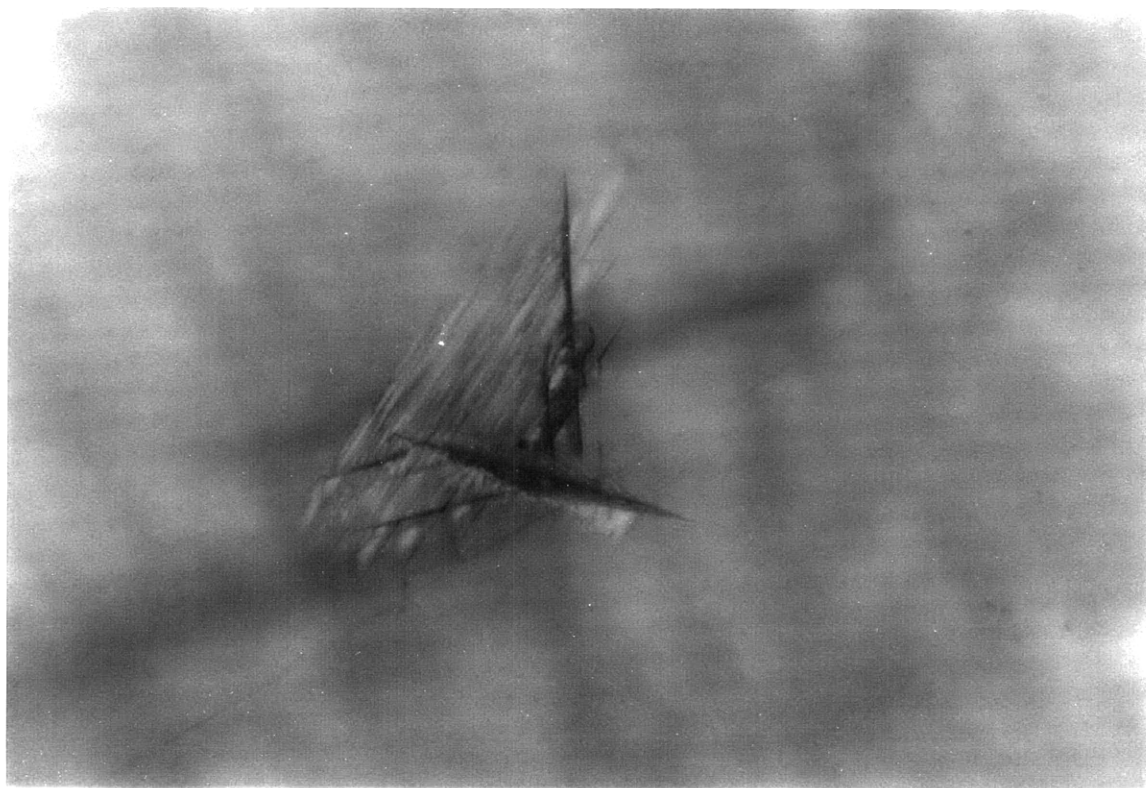
Figure 5n: Optical Photograph of Details: Slip planes.
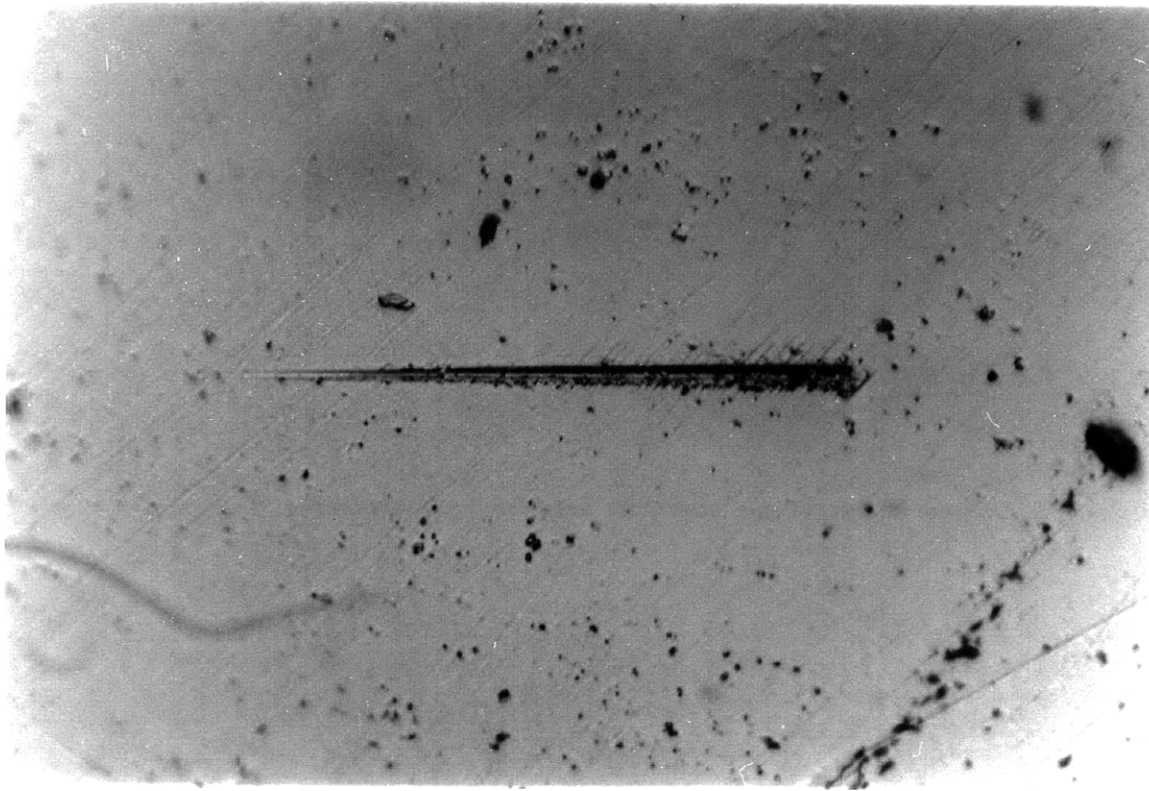
Figure 5o: Optical Photograph of Details: Pits.

145
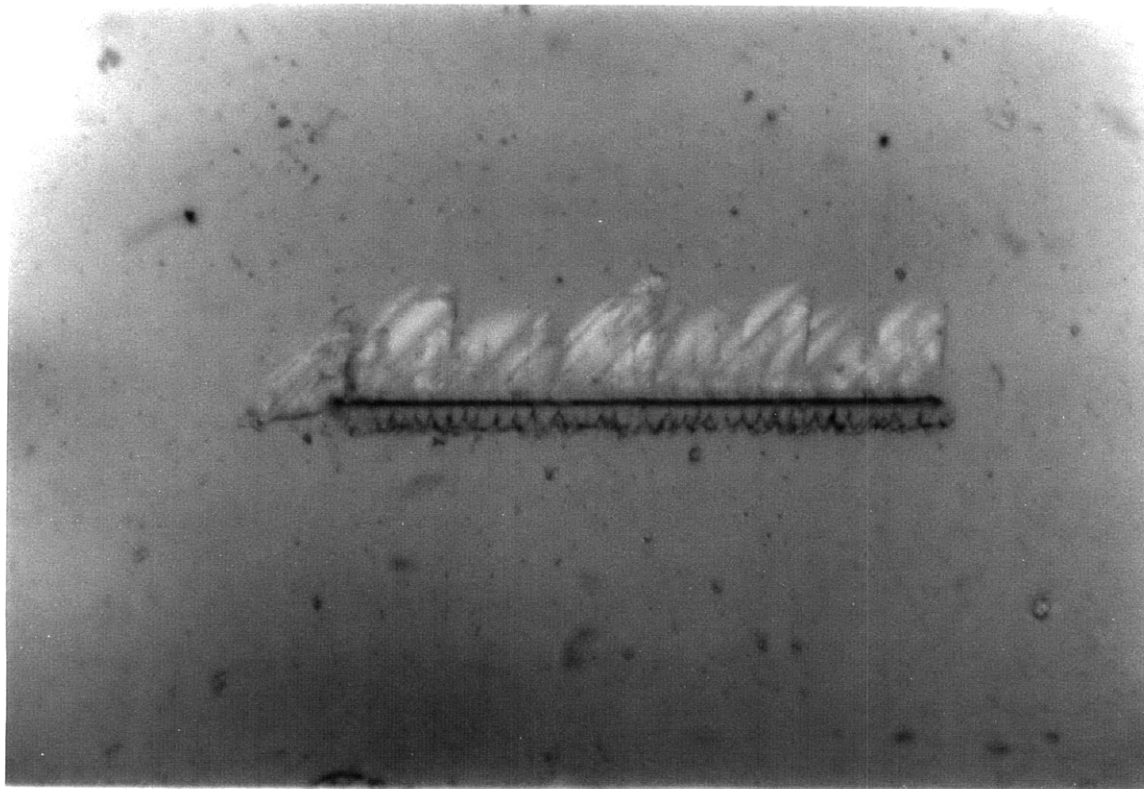
Figure 6a: Damage Features: Damage Feature Details
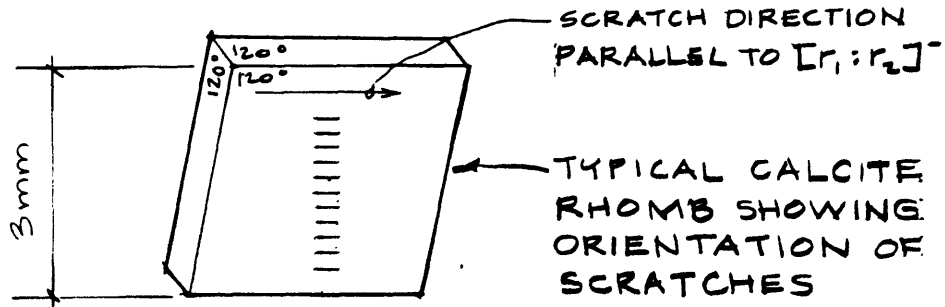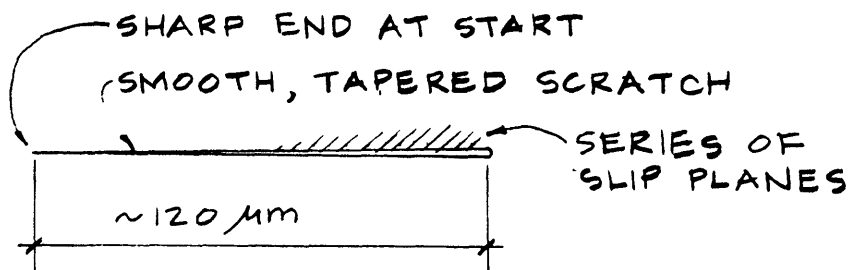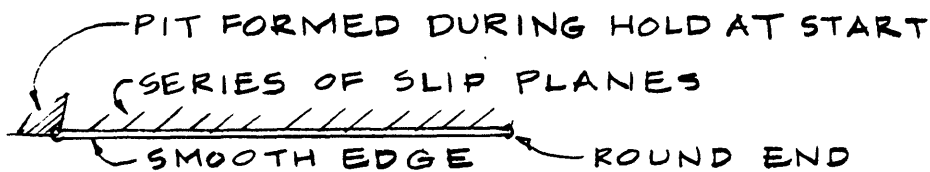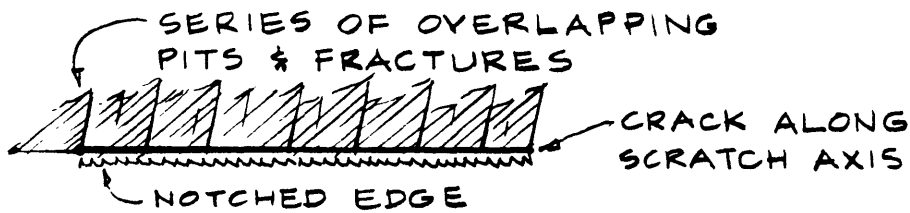
Figure 6b: Damage Features: Scratch Types
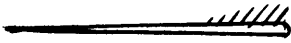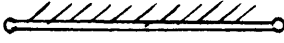
constant load tests	constant penetration rate tests
$v_s > 0$ scratch cross section	scratch cross section
$v_s > 0$ low N~3-6mN	v_s/v_i~50
$v_s > 0$ moderate: N~11mN	
$v_s > 0$ high: N~36mN	
$v_s = 0$ Knoop indentation	conical indentation

Figure 7a: Transmission Electron Microscopy: Planar features along *c*- edge of scratch 10-6 (scratch direction left to right; field of view 5 μm wide).
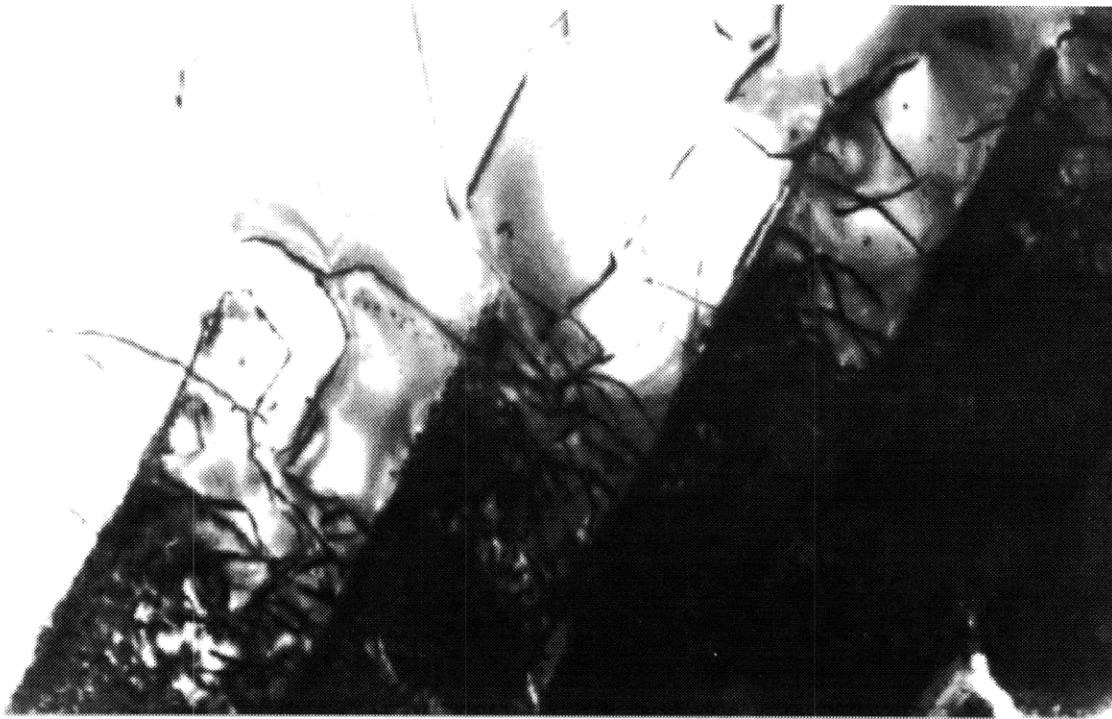
Figure 7b: Transmission Electron Microscopy: Planar features along *c*- edge of scratch 10-5: Detail (scratch direction left to right; field of view 2.5 μm wide).

Figure 7c: Transmission Electron Microscopy: Damage zone at prow of scratch 10-6 (scratch direction left to right; field of view 10 μm tall).
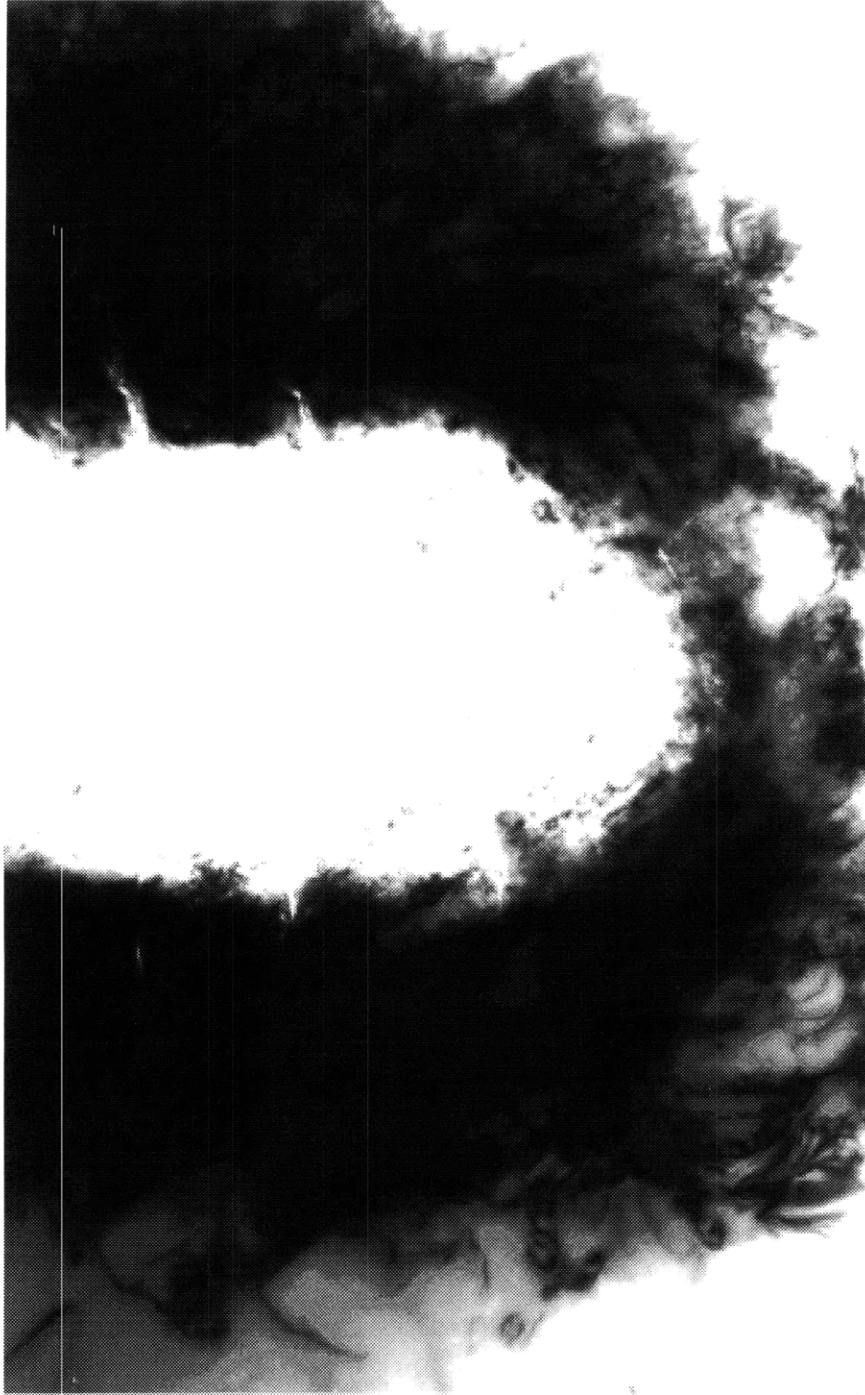
Figure 7d: Transmission Electron Microscopy: Dislocations and planar features at prow of scratch 10-6: Detail (scratch direction left to right; field of view 5 μm wide).
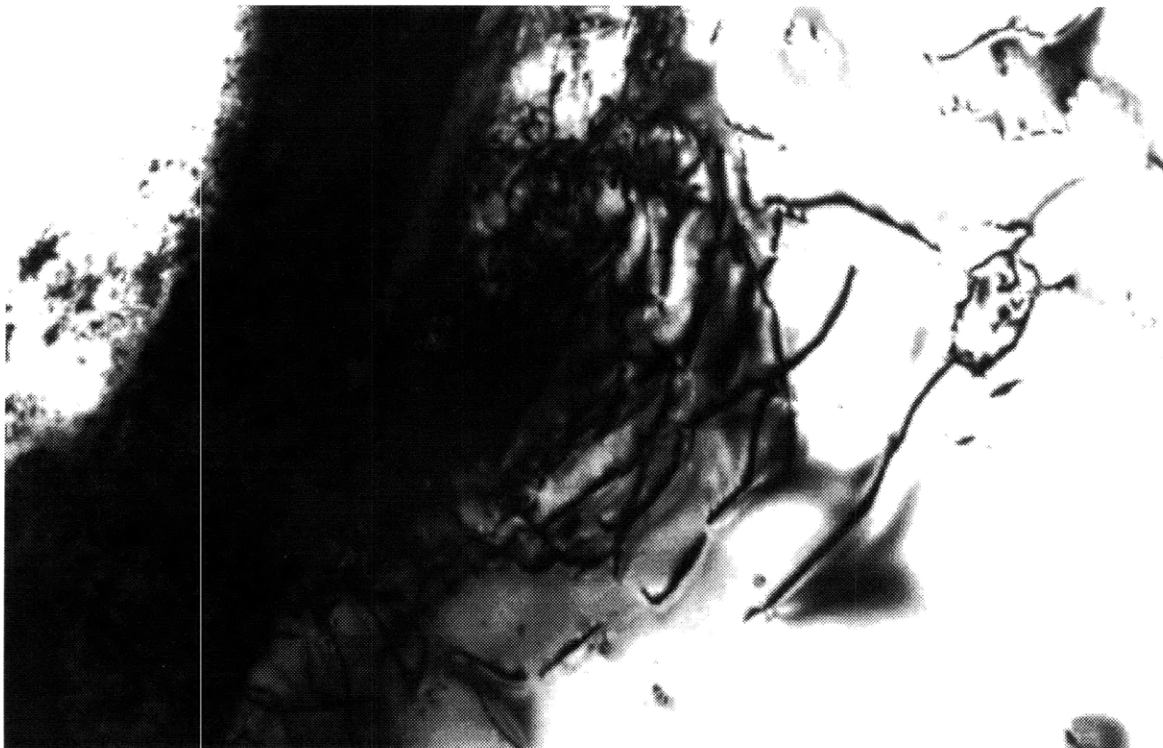
Figure 8: Plot of Scratch Damage Regimes.

scratch damage regimes
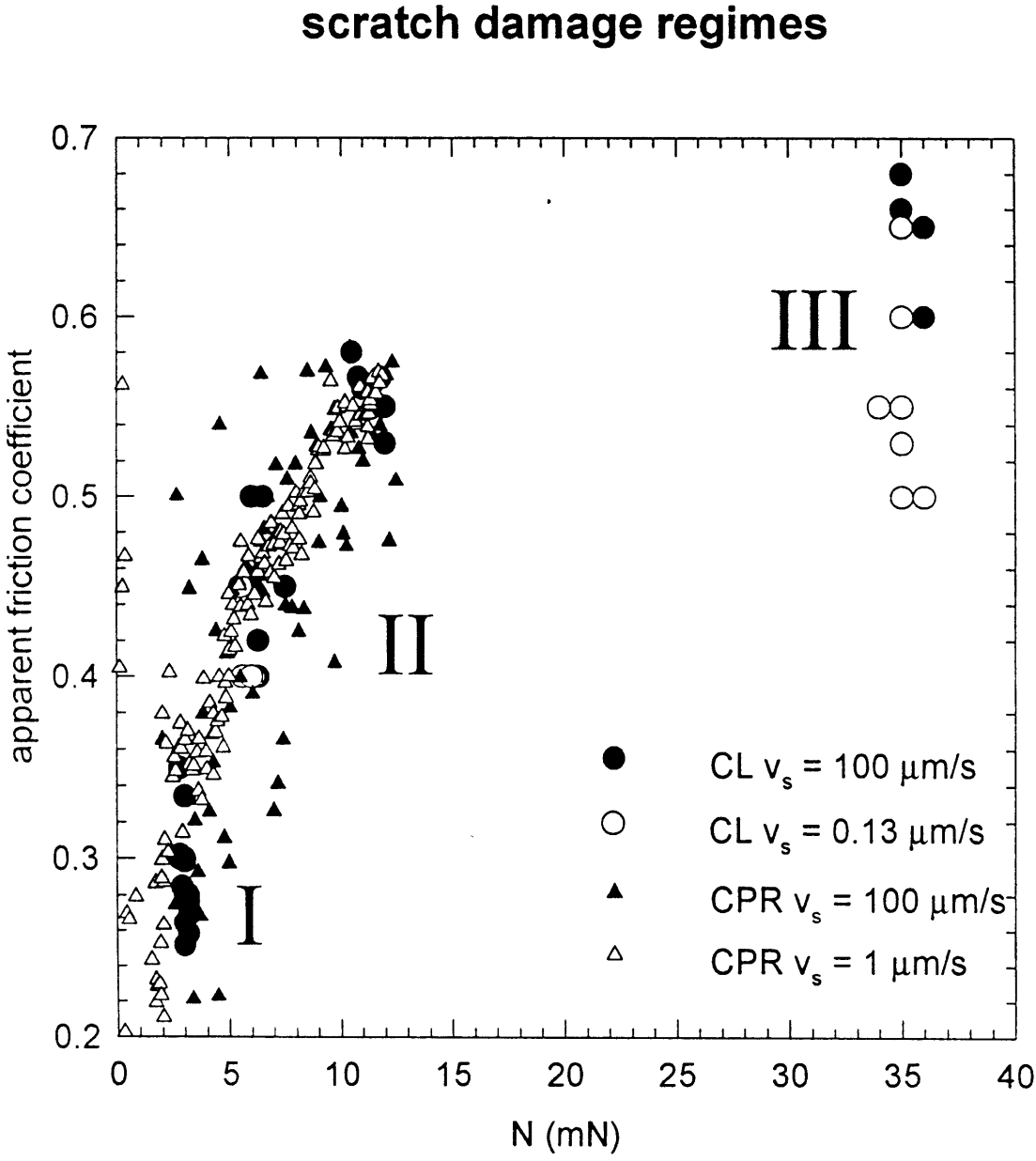
Figure 9a: Interferograms of Typical Scratches: Sample 8: constant load = 3 mN; scratch velocity = 100 μm/s (scratch direction left to right).
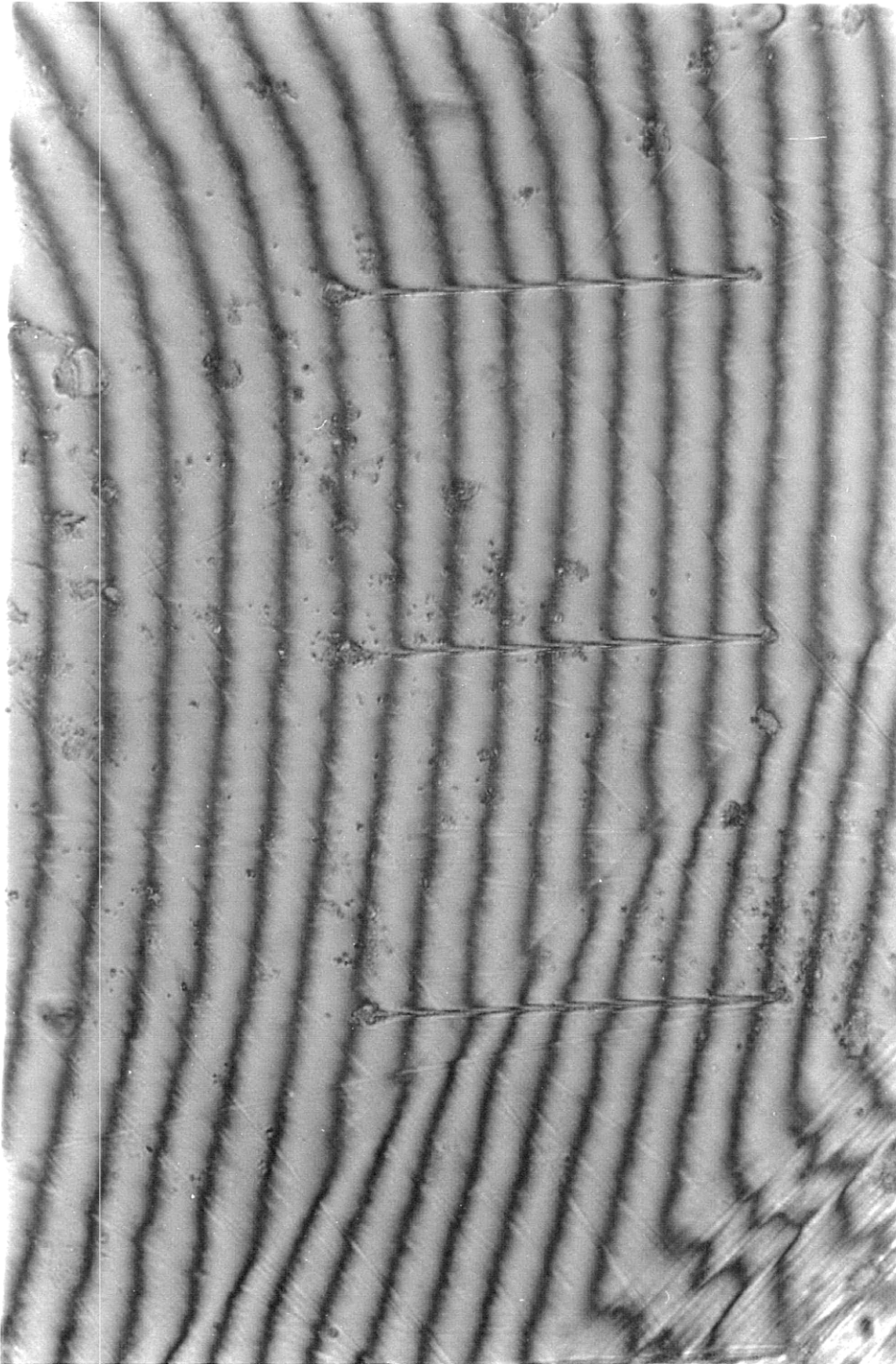
Figure 9b: Interferograms of Typical Scratches: Sample 10: constant penetration rate, scratch velocity = 1 μm/s (scratch direction left to right).
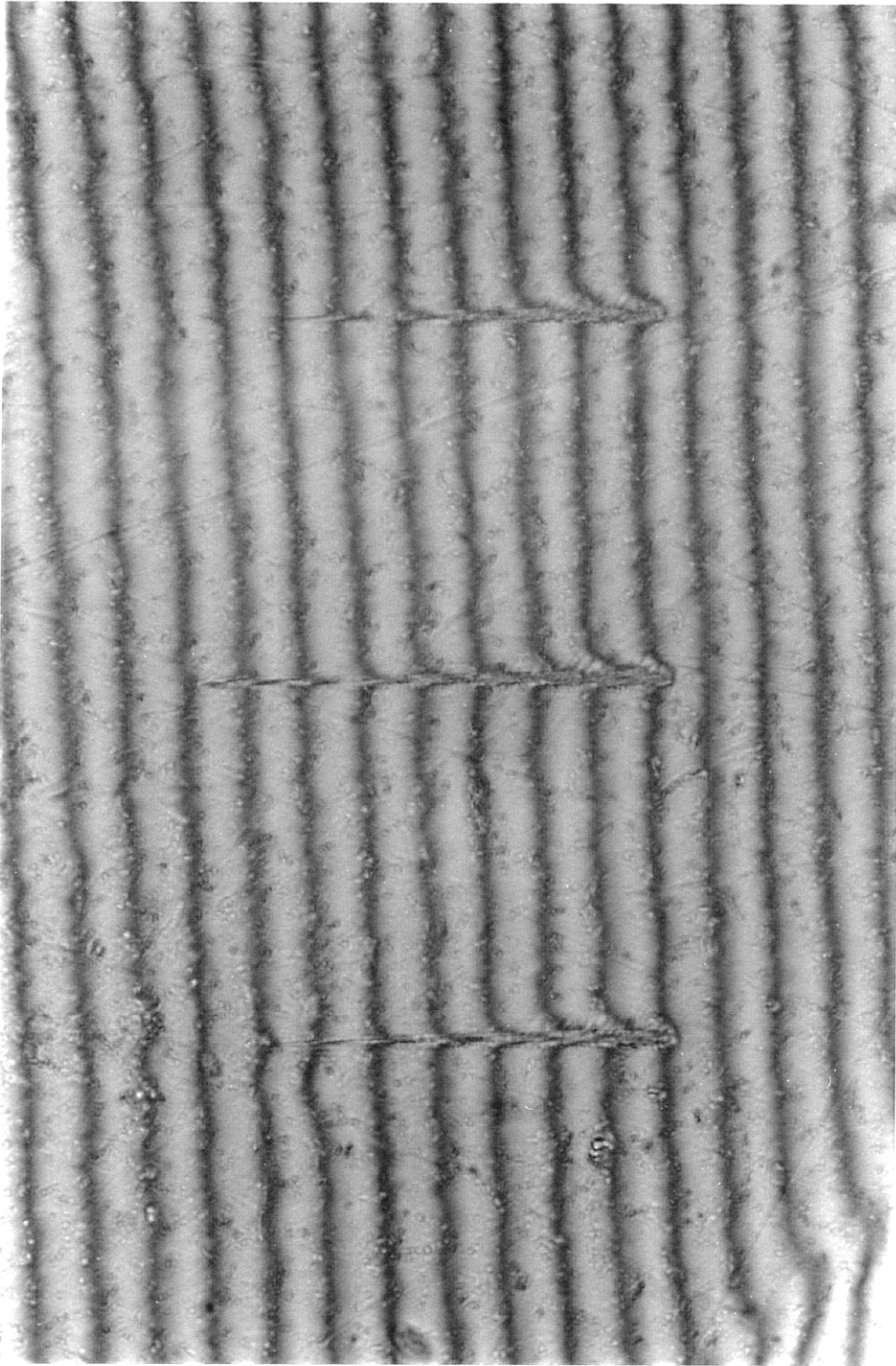
Figure 10: Geometry for Hardness Calculations

a) Projected Areas $A_{\perp N}$ and $A_{\perp T}$
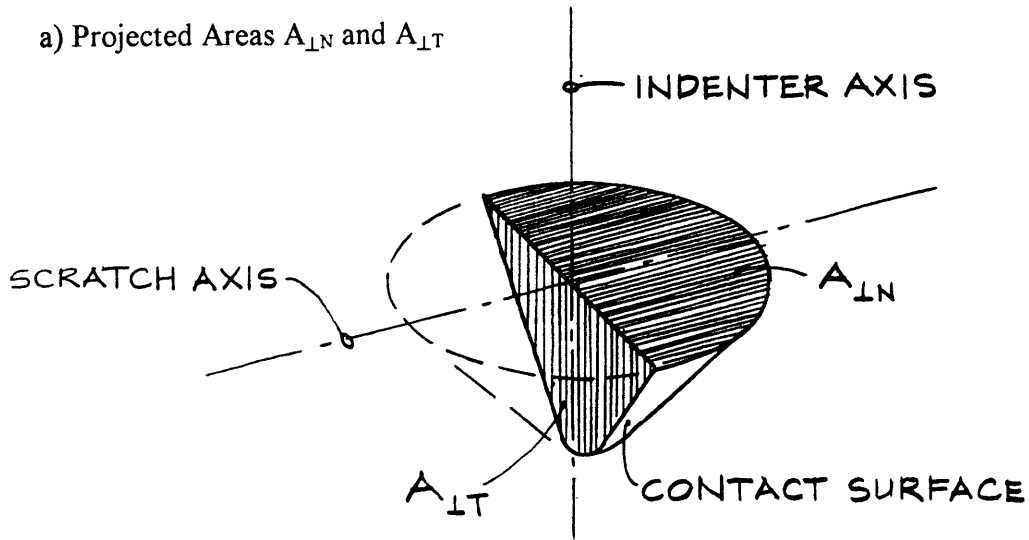
b) Force Balance
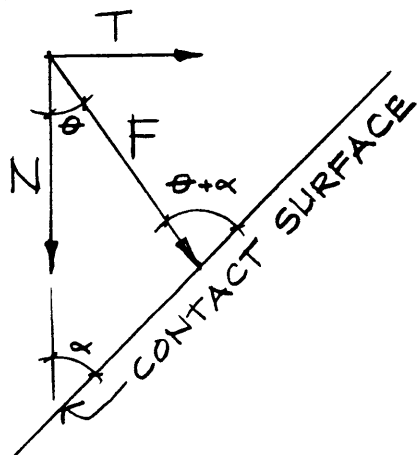
c) Mean Contact Pressure
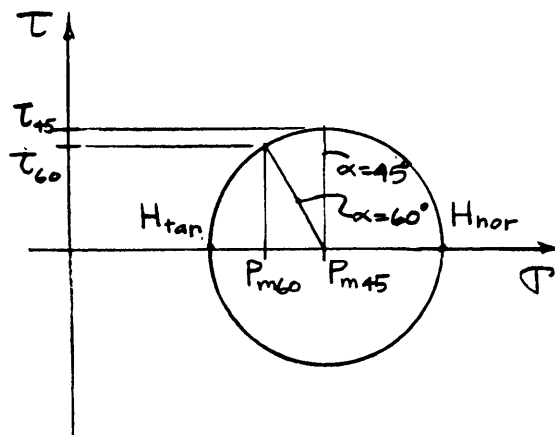
Figure 11a: Plots of Hardness Evolution: Sample 3: constant load = 35 mN, scratch velocity = 0.13 μm/s

scratch 3-1 hardness
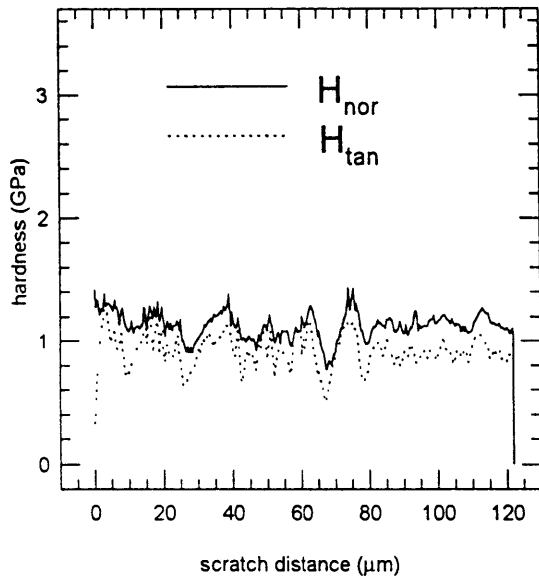
scratch 3-2 hardness
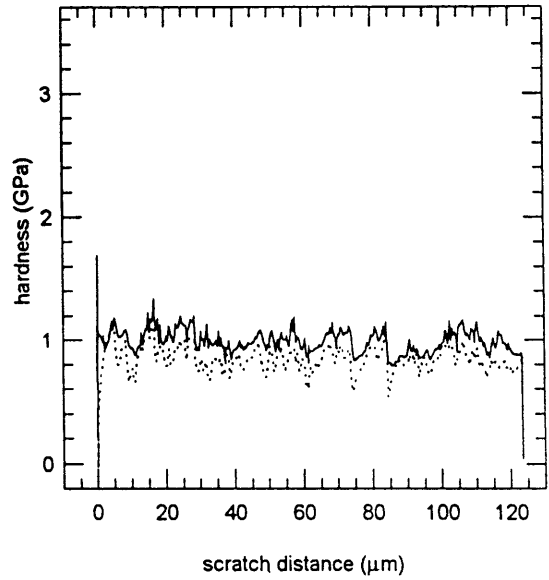
scratch 3-3 hardness
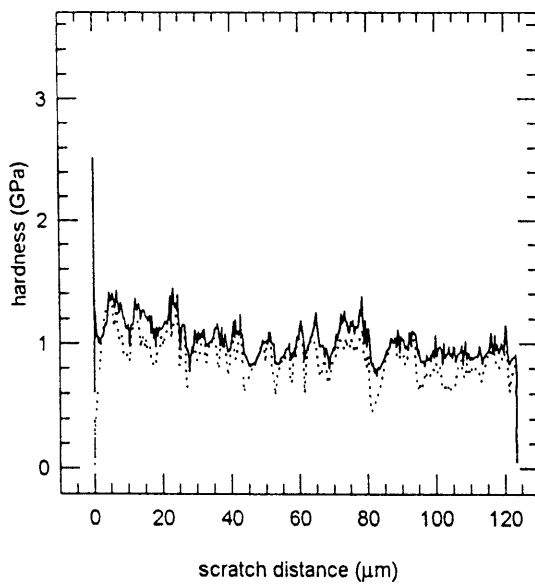
scratch 3-4 hardness
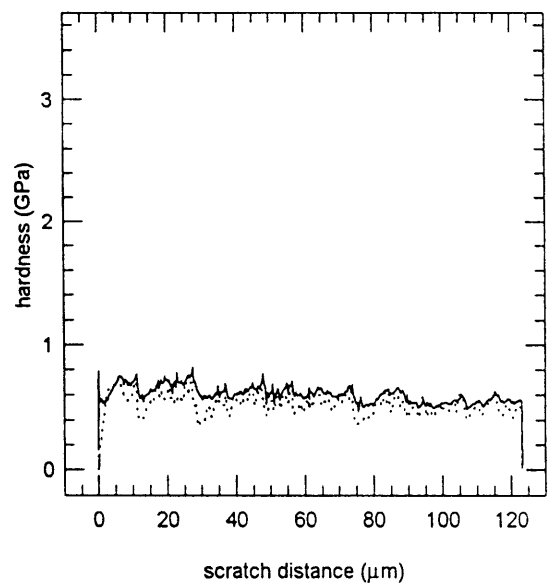
Figure 11b: Plots of Hardness Evolution: Sample 4: constant load = 35 mN, scratch
velocity = 100 μm/s

scratch 4-1 hardness
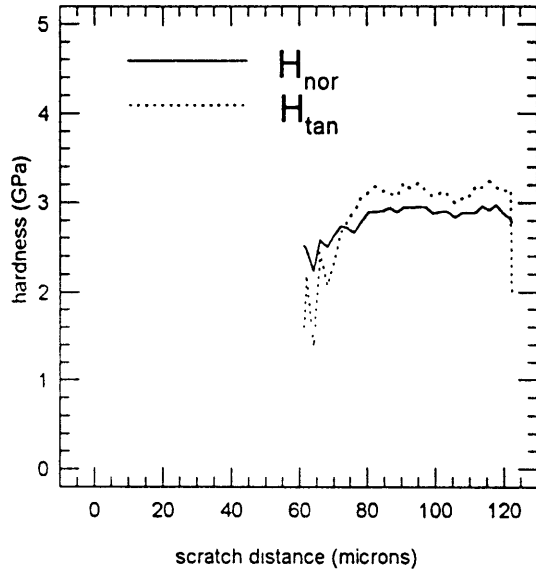
scratch 4-2 hardness
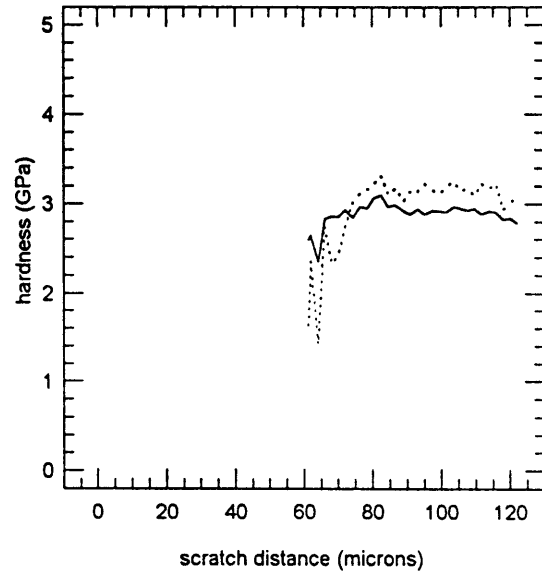
scratch 4-3 hardness
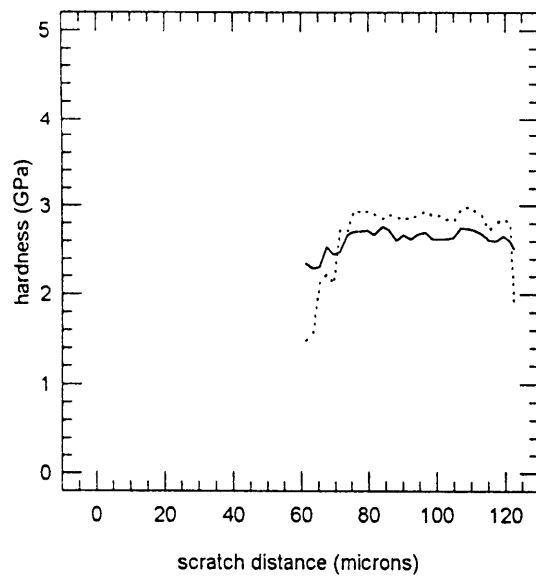
scratch 4-4 hardness
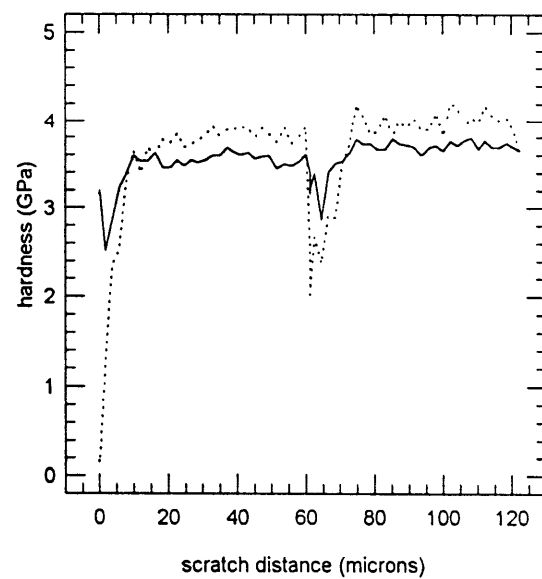
Figure 11c: Plots of Hardness Evolution: Sample 8: constant load = 3 mN, scratch
velocity = 100 μm/s
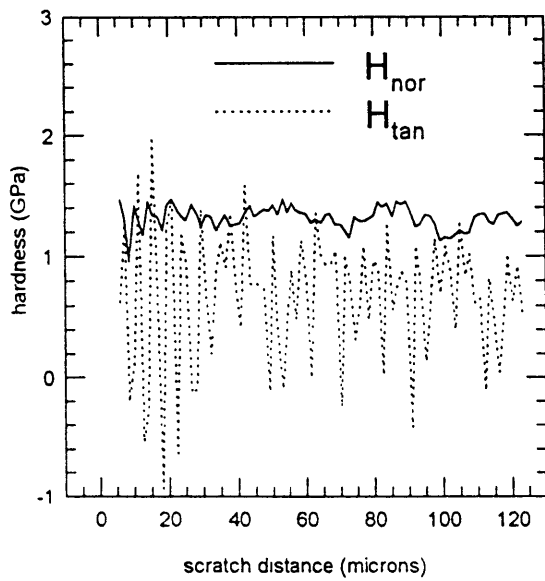
scratch 8-1

scratch 8-2
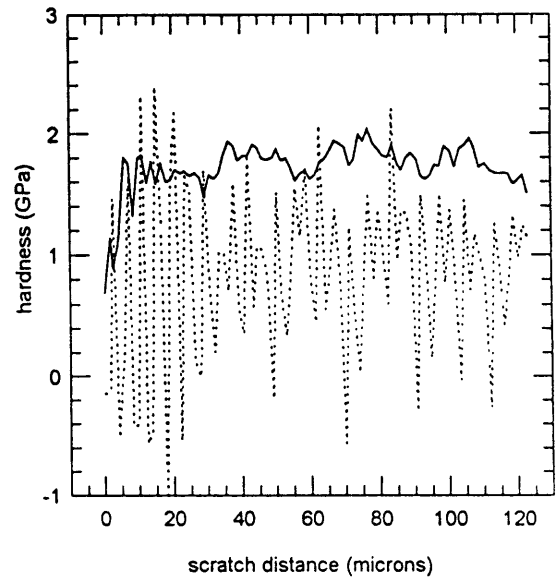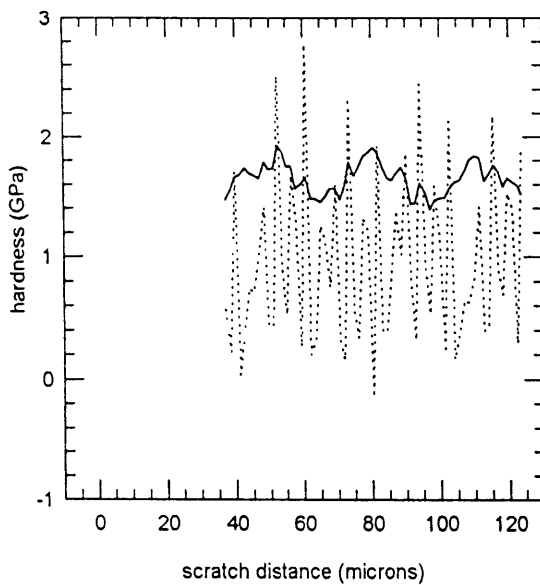
scratch 8-3
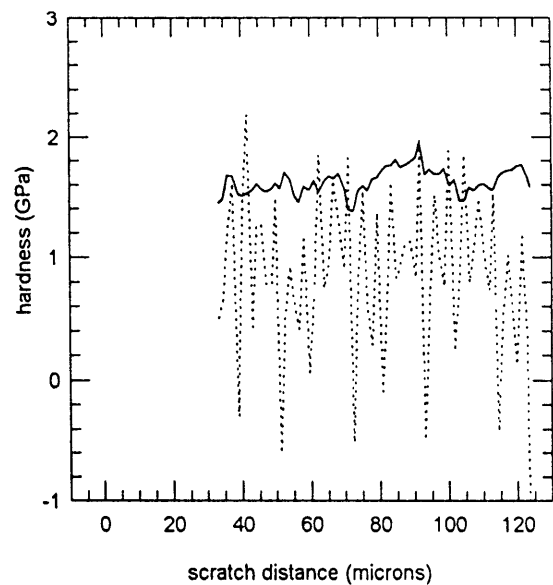
scratch 8-4

Figure 11d: Plots of Hardness Evolution: Sample 10: constant penetration rate, scratch velocity = 1 μm/s

scratch 10-5 hardness
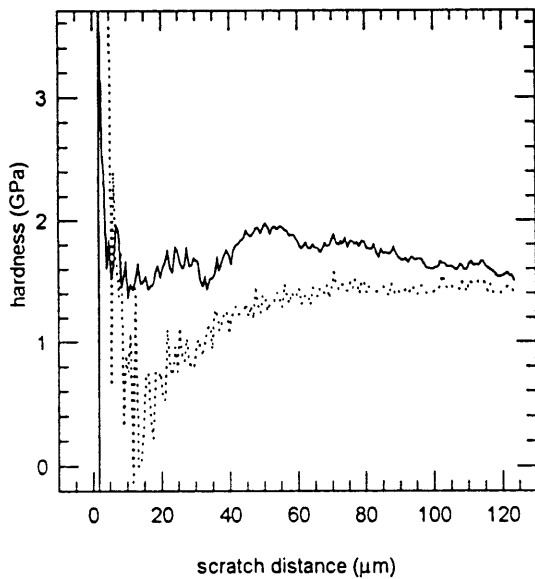
scratch 10-6 hardness
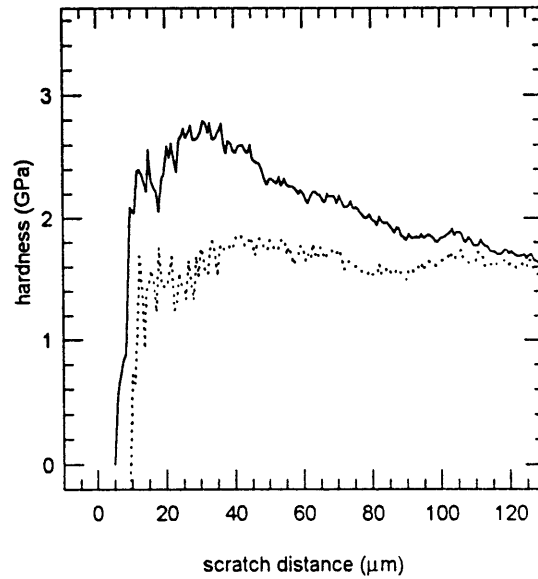
scratch 10-7 hardness
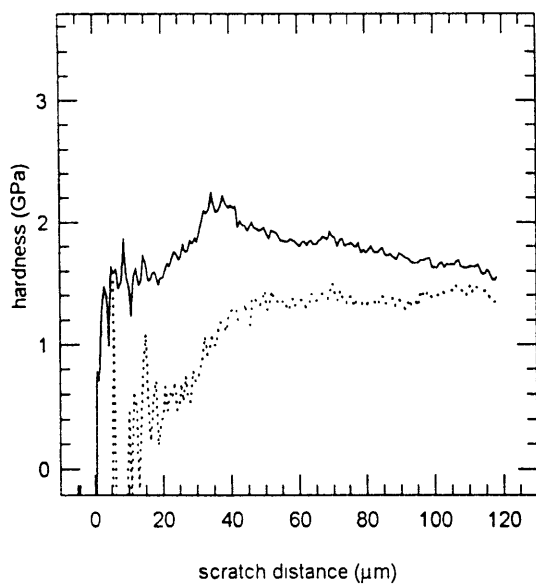
scratch 10-8 hardness
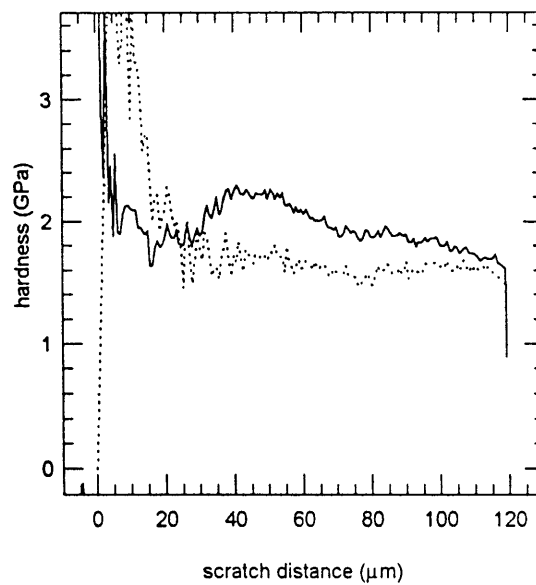
Figure 11e: Plots of Hardness Evolution: Sample 13: constant penetration rate, scratch
velocity = 100 µm/s

scratch 13-2 hardness
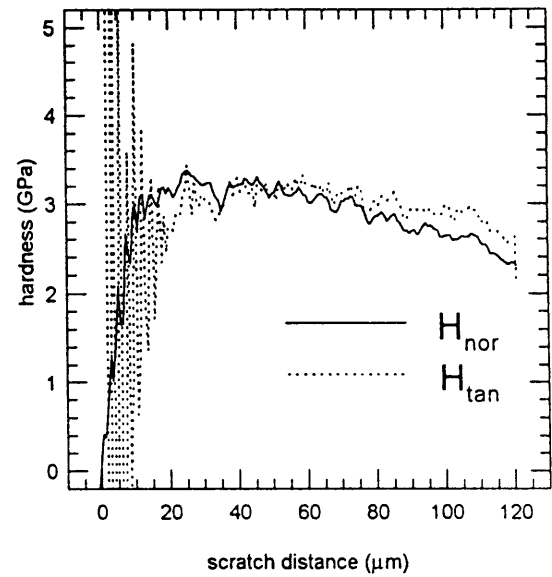
scratch 13-3 hardness
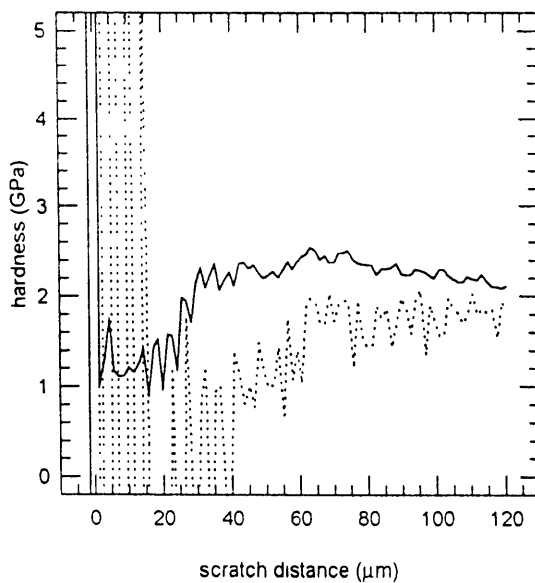
scratch 13-4 hardness
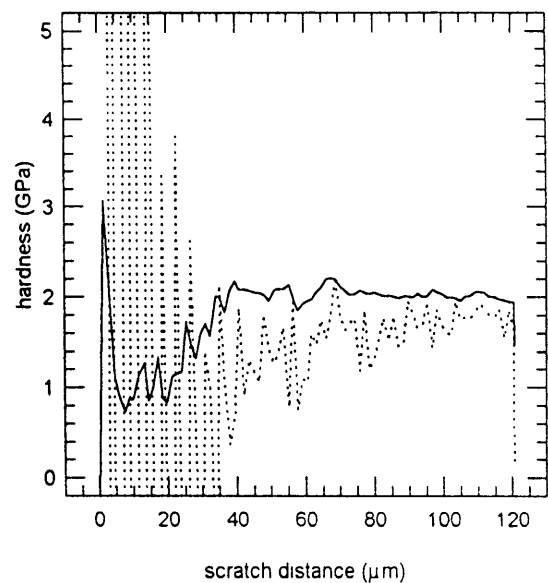
Figure 12: Plot of Contact Friction versus μ_{app}

contact friction based on force balance
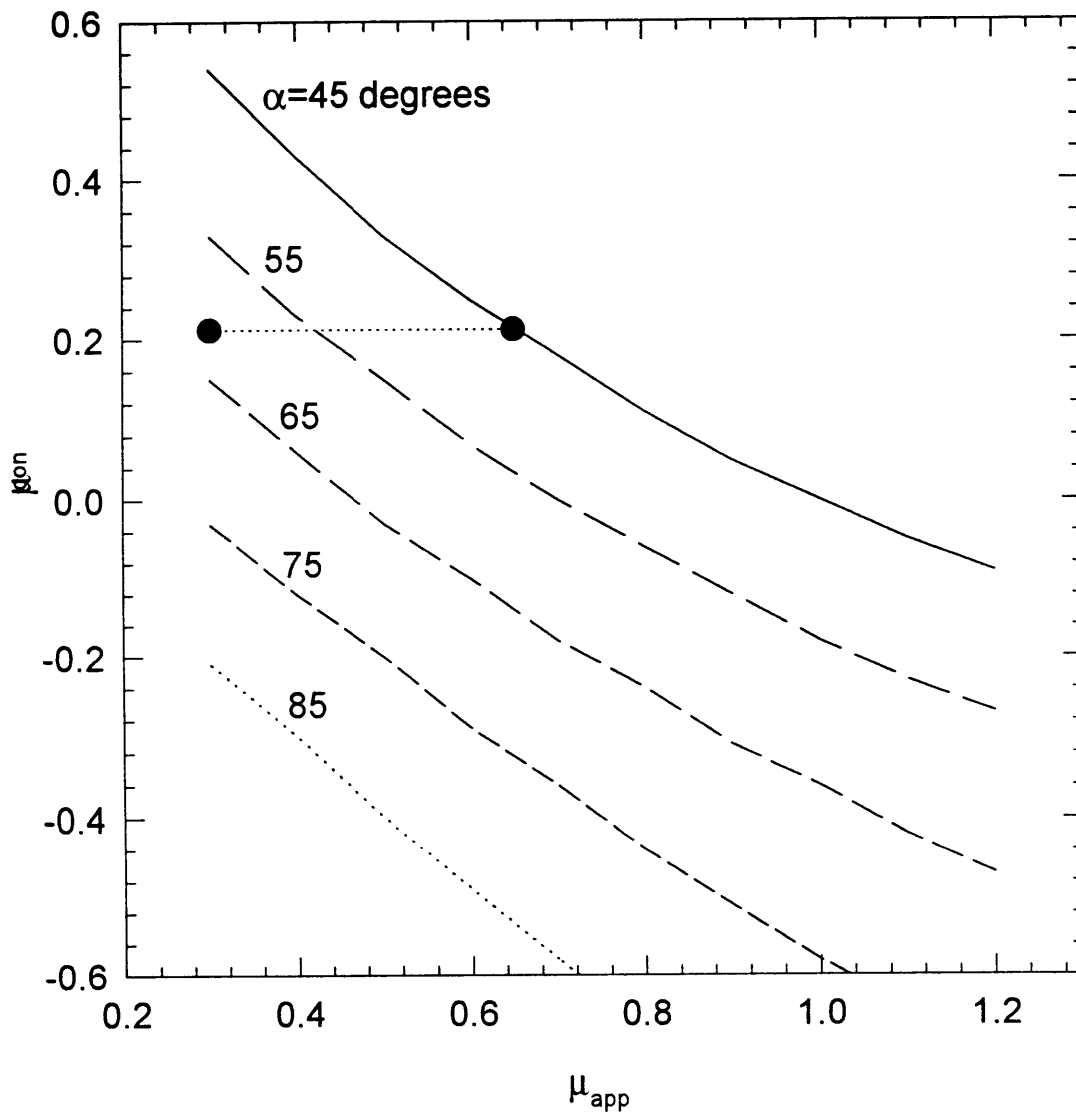
Figure 13: Stereoplot of Deformation Systems in Calcite
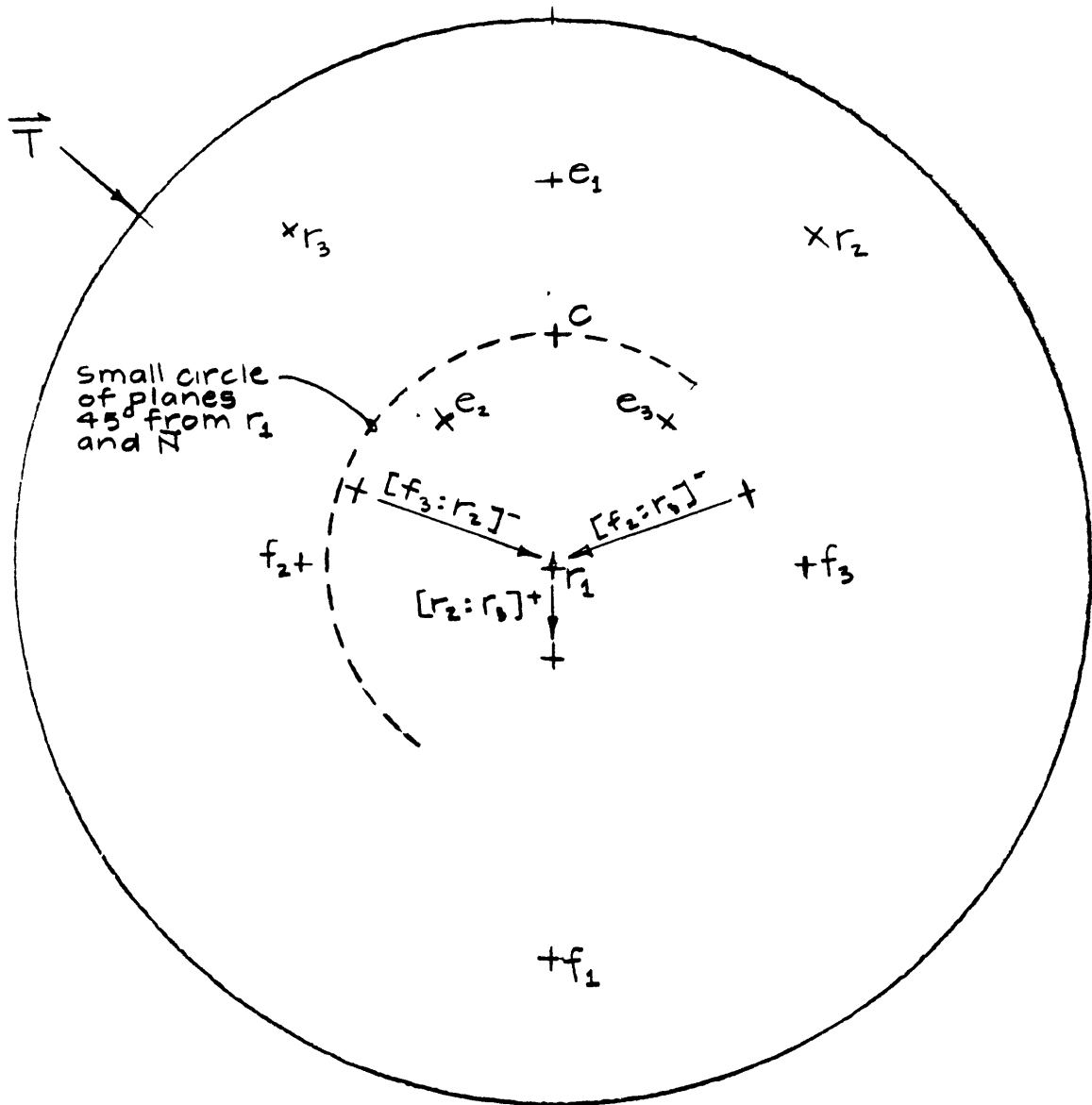
Figure 14a: Plot of i versus N: Constant Load Tests

constant load tests
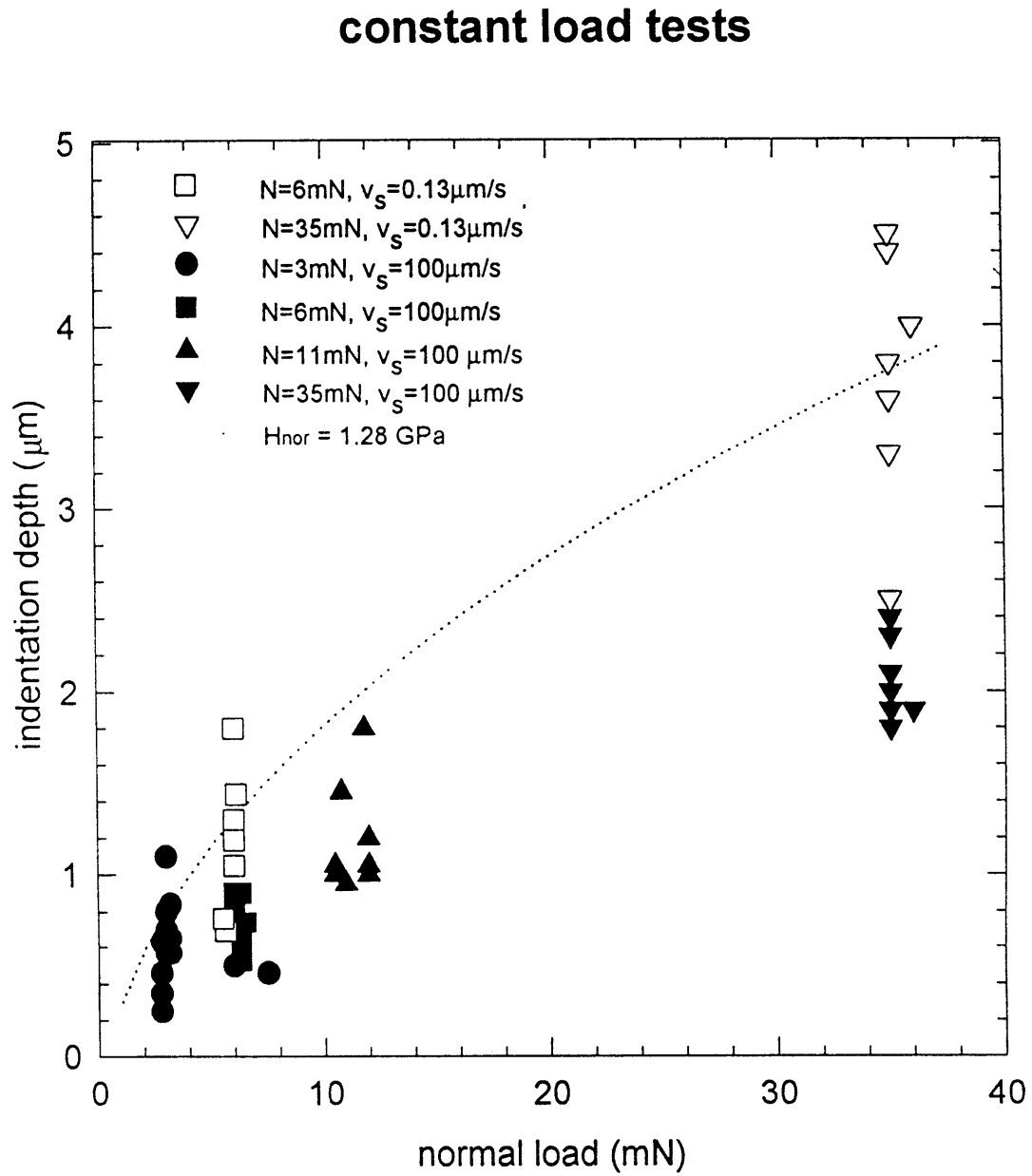
Figure 14b: Plot of i versus N: Constant Penetration Rate Tests (examples)

constant penetration rate tests 10-5 and 13-4

shape factor variation for α=45 degrees, r_t=1 μm
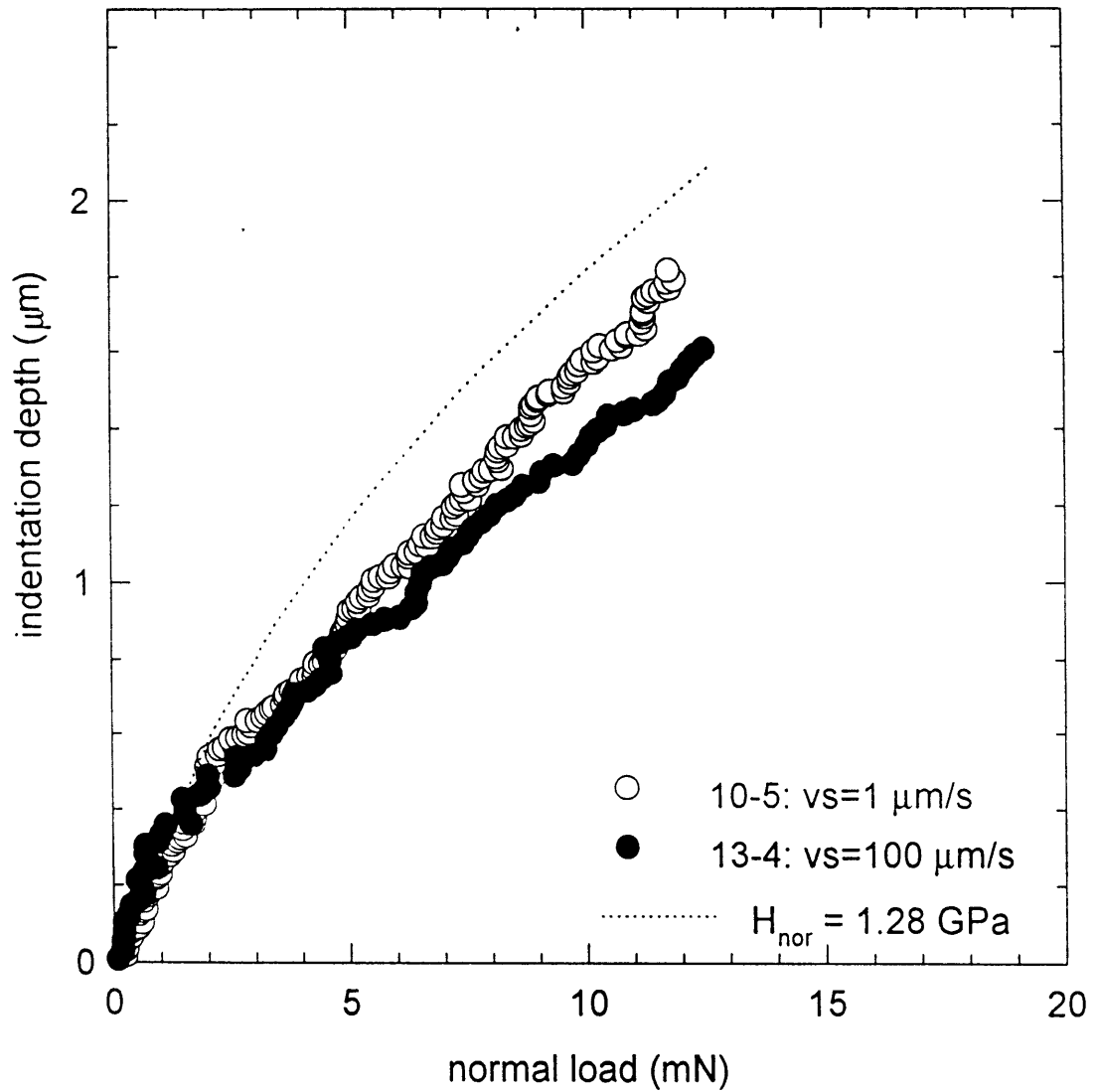
Figure 15: Plot of $A_{\perp T}/A_{\perp N}$ versus i
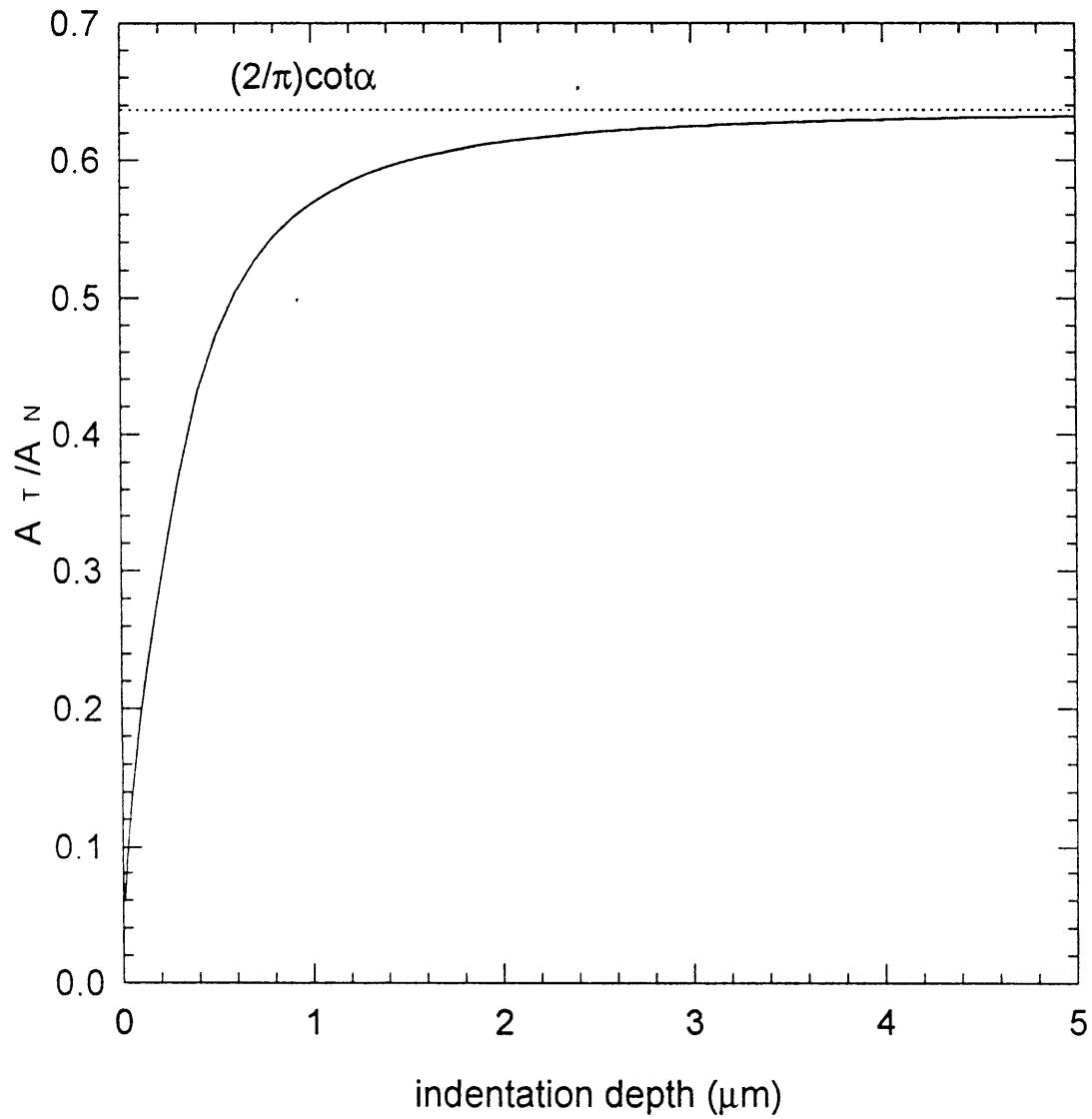
Figure 16a: Plot of μ_{app} versus $A_{\perp T}/A_{\perp N}$: Constant Load Tests

constant load tests
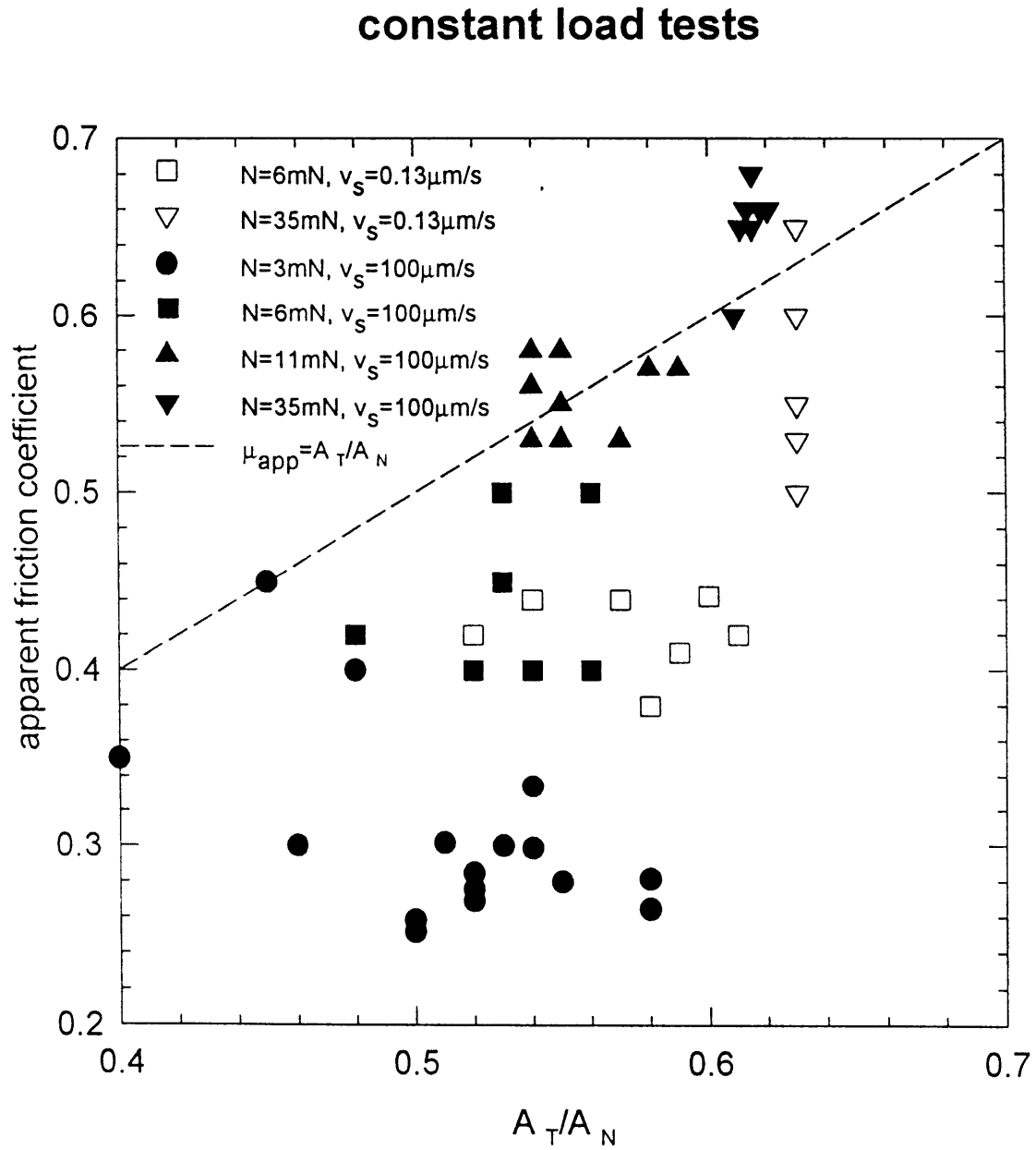
Figure 16b: Plot of μ_{app} versus $A_{\perp T}/A_{\perp N}$: Constant Penetration Rate Tests (examples)

constant penetration rate tests 10-5 and 13-4
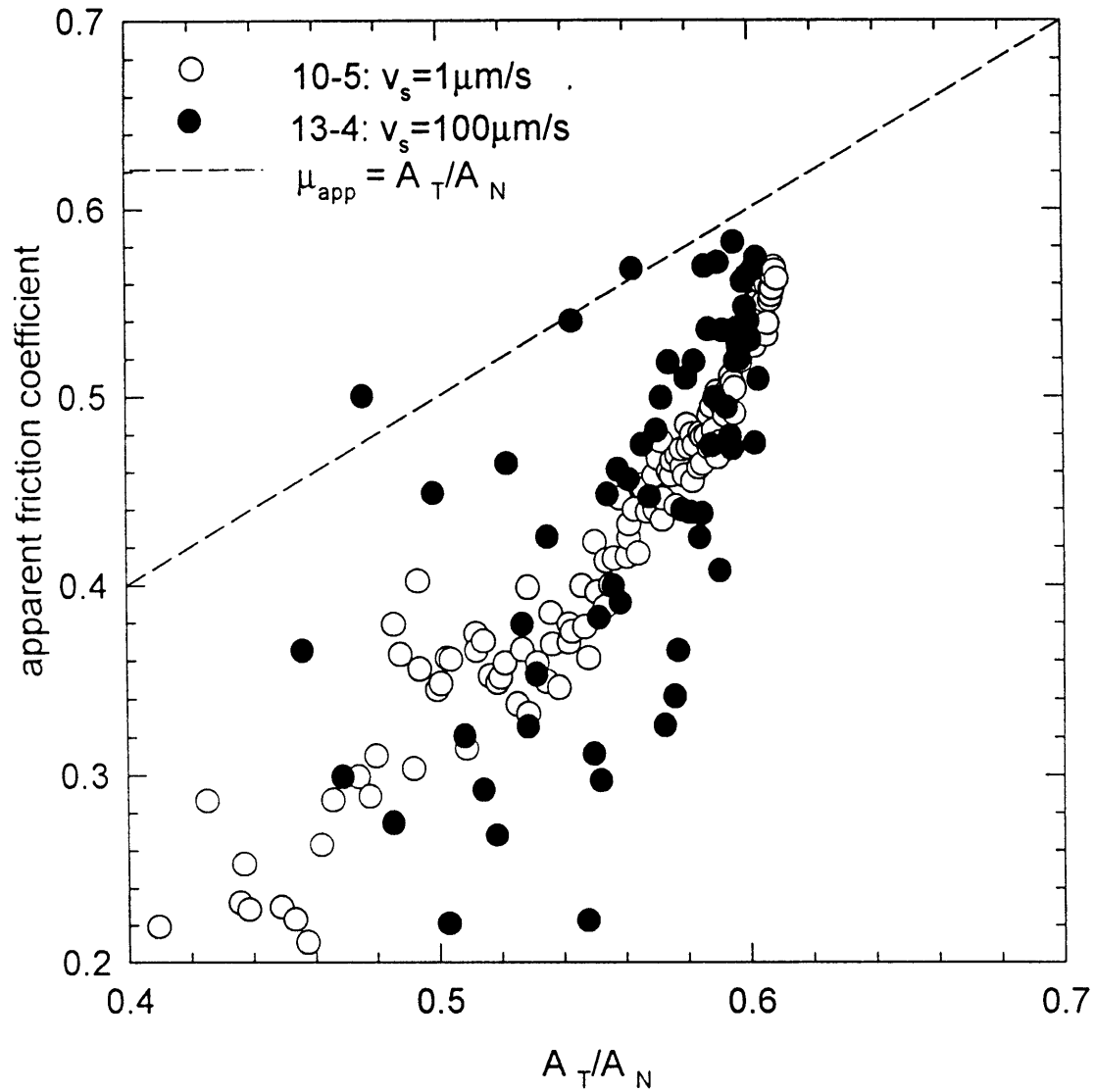
Figure 16c: Plot of μ_{app} versus $A_{\perp T}/A_{\perp N}$: Regimes

Regimes
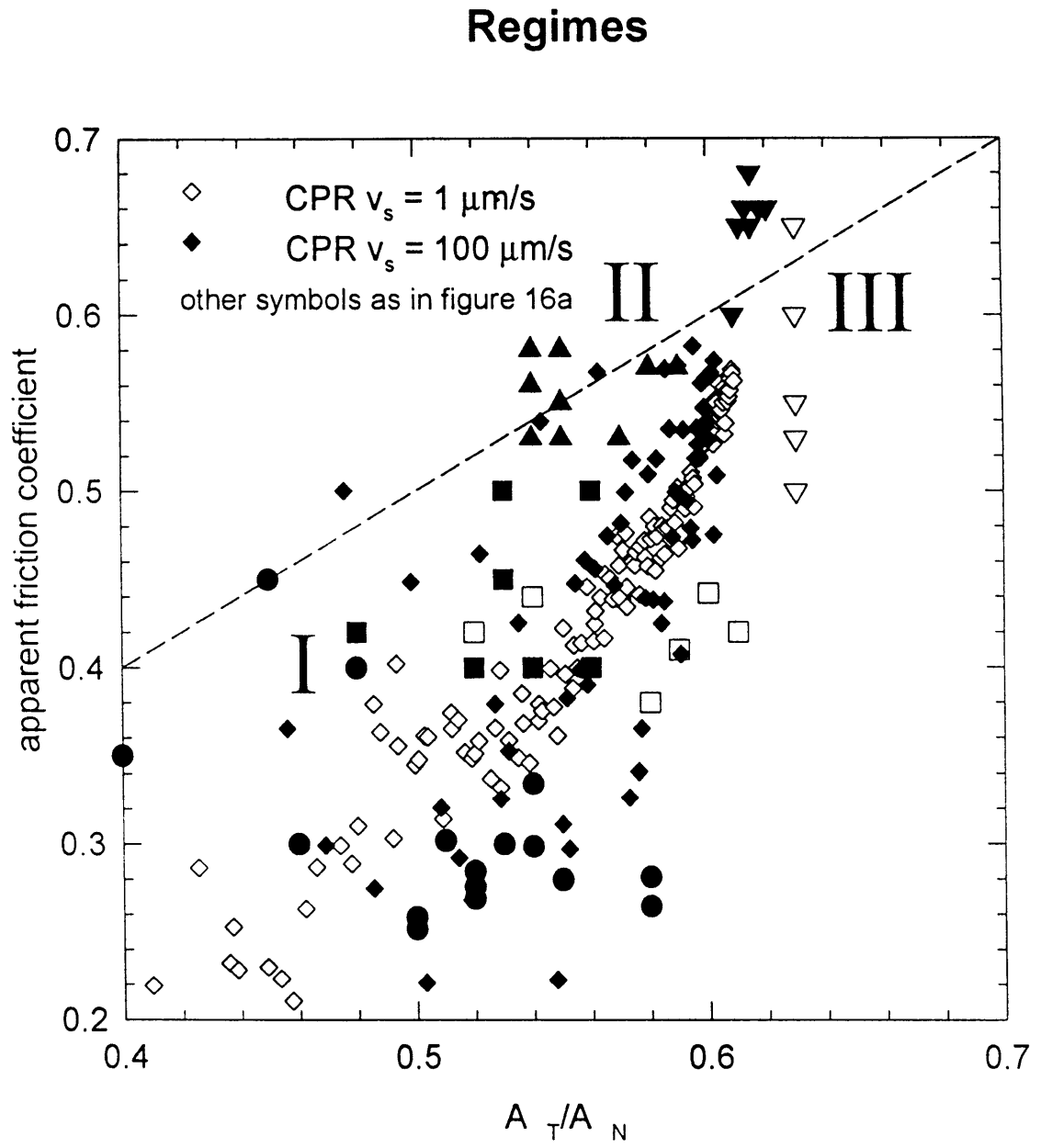
Chapter 3: Mechanical Behavior of Synthetic Marble: The Effects of Dispersed Quartz Particles.

Abstract

Strain localization in geological structures suggests that the ductile behavior of polyphase rocks at elevated temperatures and pressures in the Earth is sensitive to the relative proportions of minerals with different physical properties. I studied the strengthening effect of a varying fraction of non-deforming particles in a plastically deforming matrix through conventional triaxial deformation experiments on synthetic aggregates. Deformation experiments were performed on samples of a calcite matrix with 0%, 5% or 20% quartz particles. I evaluated the mechanical data collected during experiments in terms of existing mechanical mixing theories. Additional interpretation of data included assessment of microstructural observations of sample material before and after tests. The results of experiments conducted at 600°C and 200 MPa at a strain rate of $3 \times 10^{-5} \text{s}^{-1}$ suggest that, under these conditions, the presence of relatively strong quartz particles strengthens the synthetic marble by enhancing strain hardening, through the development of local strain gradients around the strong particles. The magnitude of strengthening is greater than that predicted by existing models.

Introduction

An accurate understanding of the rheology of earth materials is essential to the interpretation of major geological processes. The identification of features which control deformation, combined with the appropriate application of data and constitutive laws based on laboratory deformation experiments, can provide the critical link between individual geological formations and larger tectonic conditions and events (Schmid, 1982; Knipe, 1989; Groshong, 1989; Handy, 1990). To date, experiments have established the mechanical properties of common rock-forming minerals as single-crystals and in monomineralic aggregates (Evans and Kohlstedt, 1994). Several fine-grained natural rocks (Tullis,1990) and synthetic aggregates of naturally occurring minerals (Ross et al, 1987; Jordan, 1988; Peach,1991; Durham et al, 1992; Bruhn et al,1993) have also been tested. Because the great variety of polymineralic rocks of interest to earth scientists are complex multiphase aggregates, some method for assessing the interactions between minerals of differing mechanical properties is necessary.

Relatively strong particles may have a large impact upon the rheology of many rocks with a more easily deformed matrix. Strength sensitivity to small variations in strong particle content could contribute to strain localization in rocks as observed in peridotites by Drury et al (1991). The strengthening effect of strong particles in aggregates has been adressed theoretically by materials scientists in terms of self-consistent models (i.e Chen and Argon, 1979; Tanaka et al, 1991; Poech and Fischmeister, 1992; Corbin and Wilkinson, 1994) which predict aspects of continuum mechanical behavior A second approach, dispersion hardening theory, integrates evidence from microstructural features with the bulk mechanical properties of the aggregate, in order to assess evolution of strain, dislocation density and strength (Ashby, 1970; Humphreys and Kalu, 1987, 1990).

We have chosen to investigate the strengthening effect of varying volume fractions of quartz particles in marble. This material has the advantages of geological relevance and a large strength contrast between well-characterized phases. For our experiments, fine-grained synthetic aggregates of quartz and calcite were fabricated. A recent study by Dresen and Evans (1993) demonstrated the pressure sensitivity of similar materials at 300K. For the present study, samples were tested for their mechanical properties at dry conditions at temperatures just above the transition from brittle to plastic deformation, where chemical interactions between phases could be neglected.

Characteristics of stress/strain data and microstructural analysis allow us to make preliminary comparisons of our results with predictions based on theory. These comparisons allow us to identify features which are likely to be critical to the aggregate mechanical properties of marble.

Experimental materials and methods

In order to evaluate the effect of varying quartz content on the mechanical properties of the synthetic marble, we produced three sample materials: pure calcite; calcite with 5% quartz (IRE series); calcite with 20% quartz (IBLA series). The starting materials consisted of fine-grained analytical reagent grade calcite powder and crushed quartz. The grain size of the calcite powder was 5 to 10 microns; quartz particles averaged 25 microns. The two powders were mixed, and each mixture was cold-pressed into a large mold. The sample material was then hot-isostatically-pressed (HiPed), at 450°, 200 MPa for pure calcite and at 600°, 200 MPa for mixed compositions. Individual cylindrical samples were cored from the hipped aggregates and precision ground to 3.18 cm. length, 1.59 cm. diameter.

Prior to deformation, the unconnected porosity of each sample was measured using the Archimedes method. Values ranged from 3 to 5% in the two-phase samples, to 9% in the pure calcite. Examination of the undeformed sample material revealed that quartz grains were well dispersed (Figure 1a). Calcite had recrystallized in all three materials, but grain growth was limited, resulting in grain sizes of 5 to 25 microns. Quartz grains remained 25 microns in diameter. Before jacketing, the samples were cleaned in acetone in an ultrasonic bath and subsequently dried under vacuum overnight.

Standard triaxial deformation experiments were performed at 400° and 600°C in an internally heated vessel. Confining pressures of 200 to 350 MPa were obtained using argon gas as a confining medium. A strain rate of approximately $3 \times 10^{-5} s^{-1}$ was maintained by a servo-controlled ram.

Results: Mechanical Data

A summary of results from the experiments is given in table 1. Stress-strain plots for the data (Figure 2) exhibit a variety of strength-related characteristics. The features of the plots which most clearly describe the mechanical behavior of each sample are the rate of strain hardening and the magnitudes of the stress and strain at which steady state, or zero hardening rate, is reached. The conditions under which increased quartz content had the greatest strengthening effect were 600°C, 200 MPa.

Experiments at 600 °C, 200 MPa confining pressure.

Under conditions close to the calcite brittle-plastic transition, *pure calcite* aggregates exhibited very low rates of strain hardening and reached steady-state strengths of 20 and 40 MPa (Figure 2). The sample which contained 9% porosity (ZI1) appears to have reached steady state only after 10% strain. The other pure calcite sample (ZI3) was hipped a second time at 600°C, 350 MPa, to reduce its porosity to 1%. This sample was the weaker of the two but reached steady-state deformation at 3% strain, suggesting that some of the apparent strain hardening in the samples is due to pore collapse.

Samples with *5% quartz* (IRE2, IRE3, IRE4) strain hardened at moderate rates. Samples IRE3 and IRE4 reached steady-state strengths of 70 to over 100 MPa, within 4 to 6% strain. Moderately high rates of strain hardening and large strain to reach steady-state characterize the samples which contained *20% quartz* (IBLA3, IBLA5 IBLA7). The sample which was deformed to 12% strain (IBLA7) appears to have been close to steady-state deformation, at a strength close to 200 MPa, whereas samples IBLA3 and IBLA5 were continuing to harden when those experiments ended, at 6% and 8% strain, respectively.

Although there is noticeable variation among plots within each group of samples cored from the same material, clear trends are suggested by these observations. Under the given conditions, an increase in the proportion of strong particles results in an increased rate and duration of strain hardening, and therefore in a greater steady-state strength. Aggregates containing *20% quartz* have roughly twice the strength of those with *5% quartz*, and can be almost five times as strong as *pure calcite* aggregates. Comparisons with similar data obtained in experiments on Solnhofen limestone and Cararra marble (Schmid et al 1977, 1980) and fine-grained calcite (Walker et al 1990) also show that our samples which contain quartz particles deform at greater hardening rates than observed in pure calcite.

Experiments at varied temperatures and pressures.

The data for the following experiments are included to provide some information on the limits of the quartz particle hardening regime. A confining pressure of *350 Mpa* was maintained during one experiment performed on the material with *5%* quartz at *600 °C*. This increase in pressure had no quantifiable effect on the strength of the sample. Several experiments were conducted under conditions approaching the brittle regime for calcite. At *400 °C, 200 MPa*, samples with *5%* and *20%* quartz both exhibited roughly the same strength as Carrara marble. This suggests that strong particles do not have a measurable strengthening effect at lower temperatures. One experiment was performed on the material with *20% quartz* at *400 °C, 300 Mpa*, during which high confining pressure appears to have increased the hardening rate dramatically.

It appears that at 600°C, deformation of these materials at a strain rate of $3 \times 10^{-5} s^{-1}$ is not sensitive to changes in confining pressure. However, at a lower temperature of 400°C, a pressure-sensitive regime is entered, in which mechanical properties are far less sensitive to quartz fraction. Due to the small number of experiments under each set of conditions, further work is needed to verify these observed effects, and to further quantify the transition between the plastic deformation of our present experiments and the brittle deformation exhibited by experiments reported by Dresen and Evans (1993)

Results: Optical Microscopy

Variations in microstructural features among the deformed samples appear to correlate well with quartz fraction. Some differences may have originated in the starting materials. Grain size among the sample materials was fairly consistent, as noted above in the description of experimental materials. However, as the powders were packed during cold-pressing, calcite matrix grains near the rigid quartz particles may have been crushed. This porosity may have only partially collapsed during hipping, and may have been a factor in the development of a smaller matrix grain-size at interfaces (Figure 1b). Dislocation densities in the calcite also vary from sample to sample, and were not uniform within a given sample. The value for the pure calcite aggregate with 9% porosity was close to $1.5x10^9$ cm^{-2}, whereas the pure calcite sample whose porosity had been reduced to 1% by additional hipping showed reduced densities of $2.1x10^8$ to $1.0x10^9$ cm^{-2}. Dislocation densities in the two-phase aggregates were considerably higher, reaching $6.0x10^9$ cm^{-2} near quartz particles.

The deformed samples exhibit enhanced compaction. During experiments at 600°C, 200 Mpa, porosity in the pure calcite samples was reduced by up to 8%, and by 2 to 3% in the two-phase aggregates. Pore collapse adjacent to quartz particles may have contributed to a strain gradient at these interfaces. Coronas of submicron-sized strain-free calcite grains around the strong particles provide evidence for recrystallization in response to such a gradient (Figure 1c).

Dislocation densities in the calcite matrix evolve during deformation, and are generally higher in samples with greater quartz content. Typical values for pure calcite aggregates vary between $2.4x10^8$ and $7.0x10^9$ cm^{-2} after more than 10% strain at 600°C, 200 Mpa. In samples containing 20% quartz, dislocation densities were as high as $2.0x10^{10}$ cm^{-2} even for samples which had been deformed only to 5% strain. In the two-phase samples, we observed a strong increase in dislocation densities within large calcite grains near quartz particles, also indicative of the presence of a strain gradient at these interfaces (Figure 1d).

Optical microscopy provides evidence for further comparisons of microstructure in the three sample materials deformed at 600°C, 200 MPa. The pure calcite exhibits significant grain growth and a limited amount of grain elongation. The samples with quartz grains, on the other hand, show microstructures indicative of the operation of a range of deformation mechanisms. Twinning, undulatory extinction, sutured grain boundaries, recrystallization along grain boundaries and elongation can all be found to varying degrees. With increasing strain, elongation of grains perpendicular to the axis of deformation became more pronounced and twinning is less common.

Discussion

The presence of strong quartz particles increases the strain hardening rate and and strain to reach steady state, thereby enhancing steady-state strength in synthetic marble. These effects appear to be associated with the development of local strain gradients around the particles. The strengthening effect occurs under conditions which govern power-law creep in the matrix material, calcite. Stress-strain plots of our data are also typical for power-law creep. The first few percent of strain is accompanied by a rapidly increasing differential stress, which evolves into an interval with decreasing hardening rate; the initial period of transient creep is followed at 5 to 10% strain by steady-state creep. We therefore considered it appropriate to compare our results to predictions based on a continuum mechanics approach to dislocation creep in a two-phase aggregate.

The simplest type of model for assessing the strength of two-phase aggregates can be expressed in terms of a rule of mixture, which predicts variation in the strength of an aggregate as a function of the proportion of strong phase. Cho and Gurland (1987) and Tullis et al (1991) provide excellent reviews of this approach. Most such models have been developed to predict the yield strengths of elastically deformed metal alloys. However, they are sometimes used, with or without modification, to assess the aggregate viscosity or steady-state strength of materials under conditions beyond their elastic regime. In order to calculate bulk deformation properties, assumptions are made regarding the distribution of stress and strain between the two phases. A parallel loading model for elastic deformation assumes uniform strain in both phases, such that the yield strength of an aggregate can be predicted by a simple mechanical mixing law. A similar mixing law for creep deformation calculates steady-state strength, assuming uniform strain-rate in both phases. The mixing law for uniform strain or strain-rate can be used to provide a theoretical upper limit (Voigt bound) on the strength of marble, σ_{marble}, for given strength σ_i and volume fraction, V_i, of each phase i:

$$\sigma_{marble} = V_{quartz}\sigma_{quartz} + V_{calcite}\sigma_{calcite} \qquad (1)$$

184

A serial loading model assumes uniform stress in both phases. The strain of an elastically deforming aggregate is calculated as a volume weighted average of the strain in each of the two phases. The uniform stress mixing law provides a theoretical lower limit (Reuss bound) for the yield strength of marble, calculated using the estimated strain at which the yield point occurs and some choice of Young's modulus for marble:

$$\varepsilon_{marble} = V_{quartz}\varepsilon_{quartz} + V_{calcite}\varepsilon_{calcite} \tag{2}$$

$$\sigma_{marble} = E_{marble}/\varepsilon_{marble} \tag{3}$$

Similar equations can be developed for serial loaded aggregates deforming by power-law creep, but the appropriate selection of values for the parameters A,Q and n for equation (5) is not obvious:

$$d\varepsilon_{marble}/dt = V_{quartz}(d\varepsilon_{quartz}/dt) + V_{calcite}(d\varepsilon_{calcite}/dt) \tag{4}$$

$$\sigma_{marble} = ((d\varepsilon_{marble}/dt)/(Ae^{-Q/RT}))^{1/n} \tag{5}$$

Because quartz has a steady-state strength two orders of magnitude greater than calcite at our experimental conditions, it could be assumed for small quartz fractions that all strain was accomodated by the calcite, so that in equation (4) we have $(d\varepsilon_{quartz}/dt)=0$. The fact that the calcite comprised only part of the total sample volume means that the effective strain-rate within calcite would be increased above that of the sample as a whole, as in the two-block model of Jordan (1988). For a serial loading model, the marble strength could thus be estimated using calcite power law parameters and this effective strain rate in equation (5).

In figures 3 and 4, mixing law predictions for the steady-state creep strength of marble are plotted as a function of the proportion of quartz particles. Two plots are provided because actual sample temperatures during experiments were likely to have ranged between 600 and 650°C. Flow laws for the individual phases are based on results from experiments on single-phase aggregates of calcite by Walker et al (1990) and quartz by Paterson and Luan (1990). Our data fall within the bounds set by serial and parallel loading, but are not well defined by either condition. Indeed, it is reasonable to assume that neither stress nor strain is equal for calcite and quartz in our deforming samples.). Jordan (1988) predicts that the results of serial loading calculations may be modified by taking into account a strain shadow described by an angle δ around each strong particle. Qualitatively, our results agree most closely with their plot for δ=20°(figure 4, Jordan, 1988).

A simple empirical method is given by Tullis et al (1991), specifically to predict the strength of aggregates deforming by dislocation creep. Power law parameters are obtained by averaging parameters of the power laws of the two individual phases. The authors demonstrate that this method can provide a good estimate for plagioclase/pyroxene aggregates. We plotted the results obtained from equation (5), using our strain rate of $3\times10^{-5}\text{s}^{-1}$ and the appropriate parameters for calcite (Walker et al, 1990) and quartz (Paterson and Luan, 1990) to obtain aggregate parameters according to the following equations from Tullis et al (1991):

$$n_{marble} = 10^{(V_{quartz}\log(n_{quartz})+ V_{calcite}\log(n_{calcite}))} \tag{6}$$

$$Q_{marble} = (Q_{quartz}(n_{marble} - n_{calcite})-Q_{calcite}(n_{marble} - n_{quartz}))/(n_{quartz} - n_{calcite}) \tag{7}$$

$$A_{marble} = 10^{(\log A_{quartz}(n_{marble} - n_{calcite})+\log A_{calcite}(n_{marble} - n_{quartz}))} \tag{8}$$

The results of these calculations, also shown on figure 8, underestimate the strengths of our aggregates, although they do come closer than the Voigt and Reuss bounds. The great difference in mechanical properties between quartz and calcite may account for the difficulty in finding a mixing model which matches the properties of synthetic marble.

Bloomfield and Covey-Crump (1993) propose a measure of contiguity, C_i, between strong particles which could be used to modify equations (1) and (2), as follows:

$$\sigma_{marble} = C_{quartz}V_{quartz}\sigma_{quartz} + (1-C_{quartz}V_{quartz})\sigma_{calcite} \qquad (9)$$

$$\varepsilon_{marble} = C_{quartz}V_{quartz}\varepsilon_{quartz} + (1-C_{quartz}V_{quartz})\varepsilon_{calcite} \qquad (10)$$

The contiguity between quartz particles in all our samples is essentially zero, which means that the results of equations 9 and 10 would be $\sigma_{marble} = \sigma_{calcite}$ and $\varepsilon_{marble} = \varepsilon_{calcite}$, which clearly does not agree with our data. Again, it may be the large strength difference between quartz and calcite which reduces the validity of this approach to our experimental results.

Numerical methods have been used to explore interactions between two phases during creep deformation. Mixing laws may be solved iteratively (Poech and Fischmeister, 1992), so that both stress and strain evolve distinctly in the two phases, allowing for change in strain partitioning with increasing strain. Tanaka et al (1991) present a continuum mechanics model in which bulk deformation is initiated with a period of transient creep. In each time-step of the model, a new bulk strain rate is calculated based on the difference in strain response of the two phases to an applied stress. The resulting internal stresses are eventually redistributed until a steady state strain rate is achieved for the given stress. Transient creep is displayed by the results of our experiments during the initial strain interval up to 5 or 10%, whereas the plots in Tanaka et al (1991) suggest that steady state creep is achieved at much smaller strains. They recognize that increasing the volume fraction of strong particles will result in an increase in the strain to reach steady state, and that a larger strength contrast between phases, such as that between quartz and calcite, will generate a more "prominent transient creep behavior". The transient creep inherent in each individual phase, not accounted for in this model, may also add to the effects of transient creep of marble.

Corbin and Wilkinson (1994) present an effective medium approximation method for calculating the plastic deformation of two-phase aggregates, which further refines the period of transient creep. They have developed an expression which estimates Young's modulus for elastically deforming aggregates. For plastic deformation, they use incremental recalculation of an effective Young's modulus, derived from the constitutive laws for the two phases, to generate stress-strain curves which evolve rapidly to extended periods of constant hardening rates. As in our experiments, hardening rates increase with increasing strong particle fraction. Their stress-strain plots, however, settle into constant hardening rates at smaller strains than we observed. The irregular elongated shape of our quartz particles is quite unlike their assumed spherical particles, and the additional sites for stress concentration may account for a longer period of creep evolution. Another discrepancy between our results and this model is that the model does not predict the eventual attainment of steady-state creep which was reached by some of our samples

A finite element model constructed by Tullis et al (1991) explores the possible contributions of particle shape and distribution geometry to the changing strain and stress within a two-phase aggregate, and hence to the evolution of deformation. The authors conclude that, in general, isolated particles of a strong phase will result in an aggregate strength close to the Reuss bound. However, they also find that deviation of particle shape from spherical will increase the strengthening effect of rigid particles through greater local stress concentrations and resultant power dissipation. This agrees with our experiments, in which even small fraction of angular quartz particles increases the marble strength to a value approximately halfway between the Voigt and Reuss bounds. The finite element model of Shen et al (1994) also predicts increased strengthening effect of non-spherical strong particles.

The evolution of internal stress and strain required by models such as Tanaka et al (1994) can also be assessed by the dispersion-hardening theory as described by Ashby (1970) and further developed by Humphreys and Kalu (1990). Strong particles in a deforming aggregate are expected to require geometrically-necessary dislocations in the matrix, in order to maintain strain compatibility at each interface between the two phases. Such dislocations, added to the dislocations in the matrix which are statistically necessary for bulk strain, form zones of high dislocation density around the particles. These tangled zones are relatively resistant to deformation, and can increase in size with strain. Qualitatively, our samples exhibit zones of high dislocation density which are consistent with this theory. In some such zones, recrystallization has begun to produce coronas of small strain-free calcite grains around quartz particles.

Further modifications in aggregate strength can be caused by inhomogeneous distribution of strong particles. Such a distribution could be present in the original undeformed rock, due to variations in some geological process, such as sedimentation, by which the rock formed. In other cases, particle distribution may evolve during deformation through fabric development. Durham et al (1992) performed experiments on ice with varying proportions of fine-grained rock-forming minerals, where they found that hard particle fractions of over 0.1 had a much higher strengthening effect upon the aggregate than predicted by mixing laws or the pinning of dislocations. Some sample textures exhibited the evolution of bridging between rigid particles, which they interpreted to add to the strength and toughness of the aggregates. In their samples with particle fractions over 0.3, they observed the formation of lamellar features in the aggregate texture, where rigid particles were beginning to form regions of continous framework. Corbin and Wilkinson (1994) consider distribution geometry within aggregates, in terms of clustering of strong particles. Their results suggest that clustering can increase aggregate strength through higher rates of strain hardening. On the other hand, if inhomogeneous distribution reaches a stage where strong particles are segregated into layers alternating with layers of softer matrix material, conditions for serial loading will have been reached, and aggregate strength is most likely to be lowered, approaching the Reuss bound. Because the particles in our samples were evenly dispersed, both before and after deformation, we did not have the opportunity to observe either of these effects. This discussion, however, does indicate the potential for strain localization inherent in variations in hardening behavior, as discussed by Hobbs et al (1990), in this case controlled by the volume fraction of strong particles.

At present, no single model fully explains our data and observations. However, several models identify phenomena which together could produce the essential qualities of our results. Redistribution of internal stress in response to strain mismatch between phases can produce transient creep (Tanaka et al, 1991). The growth of the effective size of strong particles, due to high dislocation density building up around them (Ashby, 1970; Humphreys and Kalu, 1990), may describe the microstructural mechanics responsible for this effect. This effect may be magnified by non-spherical shape of strong particles (Tullis et al, 1991). When the energy at these tangles of dislocations reaches a certain concentration, it may lead to nucleation and growth of new grains, a recovery process which would tend to conteract other hardening processes. Thus a constant hardening rate may evolve to steady state creep when recovery and hardening reach a balance. The period of constant hardening rate in the aggregate will be enhanced by increasing strong particle fraction (Corbin and Wilkinson, 1994).

Conclusions

Our experiments have shown that even a small proportion of quartz particles in a calcite matrix can increase the strength of synthetic marble considerably, when it is deformed under conditions close to the transition between brittle and ductile behavior of the aggregate. Marble strength lies between the bounds set by predictions based on uniform strain and uniform stress, and is higher than that predicted by existing continuum mechanical models. A significant contribution to aggregate strength may be provided by angular shape in strong particles, transient creep properties of individual phases, and zones of high dislocation density and/or recrystallization around the strong particles, none of which is completely quantified by existing models.

These results suggest that the use of experimental data to predict or explain the deformation of complex earth materials is not a simple matter. Where more than one phase is present in a rock, it can not be assumed that mechanical data for either phase will succesfully approximate the mechanical properties of the aggregate. Furthermore, no currently available mixing model appears to apply to aggregates whose phases have such differing strengths as quartz and calcite.

We do offer some hope, however, in the fact that experimentalists and theoreticians have identified and begun to quantify the effects of some of the features of an aggregate which ultimately control its steady-state strength: volume fraction of rigid particles; particle/matrix strength contrast; particle shape. Additional features of the deformed aggregates may offer clues to their history: dislocation density and recrystallization at particle/matrix interfaces; redistribution of particles through fabric development. Even where these features can not be precisely quantified, their contribution to strain localization may be assessed, based on the large strengthening effects of small quantities of strong particles.

References:

Ashby, M. F., 1970. The deformation of plastically non-homogeneous crystals. Philosophical Magazine 21: 399-424.

Bloomfield, J. P., and Covey-Crump, S. J., 1993. Correlating mechanical data with microstructural observations in deformation experiments on synthetic two-phase aggregates. Journal of Structural Geology 15: 1007-1019.

Bruhn, D.; Olgaard, D.L.; Dell'Angelo, L.N., Siddiqi, G., 1993. Rheology of fine-grained rocks containing two phases of similar strengths: preliminary results. Terra Nova, Abstract Supplement 5:287.

Chen, I. W., and Argon, A. S., 1979. Steady-state power-law creep in heterogeneous alloys with coarse microstructures. Acta Metallurgica 27: 785-791.

Cho, K., and Gurland, J., 1988. The law of mixtures applied to the plastic deformation of two-phase alloys of coarse microstructures. Metallurgical Transactions 19A: 2027-2040.

Corbin, S.F.; Wilkinson, D.S, 1994. The influence of particle distribution on the mechanical response of a particulate metal matrix composite. Acta Metallurgica et Materialia 42:1311-1318.

Dresen, G., and Evans, B., 1993. Brittle and semibrittle deformation of synthetic marbles composed of two phases. Journal of Geophysical Research 98: 11,921-11,933.

Drury, M.R.; Vissers, R.L.M.; van der Wal, D.; Hoogerduijn Strating, E.H., 1991 Shear localization in upper mantle peridotites. Pure and Applied Geophysics. 137:439-460.

Durham, W.B.; Kirby, S.H., Stern, L., 1992. Effects of dispersed particulates on the rheology of water ice at planetary conditions. Journal of Geophysical research 97:20,883-20,897.

Evans, B.; Kohlstedt, D.L., 1995 Rheology of Rocks. in Rock Physics and Phase Relations: A Handbook of Physical Constants. A.G.U. Reference Shelf 3: 148-165.

Groshong, R.H, 1988. Low-temperature deformation mechanisms and their interpretation. Geological Society of America Bulletin. 100:1329-1360.

Handy, M.R., 1990. The solid-state flow of polymineralic rocks. Journal of Geophysical Research. 95:8647-8662.

Hobbs, B.E.; Mulhaus, H.B.; Ord, A., 1990. Instability, softening and localization of deformation. in Knipe, R.J.; Rutter, E.H., eds, Deformation Mechanisms, Rheology and Tectonics. Geological Society Special Publication 54:143-165.

Humphreys, F. J., and Kalu, P. N., 1990. The plasticity of particle-containing polycrystals. Acta Metallurgica et Materiala 38: 917-930.

Jordan, P. G., 1987. The deformational behaviour of bimineralic limestone-halite aggregates. Tectonophysics 135: 185-197.

Jordan, P. J., 1988. The rheology of polymineralic rocks - an approach. Geologische Rundschau 77: 285-294.

Knipe, R.J., 1989. Deformation mechanisms - recognition from natural tectonites. Journal of Structural Geology. 11:127-146.

Olgaard, D.L., 1990. The role of second phase in localizing deformation. in Knipe, R.J.; Rutter, E.H., eds, Deformation Mechanisms, Rheology and Tectonics. Geological Society Special Publication 54: 175-181.

Paterson, M. S. and Luan, F. C., 1990. Quartzite rheology under geological conditions. in Knipe, R. J., and Rutter, E. H., 1990. Deformation Mechanisms, Rheology and Tectonics, Geological Society Special Publication No. 54: 299-307.

Peach, C.J., 1991. Influence of deformation on the fluid transport properties of salt rocks. PhD-thesis Utrecht, 238 p.

Poech, M.H.; Fischmeister, H.F., 1992. Deformation of two-phase materials: a model based on strain compatibility. Acta Metallurgica et Materialia. 40:487-494.

Ross, J. V., Bauer, S. J., and Hansen, F. D., 1987. Textural evolution of synthetic anhydrite-halite mylonites. Tectonophysics 140: 307-326.

Schmid, S.M., 1982. Microfabric studies as indicators of deformation mechanisms and flow laws operative in mountain building. in Hsu, K.J, ed., Mountain Building Processes. Academic Press. 95-110.

Schmid, S. M., Boland, J. N., and Paterson, M. S., 1977. Superplastic flow in finegrained limestone. Tectonophysics 43: 257-291.

Schmid, S. M., Paterson, M. S., and Boland, J. N., 1980. High-temperature flow and dynamic recrystallization in Carrara marble. Tectonophysics 65: 245-280.

Shen, Y.L; Finot, M.; Needleman, A.; Suresh, S., 1994. Effective elastic response of two-phase composites. Acta Metallurgica et Materialia. 42:77-97.

Tanaka, M.; Sakaki, T.; Iizuka, H., 1991. Creep deformation of ductile two-phase alloys. Acta Metallurgica et Materialia. 39:1549-1554.

Tullis, J., 1990. Experimental studies of deformation mechanisms and microstructures in quartzo-feldspathic rocks. in Barber, D.; Meredith, P., eds., Deformation Processes in Minerals, Ceramics and Rocks. Unwin and Hyman, Cambridge. 190-227.

Tullis, T. E., Horowitz, F. G., and Tullis, J., 1991. Flow laws of polyphase aggregates from end-member flow laws. Journal of Geophysical Research 96: 8081-8096.

Walker, A. N., Rutter, E. H., and Brodie, K. H., 1990. Experimental study of grain-size sensitive flow of synthetic, hot-pressed calcite rocks. in Knipe, R. J., and Rutter, E. H., 1990. Deformation Mechanisms, Rheology and Tectonics, Geological Society Special Publication No. 54: 259-284.

Xue, L. A., and Raj, R., 1990. Effect of diamond dispersion on the superplastic rheology of zinc sulfide. Journal of the American Ceramic Society 73: 2213-2216.

List of Tables

List of Figures

    a) Optical Microphotograph

    b) Transmission Electron Microphotograph

    c) Transmission Electron Microphotograph

    d) Transmission Electron Microphotograph

TABLE 1: Sample Materials Used in Experiments at 600°C, 200 MPa, 3×10^{-5} s^{-1}.

Sample #	Quartz fraction (vol%)	Porosity (%) before deformation	Calcite grain size (microns) before deformation	Calcite grain size (microns) after deformation
ZI1	0	9	5 to 10	10 to 40
ZI3	0	1	-	10 to 40
IRE2	5	4.1	-	-
IRE3	5	4.0	-	10 to 20
IRE4	5	-	-	-
KBLA3	20	4.1	5 to 20	10 to 15
IBLA5	20	3.5	5 to 20	5 to 15
IBLA7	20	-	5 to 20	5 to 15

TABLE 2: Mechanical Data for Experiments at 600°C, 200 MPa, 3×10^{-5} s^{-1}

Sample #	% Quartz	Strain to Reach Steady-State (%)	Final Strain (%)	Differential Stress (MPa) at Final Strain	Final Strain Hardening Rate (MPa/%)
ZI1	0	na	10.8	39	<1
ZI3	0	1	10.8	22	0
IRE2	5	na	5.9	126	8
IRE3	5	5	9.5	97	0
IRE4	5	3	5.9	68	0
IBLA3	20	na	5.8	150	8
IBLA5	20	na	9.1	199	8
IBLA7	20	>10	12.1	197	0

a) Optical mcrophotograph of undeformed sample material
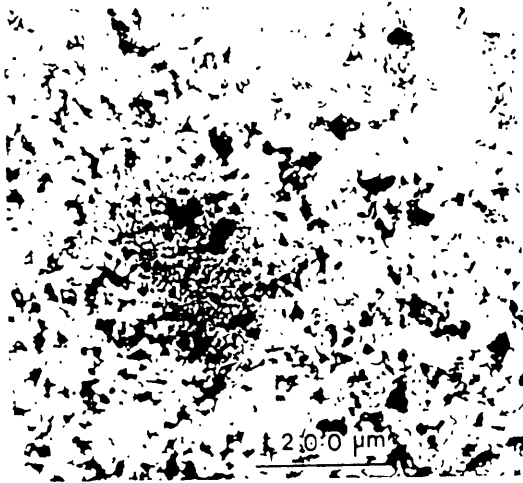
c)Transmission electron microphotograph of corona of strain-free calcite grains
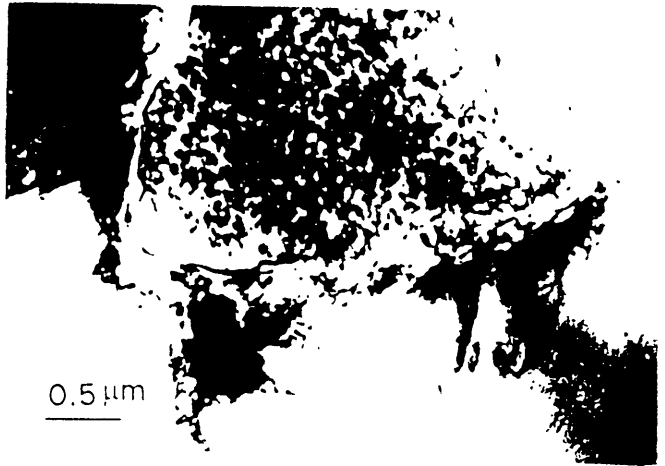
b)Transmission electron microphotograph of pore at quartz-calcite interface

d)Transmission electron microphotograph of dislocations at quartz-calcite interface

Figure 2: Plot of Experiments at 600 degrees C, 200 MPa.

Experiments at 600 degrees C, 200 MPa
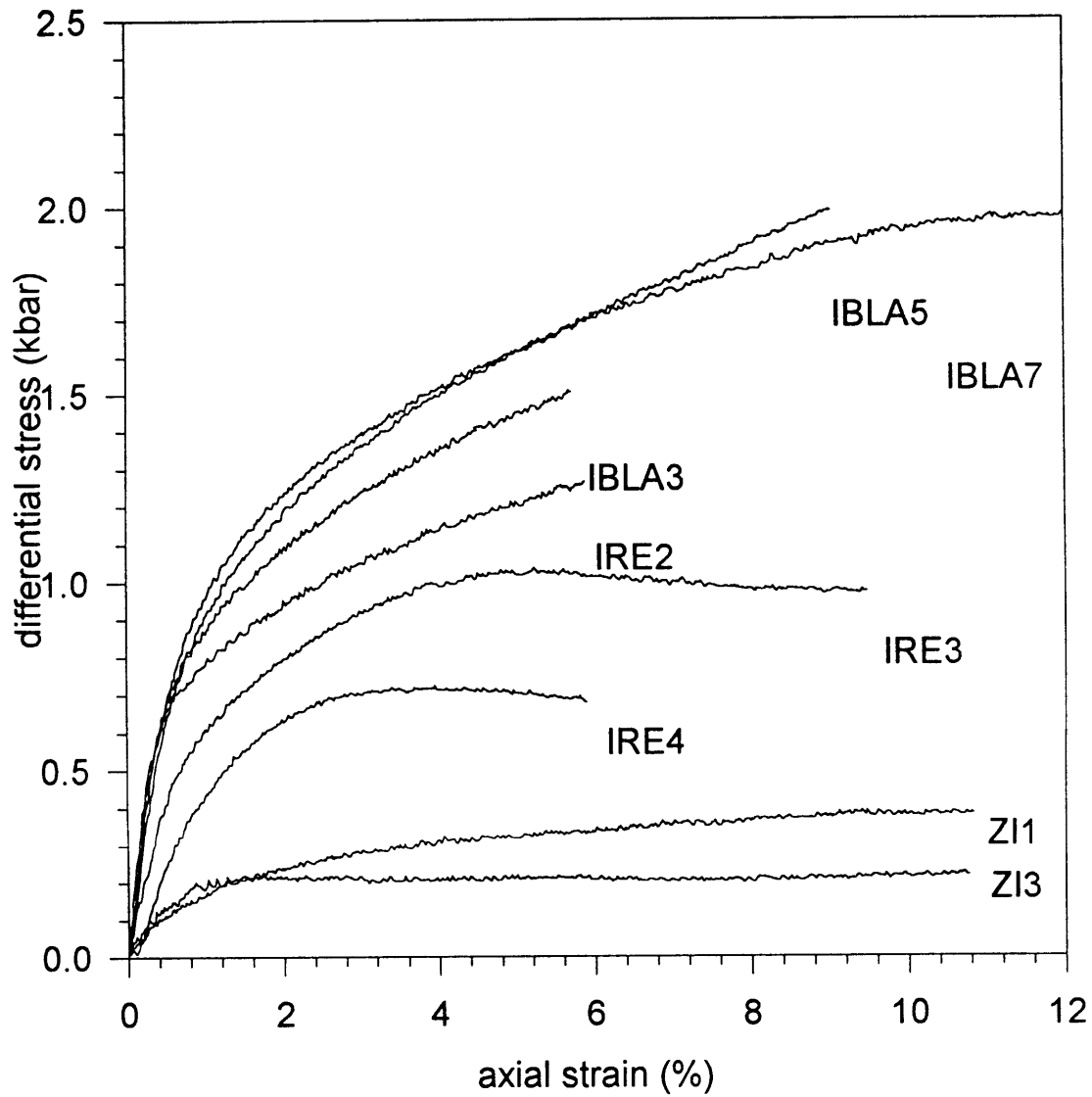
Figure 3: Plot of Mixing Law Predictions: T=873K.

Mixing Law Predictions: T=873K
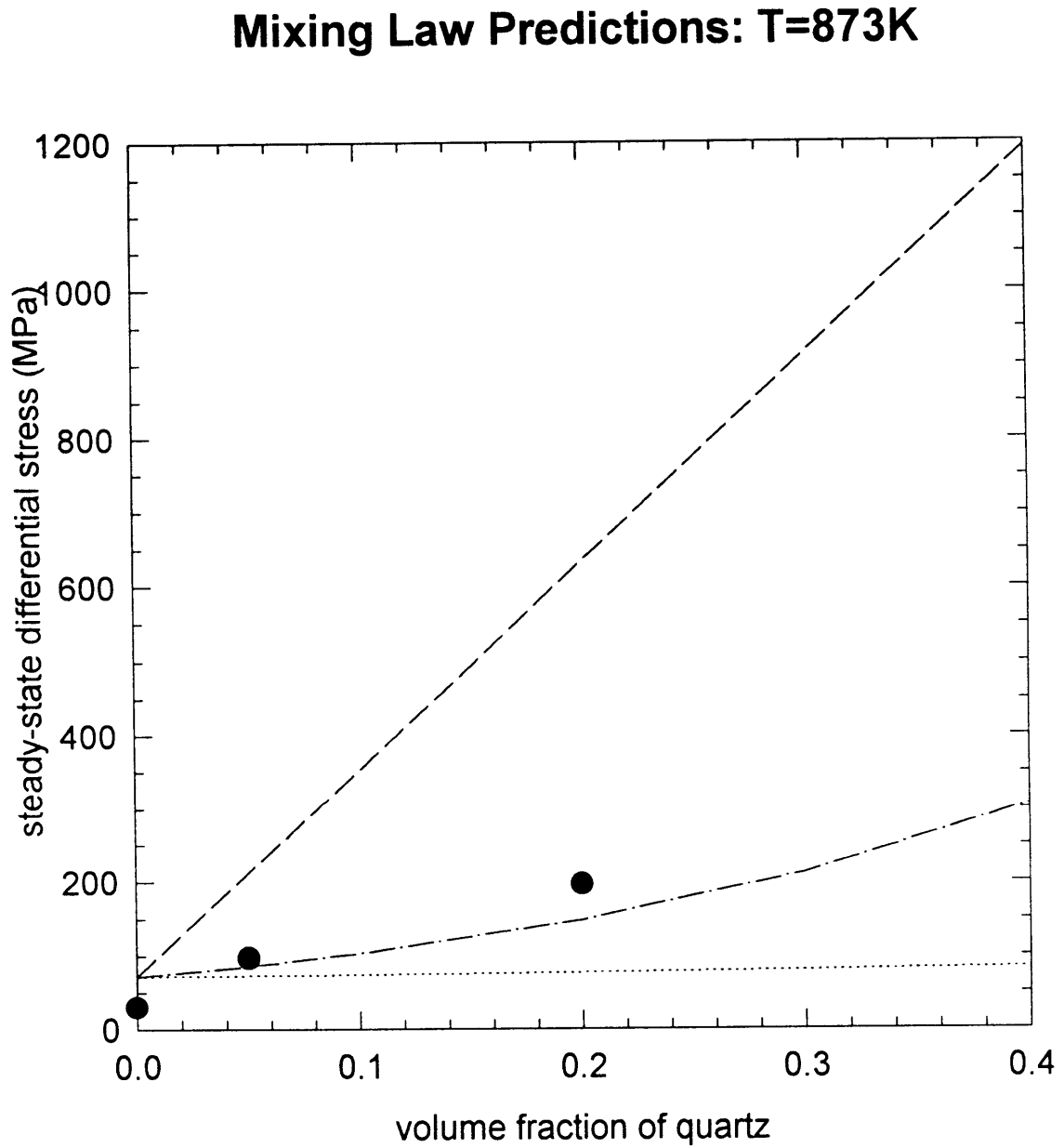
Figure 4: Plot of Mixing Law Predictions: T=923K.
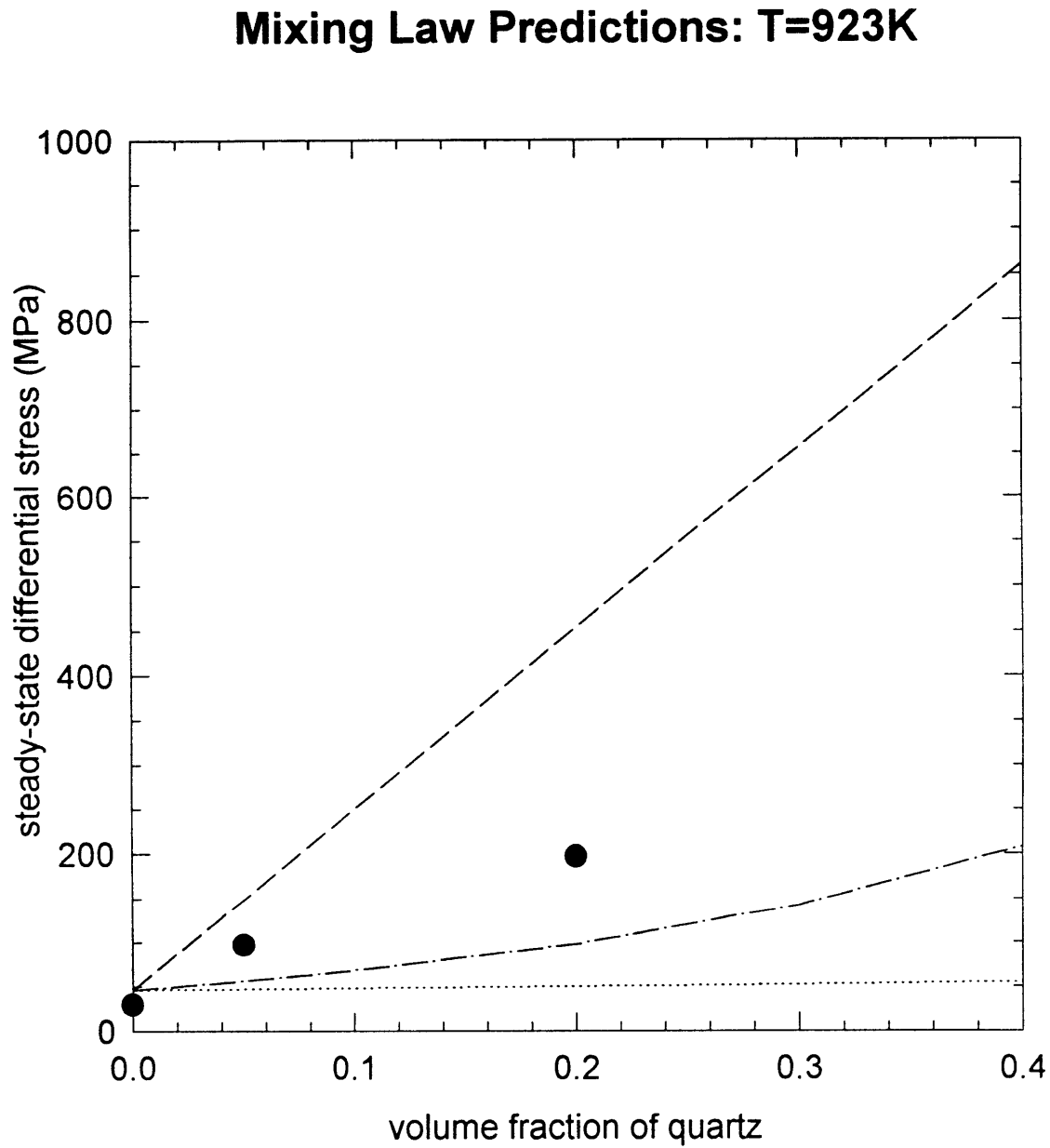
Mixing Law Predictions: T=923K

Chapter 4: Conditions For Melt Migration In Planetary Interiors: Evidence From The Brenham Pallasite

Abstract

Experiments on partially molten geological materials demonstrate that processes involved in melt segregation within a planetary interior are controlled in part by the relative interfacial energies of contacts between coexisting phases. In order to provide constraints on the formation history of the parent body of the Brenham pallasite, I assessed the interfacial energy between a metallic melt and a silicate mantle, through detailed textural observations and the analysis of interfacial angles between phases. Interfacial angle data were used to estimate the values of interfacial energy along interfaces between given phases, and to predict the conditions for formation of a connected network of metallic melt. The value calculated for olivine/metal interfaces was 660 mJ/m^2, followed by 636 mJ/m^2 for olivine/schreibersite and 615 mJ/m^2 for olivine/troilite. Further calculations provided rough estimates of interfacial energy for metal/schreibersite interfaces of less than 50 mJ/m^2, for schreibersite/troilite interfaces of approximately 50 mJ/m^2, and for metal/troilite interfaces of close to 100 mJ/m^2. The large wetting angles, all close to 90°, between olivine and non-silicate phases suggested that original chondritic material must have experienced both melting and fracturing before the observed connected network of metallic melt could have formed. During subsequent cooling of this melt, blebs of sulfide exsolved from the iron-nickel melt, followed by exsolution of phosphide blebs. The resulting minerals, troilite and schreibersite, crystallized adjacent to olivine grains. A later low-temperature deformation event opened fractures between and within olivine grains, thereby drawing non-silicate phases into cracks.

Introduction

Pallasites are of particular interest to scientists who seek to understand processes of differentiation in the formation and evolution of planetary bodies. These meteorites consist primarily of closely packed olivine crystals in a matrix of the metallic iron-nickel minerals taenite and kamacite. Minor phases include chromite, troilite and schreibersite. The coexistence of metal and silicates suggests that pallasitic meteorites originated at the interface between the metallic core of a protoplanet and its silicate mantle (e.g., Taylor, 1992). The overall texture is consistent with the existence of a connected network of metallic melt which may have been instrumental in the process of segregation of the metal core from a chondritic mineral assemblage.

In this study, I will demonstrate that the Brenham pallasite (Figure 1) represents a texture which is controlled in part by interfacial forces. The fact that metallic Fe-Ni and FeS in other meteorites frequently occur in isolated spherical droplets or pockets within the silicate framework implies that some factors are present which would inhibit the formation of a connected metallic melt network. Analysis of the pallasite texture can be used to adress the question: if this material evolved from a chondritic composition with roughly 10% metal, how did the metal form a connected network? In view of the variety of textures exhibited by meteorites in general and their multi-billion year histories, it is not unreasonable to expect that some series of distinct processes may have operated upon this material. In pallasites, these processes are likely to have involved partial melting, melt migration, minimization of interfacial energy and fracturing. A thorough review of the first two processes as associated with pallasites and related meteorites has been provided by Taylor (1992). In order to assess the relative contribution of the last two processes, I have measured wetting angles between olivine and the three non-silicate phases present in the Brenham pallasite, in conjunction with detailed textural observations. Two distinct types of features have been preserved. Features which represent an approach to textural equilibrium through minimization of interfacial energy include: wetting angles measured at cusps between adjacent olivine grains; rounding of olivine and troilite interfaces, convex toward metallic Fe-Ni; large olivine grain size (~ 5mm dia.). In contrast, disequilibrium

texture is represented by: cracks within and between olivine grains filled with troilite; sharp corners at outer edges of filled cracks.

Background

An interface can be defined as a planar feature which occurs where two volumes of distinct phases meet. A grain boundary is a special case, where the two volumes are crystals of the same phase, but with different crystallographic orientations. The presence of an interface contributes free energy to a system above that which is represented by the volumes of the phases; this free energy is referred to as interfacial energy. Its magnitude per unit area corresponds to the degree to which atomic bonding conditions are non-ideal. Minimization of free energy can be achieved both by replacement of high-energy interfaces with those of lower free energies and by any decrease in interfacial area per sample volume. Rounding of sharp edges and grain growth are two means by which area/volume ratios can be reduced.

Interfacial energy per unit area typically approximates the tensile force per unit length along any direction on the interface. At equilibrium, the forces meeting at a three-grain junction will balance, according to Newton's first law, and thus can be represented in terms of a stationary free-body diagram. Where a fluid phase meets a grain boundary between grains of a given solid A (Figure 2a), the wetting angle θ obeys the equation:

$$\gamma_{AA} = 2\gamma_{AB}\cos(\theta/2) \qquad \text{equation (1)}$$

In the case where two distinct fluid phases have wetted the approximately flat surface of a solid phase A (Figure 2b), the acute angle ψ must satisfy the equation:

$$\gamma_{AB} = \gamma_{AC} + \gamma_{BC}\cos\psi \qquad \text{equation (2)}$$

Interfacial angles at intersections between any three fluid phases (Figure 2c) can be used to calculate relative values of interfacial energy according to the general equation:

$$\gamma_{AB} = \gamma_{AC}\cos(180°-\alpha) + \gamma_{BC}\cos(180°-\beta) = -[\gamma_{AC}\cos\alpha + \gamma_{BC}\cos\beta] \qquad \text{equation (3)}$$

The melt distribution geometry for a solid/melt system with a low melt fraction can be predicted if the corresponding wetting angle θ is known, [VonBargen and Waff, 1986]. For systems with high melt fractions, wetting angle data can only be used in qualitative predictions based on extrapolations, as discussed at the end of this report. However,

interfacial angle measurements θ, ψ, α and β can be used with all three equations to estimate the magnitudes of energy at associated interfaces if data on one of the interfaces has been determined by independent means.

Method of Study

For this study, I selected sample 425b of the Brenham pallasite from the mineralogical collection at Harvard University. Sample 425b is a slab which measures 12 cm by 19 cm, cut from a much larger specimen (Figure 1). When I first observed it, one surface had been polished, whereas the other had been ground smooth only; both surfaces had been etched in order to reveal the distinction between kamacite and taenite. In order to improve the resolution of interfacial angle measurements, both surfaces were freshly polished to 600 grit for this study. Further polishing was found to be extremely difficult, due to the unevenness of the cut surface, and the size of the sample, as well as to the extremely different thermal characteristics of the olivine and metal. The surfaces were not etched a second time.

I performed the textural analysis and measurement of interfacial angles on the polished surfaces of the sample, using a Nikon SMZ-2T reflected light microscope connected to a video screen. Modal abundances shown in Table 1 are based upon a 1299-point count, and they are close to those reported by Buseck (1977). This pallasite has been oxidized to varying degrees by terrestrial weathering. Oxidized iron is referred to in Table 1 as limonite, but its exact composition has not been determined.

Results: Textural observations

The texture of the Brenham pallasite as it exists today appears to have preserved features of a solid-melt structure. For the purpose of making measurements, I have assumed this to be the case. Later, interpretations of the data allow qualitatively for the effects that the crystal structure of phases which were initially molten might have upon the melt morphology. As a solid-melt structure, this sample contains clear evidence of high values for energy at most of the interfaces between coexisting phases (Figure 2). The most abundant phase, olivine, occurs primarily in aggregates of large, rounded grains. Rounding, size and close packing all serve to minimize the interfacial area between olivine and adjacent phases, suggesting that high values of interfacial energy have a strong influence upon the texture. The olivine grains are also heavily fractured.

Metallic Fe-Ni is present as a continuous matrix, filling the large voids between olivine aggregates with the appearance of having existed as a melt within a solid olivine framework. Cusps between adjacent olivine grains which are filled with metal display broad wetting angles. The majority of such cusps, however, are filled with globules of troilite or schreibersite. Troilite exhibits convex, rounded interfaces relative to metal, suggesting that those interfaces have minimized their area in response to a value for $\gamma_{metal/troilite}$ which, while being lower than $\gamma_{olivine/metal}$, is still high. Troilite is also present as a crack-filling within and between olivine grains. Schreibersite has a varied morphology, in places forming thin rims between olivine or troilite and metal, and elsewhere occurring as euhedral crystals surrounded by metal.

These relationships suggest a heirarchy of values of interfacial energy. The following inequalities express the relative preferences of given phases for wetting olivine, from least wetting (highest interfacial energy) to most wetting (lowest interfacial energy):

$$\gamma_{olivine/metal} > \gamma_{olivine/schreibersite} > \gamma_{olivine/troilite}$$

Furthermore, the degree of rounding and relative grain sizes of each phase in the metal matrix are expressed in the following inequalities, from the largest, most rounded (highest interfacial energy) to the smallest, most euhedral (lowest interfacial energy):

$$\gamma_{olivine/metal} > \gamma_{troilite/metal} > \gamma_{schreibersite/metal}$$

Results: Interfacial Angle Measurements

I measured all angles formed at intersections of three interfaces in this sample of the Brenham pallasite. The angles can be classified according to the presence of olivine. At the edge of the grain boundary between two adjacent olivine grains, a cusp is formed, which may be filled with a non-silicate phase. Angles θ defined by the two olivine/non-silicate phase interfaces at such cusps (Figure 2a) comprise Group A. A different wetting relation exists where an interface between two distinct non-silicate phases meets an olivine grain. Angles ψ between such an interfaces and the olivine grain (Figure 2b) comprise Group B. Group C consists of angles α, which are defined by interfaces between three non-silicate phases that meet in the absense of olivine (Figure 2c).

Frequency distribution plots of the data are given in Figures 5,7 and 8. Each graph displays a plot of the measured values of a particular type of interfacial angle, as described below. Also shown on the graphs are plots of predicted distributions of apparent angles measured at arbitrary orientations relative to given true angles. These theoretical plots were produced by a program written by Amy Jurewicz and Ken Koga, according to theory presented in Jurewicz and Jurewicz (1986). For each graph, I assessed the degree to which data approximated theoretical distributions in terms of a chi-squared value, and only the best fit is shown. For some data distributions, no single angle plot provided a good fit. In these cases, normalized sums of theoretical plots for two or more true angles are shown.

Group A: Within this group, cusps between adjacent olivine grains may be filled with iron-nickel metal (OOM), troilite (OOT) or schreibersite (OOS). Measurements for OOM angles θ constitute two populations, distinguished by the presence or absence of a fine filling of metal or troilite between the olivine grains which meet at the cusp. A population of 25 angles represents cusps at which the olivine/olivine grain boundary was free of any non-silicate filling. A plot of these angles in Figure 5a matches closely the theoretical distribution for a true angle of 94°.

A plot of the second population, for the 42 OOM angles θ, at which the olivine/olivine grain boundary was filled with a non-silicate phase, is given in Figure 5b. The theoretical distribution for a single true angle of 83° comes closest to matching it, but the fit is not good. The poor fit is likely to be the result of the fact that the angles in this population do not represent the same kind of force balance as is shown in Figures 2a and 6a. In fact, these angles can not represent a stable force equilibrium, since the olivine/olivine grain boundary has been replaced by two olivine/non-silicate interfaces, giving a total of four interfaces, all of the same kind, which meet at the cusp. These interfaces occur as two pairs of connected interfaces. Each pair is unconnected to the other and therefore is independent in terms of interfacial forces. In theory, interfacial forces at a simple intersection of two interfaces are balanced only if they meet at 180°. Any smaller angle will be unstable, resulting in the tendency for it to become rounded as a means of approaching 180° (Figure 6d). The second population of angles thus may have originated as wetting angles like those in the first poplulation, but with the entry of a non-silicate phase between the olivine grains, rounding may have begun to modify the shape of the cusps. The fact that the approximate angle in the second population is 11° smaller than in the first would then be due to the initiation of rounding (Figure 6c). The preservation of distinct angles, however, suggests that the grain-boundary-filling and rounding processes occurred at low temperatures with insufficient time to allow local interfacial equilibrium to be achieved. Because of this, the filled grain boundaries represent a disruption of the overall chemical and textural equilibrium, likely to be due to a late-stage process after which complete re-equlibration did not occur.

Angles were also measured at cusps which were filled with troilite or schreibersite. Only eleven OOS angles were measured, and all were associated with filled olivine/olivine grain boundaries. A rough interpretation of the plots in Figure 5c gives an angle of 85°. The estimated true angle would then be somewhat larger. Other observations and calculations require that the OOS wetting angle be smaller than that for OOM, so an angle of 90° will be assumed. In all but four of the 34 OOT angles θ measured, the olivine/olivine grain boundary was filled with troilite. As with the second population of

OOM described above, the closest match between a plot of data and a theoretical plot for a single true angle was not good (Figure 5d). A closer fit was obtained by combining plots for a range of angles from 60° through 90°, with a mean of 75°. Following the above arguments for local disequilibrium and filled grain boundaries, it is possible that the true wetting angle is roughly 11° larger than shown by the data, giving an estimate of 86° rather than 75°.

Group B: A large number of angles was measured where interfaces between two of the non-silicate phases intersected an interface with a rounded olivine grain (Figure 2b). The distribution plot of 64 angles OMS, where the two non-silicate phases were metal and schreibersite (Figure 7a), was not well matched by the theoretical plot for any single true angle. A good fit to the data could be obtained by combining plots for three different angles, 30°, 55° and 75°, to match the three apparent peaks in the data. A normalized sum of a large range of angles, from 30° to 80° also provided a moderately good fit.

Data for 75 acute angles ψ OMT, where the two non-silicate phases were metal and troilite, are plotted in Figure 7b. No theoretical plot for a single true angle provided a good fit with the data, but a plot for 65° came the closest. A much improved fit was obtained when theoretical plots for two angles 50° and 80° were combined. An equally good fit was produced by combining a range of values from 50° to 80°.

The 76 OST angles ψ, where the two non-silicate phases were schreibersite and troilite, were the only type of angle in this group whose distribution approximated that for a single true angle (Figure 7c). The best fit was obtained for a true angle of 60°.

Group C: Interfacial angles MST measured where metal, schreibersite and troilite met at a triple junction comprise the last group. The smallest angle in all cases enclosed schreibersite and is labelled α. A distribution plot for the 13 angles of this type (Figure 7d) most closely fits a theoretical plot for a true angle of 46°. Mean values for the other two angles were 174° enclosing troilite, and 140° enclosing metal.

214

Analysis: Interpretation of plots

The preference of sulfide and phosphide phases for crystallization sites adjacent to olivine suggests two possible factors in the development of the texture. 1. The olivine presented a solid crystal surface upon which these phases might find low-energy nucleation sites for new crystal growth, as the mineral components exsolved from solution in the cooling metallic melt. 2. The interfacial energy of the system could be lowered by substitution of interfaces between troilite or schreibersite and olivine, for the higher energy olivine-metal interfaces. My results show that both are likely to have had an effect.

Interpretation of fit between theoretical plots and data: Within the three groups of data there is some variability in the degree to which theoretical plots for true angles match the distribution of a given type of angle measurement. Where a sample population is well described by the theoretical distribution of apparent angles for a single true angle, one interpretation is that the conditions are approximately isotropic and a simple force balance governs the interfacial angles. This would clearly be the case if all phases had isometric crystal structures, or if they had preserved their exact molten morphology. It could also be the case if the three phases involved in the angle had anisotropic crystal structures, but their orientations relative to each other were random to the extent that a normal distribution of true angles, centered about a single value, would result. This is a possible interpretation of the plot for OST angles in Group B, where the phases have orthorhombic, tetragonal and hexagonal symmetries, respectively. Apparent isotropy in OOM angles could result from the combined effects of the isometric crystal structure of the metal, and random orientation of adjacent olivine grains.

Another interpretation of a plot which is well fit by a single true angle is that the later-crystallizing phases have nucleated on solid interfaces epitaxially, such that a specific relative orientation is dominant. This may apply to the OOS angles in Group A, where it is clear from textural observations and phase equilibrium arguments that olivine grains had crystallized and aggregated long before the minor phases exsolved. The epitaxial interpretation could also apply to OST data as well. It is less likely to apply to angles where metal is present, because the crystal structure of the metal is isometric.

Three of the angle distributions contain more than one peak of roughly the same magnitude. If the peaks can be considered statistically significant, each one may represent a distinct condition or event. Data for OMS angles strongly suggest this interpretation, in combination with textural evidence. Some schreibersite crystals have grown along the margins of troilite or olivine grains, in which case there could be an epitaxial relationship as described above. A distinct population of schreibersite crystals appears to have nucleated within the crystal structure of the metal and/or to have developed crystal faces, thus meeting olivine grains at orientations determined by the internal structure of metal and schreibersite, rather than by minimization of interfacial energy.

Where the angle distribution is too broad to fit a single angle, and any intermediate peaks are considered insignificant, the data most likely represent a range of true interfacial angles. In this case, the anisotropy of crystal structures must have some effect, and their relative orientations be controlled to some degree, such that a random distribution does not occur. OOT and OMT angles are good candidates for this interpretation. The relative orientation between orthorhombic olivine and hexagonal troilite may respond to epitaxial constraints, and the magnitude of interfacial energy may depend to some degree upon the crystallographic orientation of an interface.

Calculations: In order to estimate interfacial energy values for each type of interface present in the Brenham pallasite, I have used the above interpretations of the data to assign a single value to each type of angle measured. These values are shown in Table 2. For OOM, OOS, OST, and MST, a single true angle plot best described the data, and this value is shown directly except for the case of OOS, where 5° was added according to the arguments discussed under Group A above. A range of values more accurately describes the distribution of OOT and OMT angles, and in this case the mean of that range is shown, with 11° added to the OOT mean. The one type of angle for which assignment of a single value is most difficult is the OMS angles. It is possible that only one of the peaks accurately represents interfacial energy minimization, but because textural observations do not strongly suggest a most likely choice, I have tentatively assumed the value of the middle peak to represent these angles.

Analysis: Interfacial Energy

Calculations of interfacial energy between olivine and the non-silicate phases were based upon a value of 900 mJ/m^2 estimated by Cooper and Kohlstedt (1982) for high-angle olivine-olivine grain boundaries. This value was used in equation (1) with values shown for Group A. Values for Group B, along with the results of the Group A calculations, were then used in equation (2) to estimate the interfacial energy between pairs of non-silicate phases. A third type of calculation used values from Group C, along with the results of some of the Group B calculations, in equation (3), as a way of checking the estimates for interfaces between the pairs of non-silicate phases. Results of calculations are shown in Table 3.

The results of the calculations support the textural observations discussed above. Among interfaces between olivine and non-silicate phases, the highest value, 660 mJ/m^2, is for olivine/metal, followed by 636 mJ/m^2 for olivine/schreibersite and 615 mJ/m^2 for olivine/troilite. These results are consistent with the preference of troilite for wetting olivine. Calculations for interfaces between non-silicate phases are less directly based upon data. In addition, they are extremely sensitive to the somewhat arbitrary choice of value for the OMS angle. Nevertheless, some agreement is found between calculations based on the two different equations (2) and (3) for metal/schreibersite and metal/troilite interfaces. The calculations suggest generally that interfacial energy for metal/schreibersite interfaces is less than 50 mJ/m^2, for schreibersite/troilite interfaces is approximately 50 mJ/m^2, and for metal/troilite interfaces is the highest, at close to 100 mJ/m^2.

Discussion

The results of this study demonstrate that interfacial energy between olivine and non-silicate phases is high enough to have produced wetting angles well above the 60° value considered as a maximum for connected melt networks at low melt fractions. However, the pallasite texture contains a large metallic melt fraction of roughly 50%, which does form a connected network. How is it possible that this meteorite evolved from originally chondritic material which contained only 10 to 20% metal?

Iron-rich metal and sulfide are typically present in chondrites either as fine-grained particles disseminated among crystallites of olivine and other silicate phases, or as very thin networks along interfaces between the other phases. In view of the high values of interfacial energy between metal and olivine, these textures store a very large amount of energy in their high interface/volume ratios. Given sufficient time and component mobility, it would be possible for connected volumes of metal to coalesce, driven by thermodynamic equilibrium requirements to lower the free energy of the system through decreasing the total area of high-energy interfaces. A heating event within the protoplanet could accelerate this process. Evidence of coalescence may be preserved in some unclassified fine-grained meteorites.

Ultimately, the coalesced volumes of metal would become isolated from each other, due to the tendency toward ponding, as described by Stevenson (1986). Acapulcoites and lodranites may serve as evidence for this portion of the process. The original chondritic metal content would be maintained, and large wetting angles would prevent the inteconnection of ponded metal, unless some process occurred by which the metal content of the material was enriched to the point where the metallic melt fraction would be high enough to form a continuous network. One relevant process, discussed by Taylor (1992), is the removal of some of the silicate material as a melt whose low wetting angle with olivine of roughly 47° (Waff and Bulau, 1979) would permit the formation of a silicate melt network. Taylor (1992) estimates that approximately 50% melting of the silicates must occur before isolated metal globules would be large enough to sink or form an

interconected network, if silicate melting were the only process operating. Gaetani and Grove (1996) have reported experimental results that sHow that an increase in the oxygen fugacity in an iron sulfide melt can cause a reduction in iron sulfide/olivine interfacial angles to below 60°, at which condition connected melt networks can form at low melt fractions. Relevant measurements of oxygen fugacity on the metallic phases in the Brenham pallasite have not been made, so this additional network-forming effect can not be ruled out.

Another process aiding the concentration of metal could have been the simultaneous fracturing of silicates and shock-melting of metal, which would have resulted from the frequent collisions with other planetary bodies likely to have occurred in the history of the protoplanet. A collision would be a source of energy which could accomodate a temporary increase in high-energy interface/volume ratios. Fractures opening in response to stress would become filled with available molten material, most likely to be iron-rich metallic melt. This process could easily have an effect on regions within the protoplanet measuring in meters to kilometers or greater. Previously isolated ponds of metal would become connected by fractures through which molten metal could flow in response to buoyant forces. As conditions changed within the molten metal, sulfide and phosphide blebs would exsolve. A more detailed analysis of this situation as a two-phase flow problem could be performed using the values of interfacial energy I have estimated above.

The cooling of the protoplanet would also have served to preserve the non-equilibrium angles I observed at filled grain boundaries. Reduced temperatures would have reduced the solubility of olivine components in the metallic melt, thus inhibiting their diffusion along pathways which would produce the rounding of sharp corners and the establishment of equilibrium wetting angles. Ohtani (1983) studied the dependence upon temperature of the rounding rate of olivine in a metallic iron matrix. His model showed that at temperatures above 1270K, the solidus of iron, rounding of 1 cm diameter olivine grains could be accomplished in less than one billion years, but at lower temperatures, rounding rates would be dramatically reduced, such that rounding of the same grains would take longer than the age of the solar system.

The Brenham pallasite was referred to by Ohtani (1983) as a pallasite with well-rounded grains, according to the two-fold classification originally proposed by Wahl (1965) and further described by Buseck (1977) and Scott (1977). These authors adressed what they referred to as "the pallasite problem" concerning the question of the relationship between pallasites with rounded grains and those with angular grains. One view of this problem held that annealed, rounded grains represented a primary texture, and that angular grains were the result of a late-stage fracturing event (Buseck, 1977). The alternative explanation was that all pallasites originated from catastrophic events which mixed the fragments of an olivine mantle with a metallic melt, and that the pallasites with rounded grains were those whose protoplanets remained at high enough temperature for sufficient time to permit the rounding of formerly angular grains (Scott, 1977). My observations of the Brenham pallasite provide an intermediate case which supports the former view for its history. The interpretation of filled olivine-olivine grain boundaries as filled late-stage fractures strongly suggests that, if further fracturing had occurred, the olivine mass would have been separated into angular olivine grains.

At roughly 50% of the volume of the texture preserved in the pallasite, olivine may or may not have formed a solid framework in three dimensions. The sample of Brenham which I examined consists roughly of 50% solid silicate and 50% metallic melt. Other samples of the same meteorite contain large regions of metal in which olivine clusters are isolated from one another. However, each cluster appears to have a well-defined edge, within which the same 50-55% silicate can be found. Outside the edge, only rare olivine crystals are isolated from the pallasitic masses. A review of the literature reveals that metal contents of pallasites are always between 25 and 50%. The textures we now observe may represent some threshold abundances for olivine: at above 50% metal, any isolated olivine grains or aggregates would rise buoyantly through the molten metal too rapidly for such a texture to be preserved, and below 25%, metal would have remained in isolated ponds, unable to form a connected melt network.

A connected framework of olivine would offer an explanation for the fact that buoyant forces have not succeeded in segregating the olivine from the much denser metallic phases,

although even with a framework, buoyancy would cause compaction to occur over a long time period (Mackenzie, 1984). The presence of cracks between and within olivine also is consistent with the idea of a solid framework responding to shock stress. A solid framework would much more effectively transmit shock stresses to olivine grains than would a surrounding metallic matrix.

Conclusions

The data obtained in this study are relevant to the assessment of the role of interfacial energy in the development of pallasites. Wetting angles between olivine and metallic iron-rich melt phases are shown to be close to 90° and therefore too high to permit formation of an interconnected melt network at low to moderate melt fractions. Therefore if the starting material resembled chondrites, it is likely that processes other than simple melting occurred in the history of the pallasite. Extensive fracturing could well have served to provide pathways for the connection and flow of otherwise isolated ponds of iron-rich phases, once they had been concentrated by other processes. Evidence of a late-stage fracturing event is preserved in the metal or troilite-filled cracks within and between olivine grains.

Interfacial angle measurements can be used in conjunction with a previously obtained estimate for interfacial energy on high-angle olivine/olivine grain boundaries to estimate the magnitude of interfacial energy between pairs of phases present in the pallasite. These estimates are presented in Table 3. Such estimates can provide the starting point for further studies in the problems of two-phase flow in planetary segregation processes.

References

Buseck, P. R., 1977. Pallasites - Mineralogy, petrology and geochemistry. Geochimica et Cosmochimica Acta 41: 711-740.

Cooper, R. F., Kohlstedt, D. L., 1982. Interfacial Energies in the Olivine-Basalt System. *in* Akimoto, S., Manghnani, M. H., editors, High-Pressure Research in Geophysics. Advances in Earth and Planetary Sciences Research. Center for Academic Publications, Tokyo, Japan, p. 217-228.

Gaetani, G.A.; Grove, T.L., 1996. The effect of variable f_{O2}/f_{S2} conditions on wetting angles in olivine/sulfide melt aggregates: mobility of sulfide melt in the Earth;s upper mantle. Lunar and Planetary Sciences Conference Abstracts XXVII:389-390.

Jurewicz, S. R., Jurewicz, A. J., 1986. Distribution of Apparent Angles on Random Sections With Emphasis on Dihedral Angle Measurements. Journal of Geophysical Research, 91: 9277-9282.

McKenzie, D. P., 1984. The generation and compaction of partially molten rock. Journal of Petrology 25: 713-765.

Ohtani, E., 1983. Formation of olivine textures in pallasites and thermal history of pallasites in tehir parent body. Physics of the Earth and Planetary Interiors 32:182-192.

Scott, E. R. D., 1977. Formation of olivine-metal textures in pallasite meteorites Geochimica et Cosmochimica Acta 41: 693-710.

Stevenson, D. J., 1986. On the role of surface tension in the migration of melts and fluids. Geophysical Research Letters 13: 1149-1152.

Taylor, G. J., 1992. Core Formation in Asteroids. Journal of Geophysical Research 97: 14,717-14,726.

Waff, H. S., Bulau, J. R., 1979. Equilibrium fluid distribution in an ultramafic partial melt under hydrostatic stress conditions.. Journal of Geophysical Research 84: 6109-6114.

TABLE 1

mineral	modal abundance	density (g/cm^3)	crystal habit
olivine (Fe,Mg)$_2$SiO$_4$	49%	3.3	rounded, equant grains, single and in small clusters
metallic iron-nickel Fe,Ni	43%	7.9	swathing kamacite; taenite with Widmanstatten structure
troilite FeS	5%	4.8	rounded blobs; interstitial to olivine
schreibersite (Fe,Ni)$_3$P	2%	7.3	irregular euhedral or skeletal; rounded
chromite FeCr$_2$O$_4$	1%	5.1	subhedral to anhedral enclosing olivine
limonite FeO·OH·nH$_2$O·	not counted separately	2.7 to 4.3	rims around olivine; anhedral
phosphates (Fe,Ni)$_n$PO$_4$	trace identified by others	varies	microscopic inclusions

TABLE 2

angle type	population	angle	comments
Group A:		θ	
OOM	25 clean	94°	single angle
OOS	11 wetted	90°	single angle + 5°
OOT	34 wetted	86°	single angle +11°
Group B:		ψ	
OMS	64 clean	55°	single angle at central peak
OMT	75 clean	65°	mean of range of angles
OST	76 clean	60°	single angle
Group C:		α	
MST - A	13 clean	174°	adjusted mean
MST - B	13 clean	140°	adjusted mean
MST - C	13 clean	46°	single angle

TABLE 3

interface type	γ (mJ/m^2)	equation used	values used in calculation
OO	900		(Cooper&Kohlstedt, 1982)
OM	660	1	θ_{OOM}, γ_{OO}
OS	636	1	θ_{OOS}, γ_{OO}
OT	615	1	θ_{OOT}, γ_{OO}
MS	41	2	ψ_{OMS}, γ_{OM}, γ_{OS}
MT	105	2	ψ_{OMT}, γ_{OM}, γ_{OT}
ST	42	2	ψ_{OST}, γ_{OS}, γ_{OT}
MS	28	3	α_{MST}, γ_{OM}, γ_{OS}
MT	97	3	α_{MST}, γ_{OM}, γ_{OT}
ST	76	3	α_{MST}, γ_{OS}, γ_{OT}

Figure 1. Brenham Pallasite: View of Sample 425b.
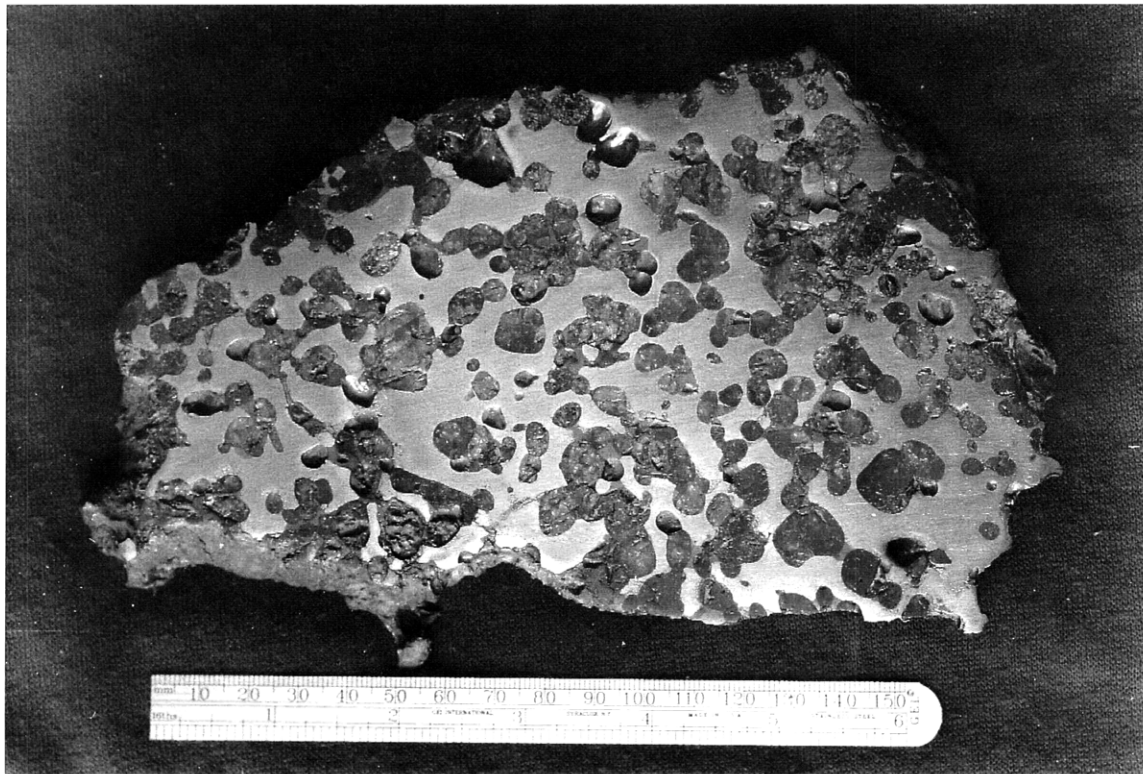
Figure 2. Brenham Pallasite: Detail showing typical texture. *Olivine*: medium dark grey, fractured, glassy grains; *metallic iron-nickel*: highly reflective matrix; *troilite*: medium grey metallic blobs; *schreibersite*: highly relective, irregularly shaped,fractured grains. Field of view: 2 cm.
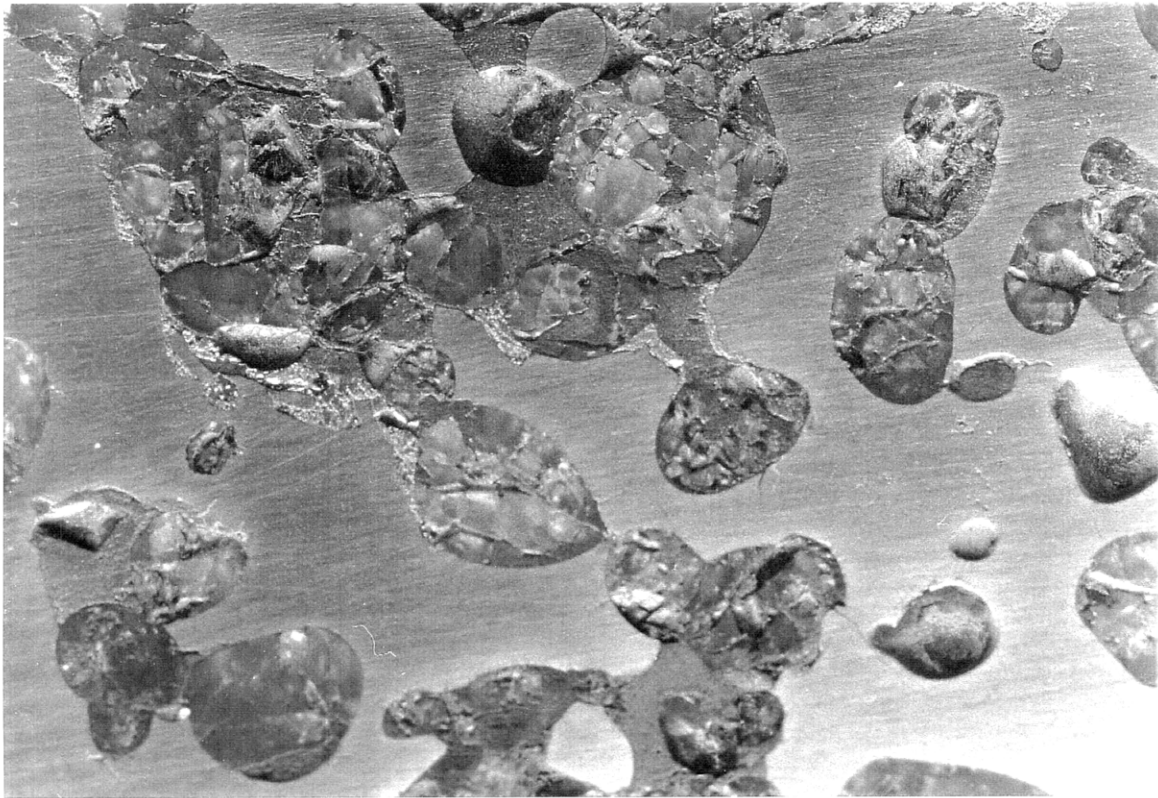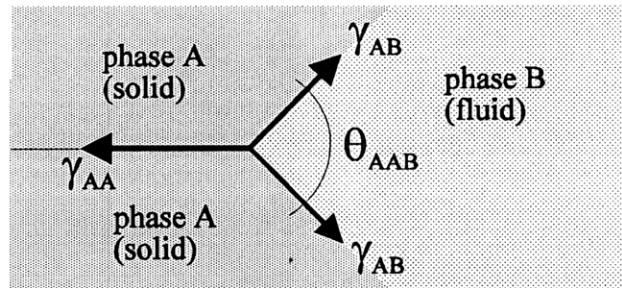
a. Wetting angle θ
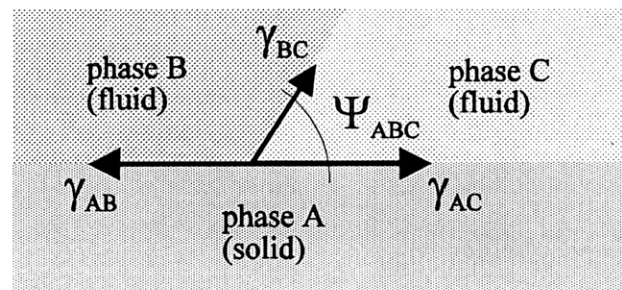
b. Interfacial angle Ψ
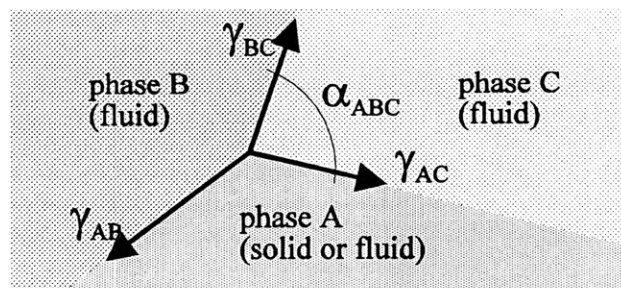
c. Interfacial angle α

figure 3. Types of interfacial angle.

232
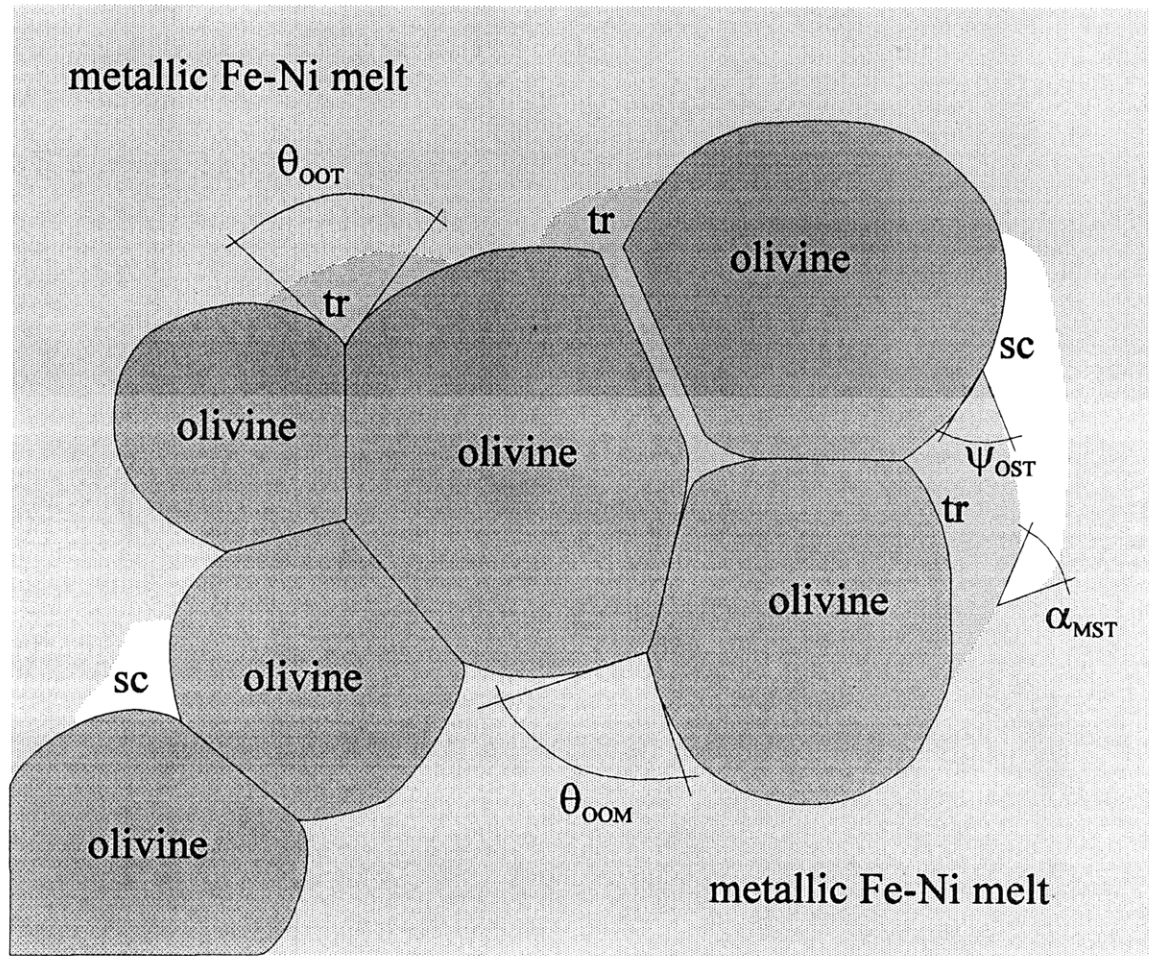
figure 4. Typical locations of interfacial angles.

Figure 5. Angle distribution plots for Group A angles

a) olivine/olivine/metal clean
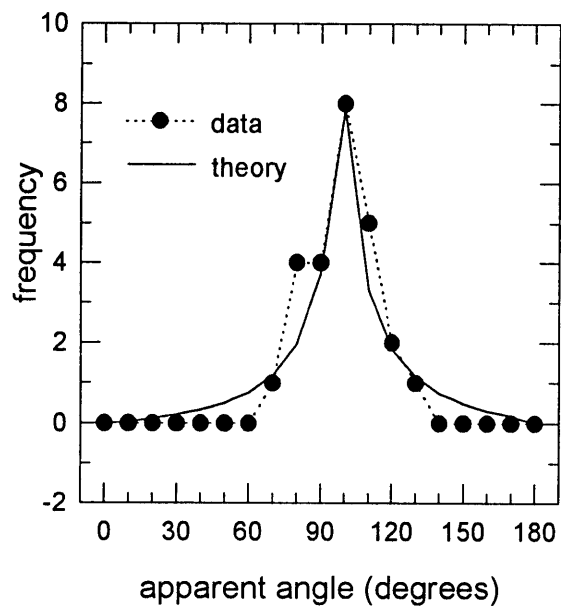
b) olivine/olivine/metal wet
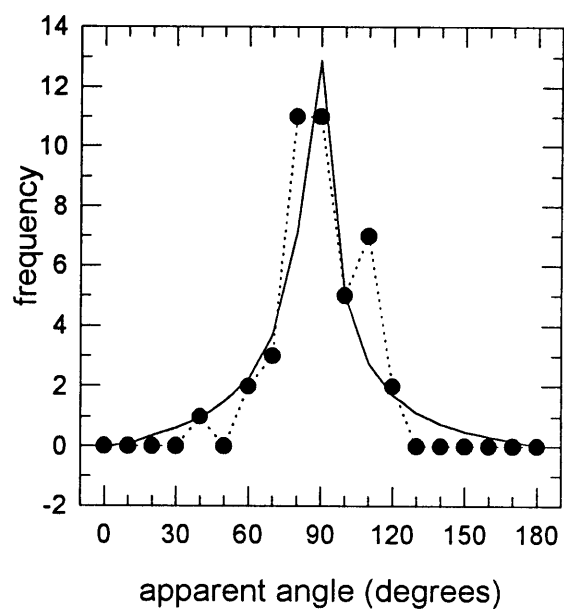
c) olivine/olivine/schreibersite
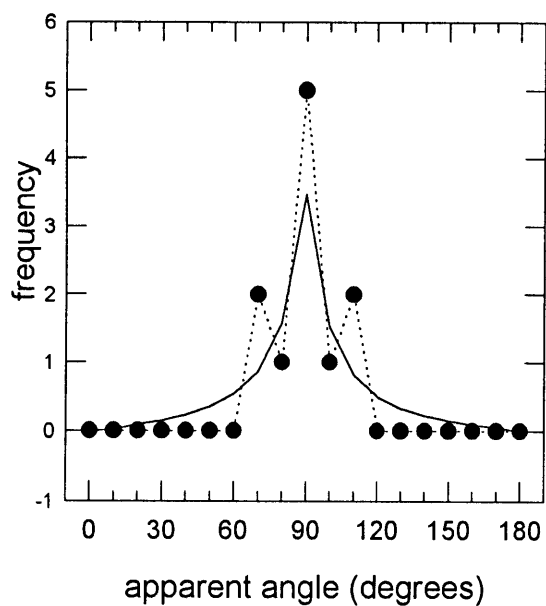
d) olivine/olivine/troilite
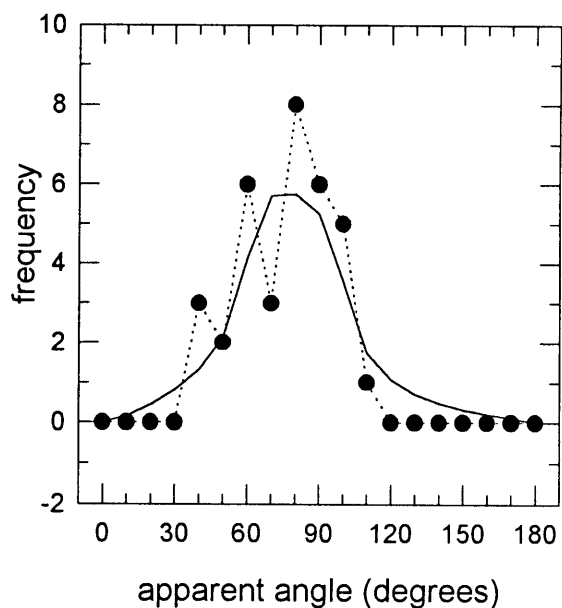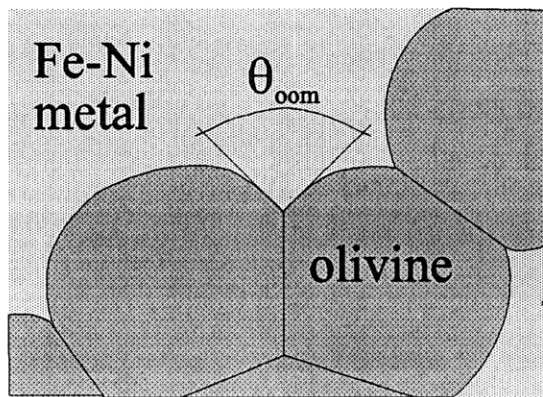
a) Annealed texture.
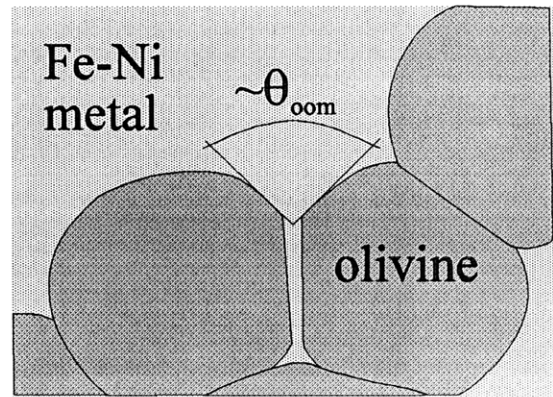
b) Crack opening and filling with metal.
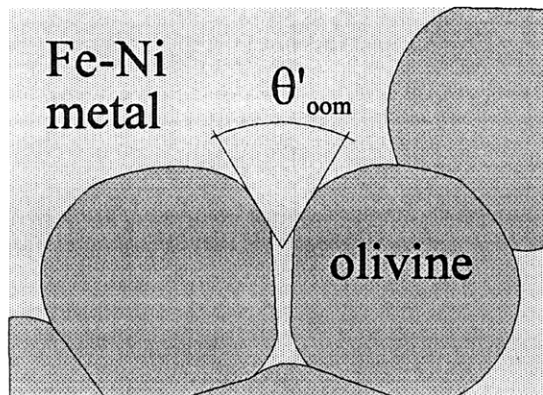
c) Rounding begins.
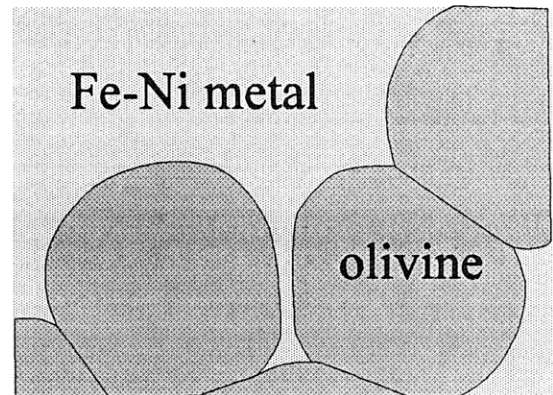
d) Rounded grains.

figure 6. Rounding of a wetting angle at filled grain boundary.

Figure 7. Angle distribution plots for Group B and C angles

a) olivine/metal/schreibersite

b) olivine/metal/troilite

c) olivine/schreibersite/troilite

d) metal/schreibersite/troilite
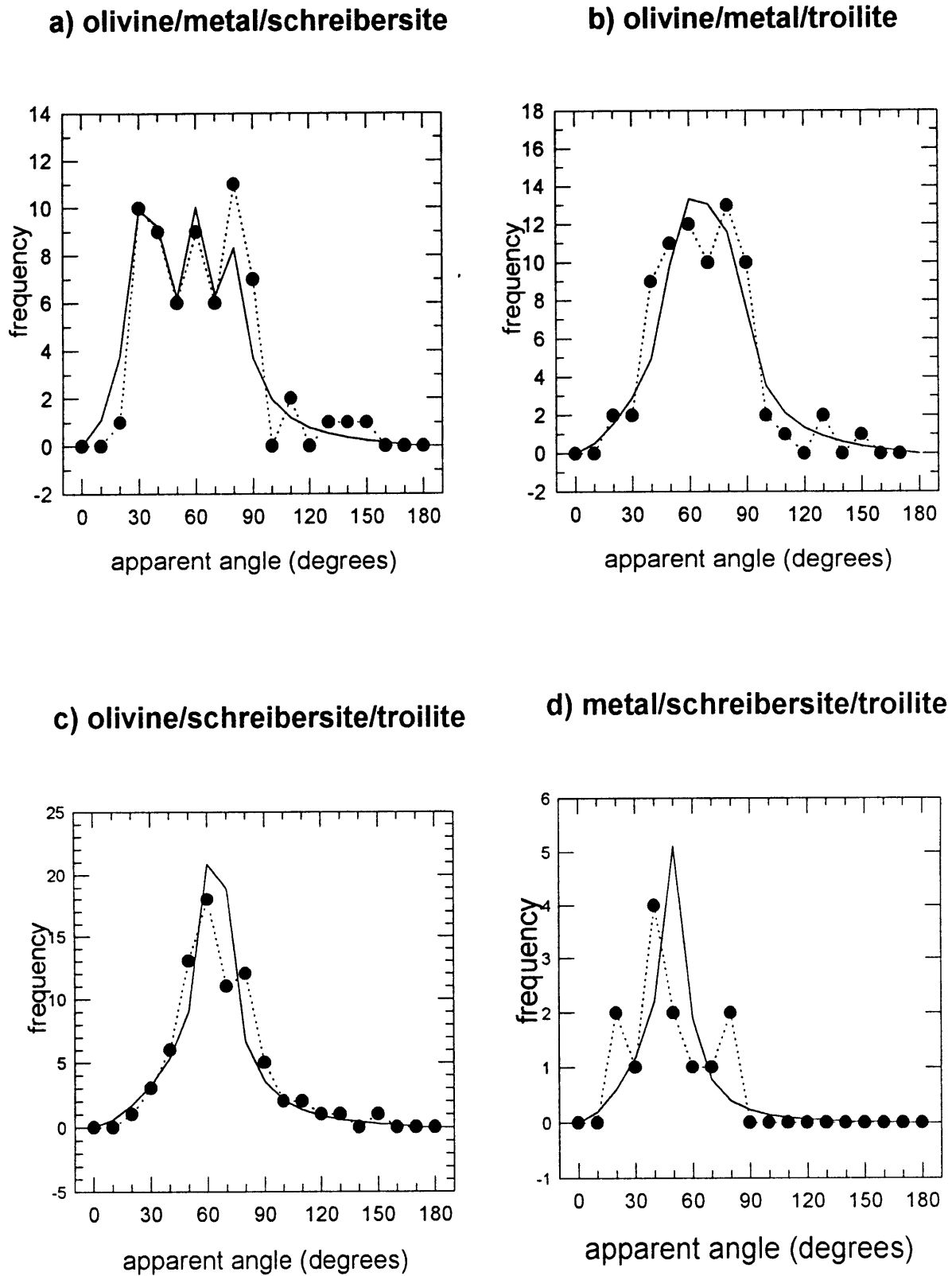
scratch 1-1 normal load
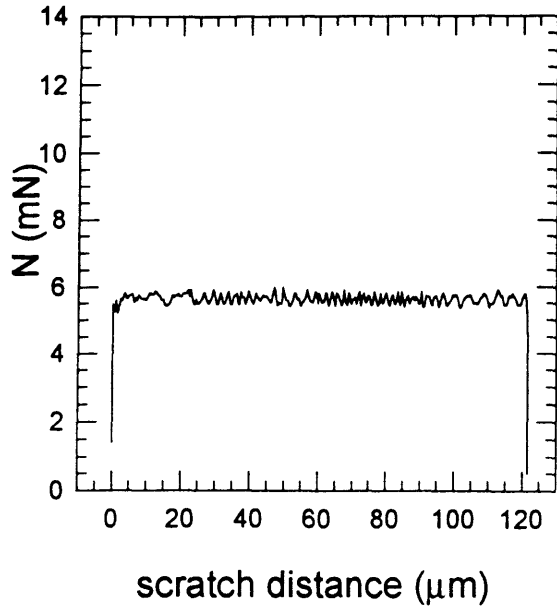
scratch 1-1 tangential load
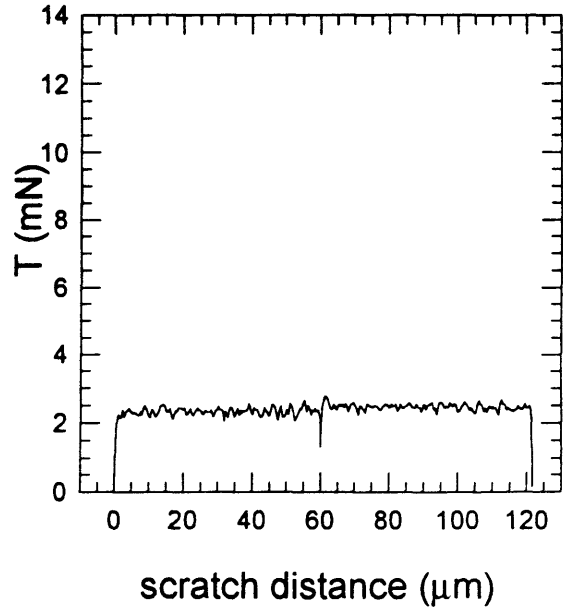
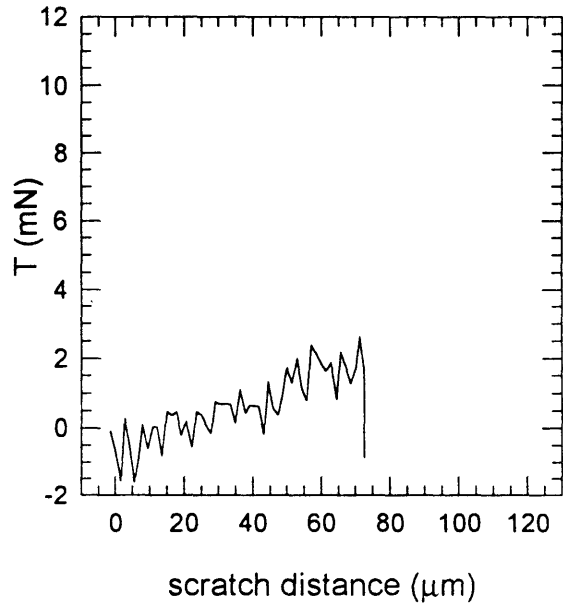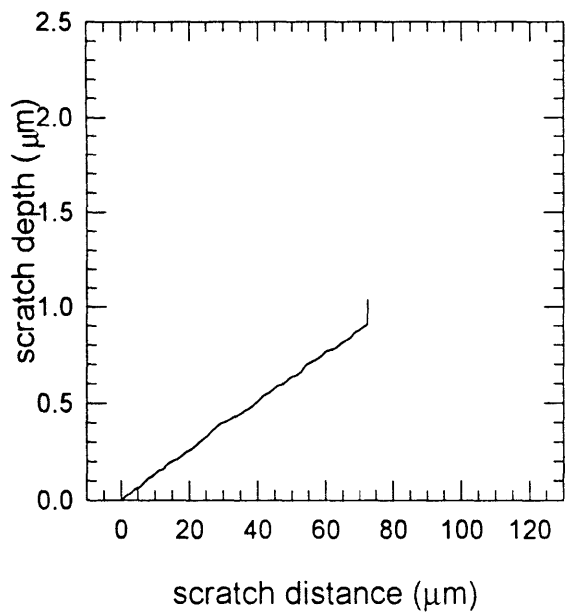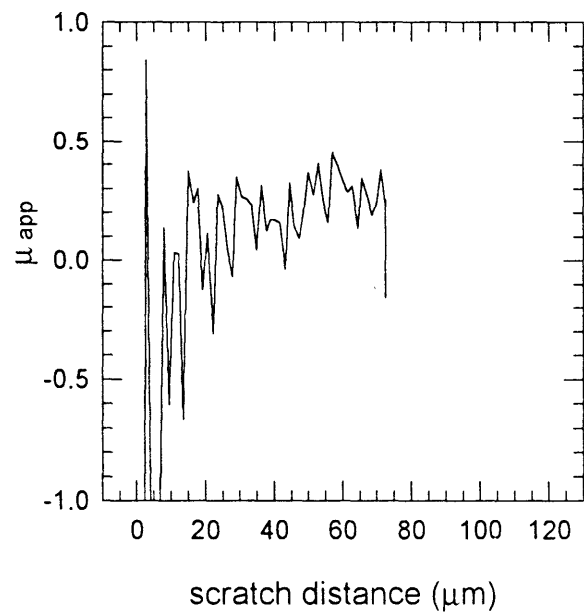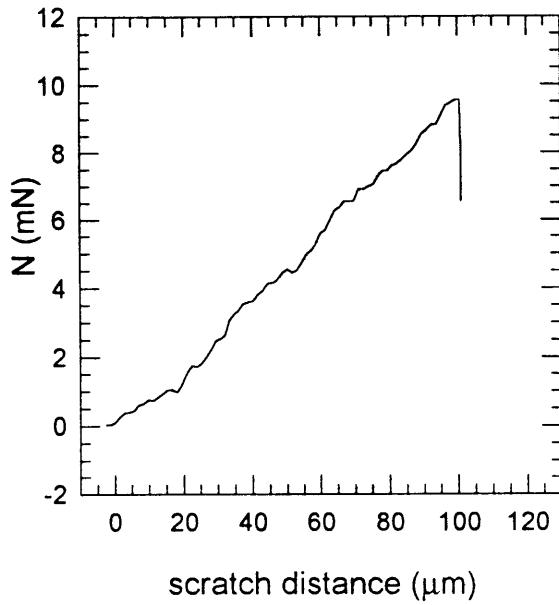## scratch 1-1 scratch depth
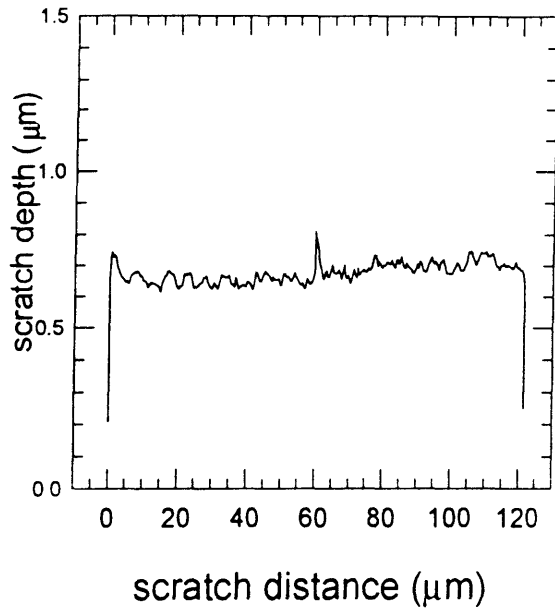
scratch 1-1 friction
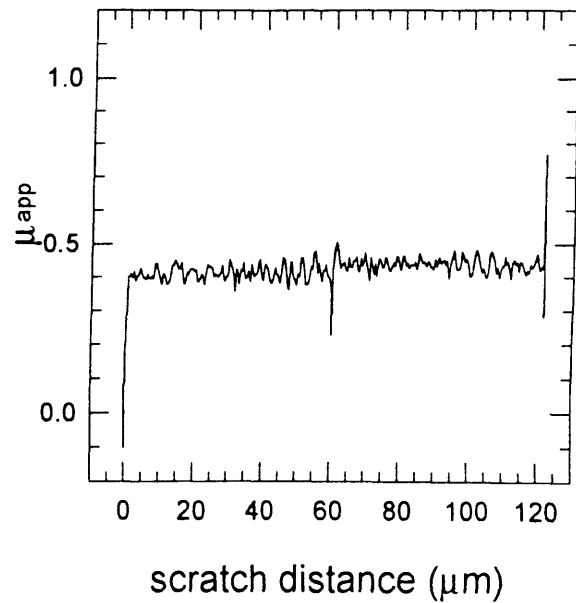
scratch 1-2 normal load
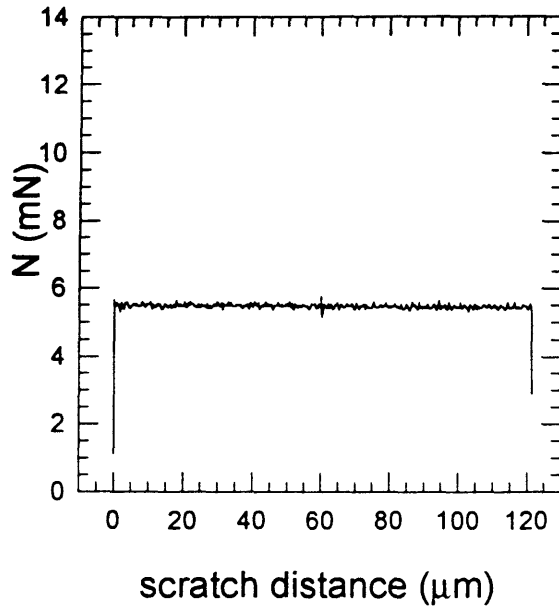
scratch 1-2 tangential load
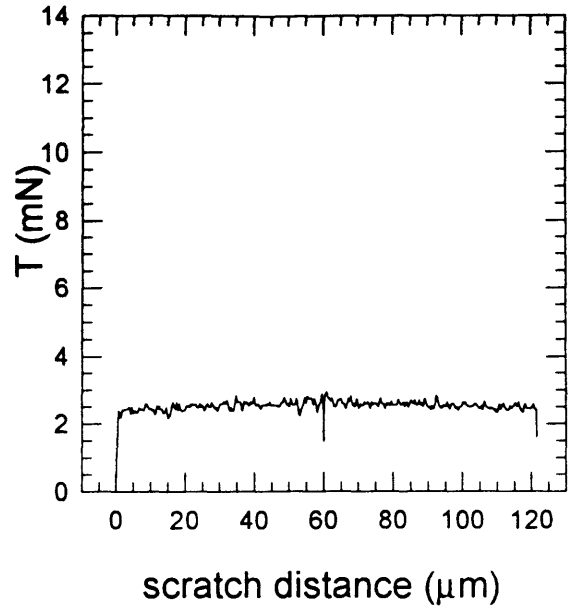
scratch 1-2 scratch depth
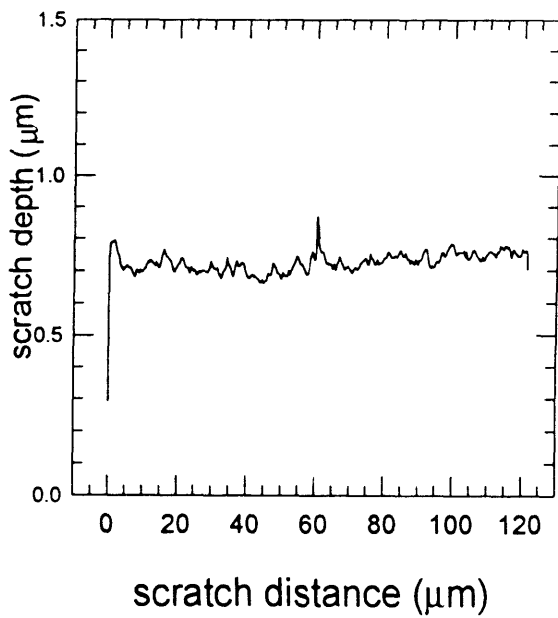
scratch 1-2 friction
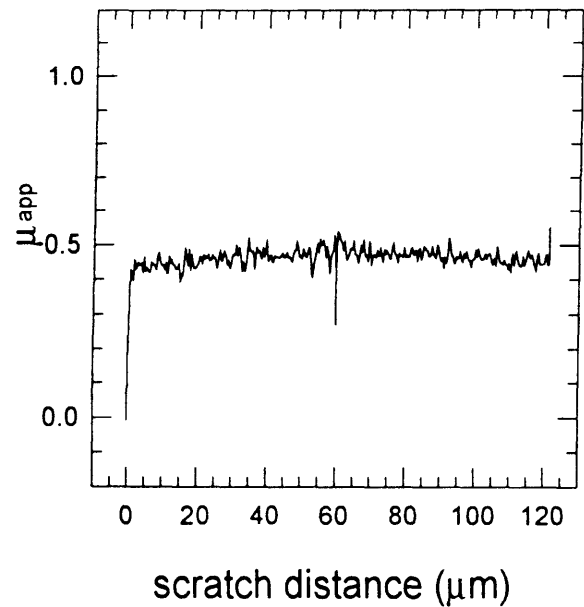
scratch 1-3 normal load
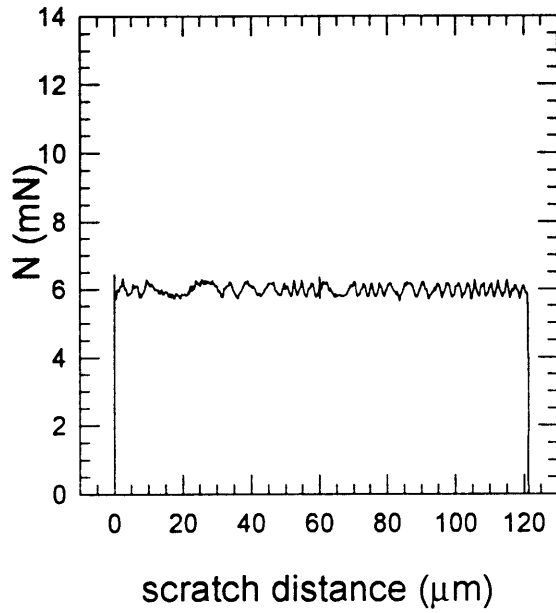
scratch 1-3 tangential load
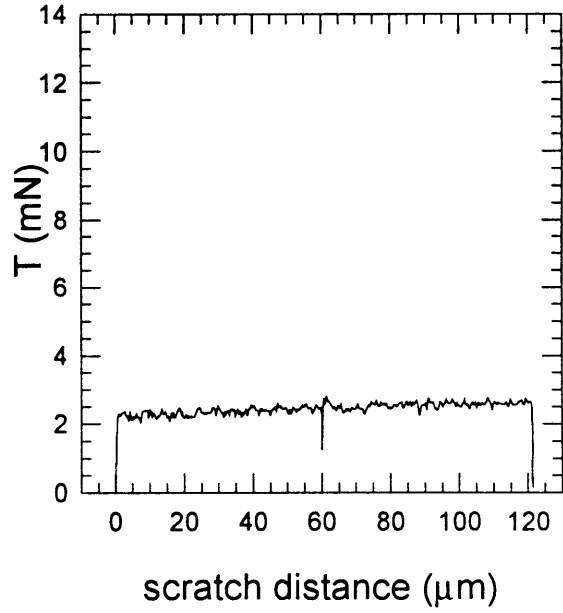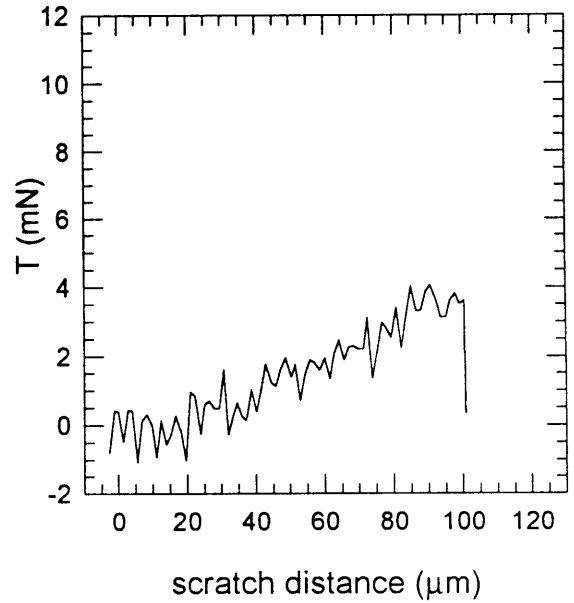

scratch 1-3 scratch depth
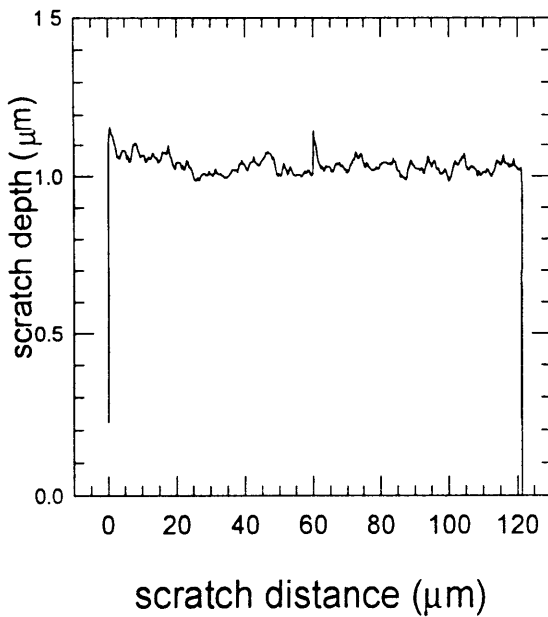
scratch 1-3 friction
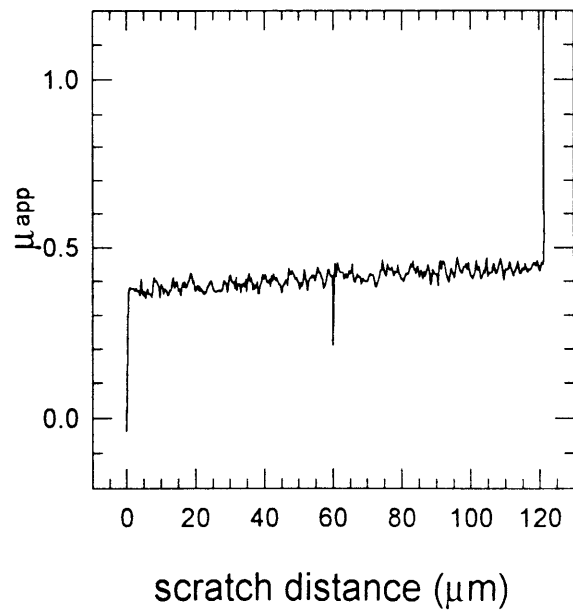
scratch 1-4 normal load
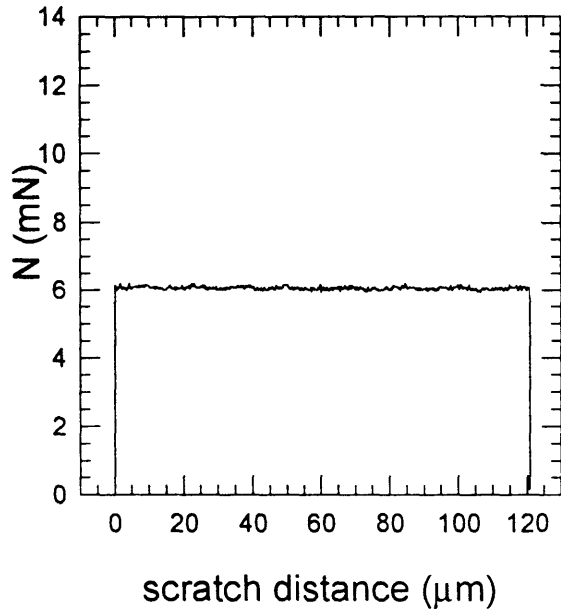
scratch 1-4 tangential load
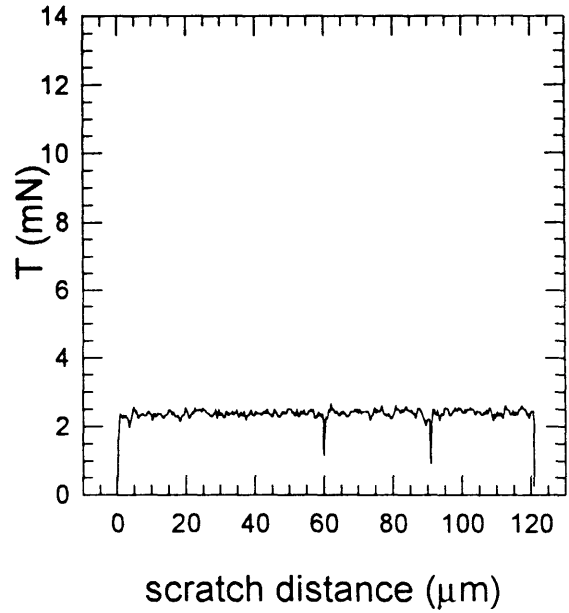
scratch 1-4 scratch depth
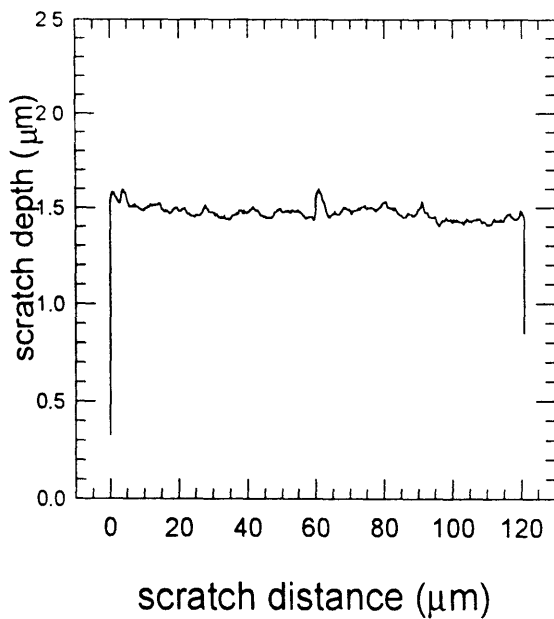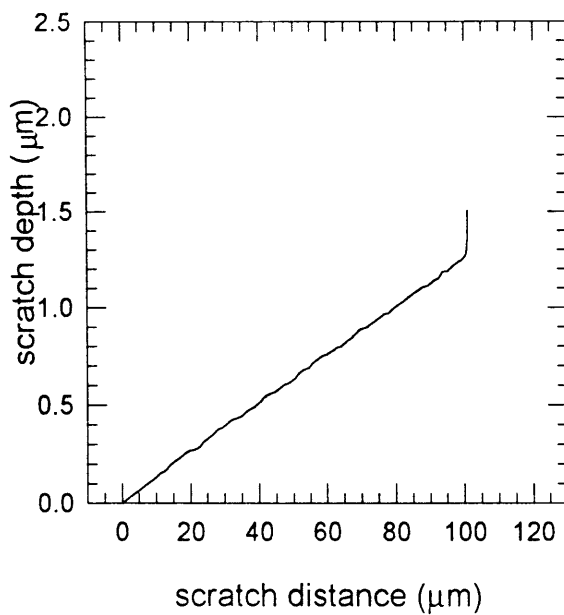
scratch 1-4 friction
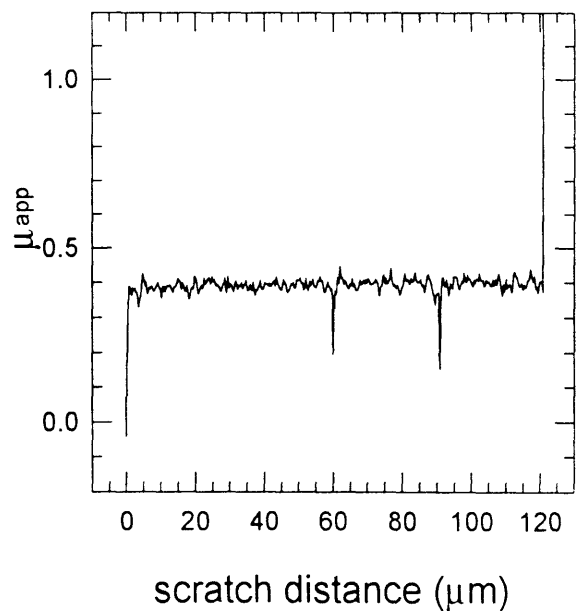
scratch 1-5 normal load
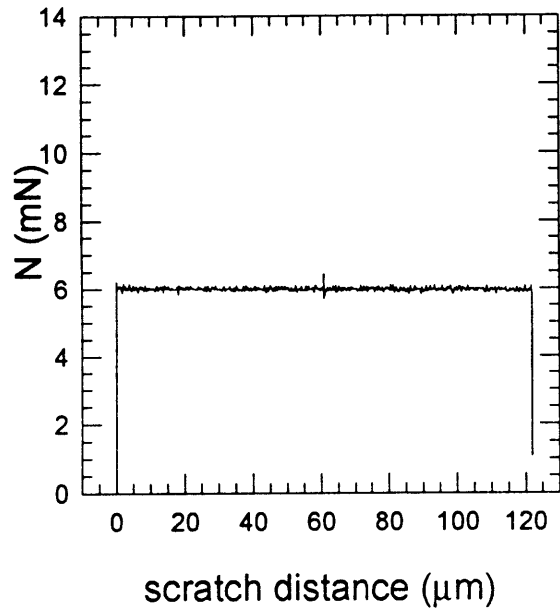
scratch 1-5 tangential load
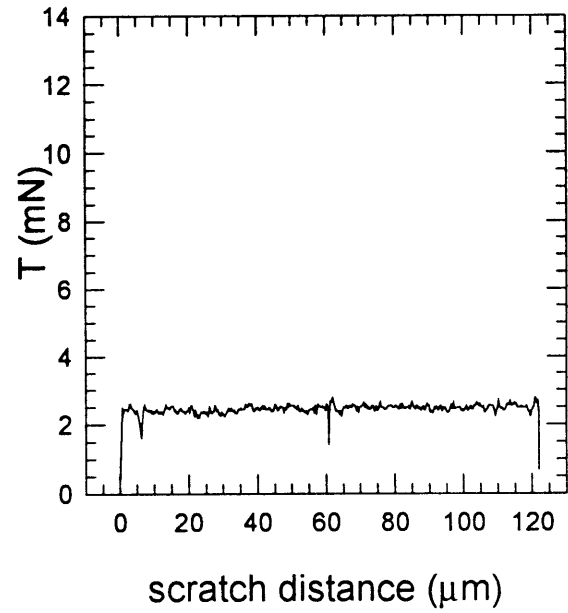
scratch 1-5 scratch depth
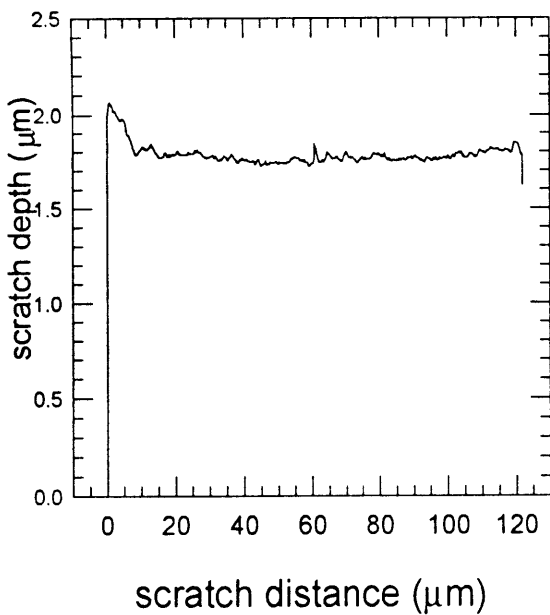
scratch 1-5 friction
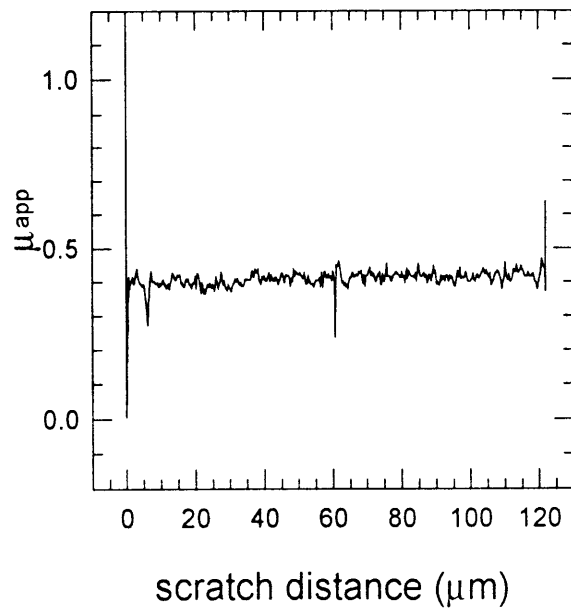
scratch 1-6 normal load
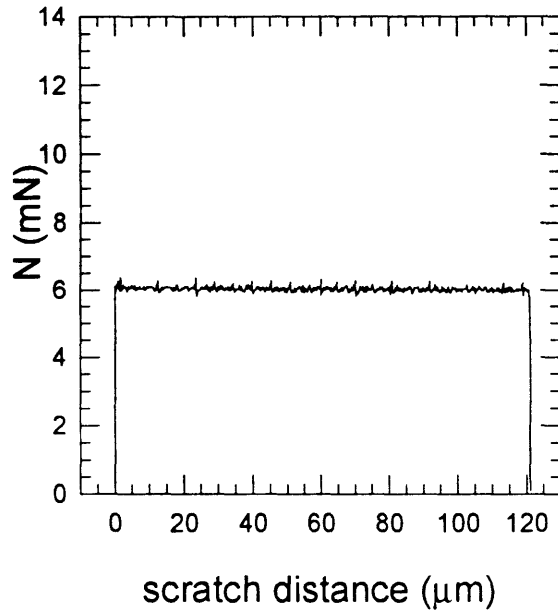
scratch 1-6 tangential load

scratch distance (μm)

scratch distance (μm)
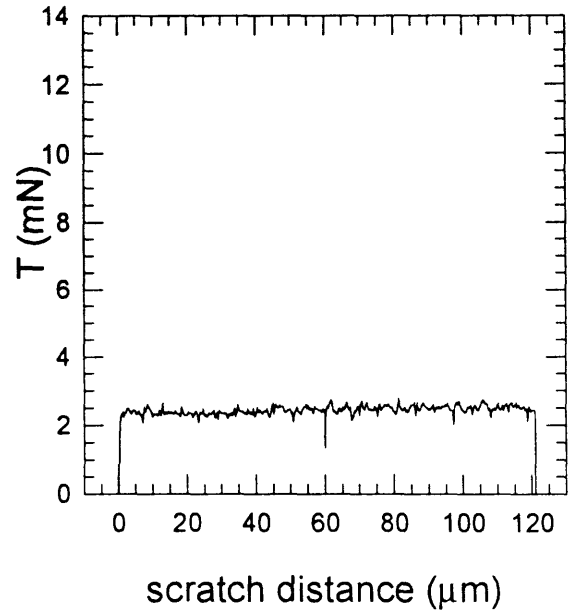
scratch 1-6 scratch depth
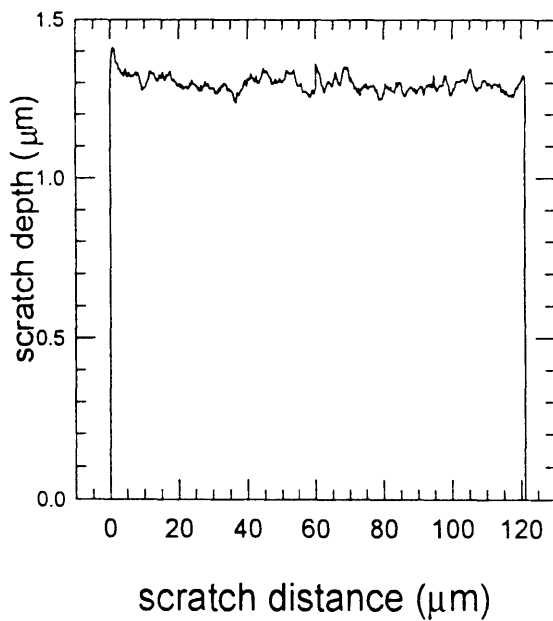
scratch 1-6 friction

scratch distance (μm)

scratch distance (μm)
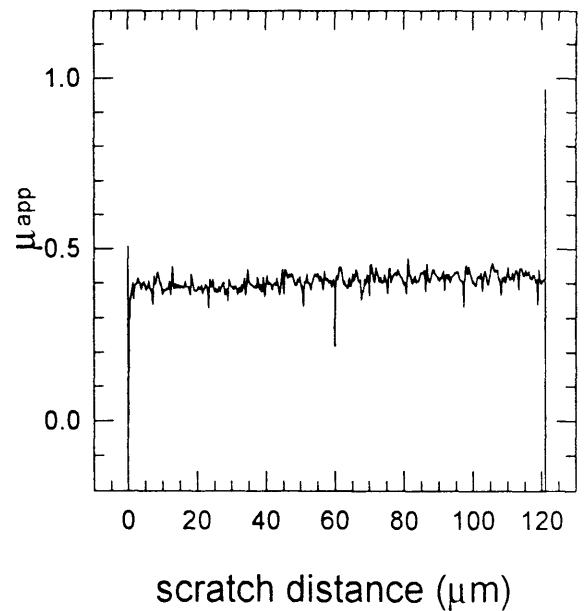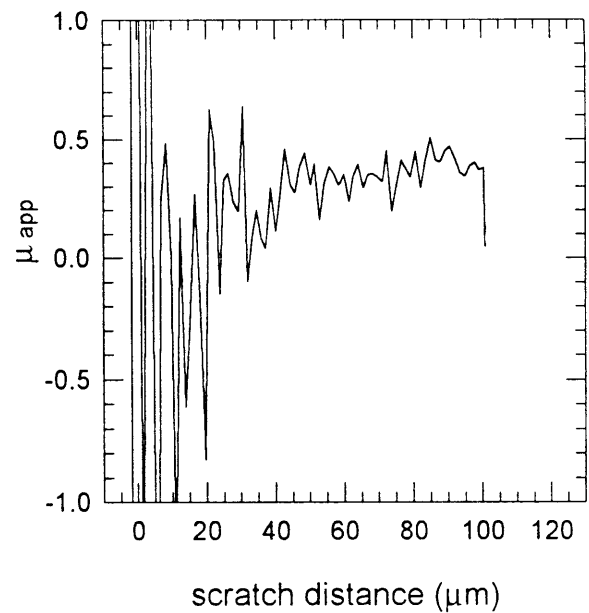
scratch 1-7 normal load
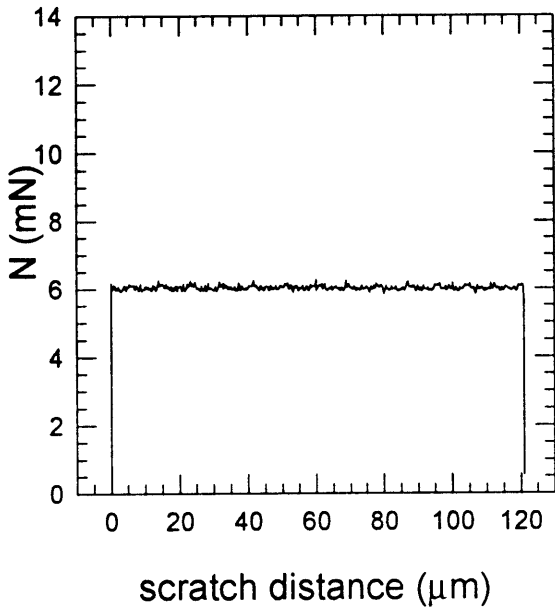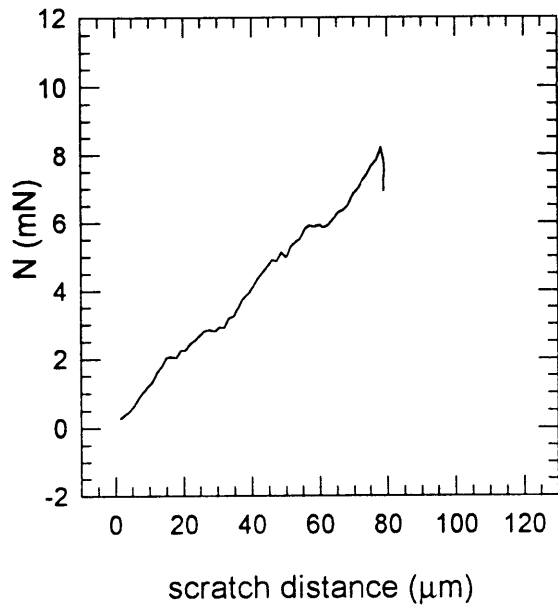

scratch 1-7 tangential load
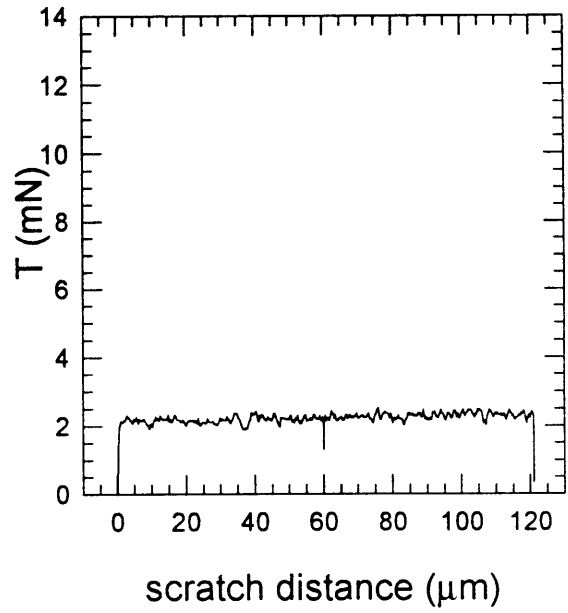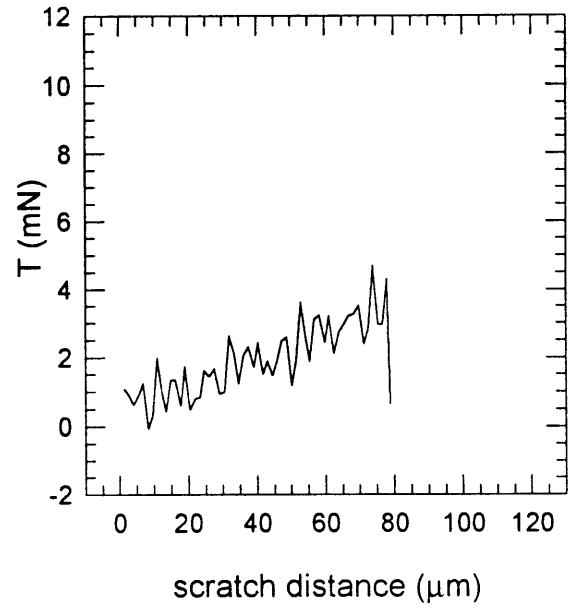

scratch 1-7 scratch depth
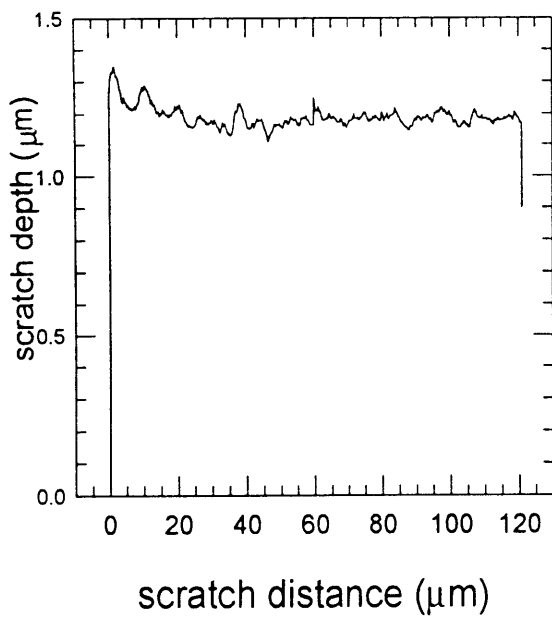
scratch 1-7 friction
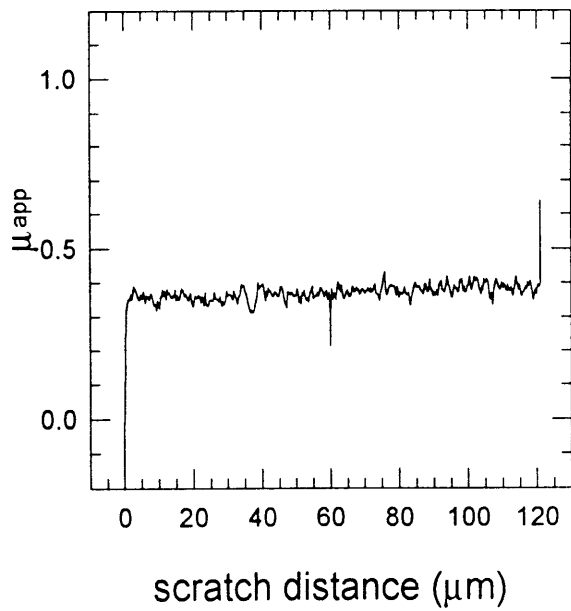
scratch 2-1 normal load
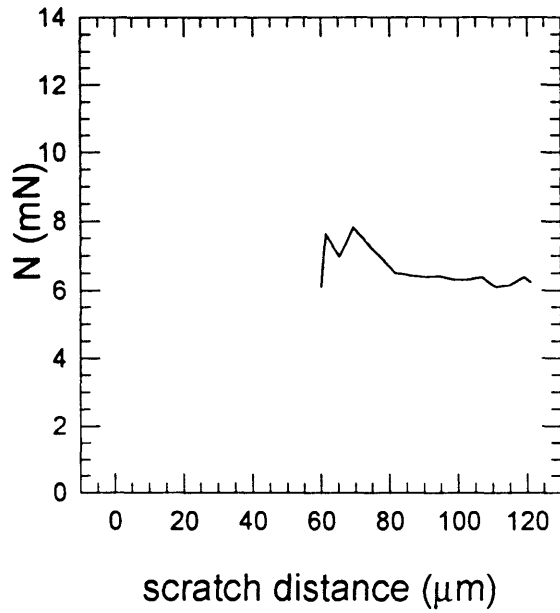
scratch 2-1 tangential load
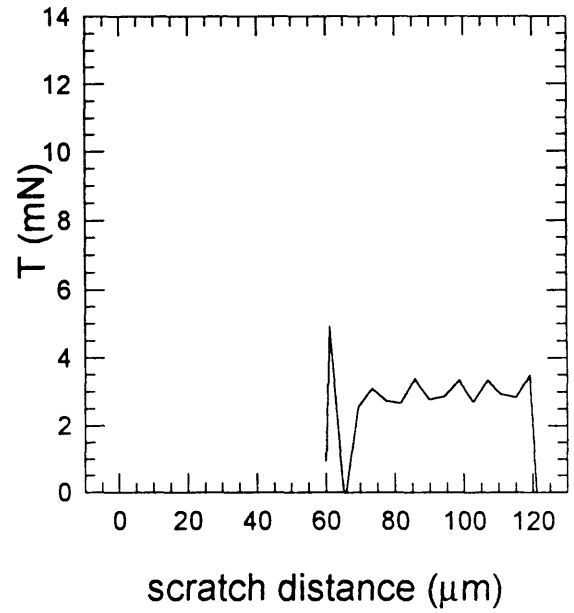
scratch 2-1 scratch depth
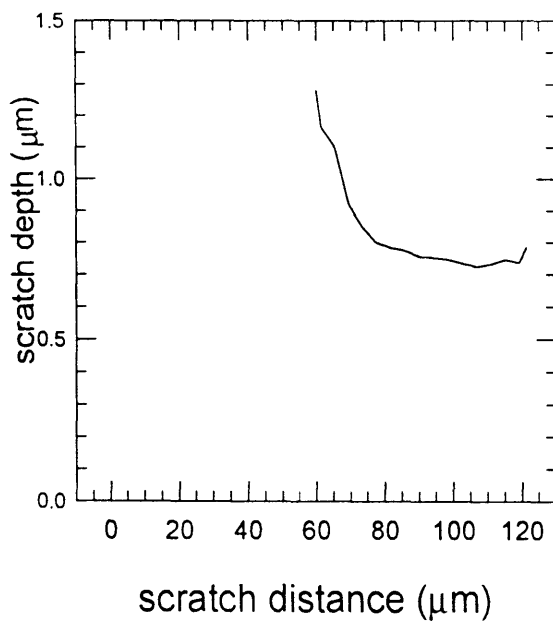
scratch 2-1 friction
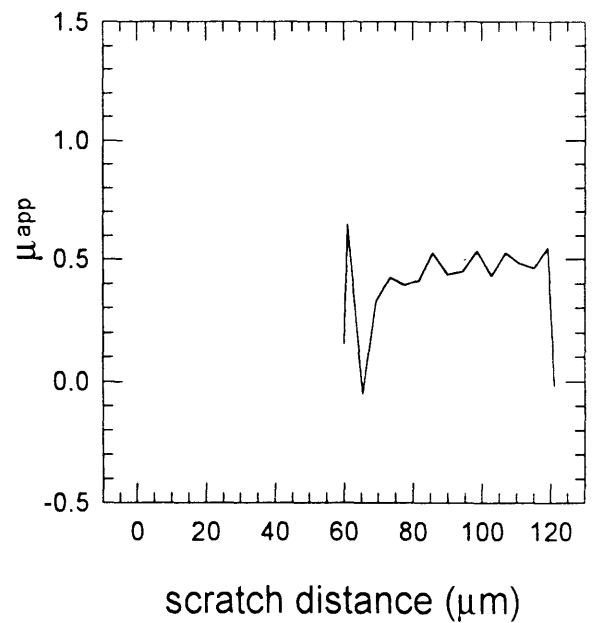
scratch 2-2 normal load
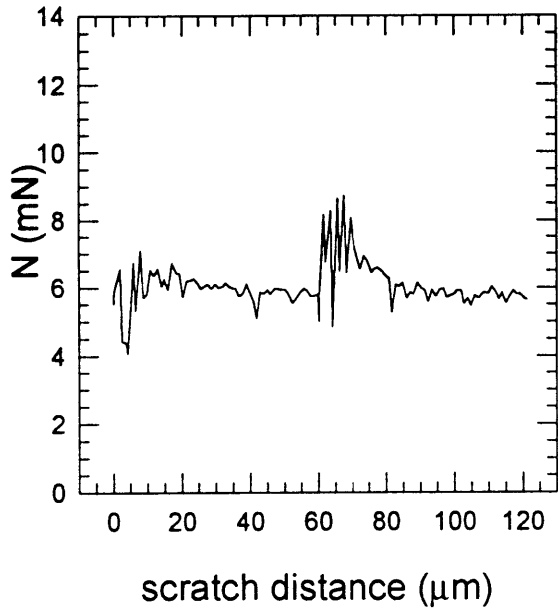
scratch 2-2 tangential load
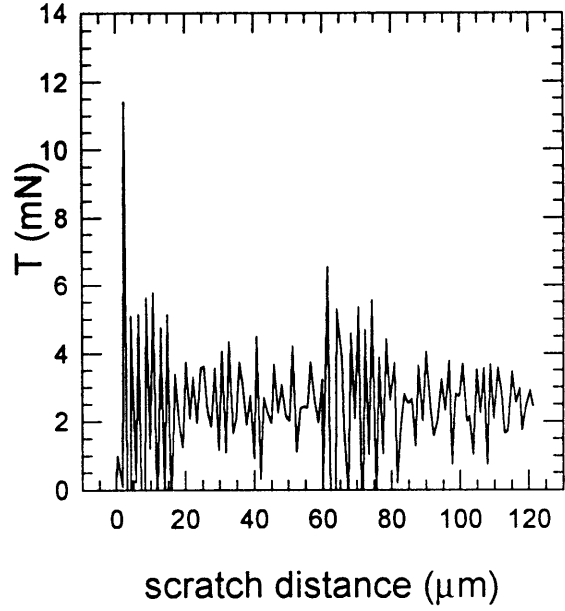
scratch 2-2 scratch depth
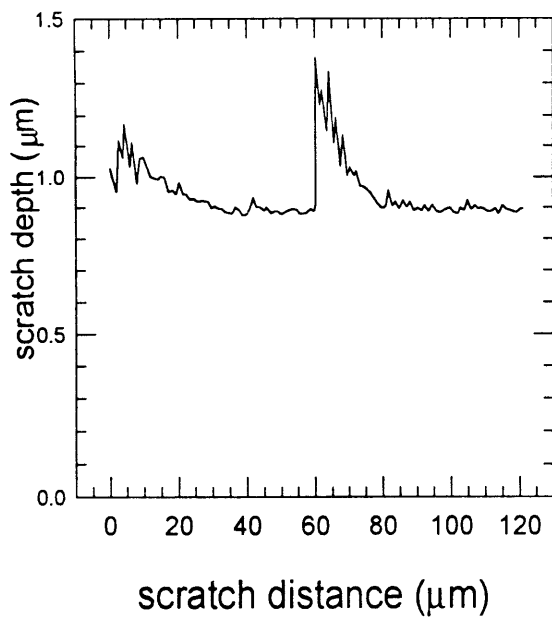
scratch 2-2 friction
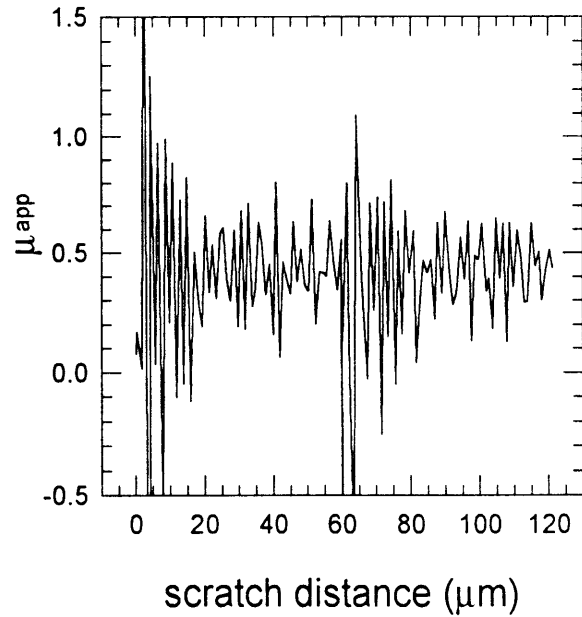
scratch 2-3 normal load
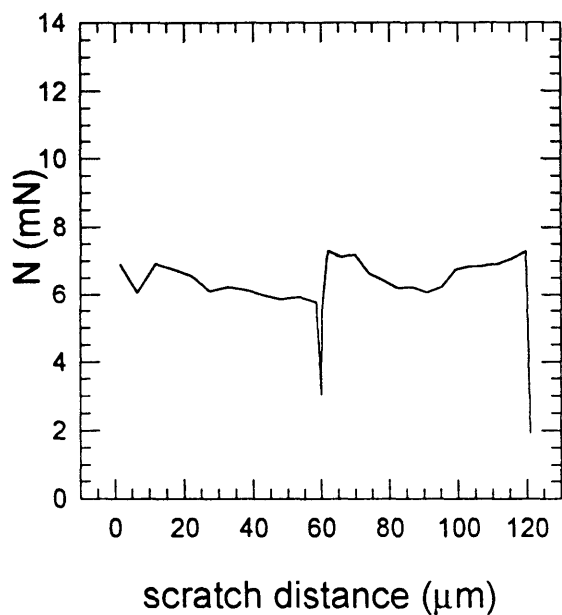
scratch 2-3 tangential load
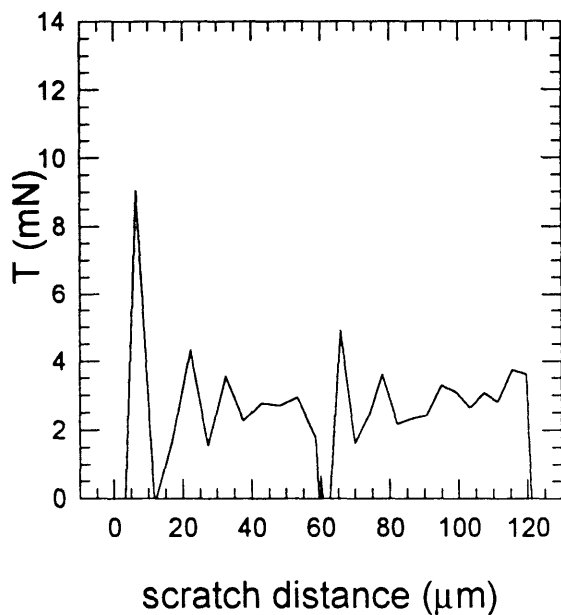
scratch 2-3 scratch depth
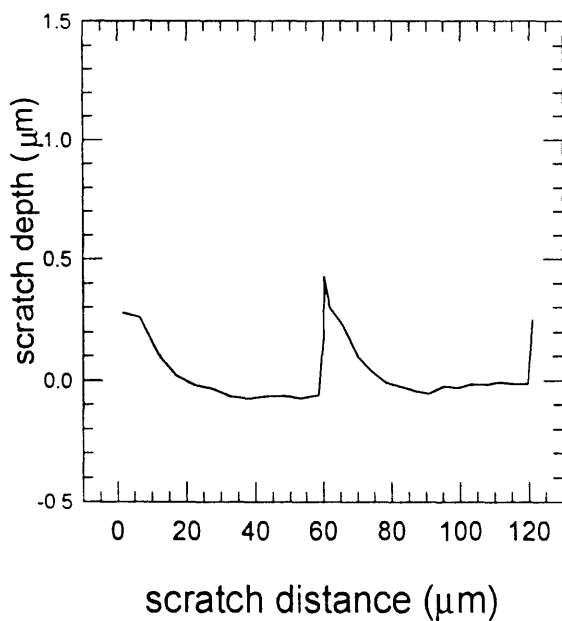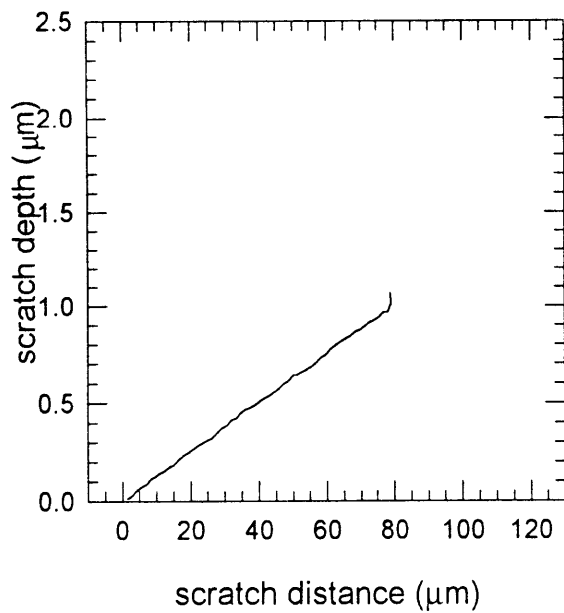

scratch 2-3 friction
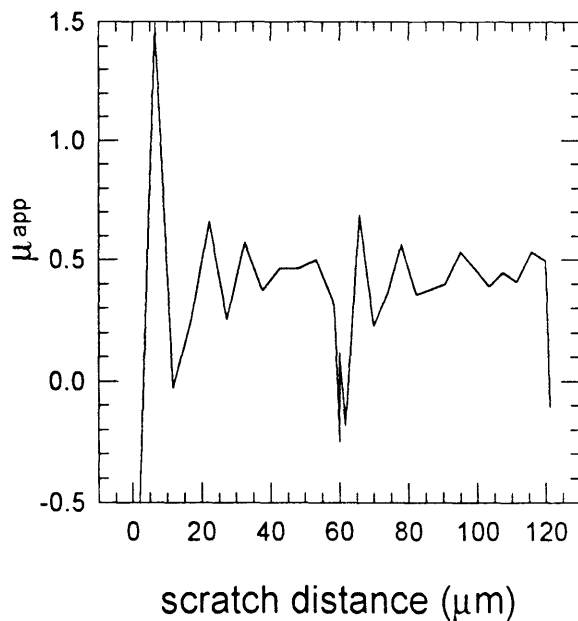
scratch 2-4 normal load
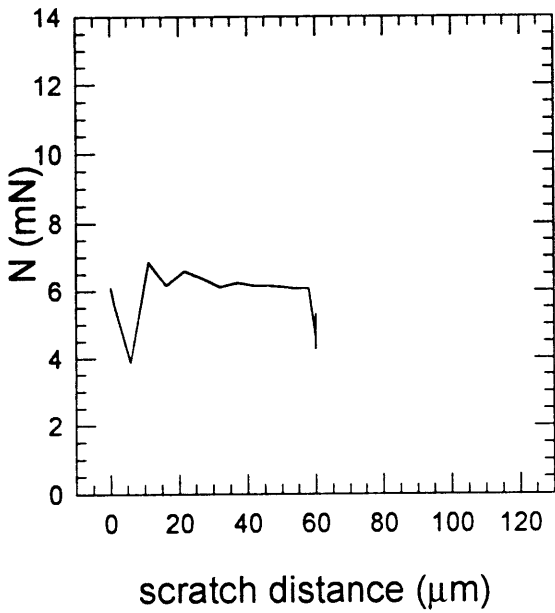
scratch 2-4 tangential load
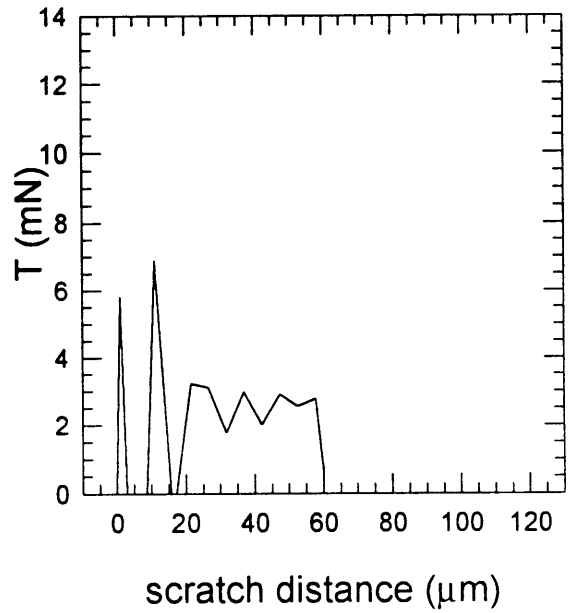
scratch 2-4 scratch depth
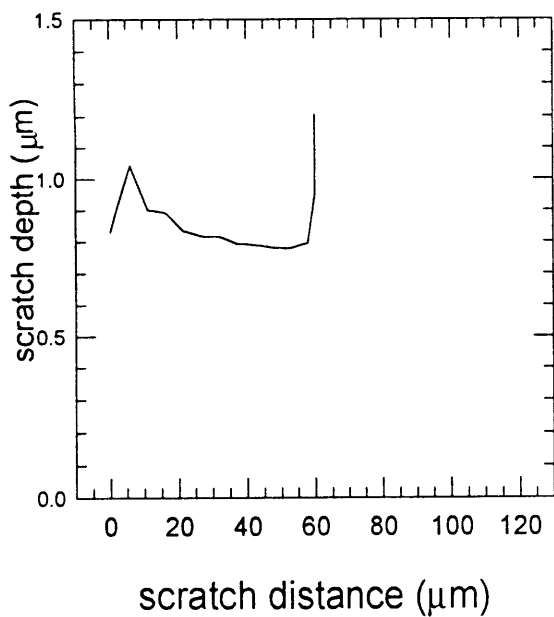
scratch 2-4 friction
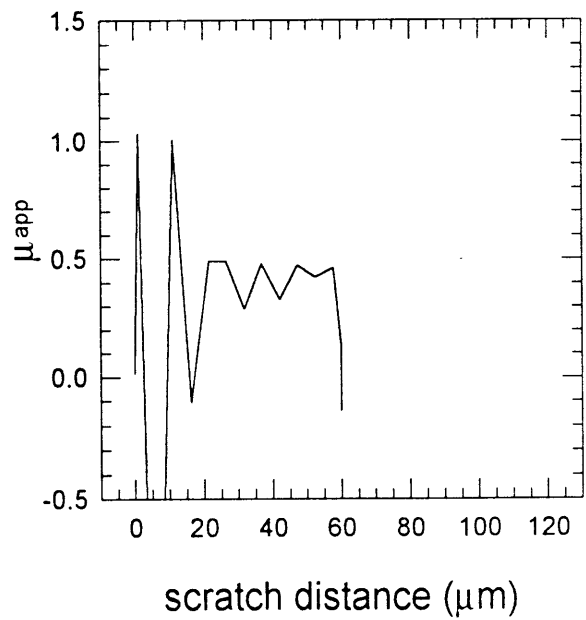
scratch 2-5 normal load
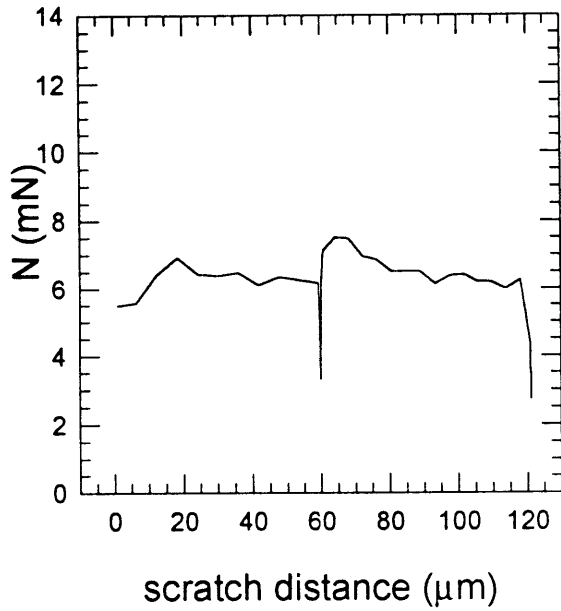
scratch 2-5 tangential load
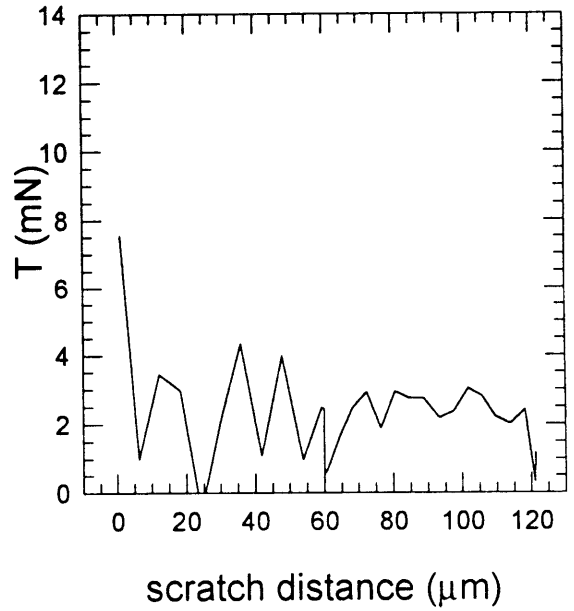
scratch 2-5 scratch depth
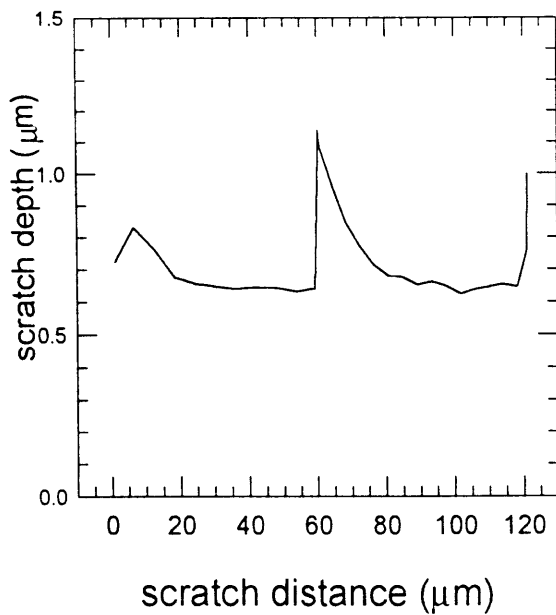
scratch 2-5 friction
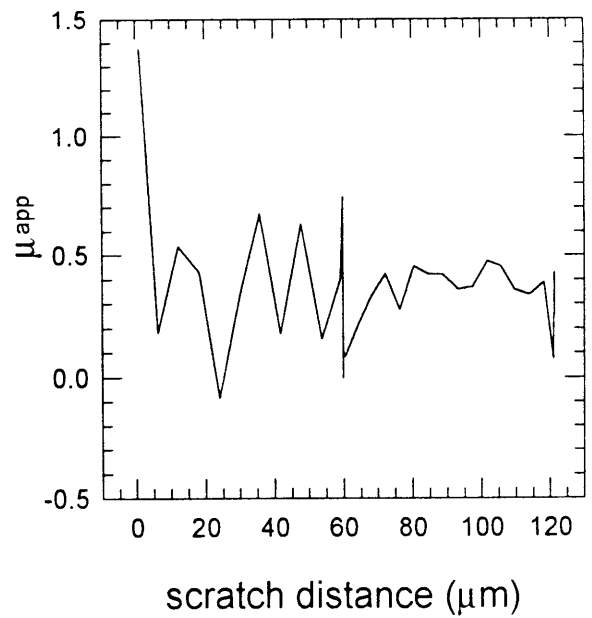
scratch 2-6 normal load
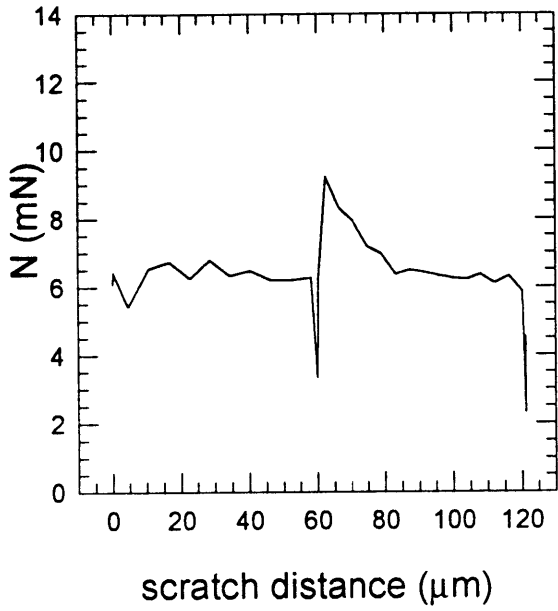
scratch 2-6 tangential load
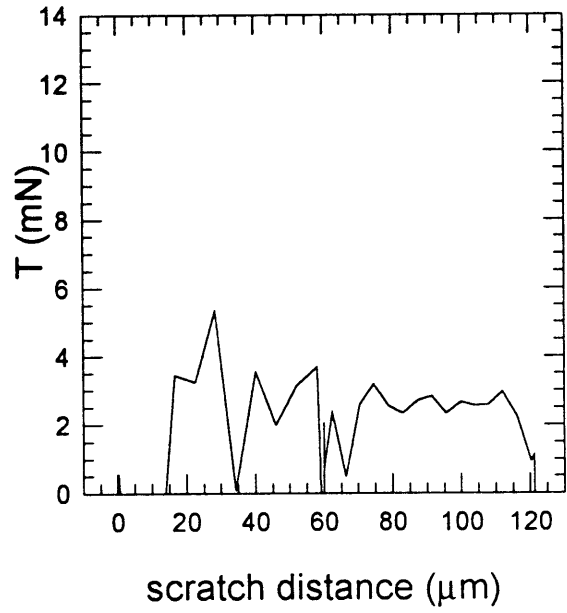
scratch 2-6 scratch depth
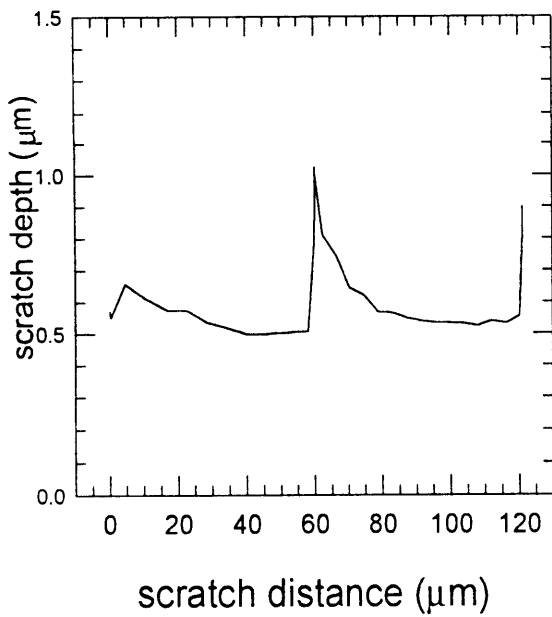
scratch 2-6 friction
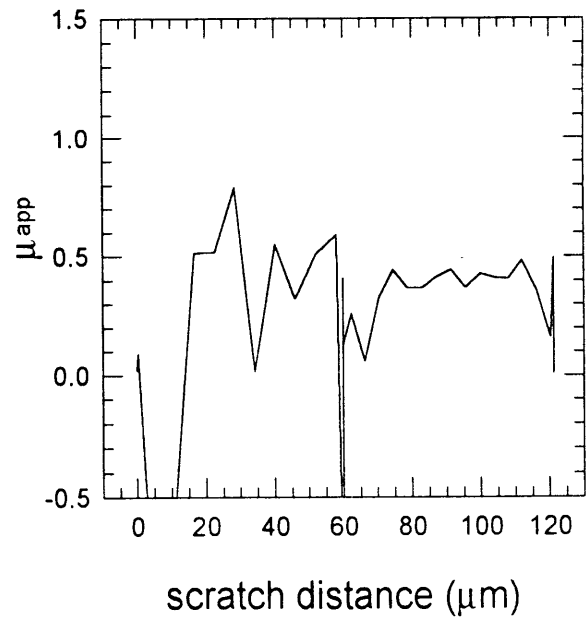
scratch 2-7 normal load
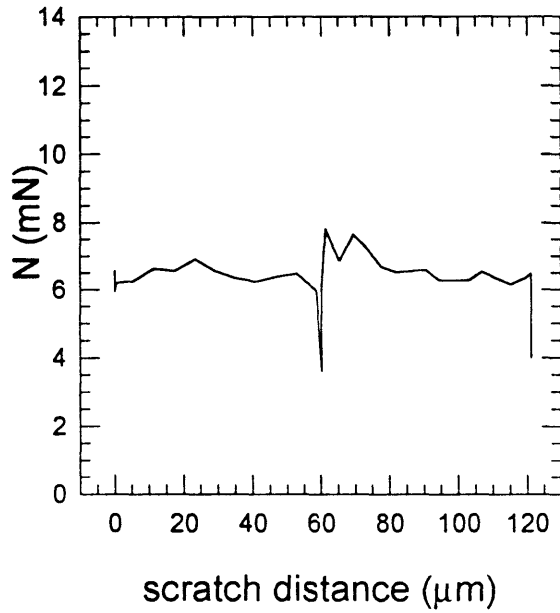
scratch 2-7 tangential load
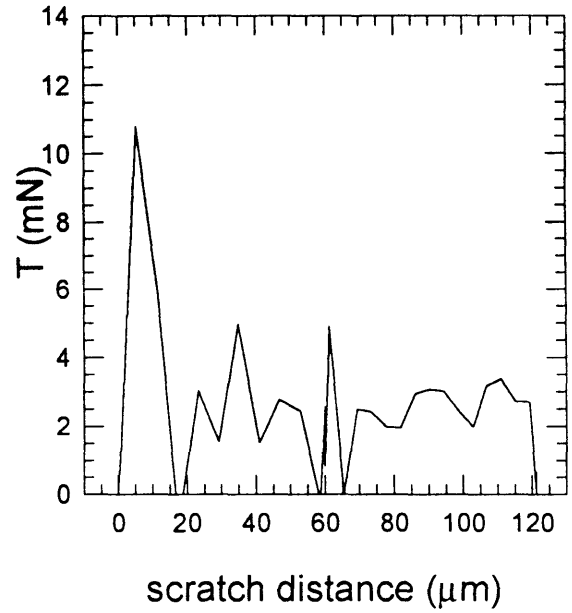
scratch 2-7 scratch depth
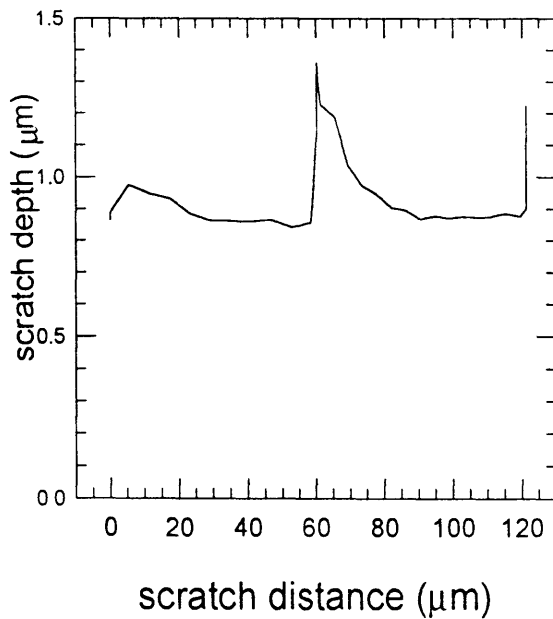
scratch 2-7 friction
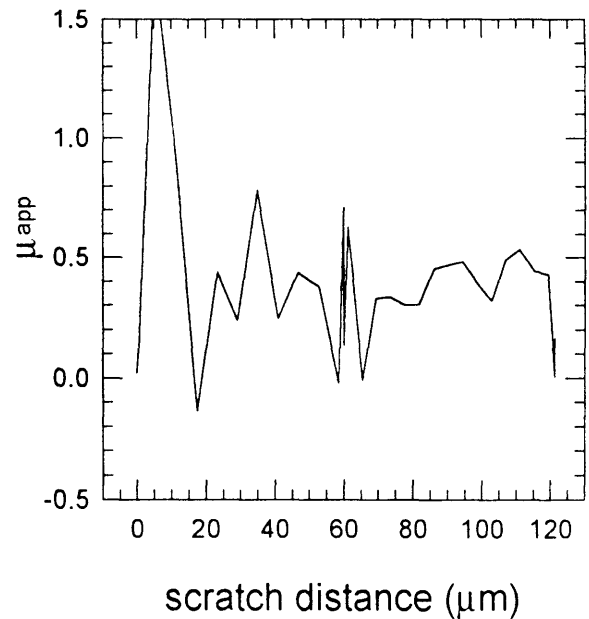
scratch 2-8 normal load
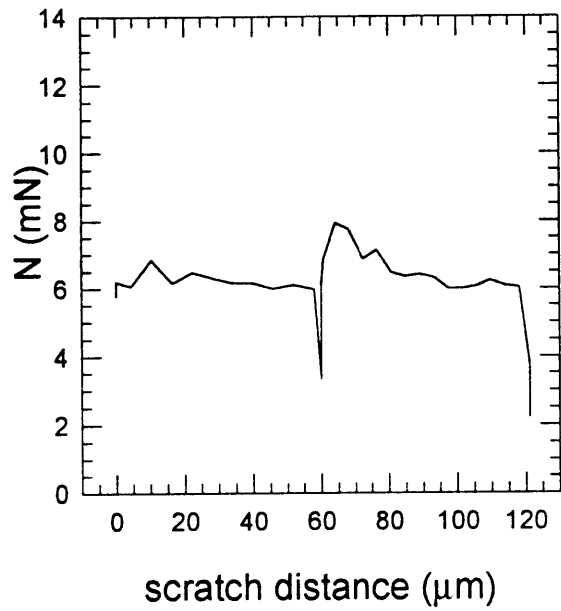
scratch 2-8 tangential load
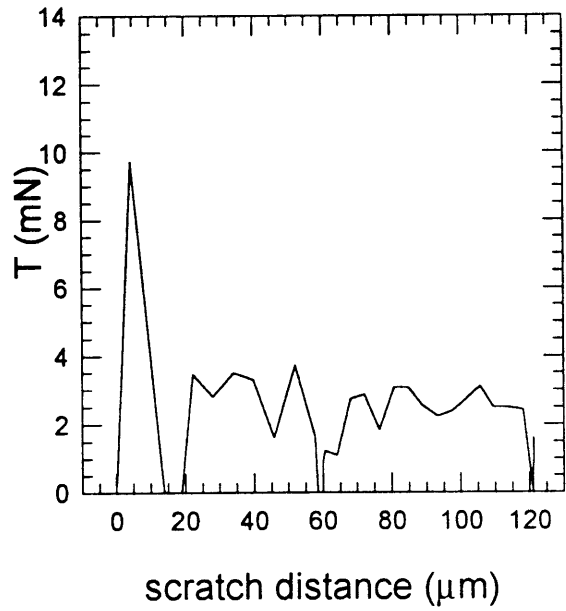
scratch 2-8 scratch depth
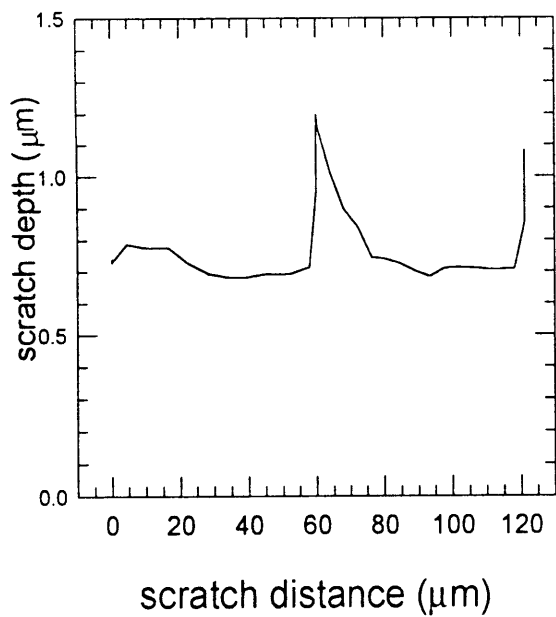
scratch 2-8 friction
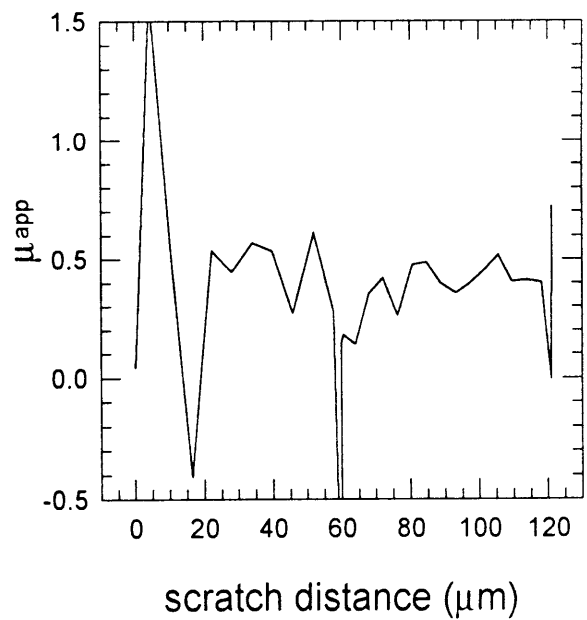
scratch 2-9 normal load
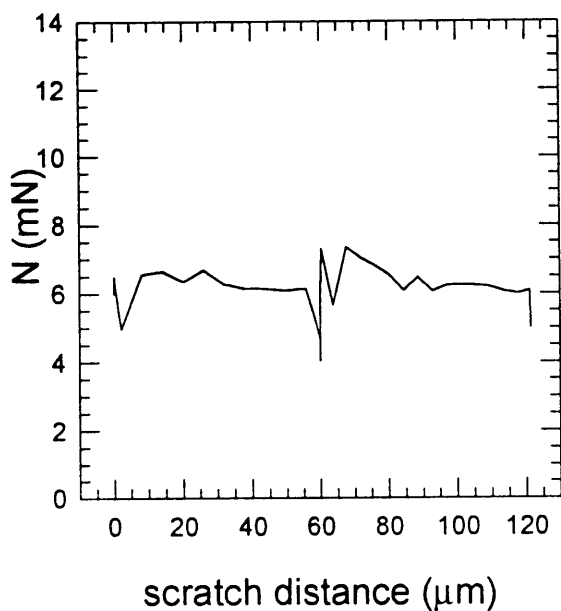
scratch 2-9 tangential load
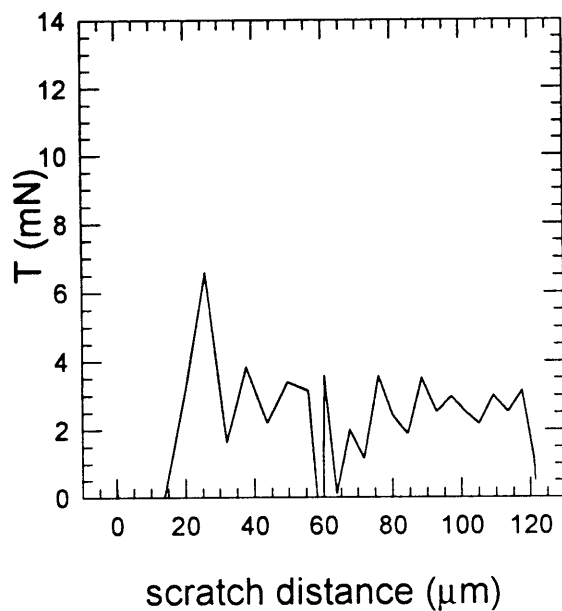
scratch 2-9 scratch depth
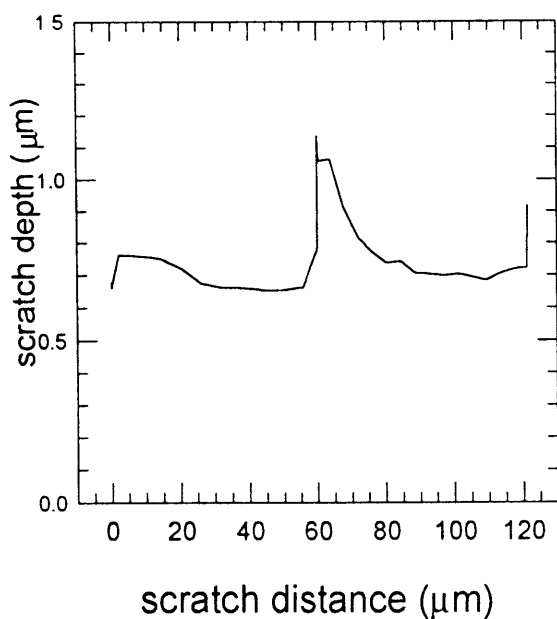
scratch 2-9 friction
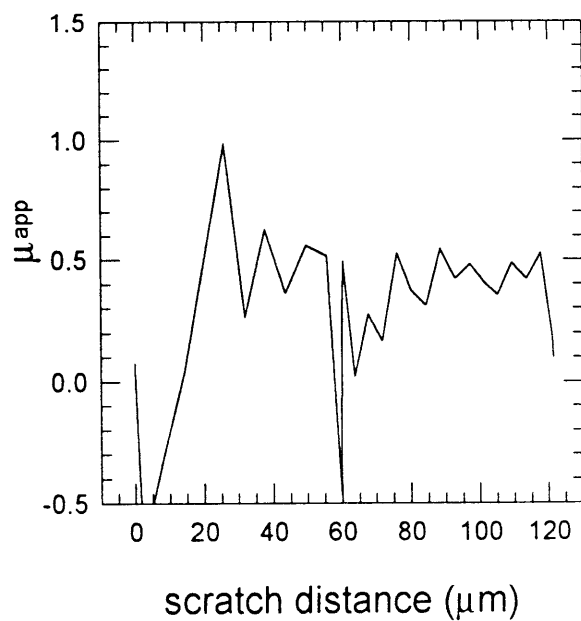
scratch 3-1 normal load
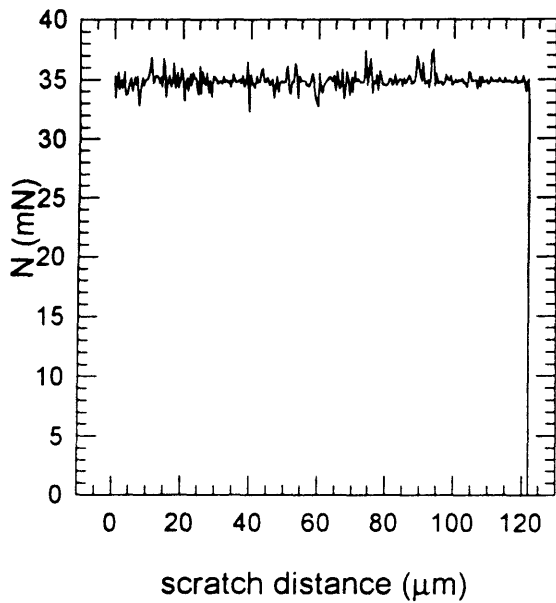
scratch 3-1 tangential load
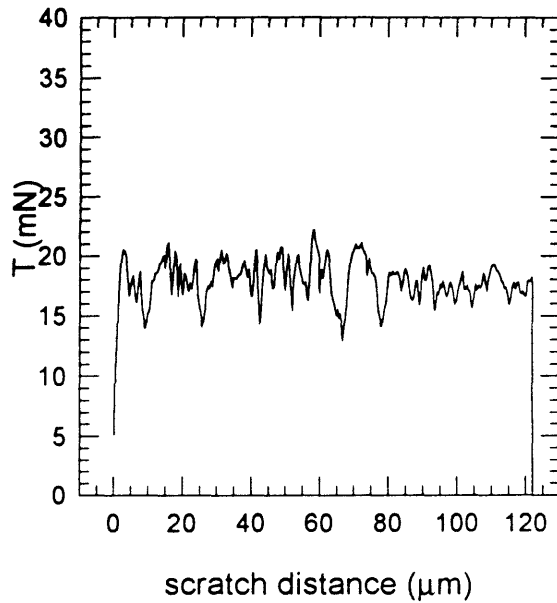
scratch 3-1 scratch depth
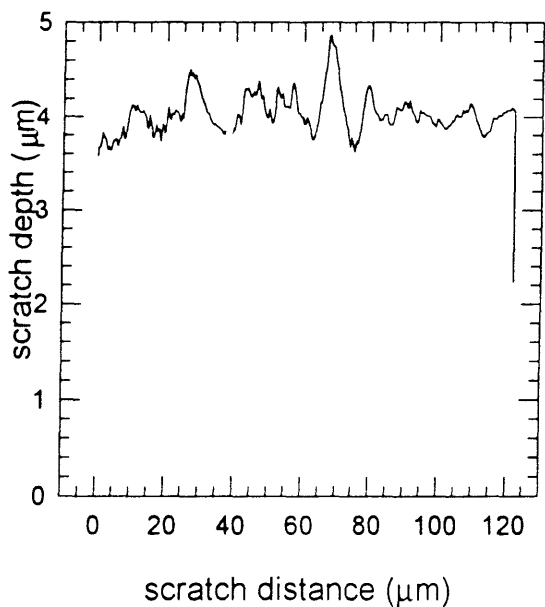
scratch 3-1 friction
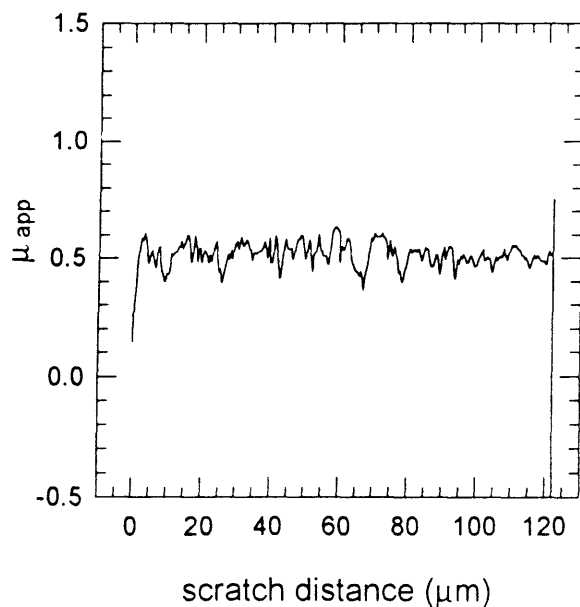
scratch 3-2 normal load
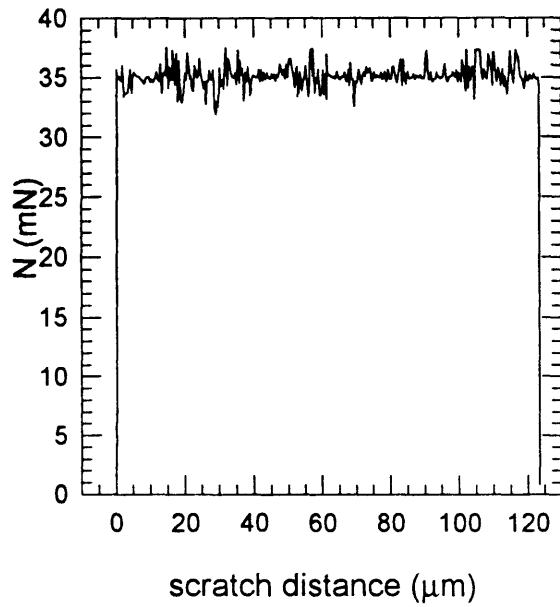
scratch 3-2 tangential load
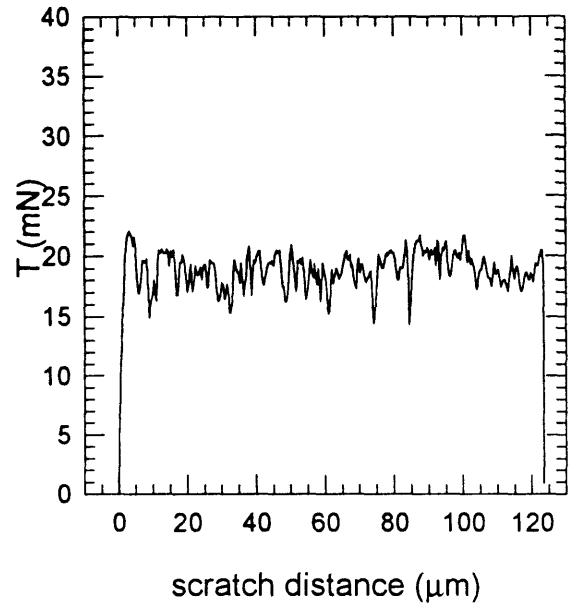
scratch 3-2 scratch depth
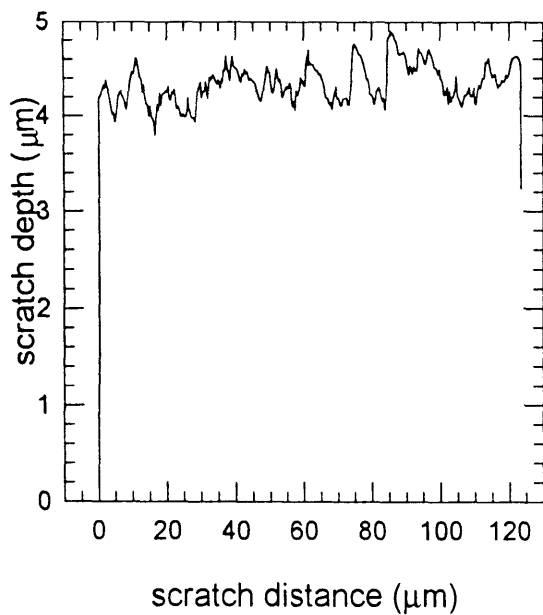
scratch 3-2 friction
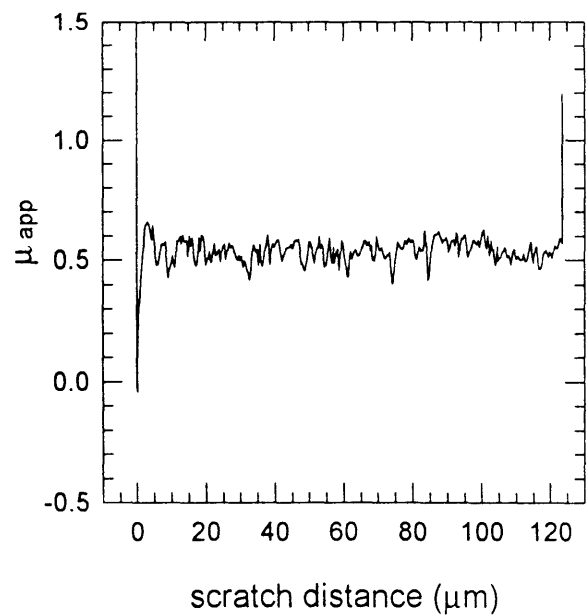
scratch 3-3 normal load
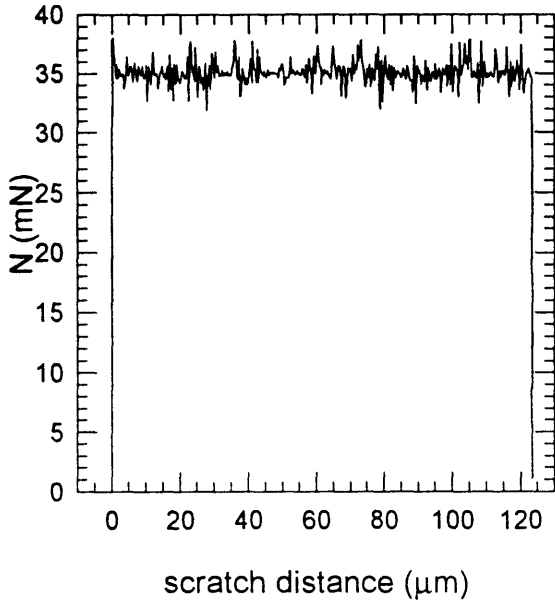
scratch 3-3 tangential load
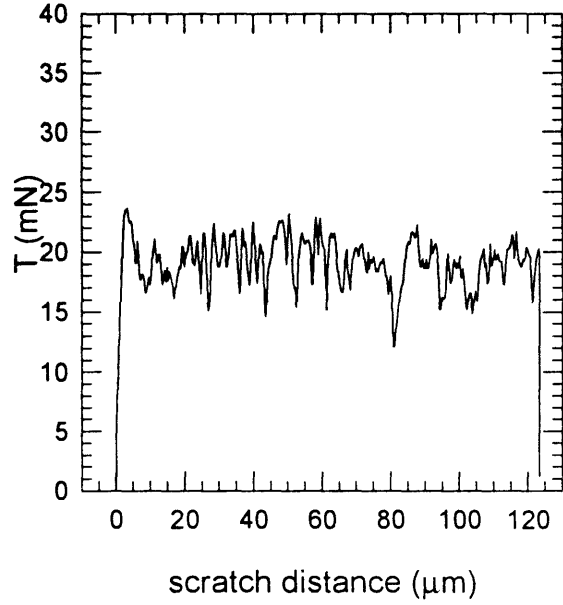
scratch 3-3 scratch depth
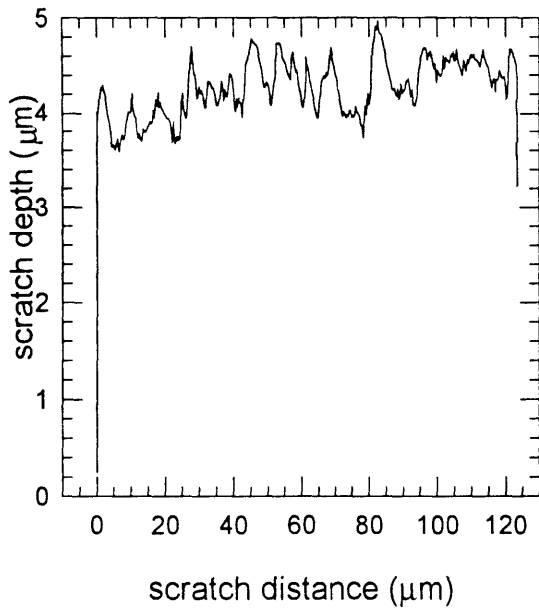
scratch 3-3 friction
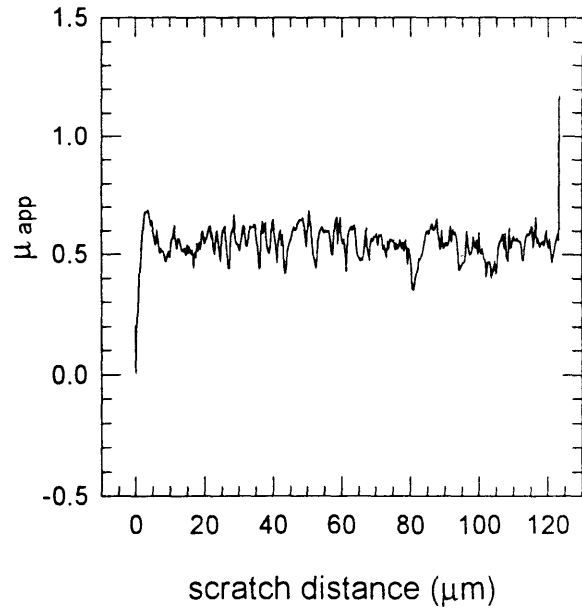
scratch 3-4 normal load
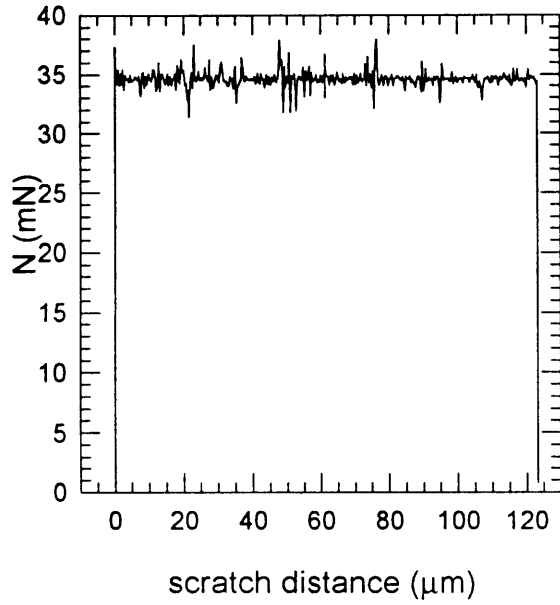
scratch 3-4 tangential load
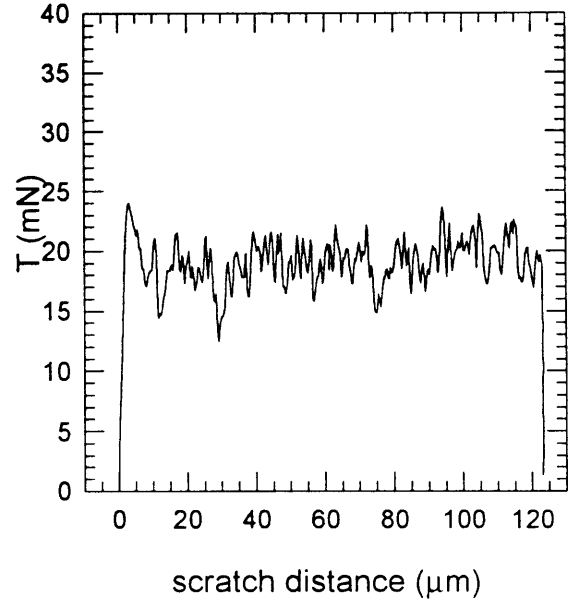
scratch 3-4 scratch depth
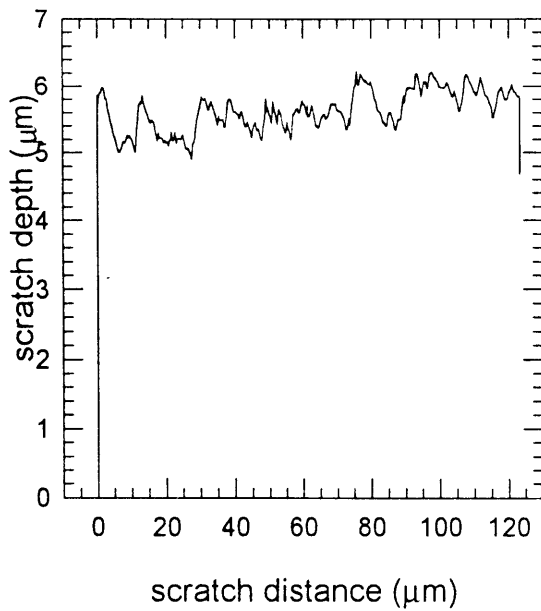
scratch 3-4 friction
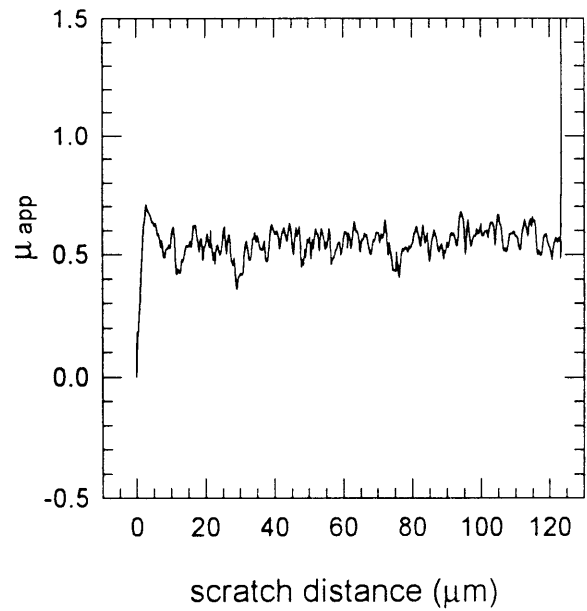
scratch 3-5 normal load
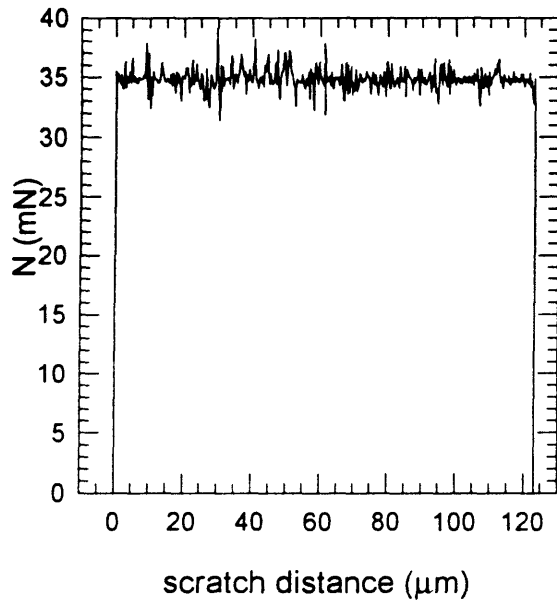
scratch 3-5 tangential load
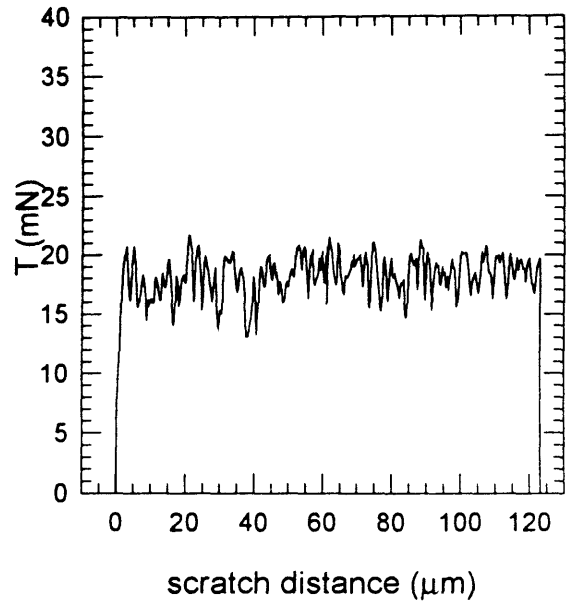
scratch 3-5 scratch depth
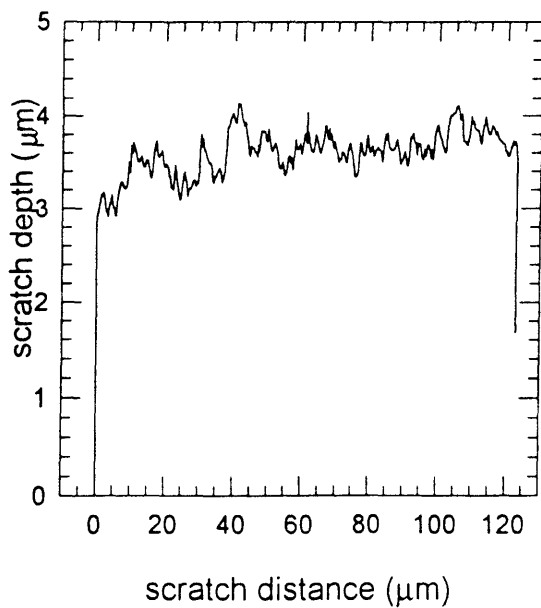
scratch 3-5 friction
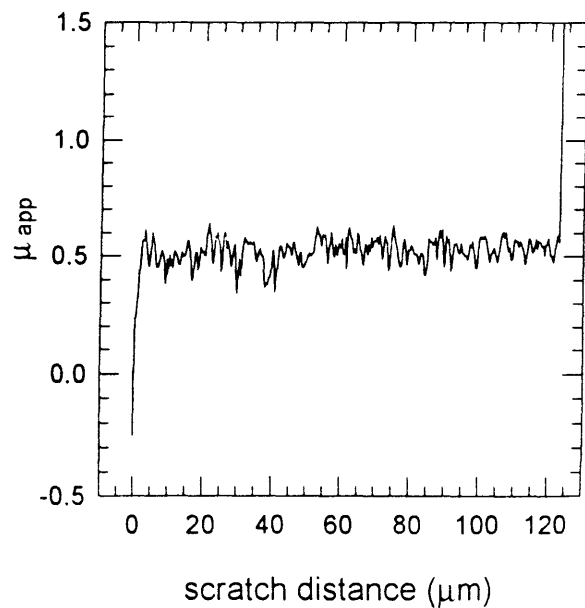
scratch 3-6 normal load
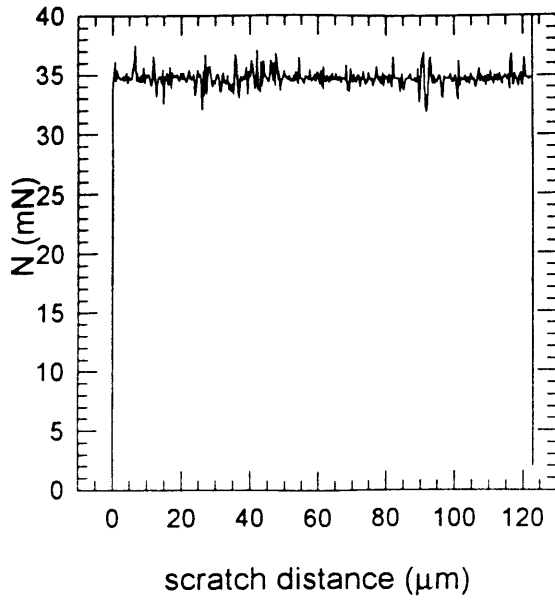
scratch 3-6 tangential load
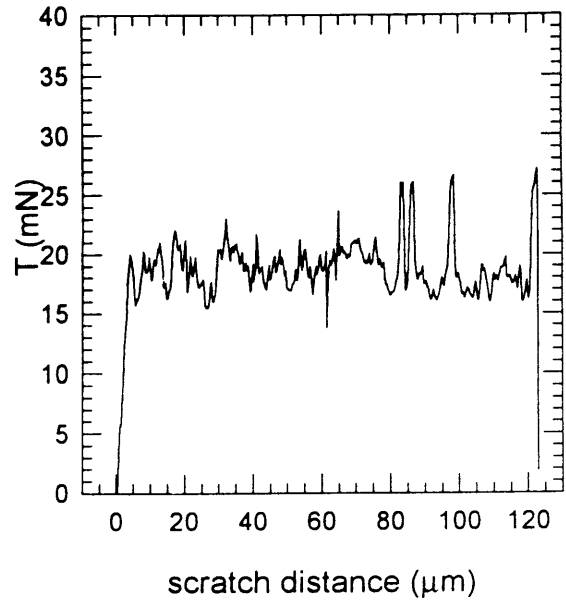
scratch 3-6 scratch depth
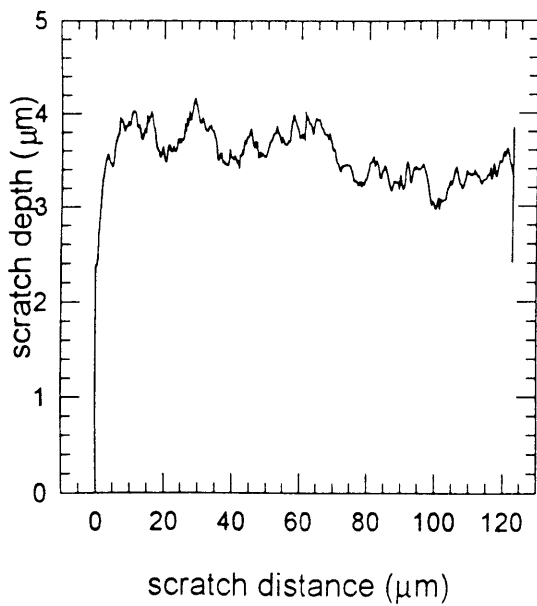
scratch 3-6 friction
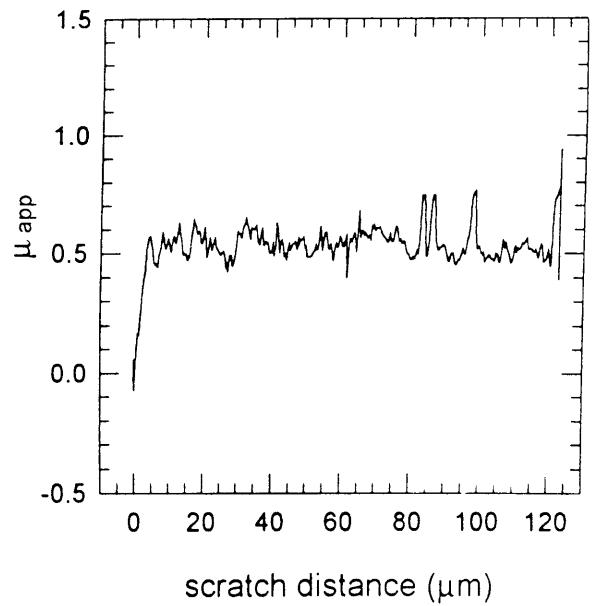
scratch 3-7 normal load
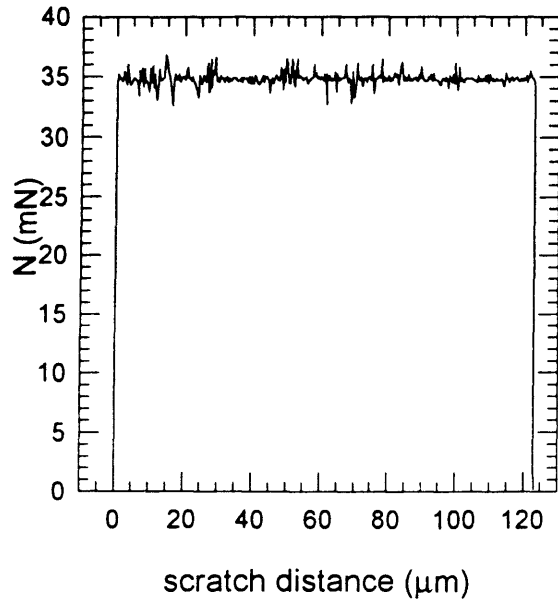
scratch 3-7 tangential load
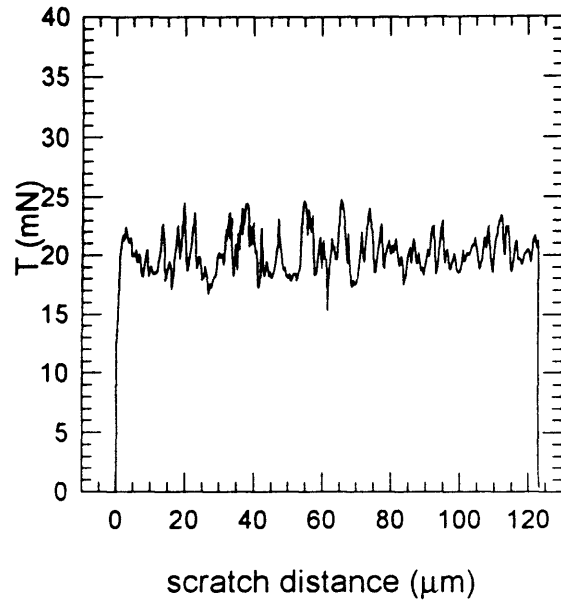
scratch 3-7 scratch depth
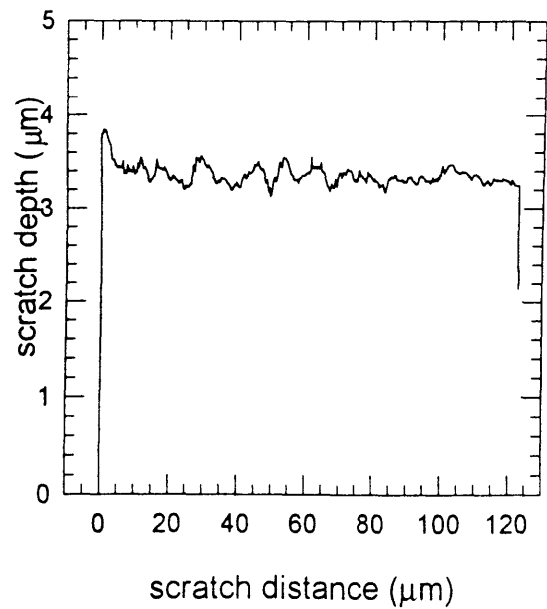
scratch 3-7 friction
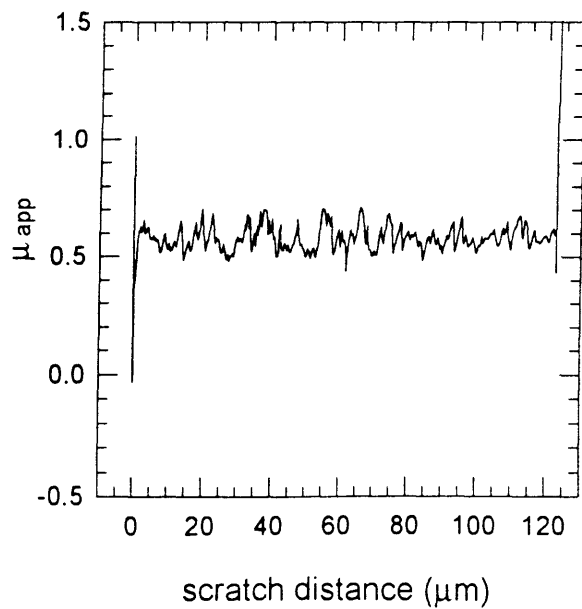
scratch 3-8 normal load
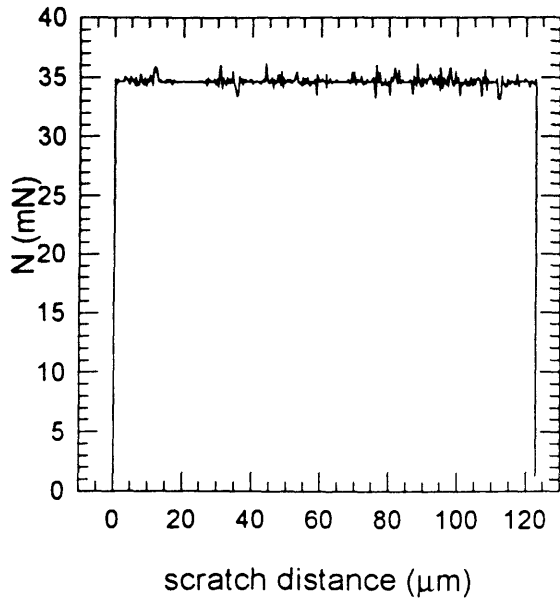
scratch 3-8 tangential load
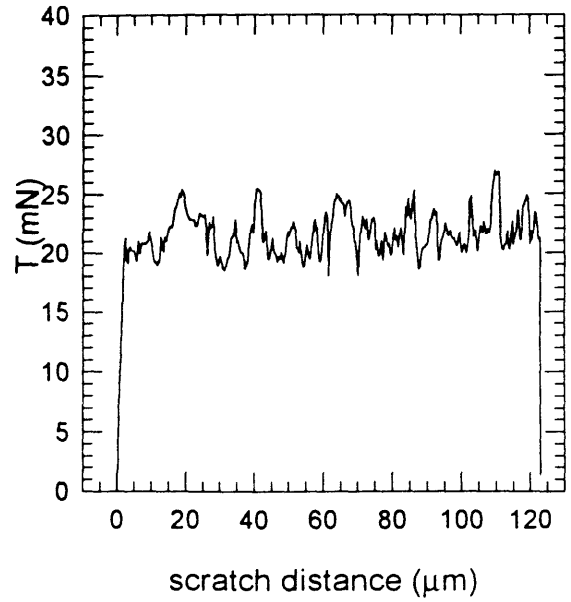
scratch 3-8 scratch depth
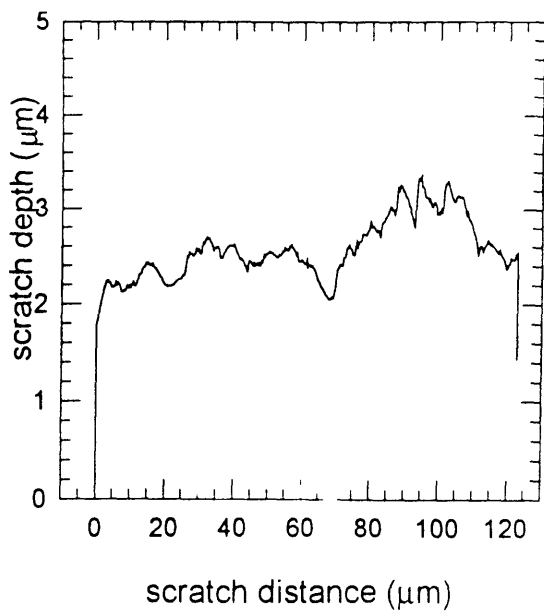
scratch 3-8 friction
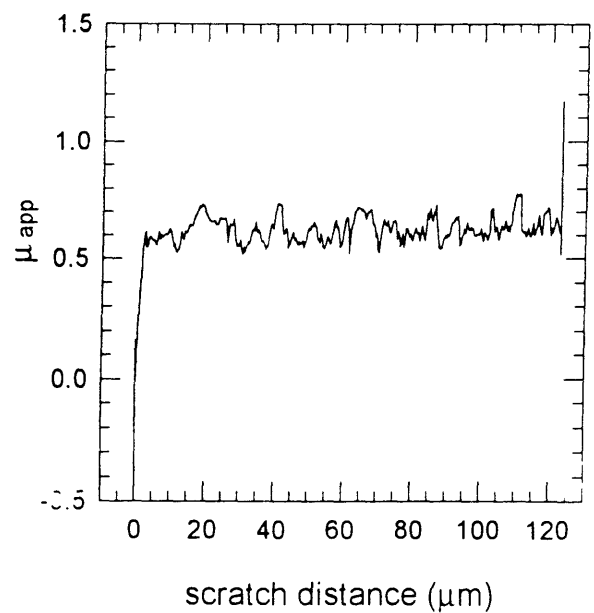
scratch 3-9 normal load
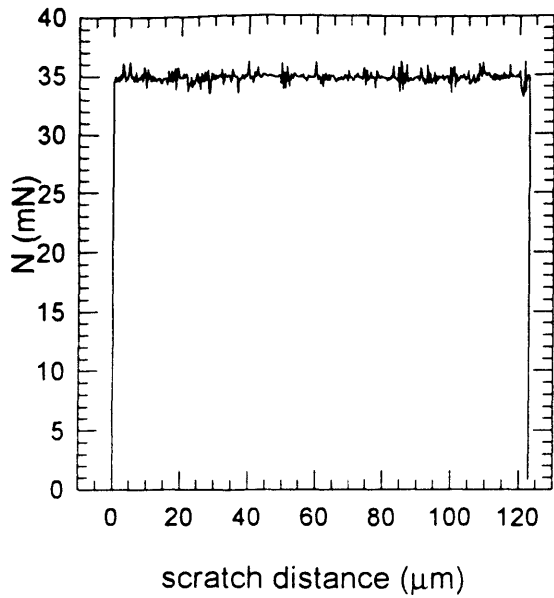
scratch 3-9 tangential load
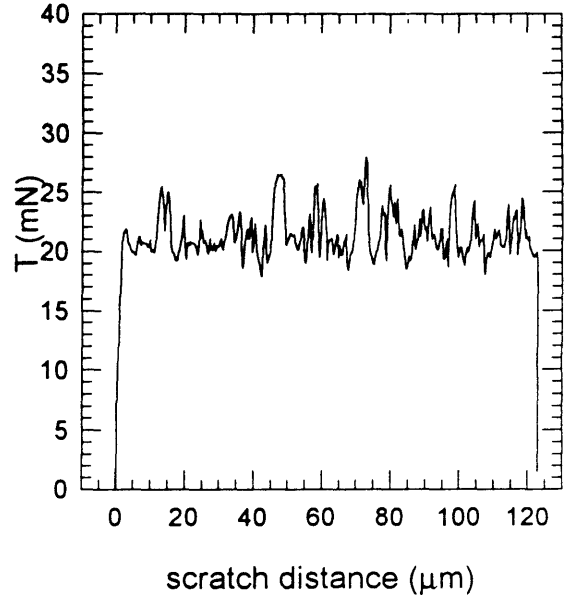
scratch 3-9 scratch depth
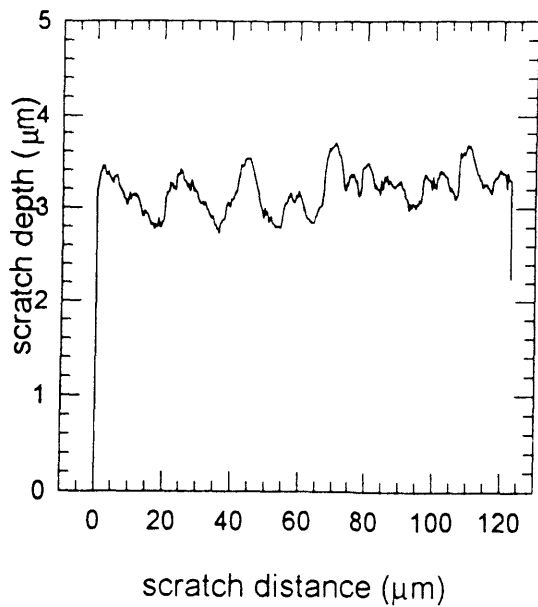
scratch 3-9 friction
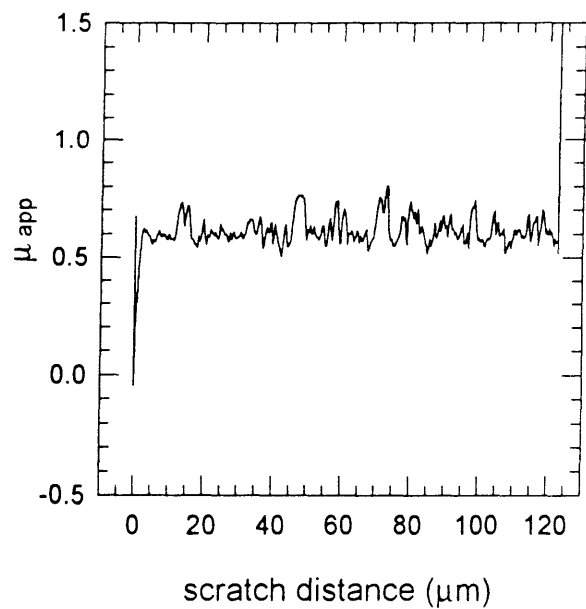
scratch 3-10 normal load
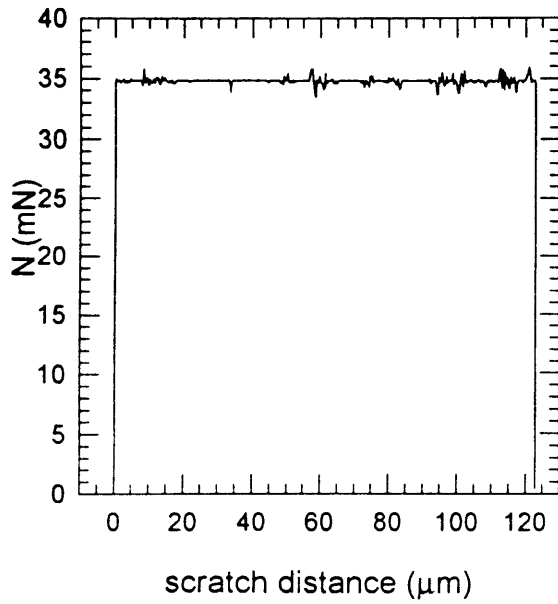
scratch 3-10 tangential load
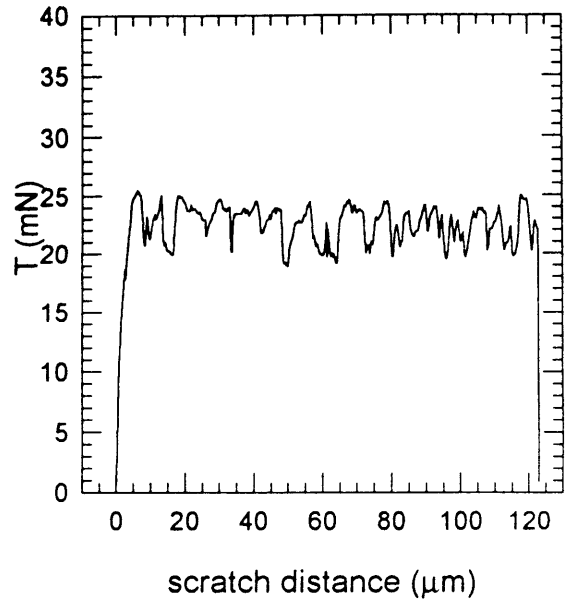
scratch 3-10 scratch depth
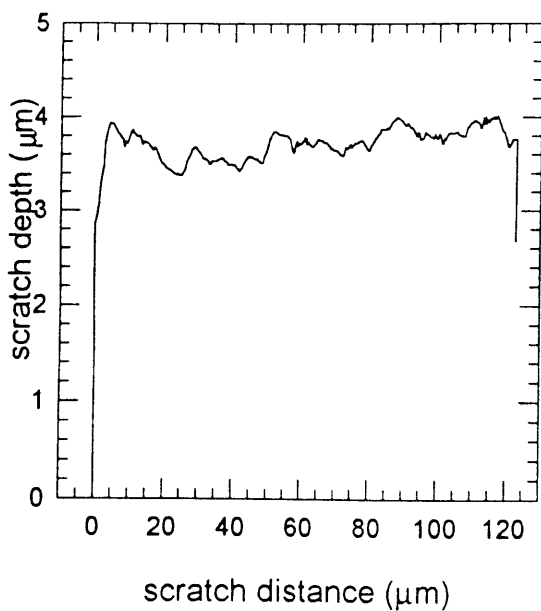
scratch 3-10 friction
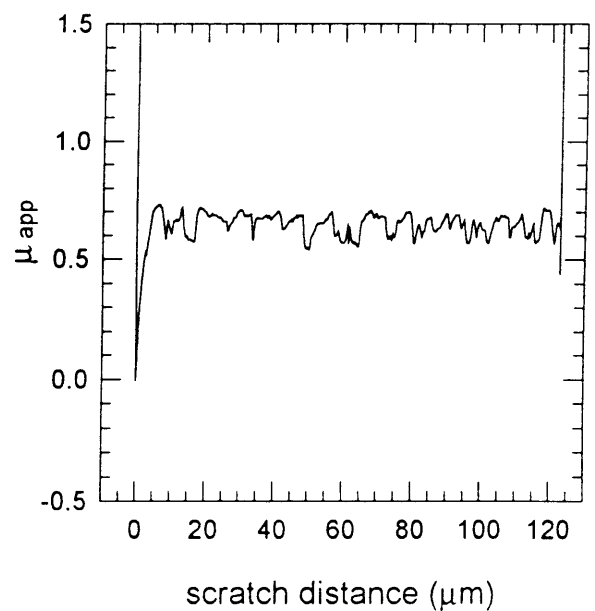
scratch 4-1 normal load
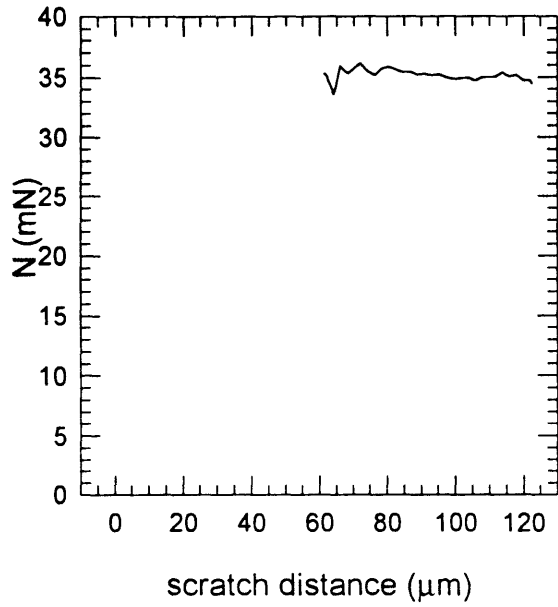
scratch 4-1 tangential load
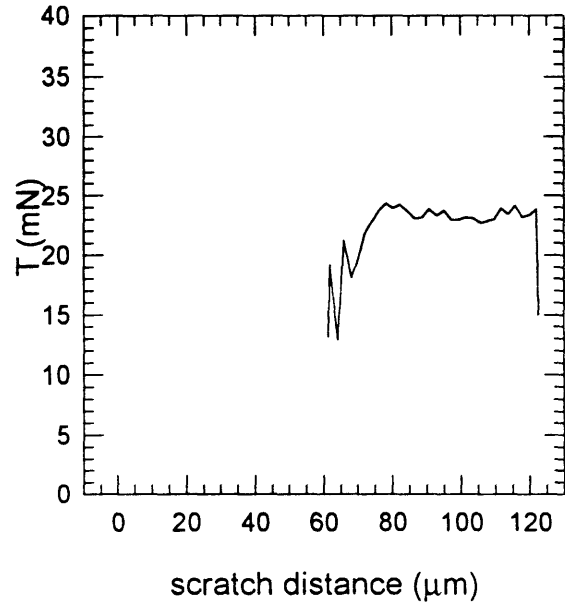
scratch 4-1 scratch depth
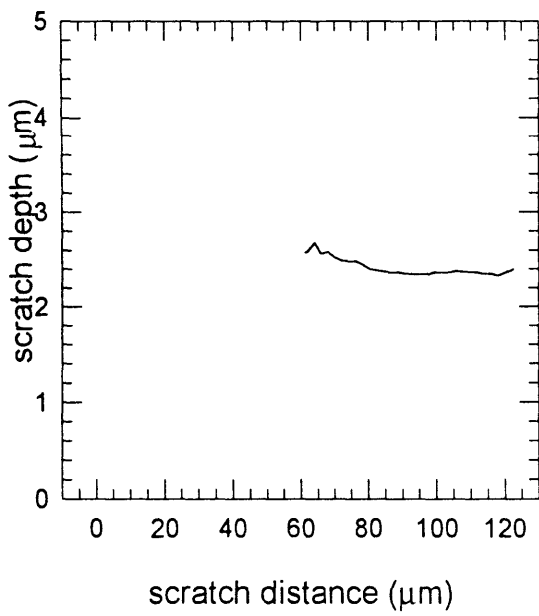
scratch 4-1 friction
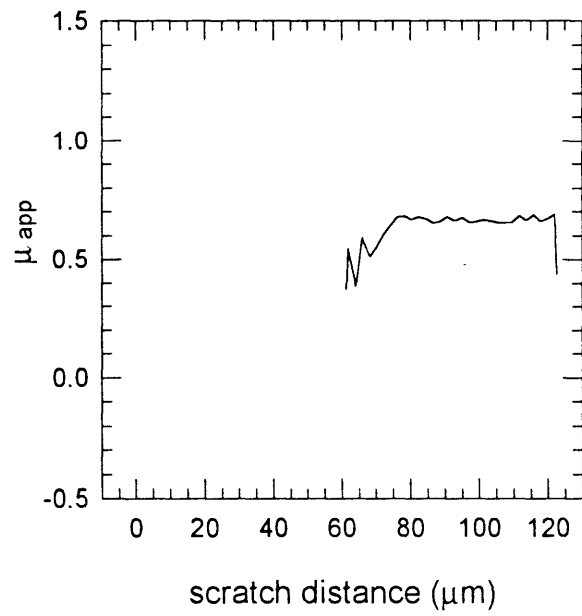
scratch 4-2 normal load
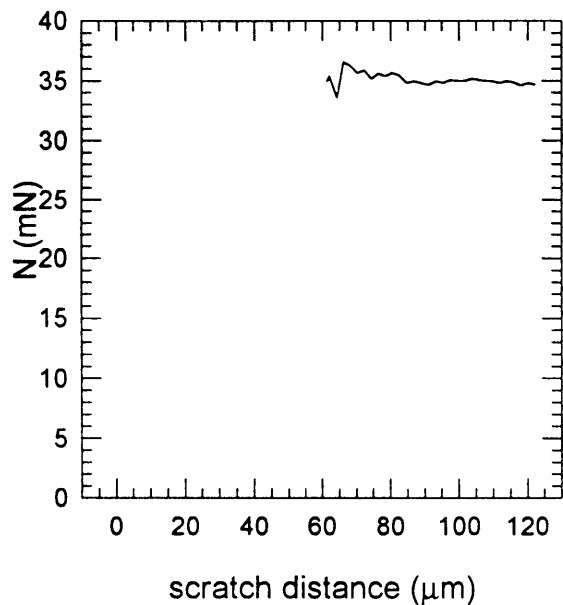
scratch 4-2 tangential load
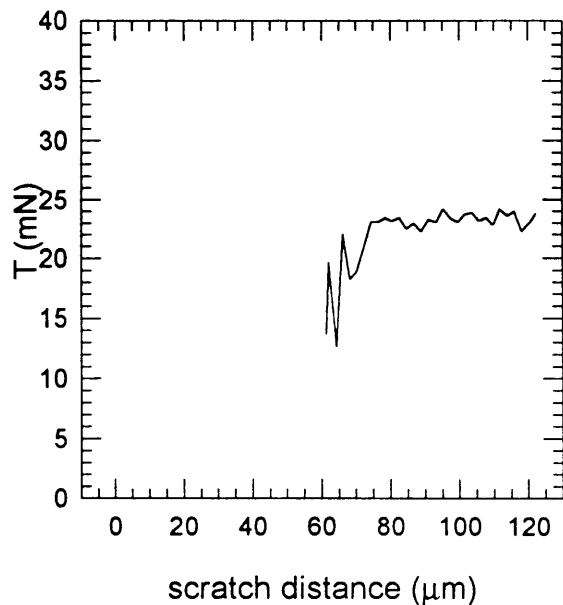
scratch 4-2 scratch depth
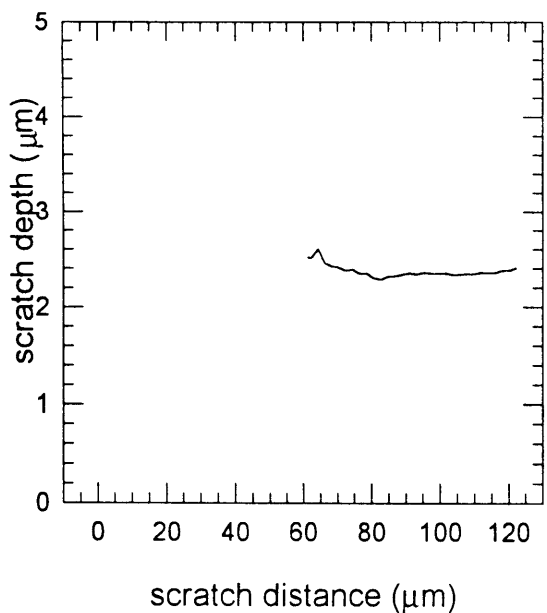
scratch 4-2 friction
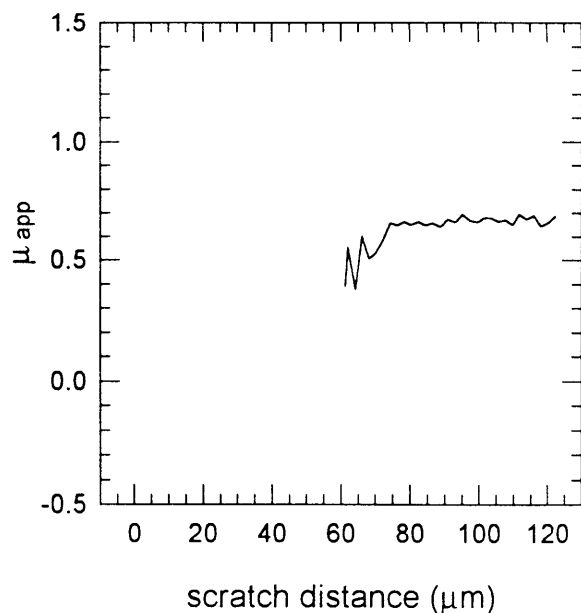
scratch 4-3 normal load
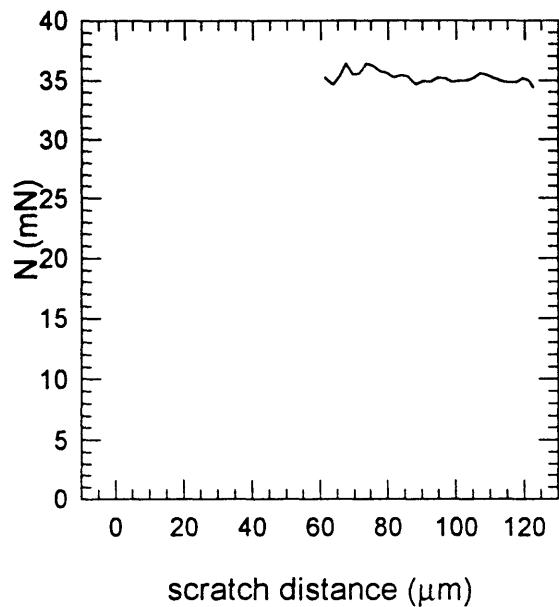
scratch 4-3 tangential load
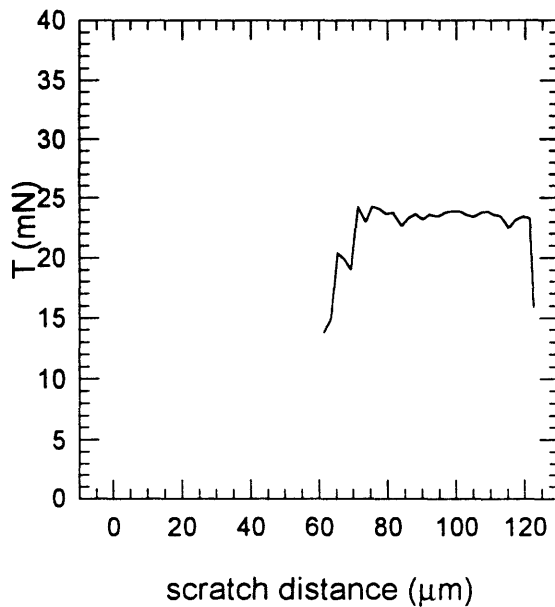
scratch 4-3 scratch depth
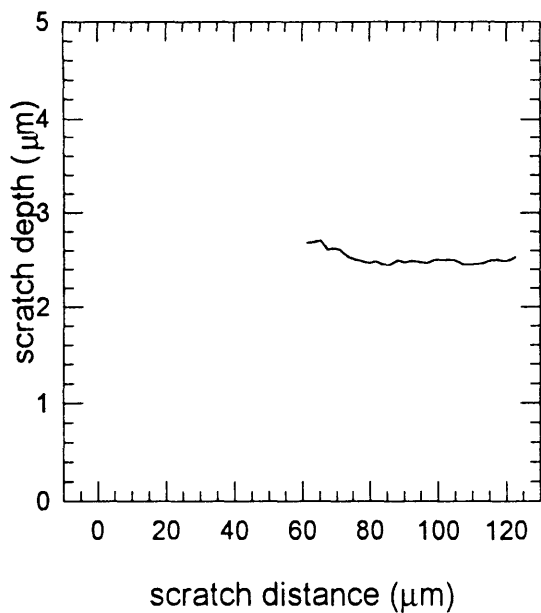
scratch 4-3 friction
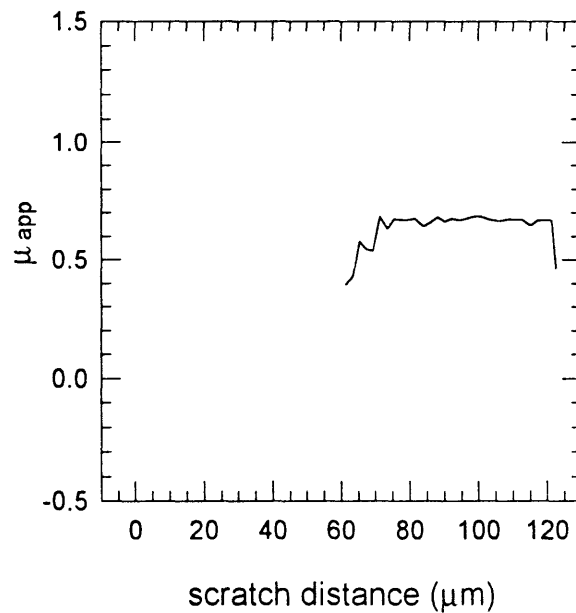
scratch 4-4 normal load
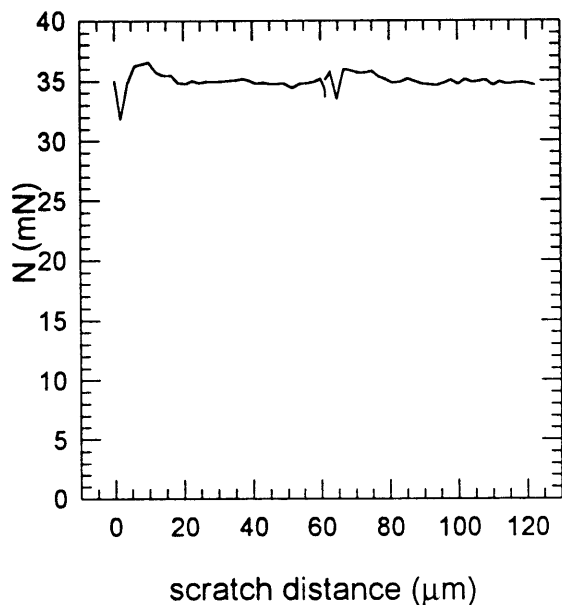
scratch 4-4 tangential load
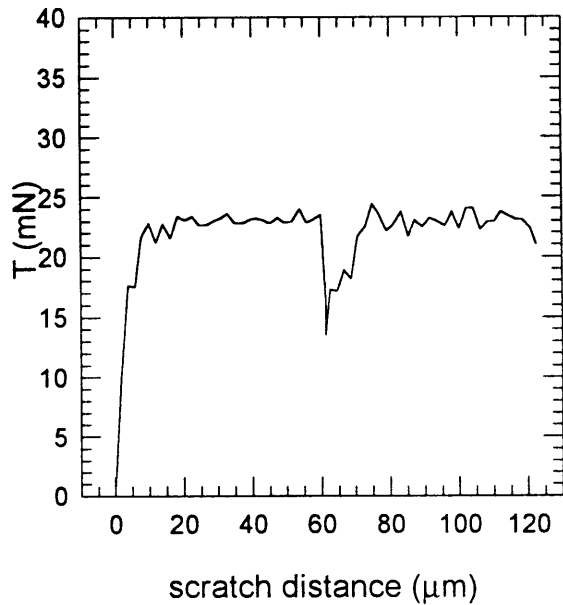
scratch 4-4 scratch depth
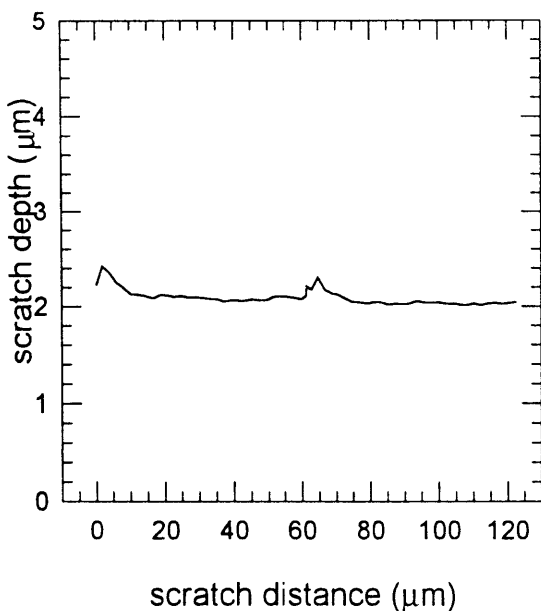
scratch 4-4 friction
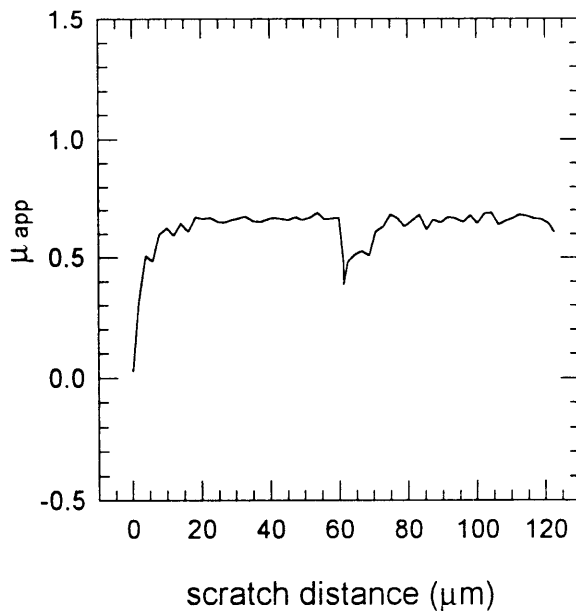
scratch 4-5 normal load
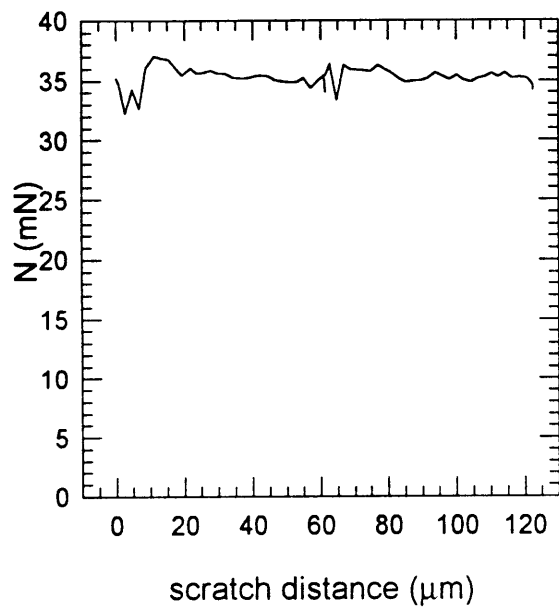
scratch 4-5 tangential load
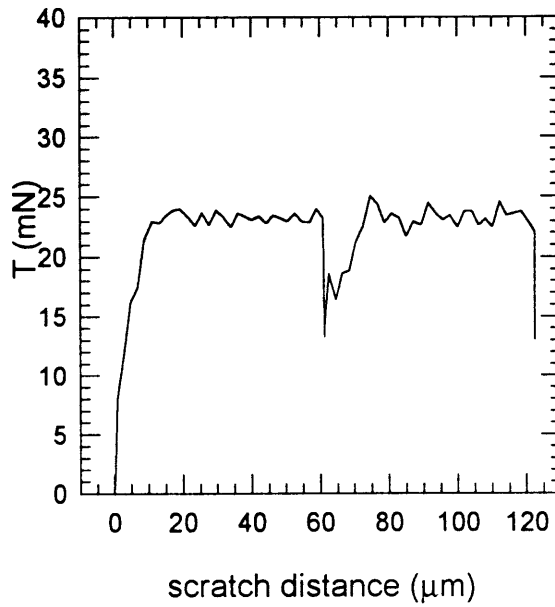
scratch 4-5 scratch depth
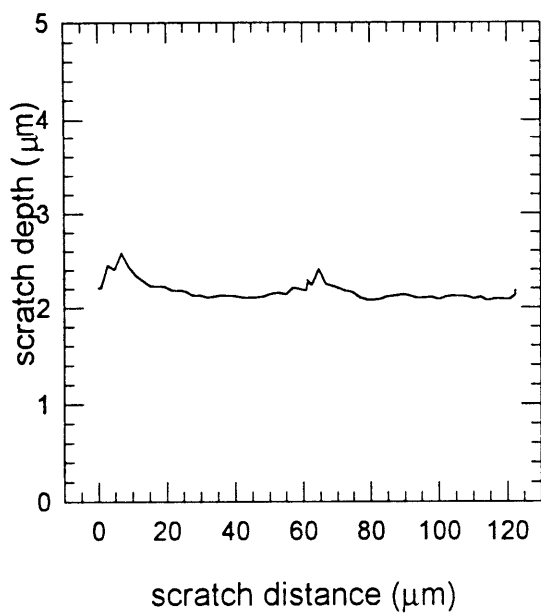
scratch 4-5 friction
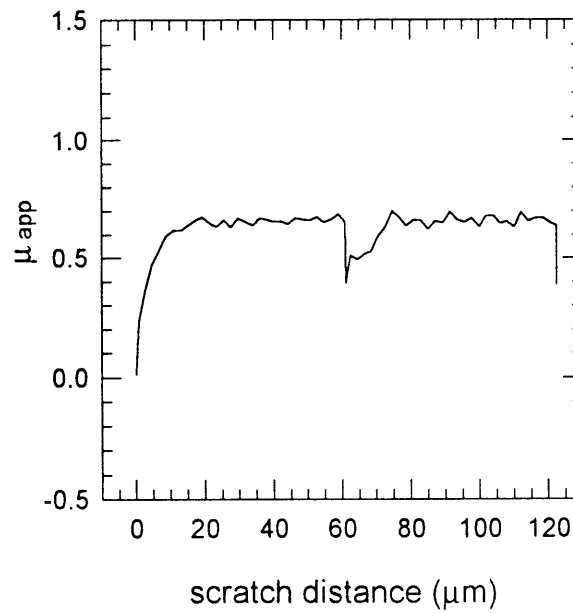
scratch 4-6 normal load
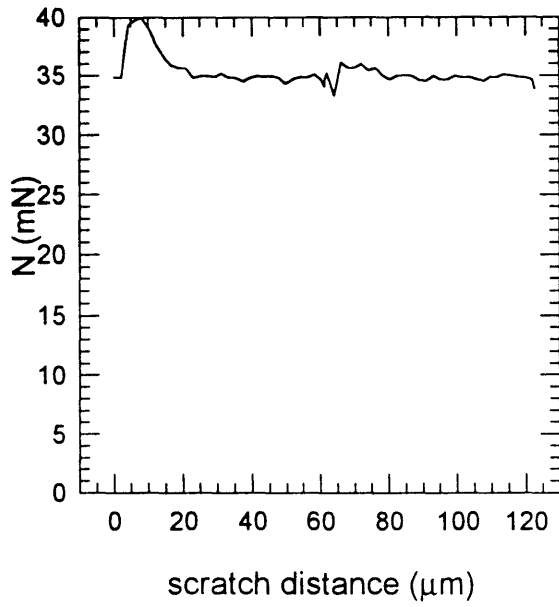
scratch 4-6 tangential load
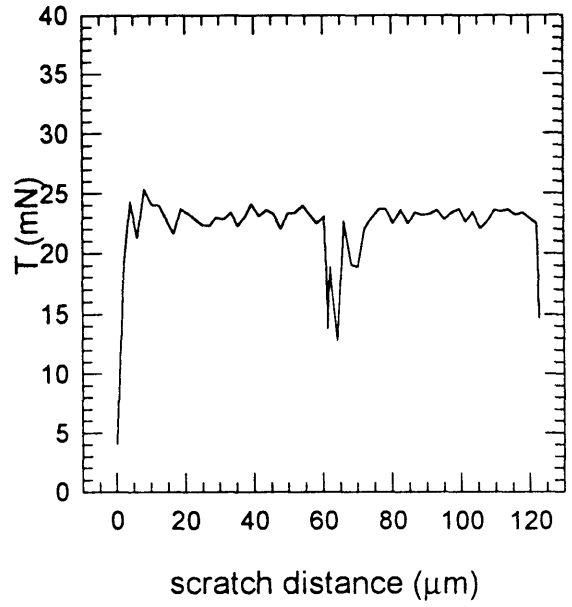
scratch 4-6 scratch depth
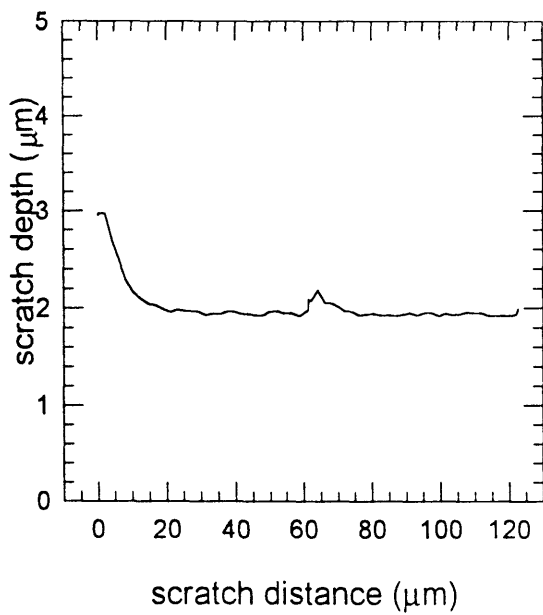
scratch 4-6 friction
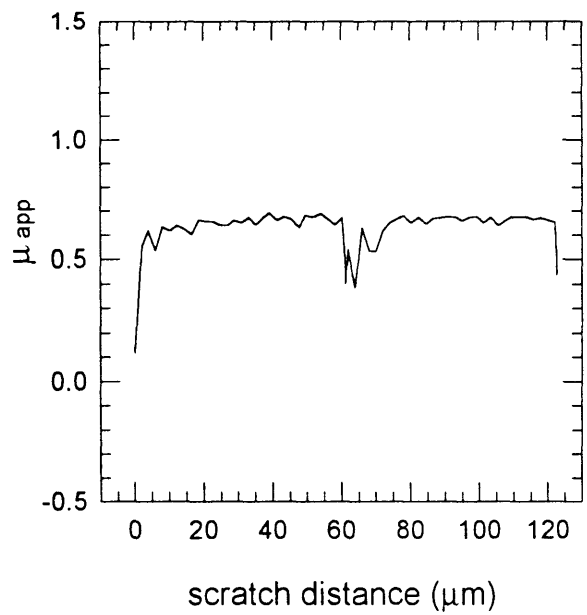
scratch 4-7 normal load
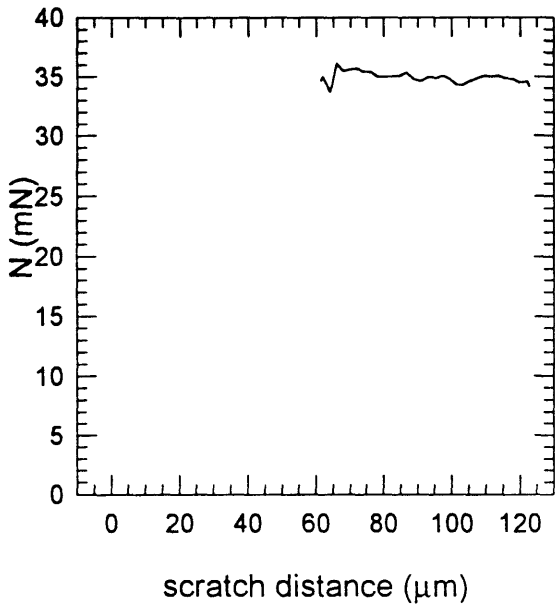
scratch 4-7 tangential load
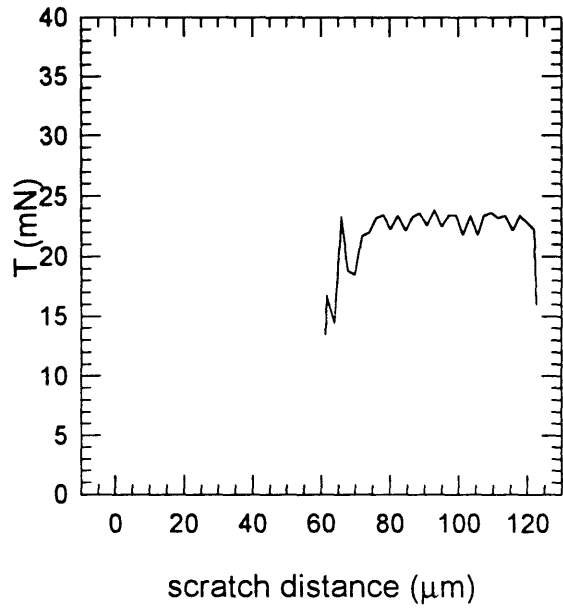
scratch 4-7 scratch depth
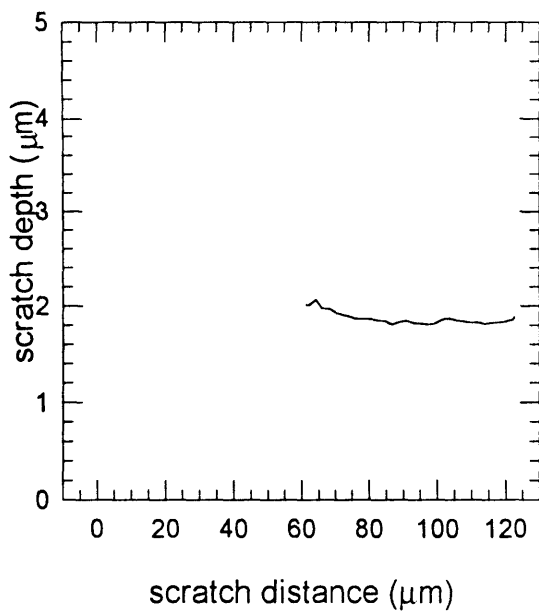
scratch 4-7 friction
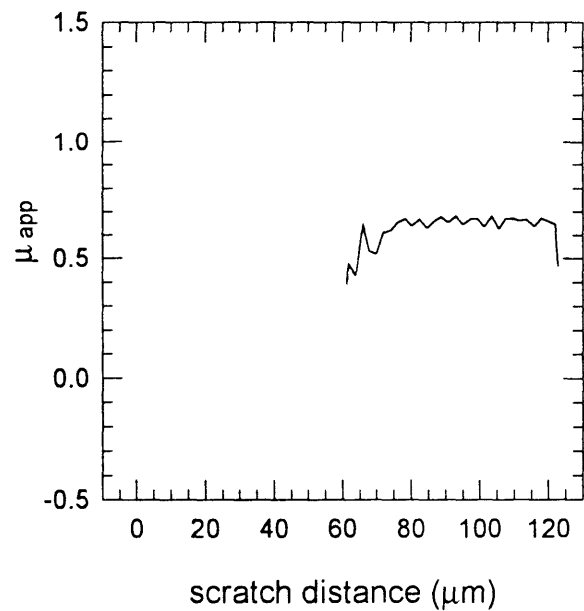
scratch 4-8 normal load
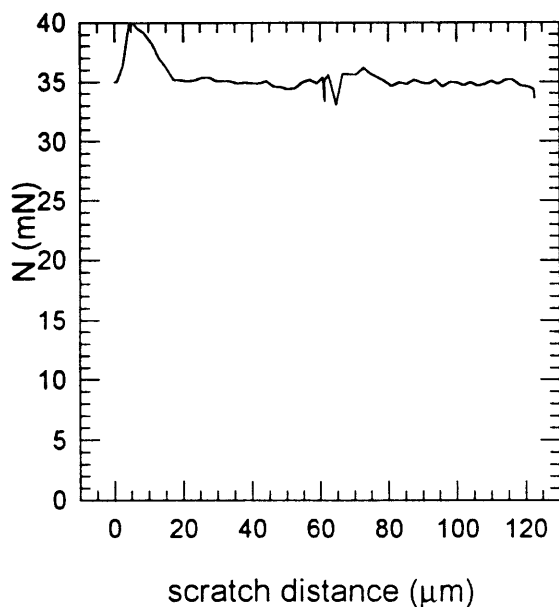
scratch 4-8 tangential load
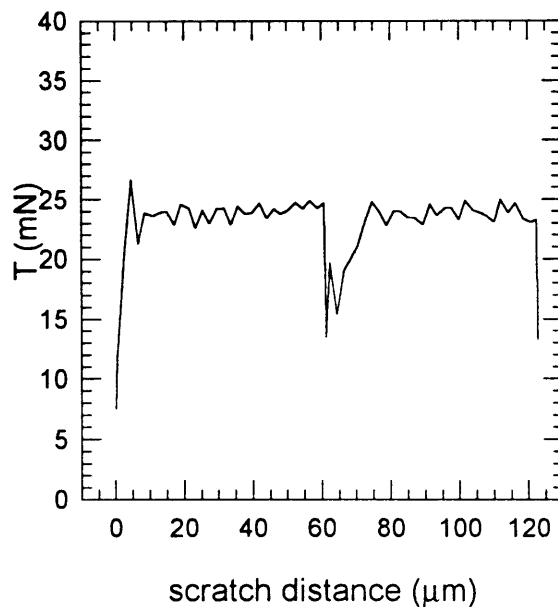
scratch 4-8 scratch depth
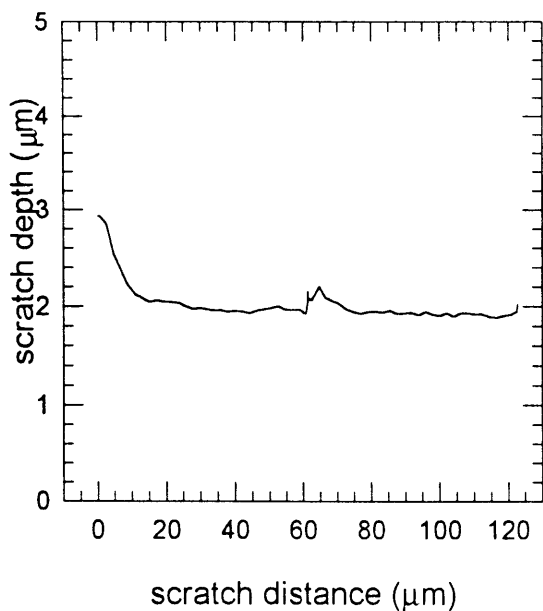
scratch 4-8 friction
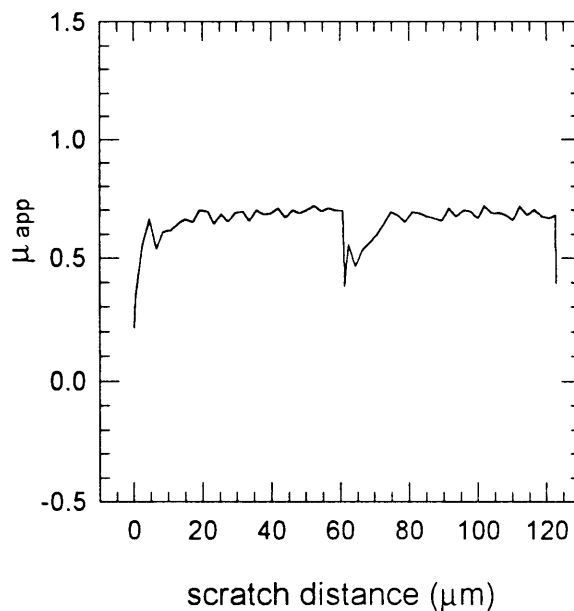
scratch 4-9 normal load
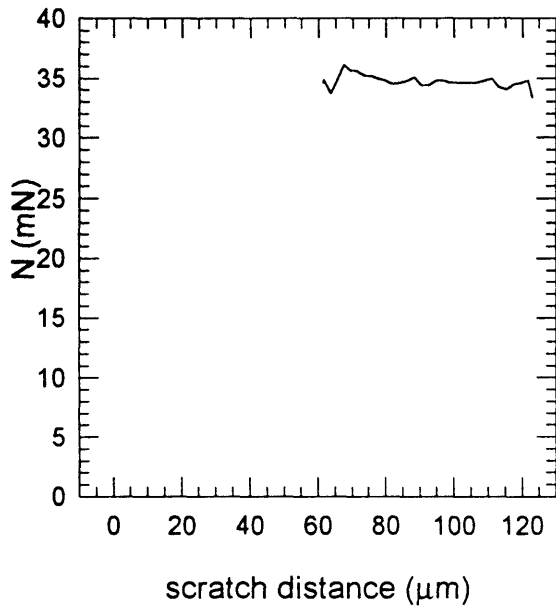
scratch 4-9 tangential load
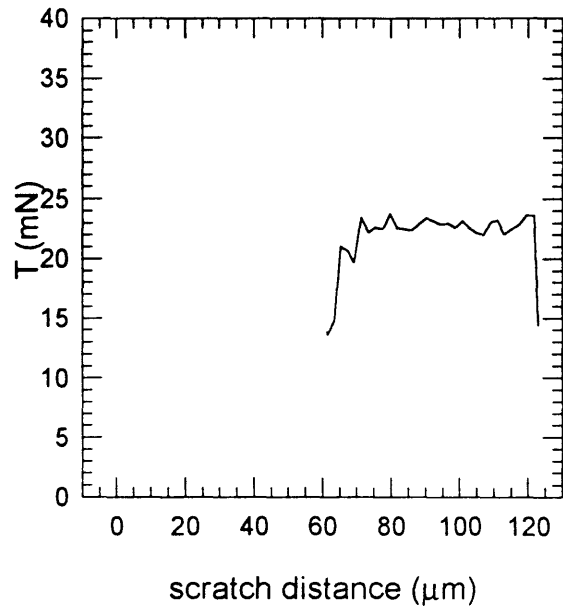
scratch 4-9 scratch depth
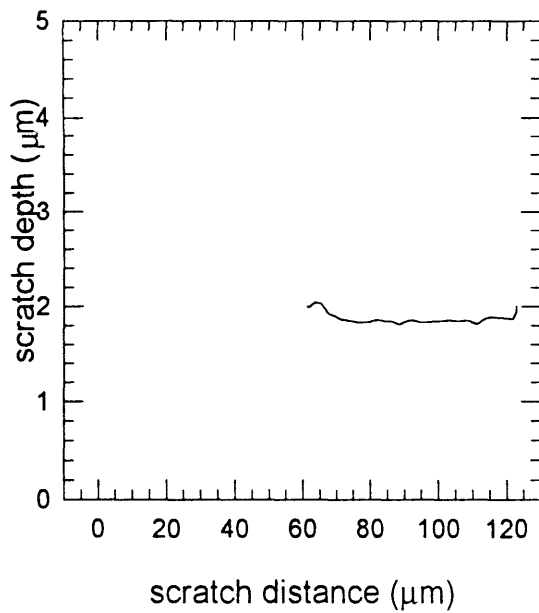
scratch 4-9 friction
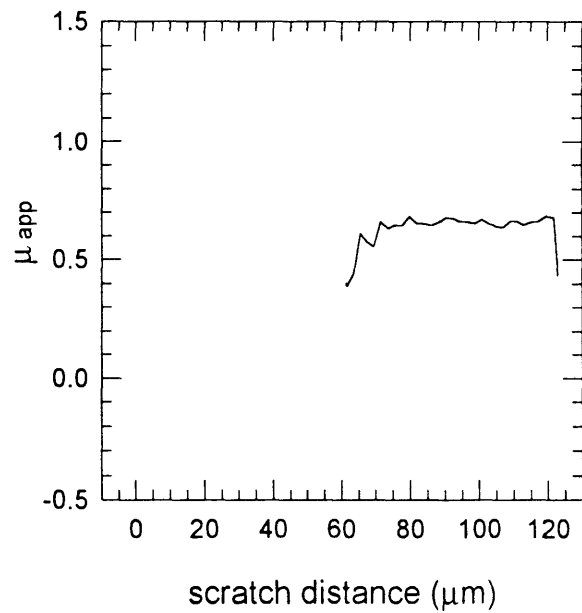
scratch 4-10 normal load
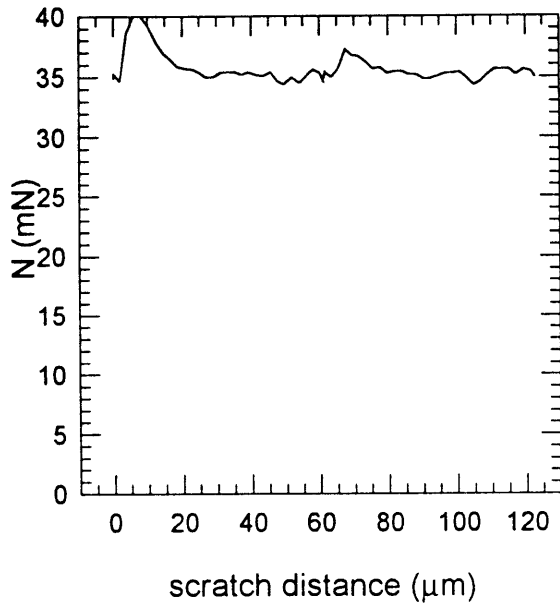
scratch 4-10 tangential load
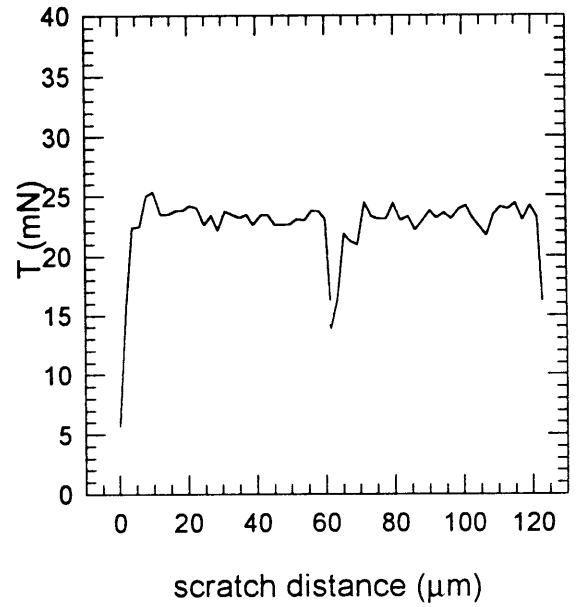
scratch 4-10 scratch depth
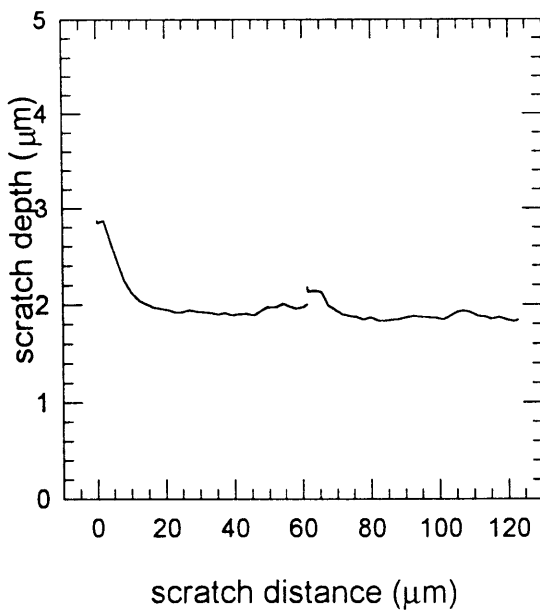
scratch 4-10 friction
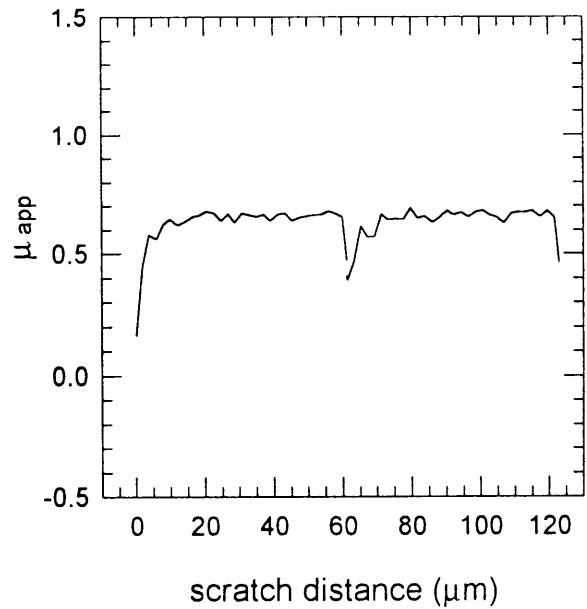
scratch 7-1 normal load
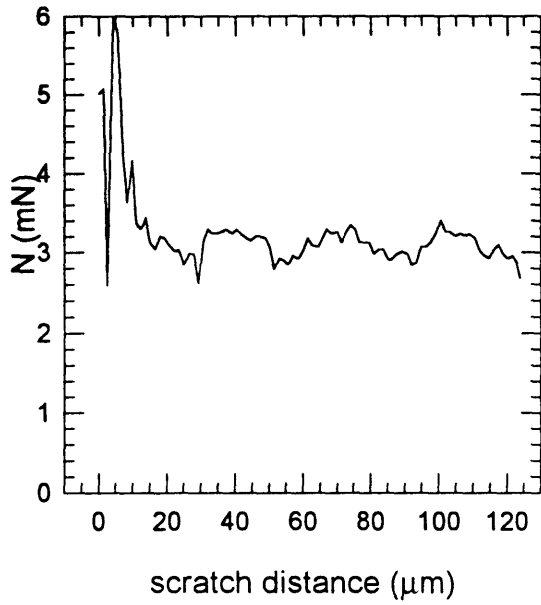
scratch 7-1 tangential load
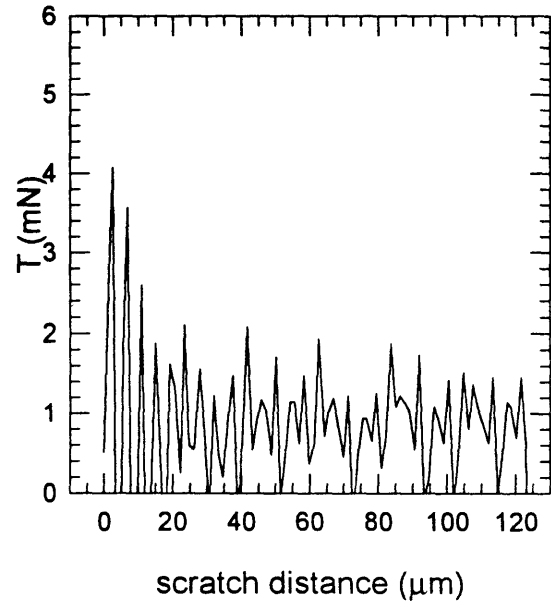
scratch 7-1 scratch depth
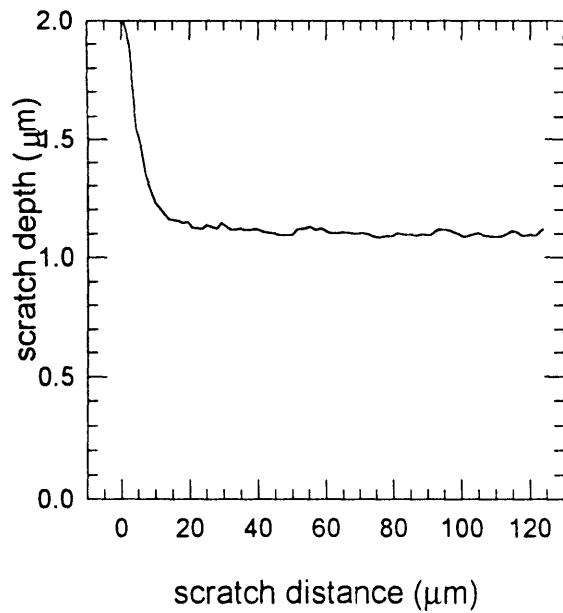
scratch 7-1 friction
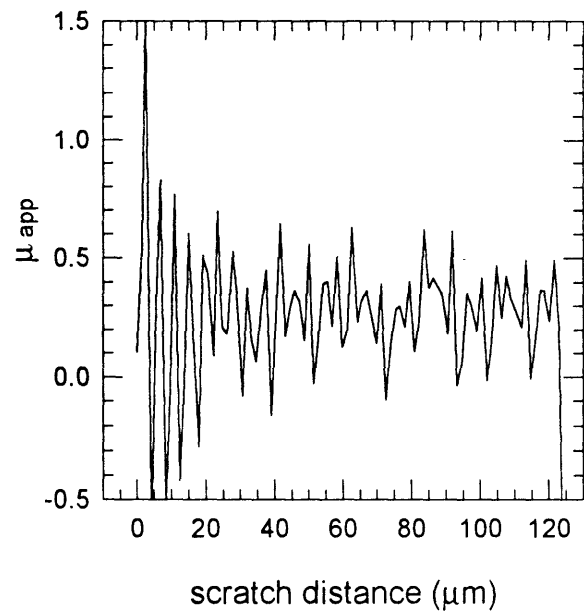
scratch 7-2 normal load
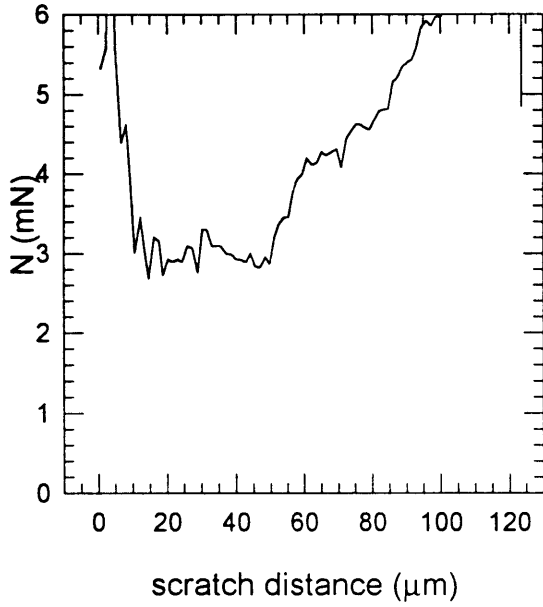
scratch 7-2 tangential load
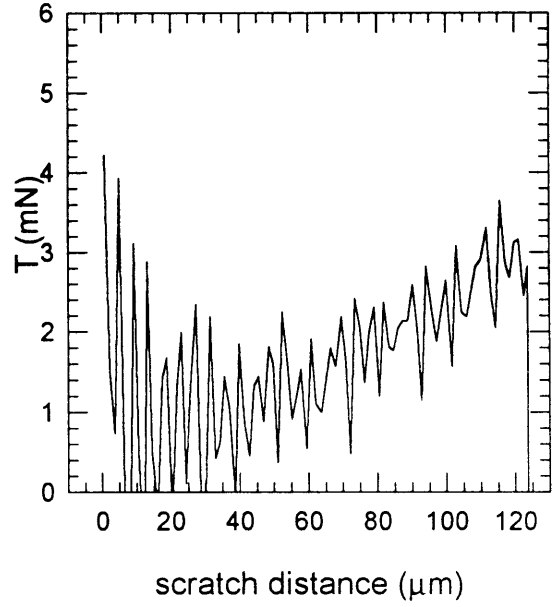
scratch 7-2 scratch depth
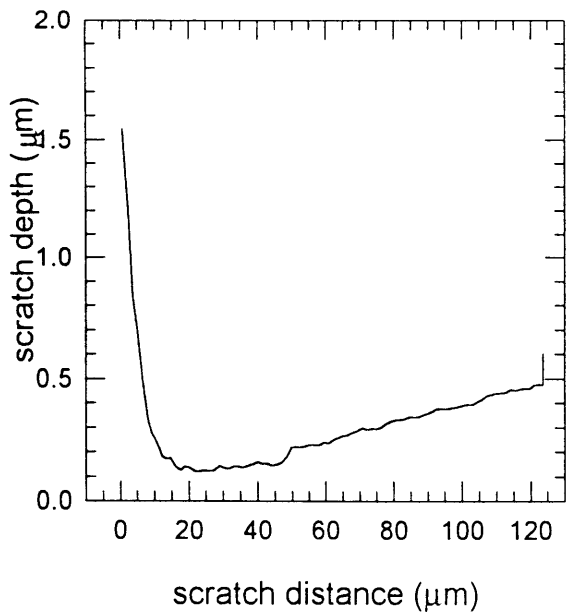
scratch 7-2 friction
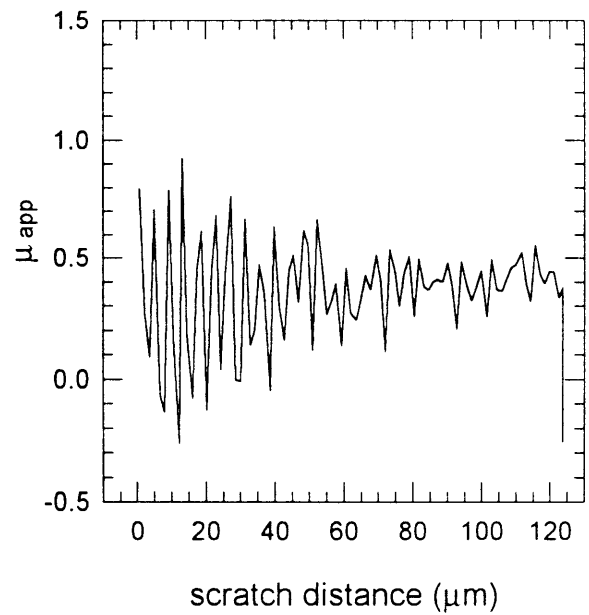
scratch 7-3 normal load
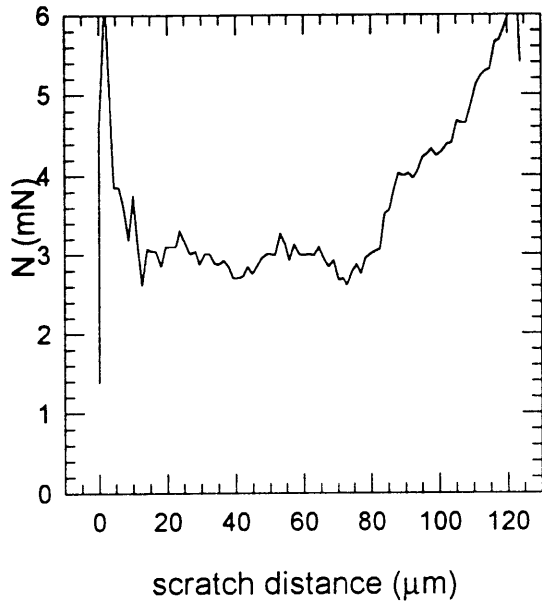
scratch 7-3 tangential load
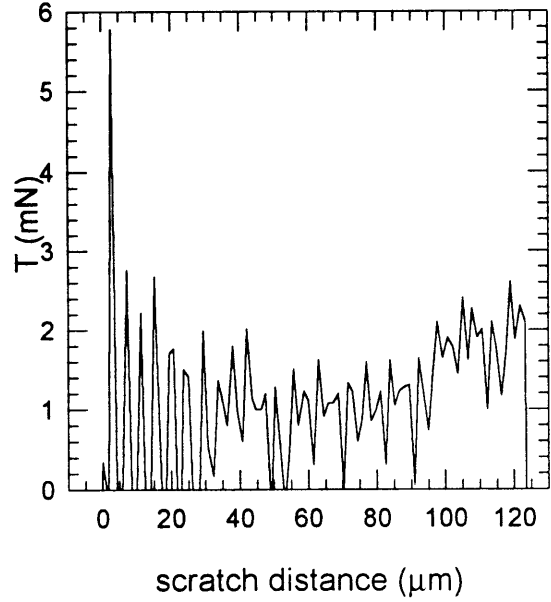
scratch 7-3 scratch depth
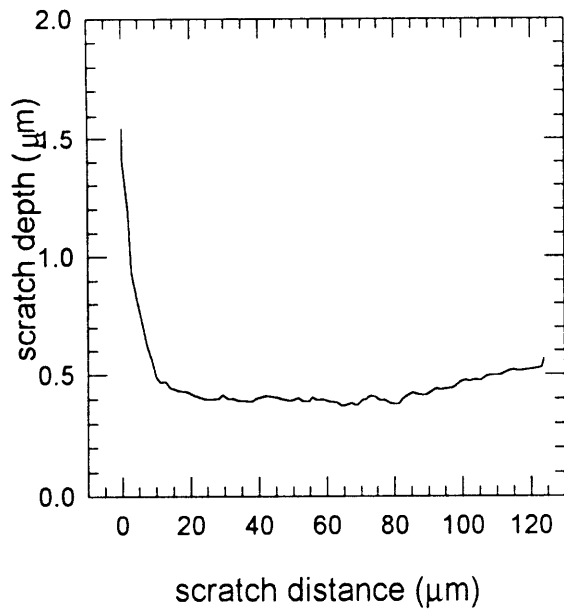
scratch 7-3 friction
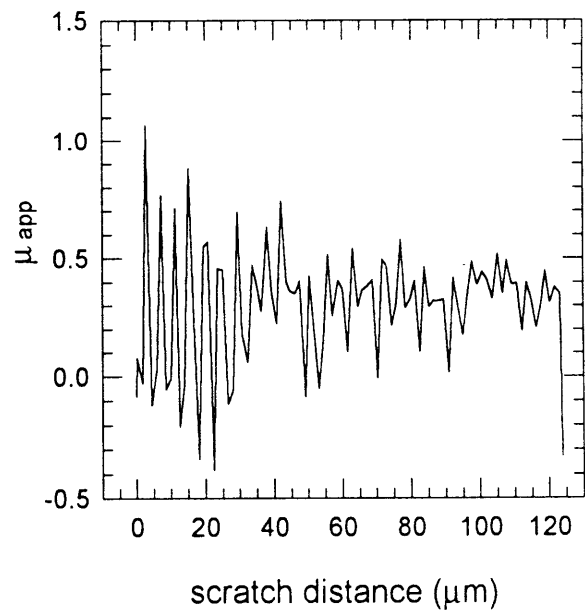
scratch 7-4 normal load
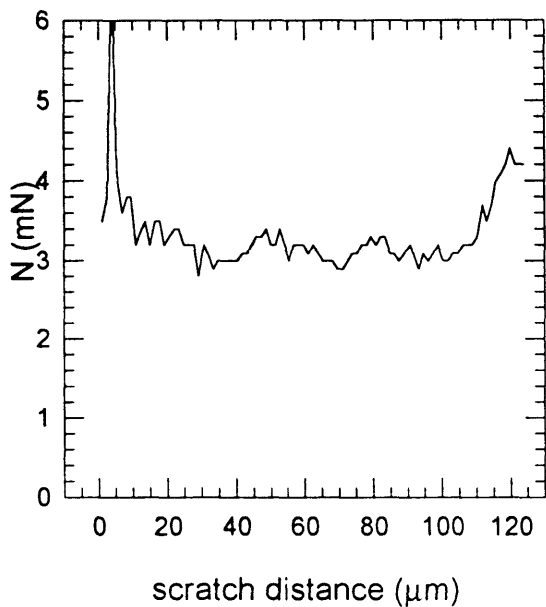
scratch 7-4 tangential load
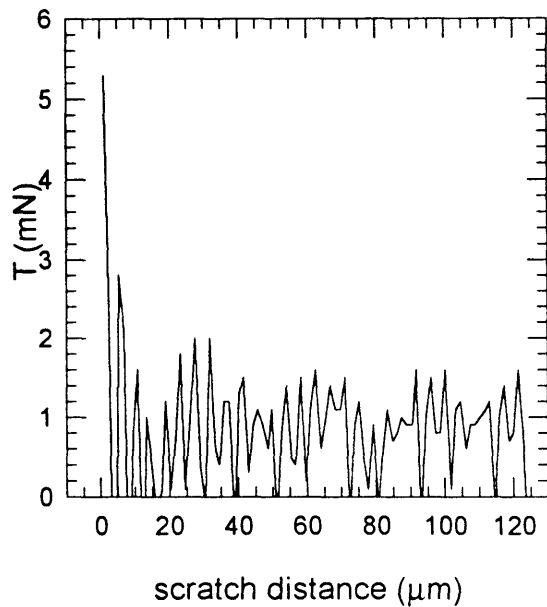
scratch 7-4 scratch depth
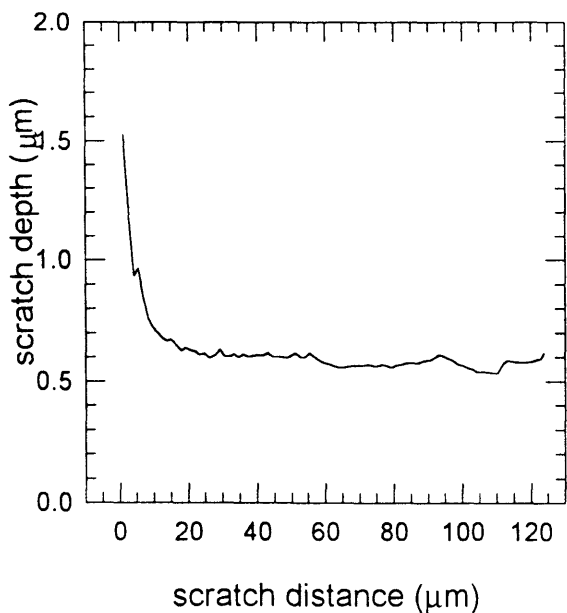
scratch 7-4 friction
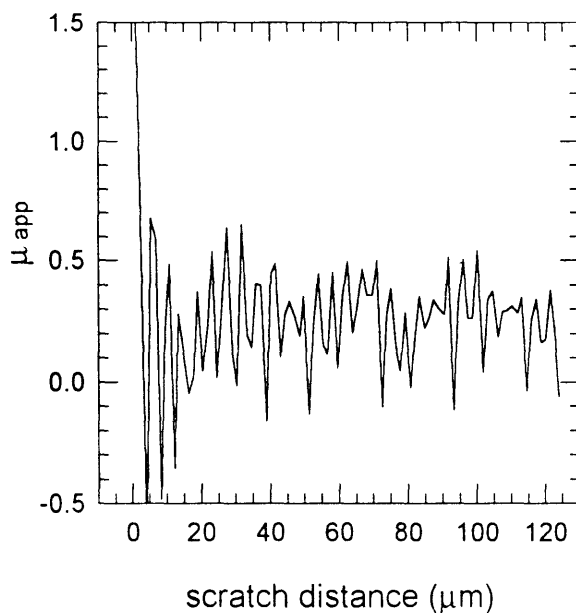
scratch 7-5 normal load
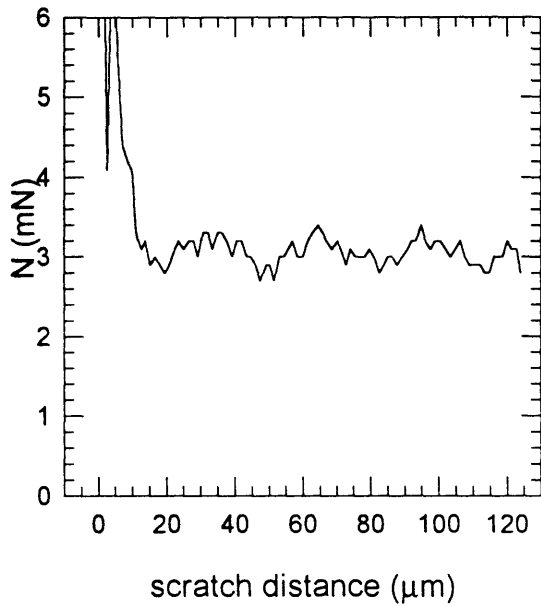
scratch 7-5 tangential load
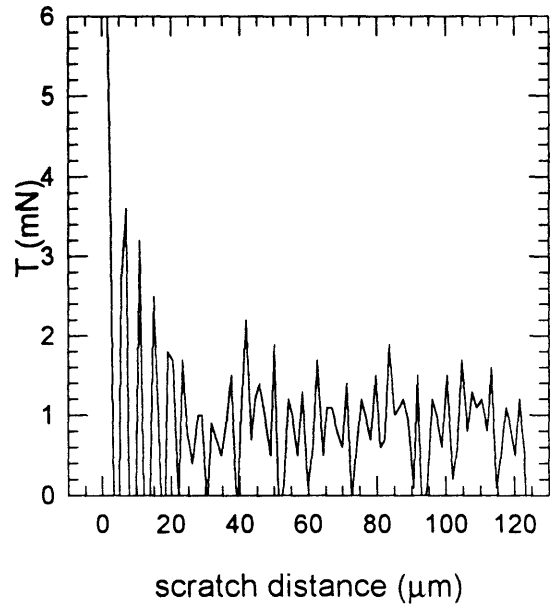
scratch 7-5 scratch depth
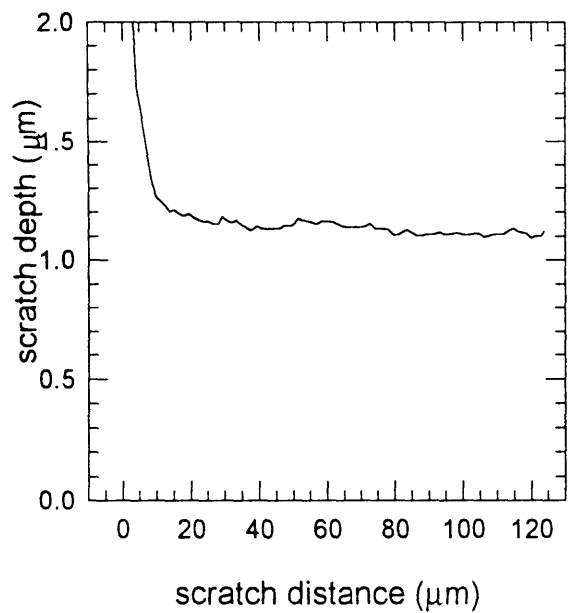
scratch 7-5 friction
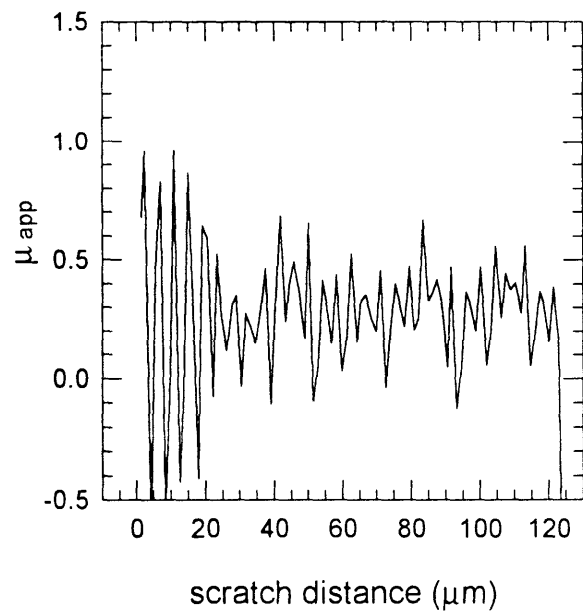
scratch 7-6 normal load
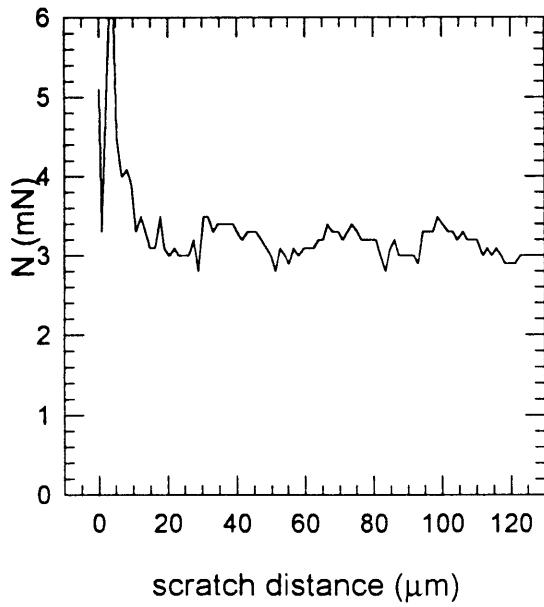
scratch 7-6 tangential load
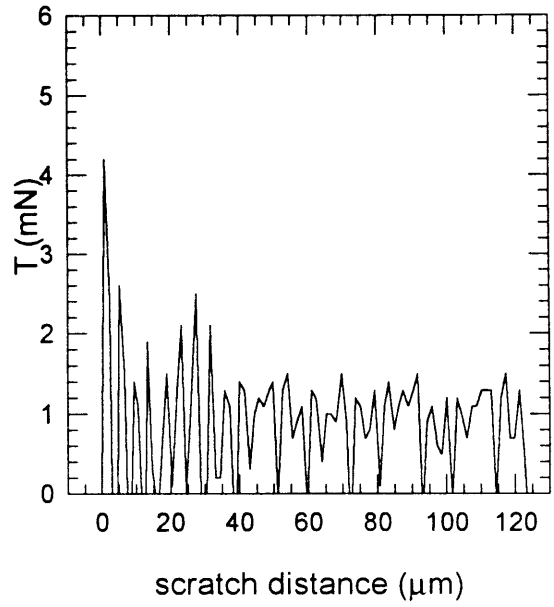
scratch 7-6 scratch depth
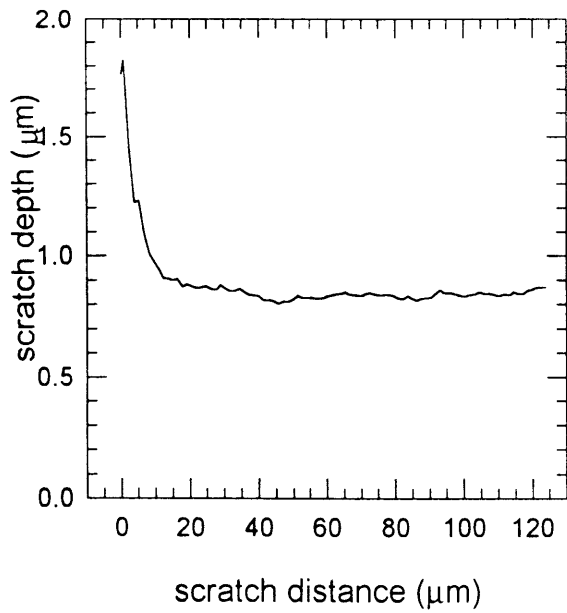
scratch 7-6 friction
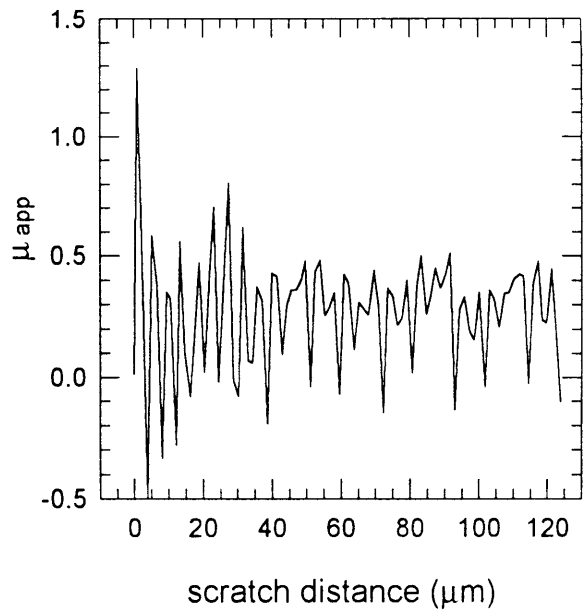
scratch 7-7 normal load
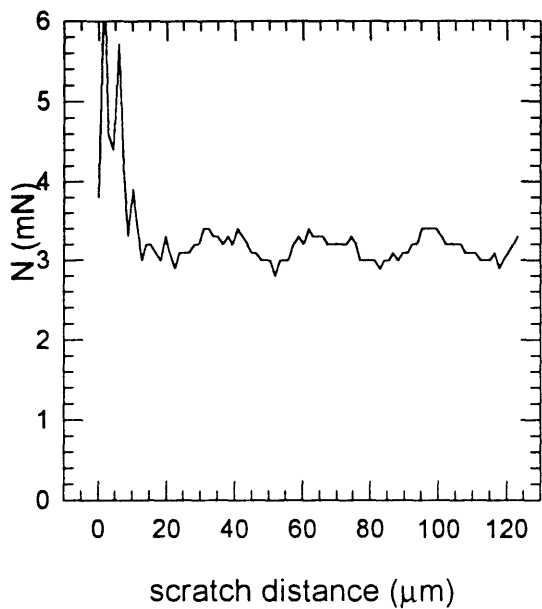
scratch 7-7 tangential load
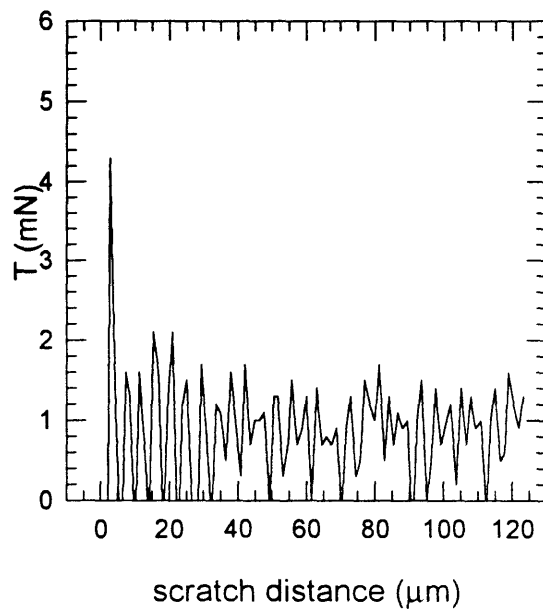
scratch 7-7 scratch depth
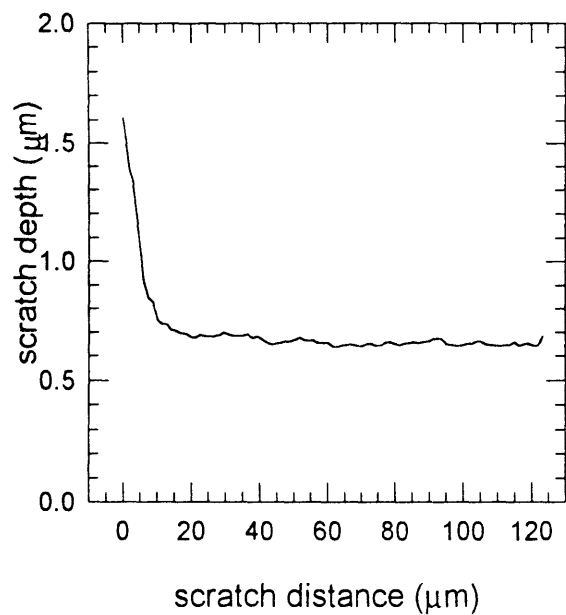
scratch 7-7 friction
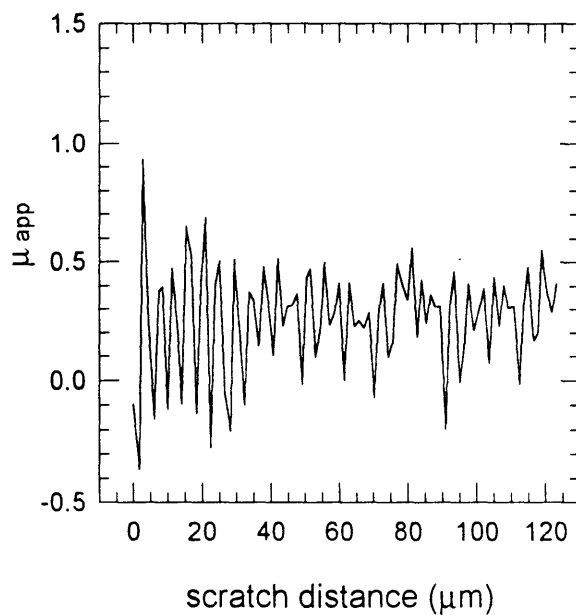
scratch 7-8 normal load
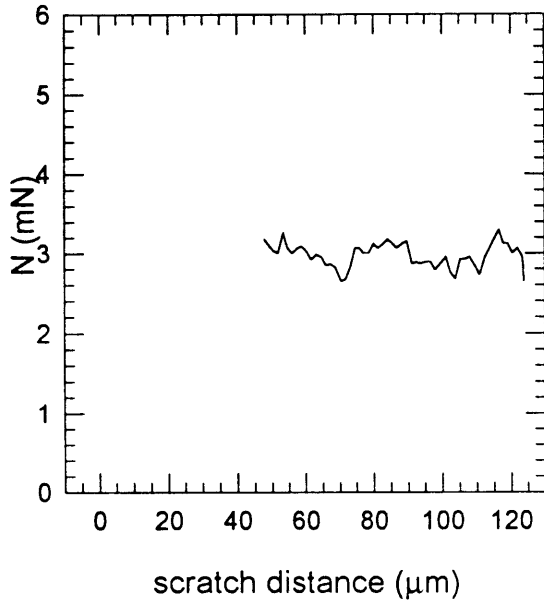
scratch 7-8 tangential load
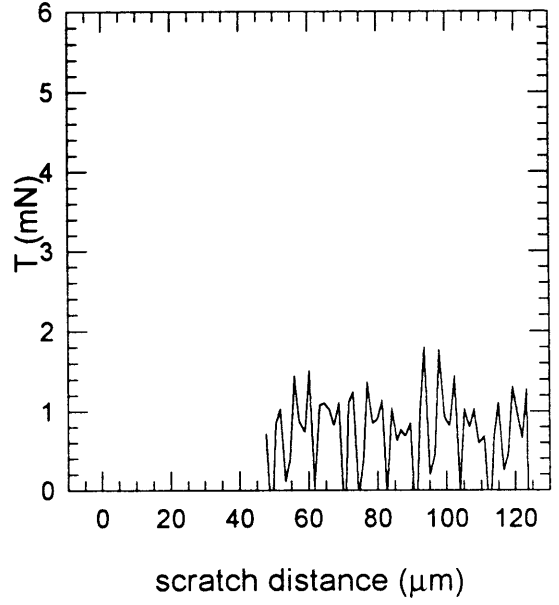
scratch 7-8 scratch depth
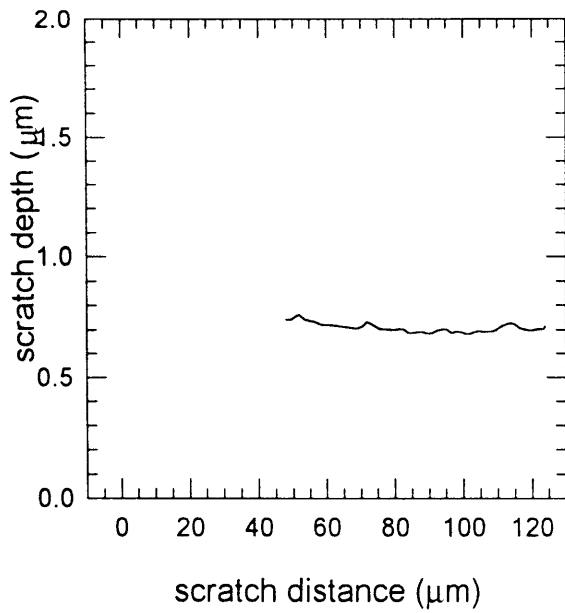
scratch 7-8 friction
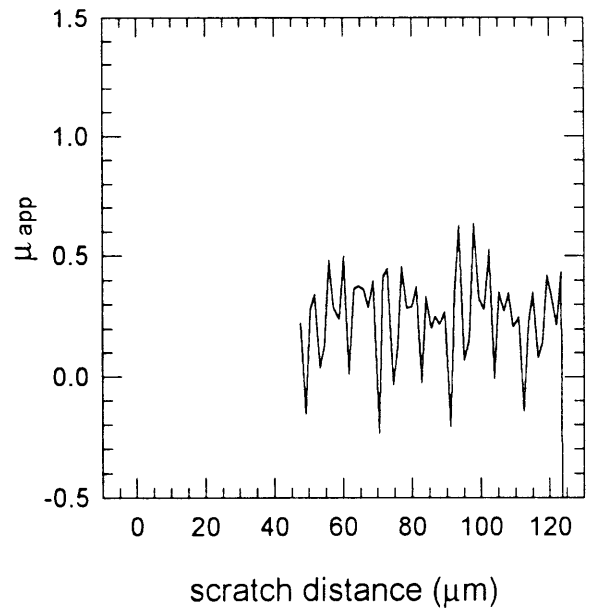
scratch 7-9 normal load
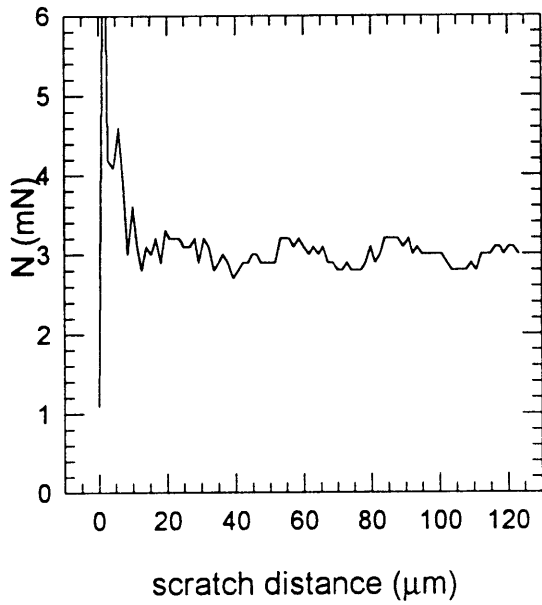
scratch 7-9 tangential load
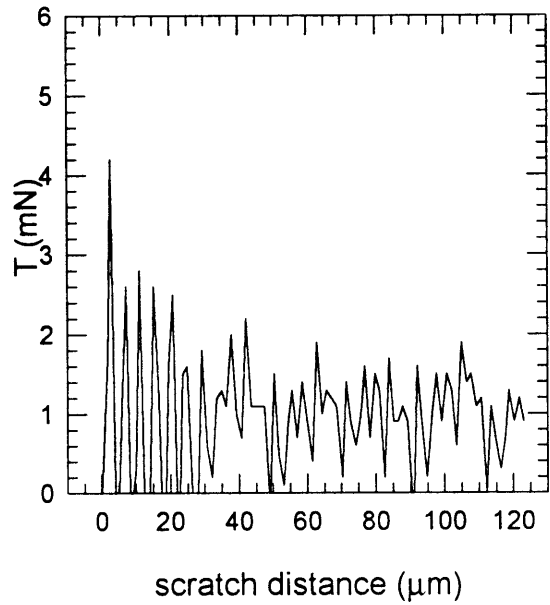
scratch 7-9 scratch depth
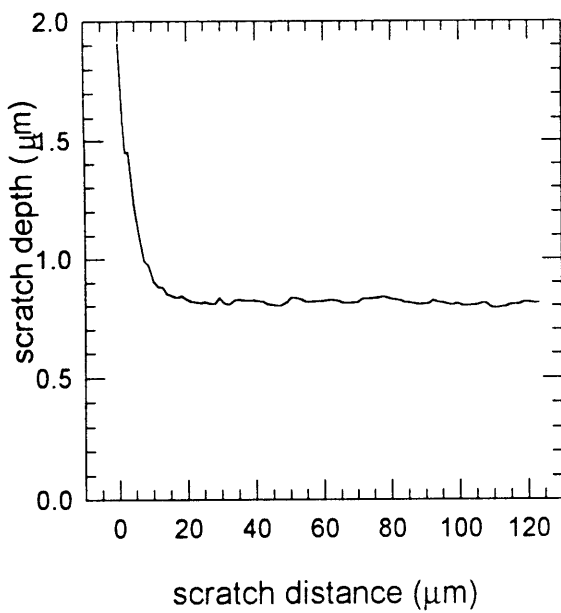
scratch 7-9 friction
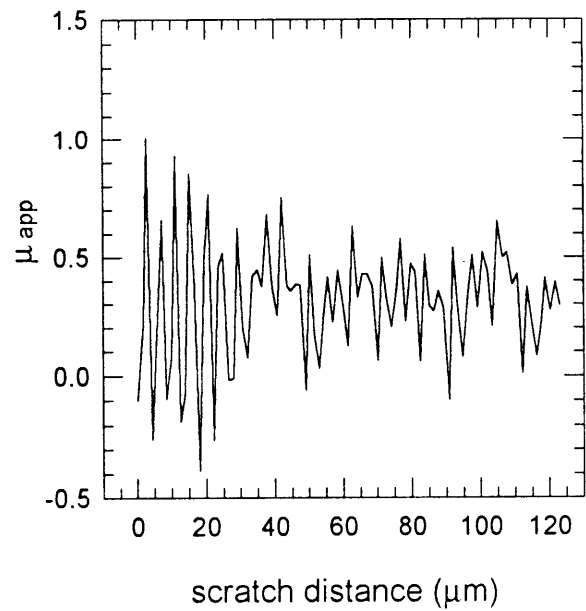
scratch 8-1 normal load
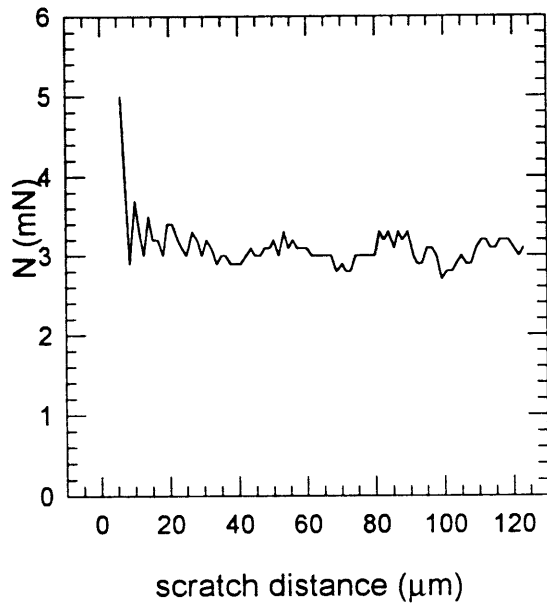
scratch 8-1 tangential load
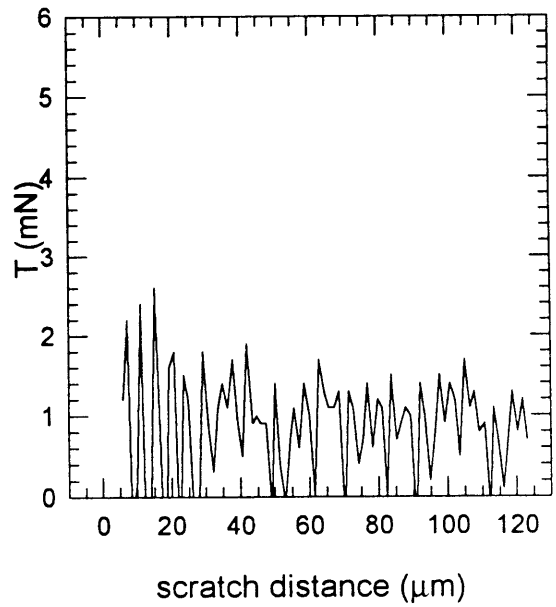
scratch 8-1 scratch depth
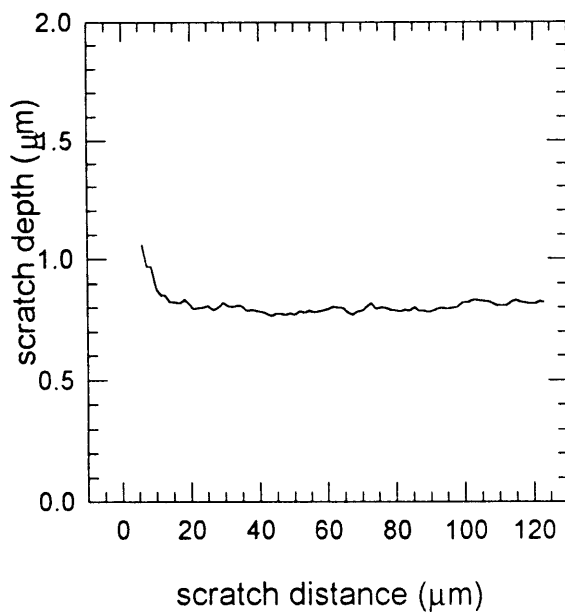
scratch 8-1 friction
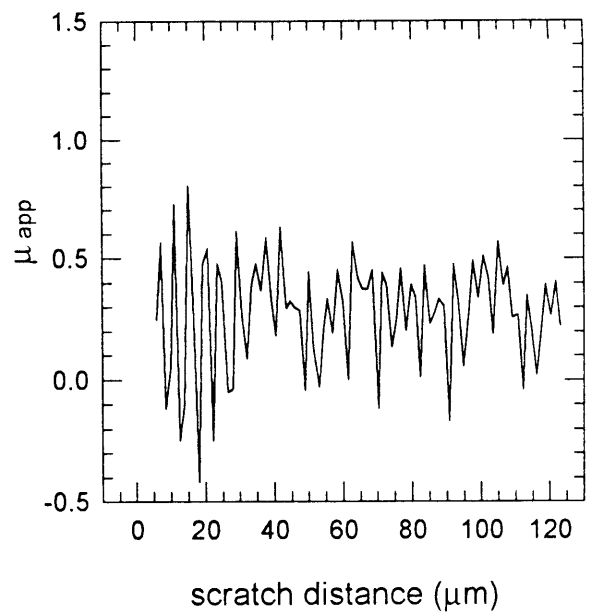
scratch 8-2 normal load
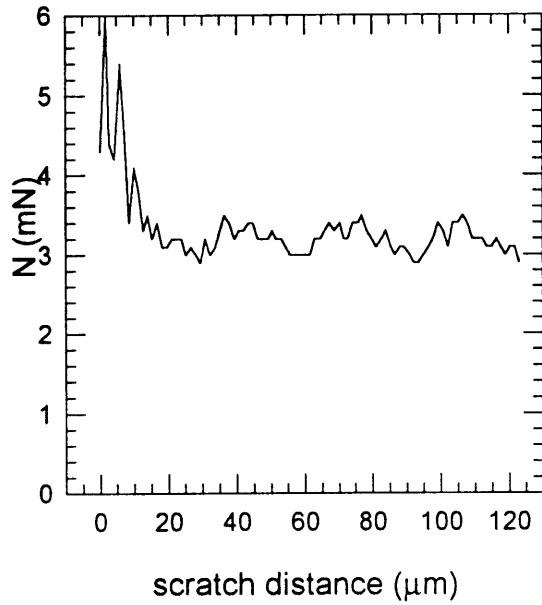
scratch 8-2 tangential load
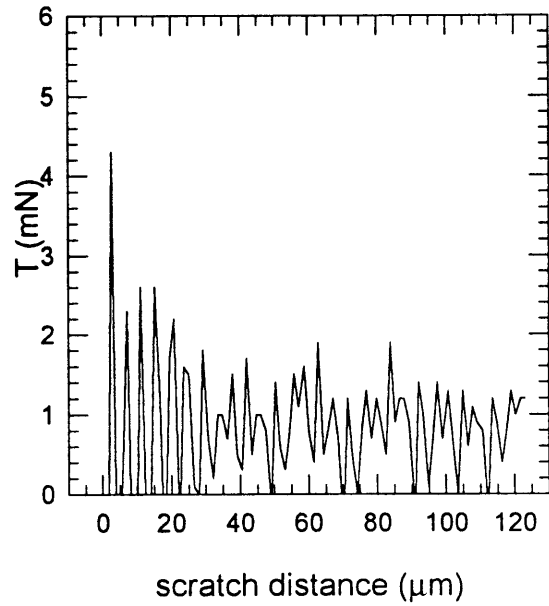
scratch 8-2 scratch depth
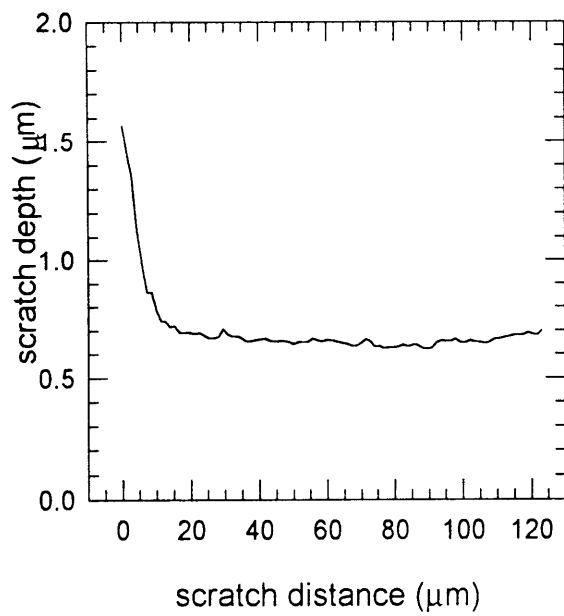
scratch 8-2 friction
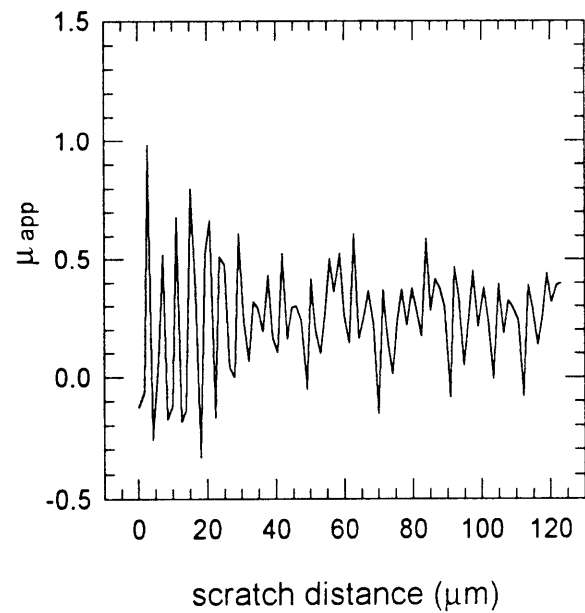
scratch 8-3 normal load
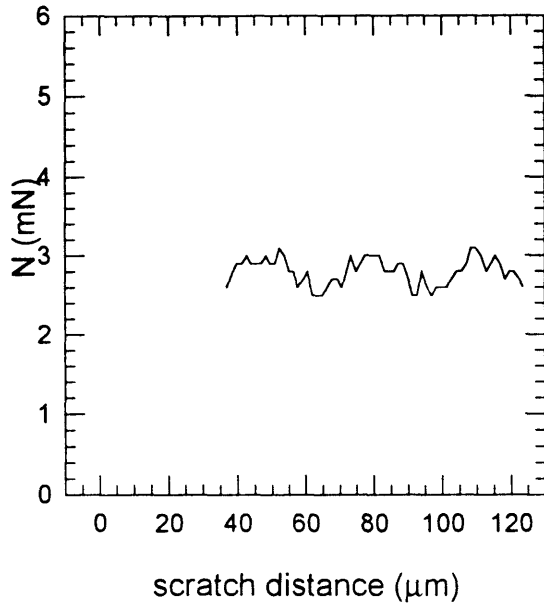
scratch 8-3 tangential load
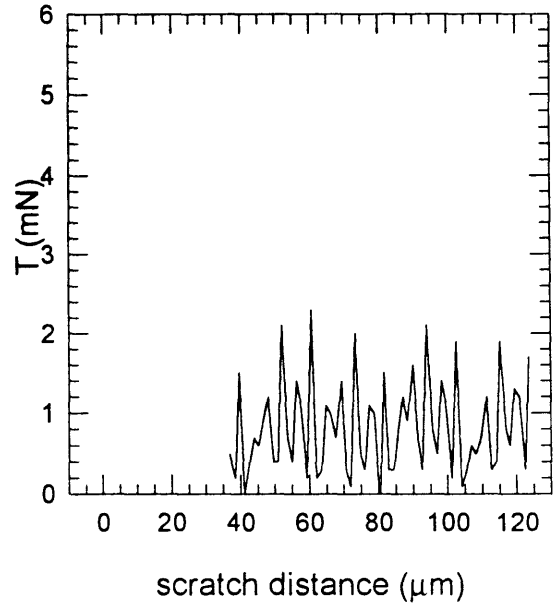
scratch 8-3 scratch depth
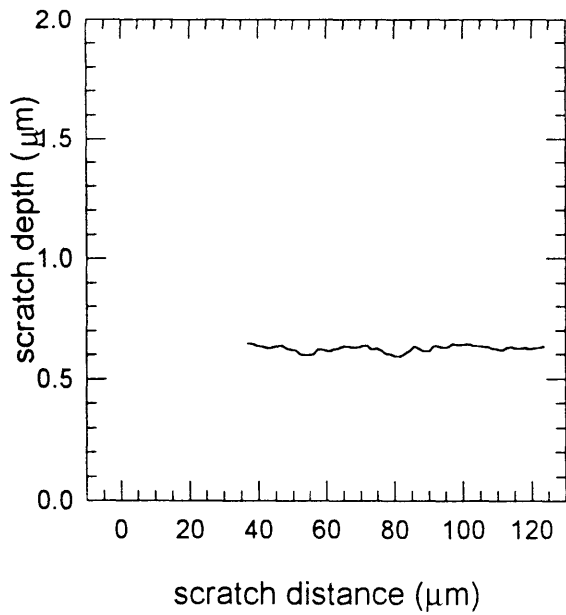
scratch 8-3 friction
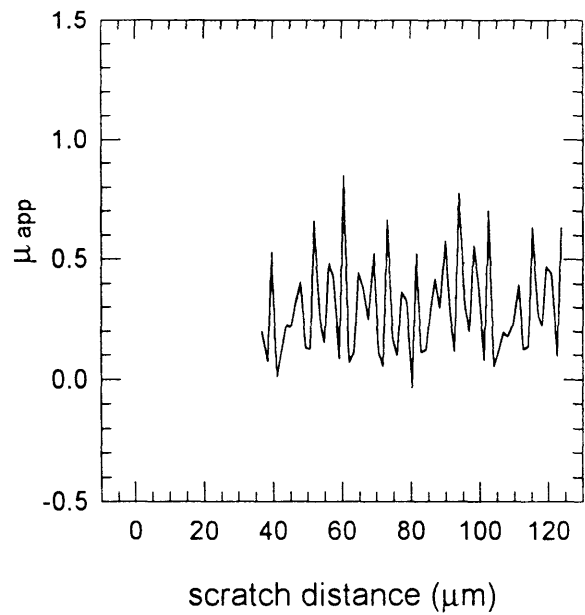
scratch 8-4 normal load
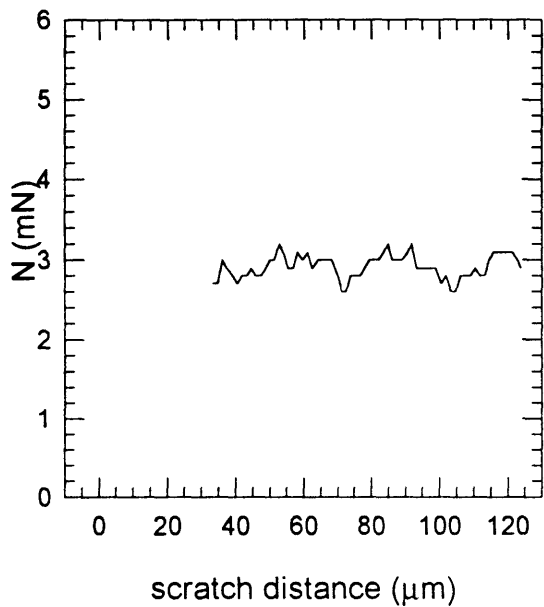
scratch 8-4 tangential load
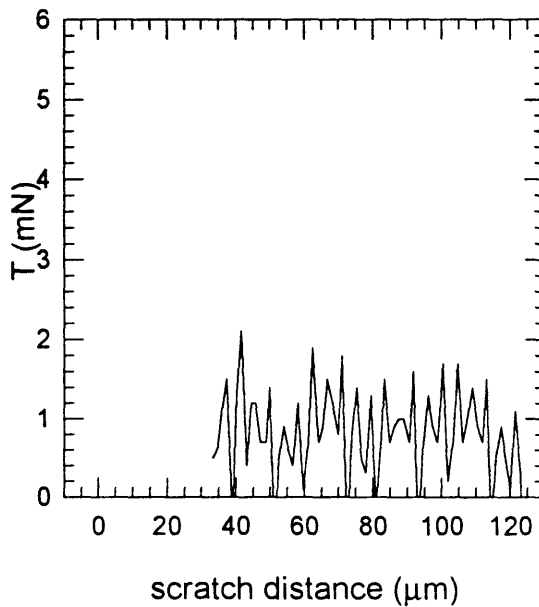
scratch 8-4 scratch depth
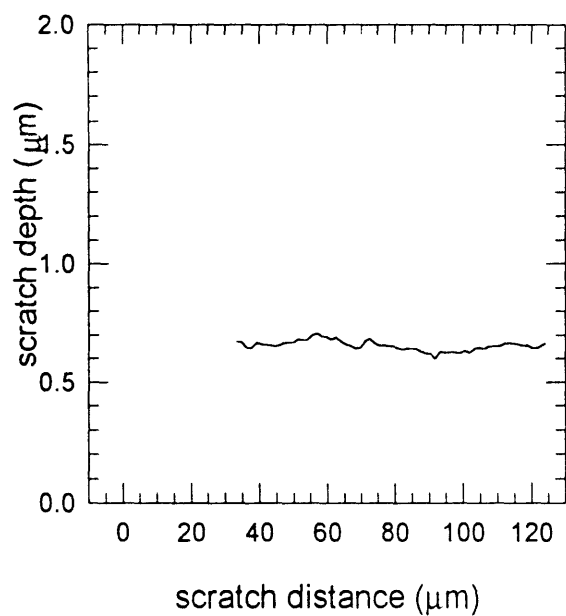
scratch 8-4 friction
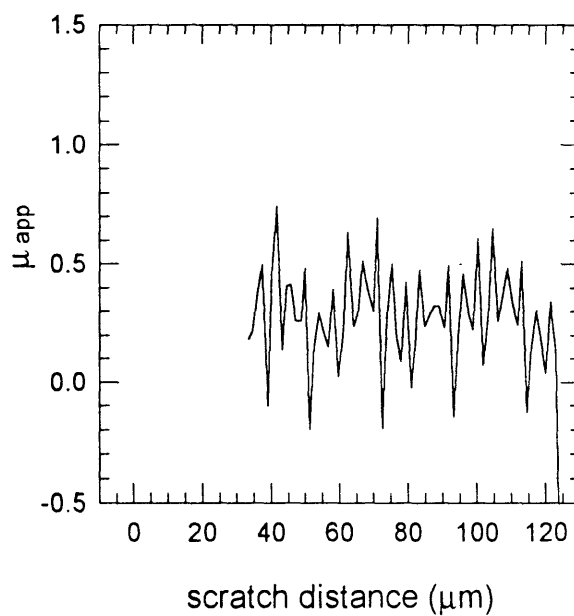
scratch 8-5 normal load
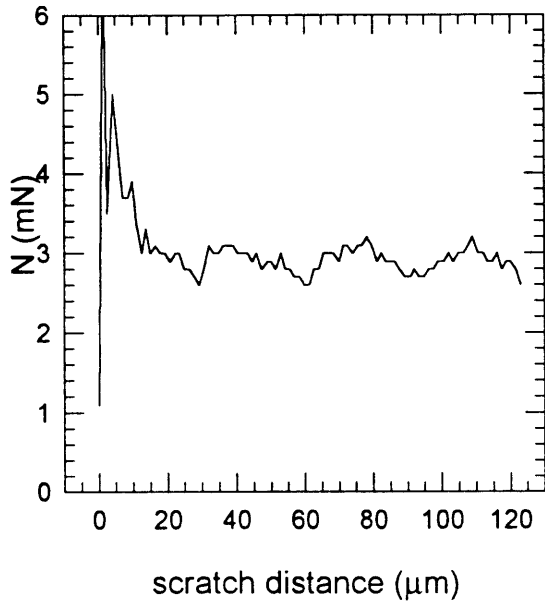
scratch 8-5 tangential load
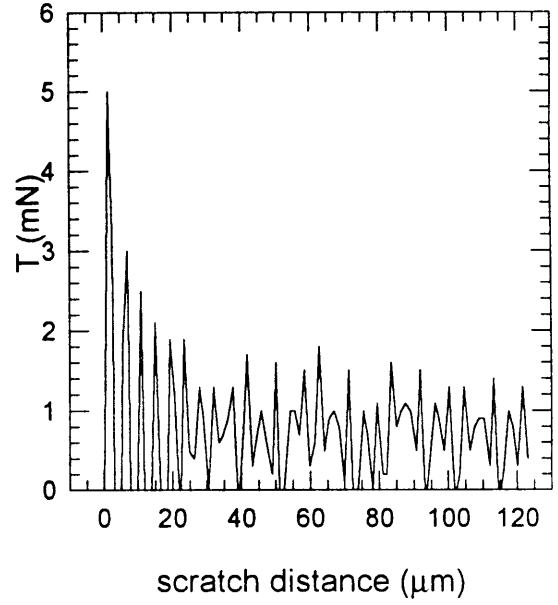
scratch 8-5 scratch depth
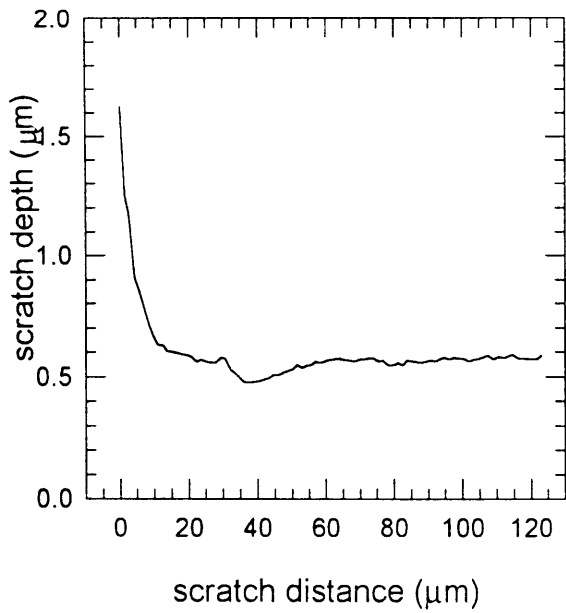
scratch 8-5 friction
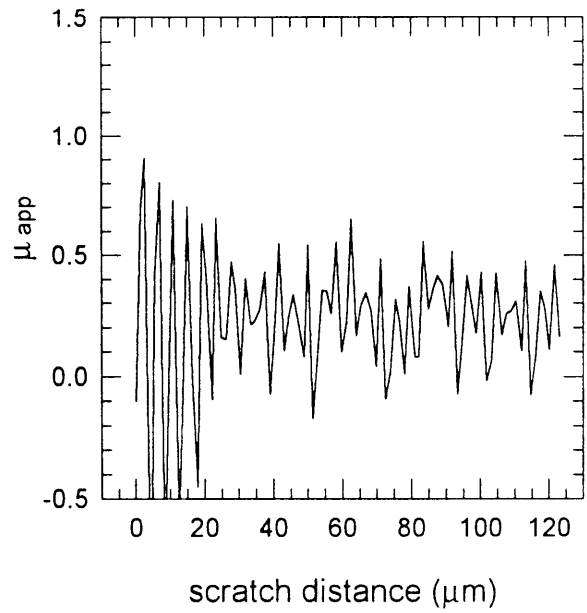
scratch 8-6 normal load
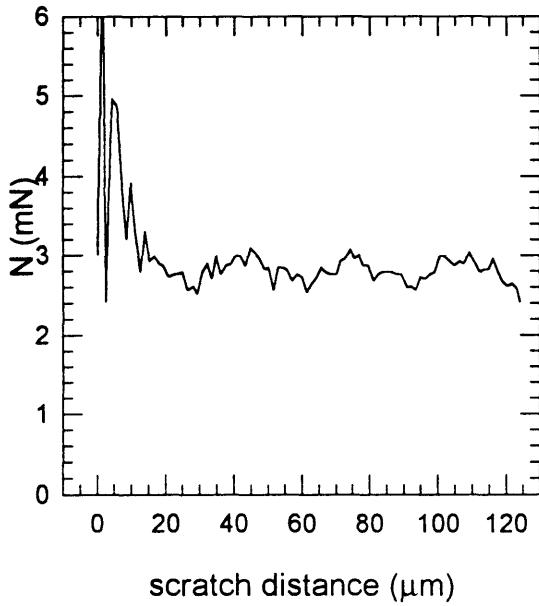
scratch 8-6 tangential load
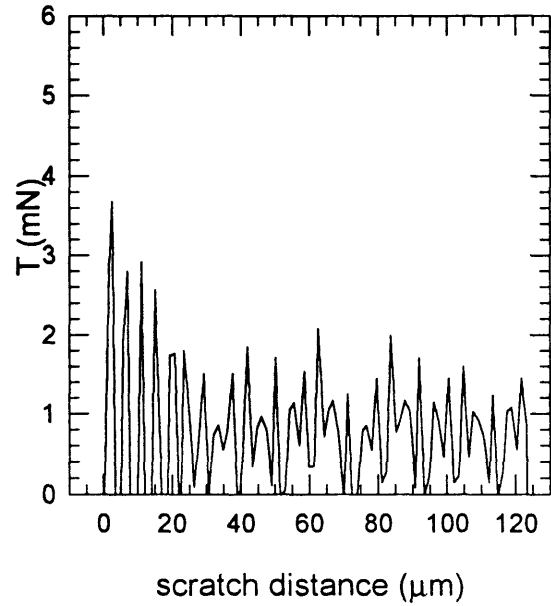
scratch 8-6 scratch depth
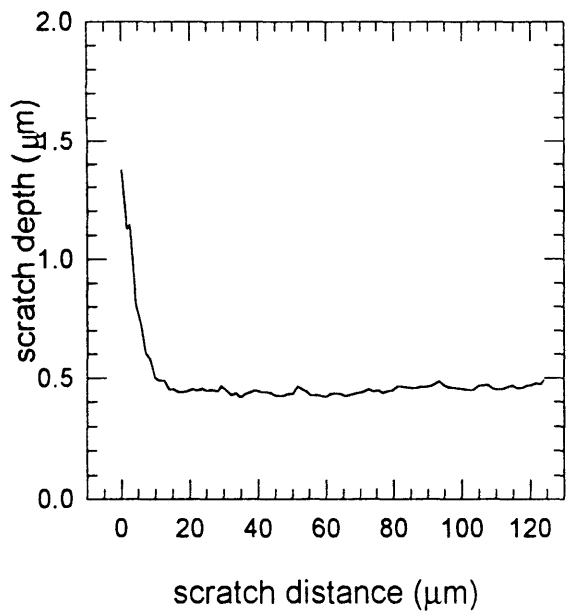
scratch 8-6 friction
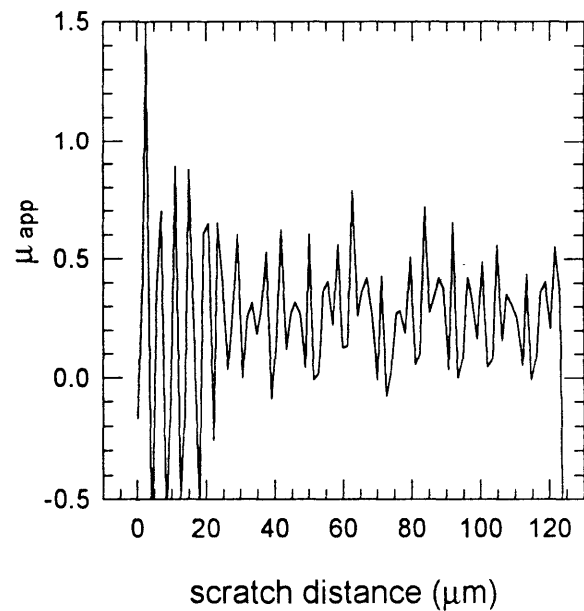
scratch 8-7 normal load
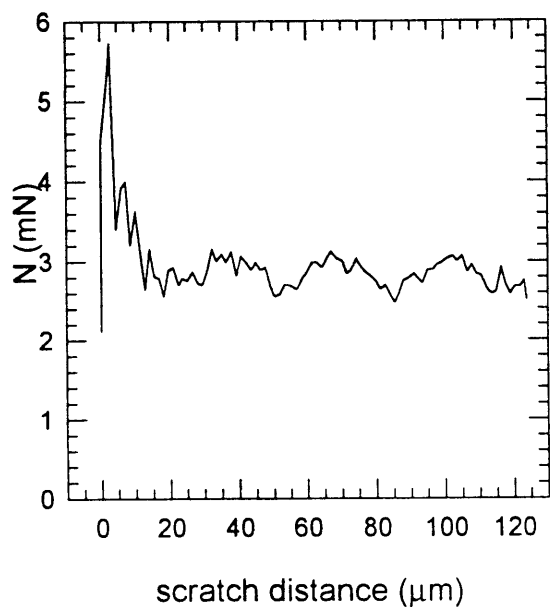
scratch 8-7 tangential load
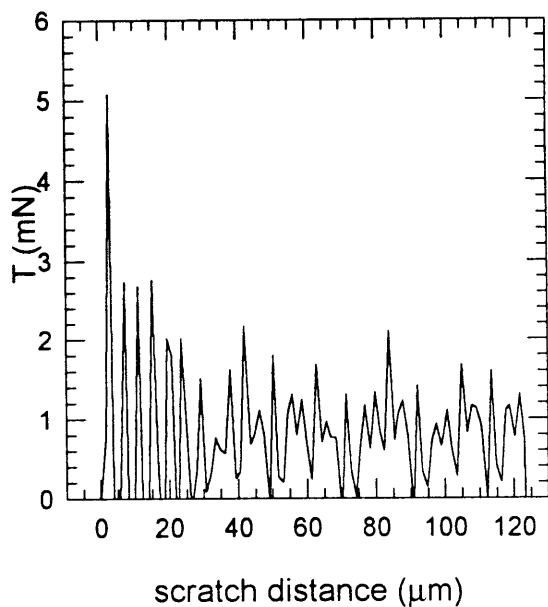
scratch 8-7 scratch depth
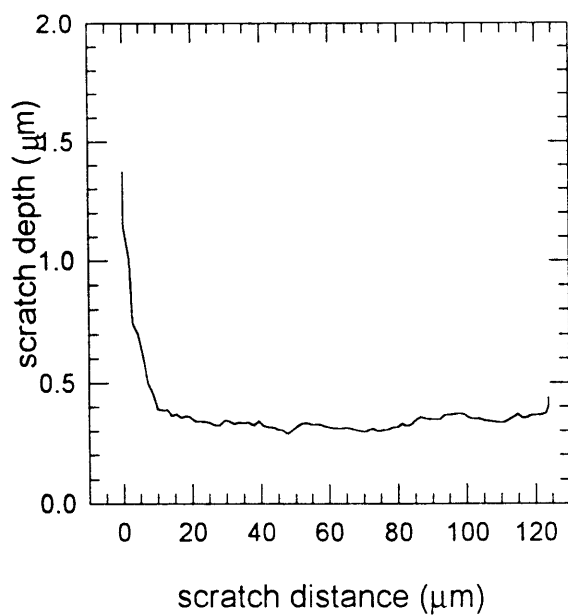
scratch 8-7 friction
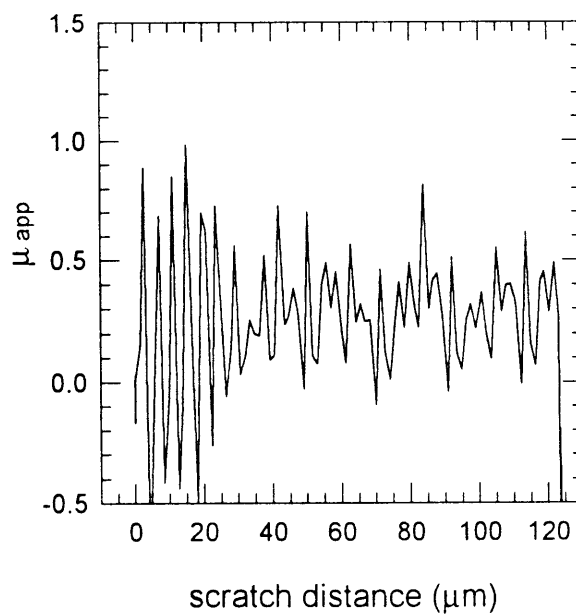
scratch 8-8 normal load
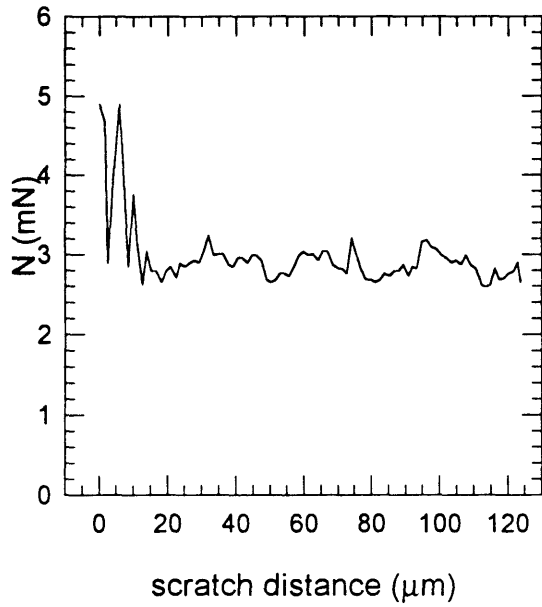
scratch 8-8 tangential load
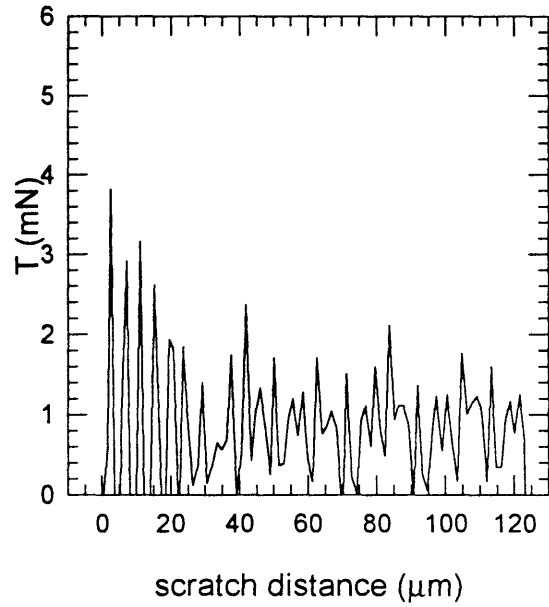
scratch 8-8 scratch depth
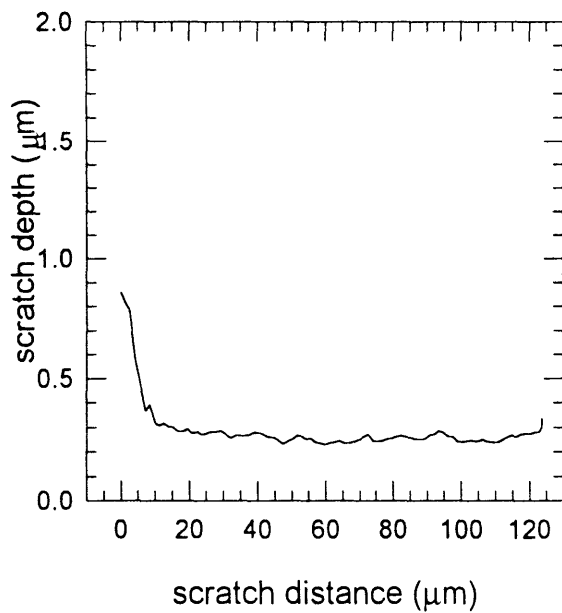
scratch 8-8 friction
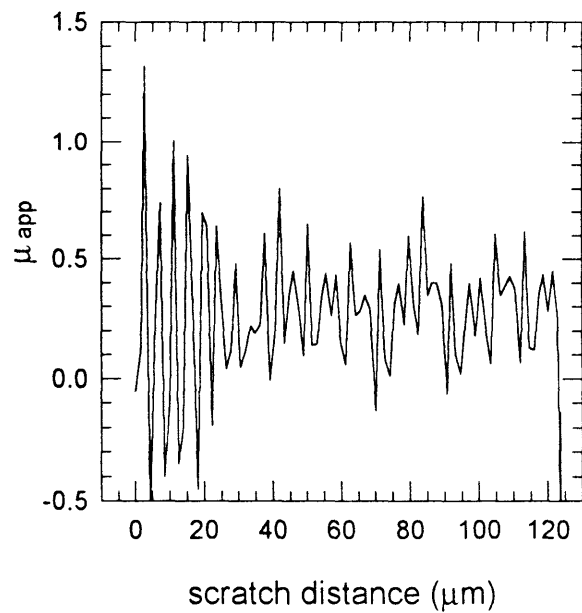
scratch 8-9 normal load
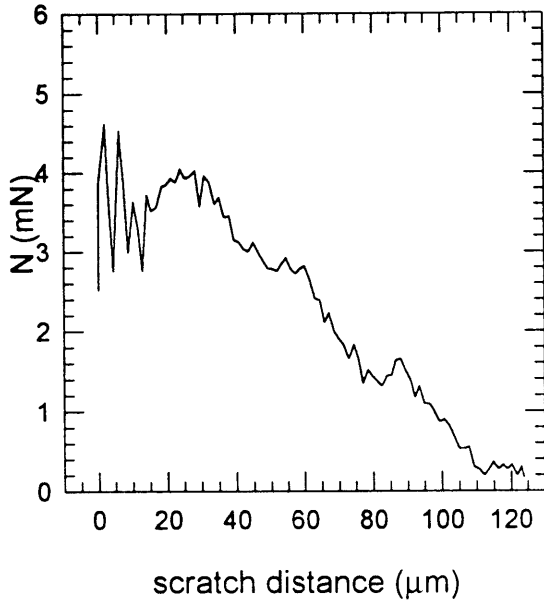
scratch 8-9 tangential load
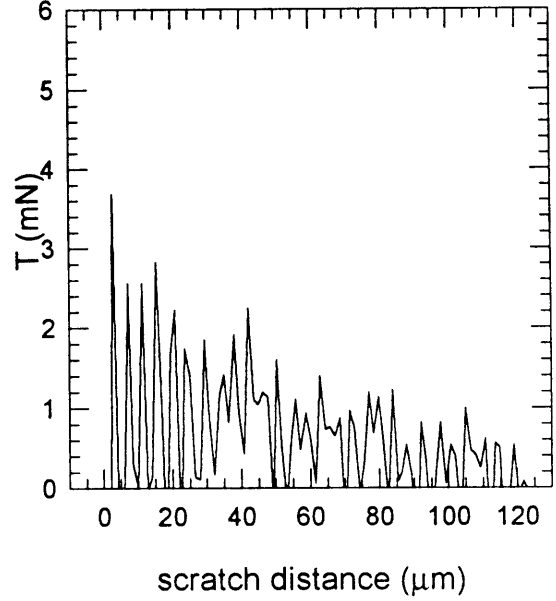
scratch 8-9 scratch depth
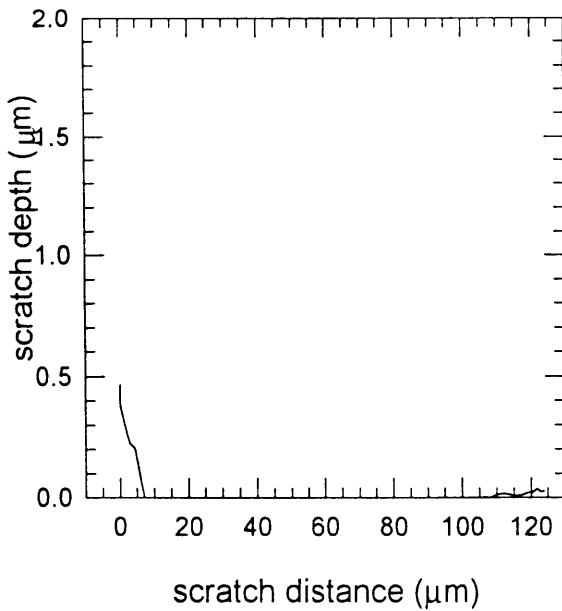
scratch 8-9 friction
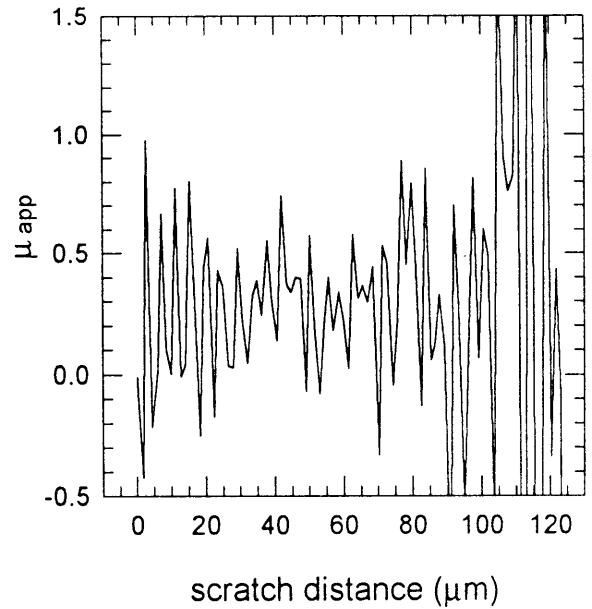
scratch 9-1 normal load
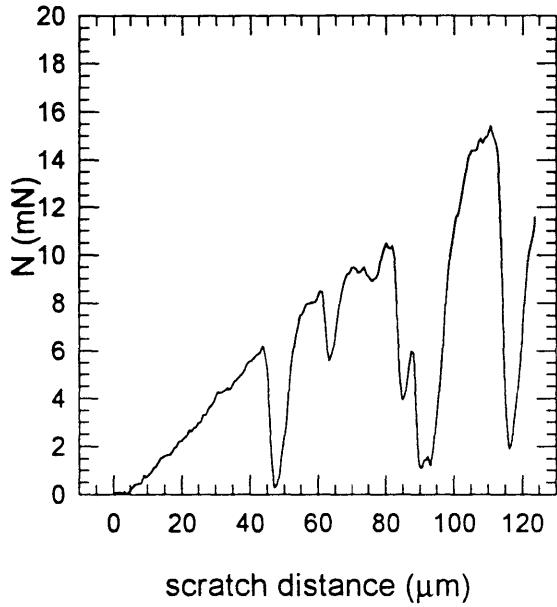
scratch 9-1 tangential load
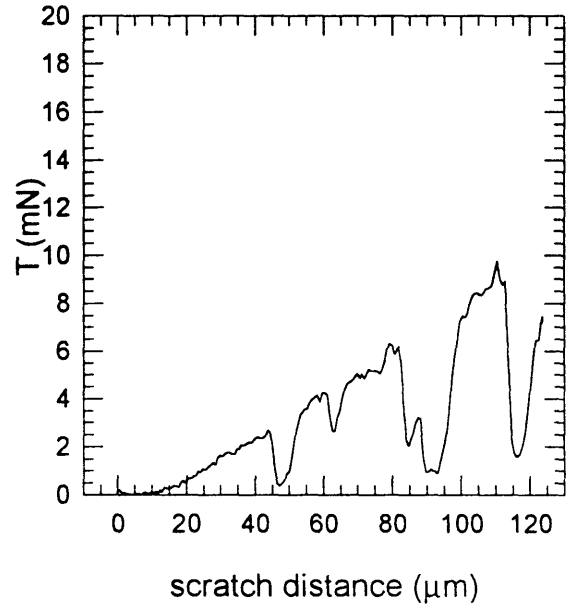
scratch 9-1 scratch depth
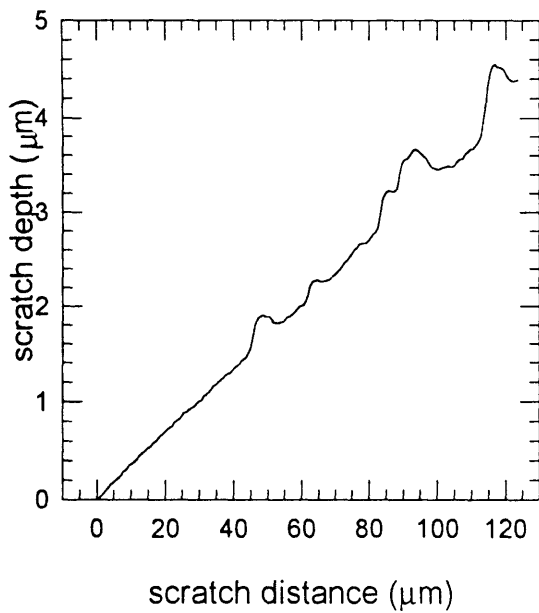
scratch 9-1 friction
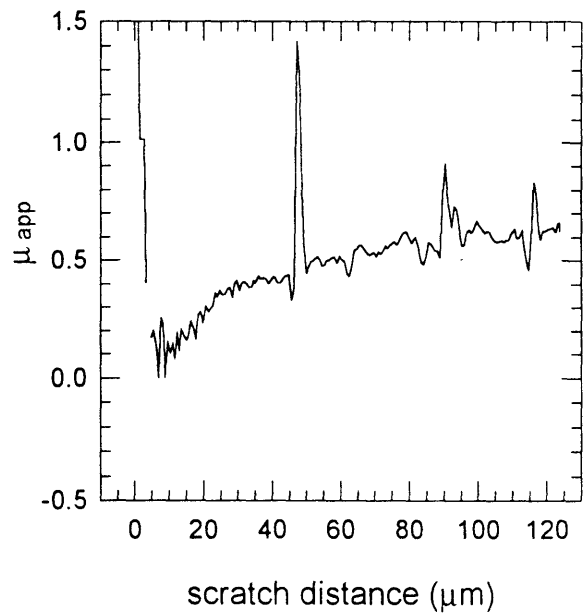
scratch 9-3 normal load
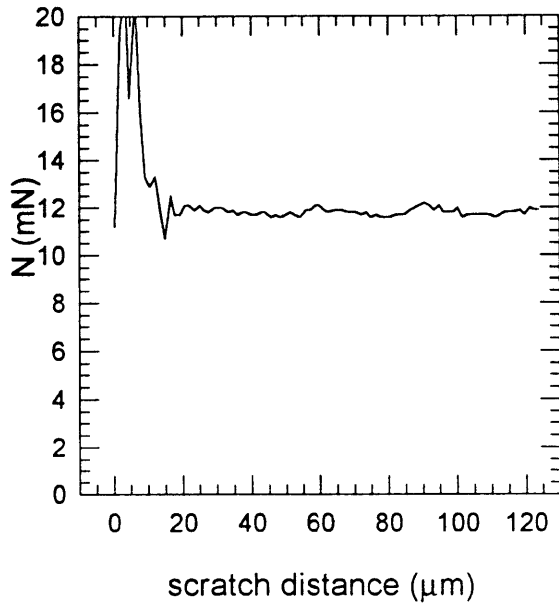
scratch 9-3 tangential load
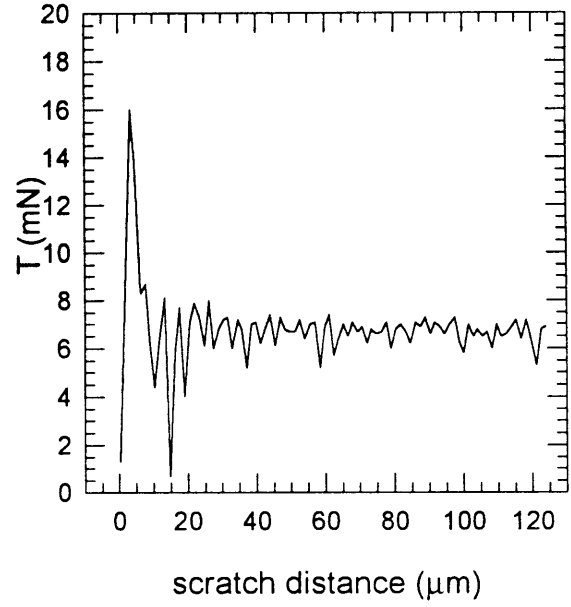
scratch 9-3 scratch depth
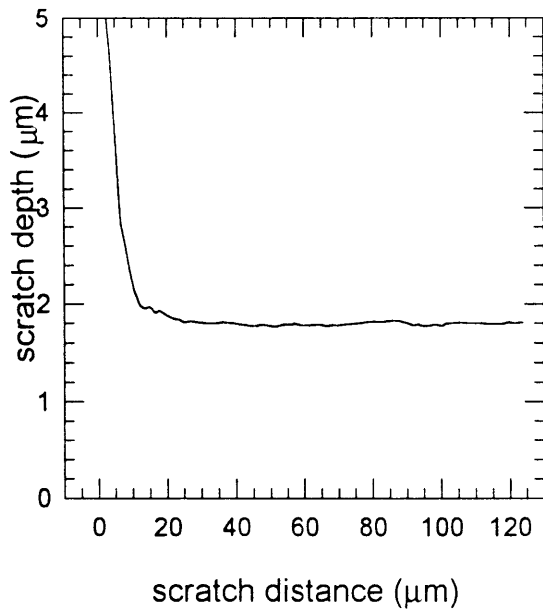
scratch 9-3 friction
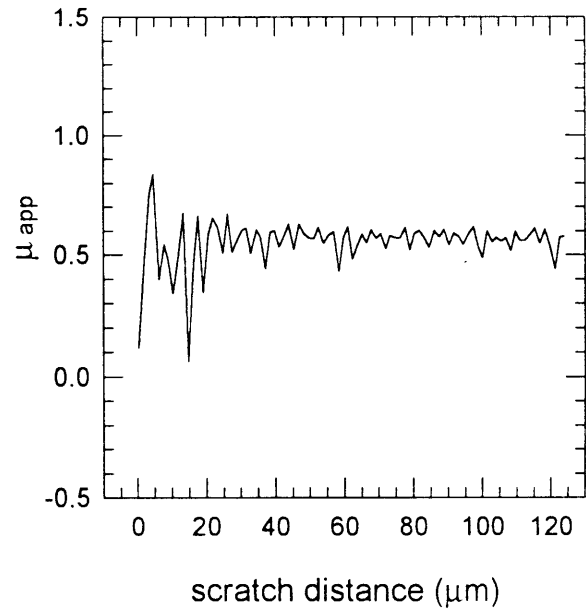
scratch 9-4 normal load
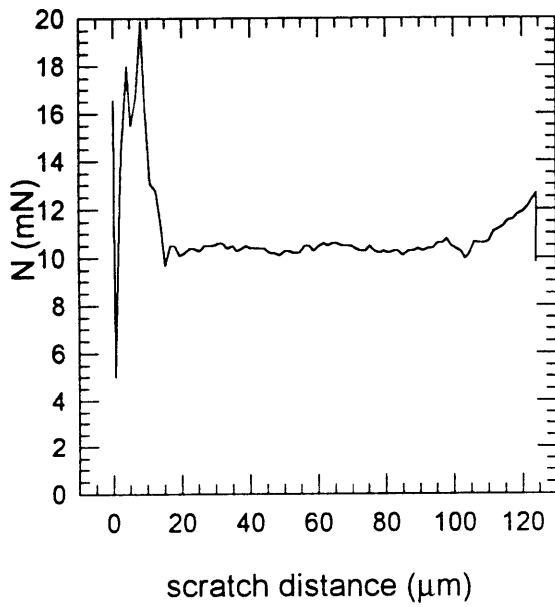
scratch 9-4 tangential load
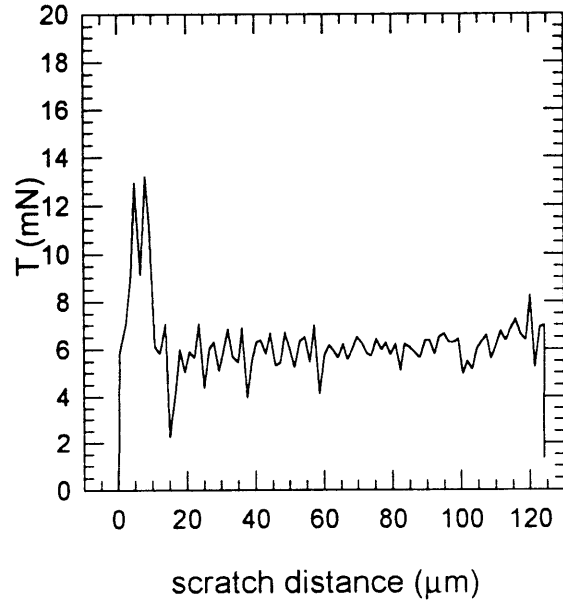
scratch 9-4 scratch depth
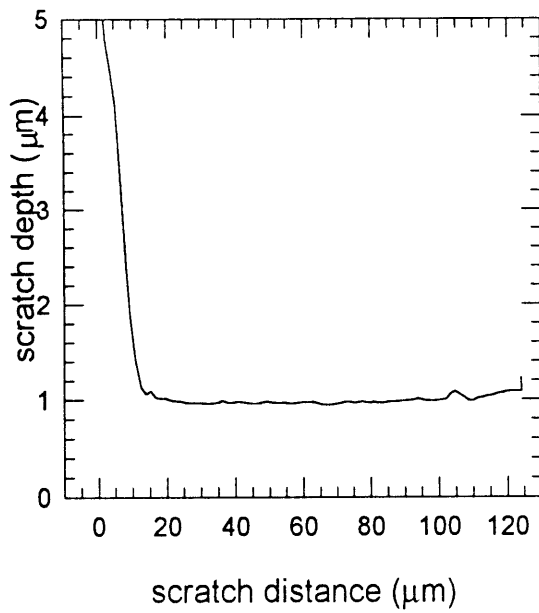
scratch 9-4 friction
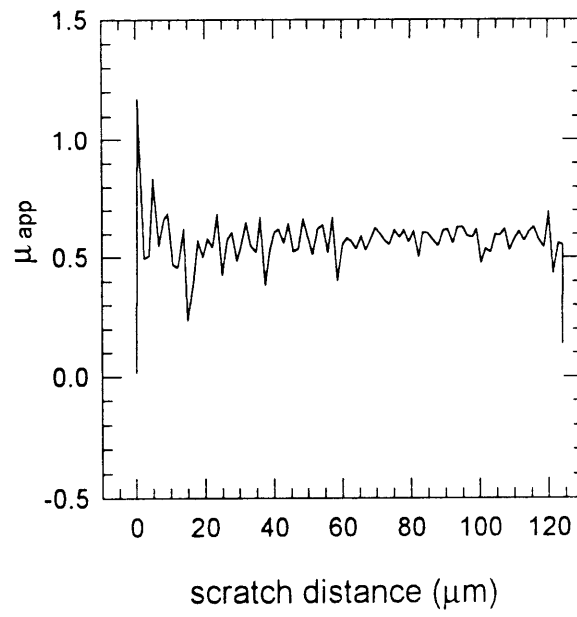
scratch 9-5 normal load
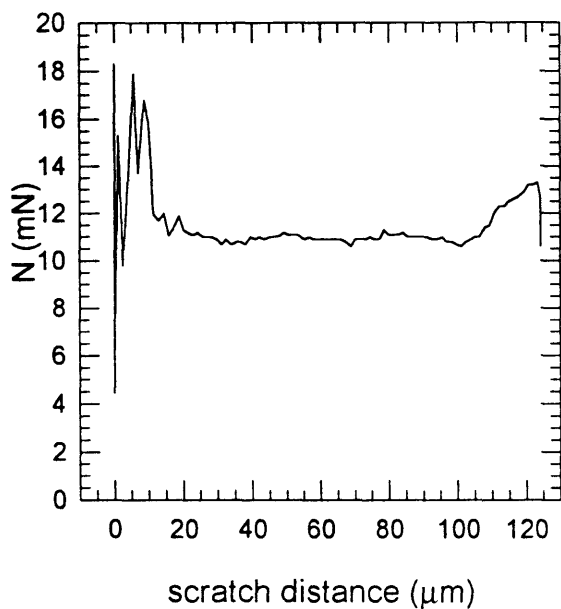
scratch 9-5 tangential load
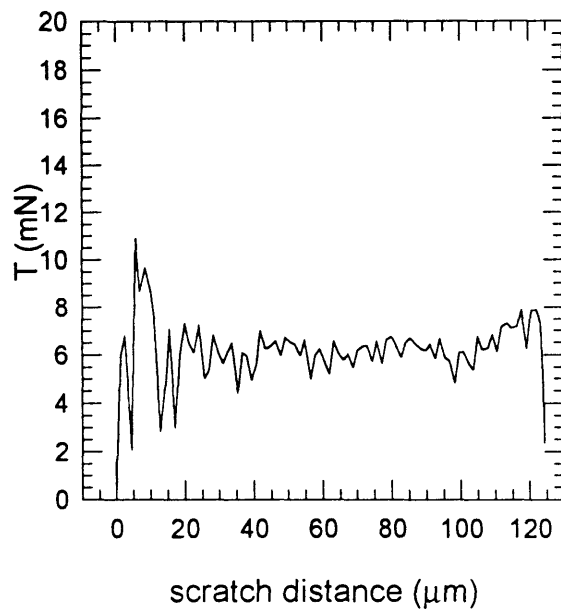
scratch 9-5 scratch depth
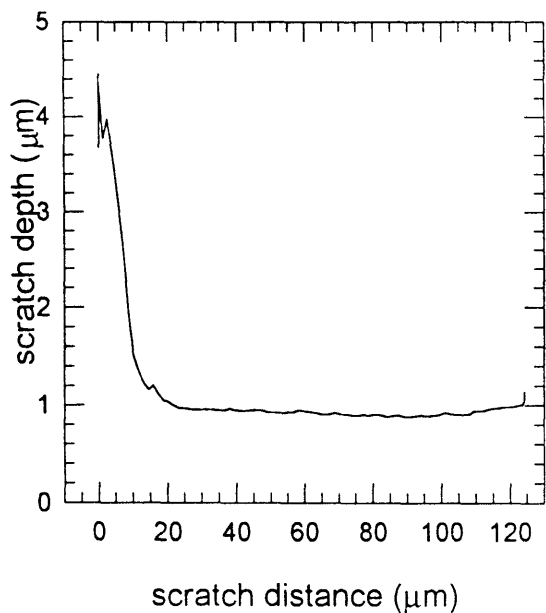
scratch 9-5 friction
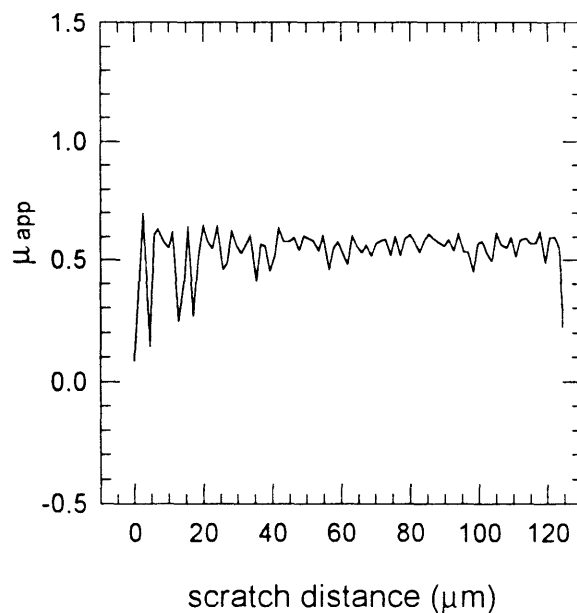
scratch 9-6 normal load
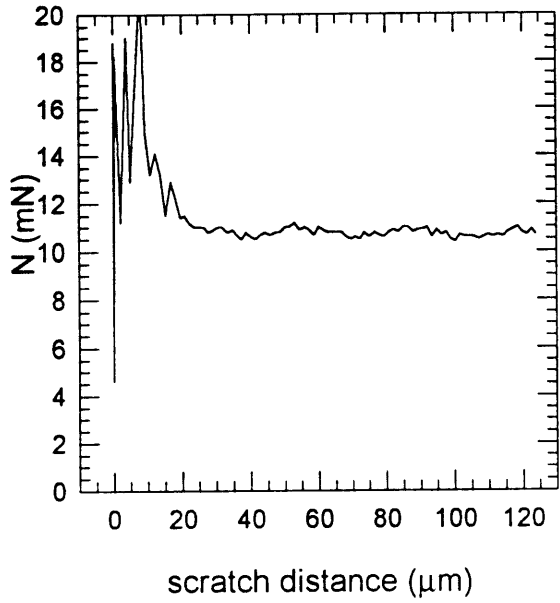
scratch 9-6 tangential load
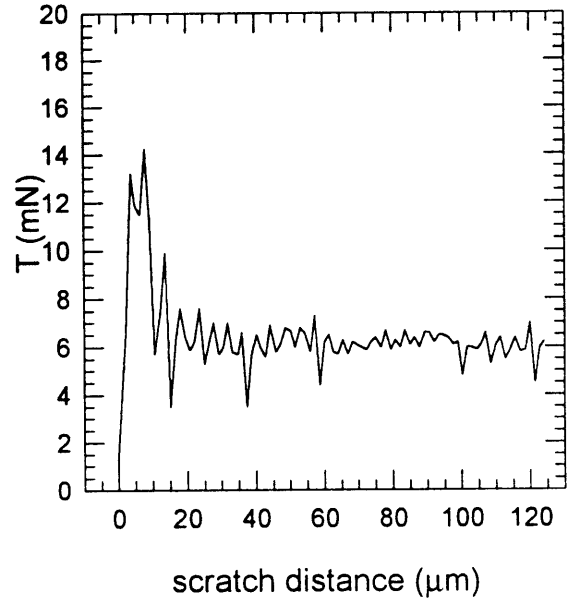
scratch 9-6 scratch depth
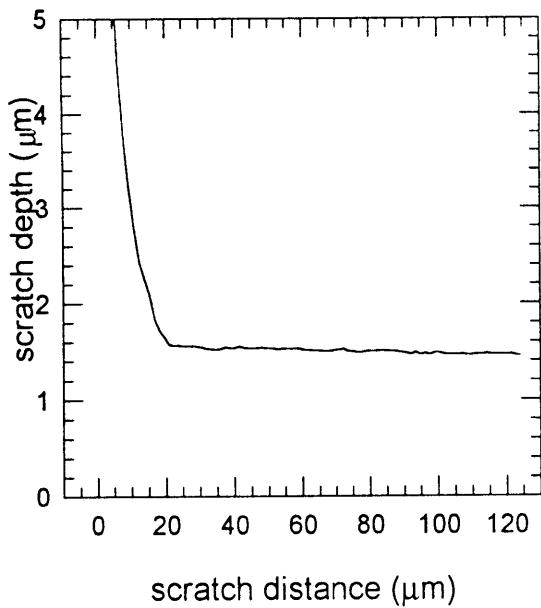
scratch 9-6 friction
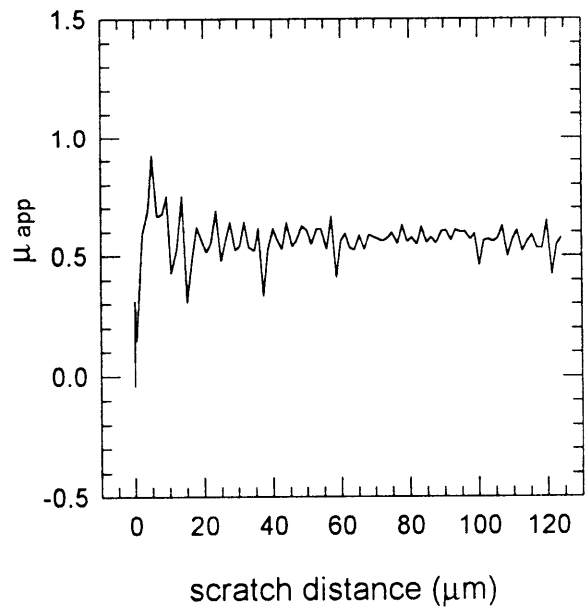
scratch 9-7 normal load
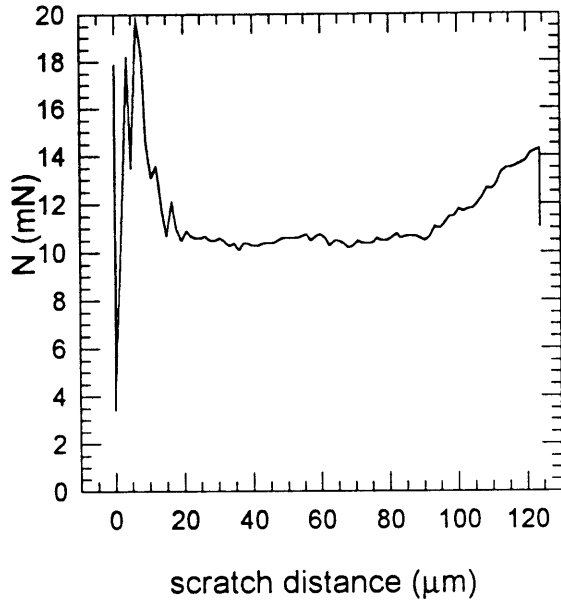
scratch 9-7 tangential load
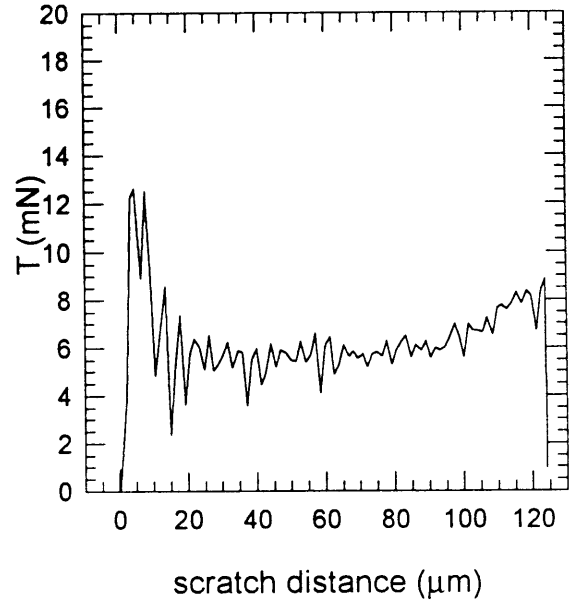
scratch 9-7 scratch depth
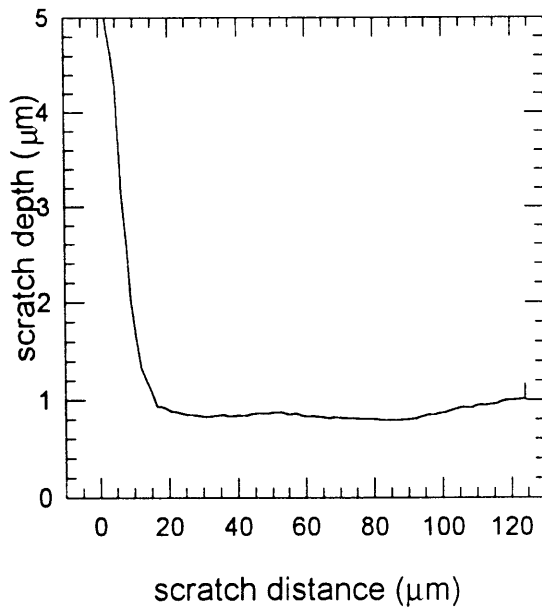
scratch 9-7 friction
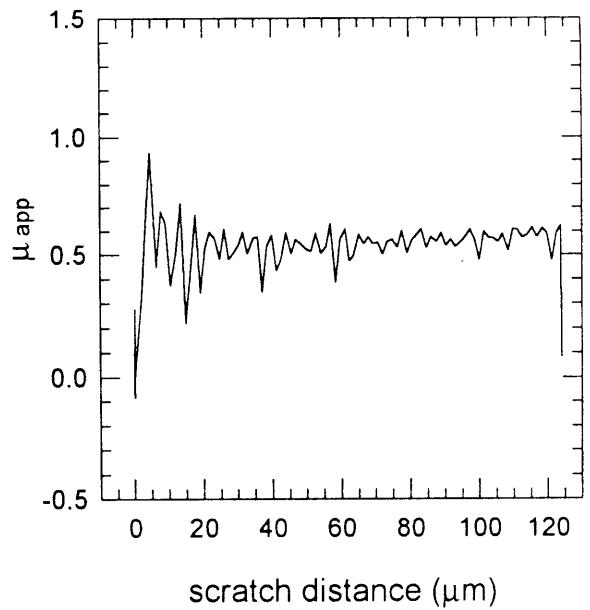
scratch 9-8 normal load
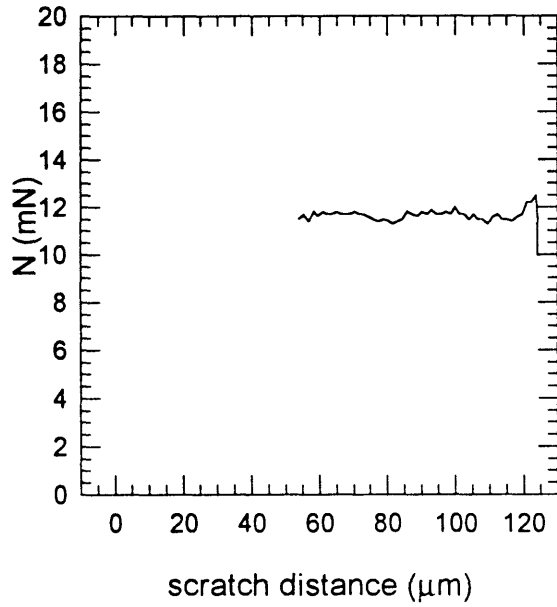
scratch 9-8 tangential load
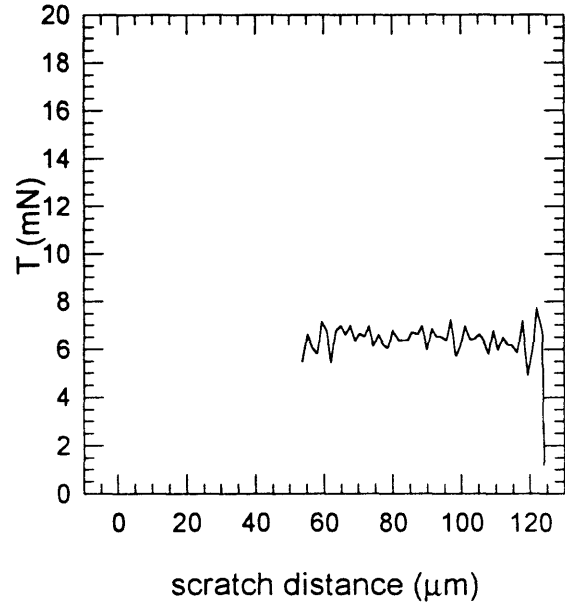
scratch 9-8 scratch depth
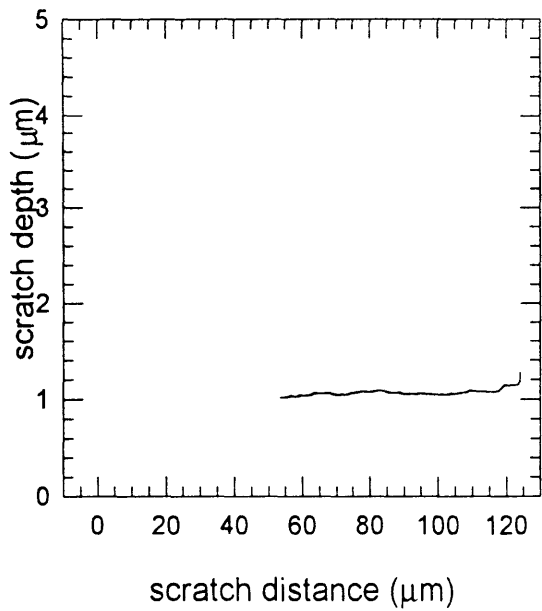
scratch 9-8 friction
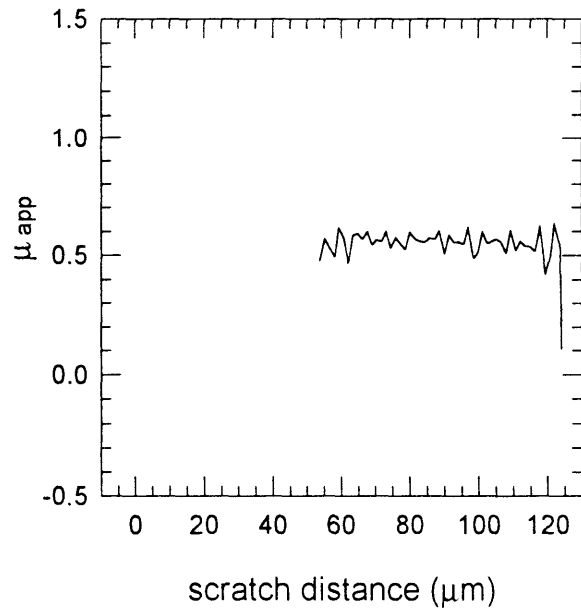
scratch 9-9 normal load
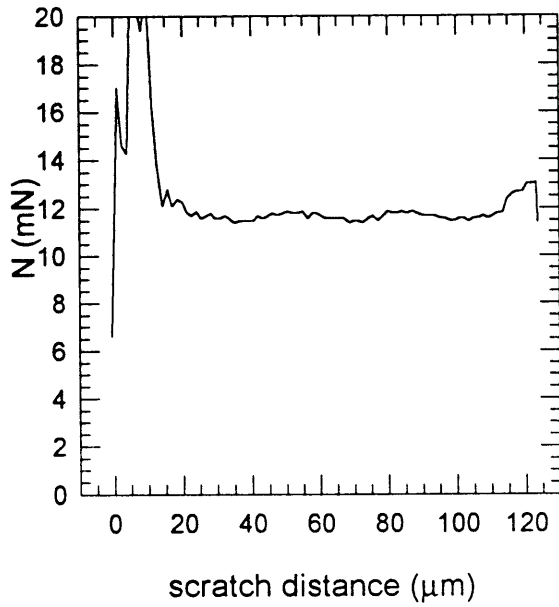
scratch 9-9 tangential load
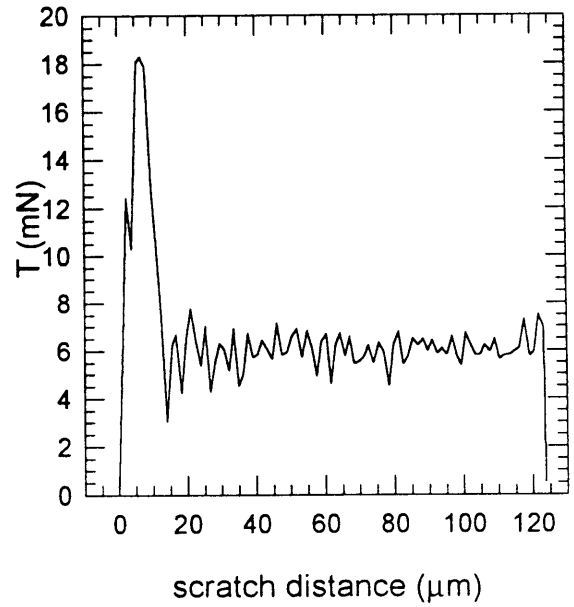
scratch 9-9 scratch depth
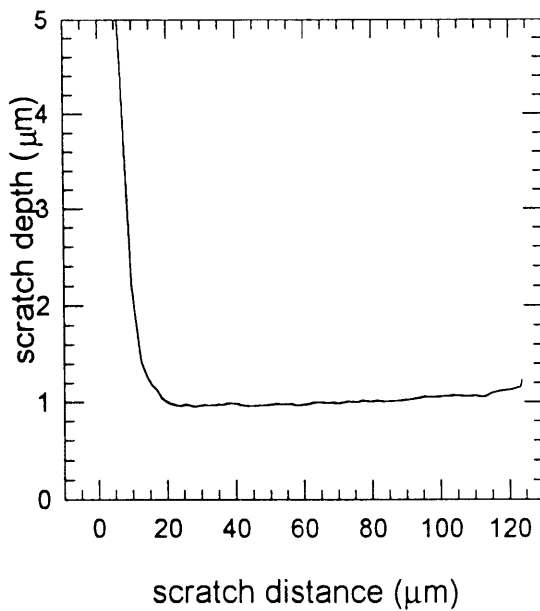
scratch 9-9 friction
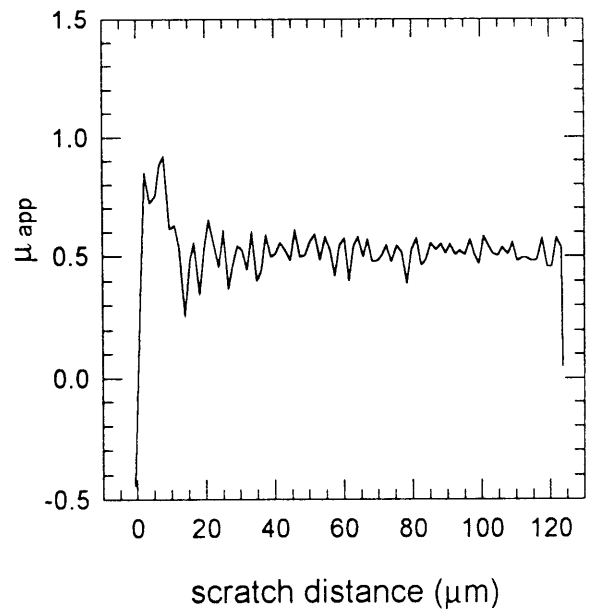
scratch 9-10 normal load
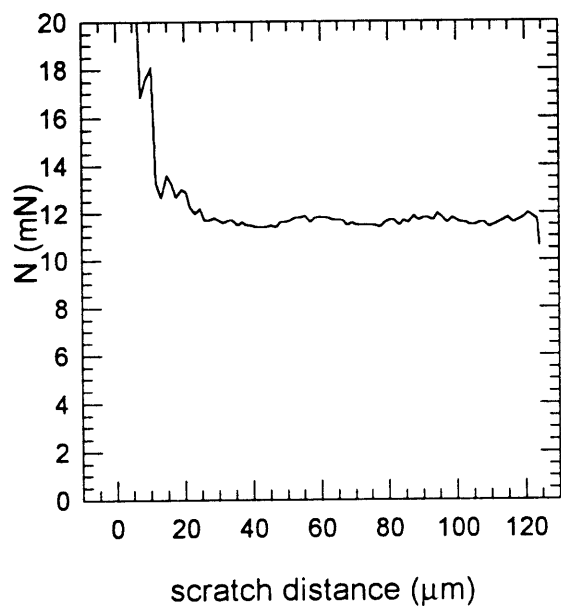
scratch 9-10 tangential load
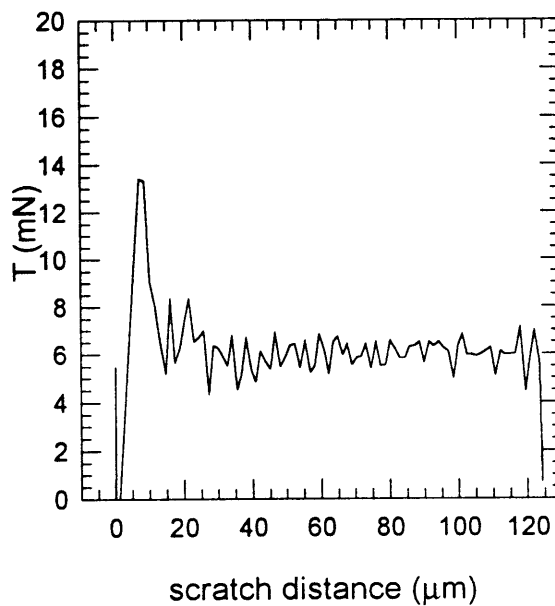
scratch 9-10 scratch depth
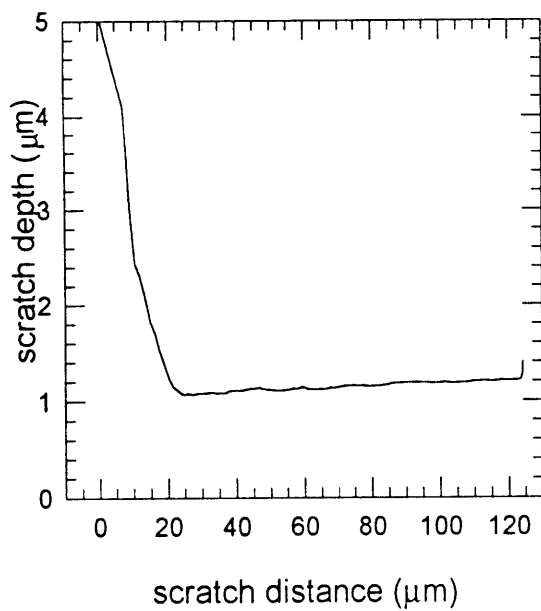
scratch 9-10 friction
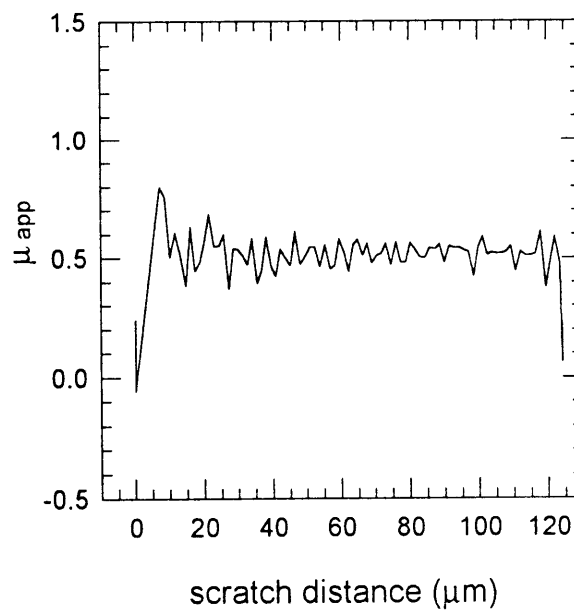
scratch 9-11 normal load
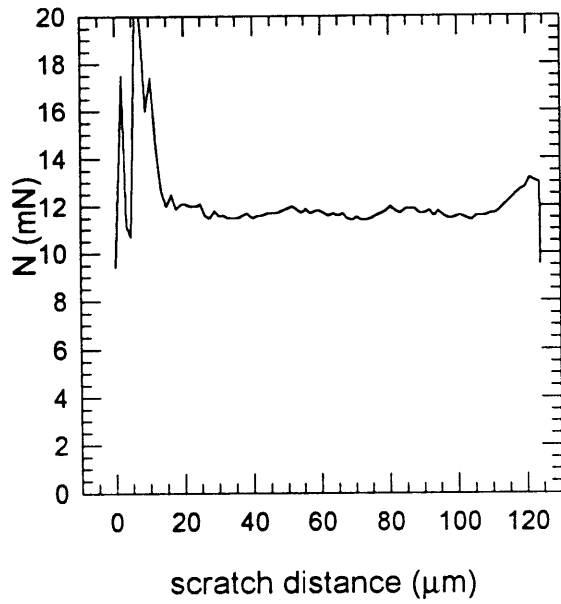
scratch 9-11 tangential load
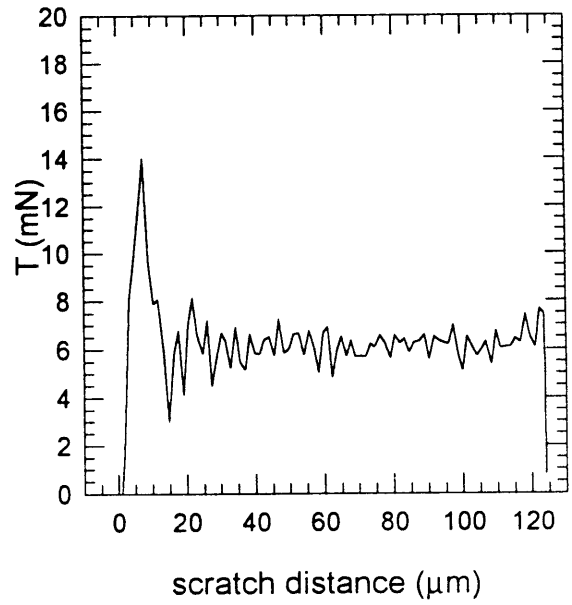
scratch 9-11 scratch depth
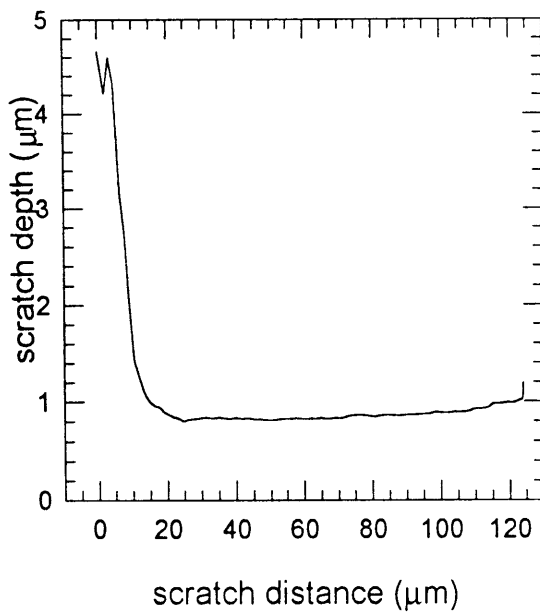
scratch 9-11 friction
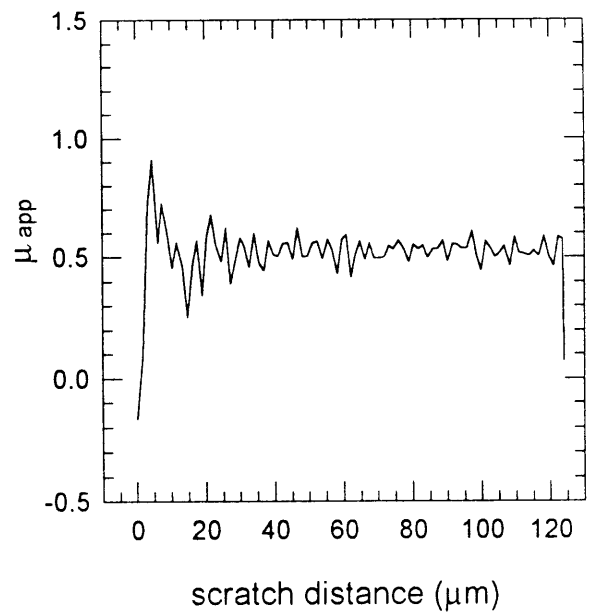
scratch 10-2 normal load
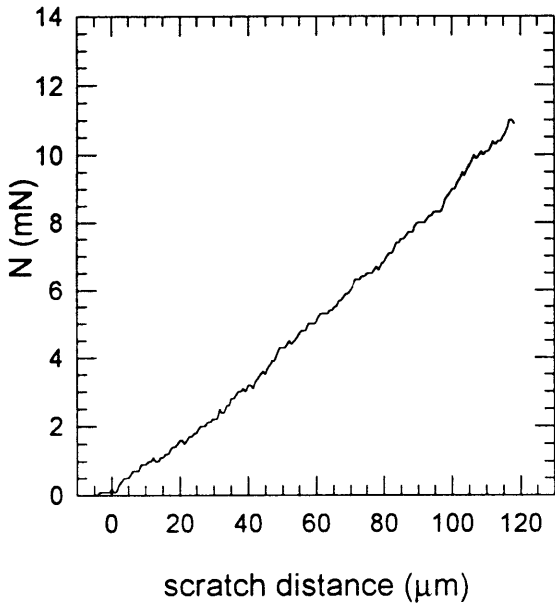
scratch 10-2 tangential load
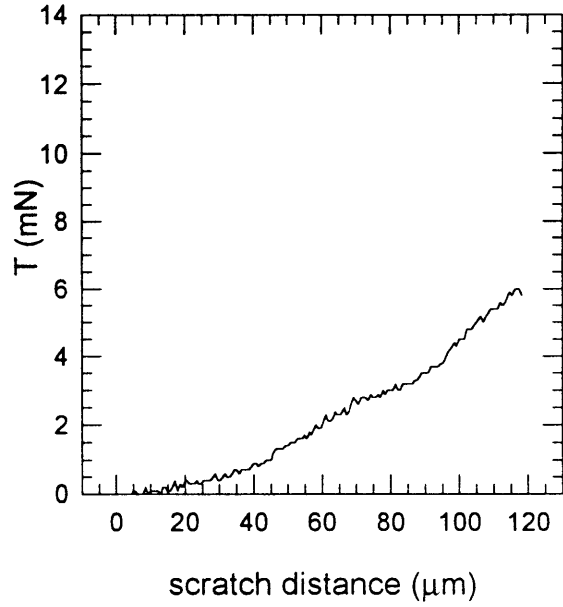
scratch 10-2 scratch depth
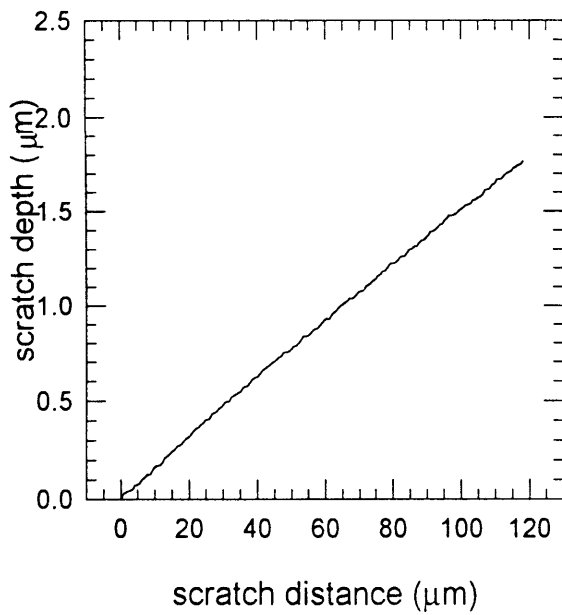
scratch 10-2 friction
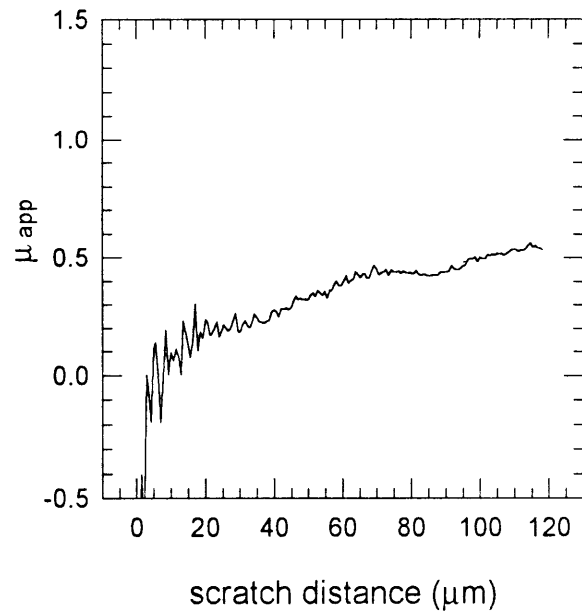
scratch 10-3 normal load
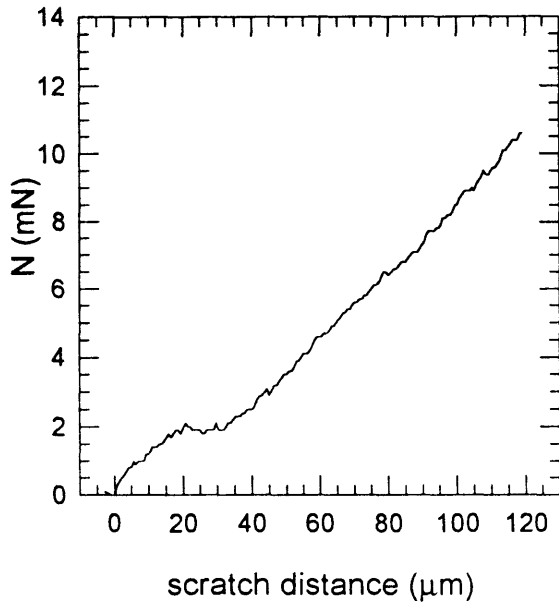
scratch 10-3 tangential load
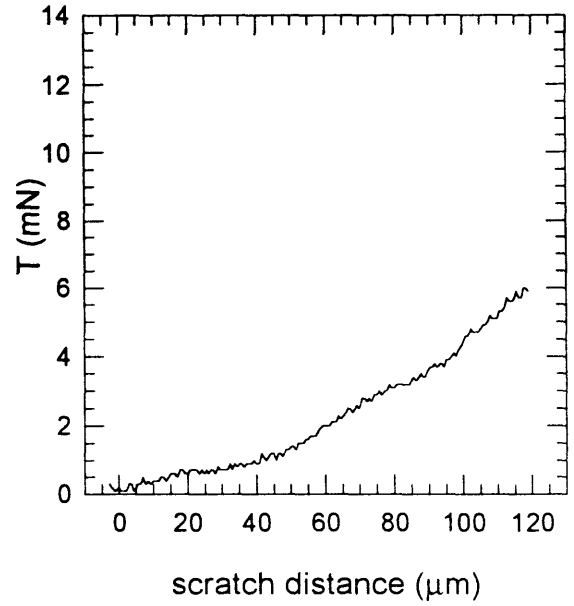
scratch 10-3 scratch depth
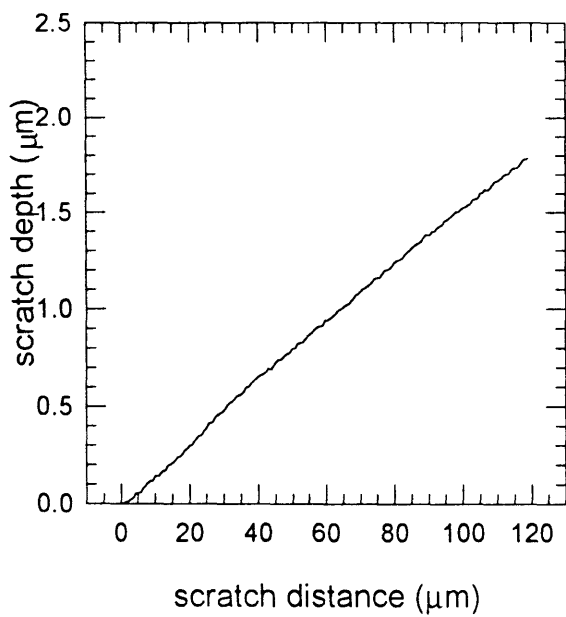
scratch 10-3 friction
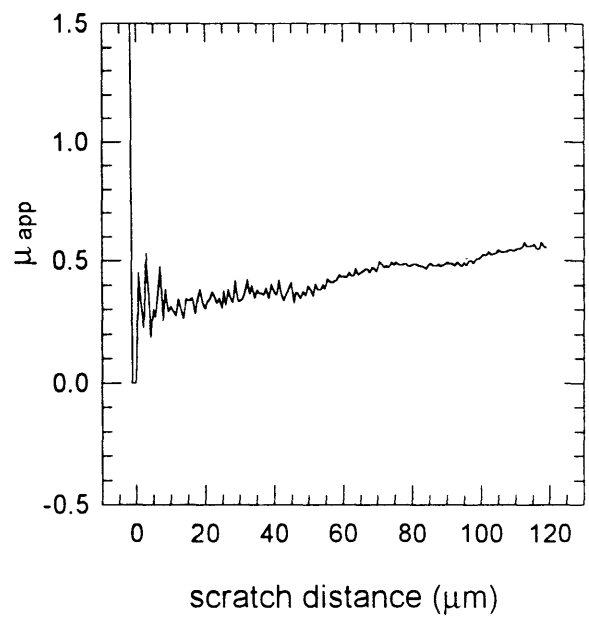
scratch 10-4 normal load
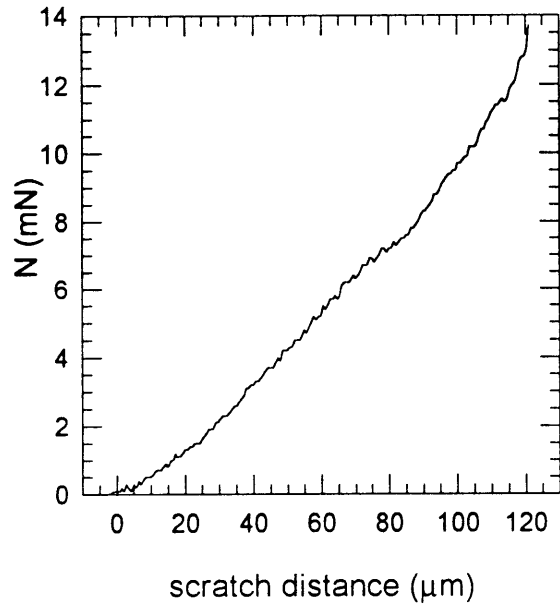
scratch 10-4 tangential load
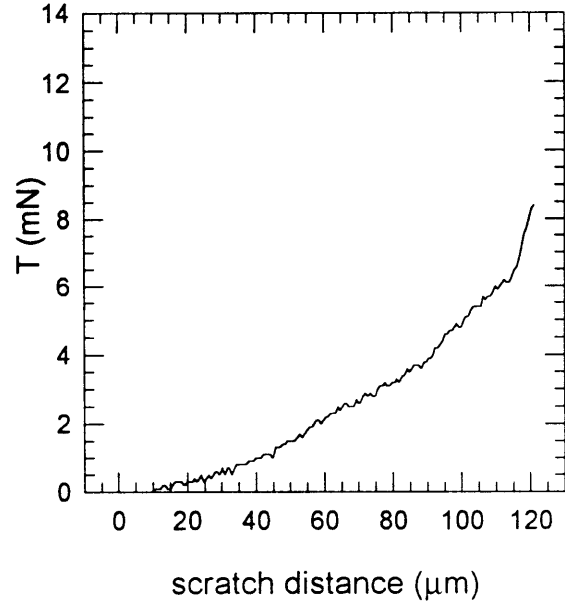
scratch 10-4 scratch depth
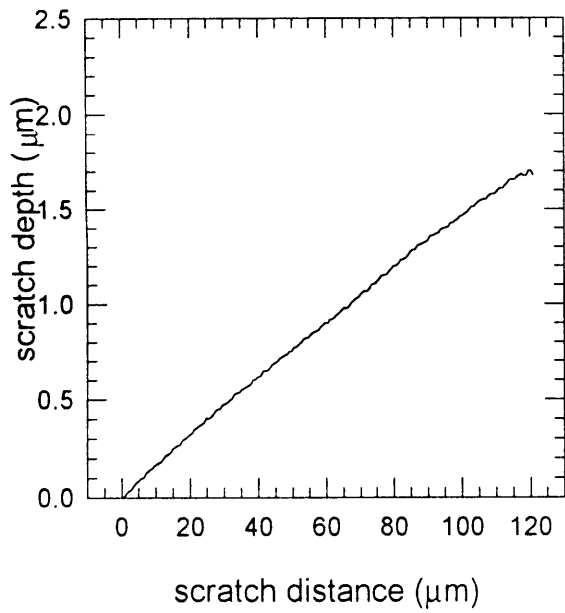
scratch 10-4 friction
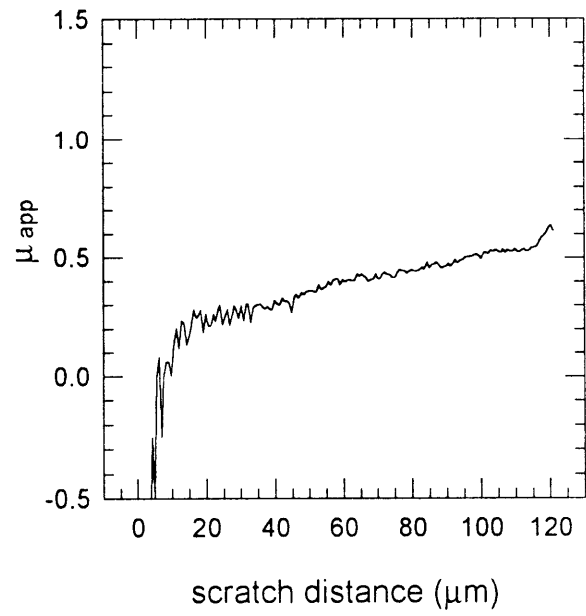
scratch 10-5 normal load
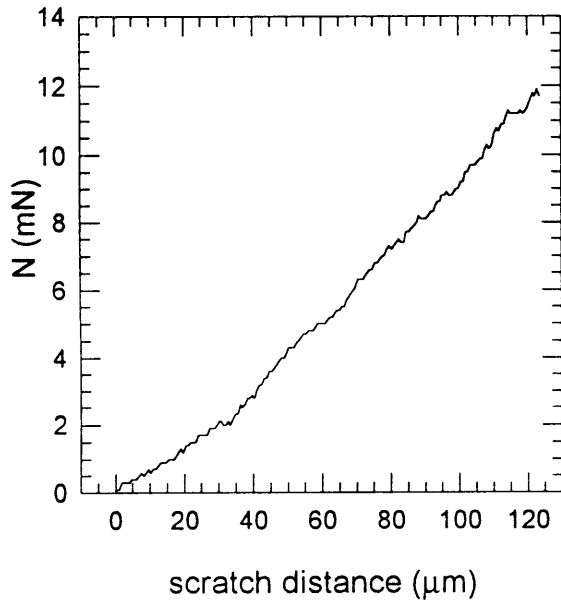
scratch 10-5 tangential load
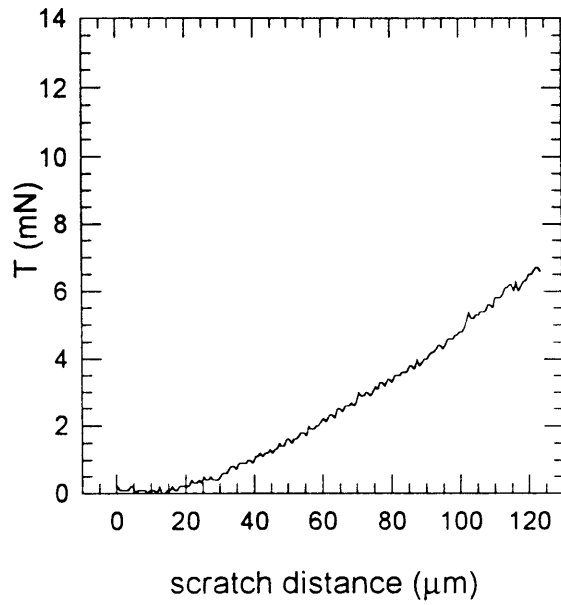
scratch 10-5 scratch depth
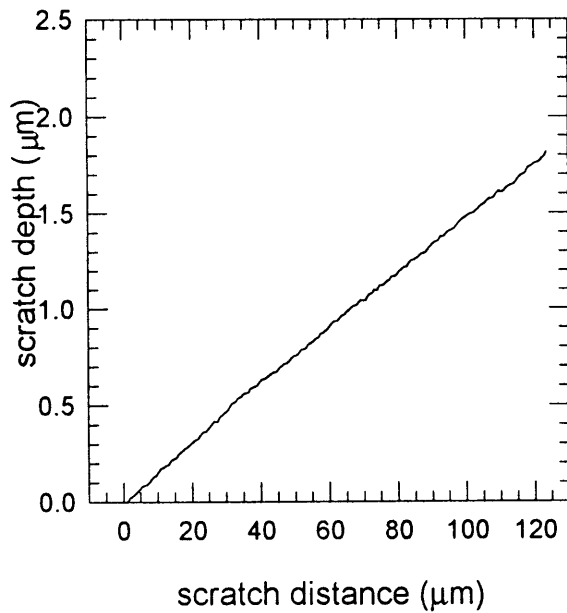
scratch 10-5 friction
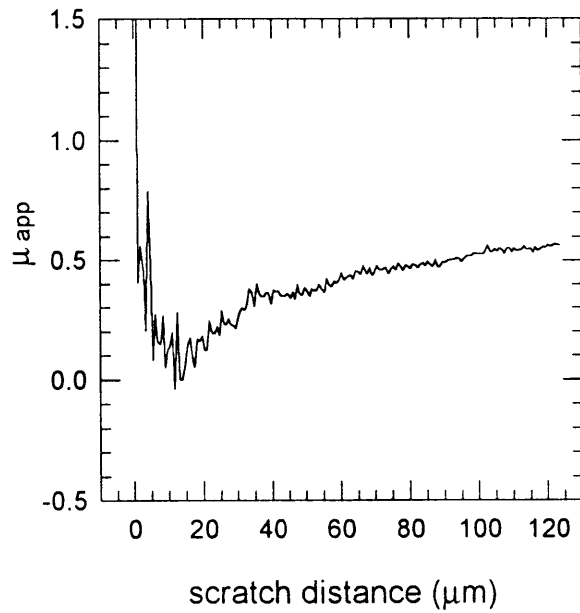
scratch 10-6 normal load
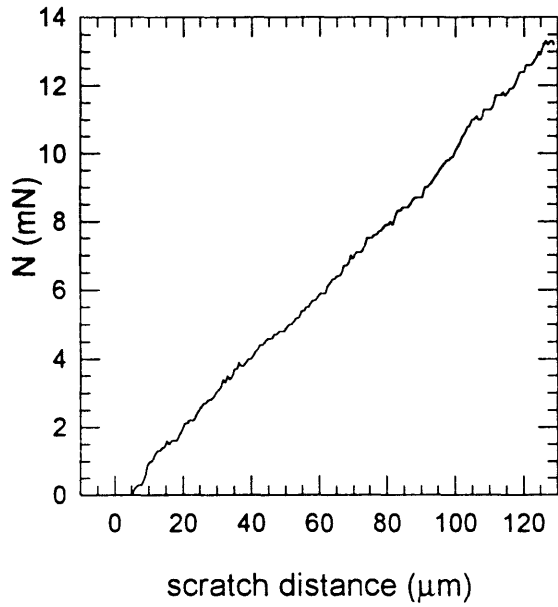
scratch 10-6 tangential load
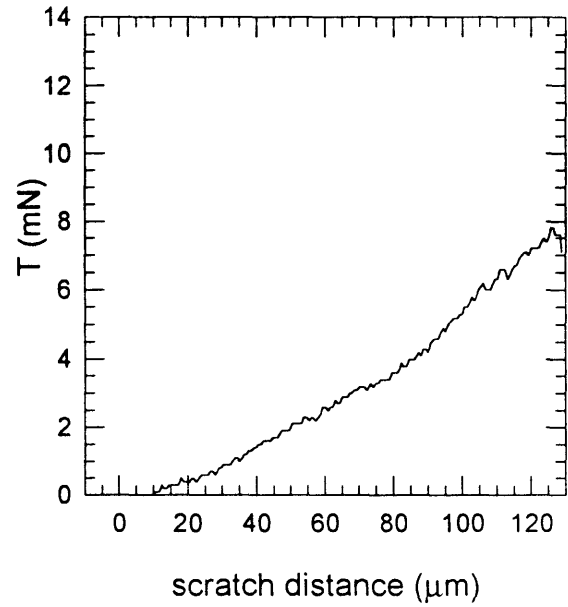
scratch 10-6 scratch depth
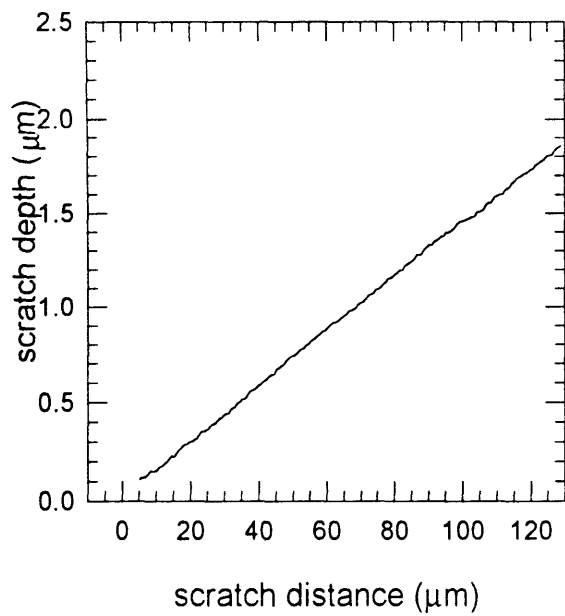
scratch 10-6 friction
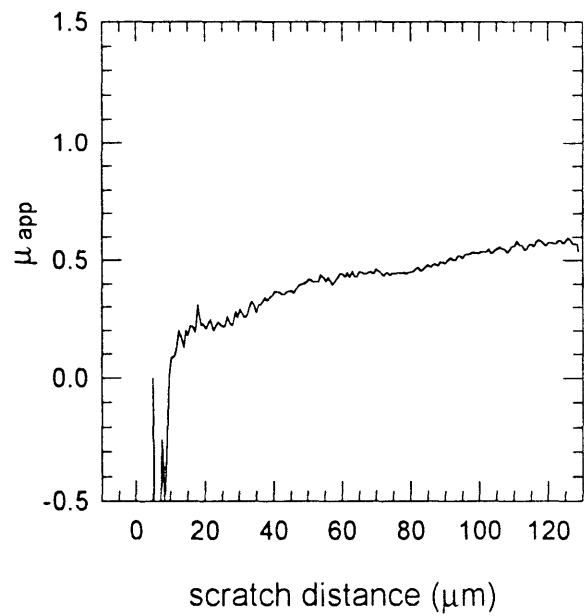
scratch 10-7 normal load
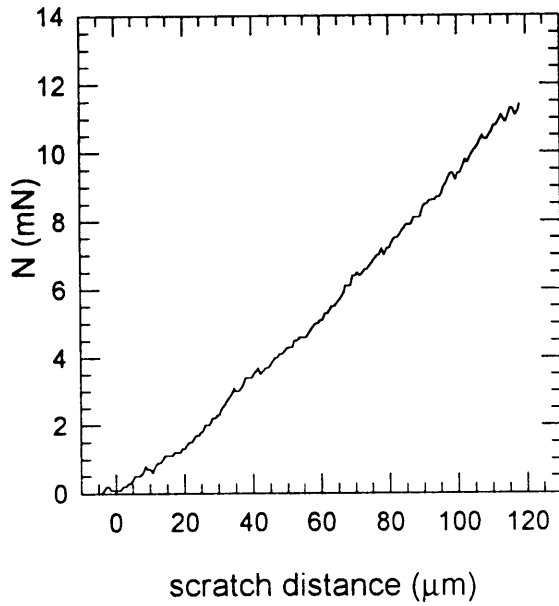
scratch 10-7 tangential load
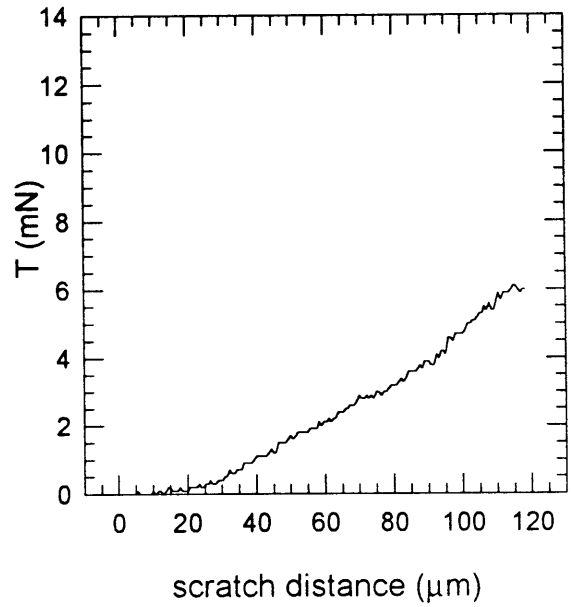
scratch 10-7 scratch depth
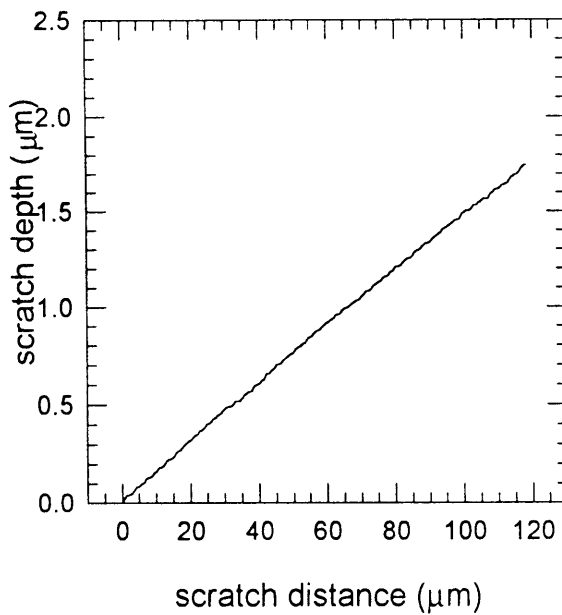
scratch 10-7 friction
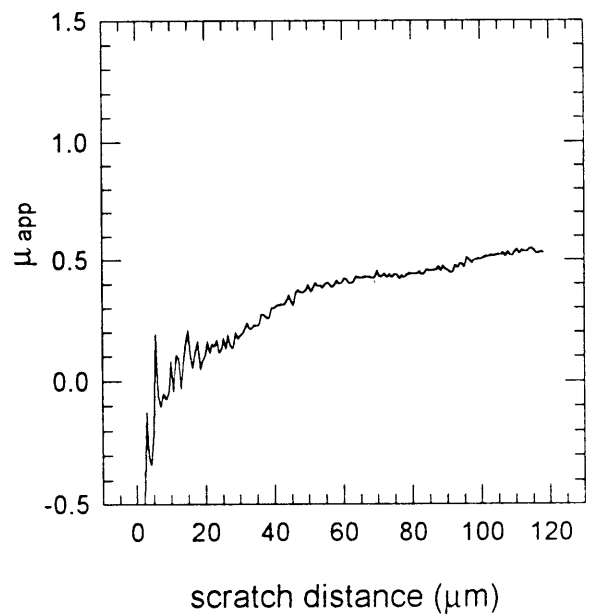
scratch 10-8 normal load
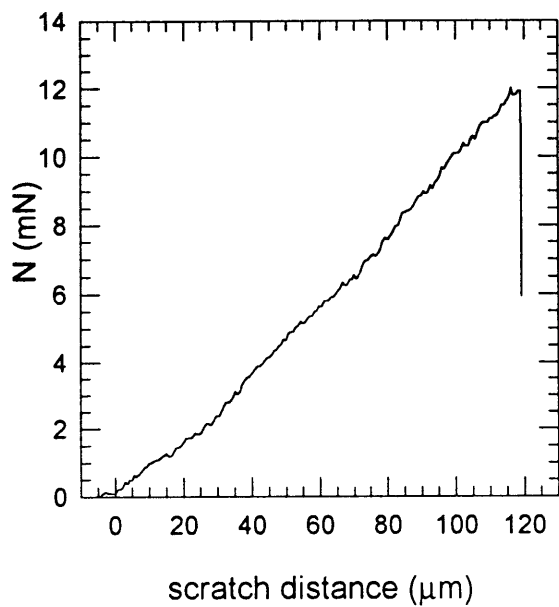
scratch 10-8 tangential load
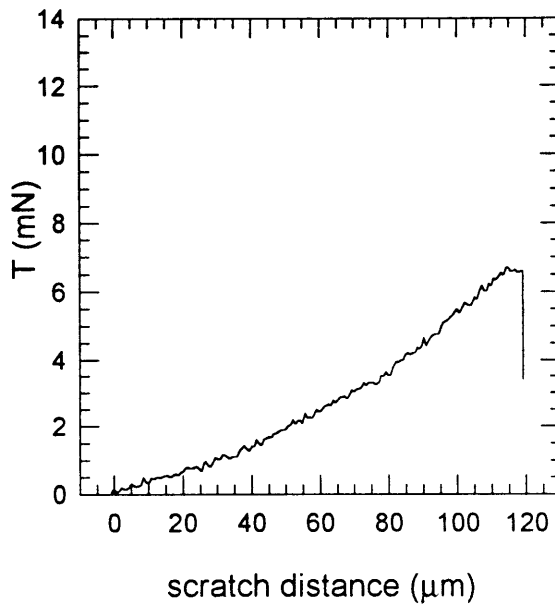
scratch 10-8 scratch depth
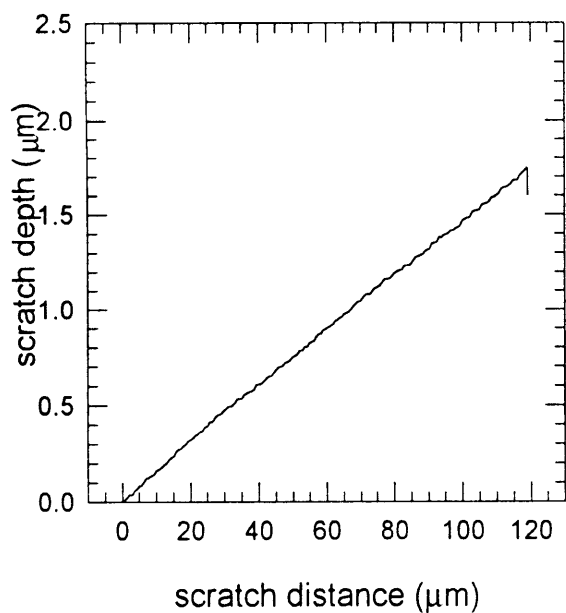
scratch 10-8 friction
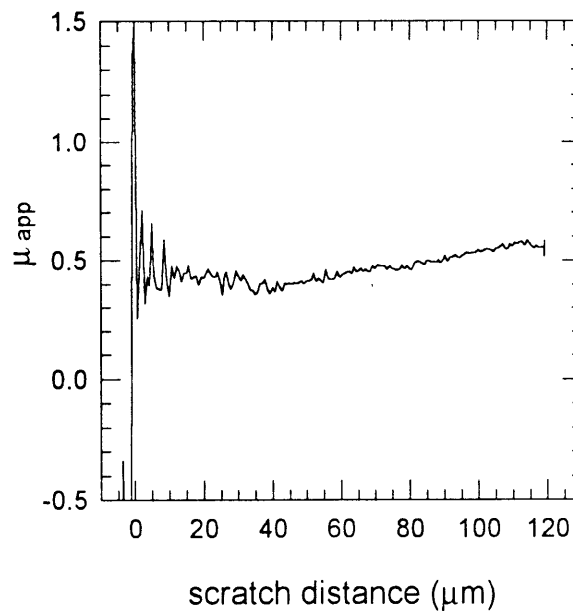
scratch 10-9 normal load
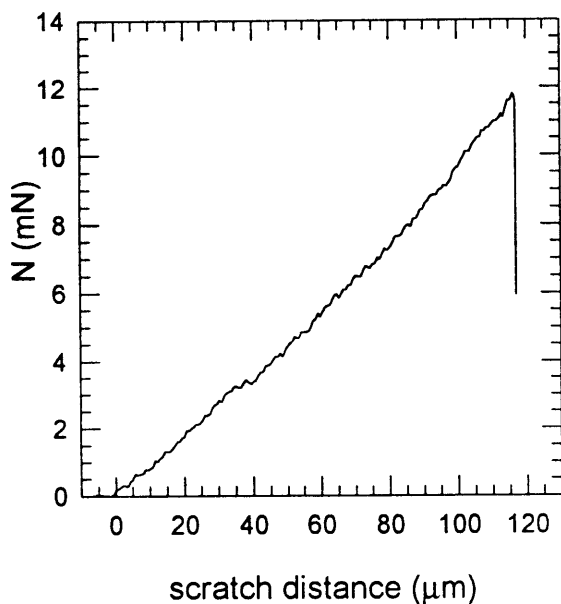
scratch 10-9 tangential load
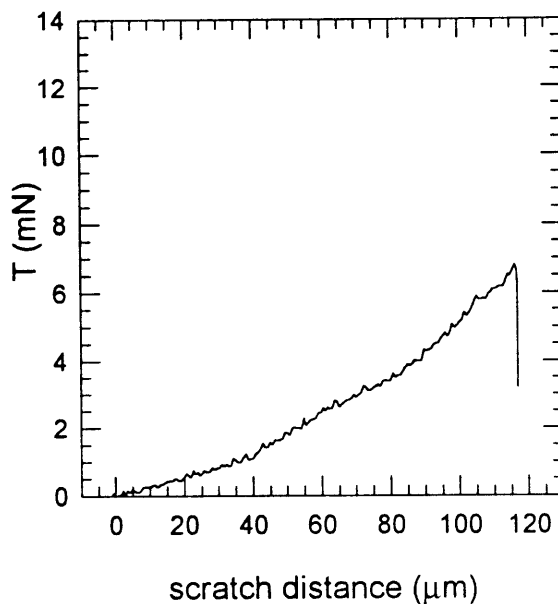
scratch 10-9 scratch depth
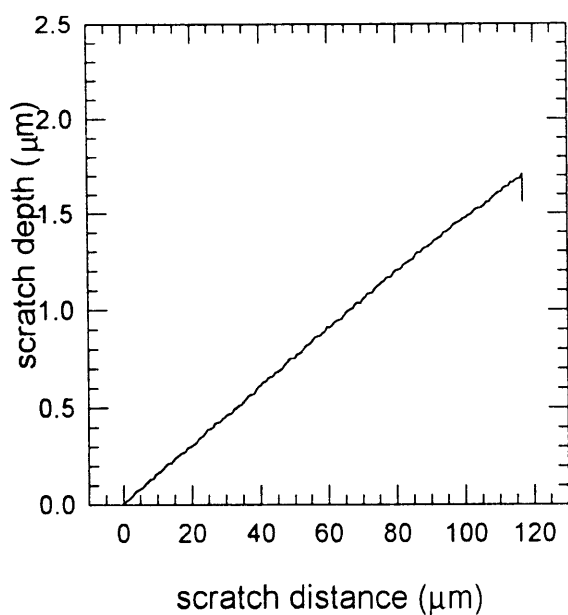
scratch 10-9 friction
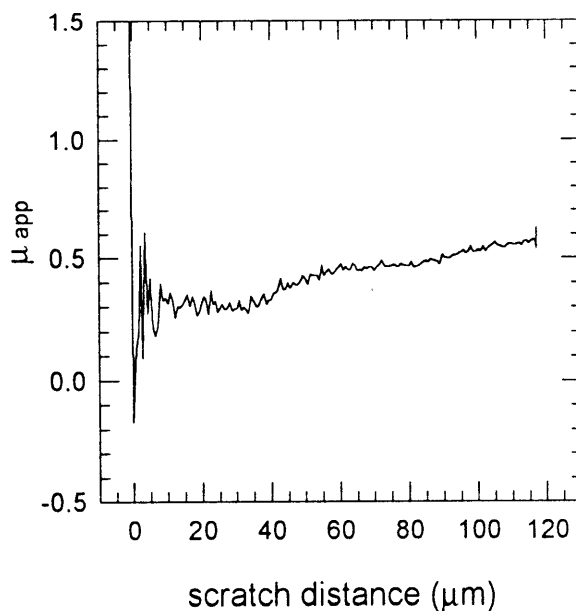
scratch 10-10 normal load
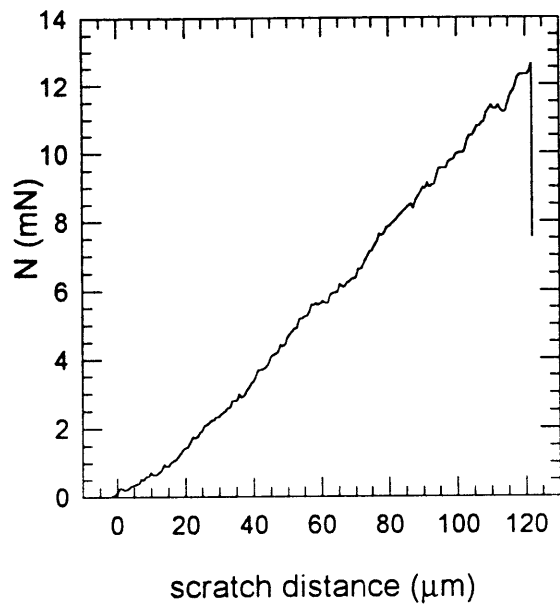
scratch 10-10 tangential load
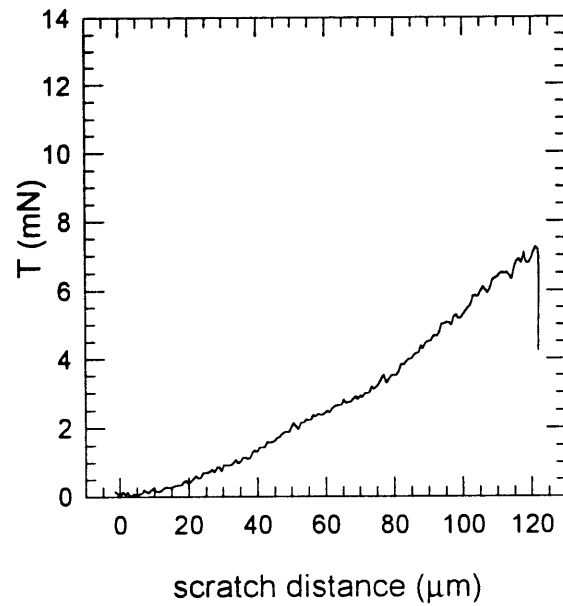
scratch 10-10 scratch depth
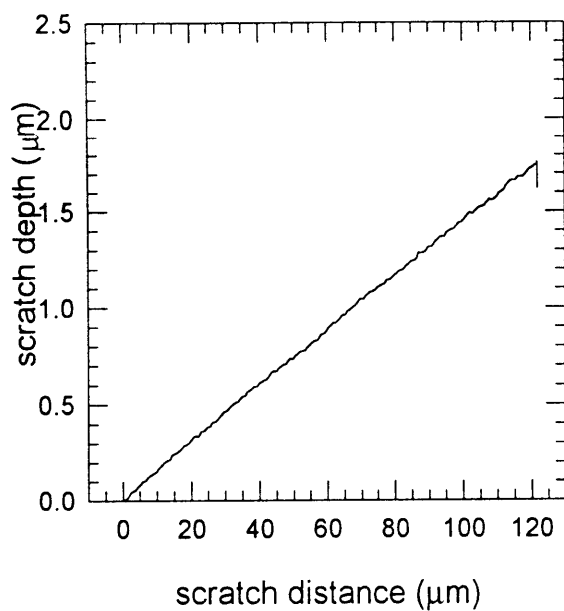
scratch 10-10 friction
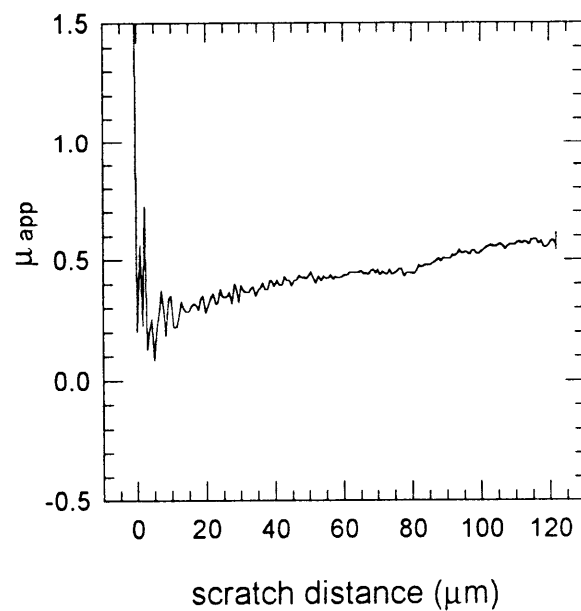
scratch 10-11 normal load
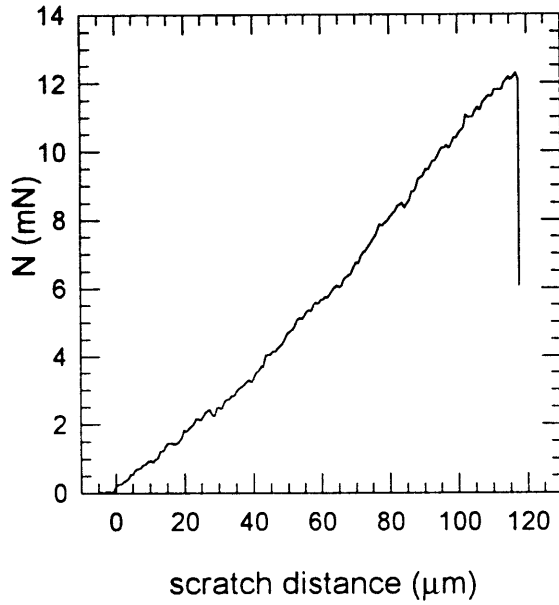
scratch 10-11 tangential load
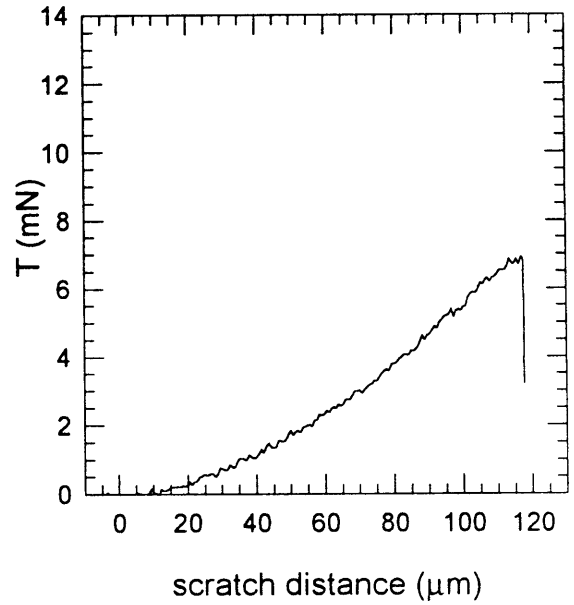
scratch 10-11 scratch depth
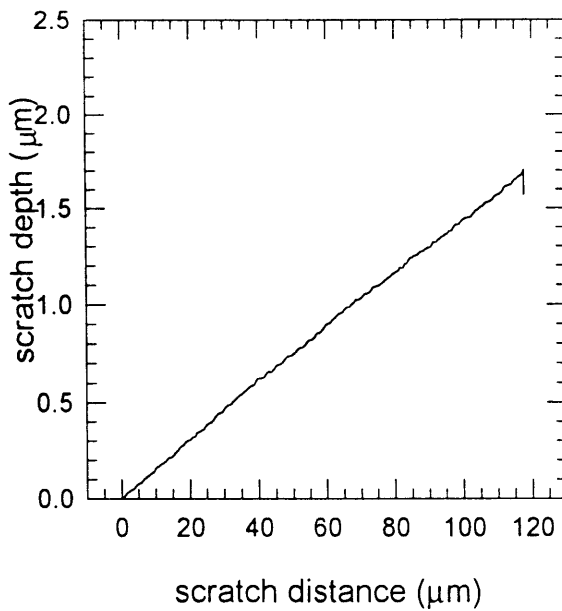
scratch 10-11 friction
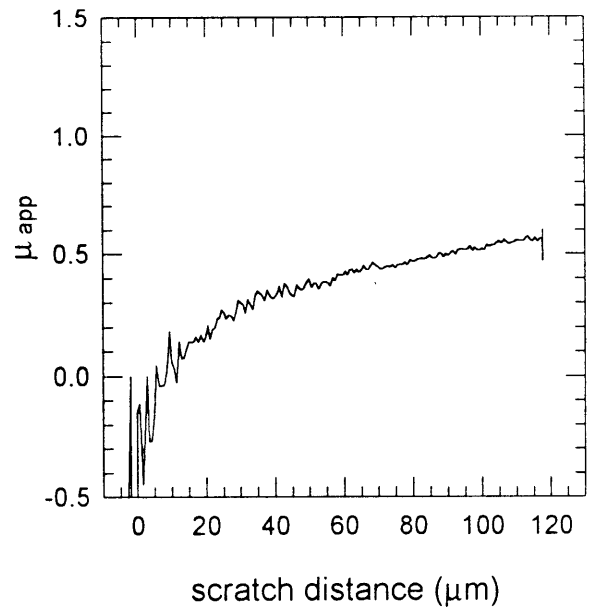
scratch 10-12 normal load
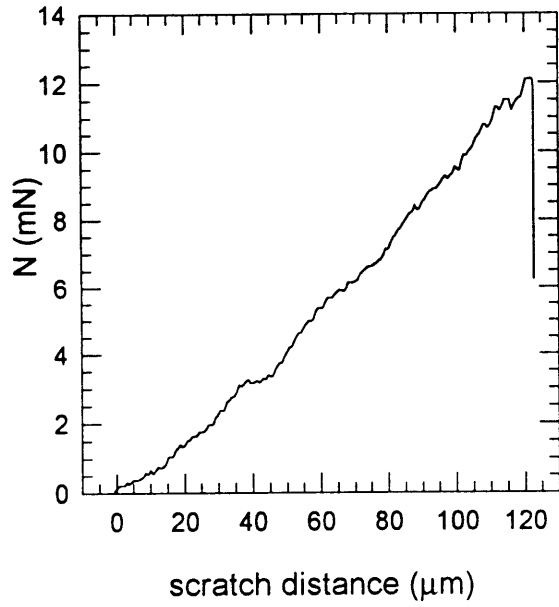
scratch 10-12 tangential load
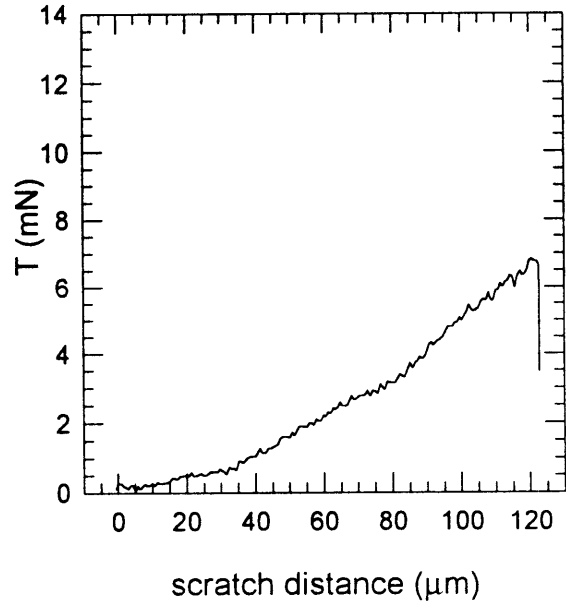
scratch 10-12 scratch depth
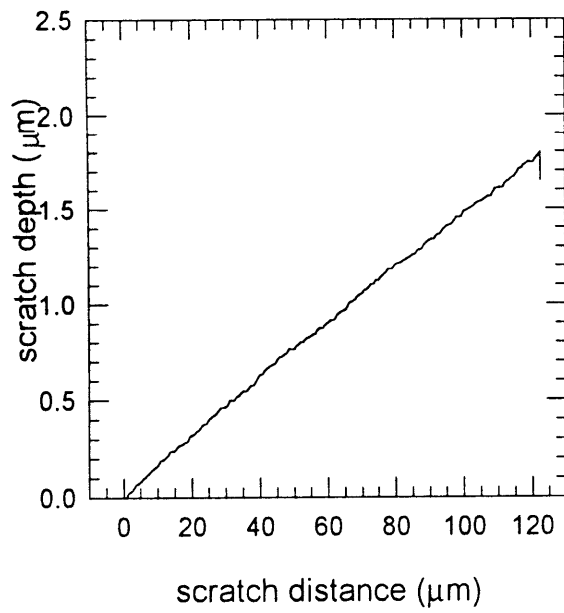
scratch 10-12 friction
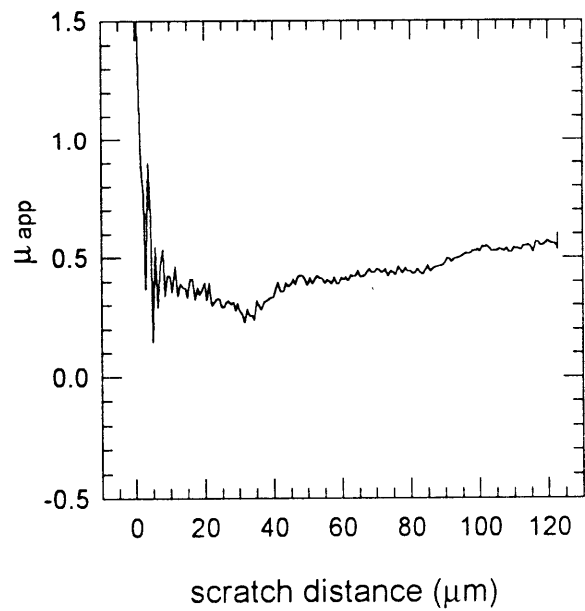
scratch 10-13 normal load
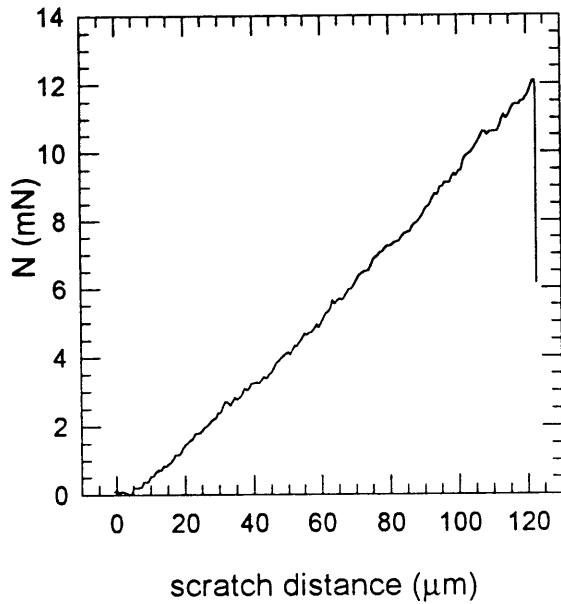
scratch 10-13 tangential load
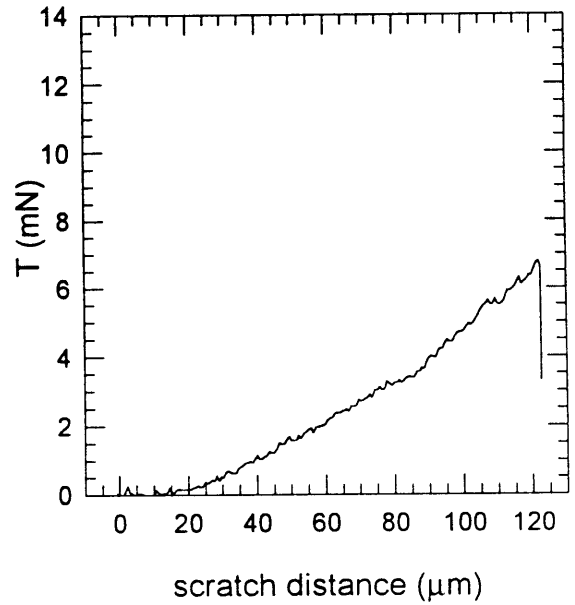
scratch 10-13 scratch depth
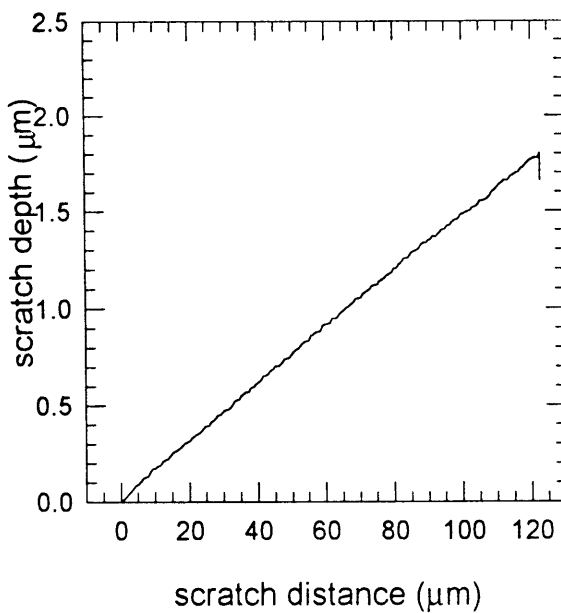
scratch 10-13 friction
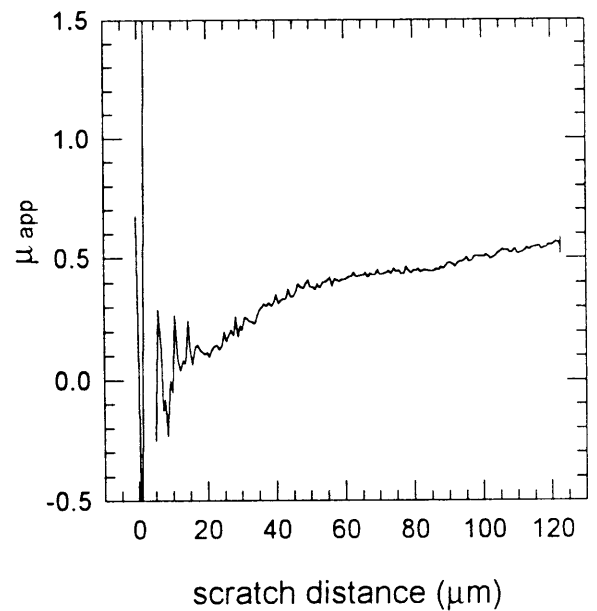
scratch 10-14 normal load
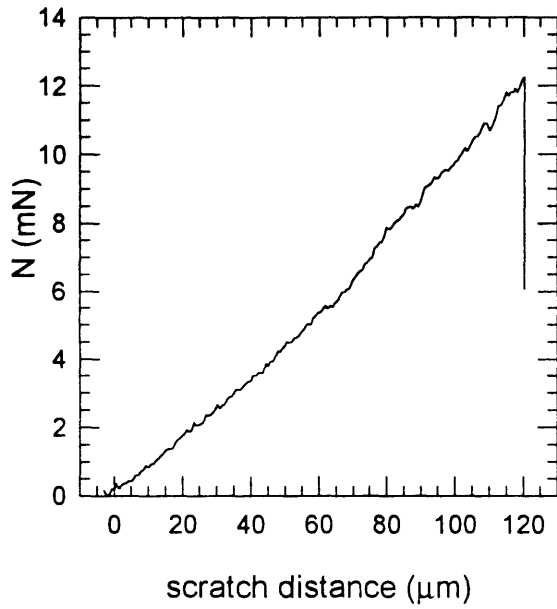
scratch 10-14 tangential load
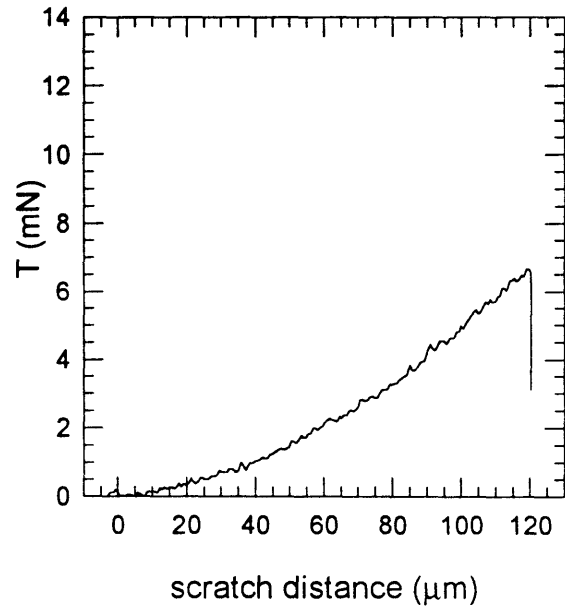
scratch 10-14 scratch depth
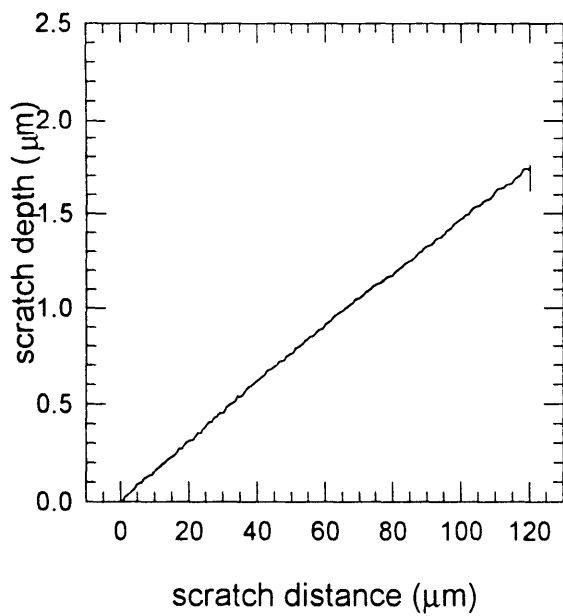
scratch 10-14 friction
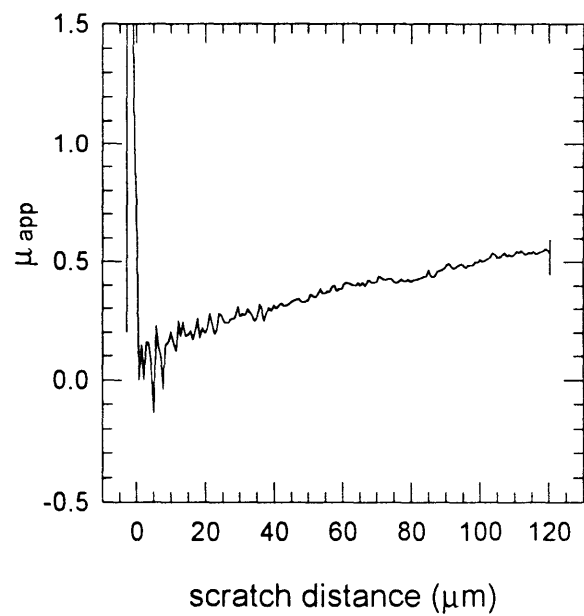
scratch 11-1 normal load
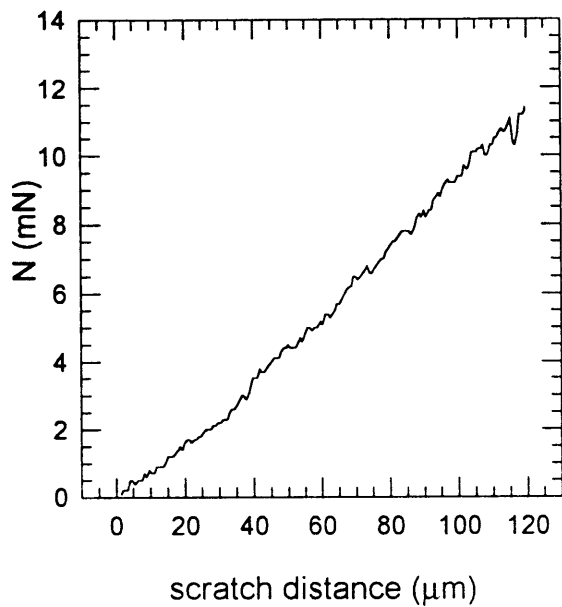
scratch 11-1 tangential load
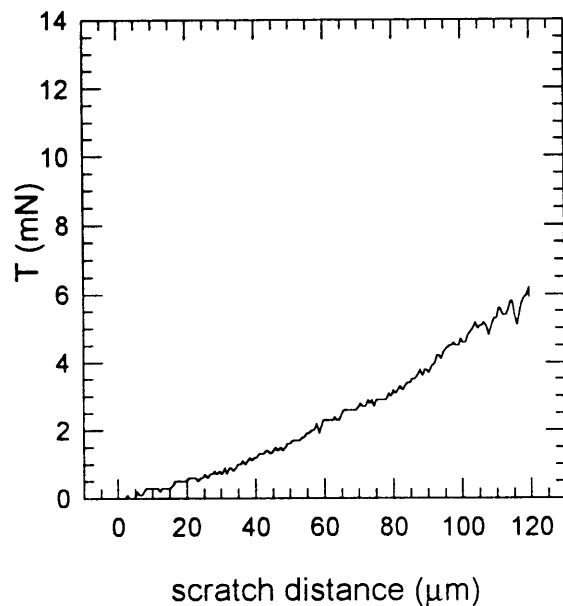
scratch 11-1 scratch depth
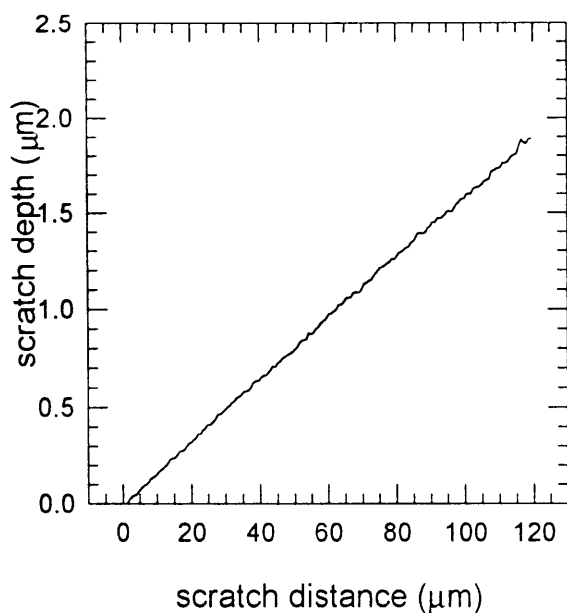
scratch 11-1 friction
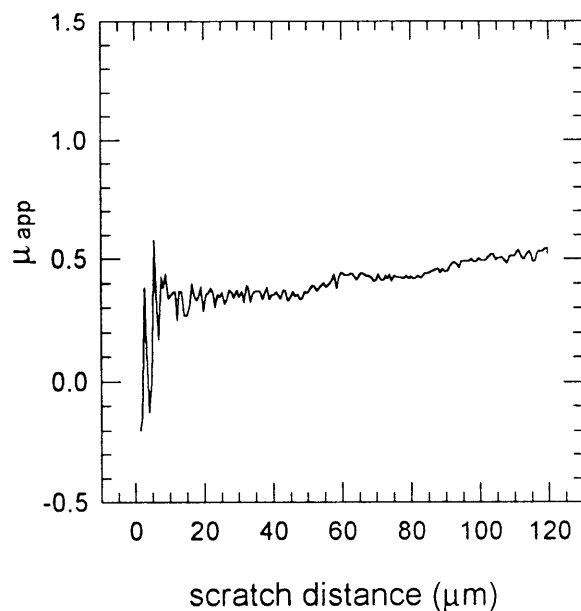
scratch 11-2 normal load
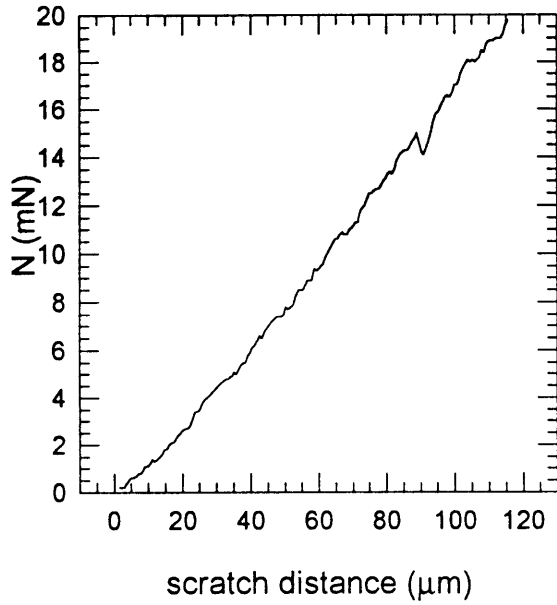
scratch 11-2 tangential load
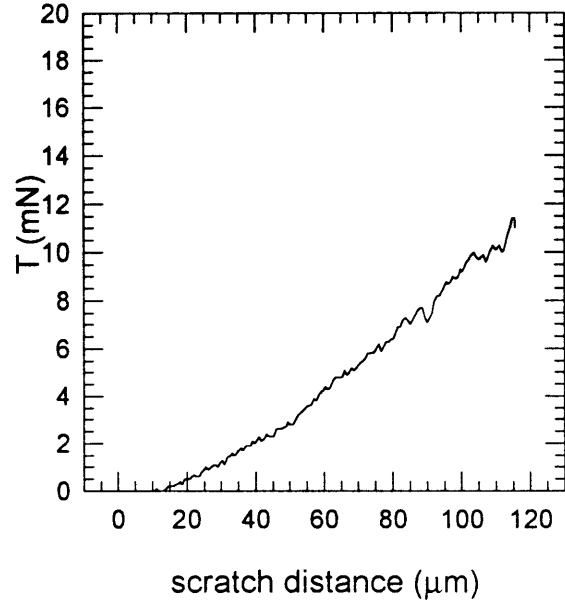
scratch 11-2 scratch depth
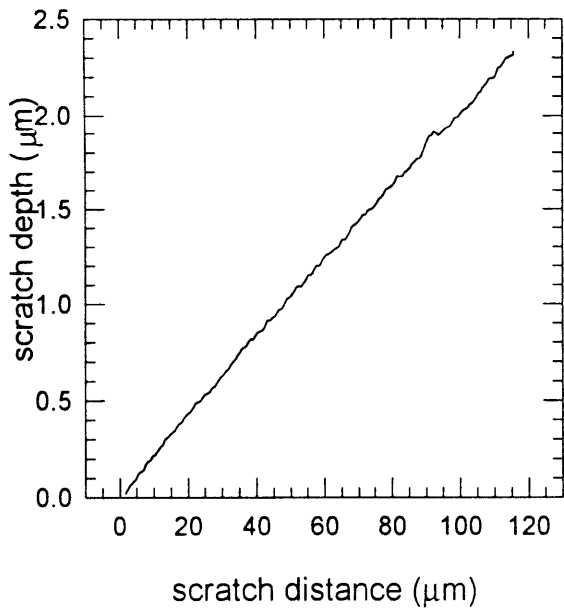
scratch 11-2 friction
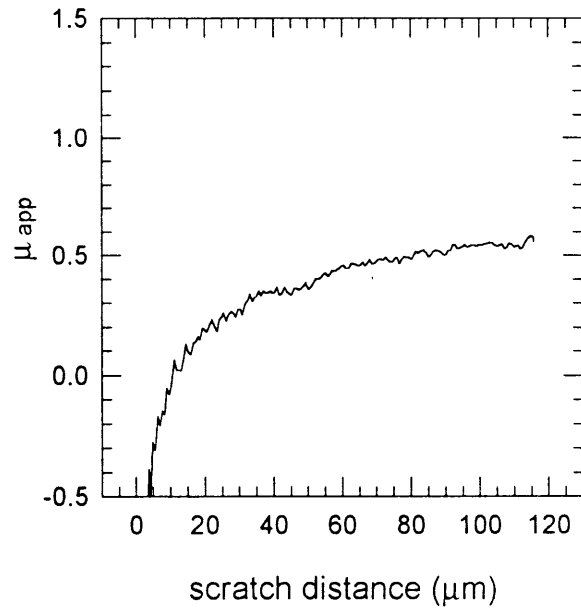
scratch 11-3 normal load
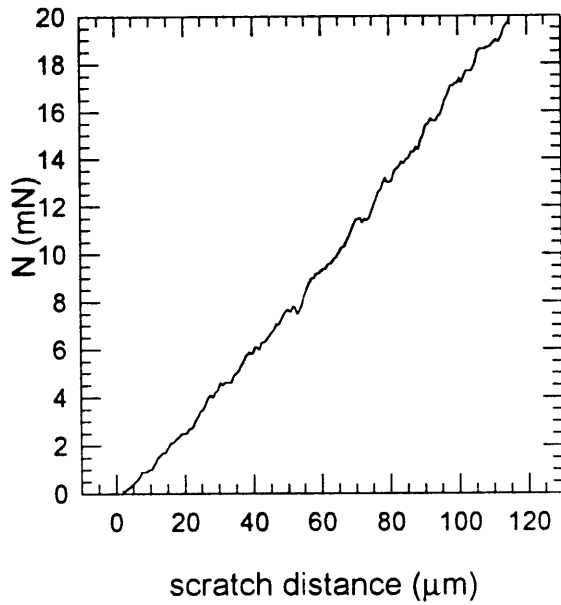
scratch 11-3 tangential load
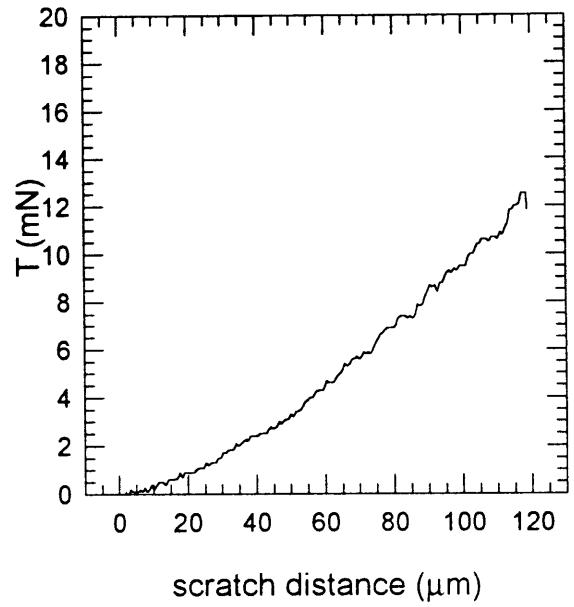
scratch 11-3 scratch depth
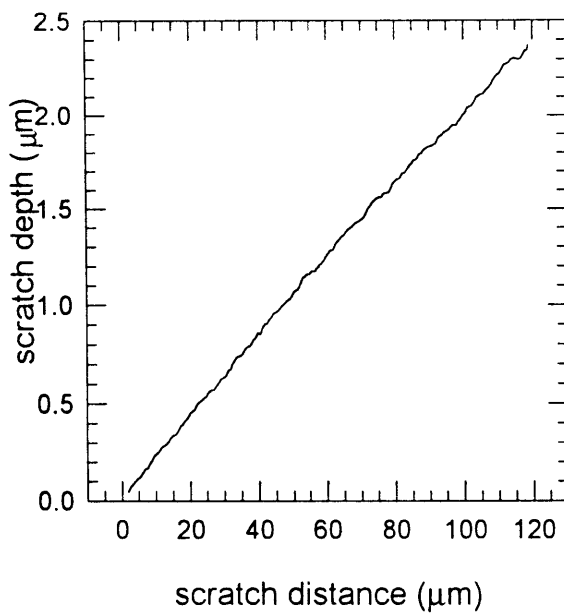
scratch 11-3 friction
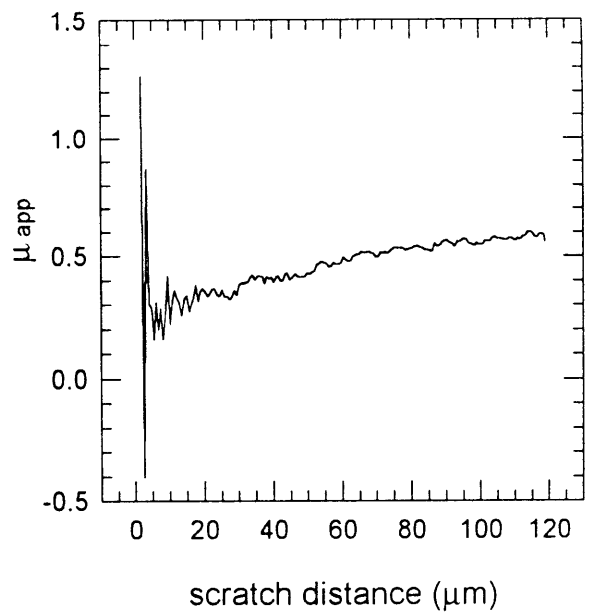
scratch 11-4 normal load
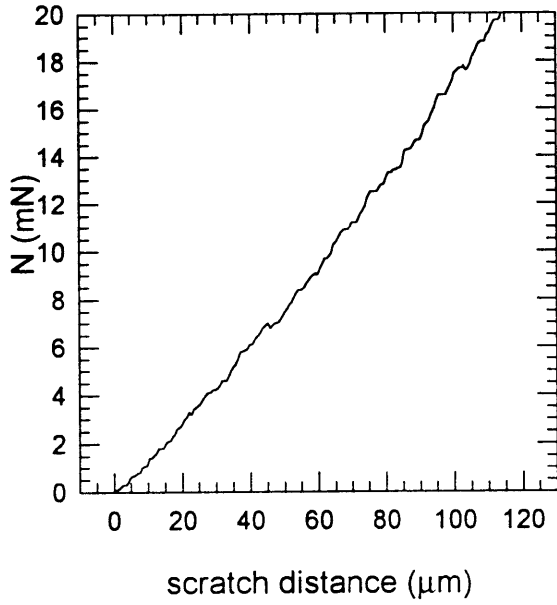
scratch 11-4 tangential load
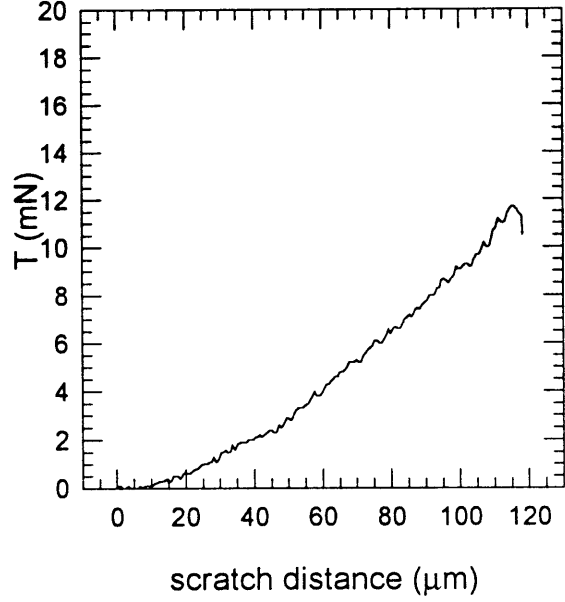
scratch 11-4 scratch depth
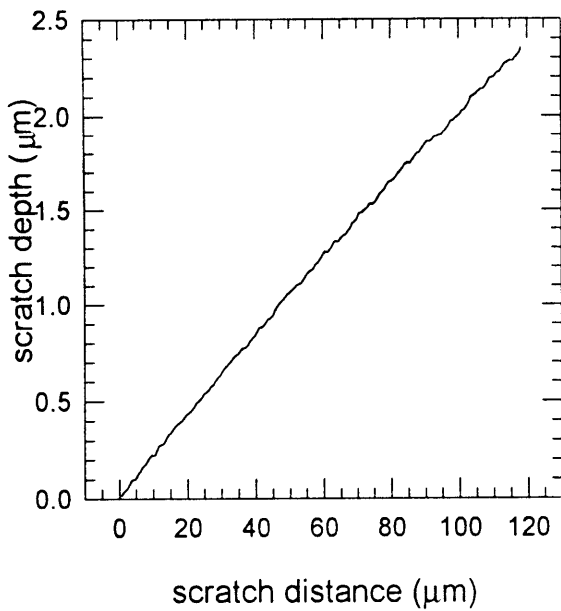
scratch 11-4 friction
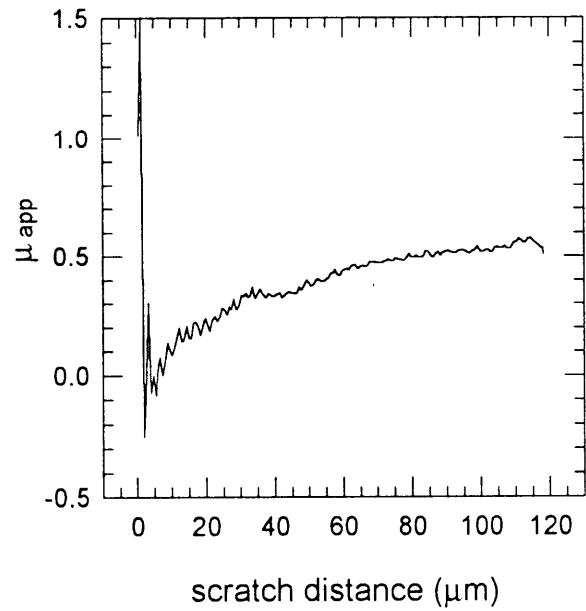
scratch 11-5 normal load
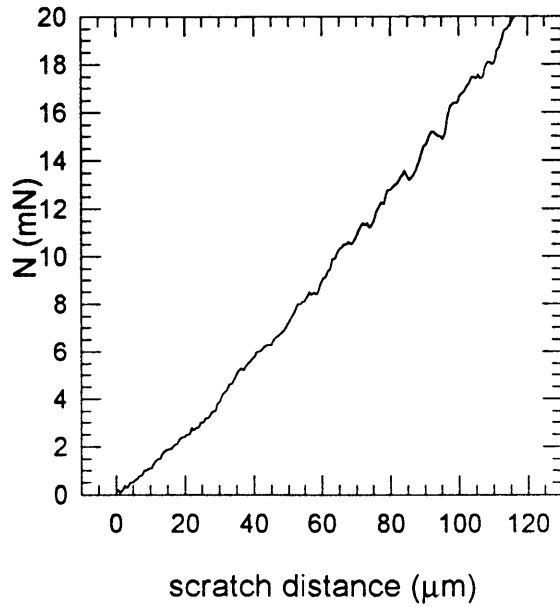
scratch 11-5 tangential load
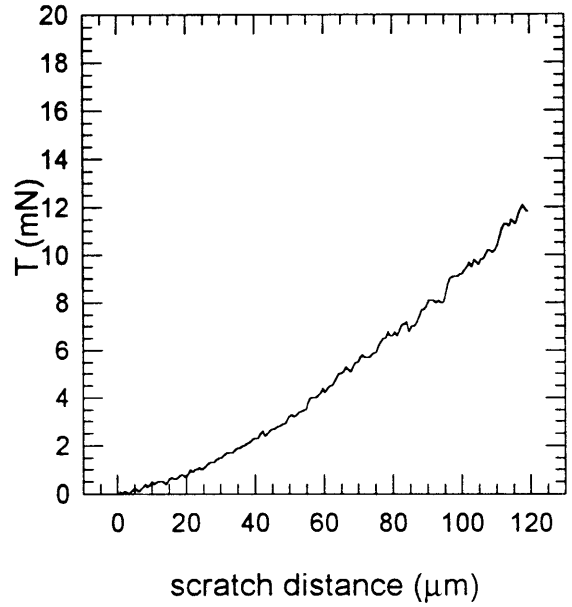
scratch 11-5 scratch depth
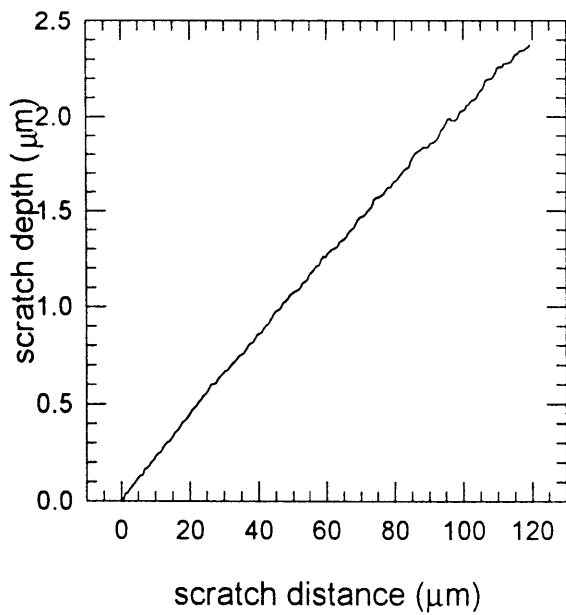
scratch 11-5 friction
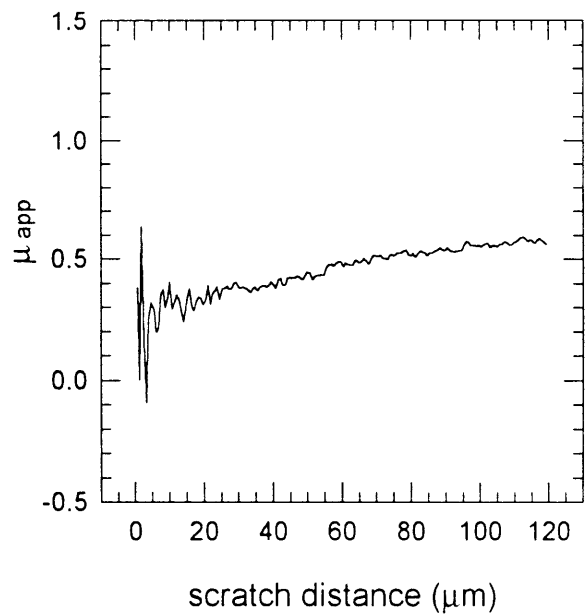
scratch 11-6 normal load
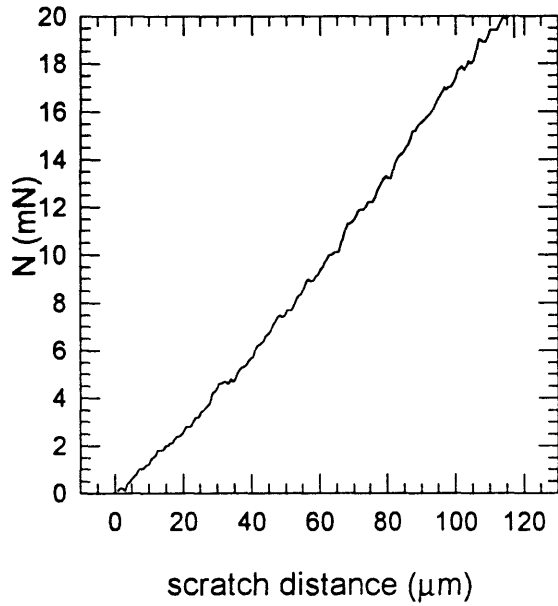
scratch 11-6 tangential load
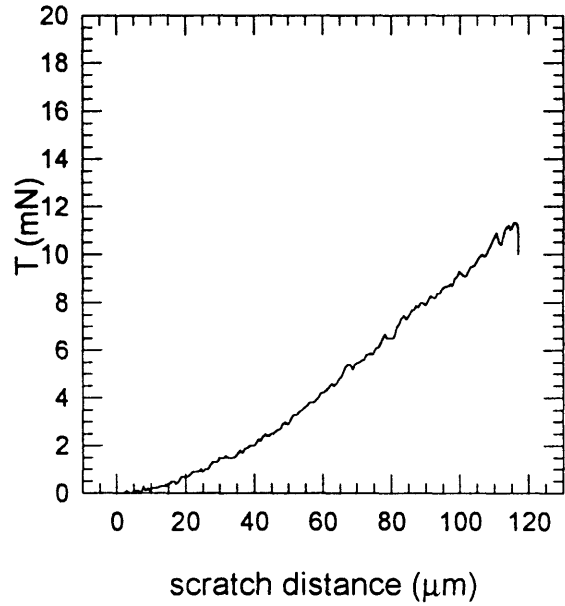
scratch 11-6 scratch depth
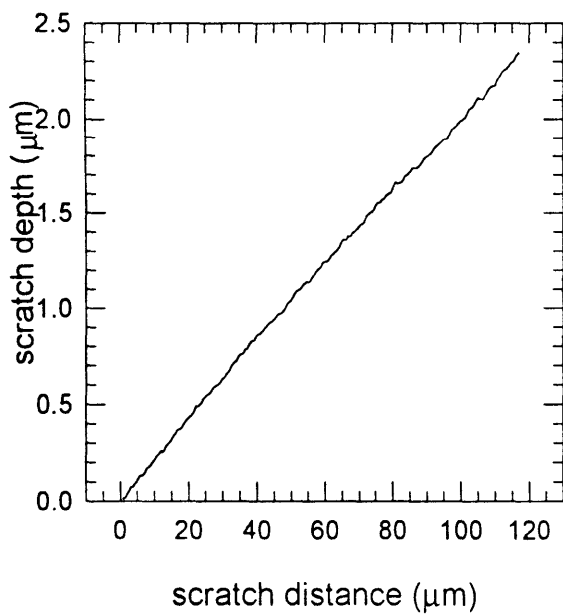
scratch 11-6 friction
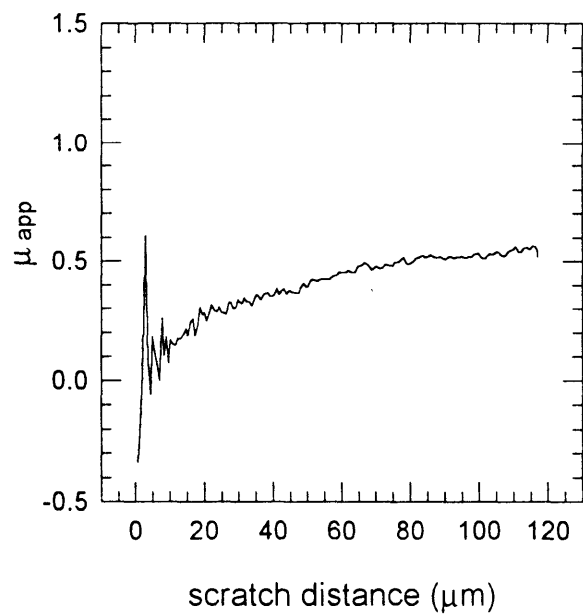
scratch 11-7 normal load
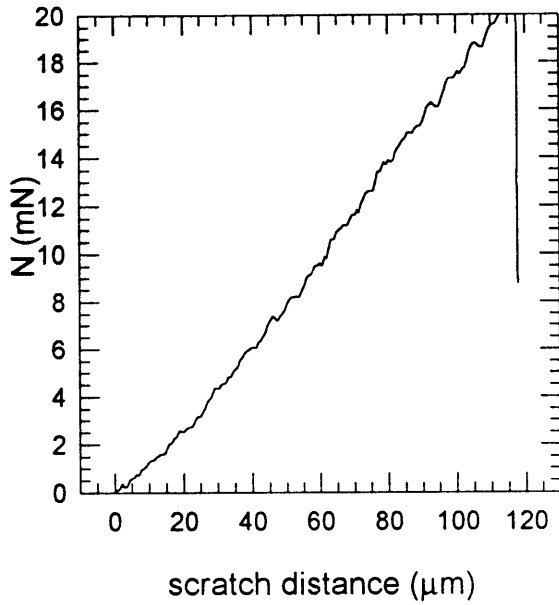
scratch 11-7 tangential load
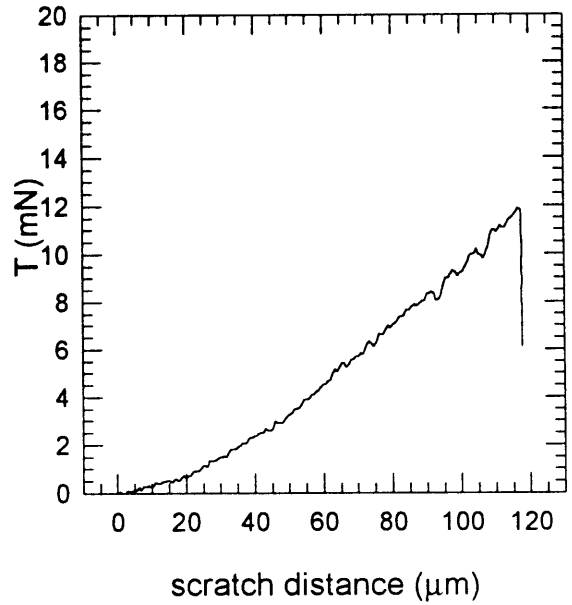
scratch 11-7 scratch depth
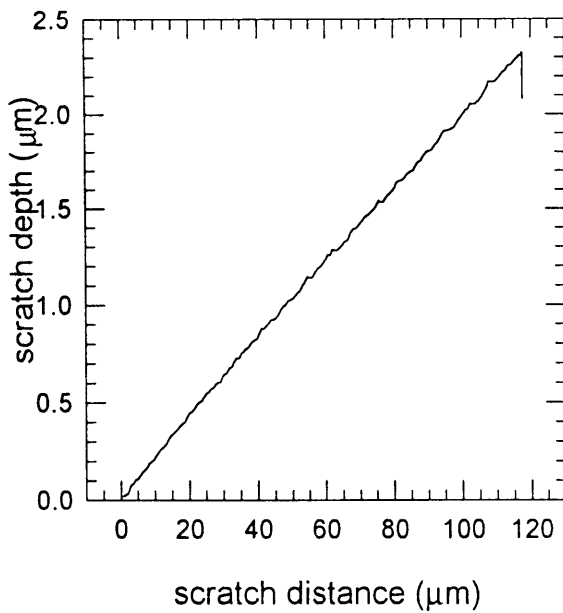
scratch 11-7 friction
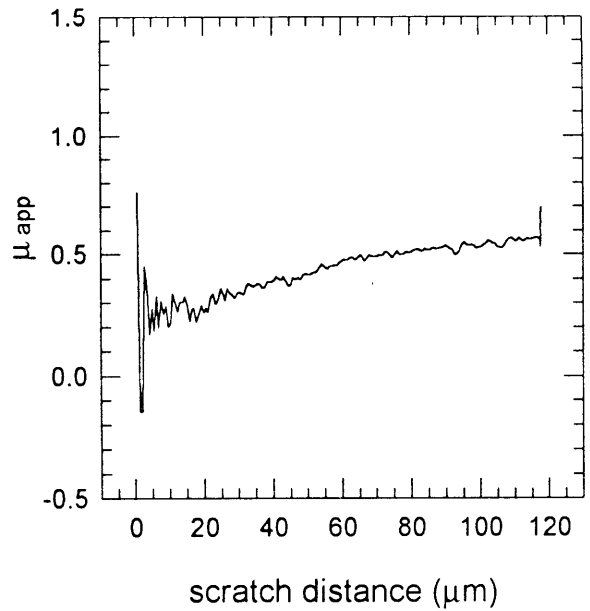
scratch 11-8 normal load
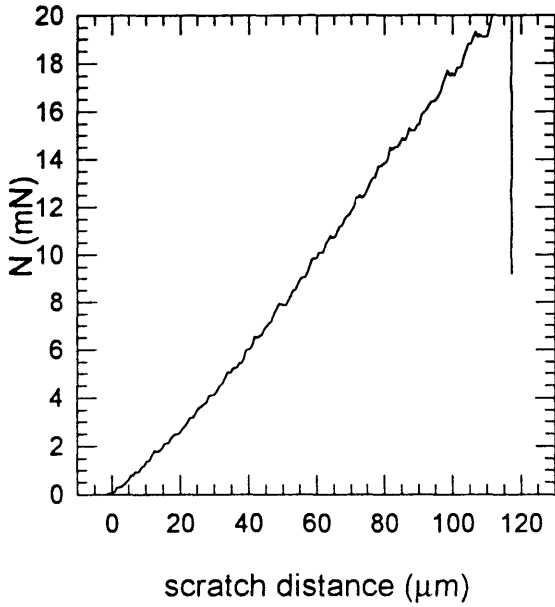
scratch 11-8 tangential load
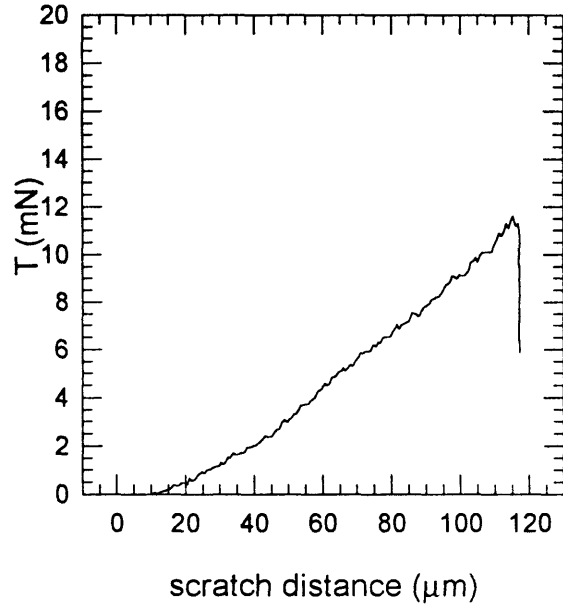
scratch 11-8 scratch depth
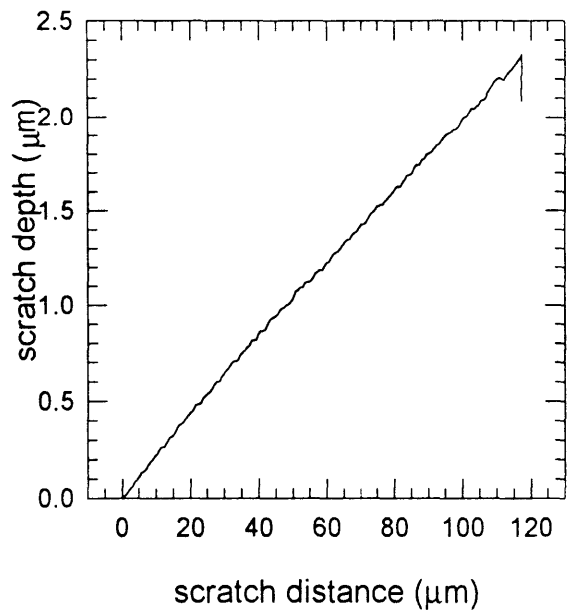
scratch 11-8 friction
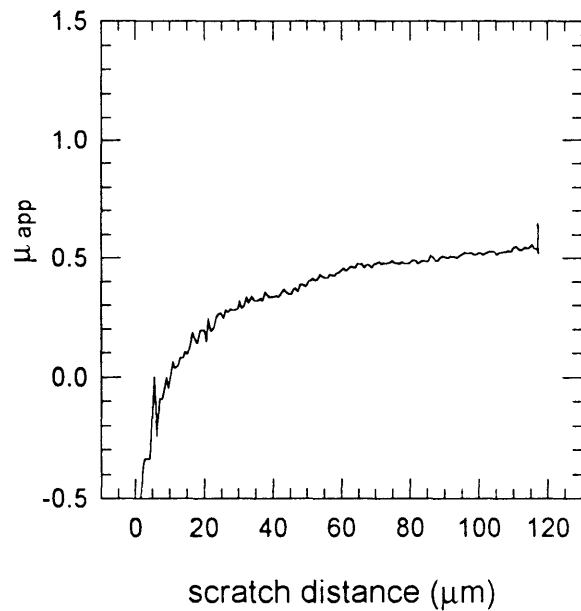
scratch 11-9 normal load
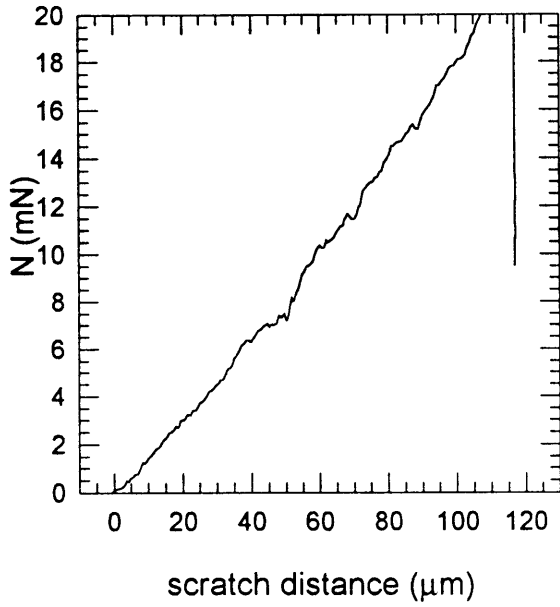
scratch 11-9 tangential load
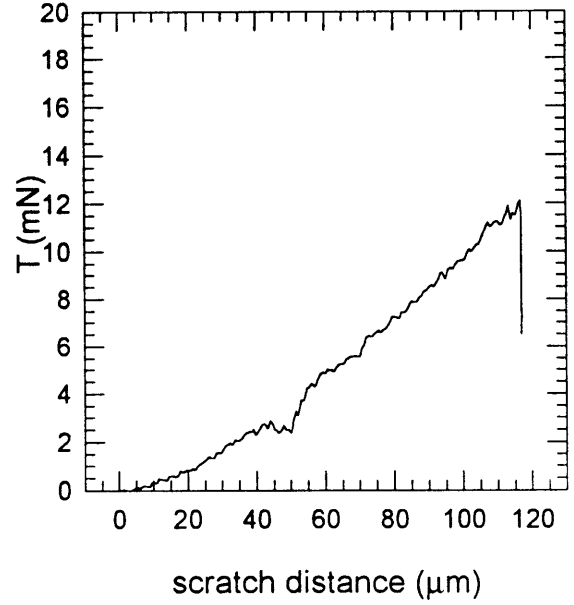
scratch 11-9 scratch depth
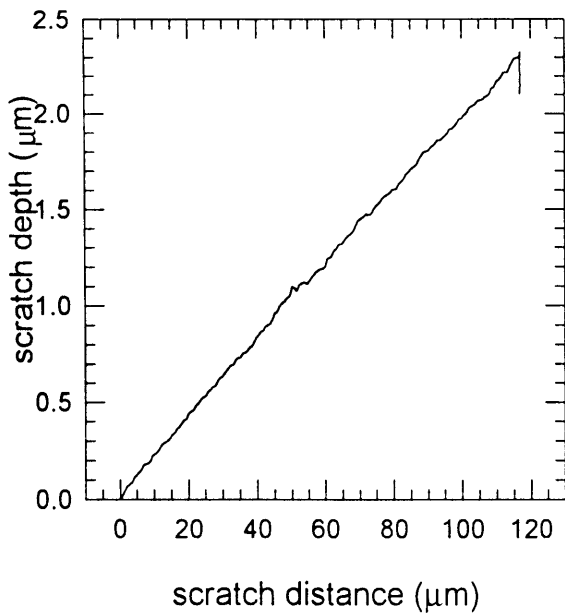
scratch 11-9 friction
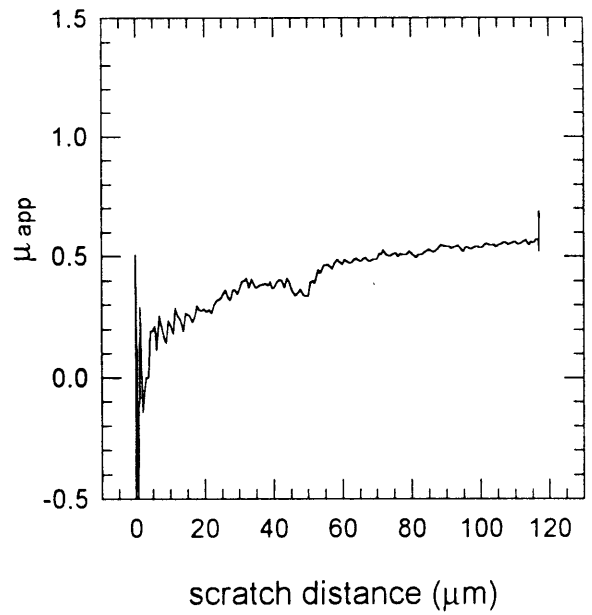
scratch 11-10 normal load
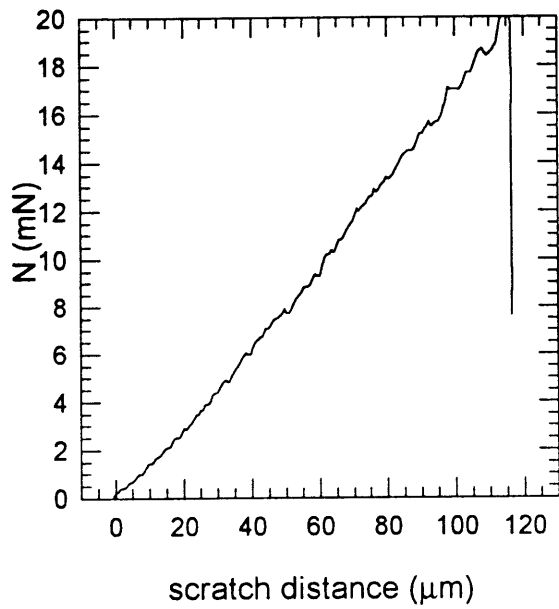
scratch 11-10 tangential load
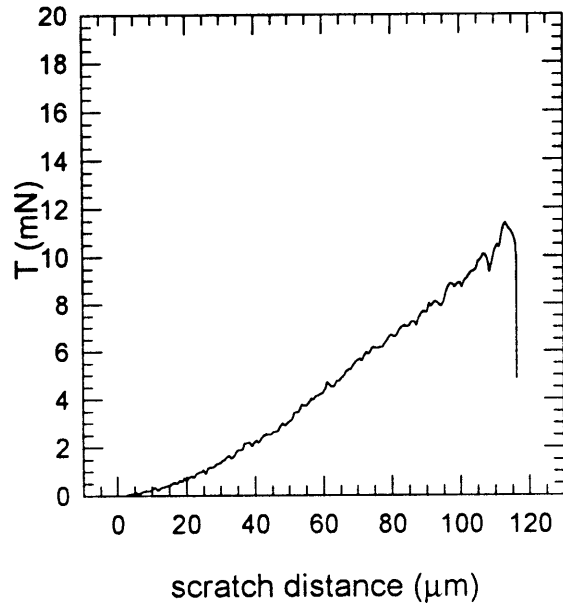
scratch 11-10 scratch depth
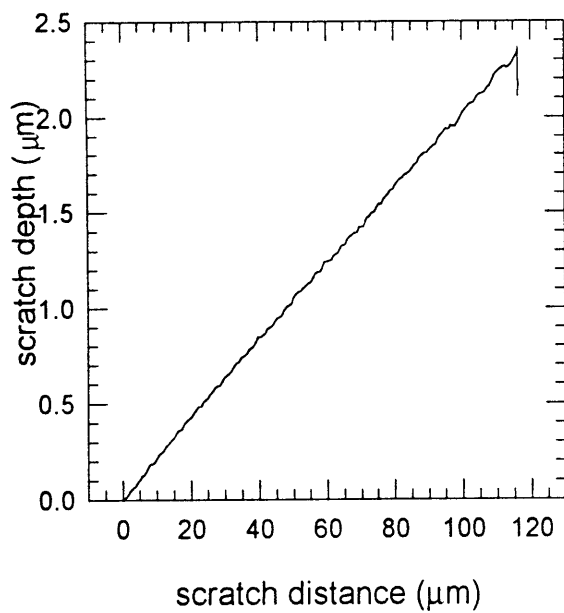
scratch 11-10 friction
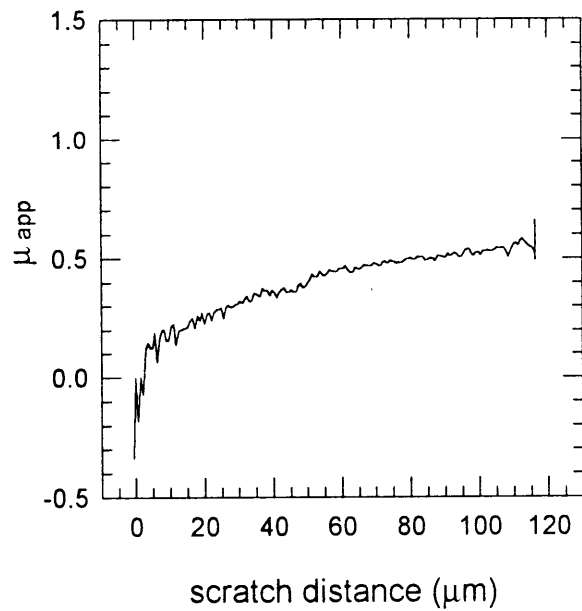
scratch 11-11 normal load
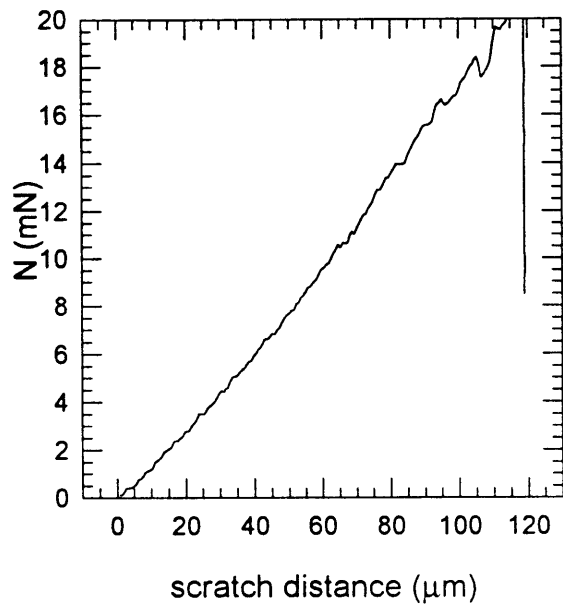
scratch 11-11 tangential load
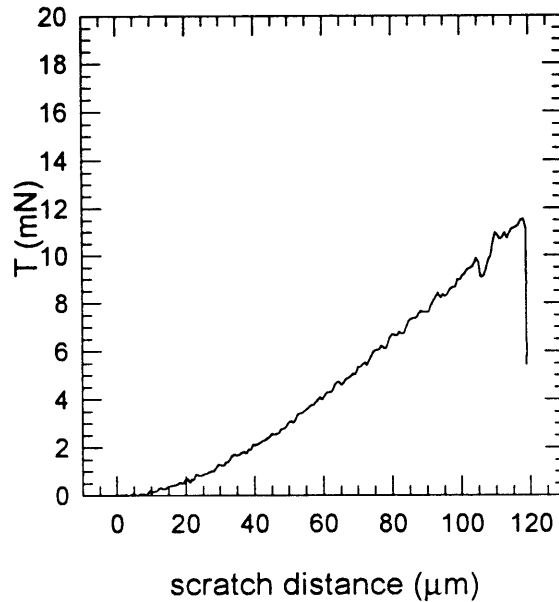
scratch 11-11 scratch depth
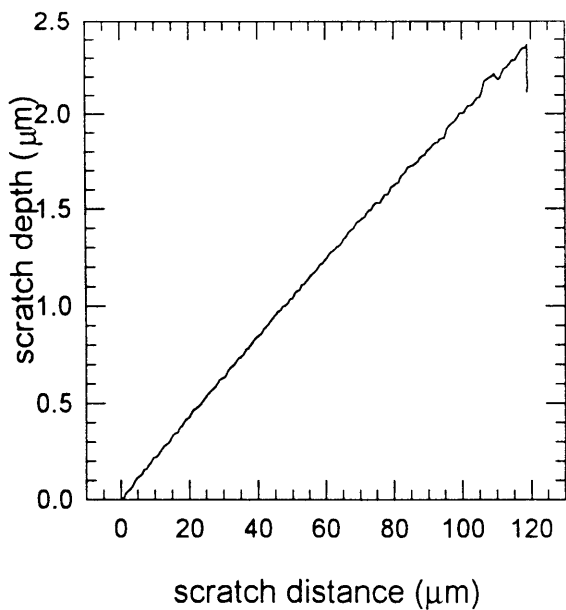
scratch 11-11 friction
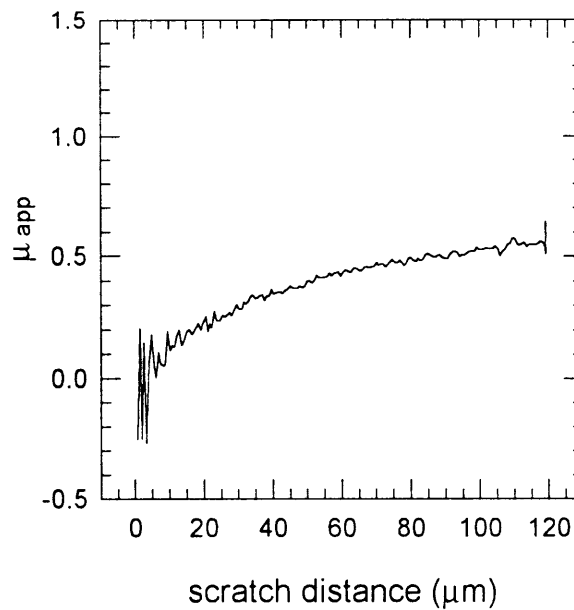
scratch 11-12 normal load
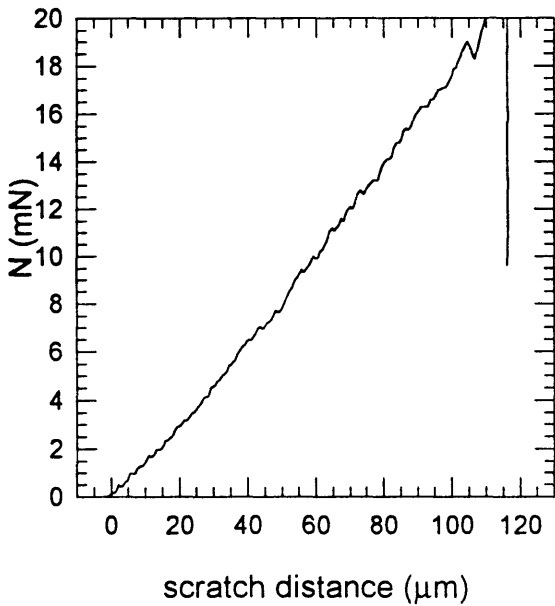
scratch 11-12 tangential load
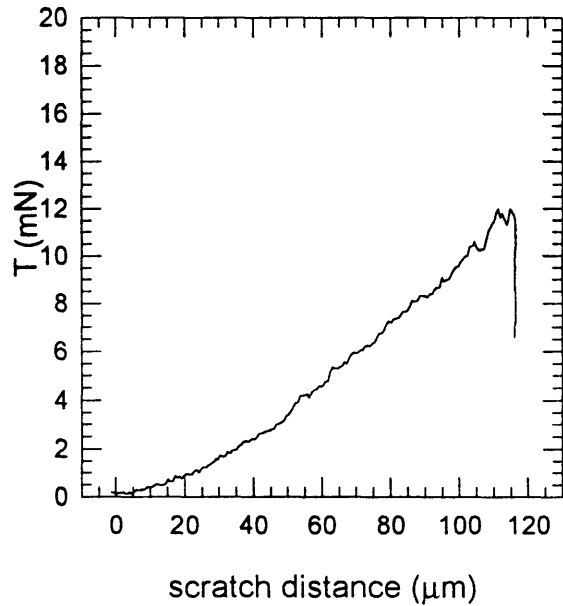
scratch 11-12 scratch depth
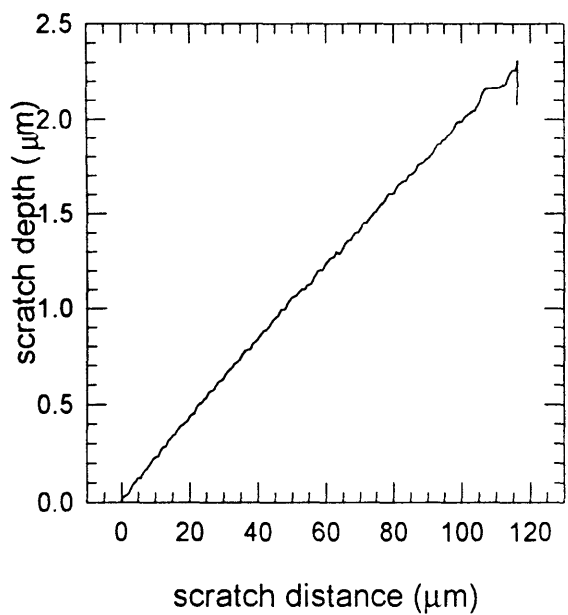
scratch 11-12 friction
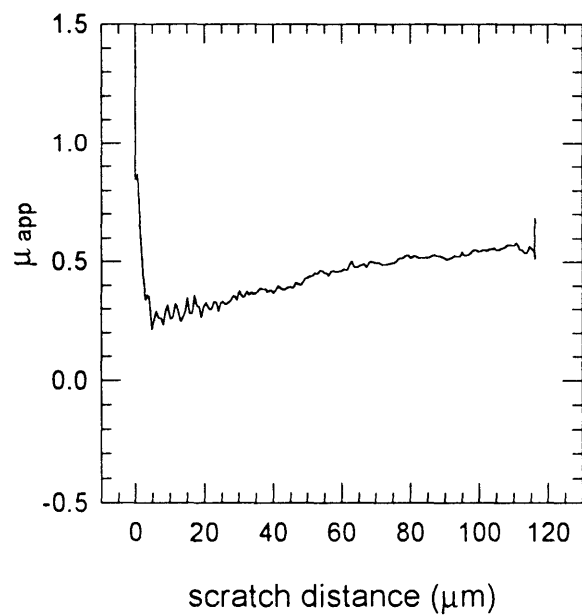
scratch 11-13 normal load
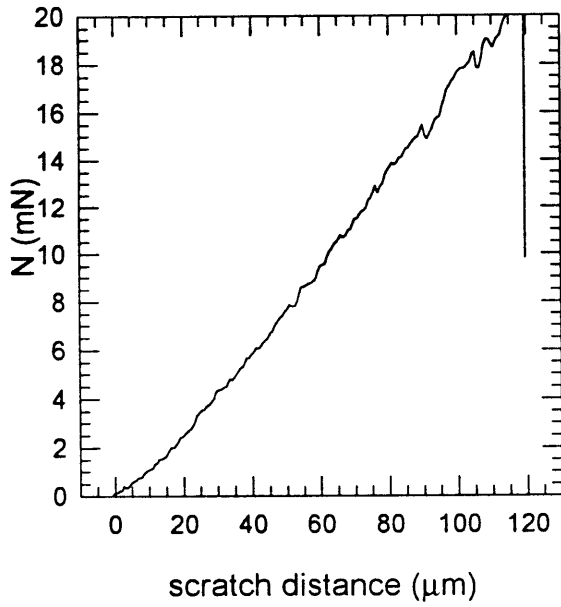
scratch 11-13 tangential load
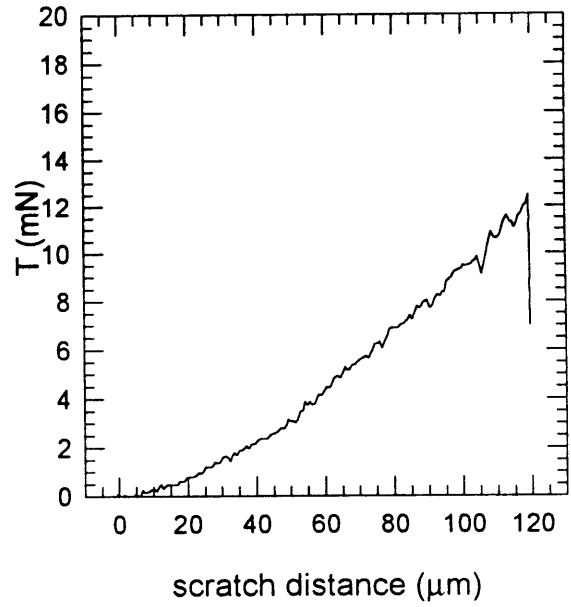
scratch 11-13 scratch depth
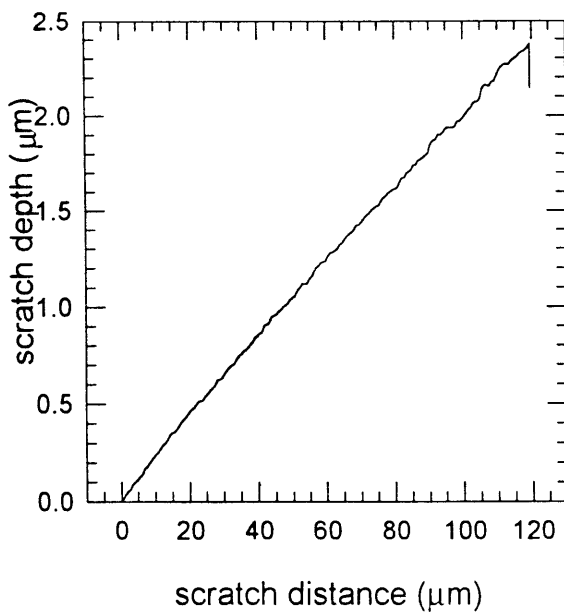
scratch 11-13 friction
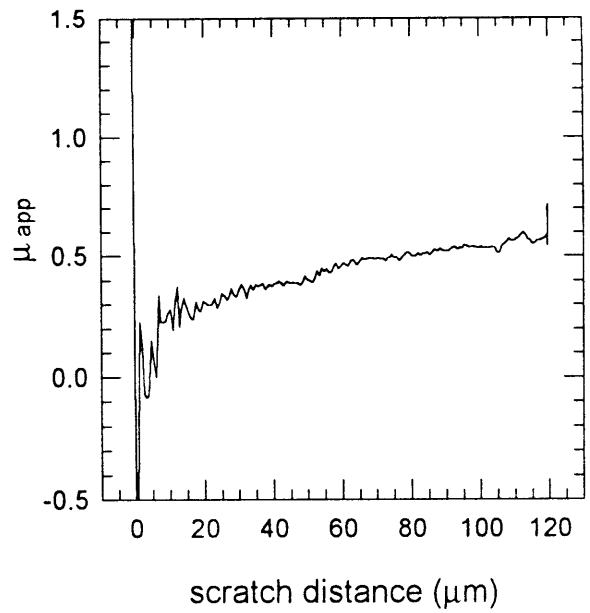
scratch 11-14 normal load
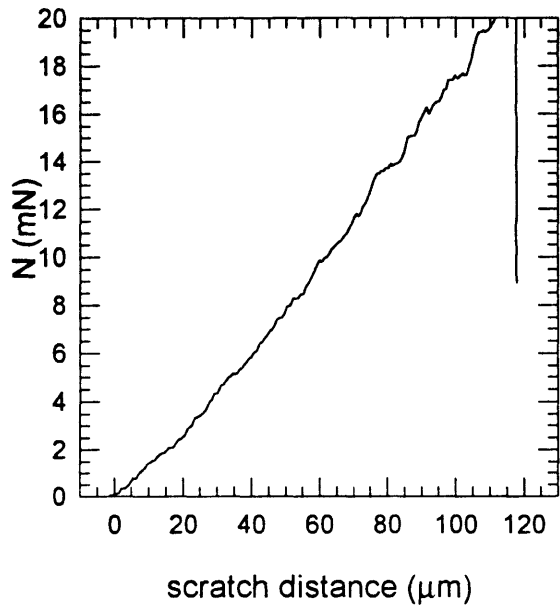
scratch 11-14 tangential load
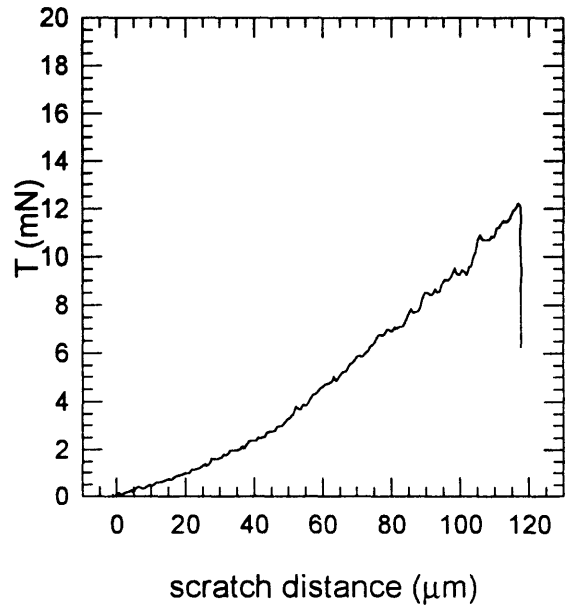
scratch 11-14 scratch depth
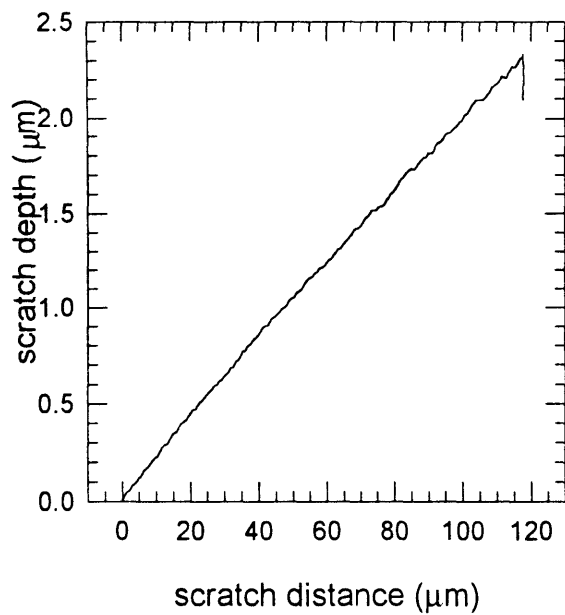
scratch 11-14 friction
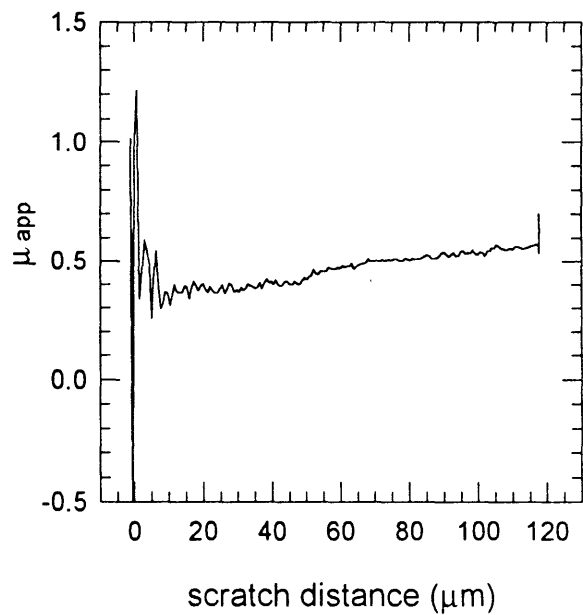
scratch 12-2 normal load
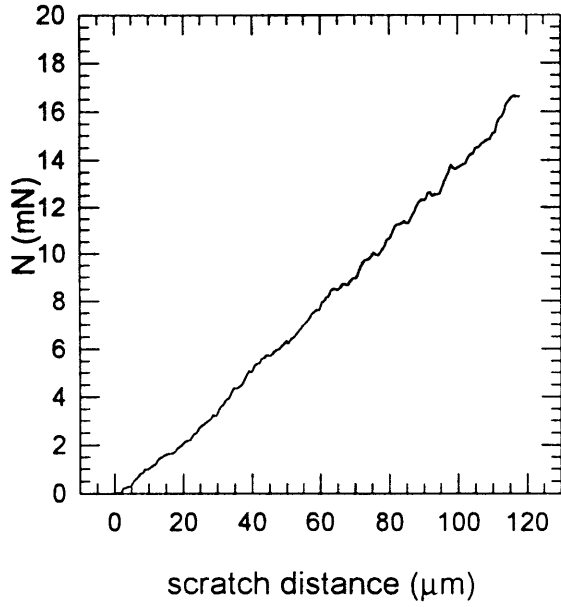
scratch 12-2 tangential load
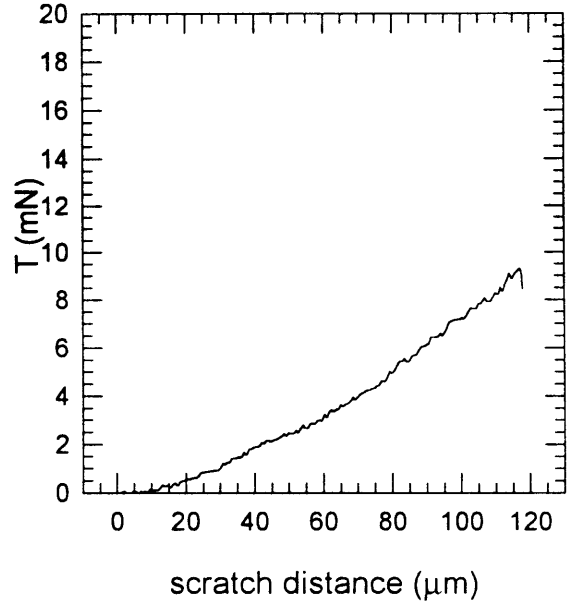
scratch 12-2 scratch depth
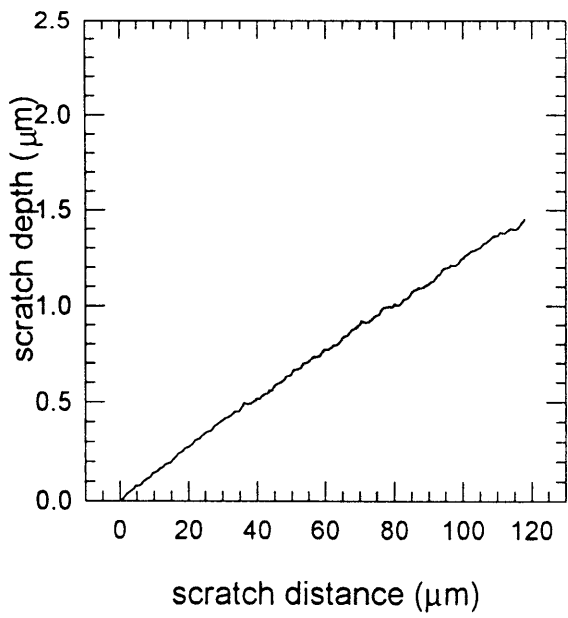
scratch 12-2 friction
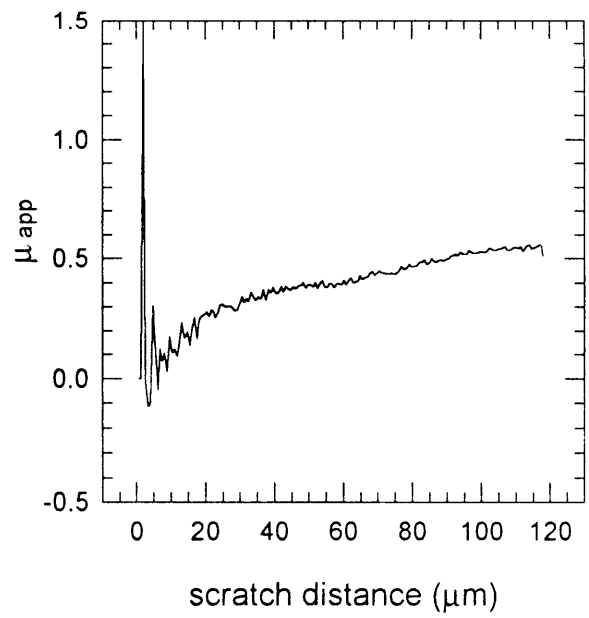
scratch 12-3 normal load
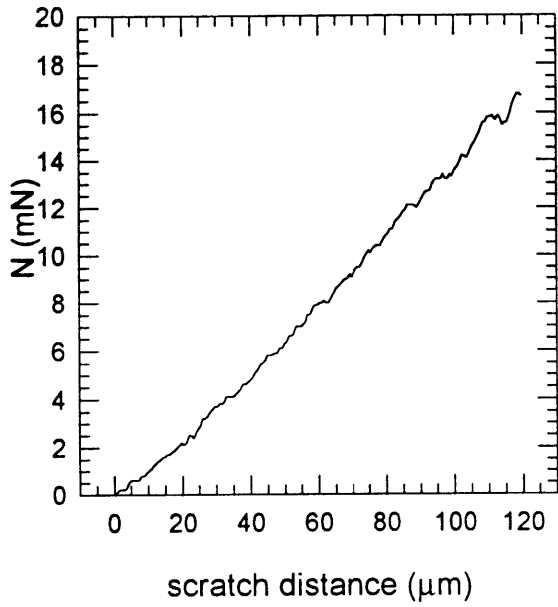
scratch 12-3 tangential load
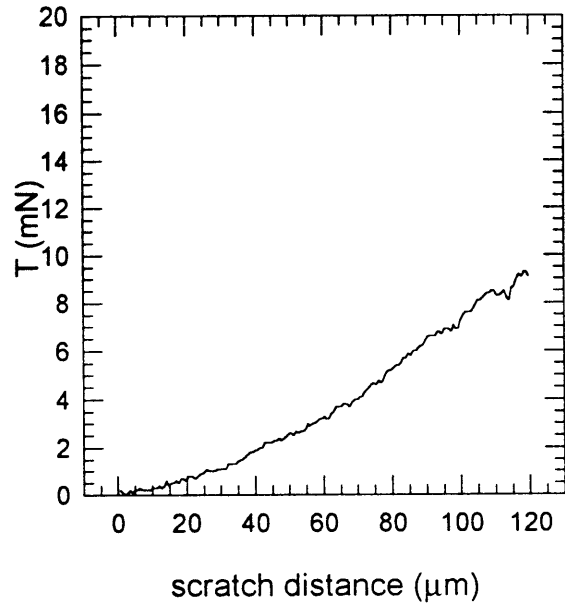
scratch 12-3 scratch depth
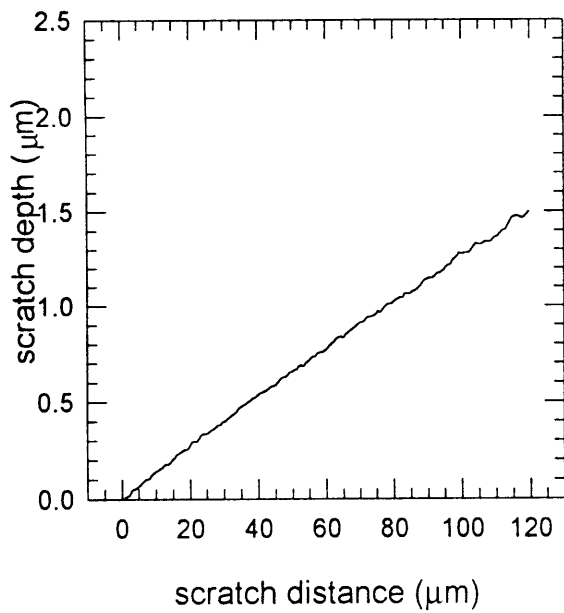
scratch 12-3 friction
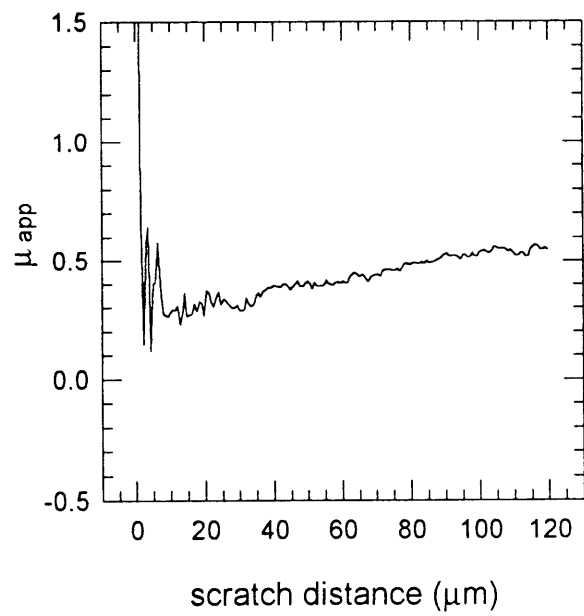
scratch 12-4 normal load
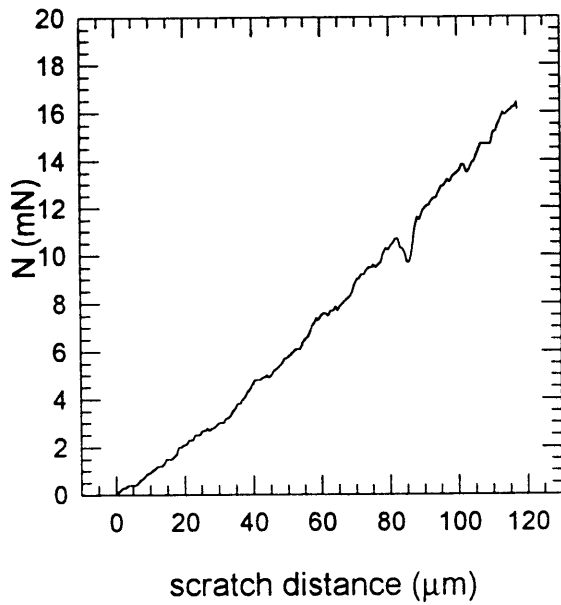
scratch 12-4 tangential load
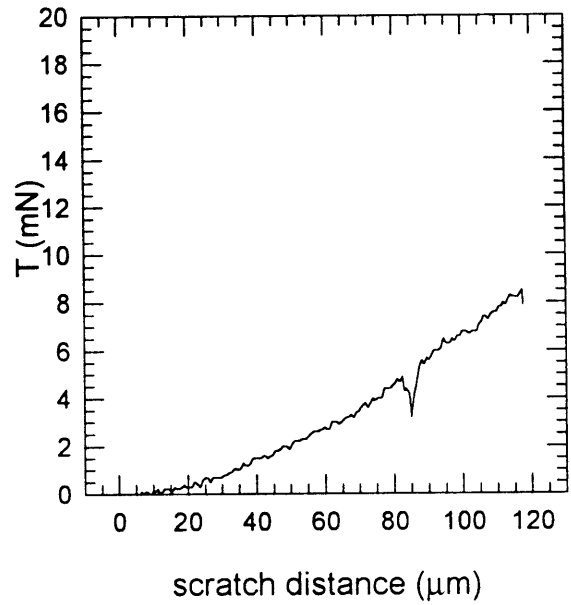
scratch 12-4 scratch depth
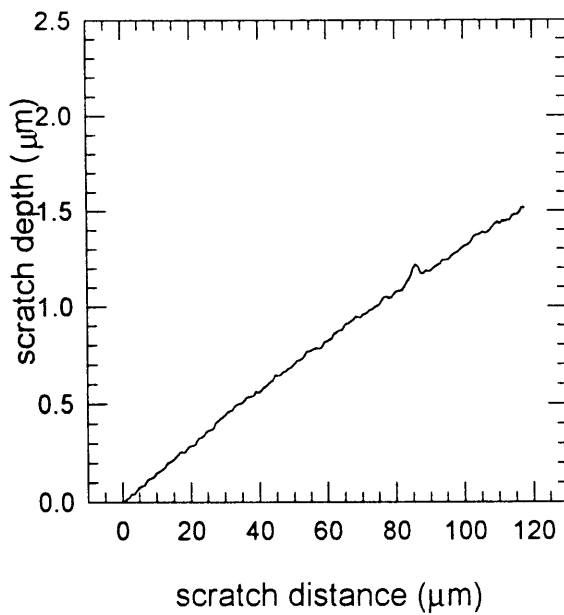
scratch 12-4 friction
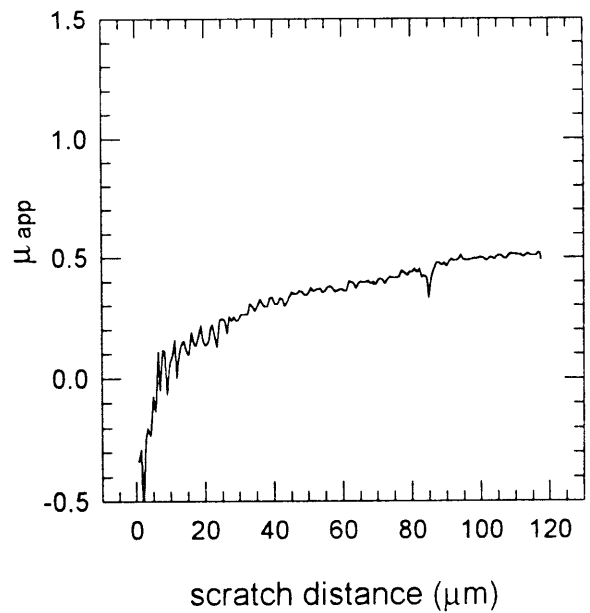
scratch 12-5 normal load
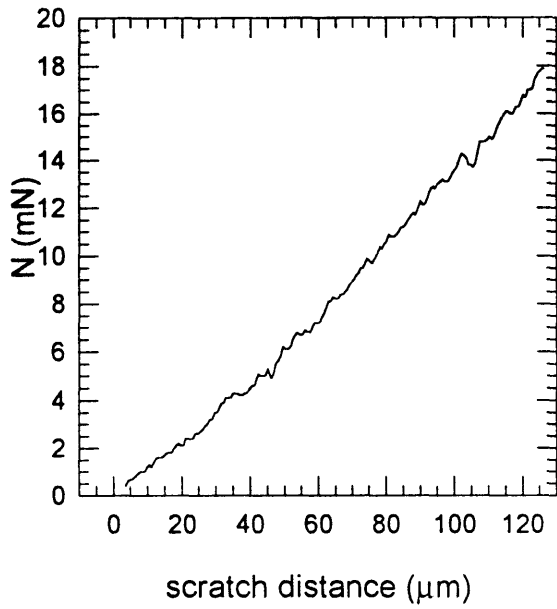
scratch 12-5 tangential load
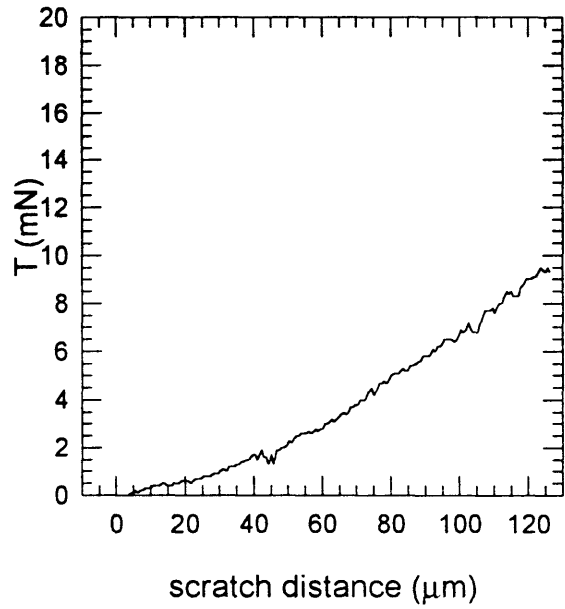
scratch 12-5 scratch depth
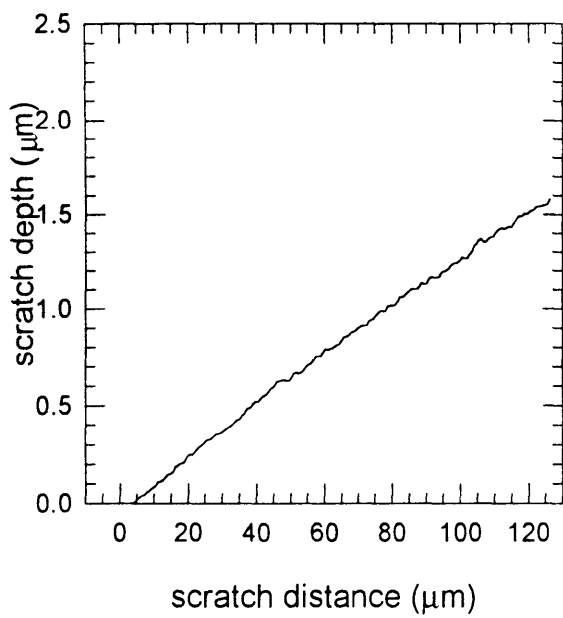
scratch 12-5 friction
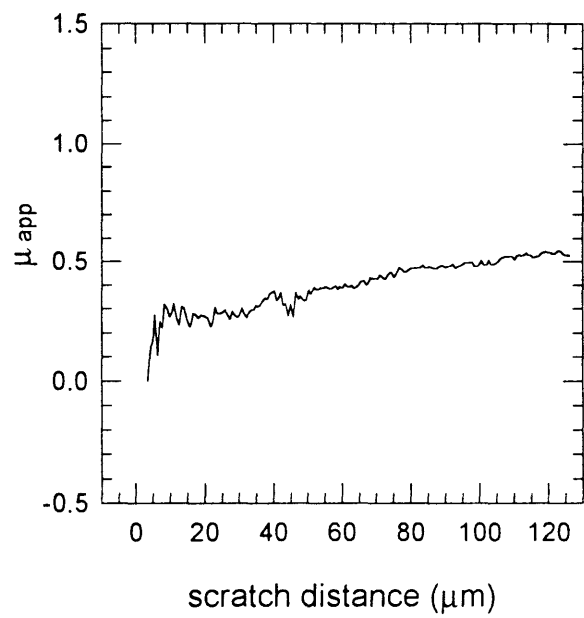
scratch 12-6 normal load
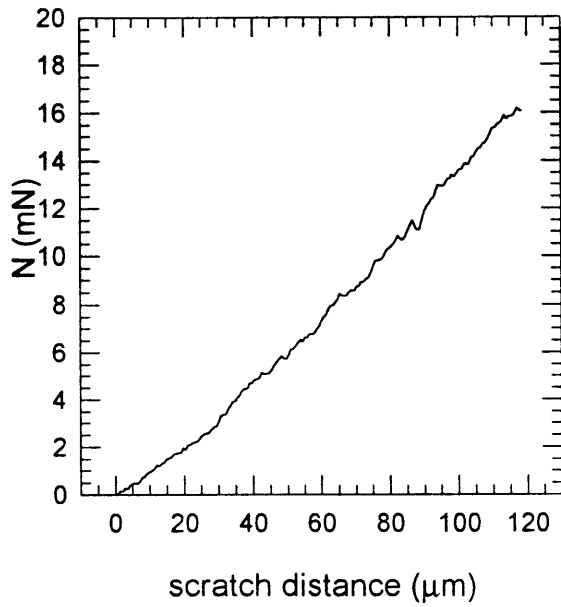
scratch 12-6 tangential load
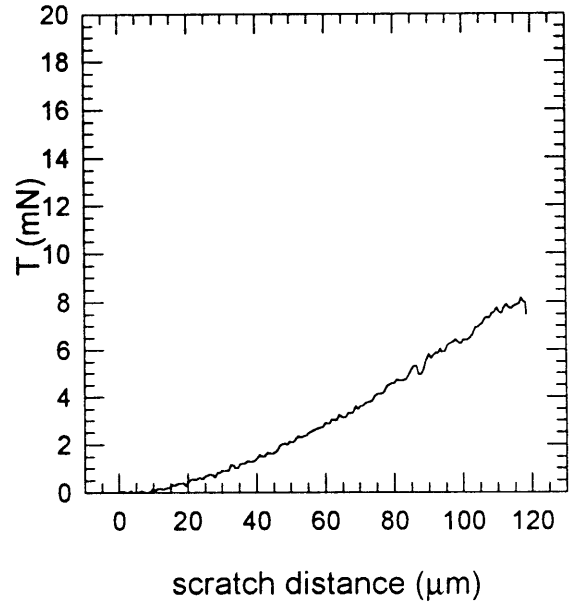
scratch 12-6 scratch depth
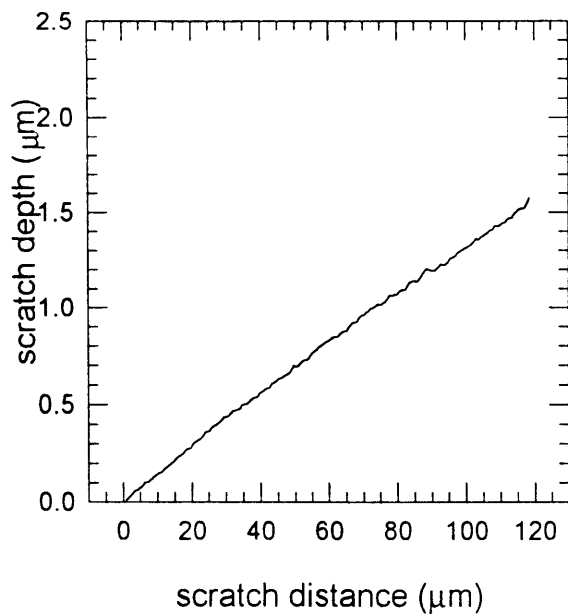
scratch 12-6 friction
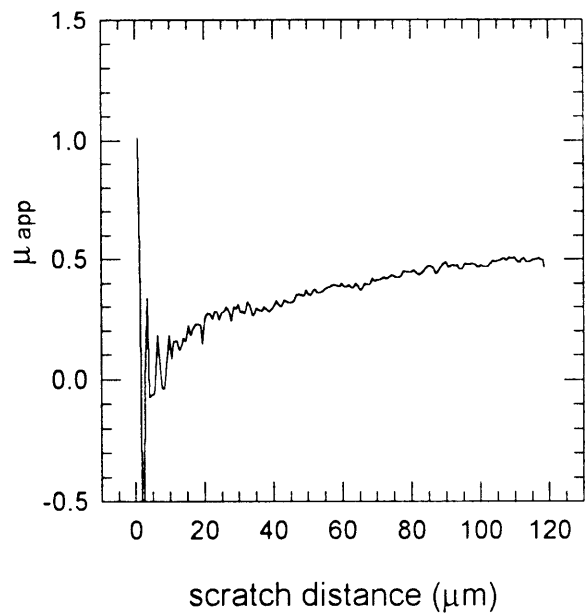
scratch 12-7 normal load
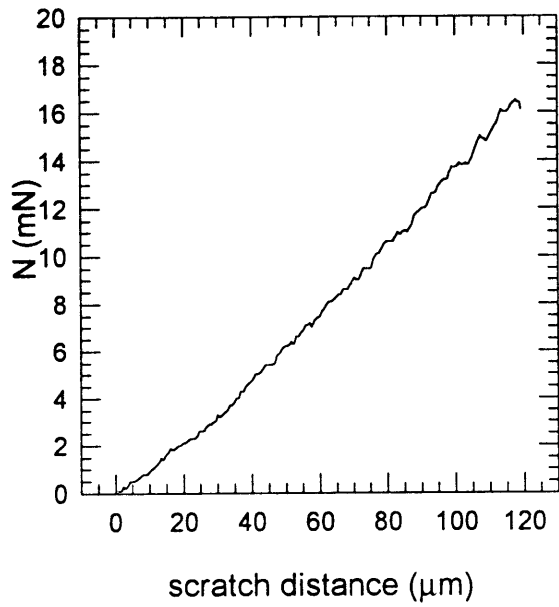
scratch 12-7 tangential load
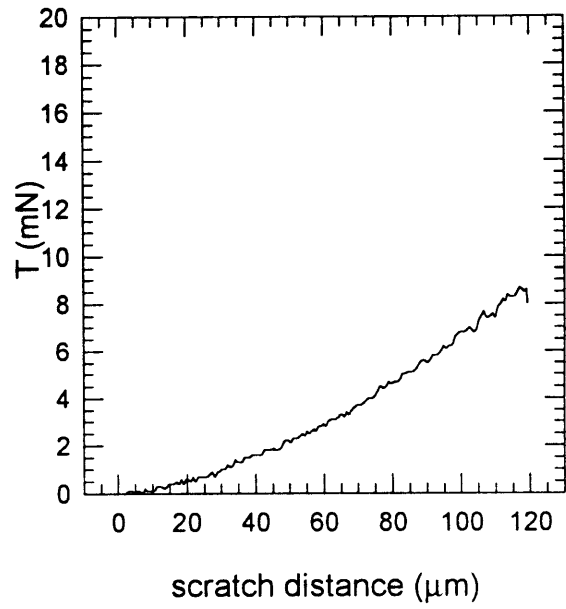
scratch 12-7 scratch depth
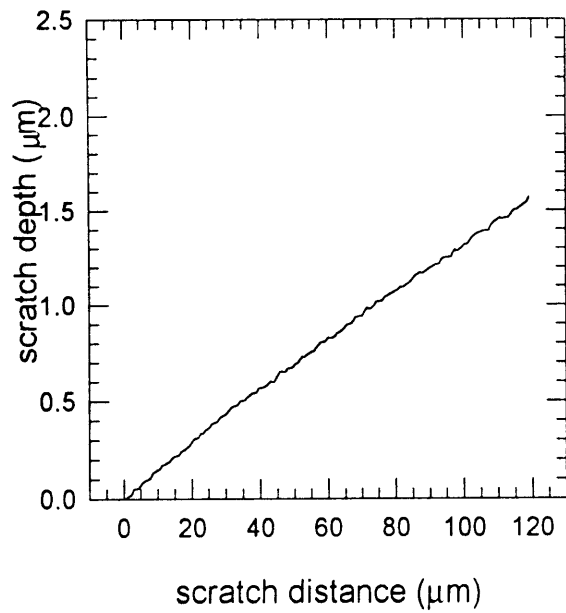
scratch 12-7 friction
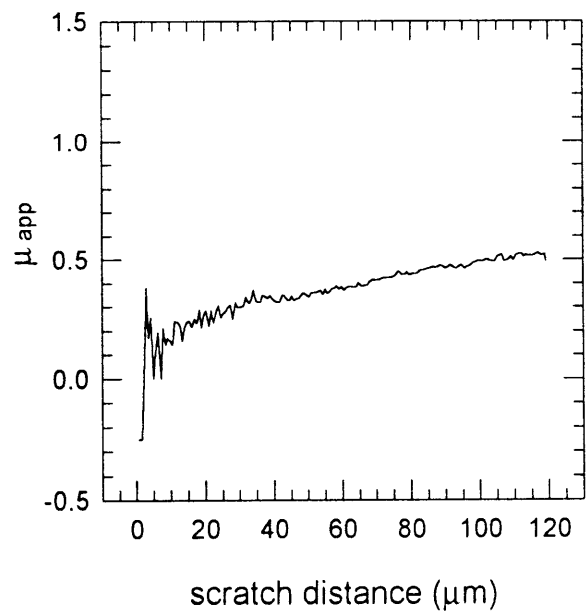
scratch 12-8 normal load
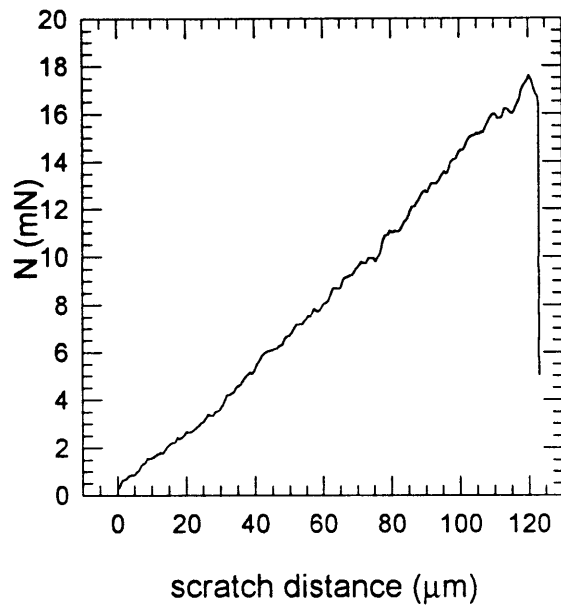
scratch 12-8 tangential load
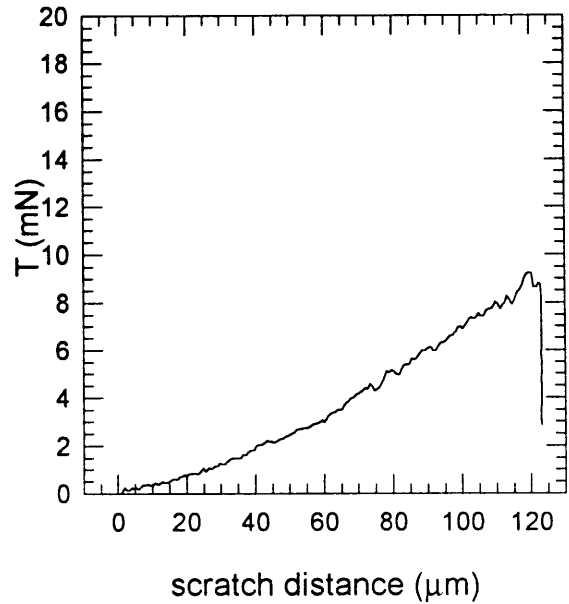
scratch 12-8 scratch depth
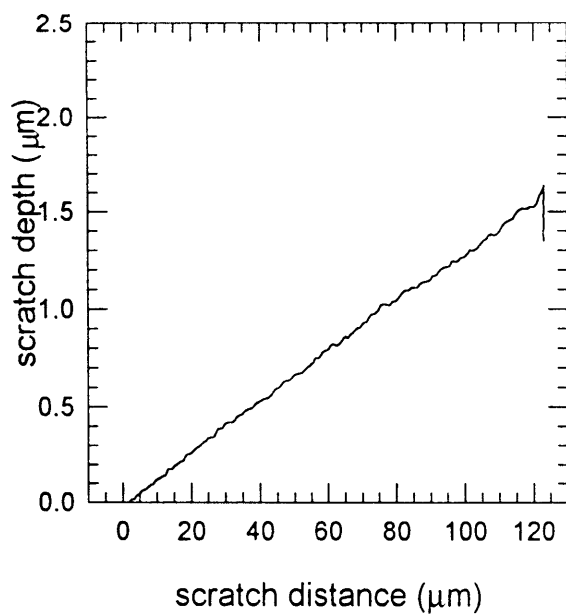
scratch 12-8 friction
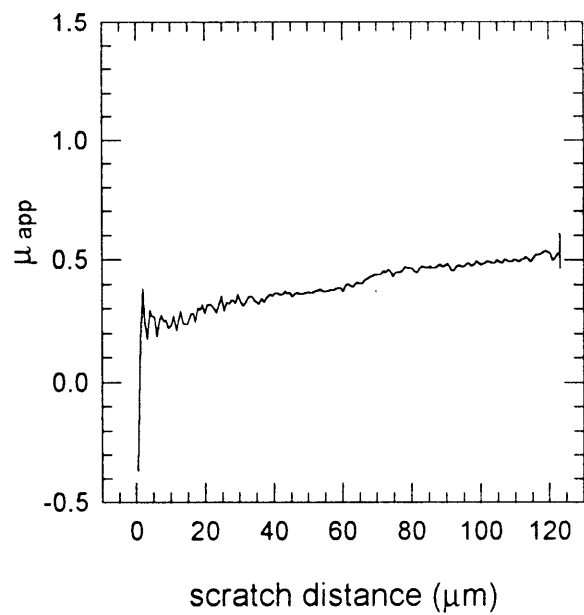
scratch 12-9 normal load
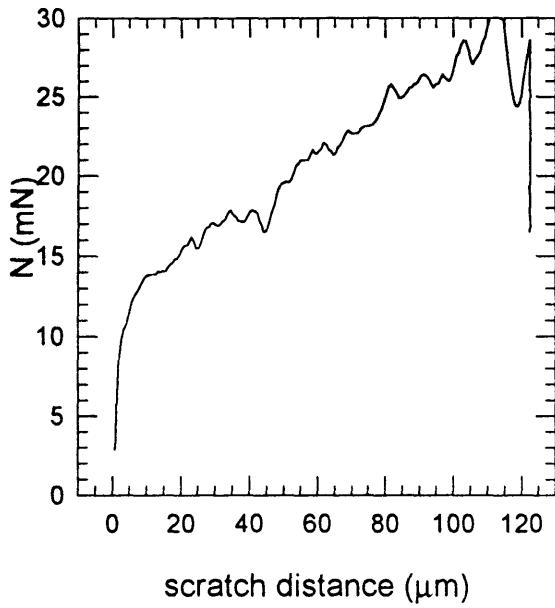
scratch 12-9 tangential load
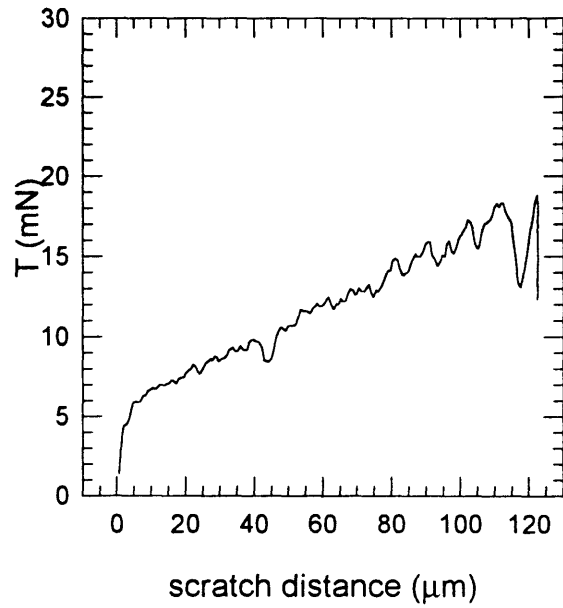
scratch 12-9 scratch depth
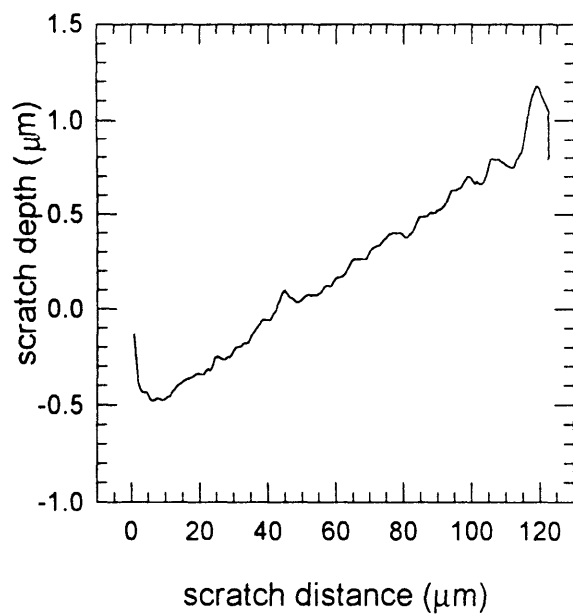
scratch 12-9 friction
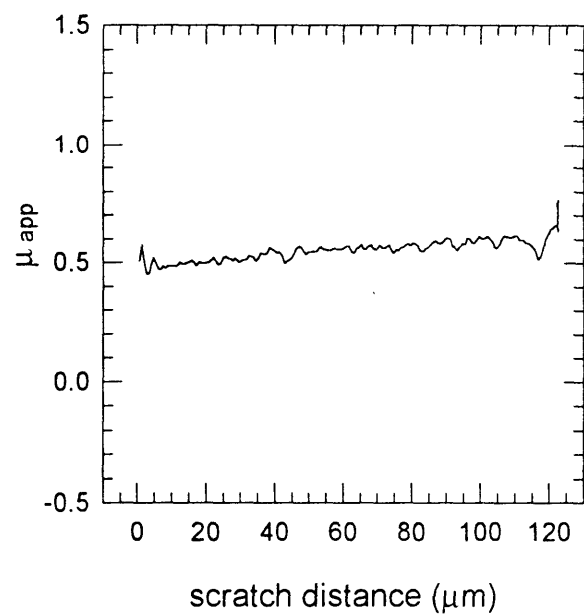
scratch 12-10 normal load
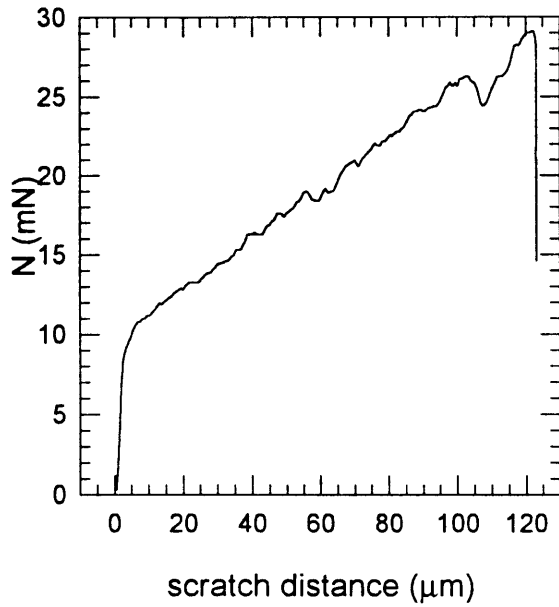
scratch 12-10 tangential load
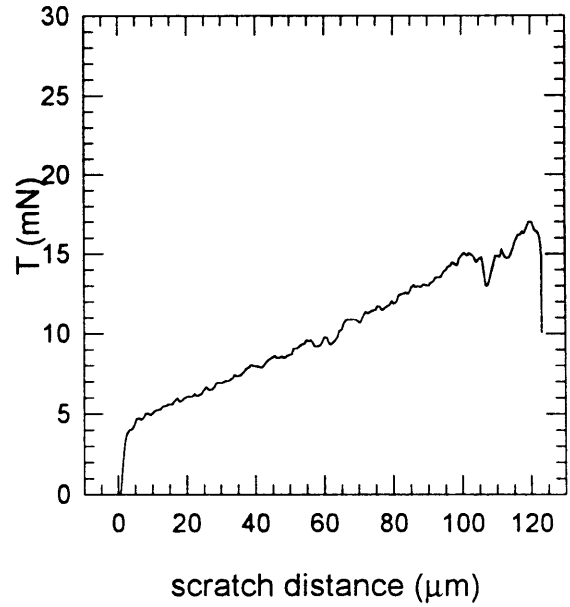
scratch 12-10 scratch depth
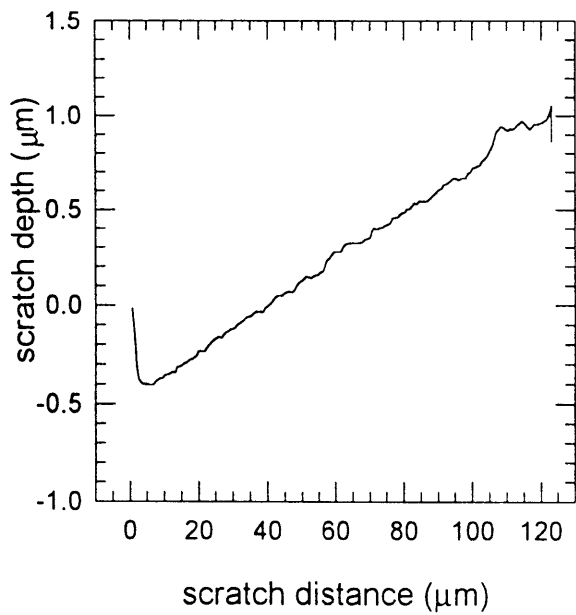
scratch 12-10 friction
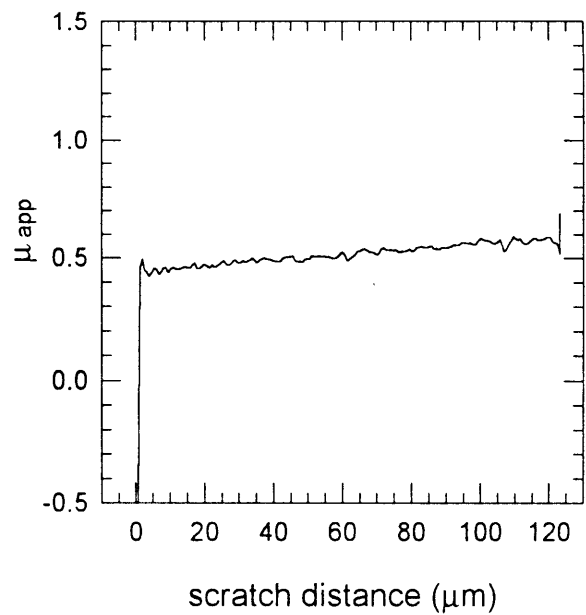
scratch 12-11 normal load
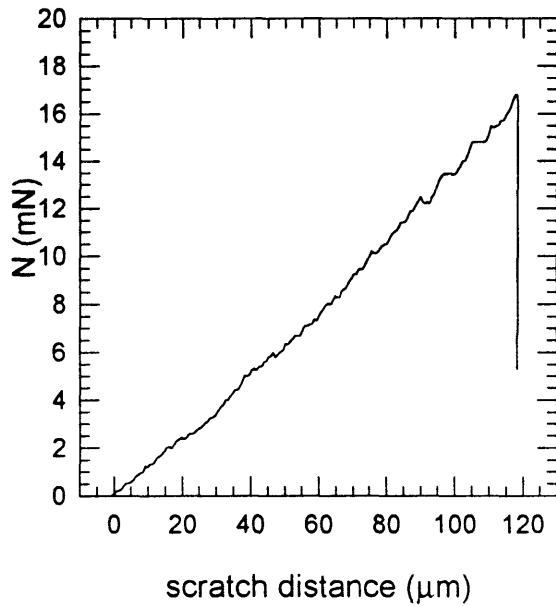
scratch 12-11 tangential load
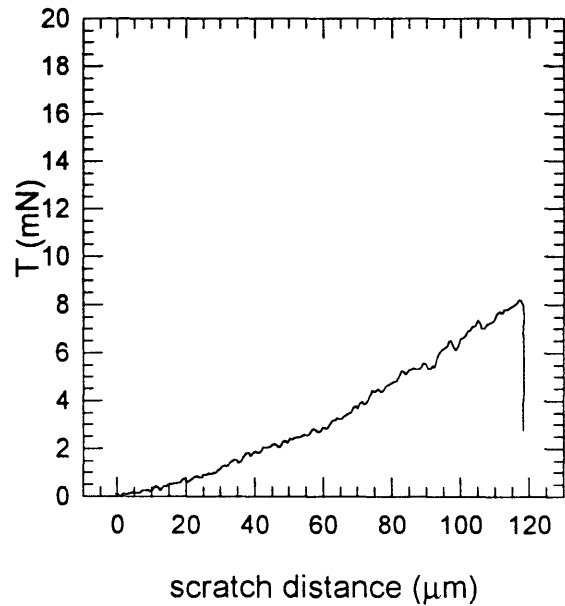
scratch 12-11 scratch depth
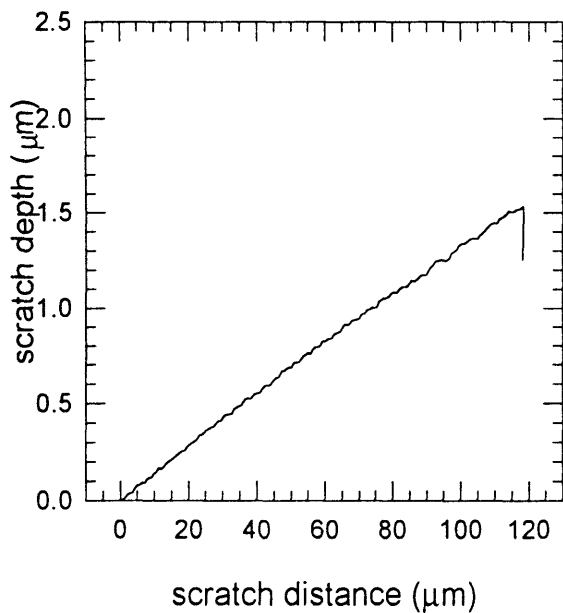
scratch 12-11 friction
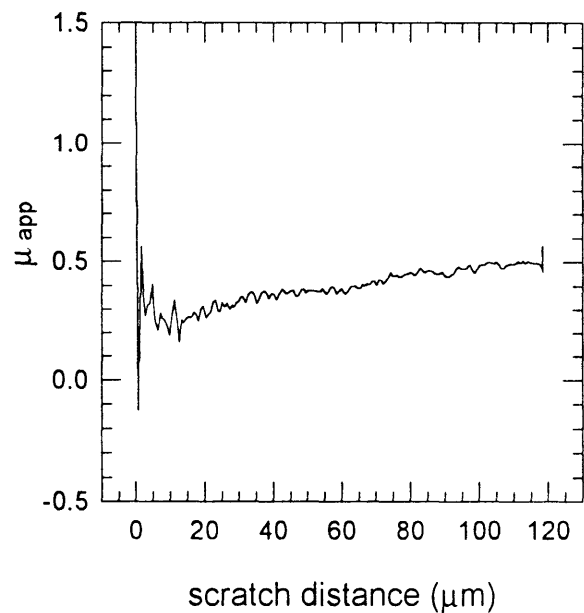
scratch 13-2 normal load
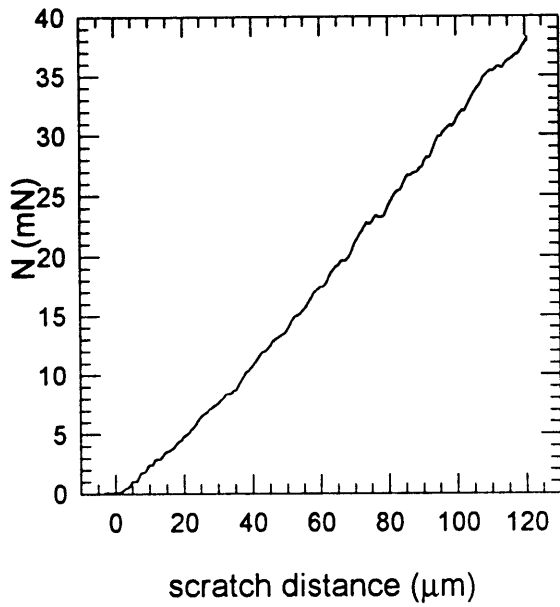
scratch 13-2 tangential load
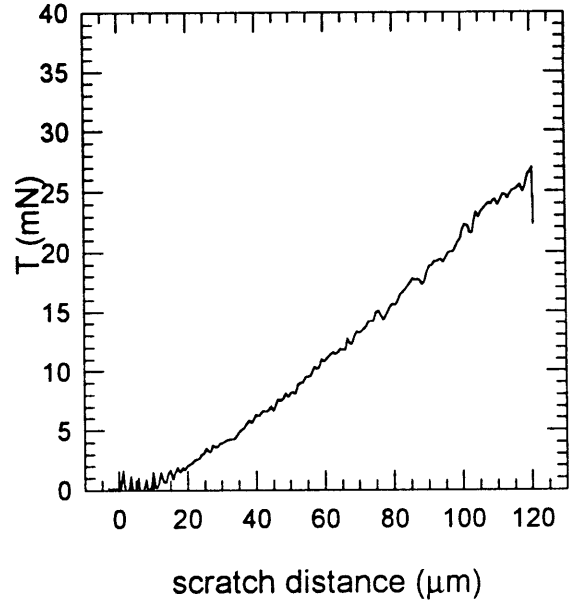
scratch 13-2 scratch depth
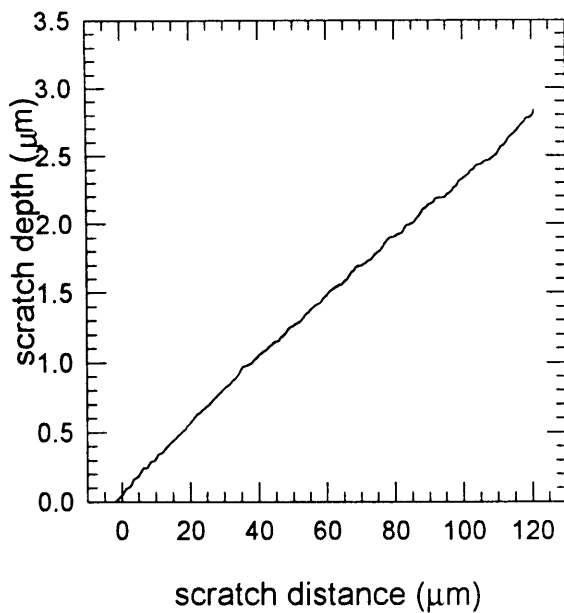
scratch 13-2 friction
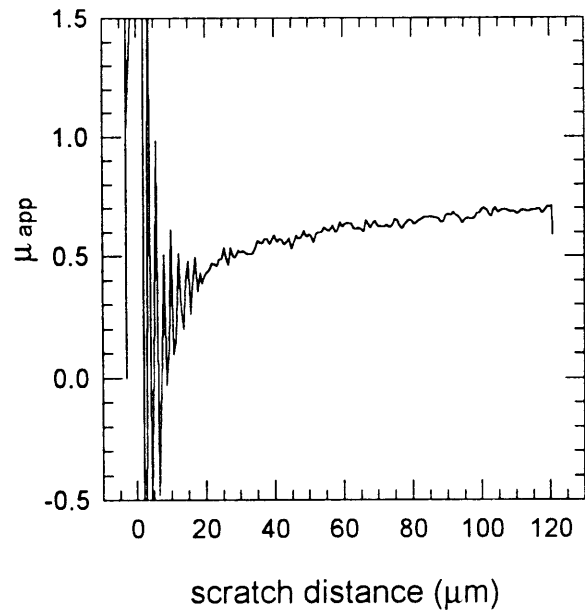
scratch 13-3 normal load
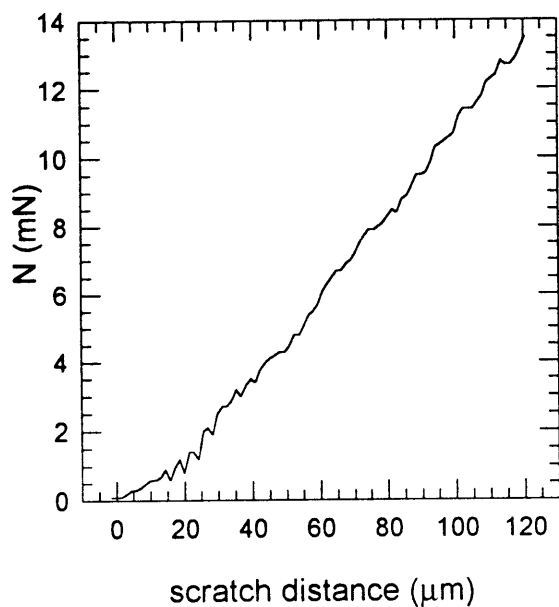
scratch 13-3 tangential load
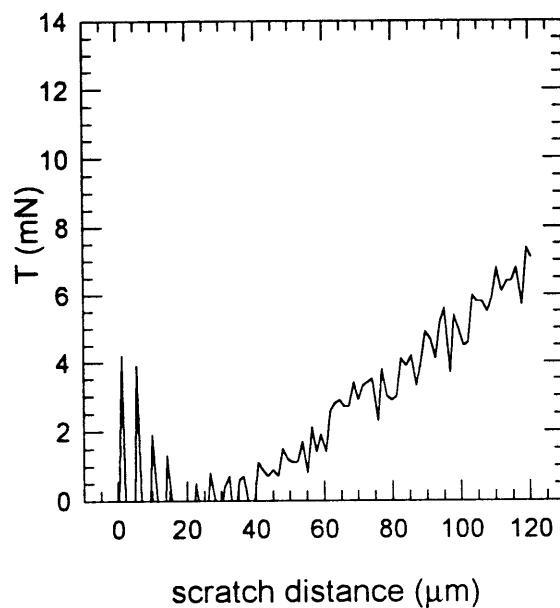
scratch 13-3 scratch depth
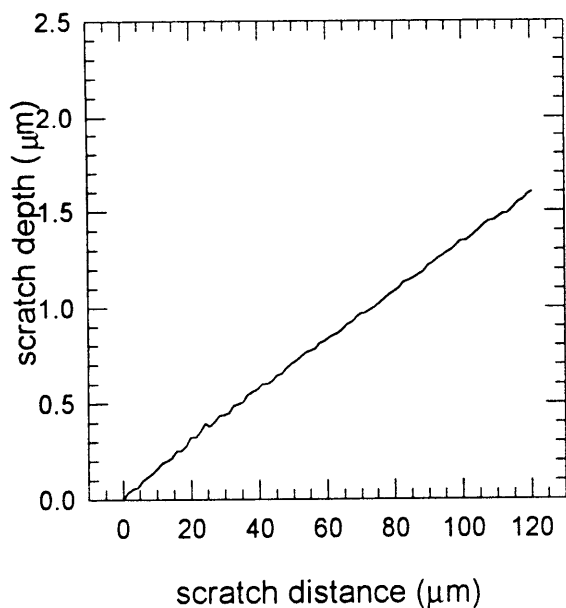
scratch 13-3 friction
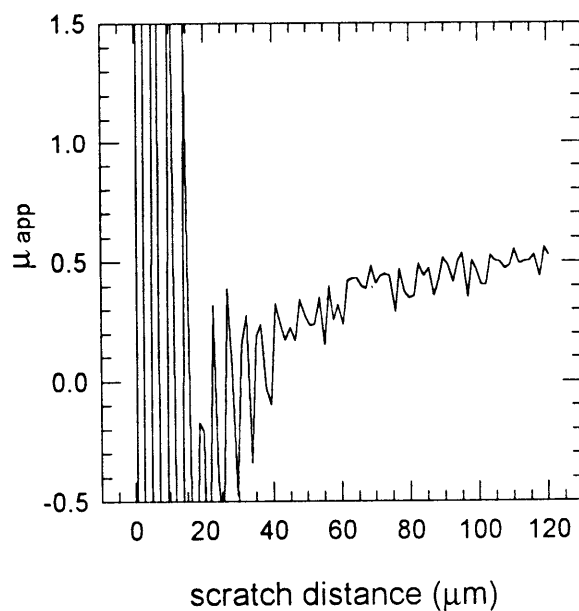
scratch 13-4 normal load
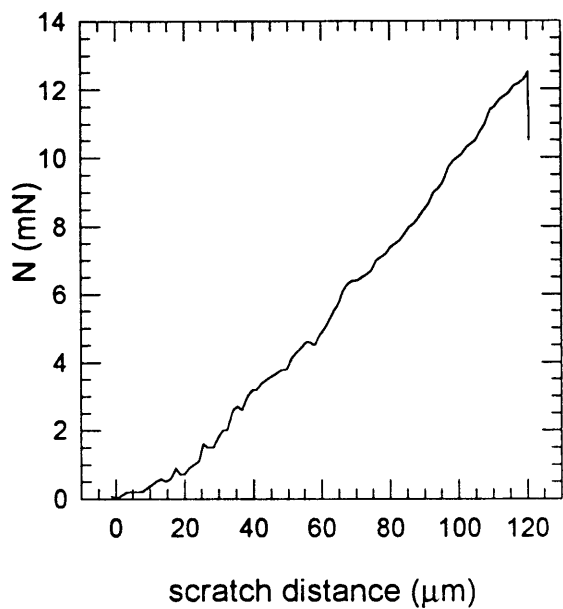
scratch 13-4 tangential load
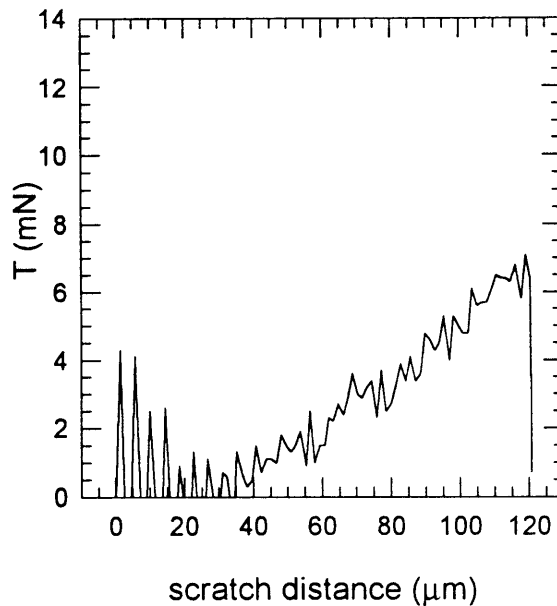
scratch 13-4 scratch depth
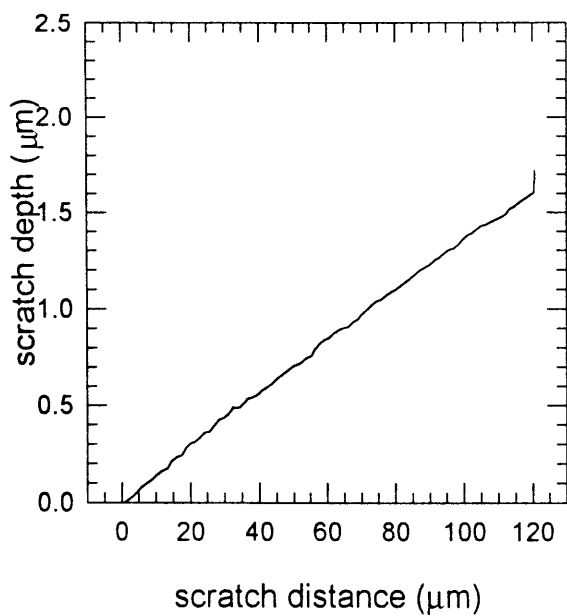
scratch 13-4 friction
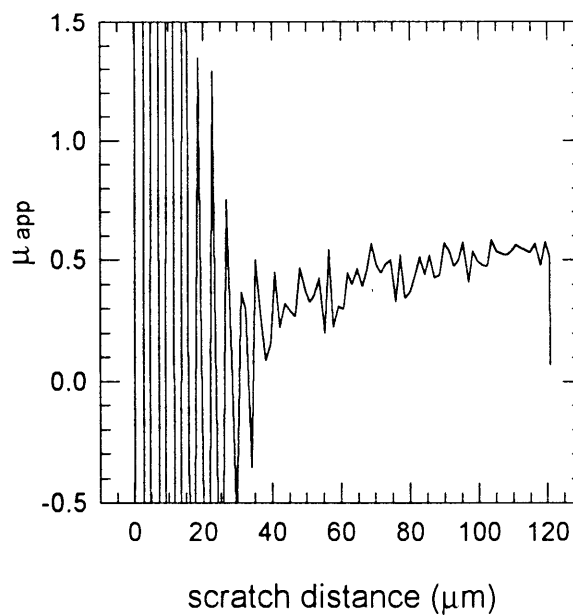
scratch 13-5 normal load
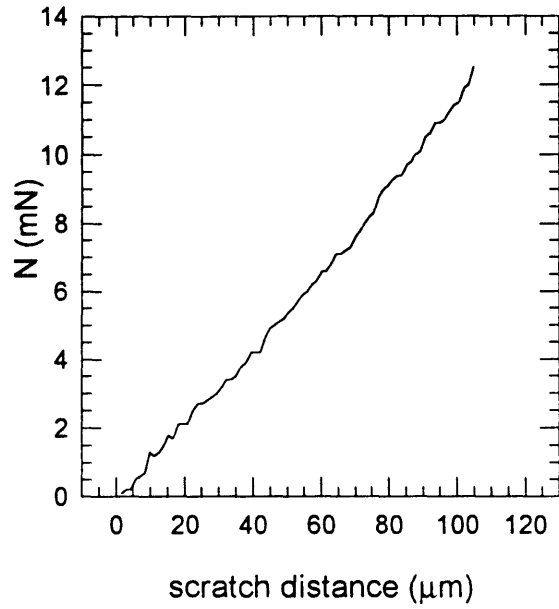
scratch 13-5 tangential load
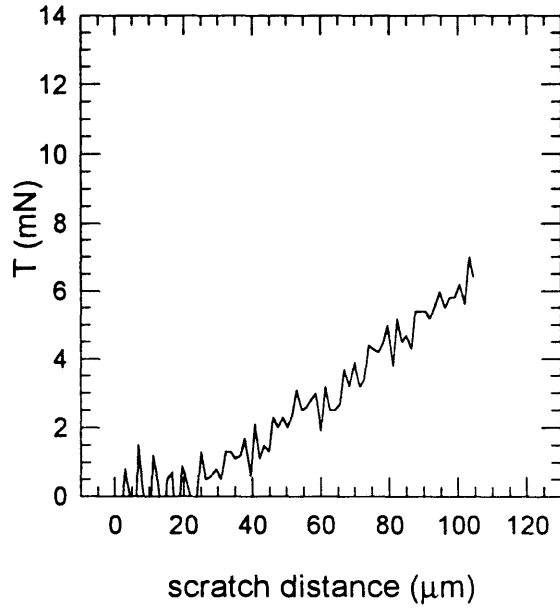
scratch 13-5 scratch depth
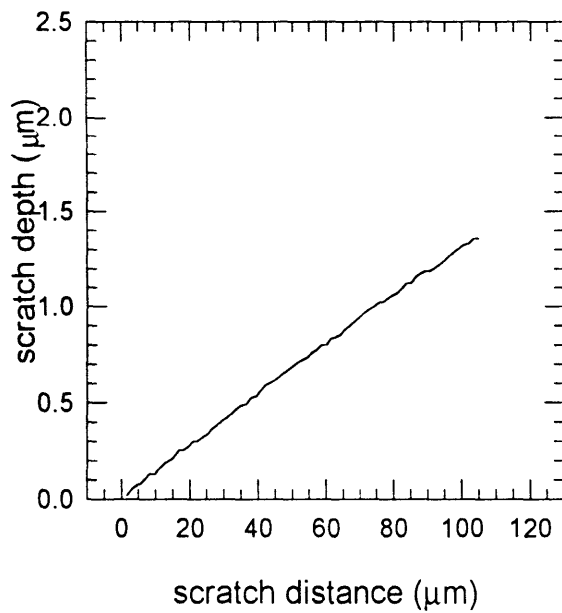
scratch 13-5 friction
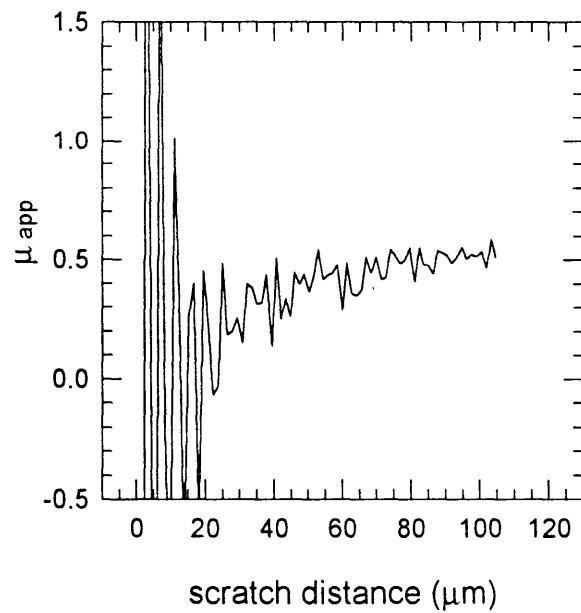
scratch 13-6 normal load
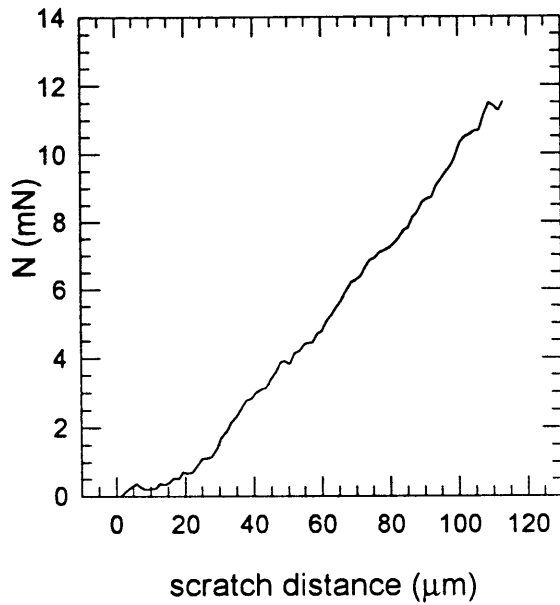
scratch 13-6 tangential load
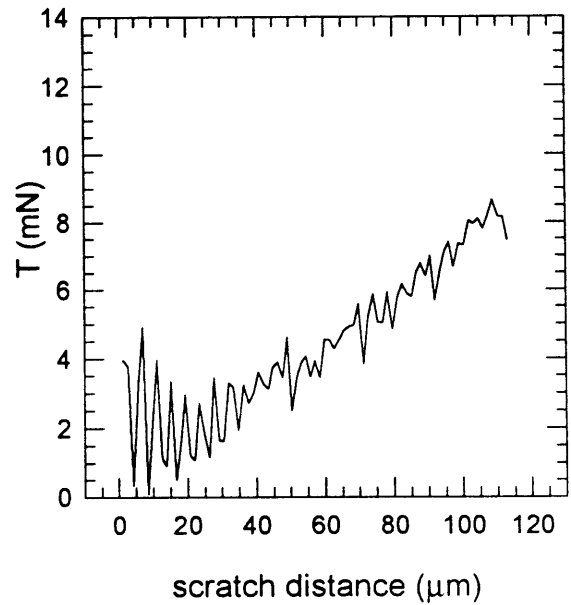
scratch 13-6 scratch depth
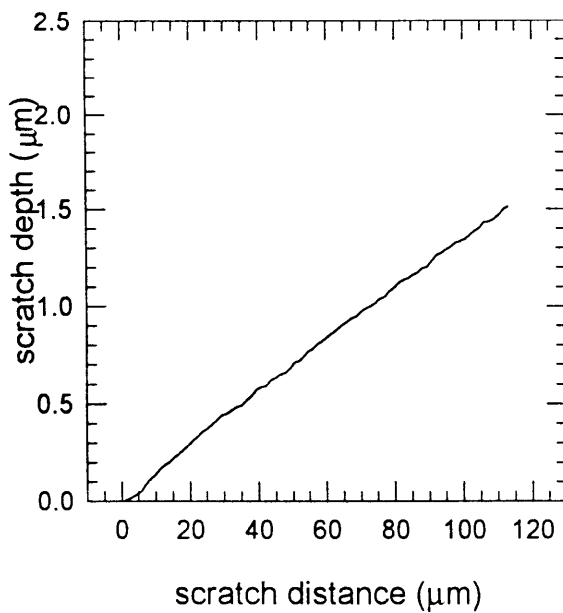
scratch 13-6 friction
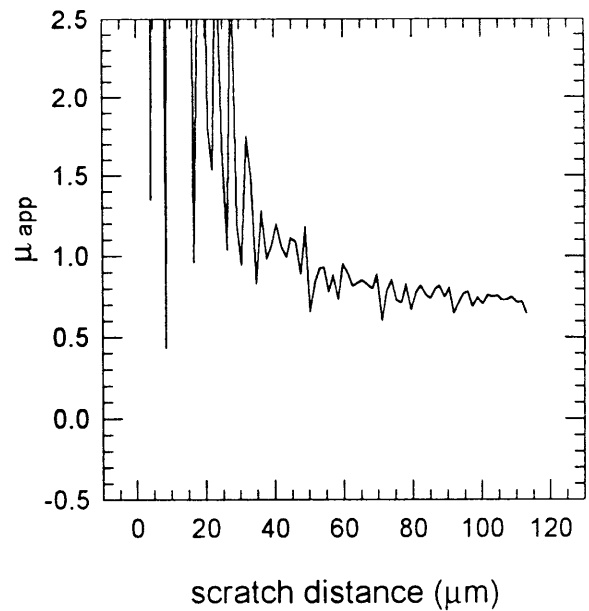
scratch 13-7 normal load
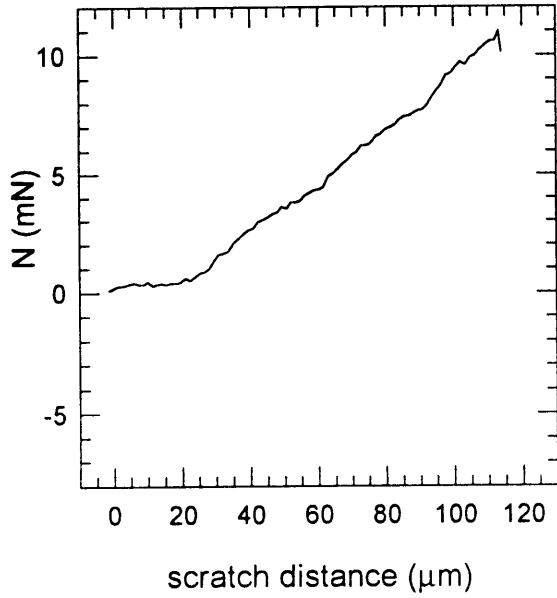
scratch 13-7 tangential load
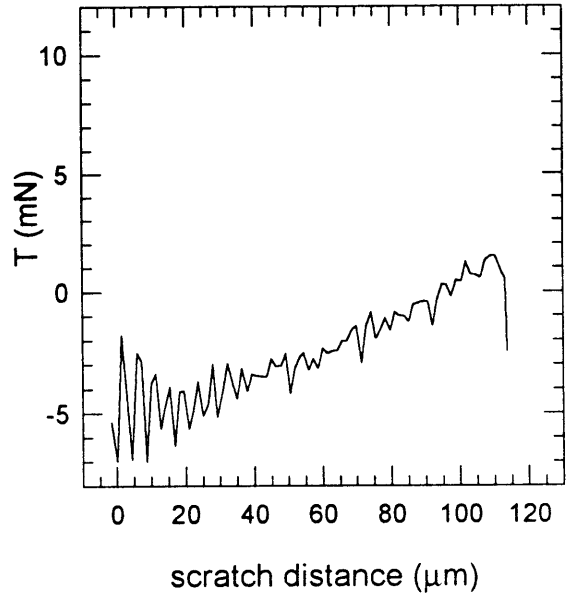
scratch 13-7 scratch depth
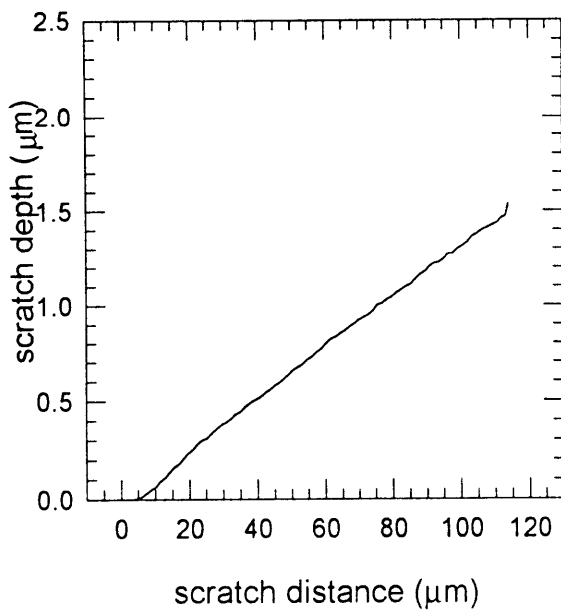
scratch 13-7 friction
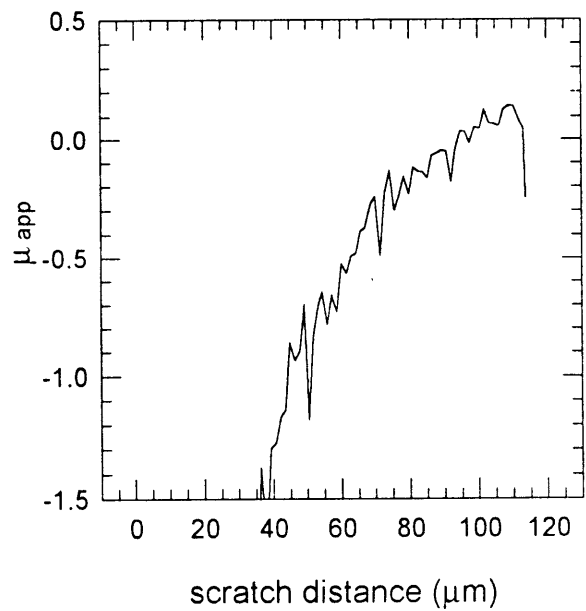
scratch 13-8 normal load
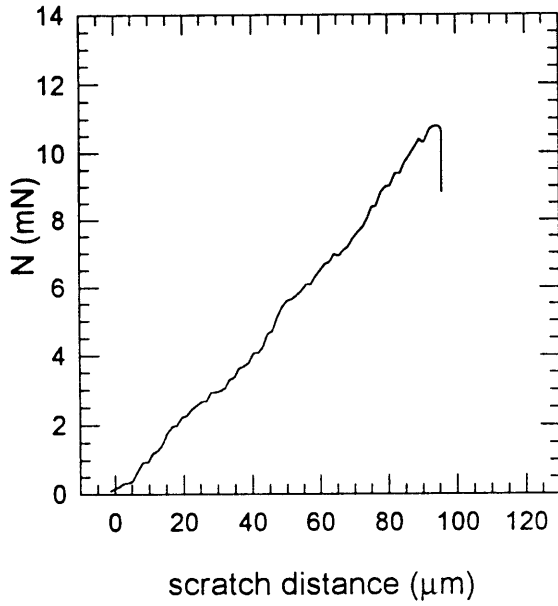
scratch 13-8 tangential load
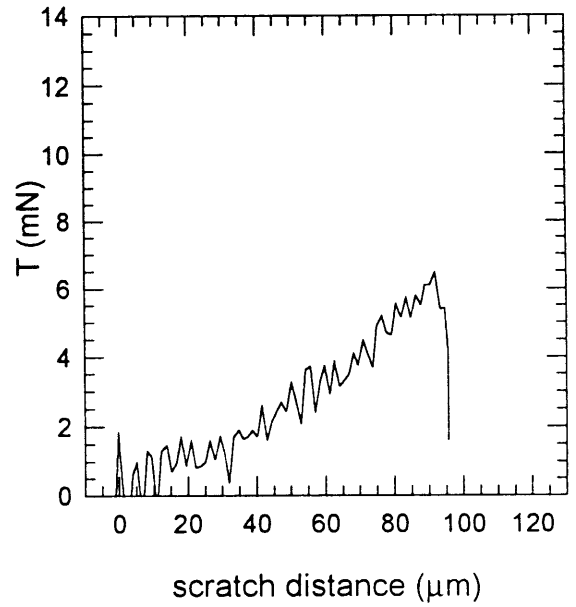
scratch 13-8 scratch depth
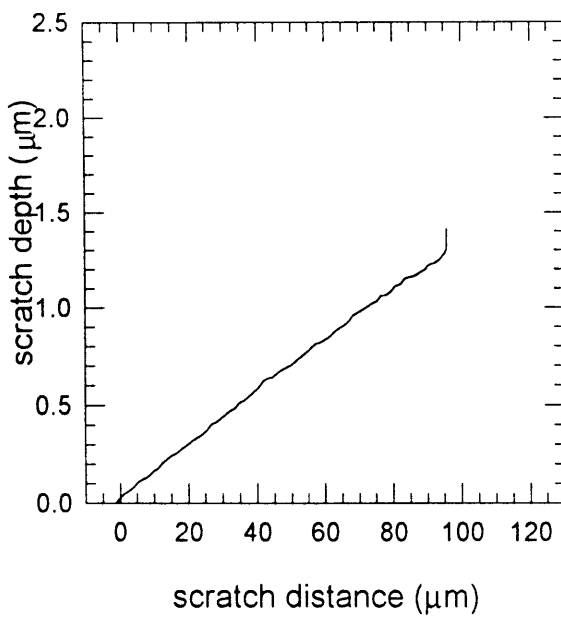
scratch 13-8 friction
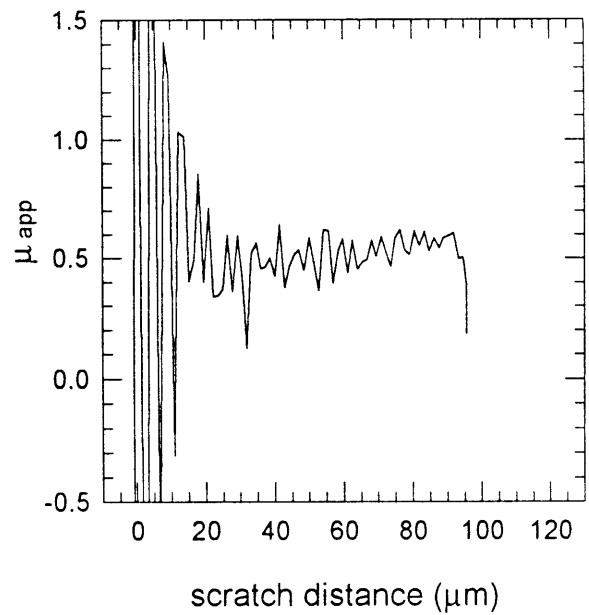
scratch 13-9 normal load
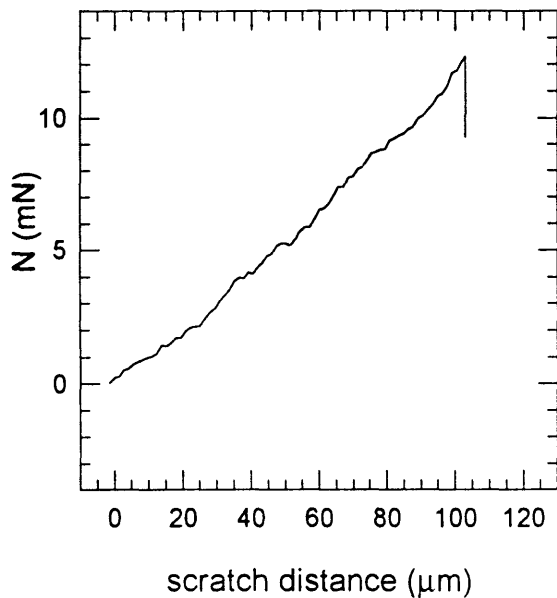
scratch 13-9 tangential load
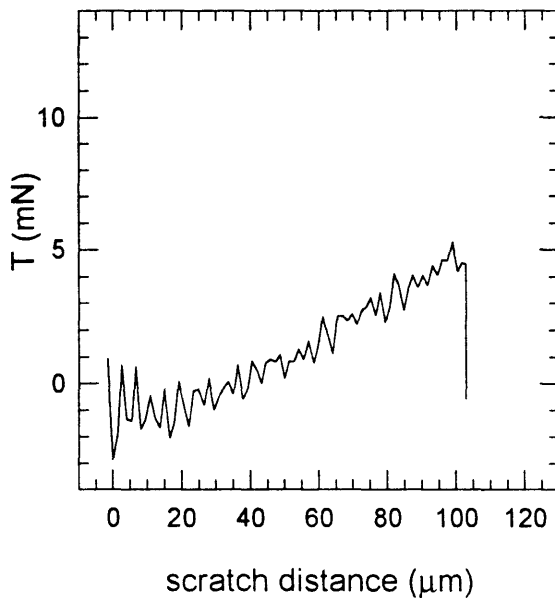
scratch 13-9 scratch depth
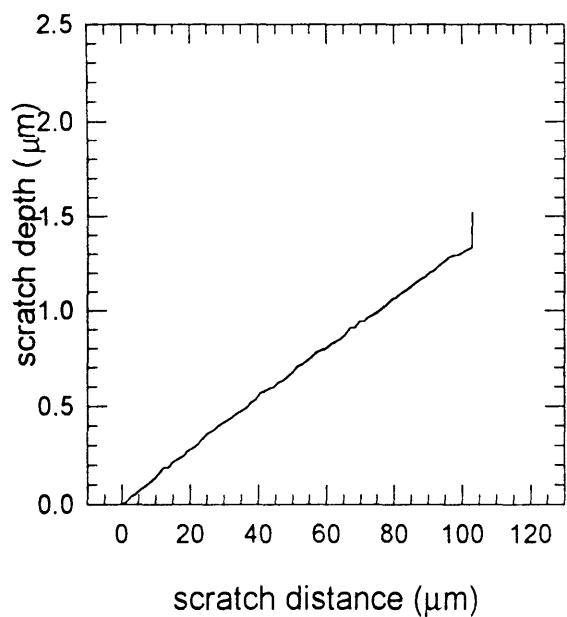
scratch 13-9 friction
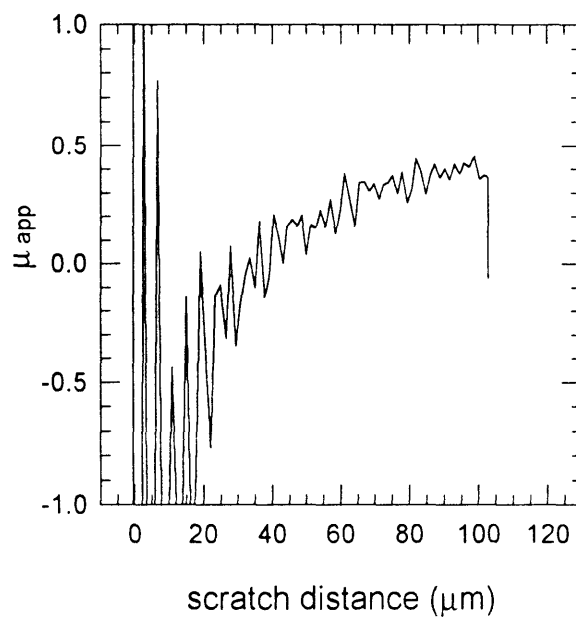
scratch 13-10 normal load
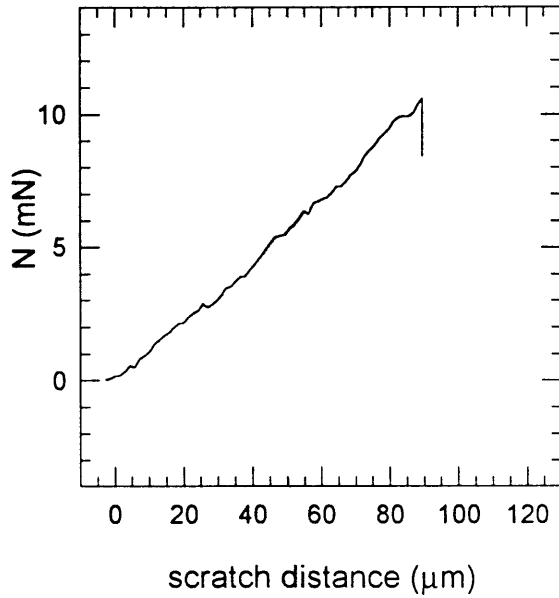
scratch 13-10 tangential load
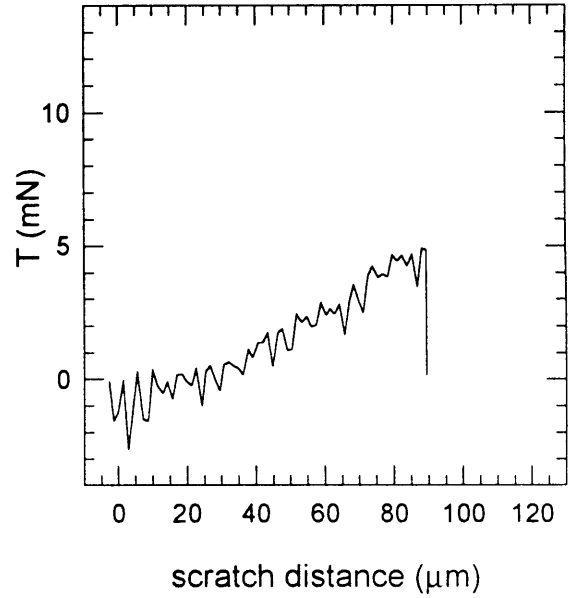
scratch 13-10 scratch depth
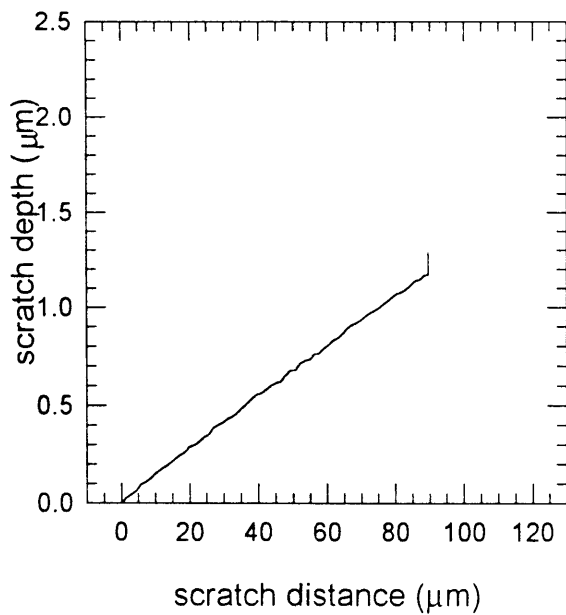
scratch 13-10 friction
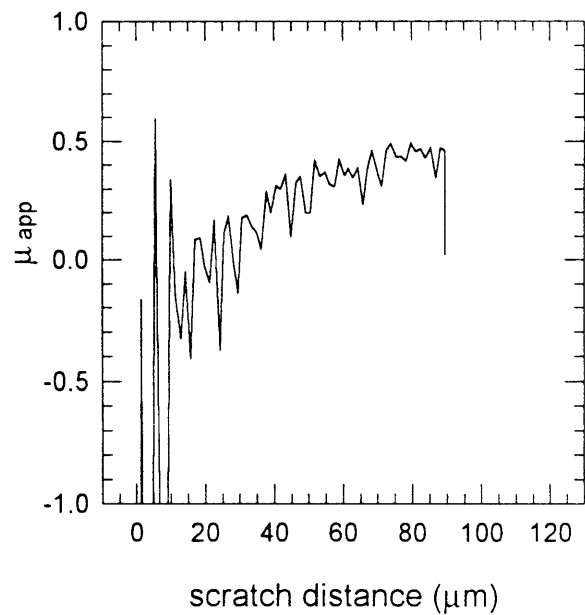
scratch 14-2 normal load
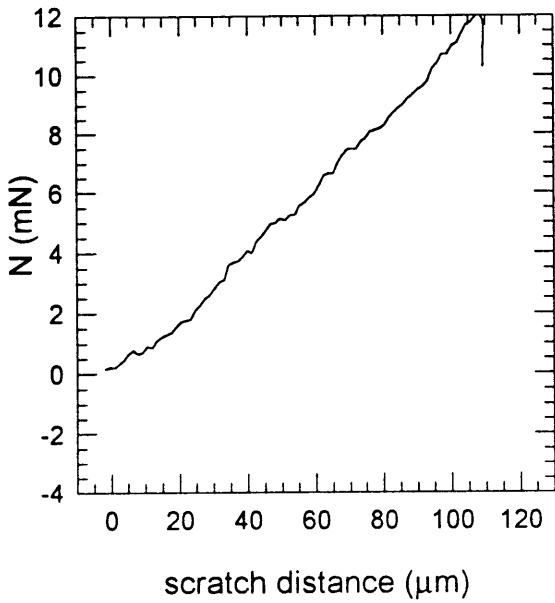
scratch 14-2 tangential load
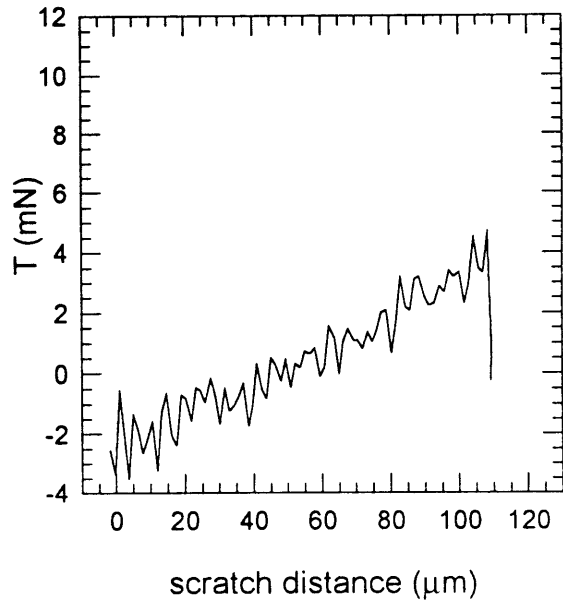
scratch 14-2 scratch depth
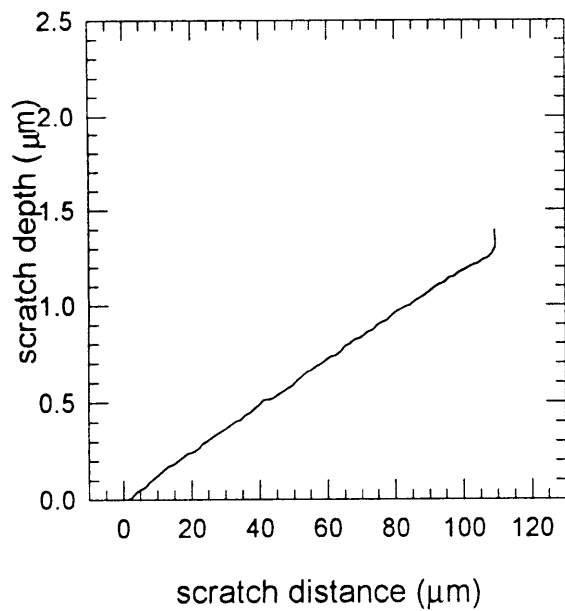
scratch 14-2 friction
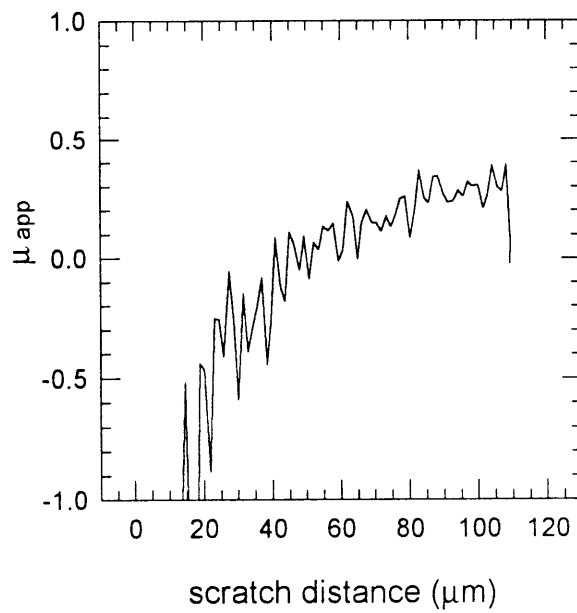
scratch 14-3 normal load
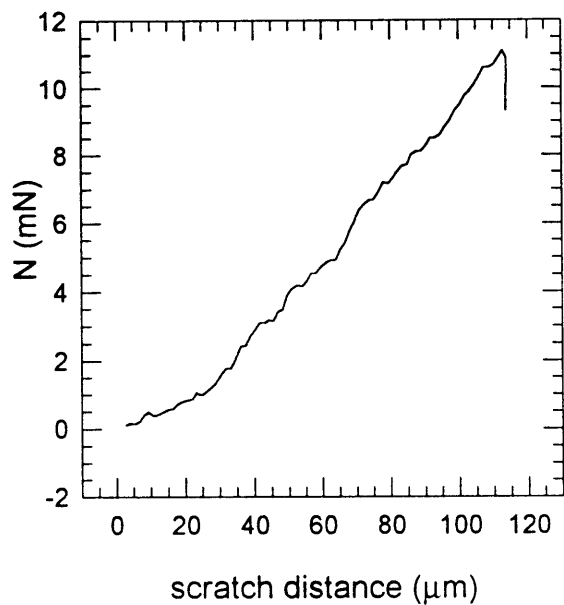
scratch 14-3 tangential load
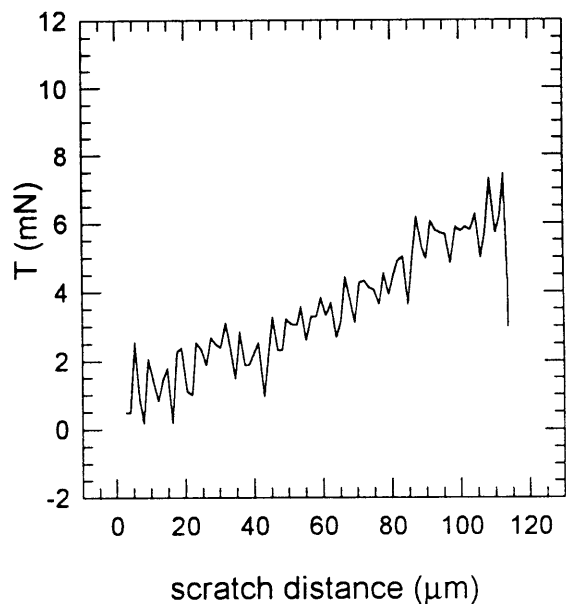
scratch 14-3 scratch depth
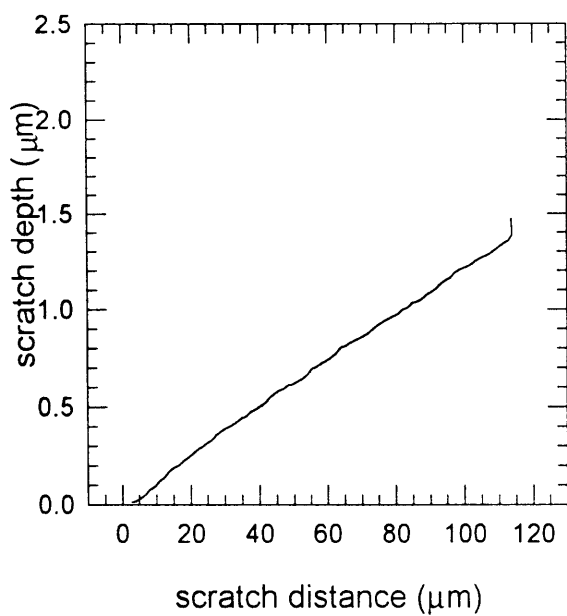
scratch 14-3 friction
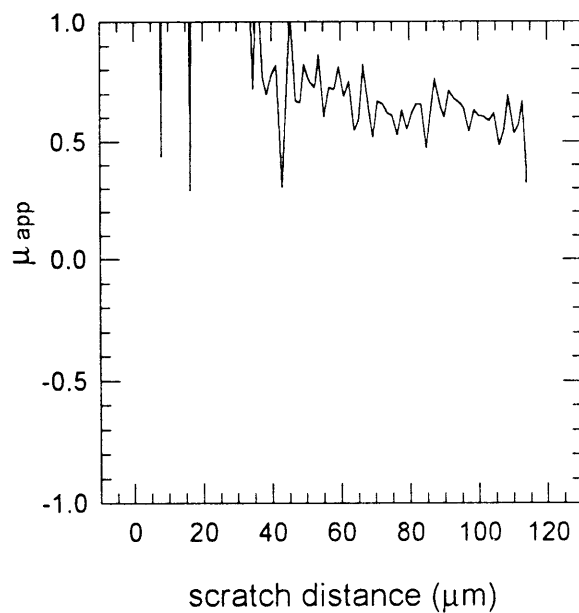
scratch 14-4 normal load
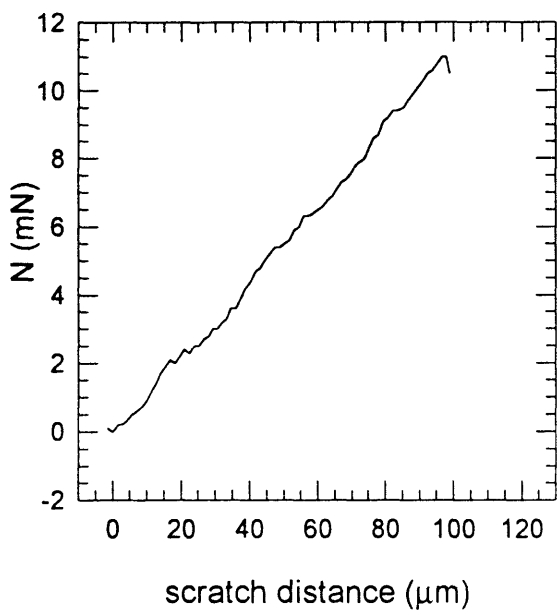
scratch 14-4 tangential load
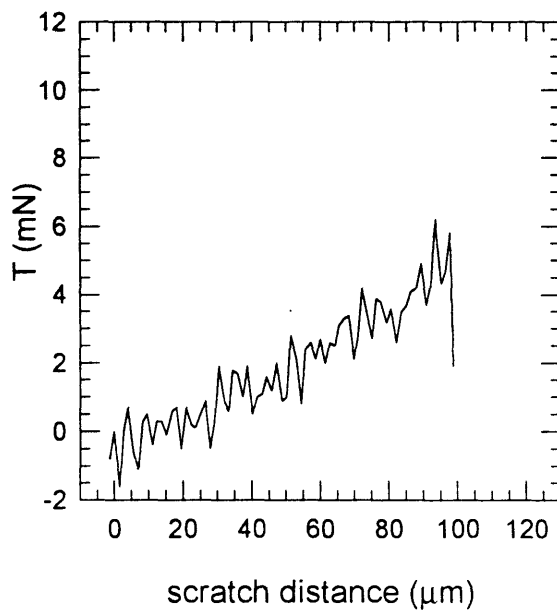
scratch 14-4 scratch depth
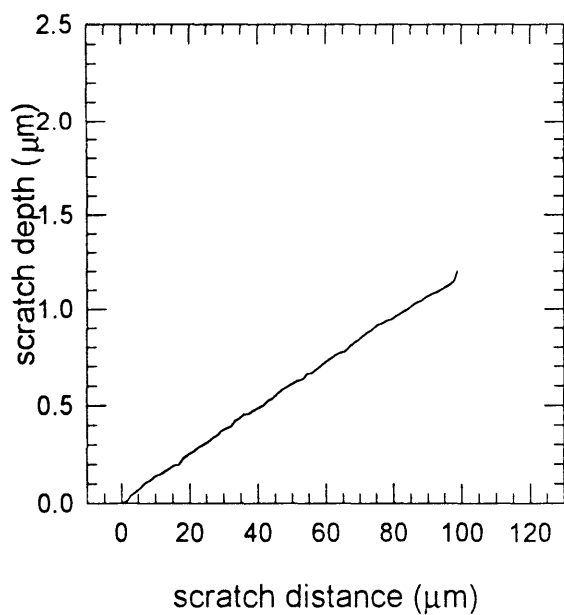
scratch 14-4 friction
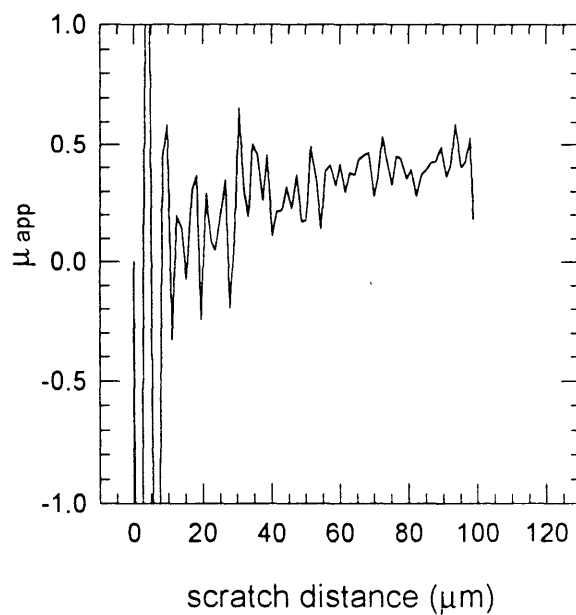
scratch 14-5 normal load
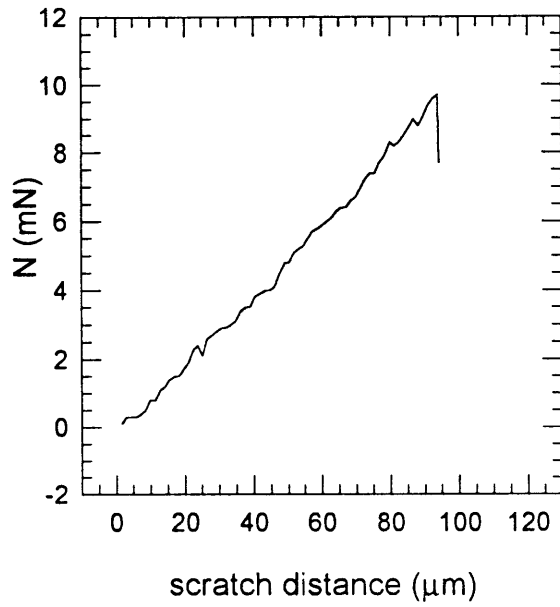
scratch 14-5 tangential load
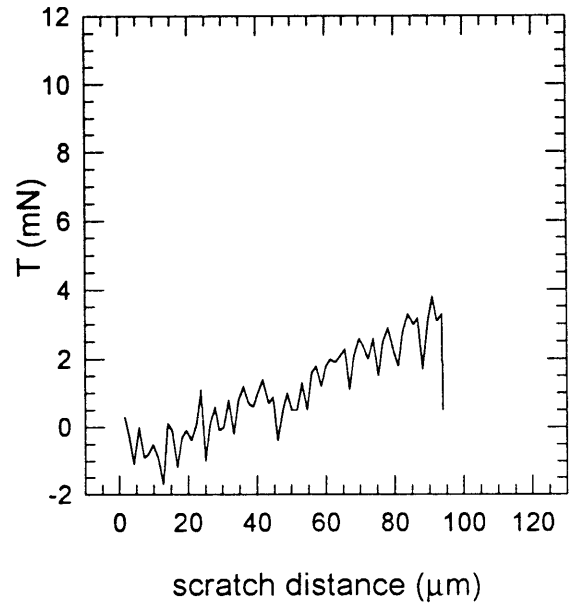
scratch 14-5 scratch depth
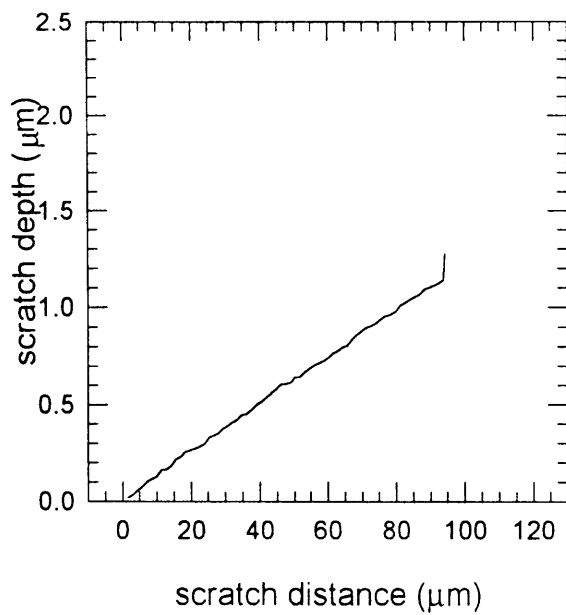
scratch 14-5 friction
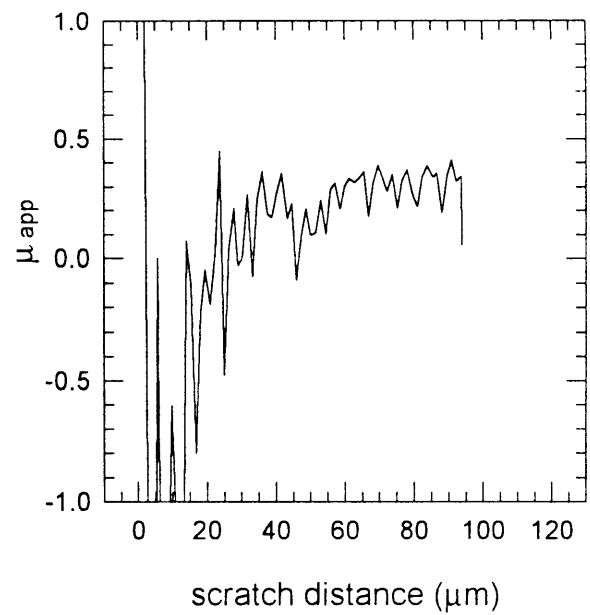
scratch 14-6 normal load
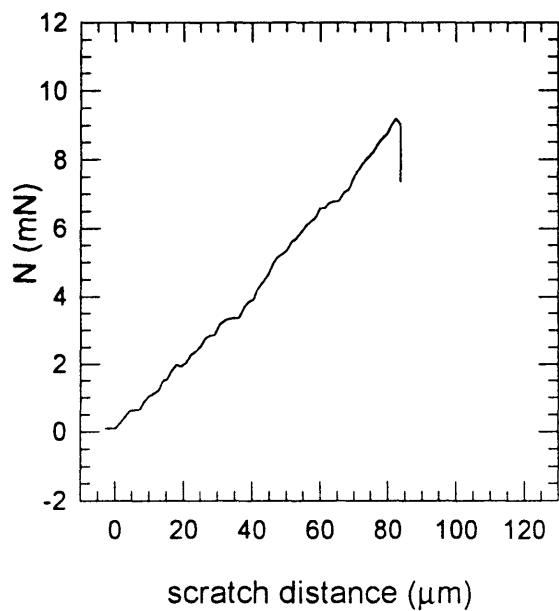
scratch 14-6 tangential load
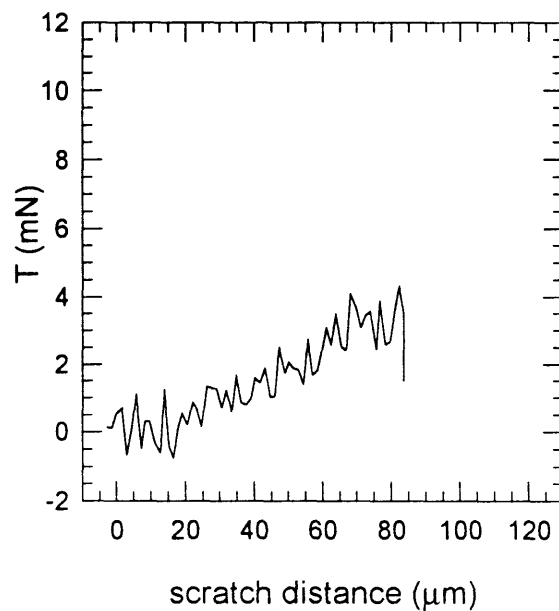
scratch 14-6 scratch depth
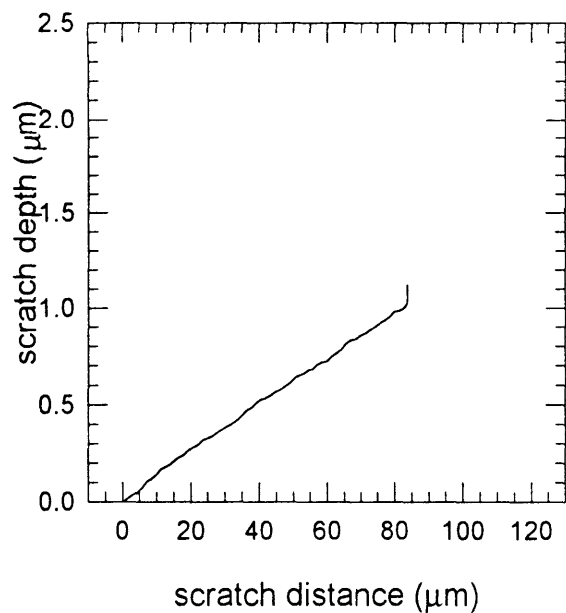
scratch 14-6 friction
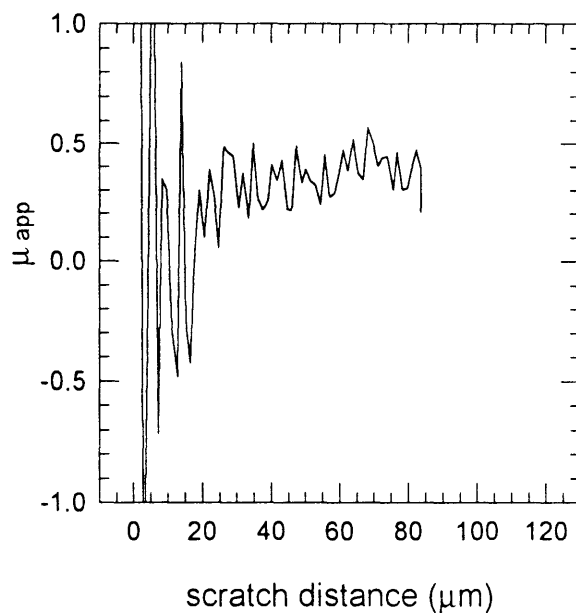
scratch 14-7 normal load
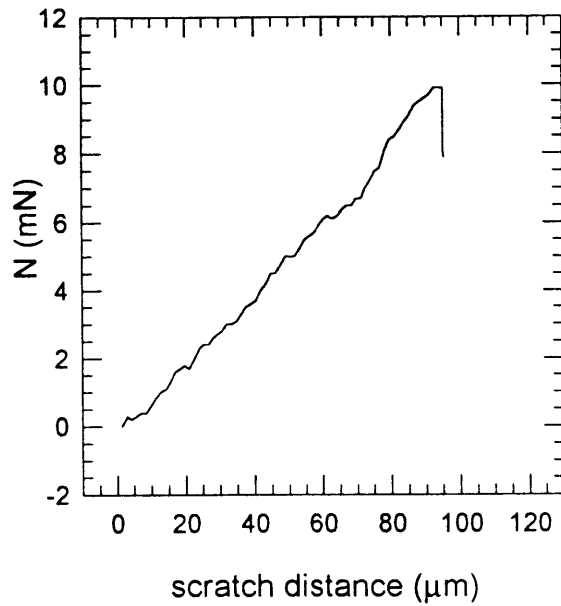
scratch 14-7 tangential load
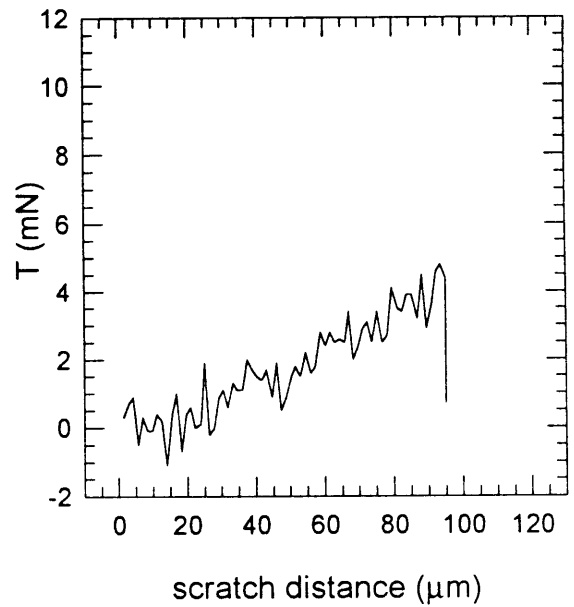
scratch 14-7 scratch depth
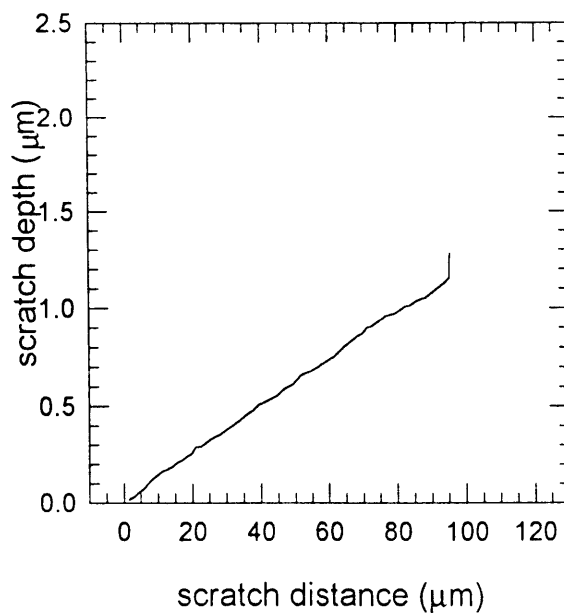
scratch 14-7 friction
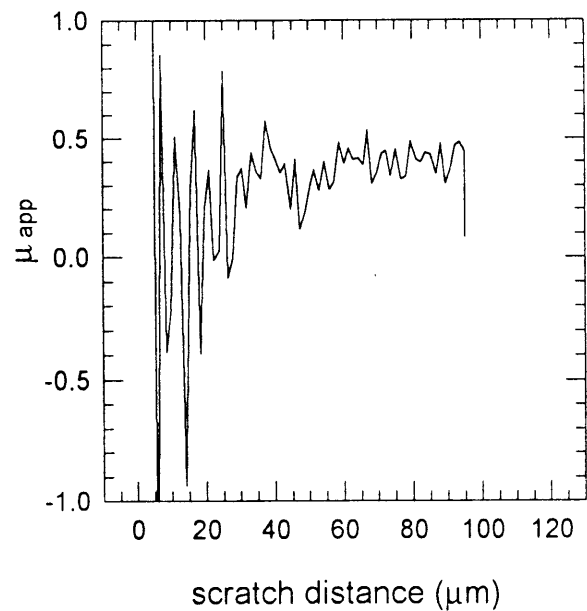
scratch 14-8 normal load
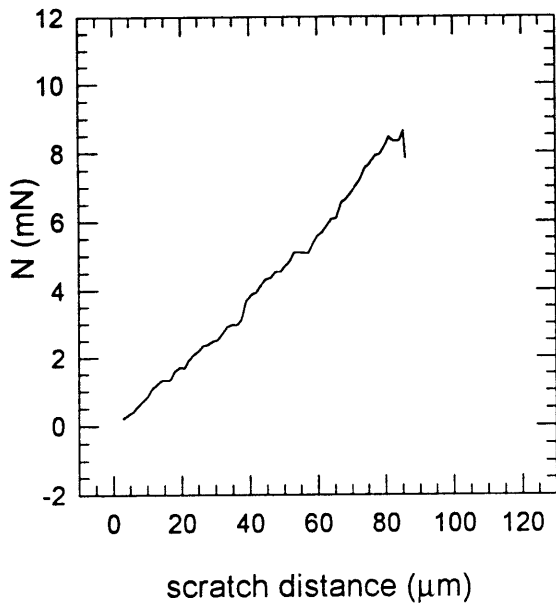
scratch 14-8 tangential load
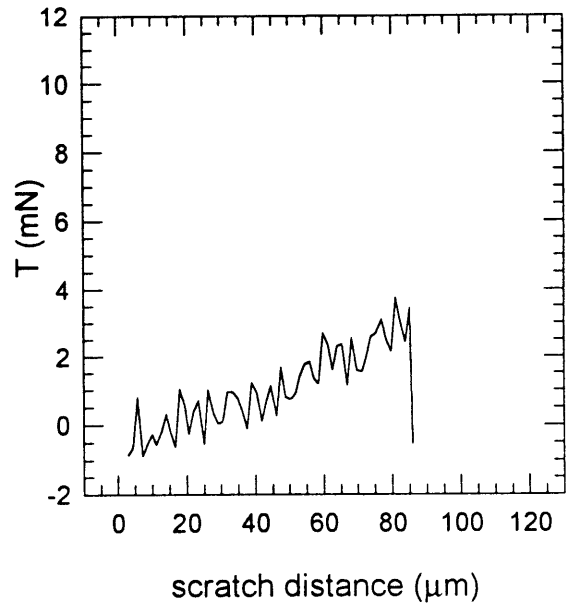
scratch 14-8 scratch depth
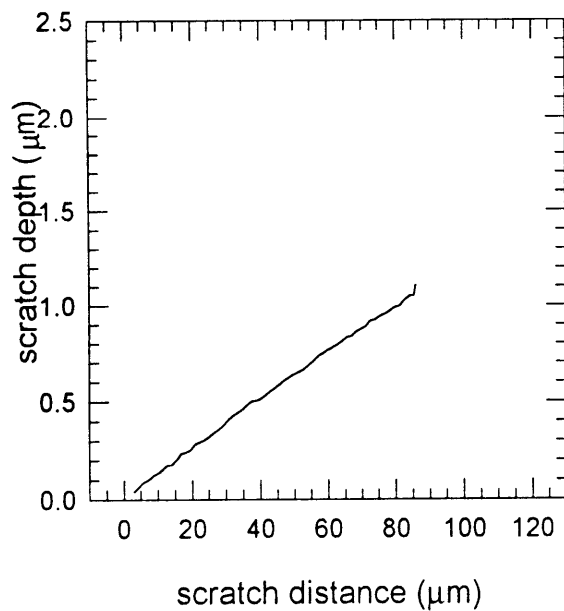
scratch 14-8 friction
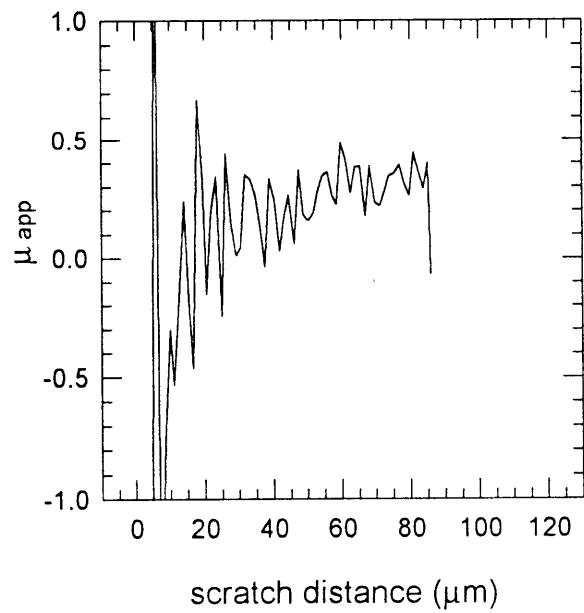
scratch 14-9 normal load
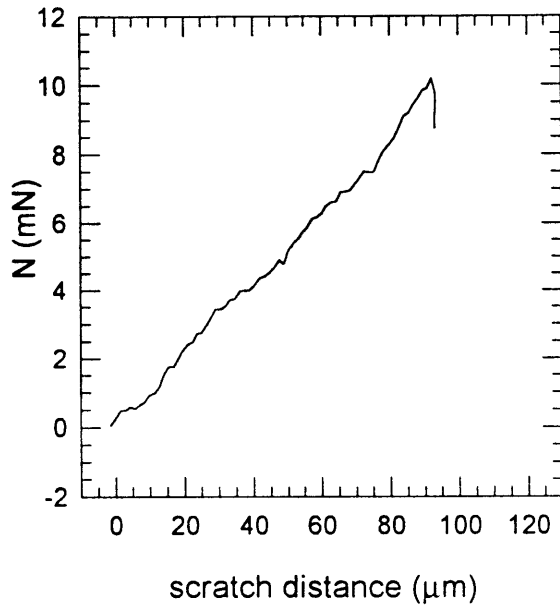
scratch 14-9 tangential load
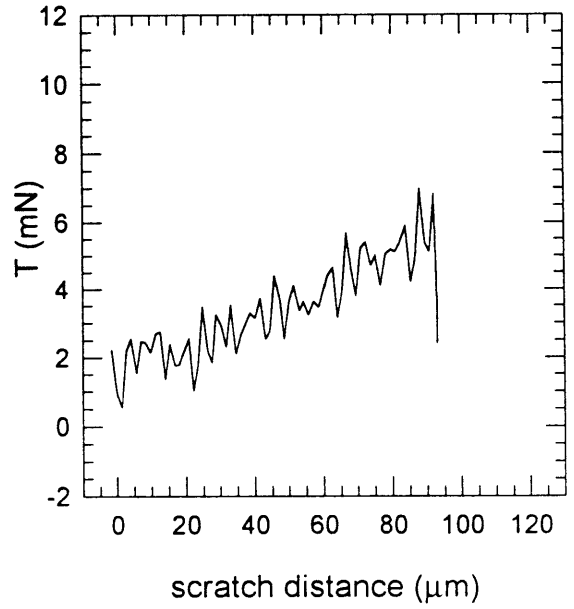
scratch 14-9 scratch depth
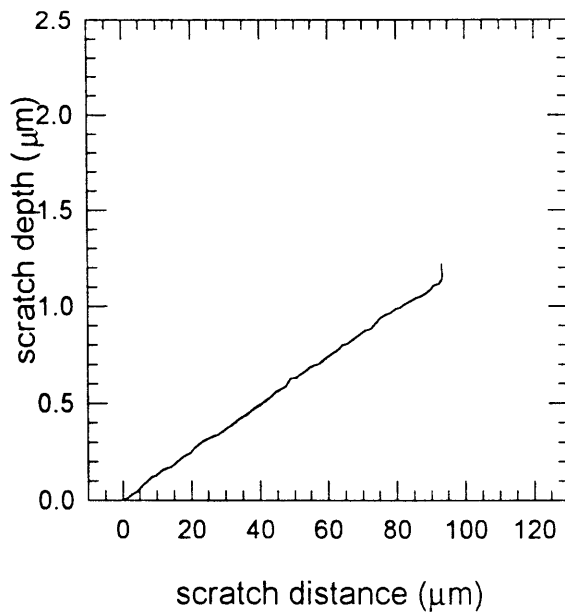
scratch 14-9 friction
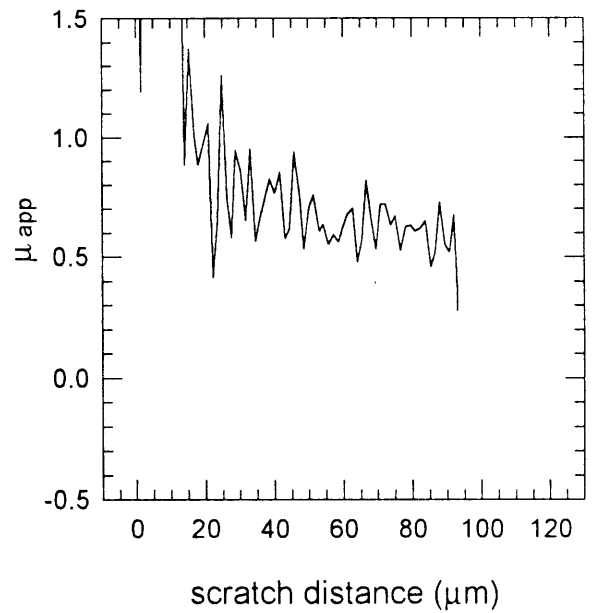
scratch 14-10 normal load
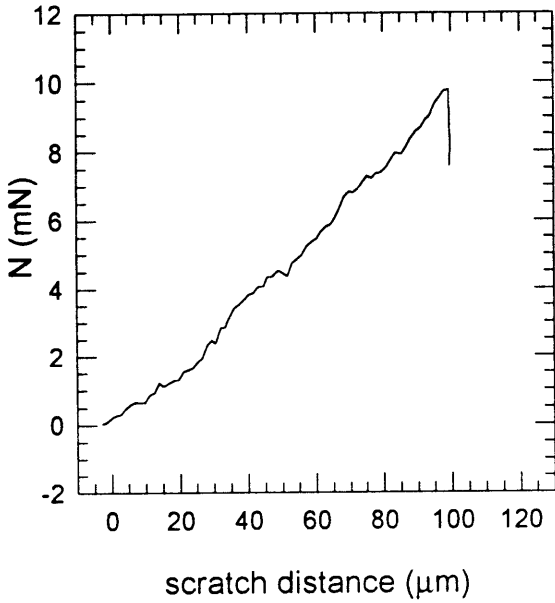
scratch 14-10 tangential load
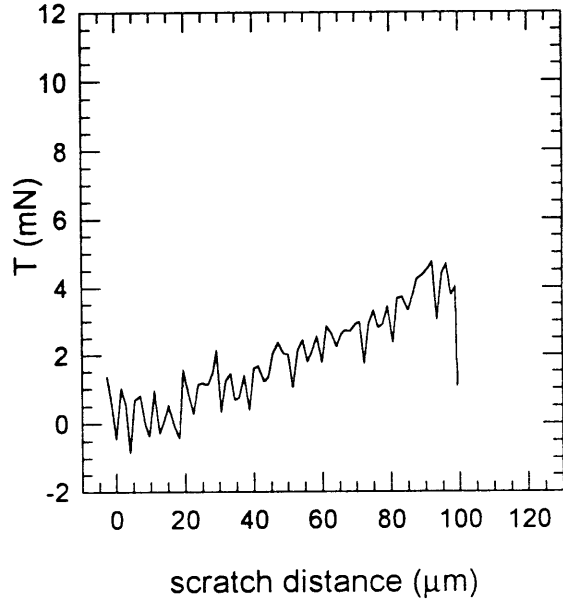
scratch 14-10 scratch depth
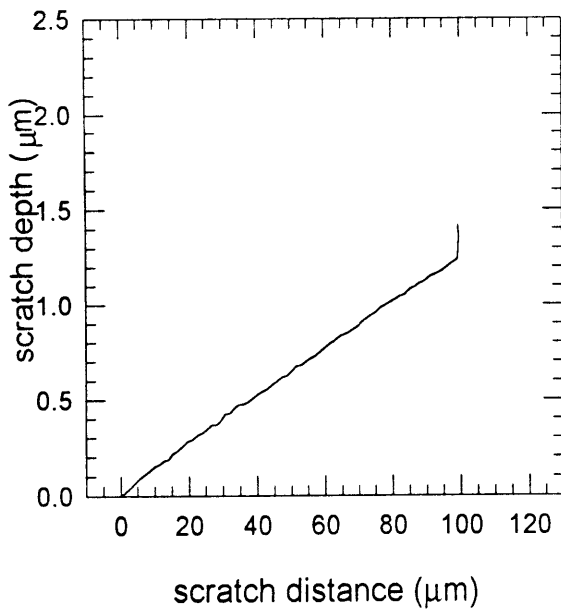
scratch 14-10 friction
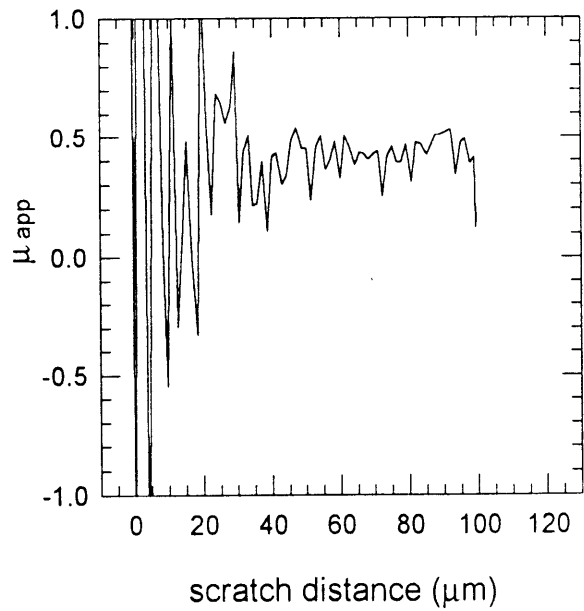
scratch 14-11 normal load
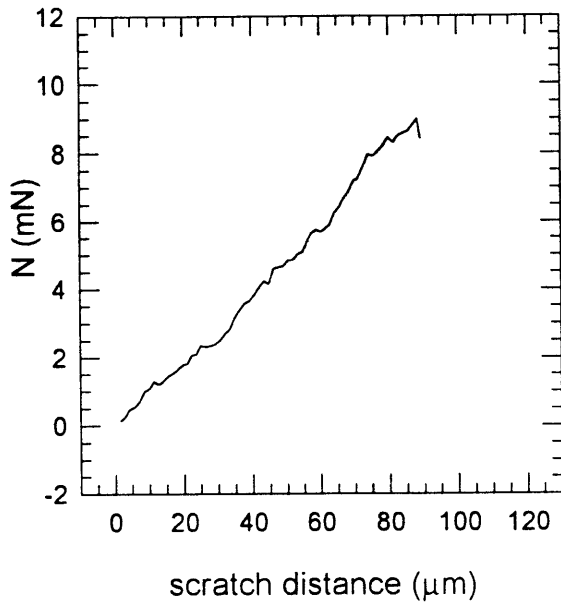
scratch 14-11 tangential load
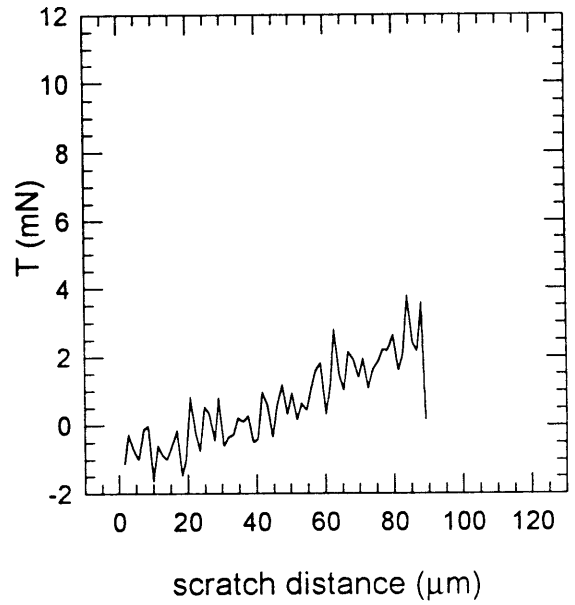
scratch 14-11 scratch depth
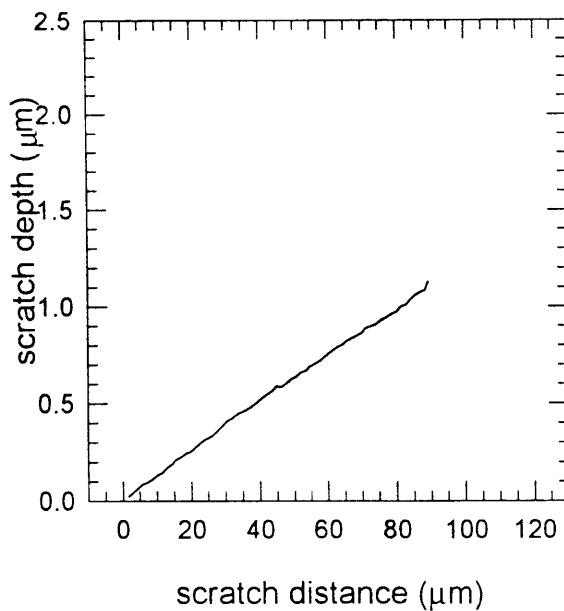
scratch 14-11 friction
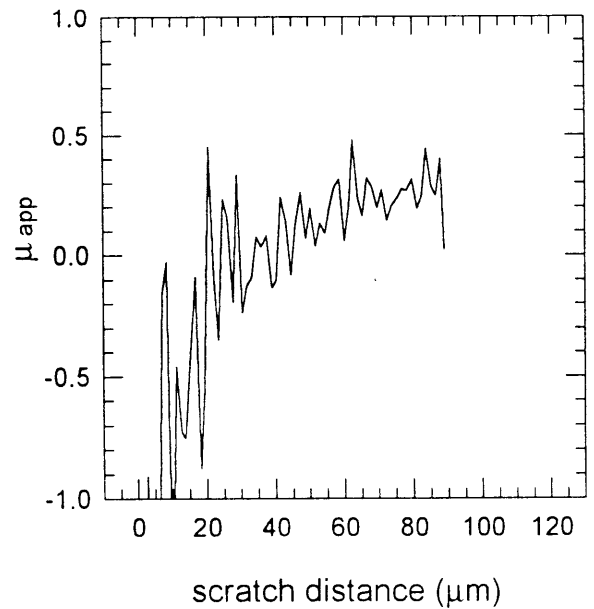
scratch 14-12 normal load
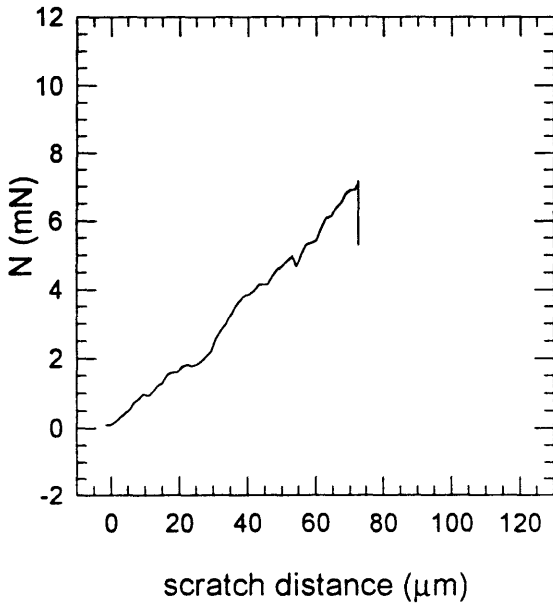
scratch 14-12 tangential load

scratch 14-12 scratch depth

scratch 14-12 friction

scratch 14-13 normal load

scratch 14-13 tangential load

scratch 14-13 scratch depth

scratch 14-13 friction

scratch 14-14 normal load

scratch 14-14 tangential load

scratch 14-14 scratch depth

scratch 14-14 friction
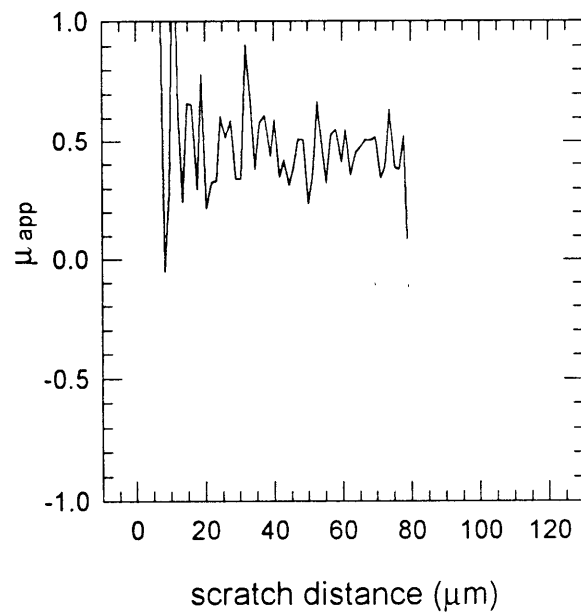
scratch 1-1 hardness
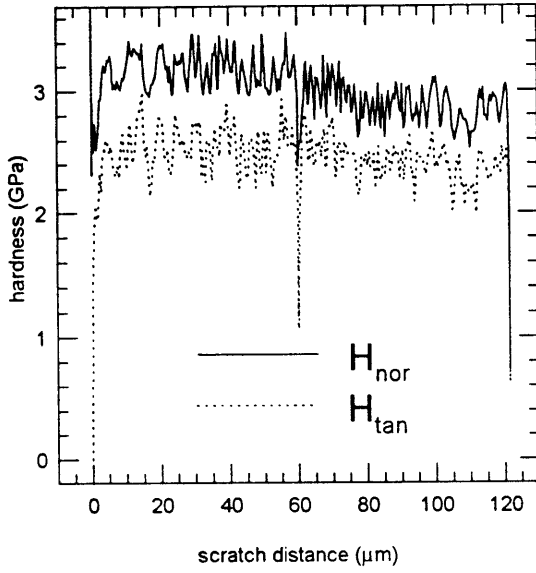
scratch 1-2 hardness
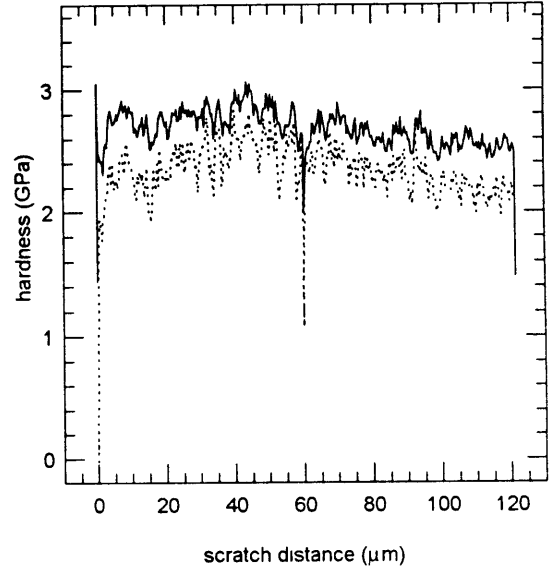
scratch 1-3 hardness
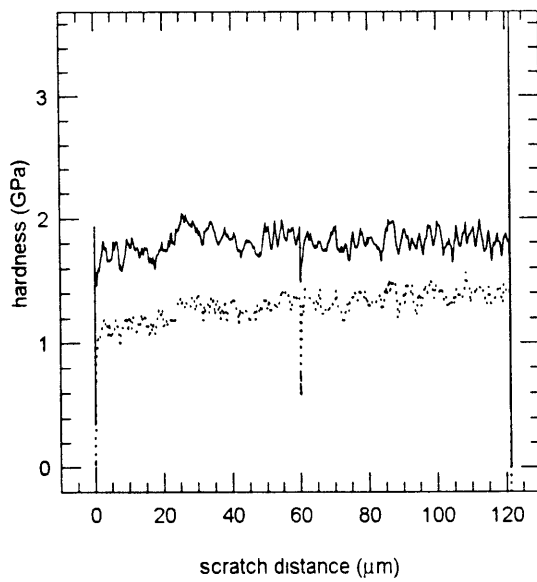
scratch 1-4 hardness
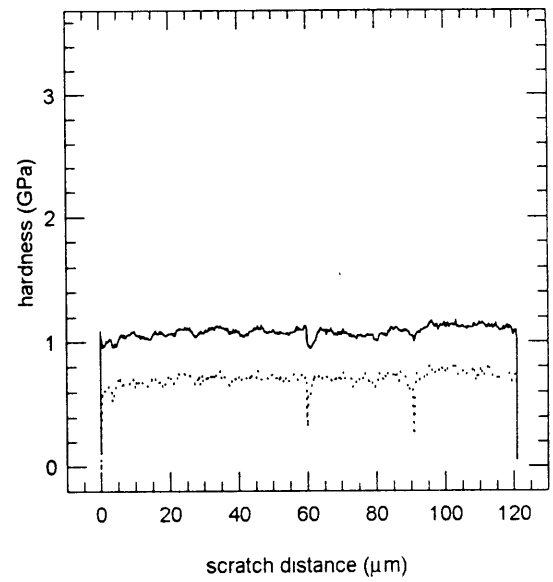
scratch 1-5 hardness
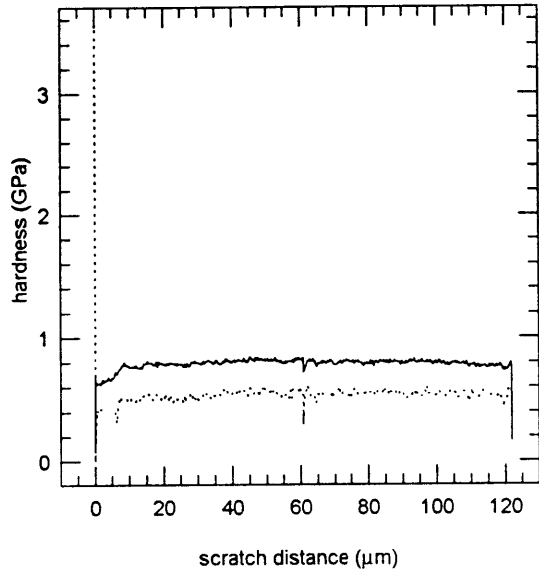
scratch 1-6 hardness
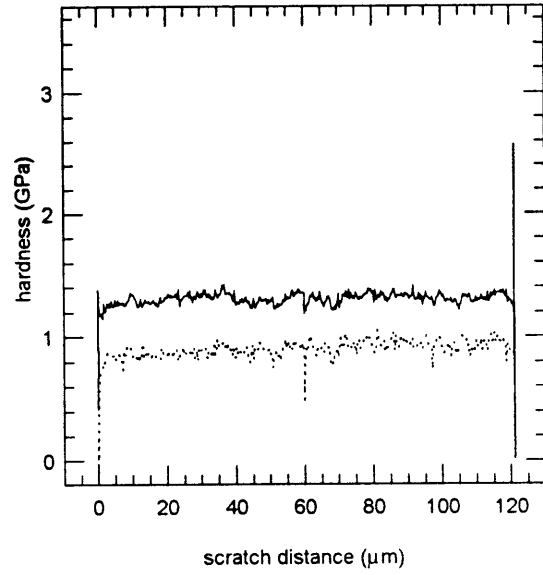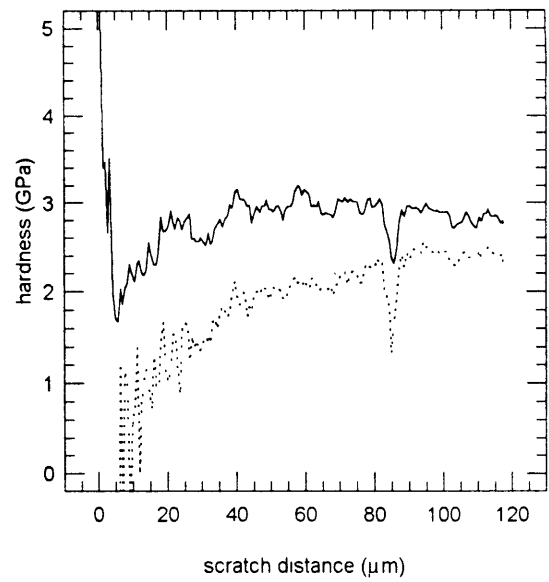

scratch 1-7 hardness
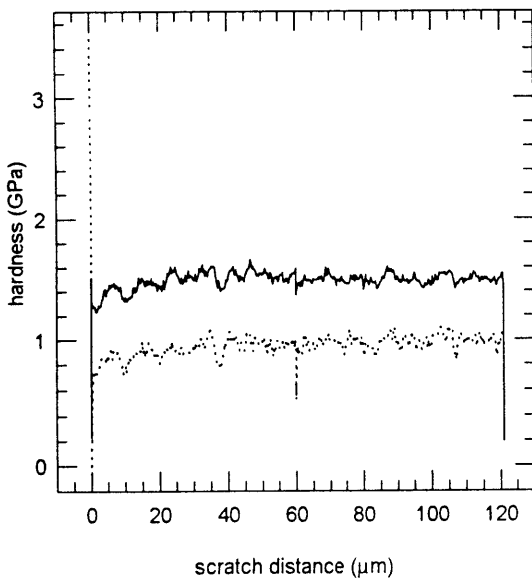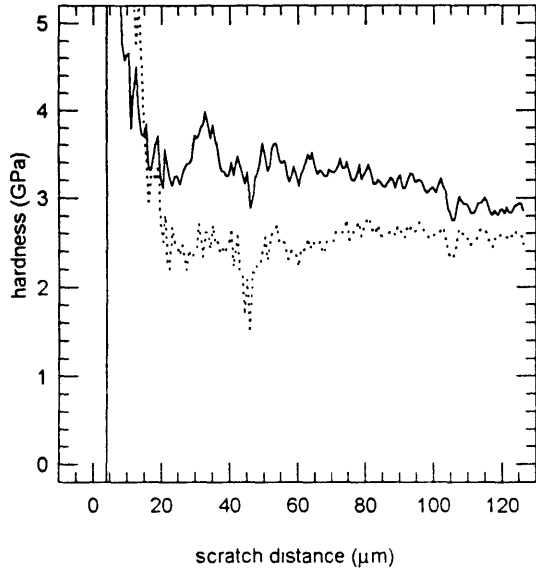
scratch 2-1 hardness
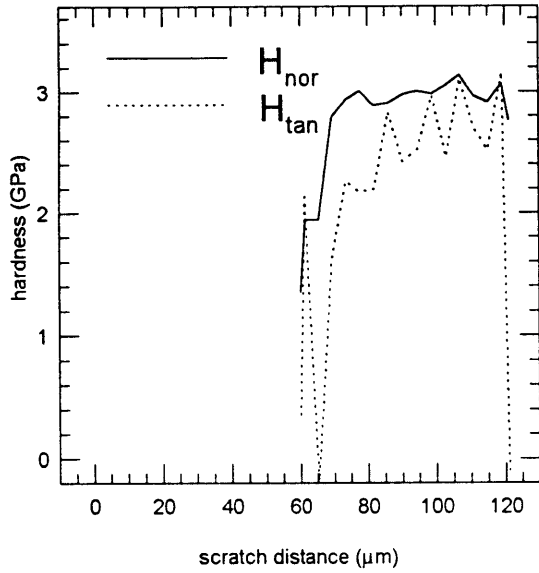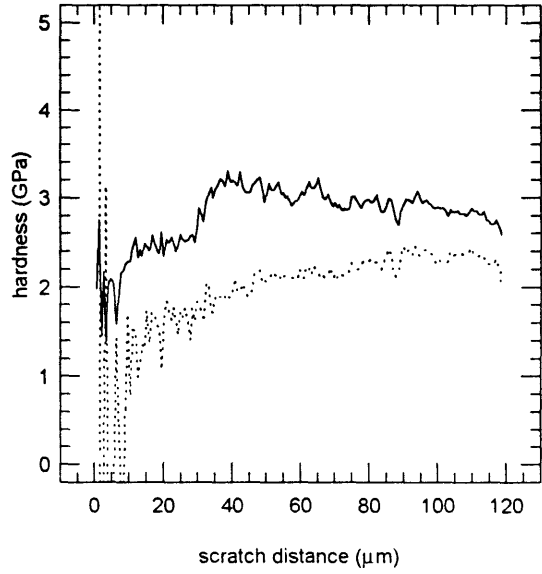

scratch 2-2 hardness
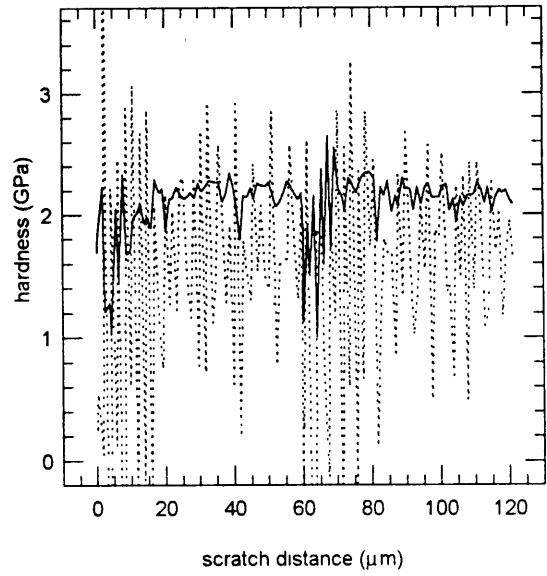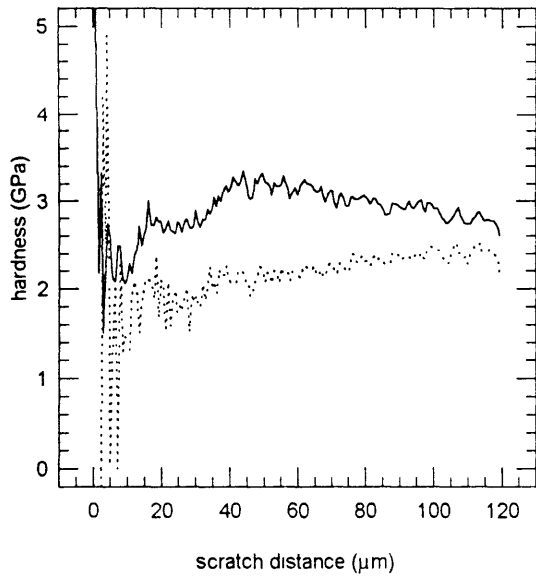

scratch 2-3 hardness
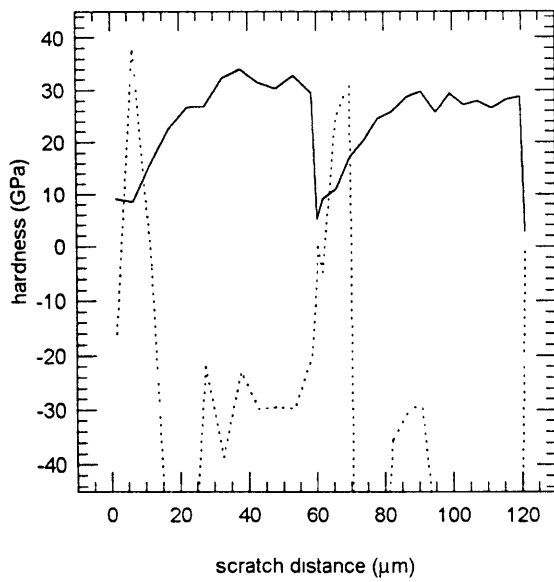
scratch 2-4 hardness
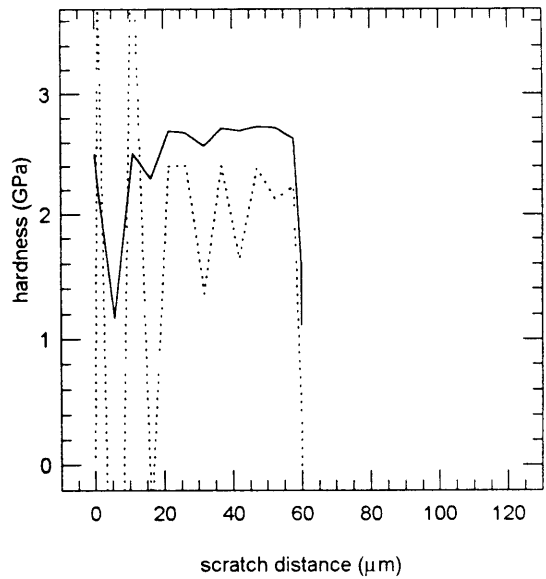
scratch 2-5 hardness
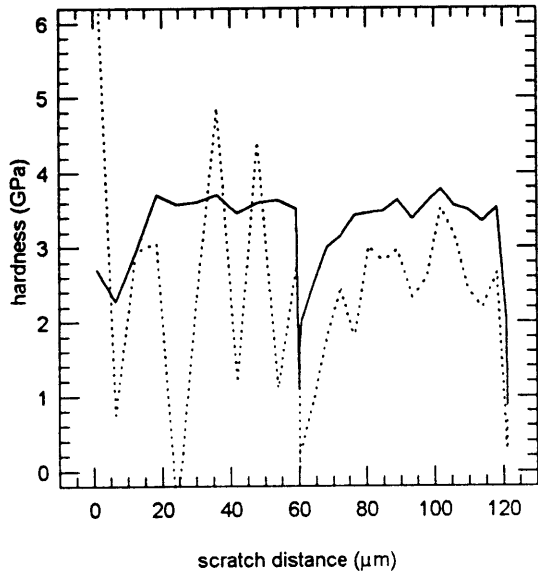
scratch 2-6 hardness
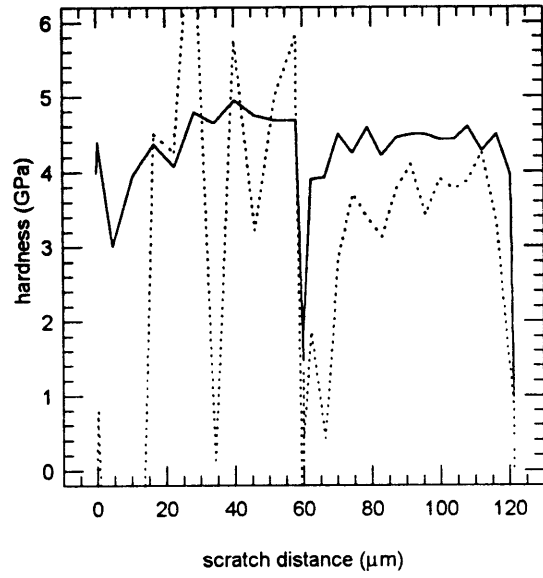
scratch 2-7 hardness
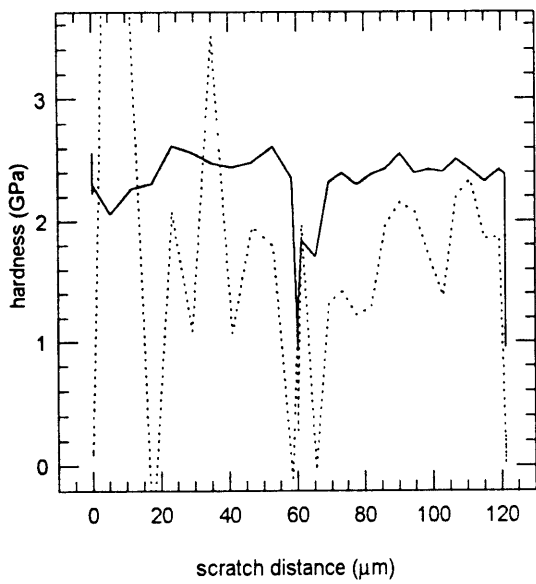
scratch 2-8 hardness
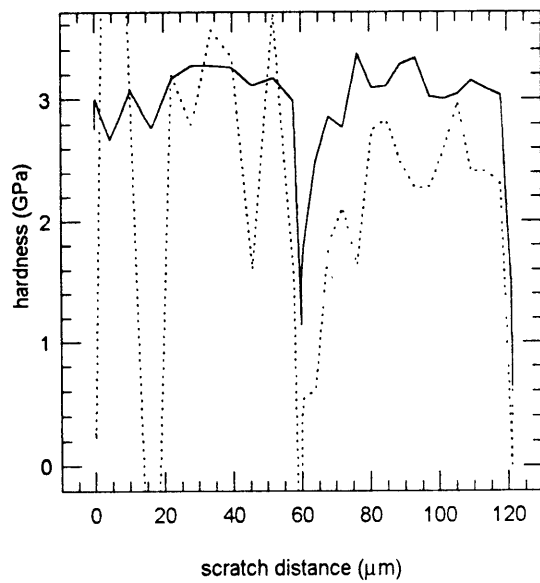
scratch 2-9 hardness

scratch distance (μm)
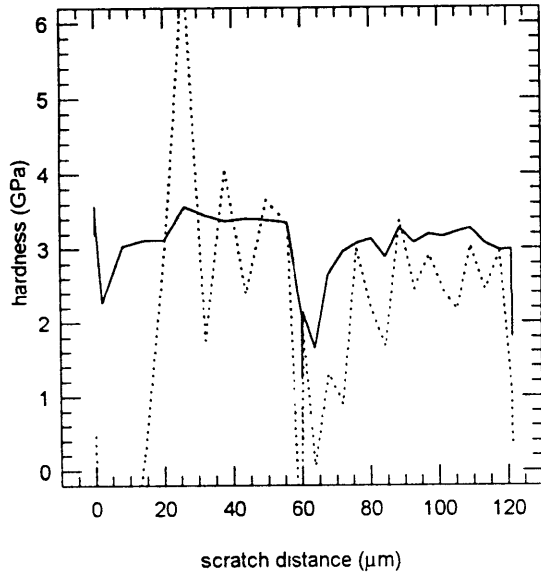
scratch 3-1 hardness
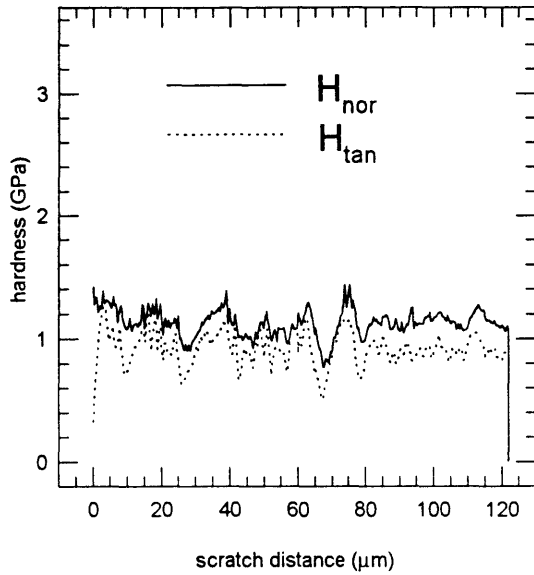
scratch 3-2 hardness
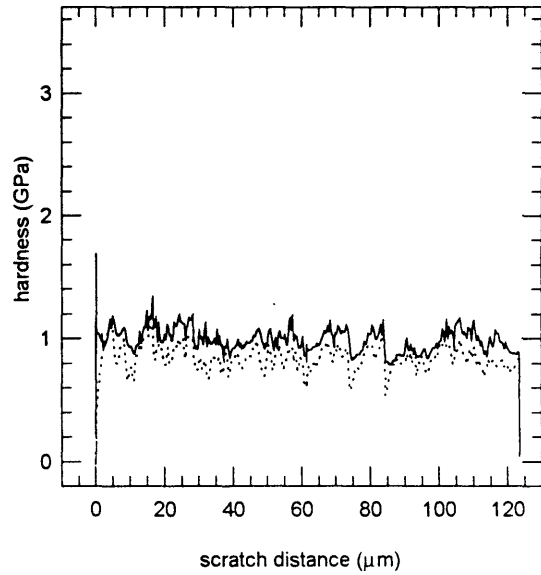
scratch 3-3 hardness
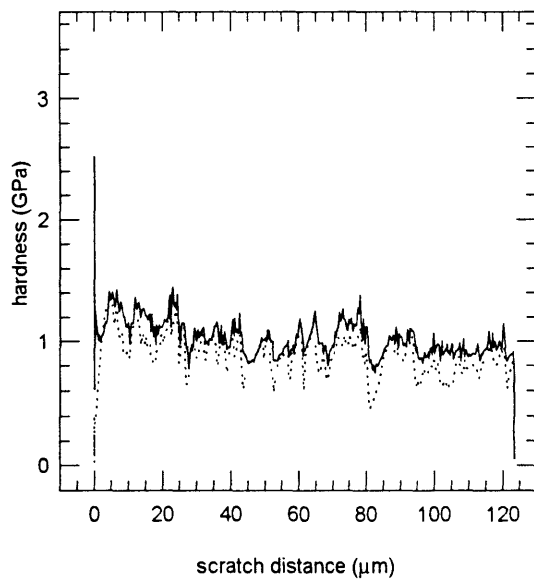
scratch 3-4 hardness
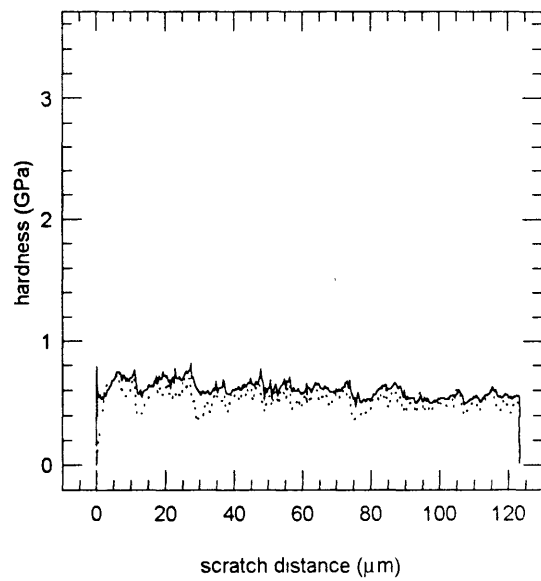
scratch 3-5 hardness
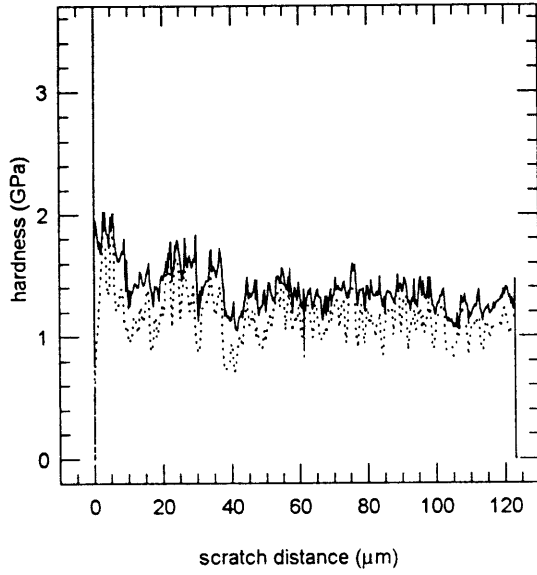
scratch 3-6 hardness
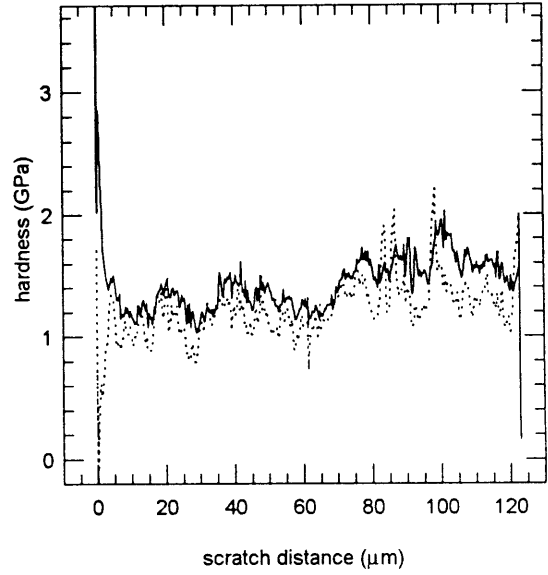
scratch 3-7 hardness
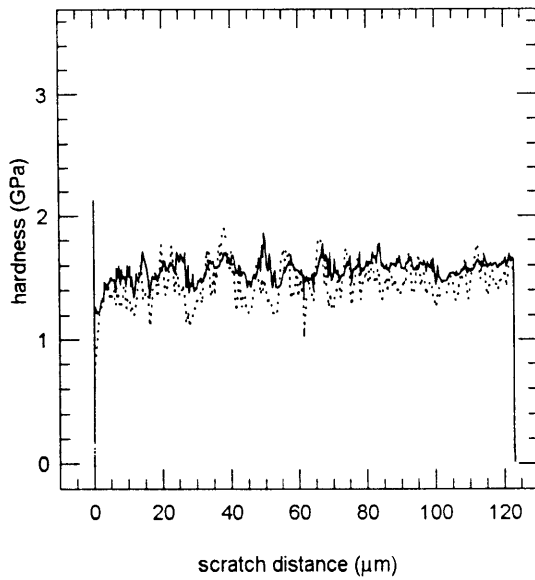
scratch 3-8 hardness
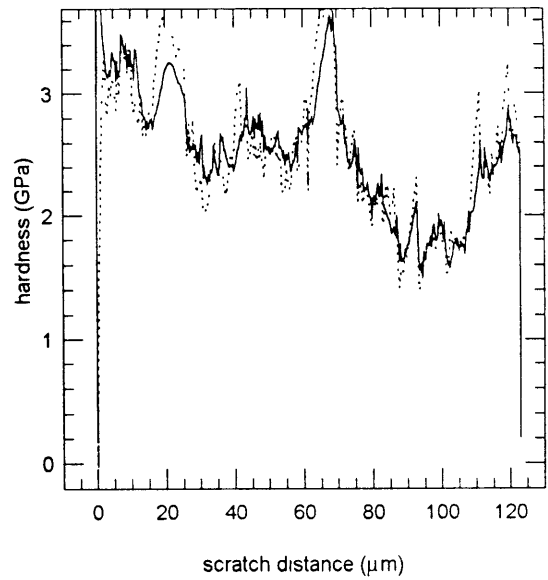
scratch 3-9 hardness
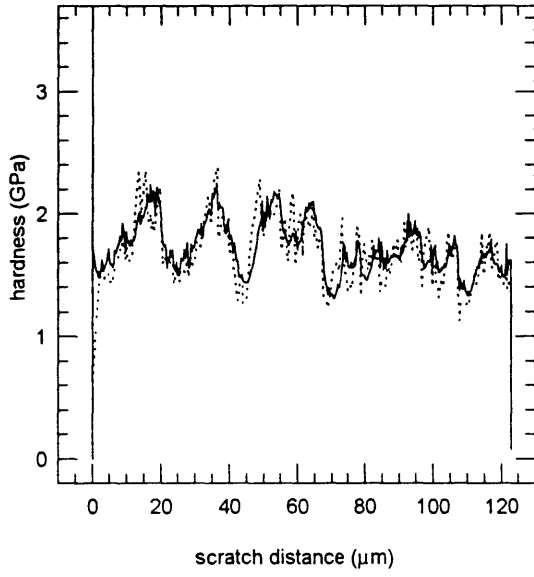
scratch 3-10 hardness
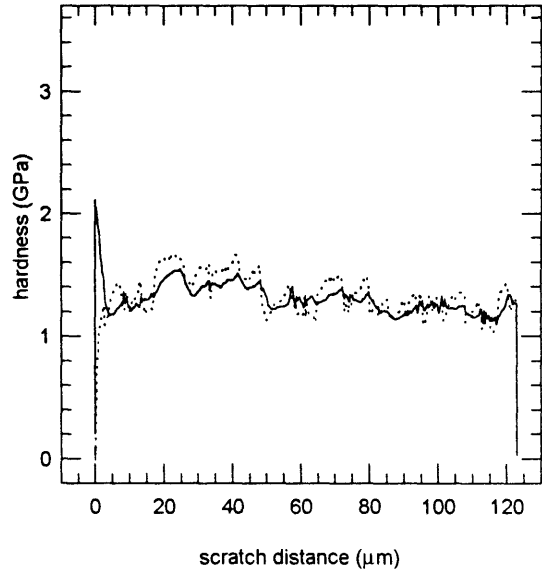
scratch 4-1 hardness
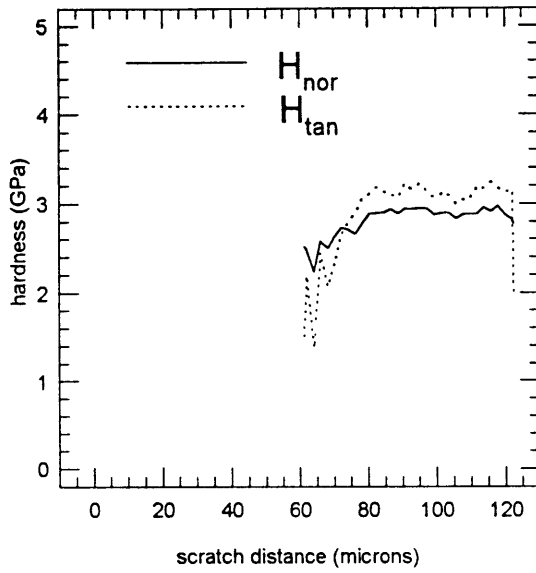
scratch 4-2 hardness
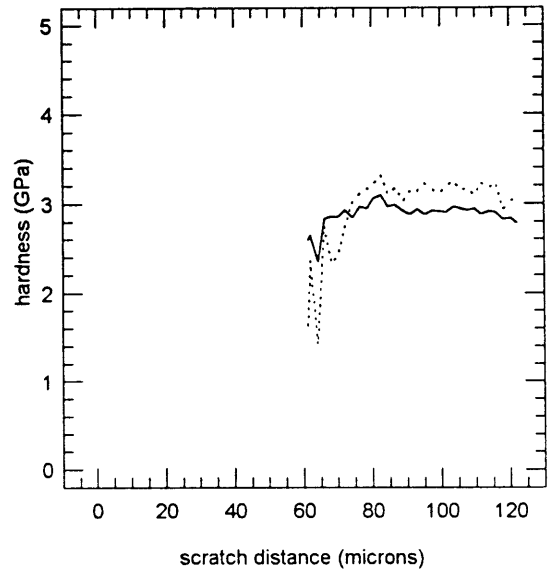
scratch 4-3 hardness
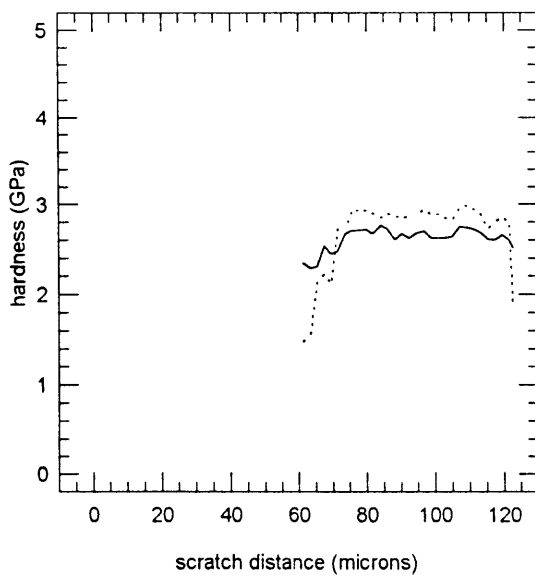
scratch 4-4 hardness
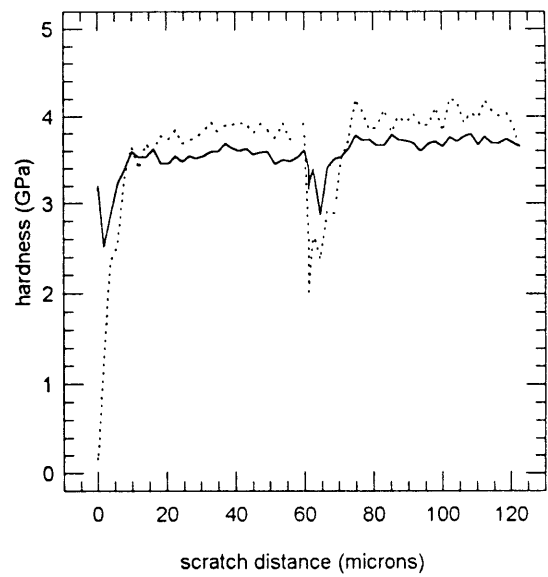
scratch 4-5 hardness
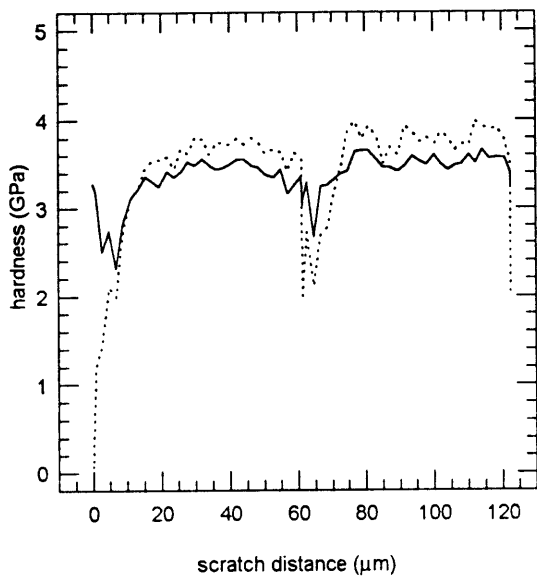
scratch 4-6 hardness
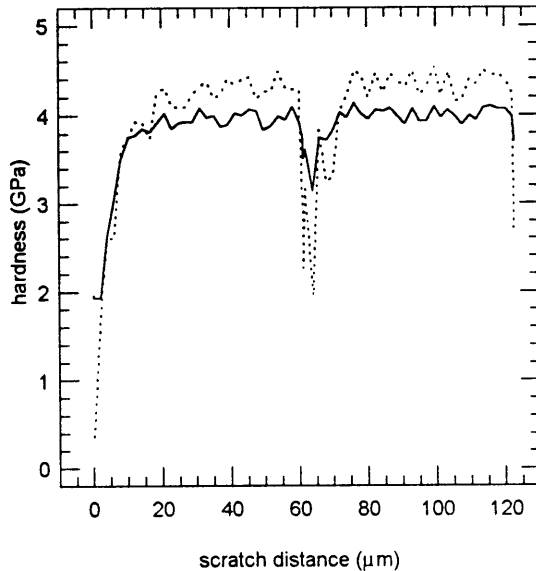
scratch 4-7 hardness
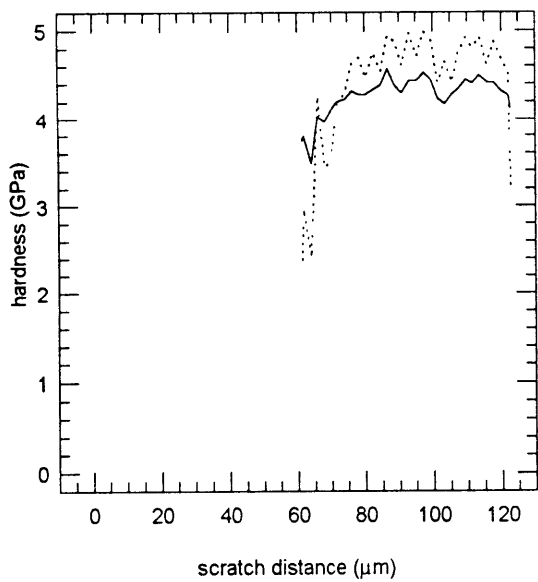
scratch 4-8 hardness
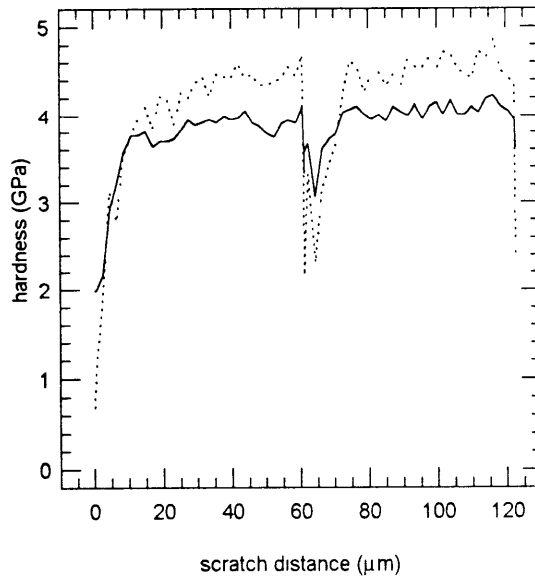
scratch 4-9 hardness
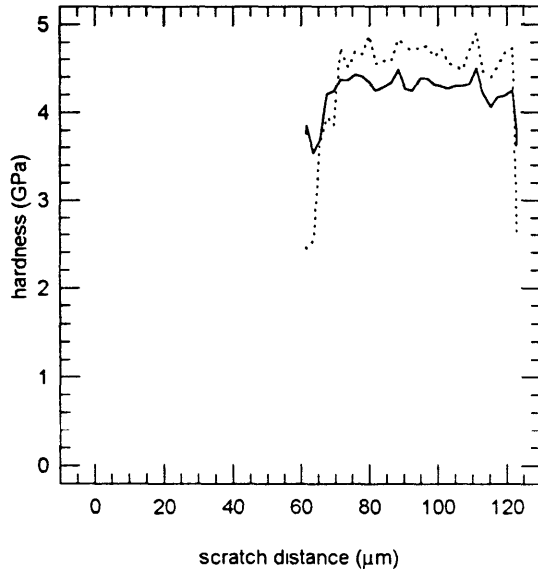
scratch 4-10 hardness
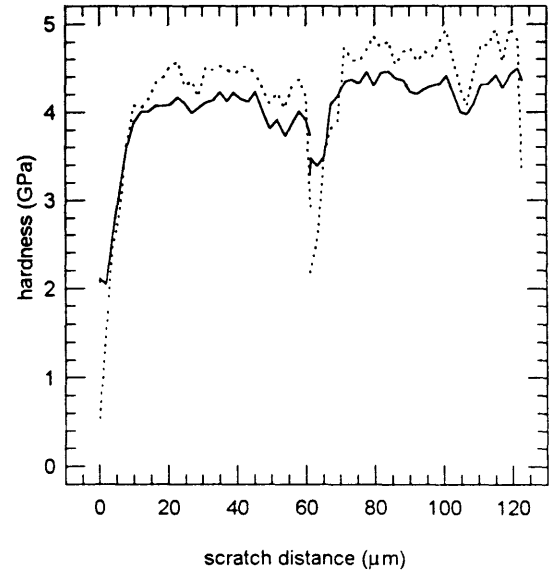
hardness (GPa) vs scratch distance (μm)

hardness (GPa) vs scratch distance (μm)

scratch 7-1 hardness

Legend: —— H_{nor}, ······ H_{tan}

hardness (GPa) vs scratch distance (μm)

scratch 7-2 hardness

hardness (GPa) vs scratch distance (μm)

scratch 7-3 hardness

hardness (GPa) vs scratch distance (μm)

scratch 7-4 hardness

hardness (GPa) vs scratch distance (μm)
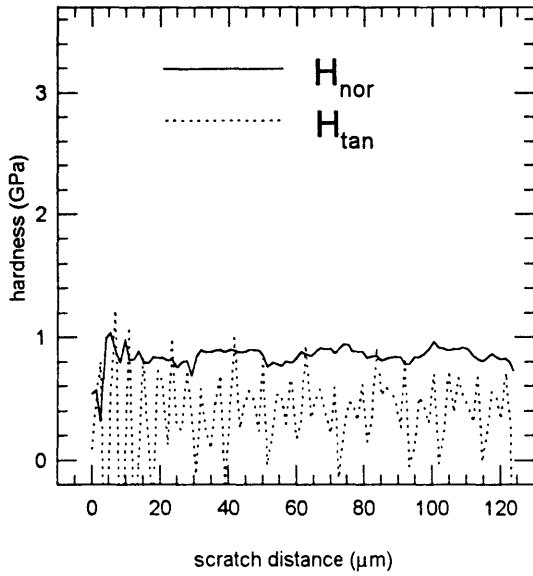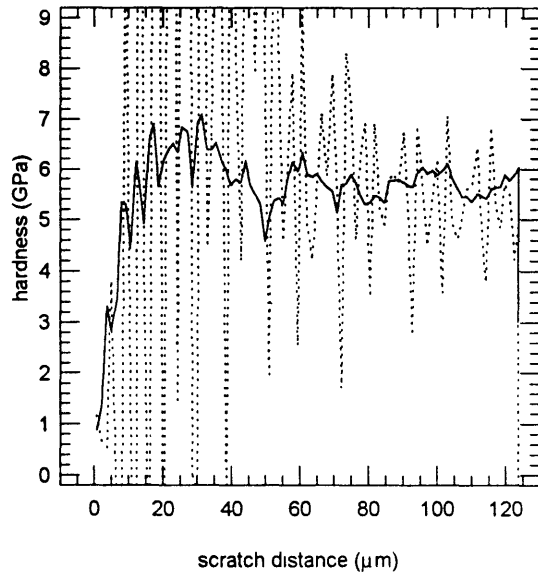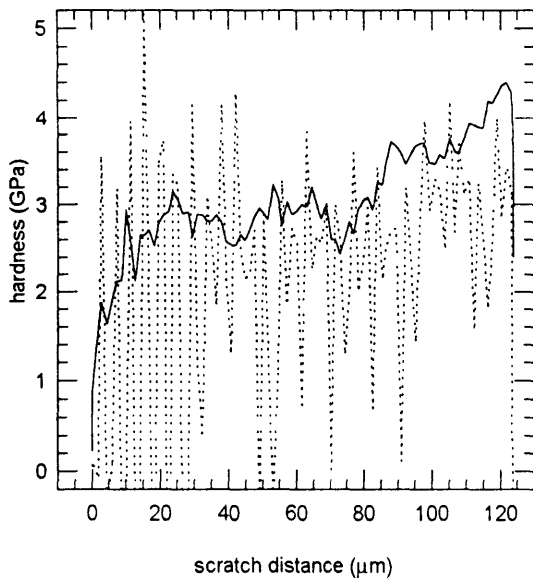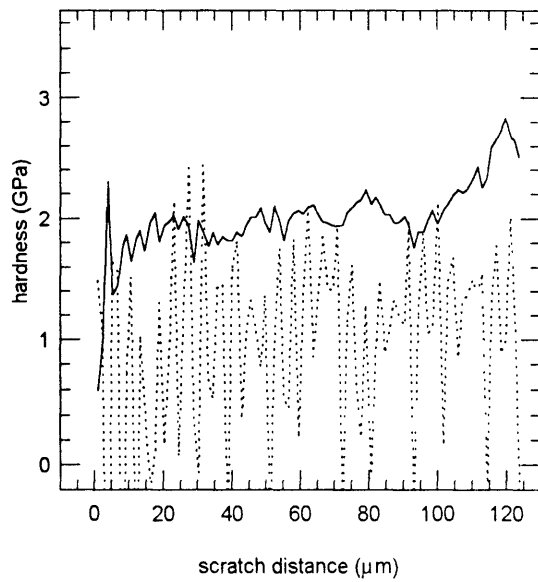
scratch 7-5 hardness
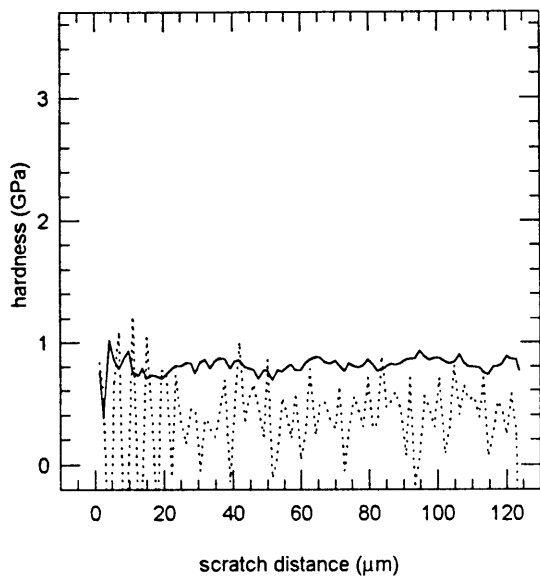
scratch 7-6 hardness
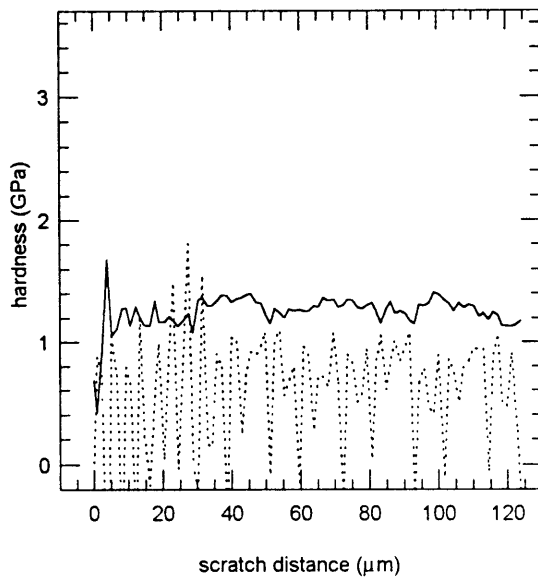
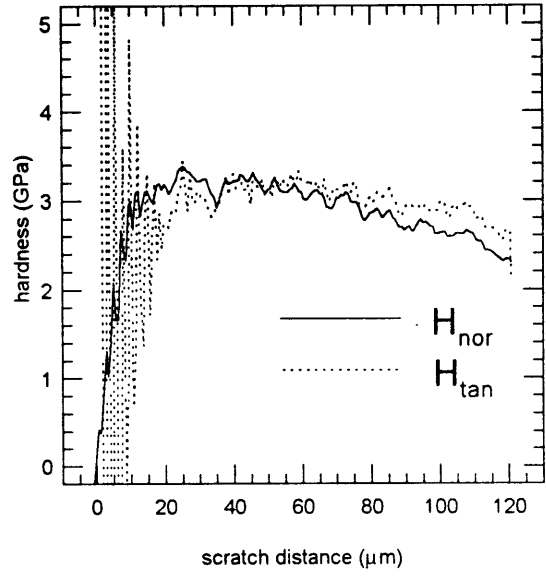# scratch 7-7 hardness
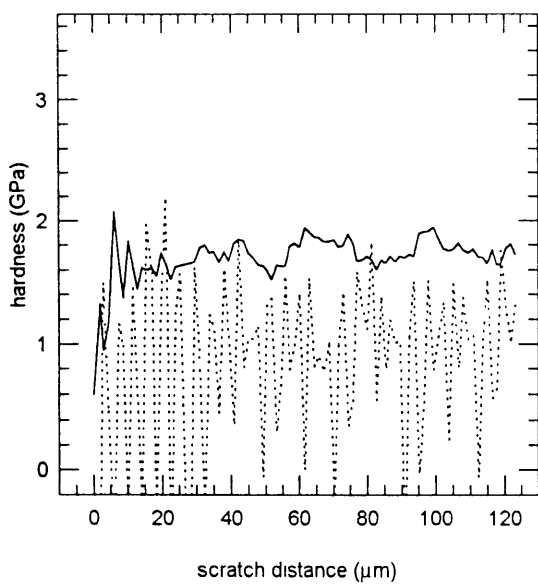
scratch 7-8 hardness
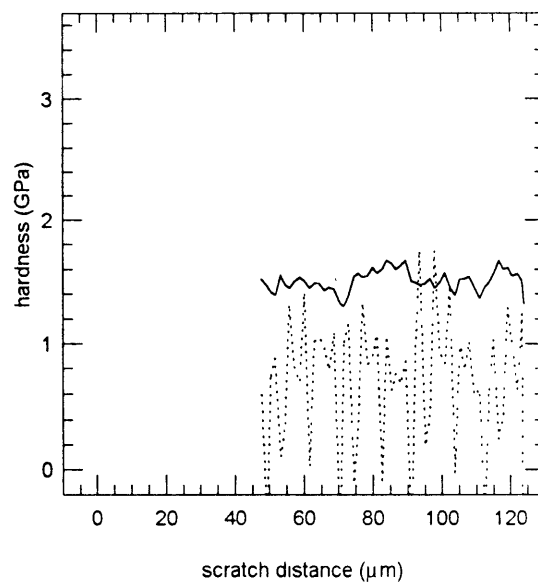
scratch 7-9 hardness

scratch distance (μm)
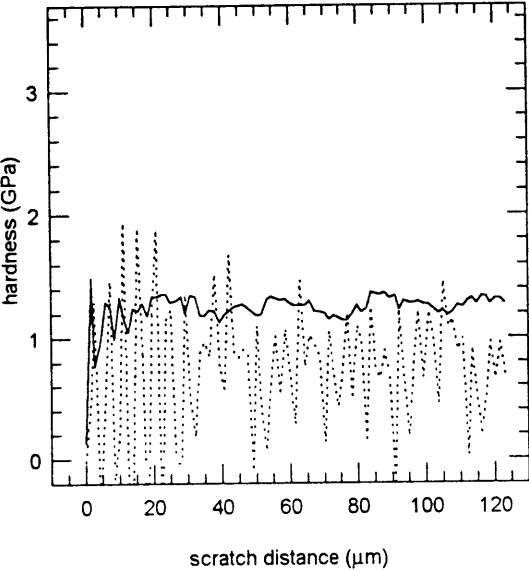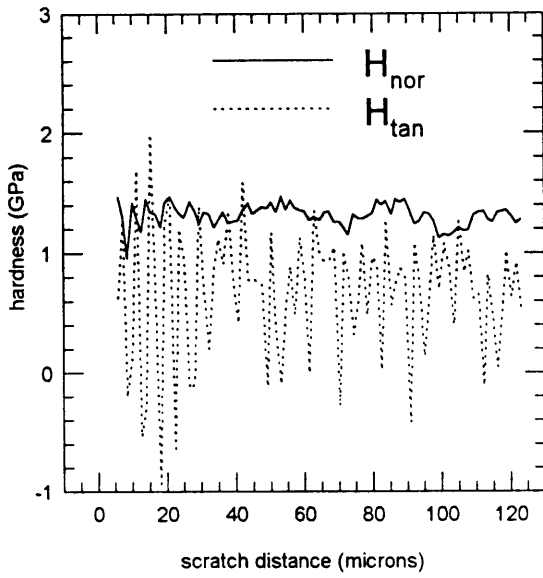
scratch 8-1
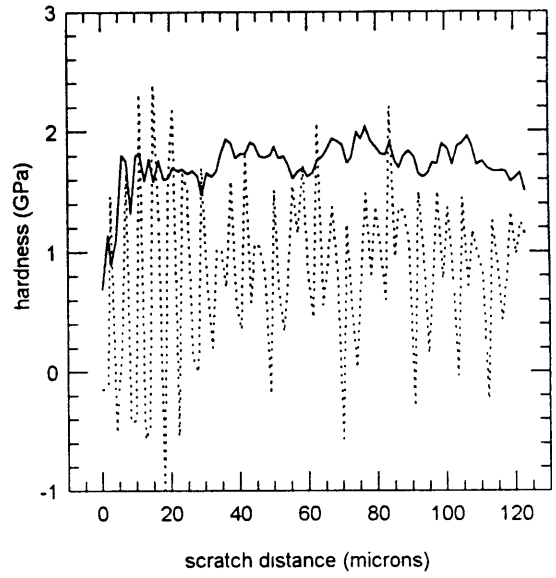
scratch 8-2
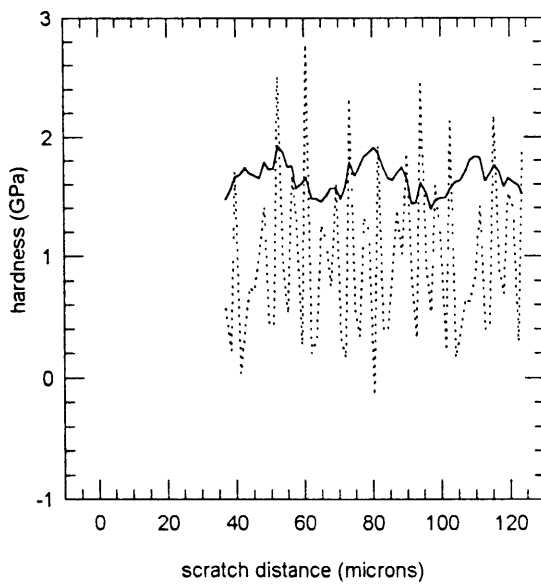
scratch 8-3
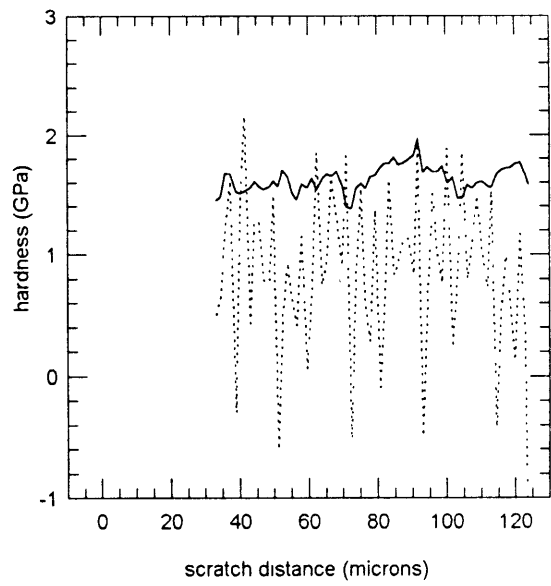
scratch 8-4

scratch 8-5 hardness
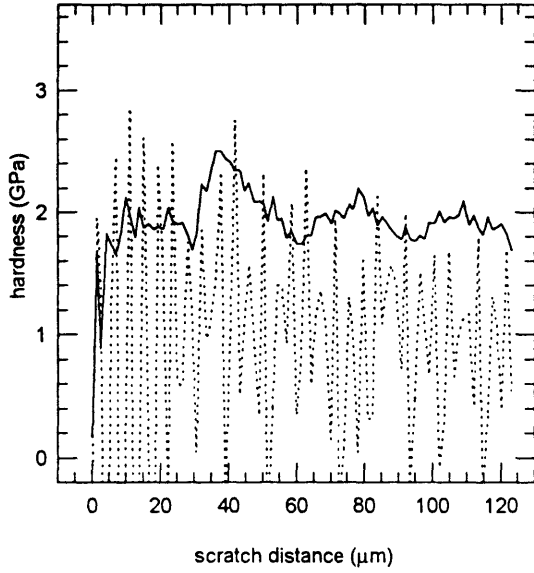
scratch 8-6 hardness
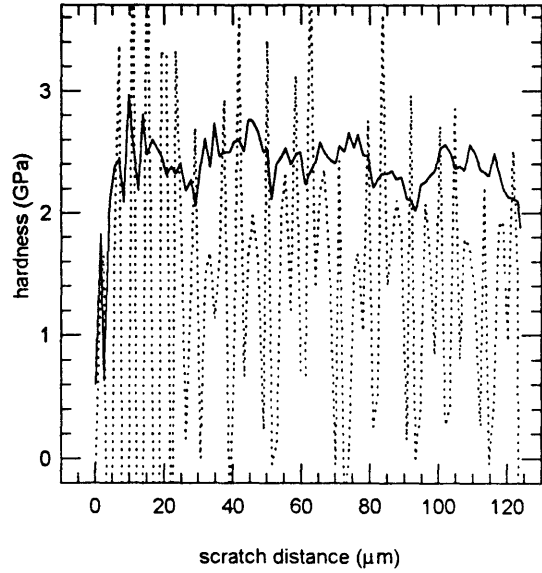
scratch 8-7 hardness
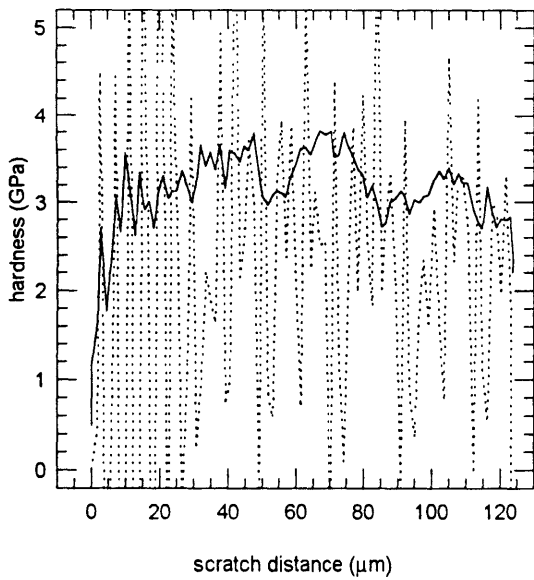
scratch 8-8 hardness
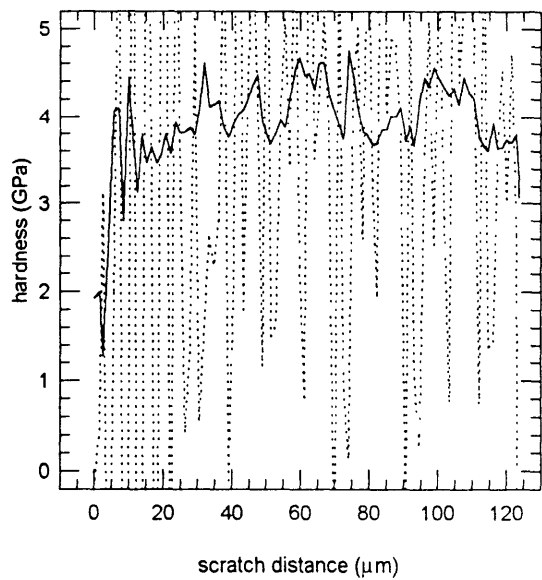
scratch 8-9 hardness
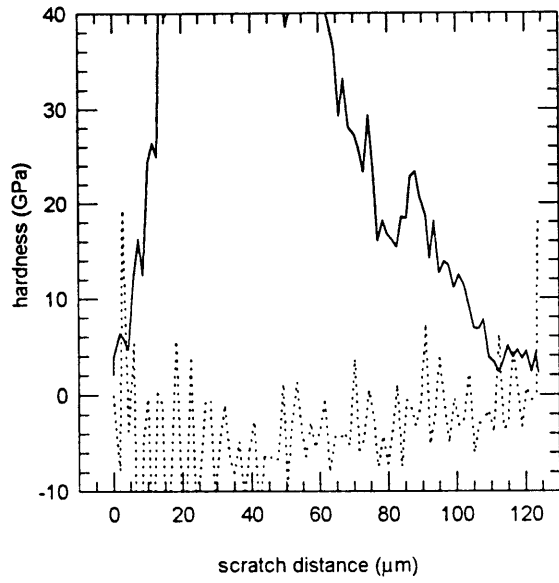
scratch 9-1 hardness
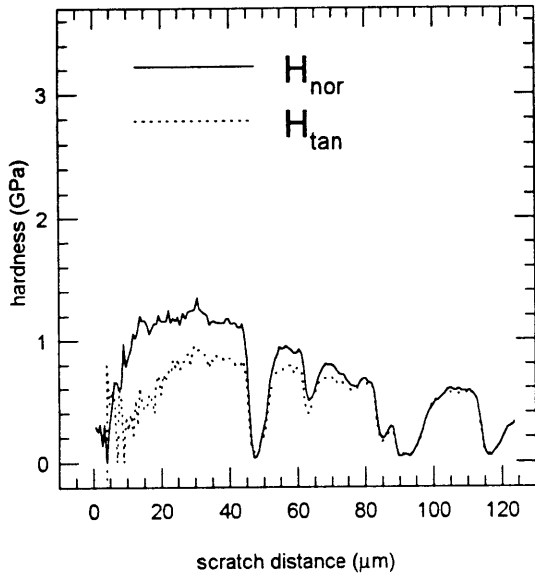
scratch 9-3 hardness
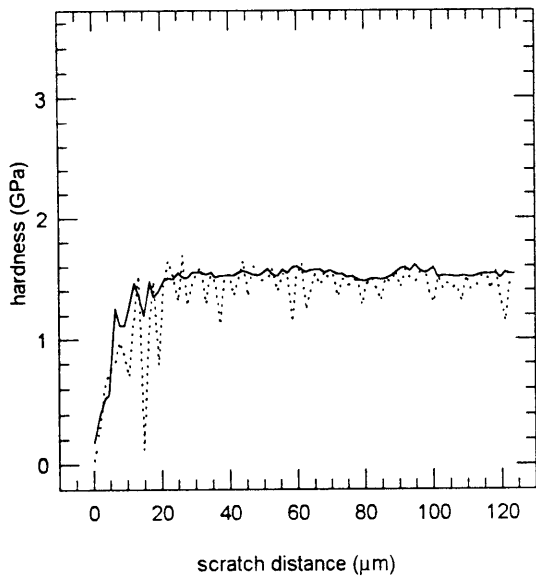
scratch 9-4 hardness
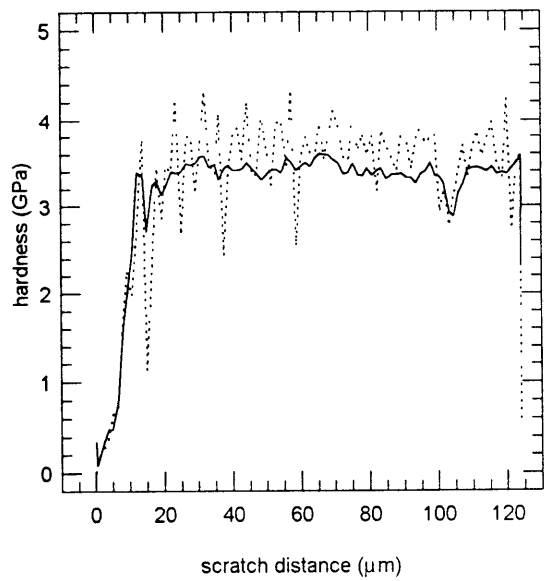
scratch 9-5 hardness
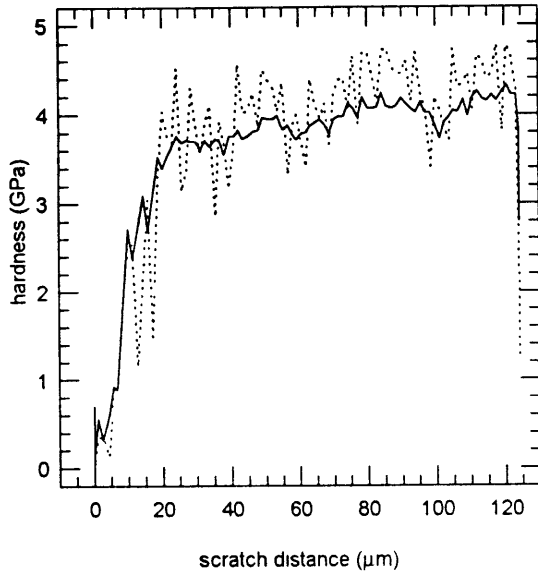
scratch 9-6 hardness
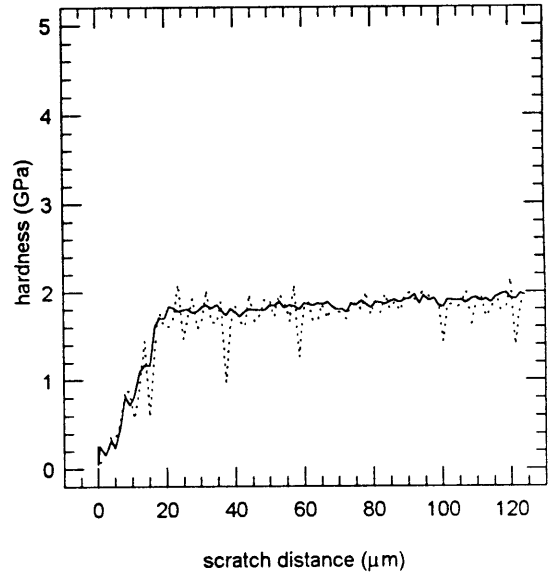
scratch 9-7 hardness
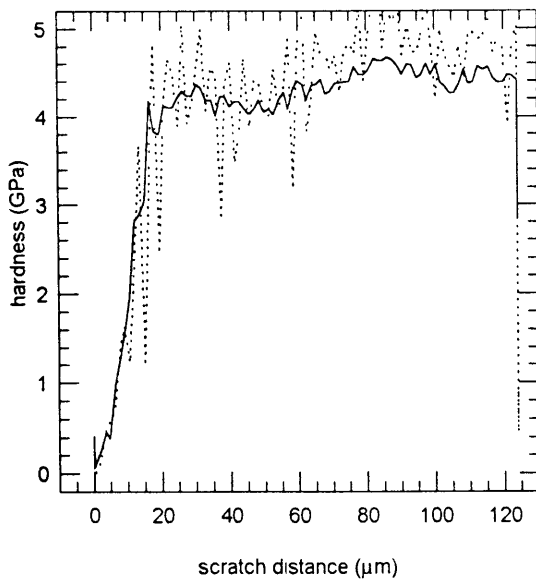
scratch 9-8 hardness
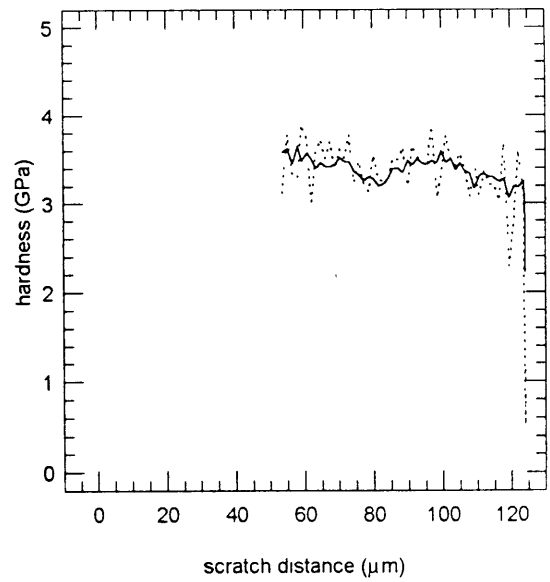
scratch 9-9 hardness
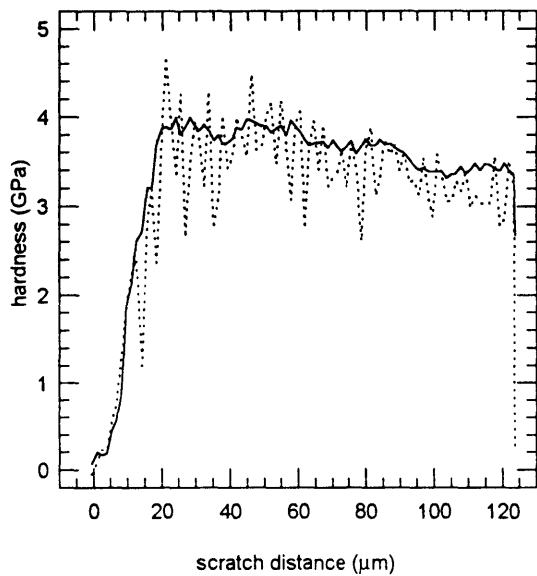
scratch 9-10 hardness
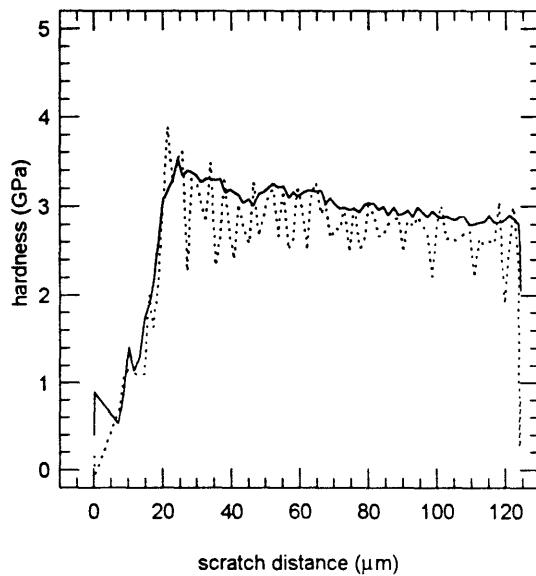
scratch 9-11 hardness
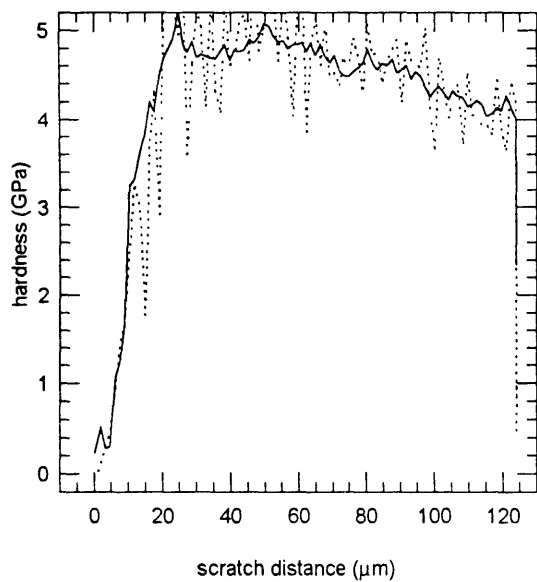
scratch 10-2 hardness
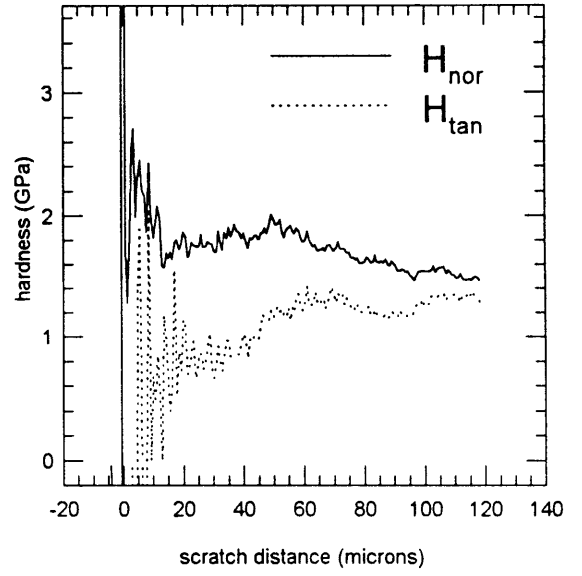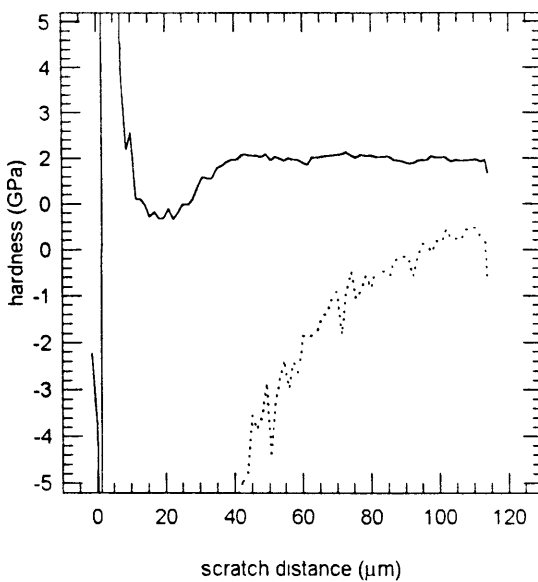

scratch 10-3 hardness
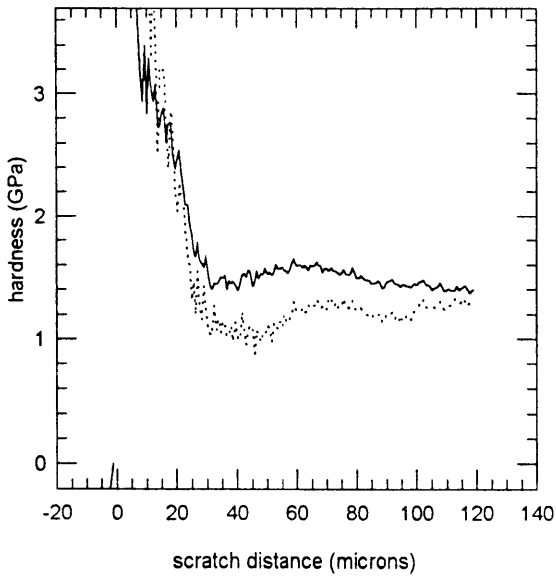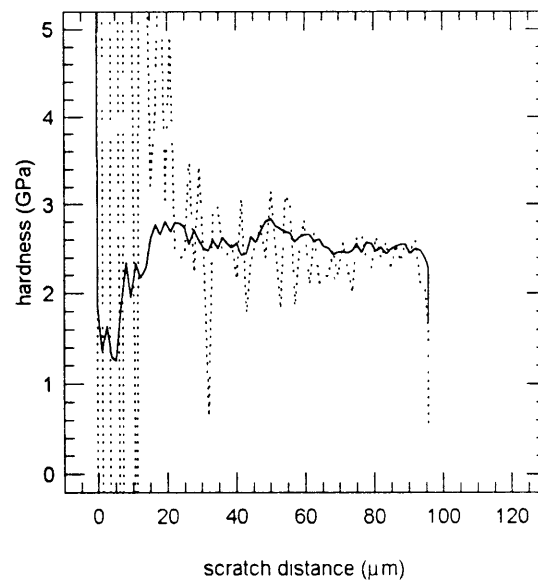

scratch 10-4 hardness
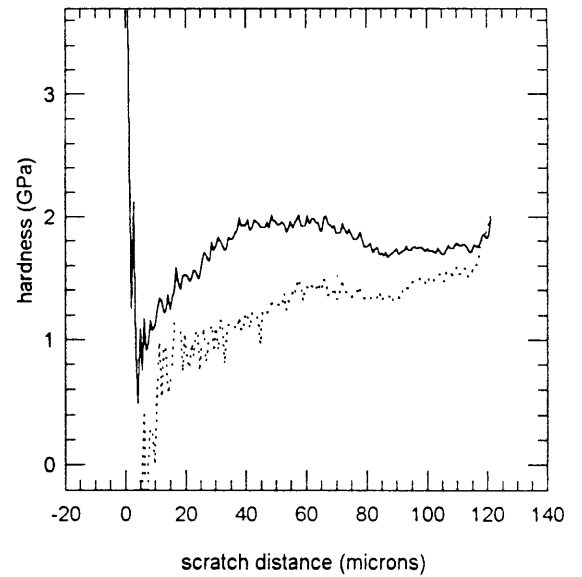
scratch 10-5 hardness

hardness (GPa)

scratch distance (μm)

scratch 10-6 hardness

hardness (GPa)

scratch distance (μm)

scratch 10-7 hardness

hardness (GPa)

scratch distance (μm)

scratch 10-8 hardness

hardness (GPa)

scratch distance (μm)
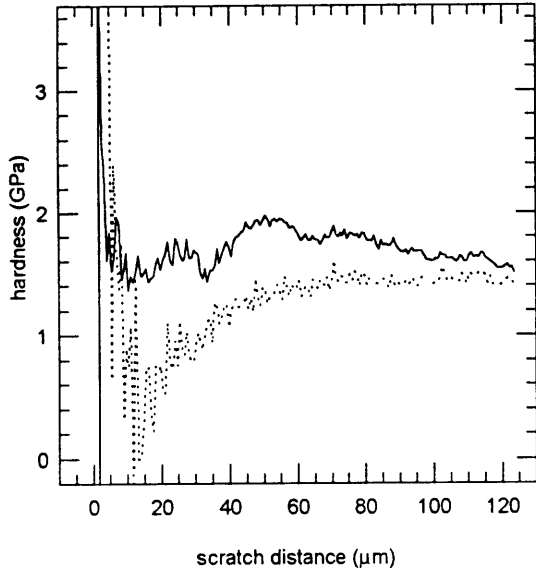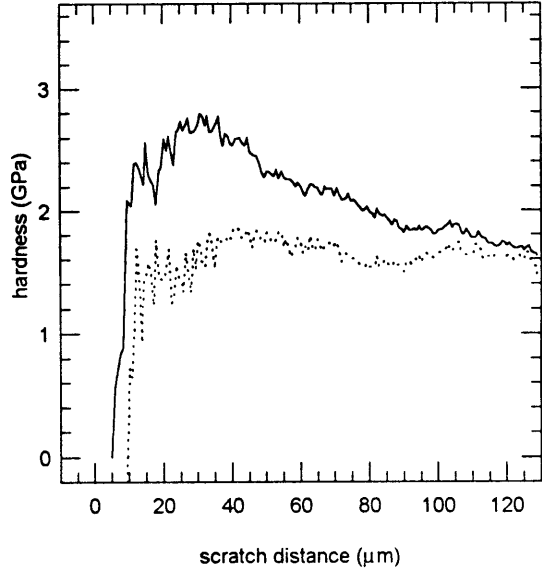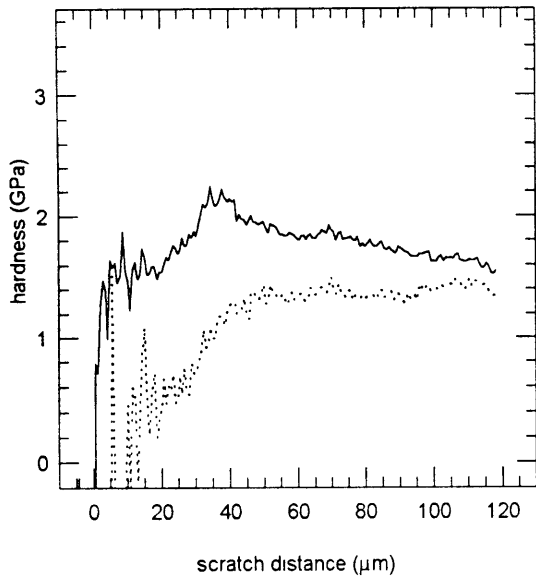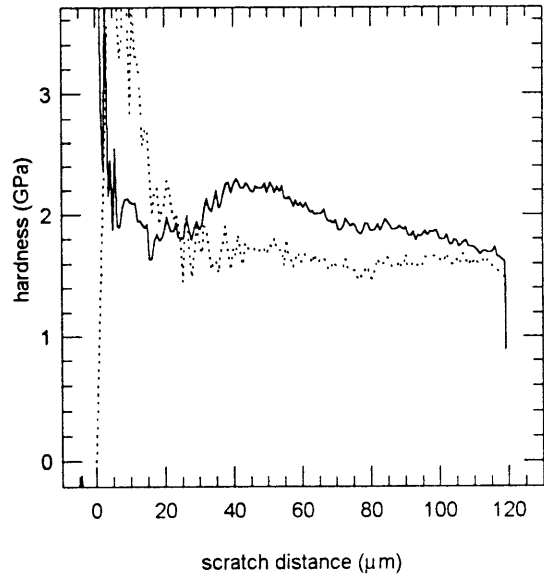
scratch 10-9 hardness
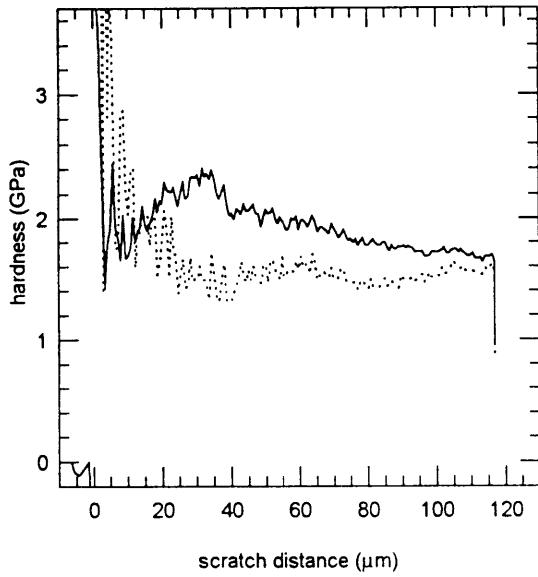
scratch 10-10 hardness
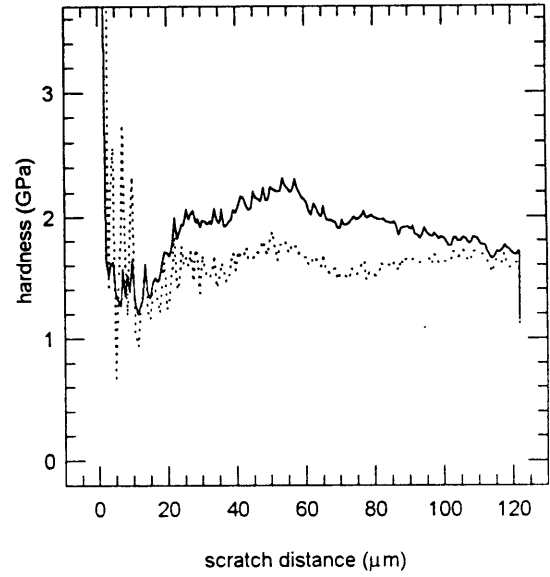
scratch 10-11 hardness
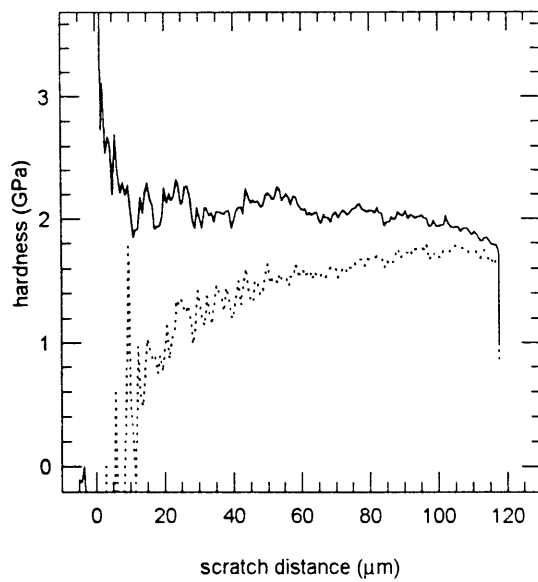
scratch 10-12 hardness

scratch 10-13 hardness

hardness (GPa)

scratch distance (μm)

scratch 10-14 hardness

hardness (GPa)

scratch distance (μm)
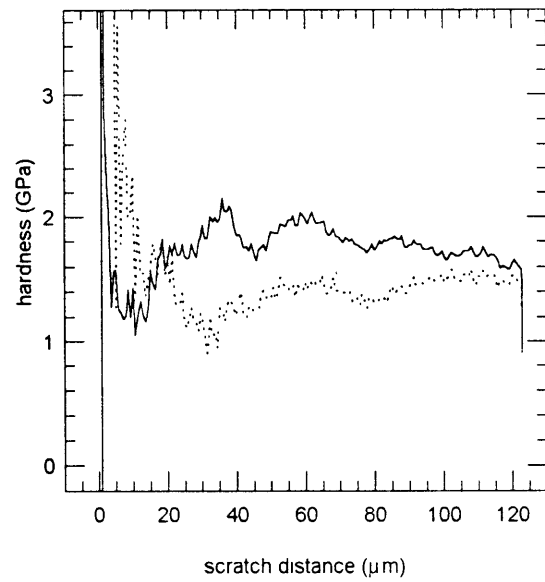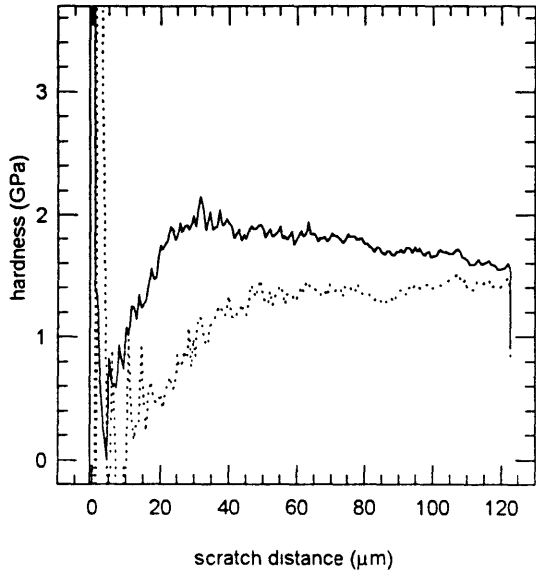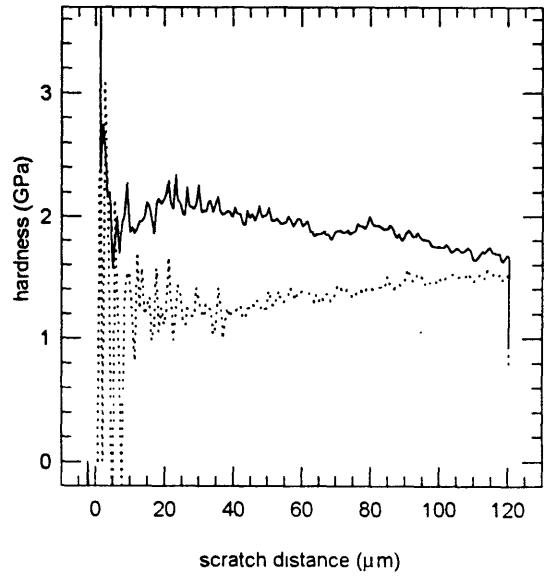
scratch 11-1 hardness
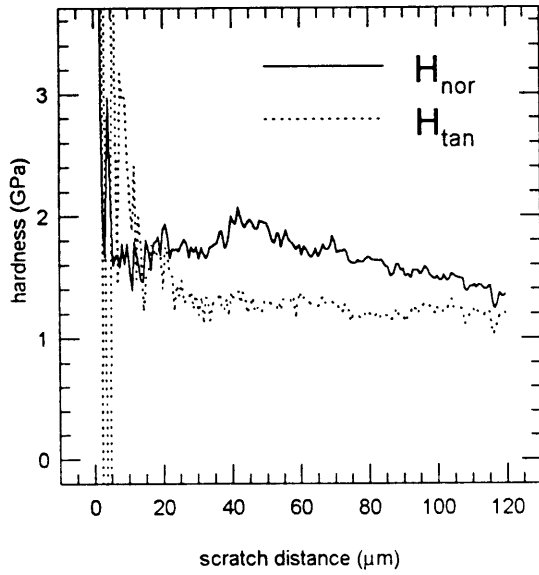
scratch 11-2 hardness
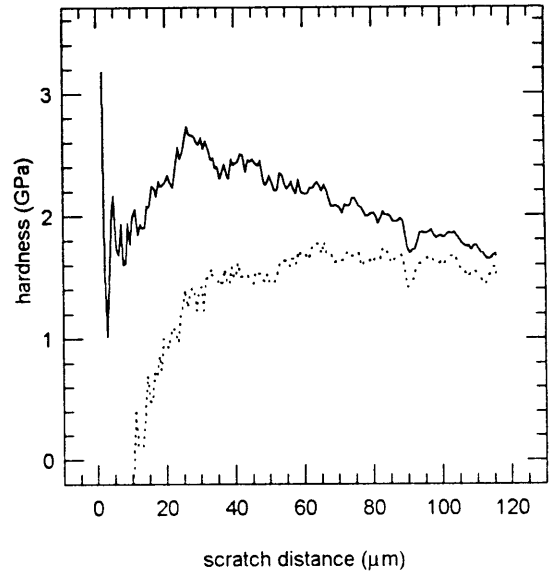
scratch 11-3 hardness
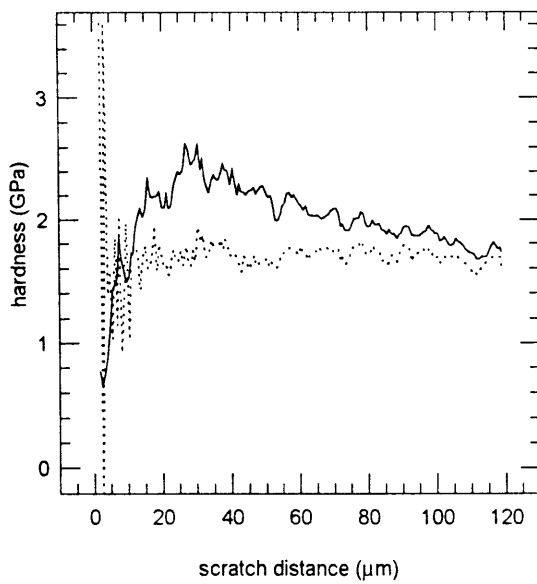
scratch 11-4 hardness
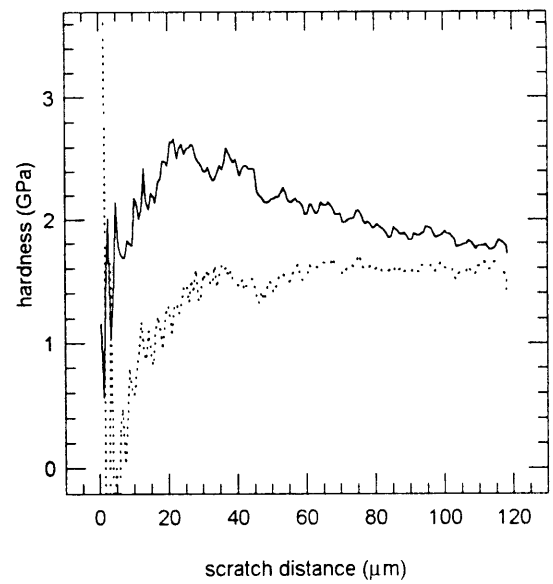
scratch 11-5 hardness
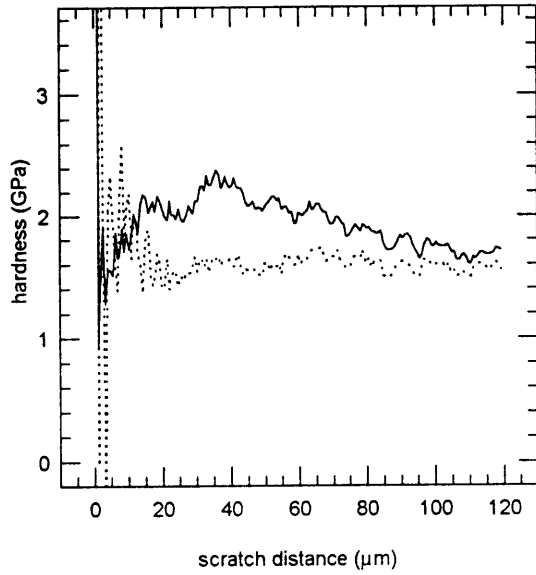
scratch 11-6 hardness
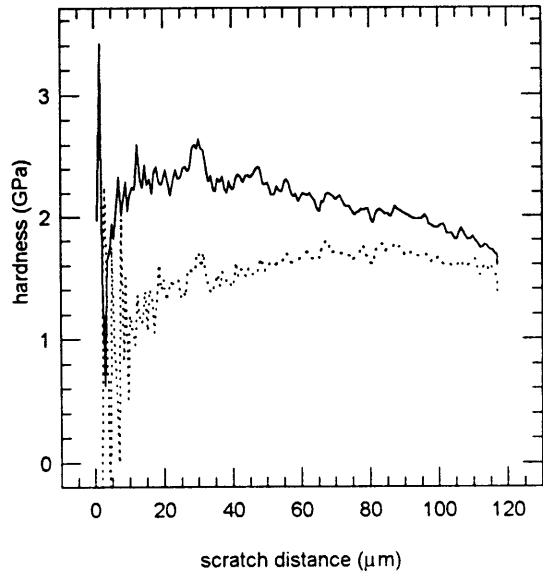
scratch 11-7 hardness
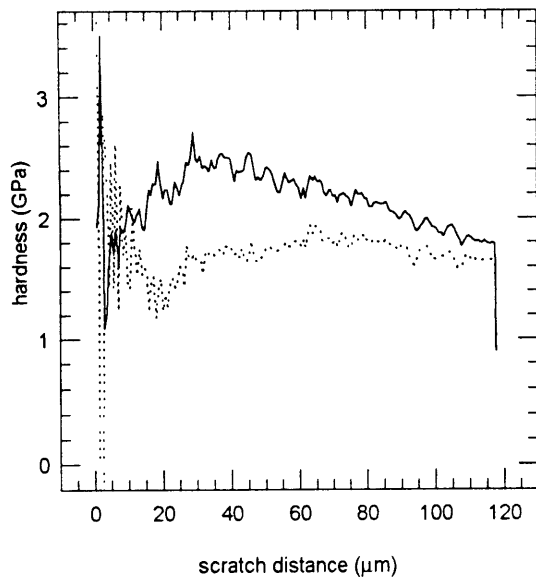
scratch 11-8 hardness
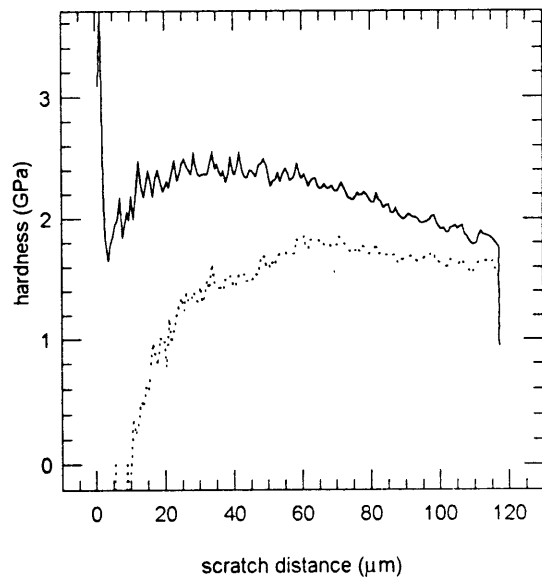
scratch 11-9 hardness
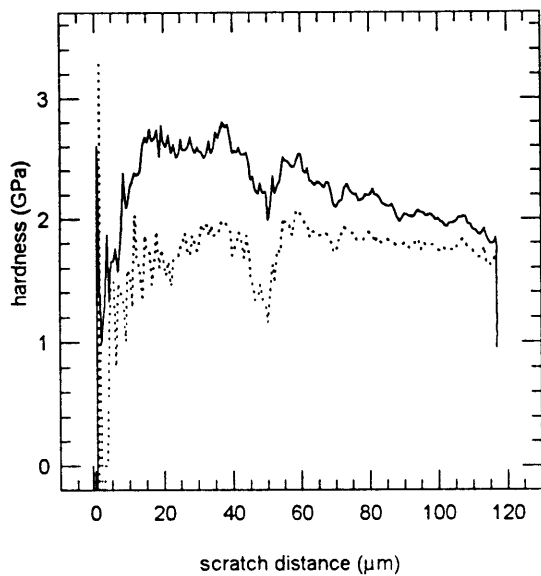
scratch 11-10 hardness
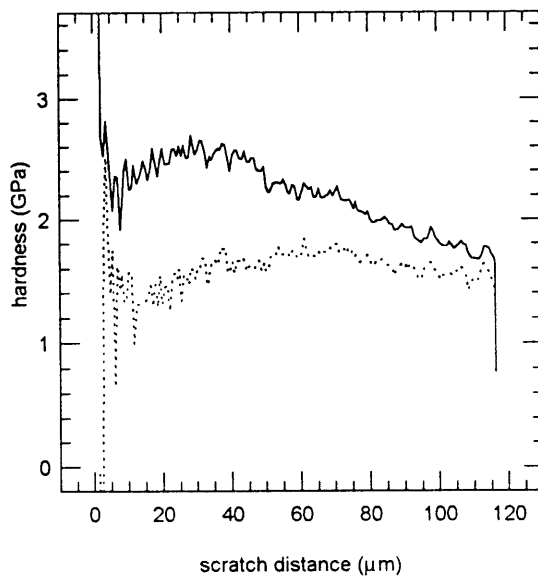
scratch 11-11 hardness
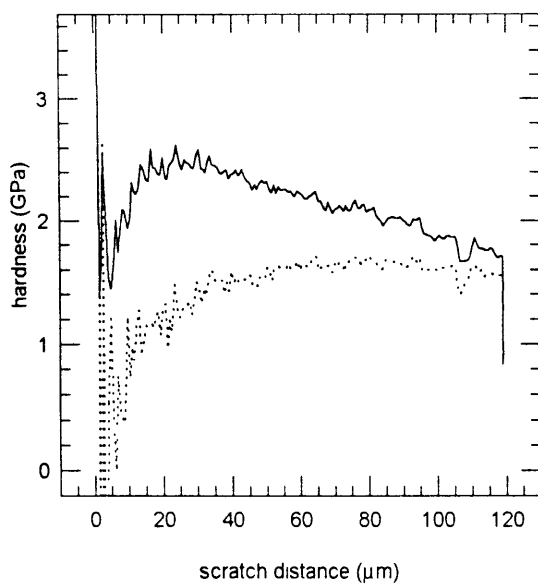
scratch 11-12 hardness
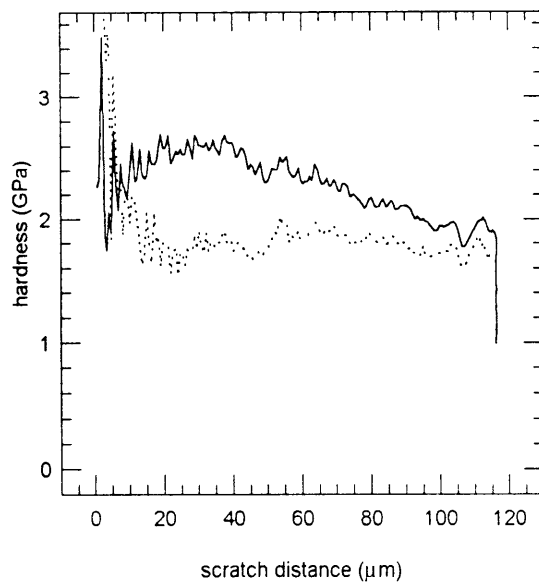
scratch 11-13 hardness
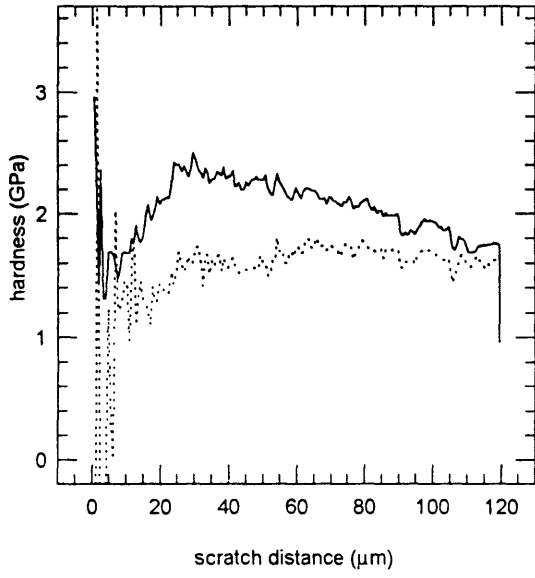
hardness (GPa)

scratch distance (μm)

scratch 11-14 hardness

hardness (GPa)

scratch distance (μm)

scratch 12-2 hardness

Legend: H_{nor} (solid line), H_{tan} (dotted line)

Y-axis: hardness (GPa)
X-axis: scratch distance (μm)

scratch 12-3 hardness

Y-axis: hardness (GPa)
X-axis: scratch distance (μm)

scratch 12-4 hardness

Y-axis: hardness (GPa)
X-axis: scratch distance (μm)
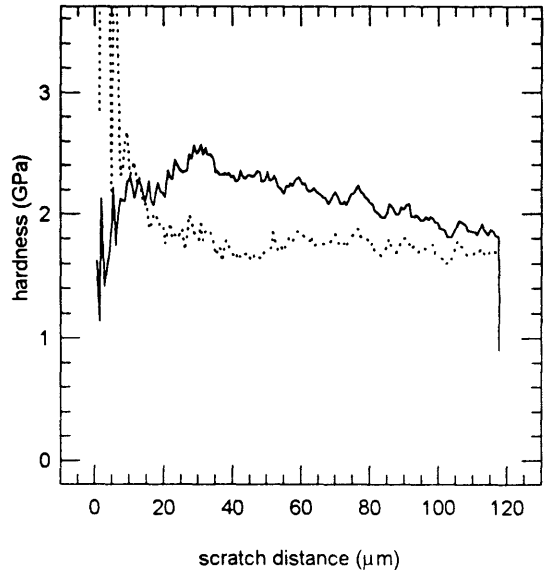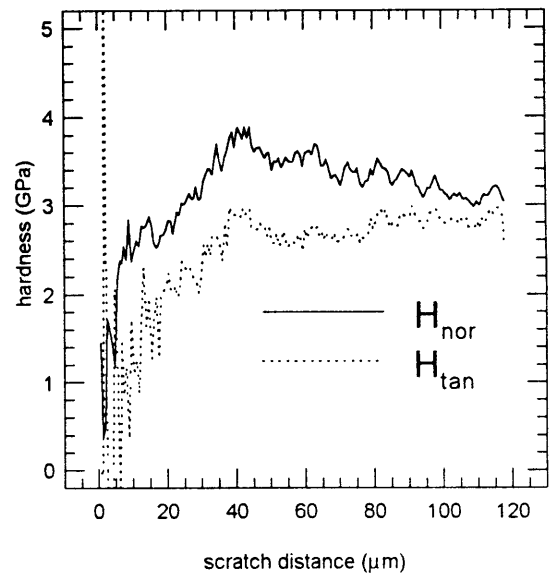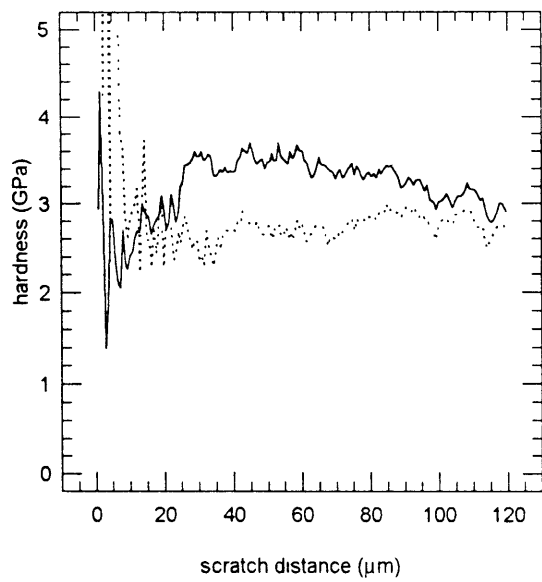
scratch 12-5 hardness

scratch 12-6 hardness

scratch 12-7 hardness

scratch 12-8 hardness
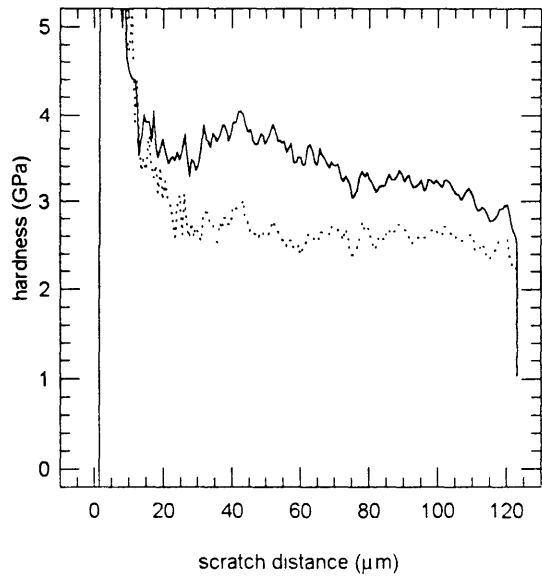
scratch 12-9 hardness
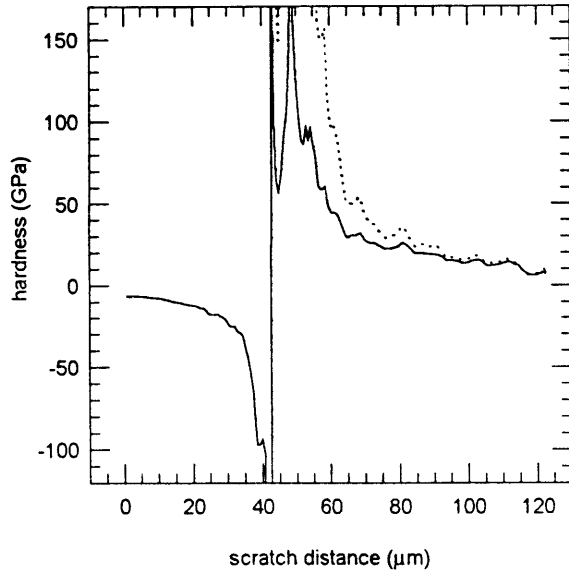
scratch 12-10 hardness
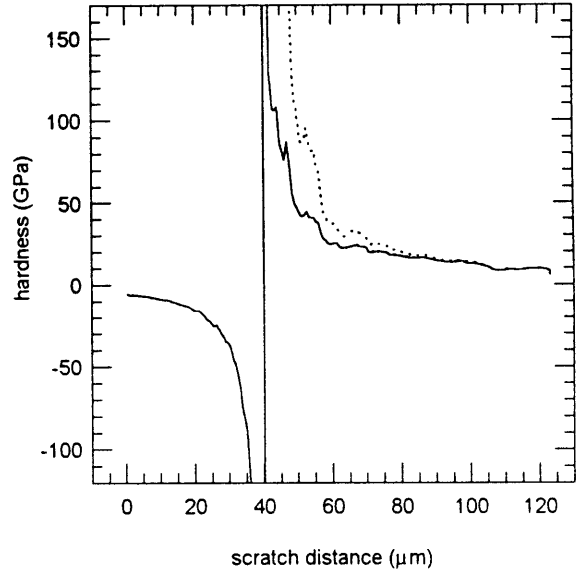
scratch 12-11 hardness
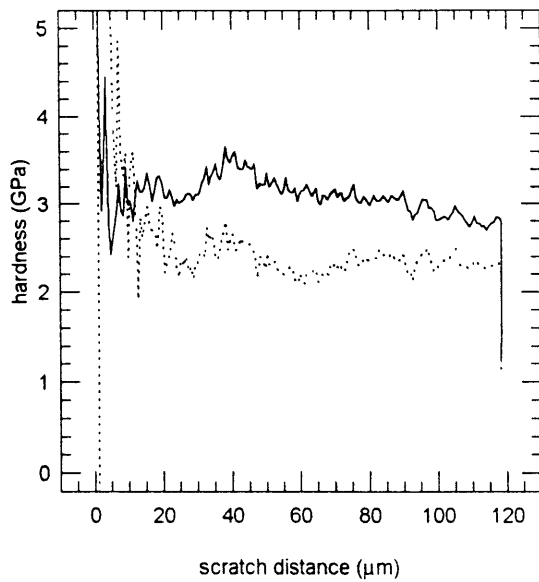
scratch 13-2 hardness
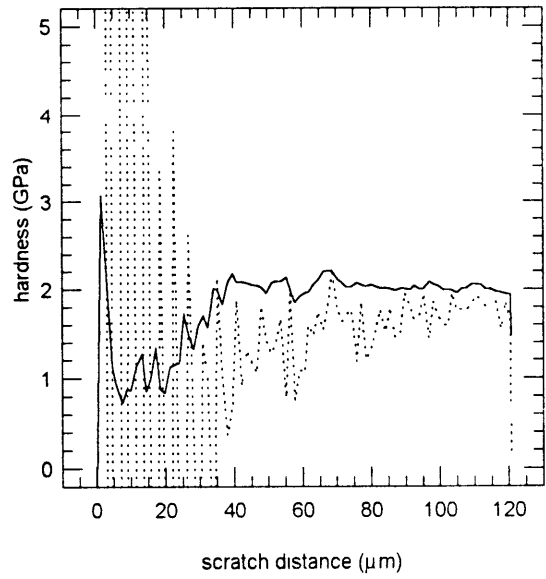
scratch 13-3 hardness

scratch 13-4 hardness
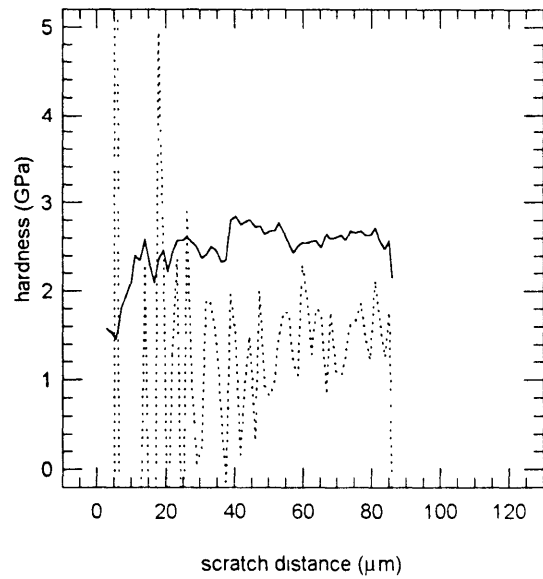
scratch 13-5 hardness

hardness (GPa)

scratch distance (µm)

scratch 13-6 hardness

hardness (GPa)

scratch distance (µm)

scratch 13-7 hardness

hardness (GPa)

scratch distance (µm)

scratch 13-8 hardness

hardness (GPa)

scratch distance (µm)
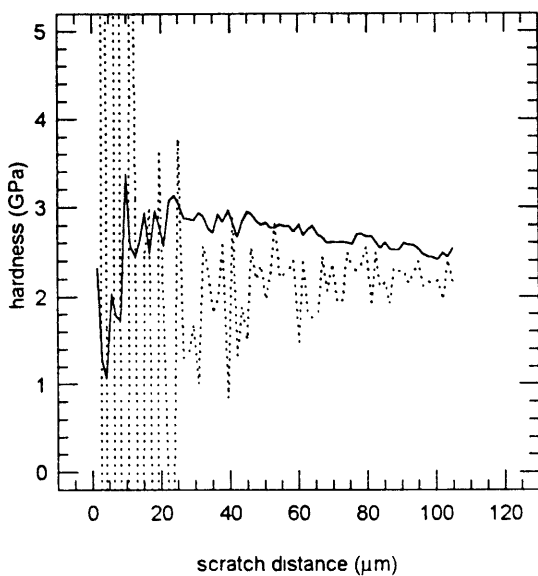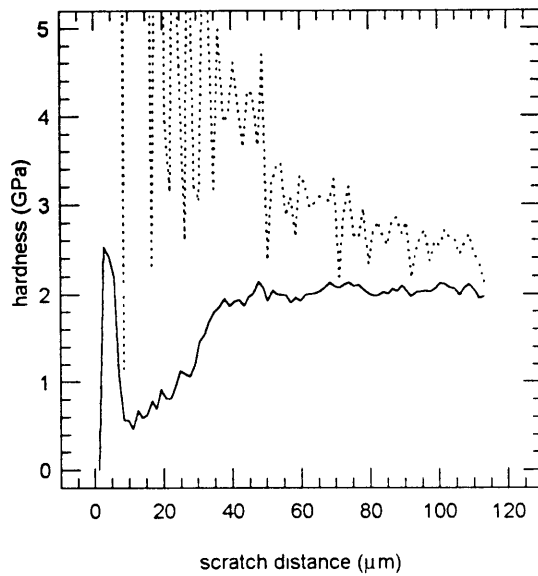
scratch 13-9 hardness
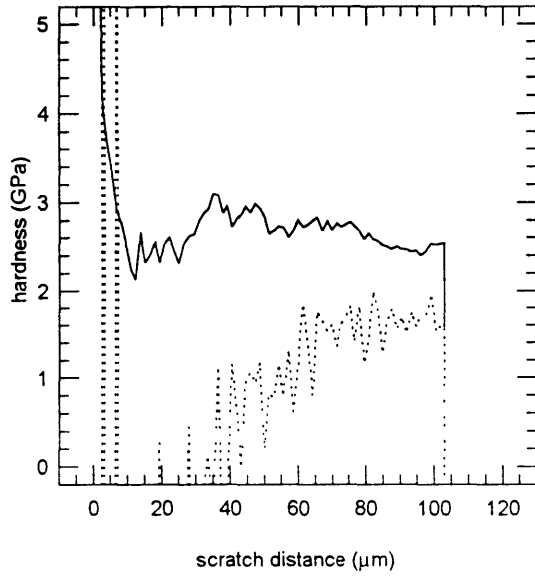
scratch 13-10 hardness
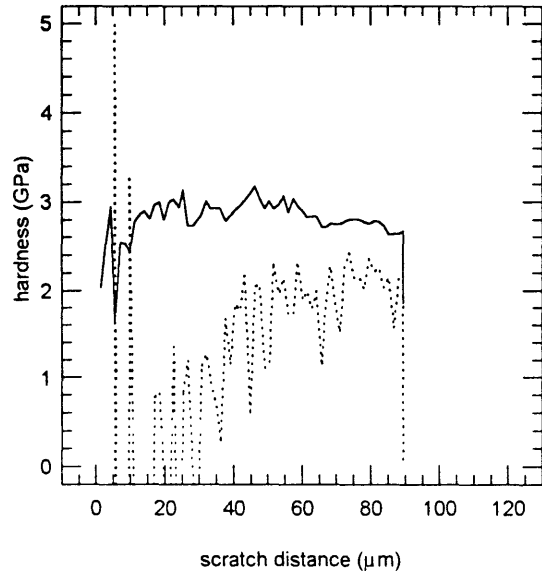
scratch 14-2 hardness
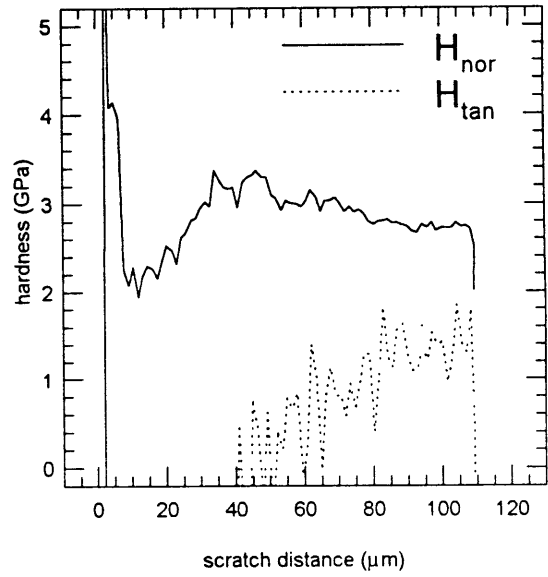
scratch 14-3 hardness
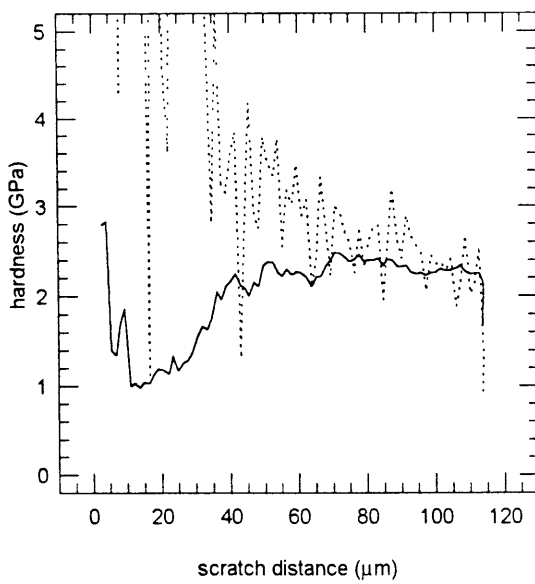
scratch 14-4 hardness
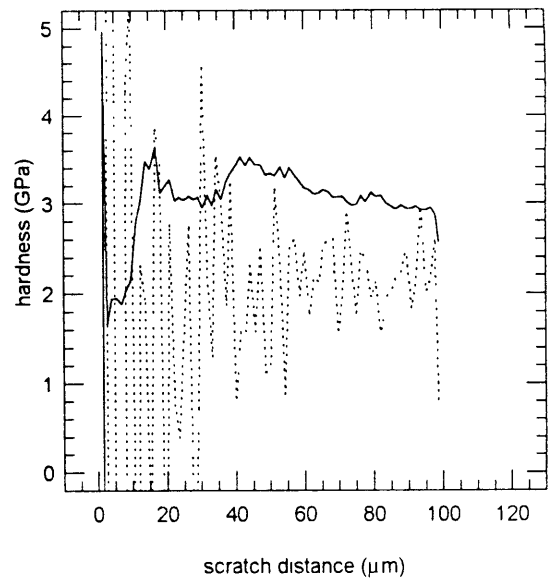
scratch 14-5 hardness
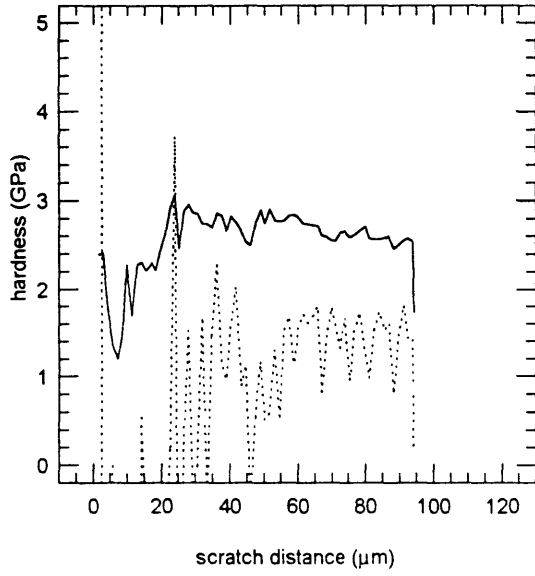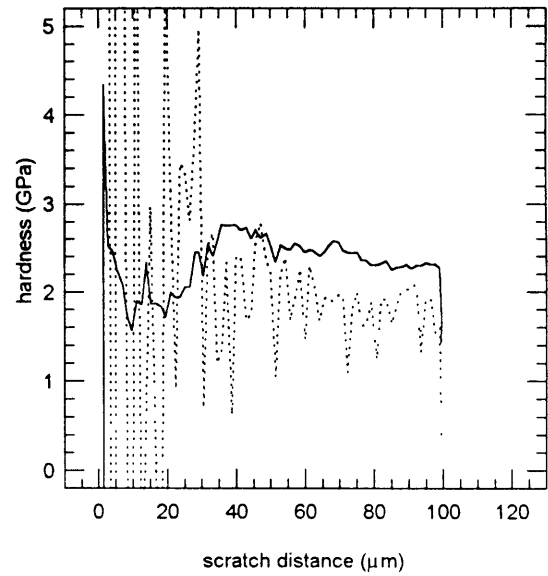

scratch 14-6 hardness
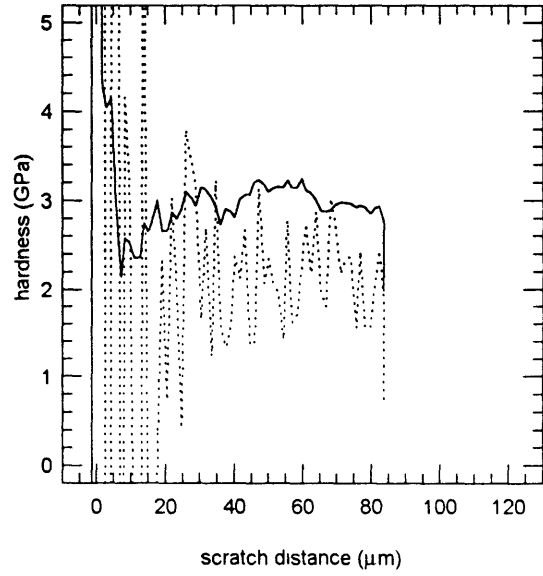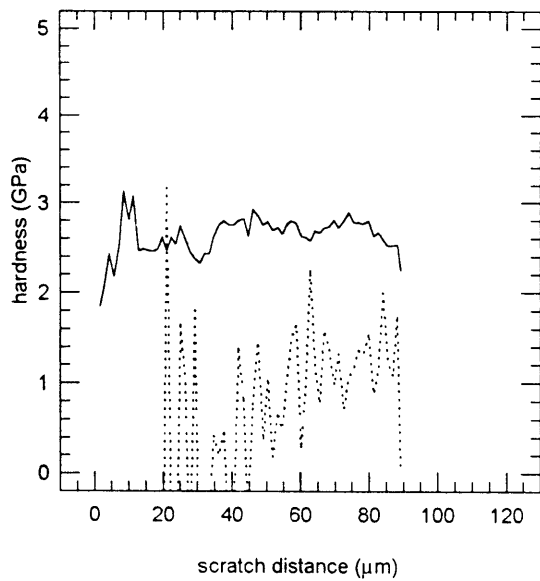

scratch 14-7 hardness
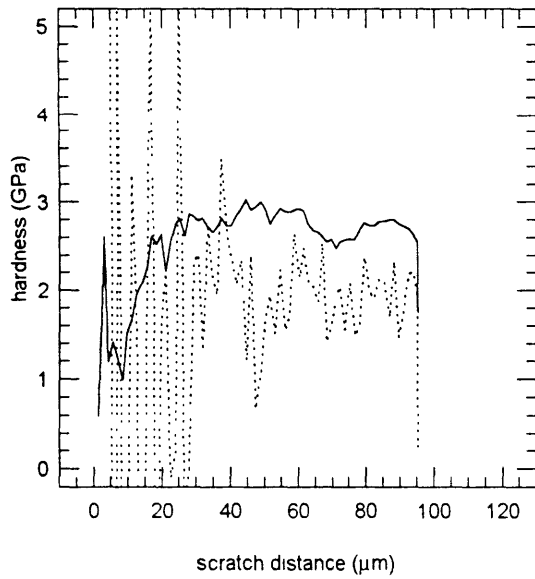
scratch 14-8 hardness

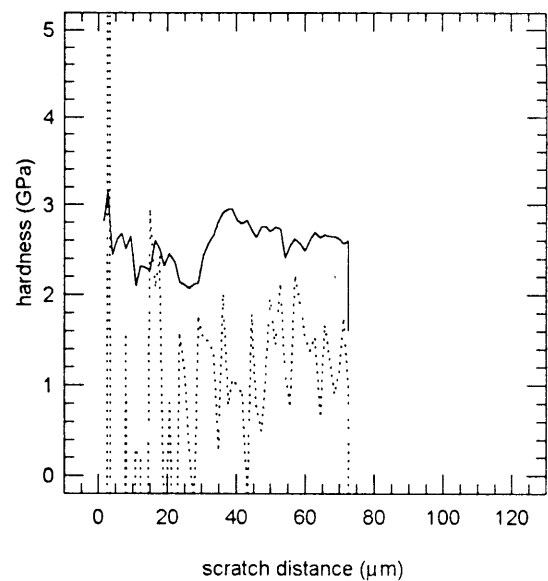## scratch 14-9 hardness
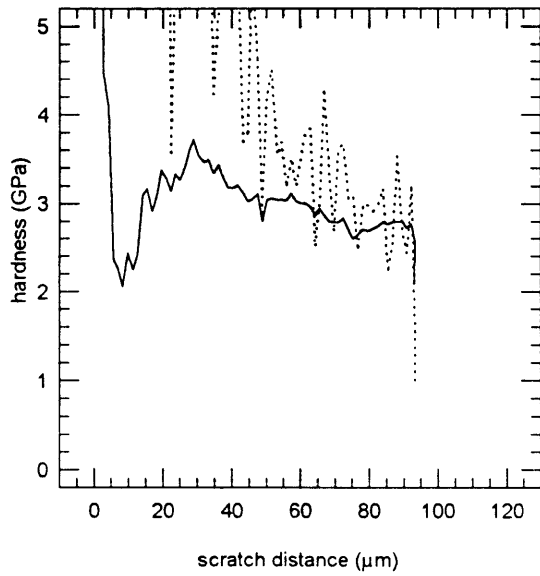
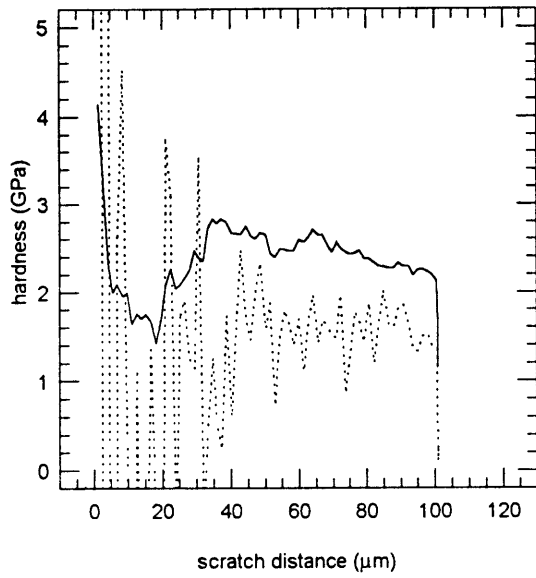## scratch 14-10 hardness

scratch 14-11 hardness

scratch 14-12 hardness

scratch 14-13 hardness

scratch 14-14 hardness